WILEY-VCH

Biomineralization

From Biology to Biotechnology and Medical Application

Edited by Edmund Baeuerlein

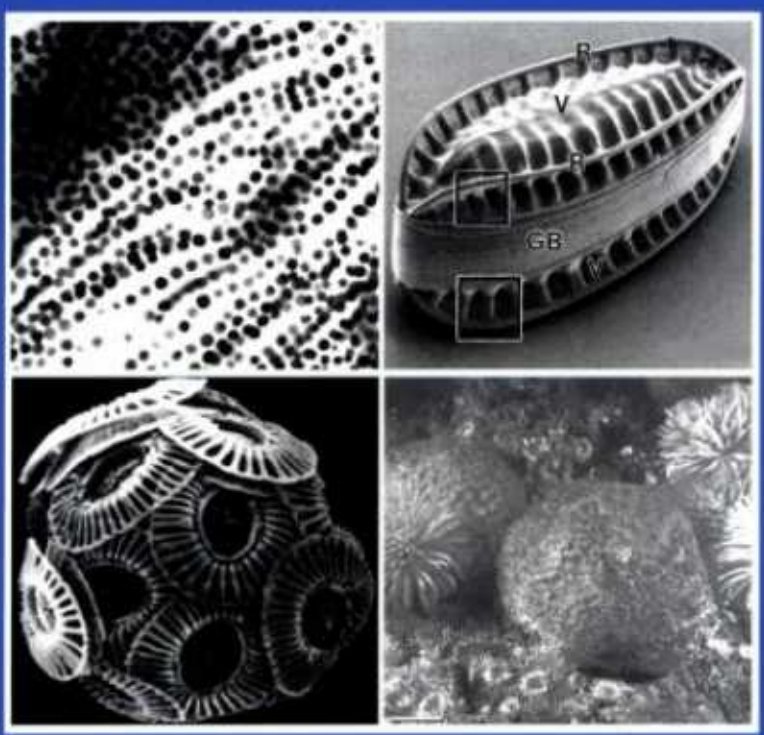

Edmund Bäuerlein (Ed.)

Biomineralization
From Biology to Biotechnology and Medical Application

Second, Completely Revised and Extended Edition

WILEY-VCH Verlag GmbH & Co. KGaA

Prof. (em.) Dr. Edmund Bäuerlein
Max-Planck-Institute of Biochemistry
Dept. of Membrane Biochemistry
Am Klopferspitz 18 A
82152 Martinsried
Germany

Cover Illustration (Designed by Felix Bäuerlein):
Top left: Elongated prismatic magnetite crystals in membrane vesicles of a magnetic bacterium (D. Schüler, Chap. 4, p. 62).
Top right: Calcein-stained calcified skeletal structures in the caudal fin of zebrafish larvae (S. J. Du, Y. Haga, Chap. 17, p. 296).
Bottom left: From aragonite to calcite. The change of shape from "ear-stone" through star-like aragonite to pur calcite crystals in a down-regulation of the starmaker protein in the zebrafish (C. Söllner, T. Nicolson, Chap. 14, p. 236).
Bottom right: A micromechanical method to study stability of diatoms (C. Hamm, R. Merkel, Chap. 18, p. 322).

Library of Congress Card No.: applied for

A catalogue record for this book is available from the British Library.

Bibliographic information published by Die Deutsche Bibliothek
Die Deutsche Bibliothek lists this publication in the Deutsche Nationalbibliografie; detailed bibliographic data is available in the Internet at http://dnb.ddb.de

First Edition 2000
Second, Completely Revised and Extended Edition 2004

Printed in the Federal Republic of Germany.
Printed on acid-free paper.

Typesetting Asco Typesetters, Hong Kong
Printing betz-druck gmbh, Darmstadt
Bookbinding Litges & Dopf Buchbinderei GmbH, Heppenheim

ISBN 3-527-31065-7

This book is dedicated to

my wife Cornelia

for her permanent encouragement and
editorial support also for this 2. edition
and to

my daughter Henrike and *my son Felix*

for their indefatigable cooperation in difficult computer work

Foreword

The term biomineralization summarizes the natural processes by which living organisms form materials from bioorganic molecules and inorganic solids. This is a fascinating topic, uniting the living and the (not always really) dead world surrounding us. In fact, all of us have a direct relation to biomineralization, as we are "biomineralisateurs" – producing each day crystals of a calcium phosphate (apatite), embedded in an organic matrix (mostly collagen), as part of the formation of bone material. These crystals are mere nanometers in size and are arranged in a well-defined hierarchical structure, so that any of us may be rightly called a bio-nano-engineer (a feat that might prove useful in grant applications).

The field of biomineralization not only connects the living and the mineral world, but also brings together scientists from very diverging fields, ranging from geology, mineralogy and crystallography via chemistry and biochemistry to biology and medicine, as well as, possibly, biotechnology. Whereas research in this field was dominated by a mostly descriptive approach throughout much of the last century, the last ten to twenty years have witnessed an increasingly profound scientific understanding of the formation mechanisms of biominerals. This progress has been fuelled by the application of modern molecular biology methods and the advent of novel solid-state analytical techniques, but, most significantly, by their mutual interaction. From the point of view of biology, the ability of an organism to form an inorganic solid material is a special feature that provides evolutionary advantages, and thus certainly deserves elaborate biochemical and molecular-biological studies. The growing interest among solid-state chemists and materials scientists lies in the processes by which the often complex and intricate hierarchical architectures of biominerals can be formed under conditions, which are incredibly mild, compared to the usual techniques of preparative solid-state chemistry. This is combined with a common general interest in the structures and processes occurring at the interfaces between organic matter (not necessarily of biological origin) and inorganic solids which are of utmost importance in many topical regimes of modern science (for example, in heterogeneous catalysis, organic-inorganic hybrid materials, biomaterials or in the attachment of cells to electronic devices). The idea of using synthesis methods taken from nature in order to generate materials with superior properties leads to bio-inspired preparation procedures (which take some key elements from biomineralization, for example the templating action of bioorganic polymers during precipitation of a solid) or bio-mimetic syntheses (which try to fully exploit the mechanisms active in biomineral formation and which may thus also provide an

insight into the natural processes themselves). Finally, if organisms could be convinced by genetic engineering to produce certain materials with selected properties, the biotechnological production of high-tech materials might become feasible.

The importance of biomineralization and its possible applications has recently been reflected in the set-up of dedicated research programs, such as the establishment of an Institute for Biologically Inspired Materials by NASA in the United States. In Germany, research on the "Principles of Biomineralization" has been focused on the priority research program of the Deutsche Forschungsgemeinschaft.

Of course, another clear indicator of the topical nature of this field is this volume and the great success of its predecessor. Within only four years, it has become necessary to publish a sequel, and as opposed to movies, in science sequels usually represent true progress. Many chapters are new (in that they were not part of the first edition) or novel (in that they have been totally rewritten by the authors) and most of the others have been thoroughly reviewed, a stringent necessity in view of the current progress in the field. Edmund Baeuerlein, as a *professor emeritus* now (mostly) freed from his time-consuming research work at the bench and the burden of administration, has devoted a lot of time and much effort to make this volume not only a compendium of the latest research results but also a valuable introduction for newcomers to this field. He did this by careful selecting the contributions and authors and by rigorous editing.

My wish is that this book will be at least as successful as its predecessor. May the research results and ideas compiled here enlighten the reader.

Peter Behrens
Professor of Inorganic Chemistry at the
University of Hanover, Germany
Coordinator of the
DFG-Schwerpunktsprogramm 1117
"Prinzipien der Biomineralisation"

Contents

Preface

Modern research in biomineralization was first summarized in 1989 in the basic work ''On Biomineralization'' by two of the pioneers in the field, M. A. Lowenstam and S. Weiner. Parallel to this more biological review, its inorganic counterpart was published the same year ''On Biomineralization: chemical and biochemical perspectives'' by three pioneers of the chemical approach, S. Mann, J. Webb and R. P. R. William. These perspectives were highlighted in 2001 in ''Biomineralization: Principles and Concepts in Bioinorganic Materials Chemistry'' by its guiding chemical initiator Stephen Mann. It is obvious by these comprehensive volumes that biomineralization was dominated for about 20 years by excellent and extended structural and physiological research.

At the end of this period I had began to study magnetite crystal formation in bacteria. Parallel to progress in bacterial genetics the conviction was and is still growing on me that mechanisms in biomineralization will be predominantly elucidated by methods of molecular biology. The term ''mechanism in biomineralization'' is permanently discussed between chemists and biologists, whether the molecular process or the coupled process of transport, directed saturation and interaction of several organic compounds may be designated a mechanism.

A ''Workshop on Biomineralization and Nanofabrication'', organized by Richard B. Frankel in May 1996, inspired me to edit a multi-author volume on ''Biomineralization. From Biology to Biotechnology and Medical Application'' in November 2000. The aim of this edition was to compare structure formation of inorganic materials in those organisms that were expected to be analyzed most likely in the near future by genetics and molecular biology. At this time, prokaryotic and eukaryotic unicellular organisms, the magnetotactic bacteria and the mineralizing algae, coccolithophores and diatoms, were the prime candidates for these very biological approaches in biomineralization.

Almost complete genome sequences of 15 bacteria, including those of two magnetotactic bacteria, have been made available to the public domain surprisingly fast by the Joint Genome Institute (IGE) of the U.S. Department of Energy. These two genome sequences allowed studying magnetite nanocrystal formation at the genomic level. The human genome project was accomplished just before this work. In addition sequencing of the genome of the zebra fish, an important model organism for the human being, began in 2001 (and should be finished in 2005). Because of extended mutant analyses, I intended to introduce studies on mineral formation of

this simple organism in this new edition, and at the beginning of this year I fortunately succeeded in finding two such reports.

This progress by modern biological methods was paralleled by extraordinary developments in modern physical methods, the highlight of which is cryo-electron tomography, elaborated by W. Baumeister. Research in biomineralization not only comes together with material science from the very edges of its biological and physical parts, but also directly in the recent, epoch-making publication by M. O. Stone and co workers on ''Peptide Templates for Nanoparticle Synthesis derived from Polymerase Chain Reaction-Driven Phage Display''.

I am very grateful to Professor Dieter Oesterhelt for the opportunity to stay as a guest in his department, an opportunity which remarkably facilitates my task as editor and author.

I thank very much to Professor Peter Behrens, the Organizer of the DFG-Priority Program ''Principles of Biomineralization'', for inviting me to several workshops of this very interdisciplinary project.

The various information encouraged me to select new topics for this new edition, among these are models of human biomineralization and modern physical methods.

July 2004

Edmund Bäuerlein
Munich/Martinsried
Germany

List of Contributors

Rudolf I. Amann
Max-Planck-Institute for Marine Microbiology
Dept. of Molecular Ecology
Celsiusstraße 1
28359 Bremen
Germany
Fax: +49-421-2028-790
E-mail: ramann@mpi-bremen.de
Chapter 3

Edmund Bäuerlein
Max-Planck-Institute for Biochemistry
Dept. Membrane Biochemistry
Am Klopferspitz 18A
82152 Martinsried
Germany
Fax: +49-89-8578-3777
E-mail: e_baeuerlein@yahoo.de
Chapter 1

Dennis A. Bazylinski
Dept. of Biochemistry, Biophysics and Molecular Biology, 207 Science 1
Iowa State University
Ames, IA 50011
USA
Fax: +1-515-294-6019
E-mail: dbazylin@iastate.edu
Chapter 2

Simon Crawford
School of Botany
The University of Melbourne
Parkville, Victoria 3052
Australia
Fax: +61-3-9347-5460
E-mail: richardw.@botany.unimelb.edu.au
Chapter 11

Shaojun Du
Center for Marine Biotechnology
University of Maryland Biotechnology Institute
Suite 236, Columbus Center
701 East Pratt Street
Baltimore, Maryland 21202
USA
Fax: +1-410-234-8896
E-mail: dus@umbi.umd.edu
Chapter 17

Matthias Epple
Institute of Inorganic Chemistry
University of Duisburg-Essen
Universitaetsstraße 5-7
45117 Essen
Germany
Fax: +49-201-183-2621
E-mail: matthias.epple@uni-essen.de
Chapter 18

Lars–Oliver Essen
Dept. of Chemistry
Phillips-University
Hans-Meerwein-Straße
35032 Marburg
Germany
Fax: +49-6421-28-22191
E-mail: essen@chemie.uni-marburg.de
Chapter 8

Christine Flies
Göttinger Center for Geosciences
Dept. Geology
University Göttingen
Goldschmittstr. 3
D-37077 Göttingen
Germany
Fax: +49-551-397 918
Chapter 3

Richard B. Frankel
Physics Dept.
California Polytechnic State University
San Louis Obispo, CA 93407
USA
Fax: +1-805-756-2435
E-mail: rfrankel@calpoly.edu
Chapter 2

Yoshihiro Fukumori
Dept. of Biology
Faculty of Science
Kanazawa-University
Kakuma-machi
Kanazawa 920-1192
Japan
Fax: +81-76-264-5978
E-mail: fukumor@kenroku.
kanazawa-u.ac.jp
Chapter 5

Elma González
Dept. of Ecology and Evolutionary
Biology
UCLA University of California
Los Angeles
Los Angeles, CA 90095-1606
USA
Fax: +1-310-206-3987
E-mail: gonzalez@lifesci.ucla.edu
Chapter 13

Yutaka Haga
Center for Marine Biotechnology
University of Maryland
Biotechnology Institute Suite 326
Columbus Center
701 East Pratt Street
Baltimore, Maryland 21202
USA
E-mail: Haga@umbi.umd.edu
Chapter 17

Christian Hamm
Alfred Wegener Institute
for Polar and Marine Research
Plankton Biomechanics Pelagic
Ecosystems/Biological Oceanography
Am Handelshafen 12/Co9
27570 Bremerhaven
Germany
Fax: +49-471-4831-1425
E-mail: chamm@awi-bremerhaven.de
In Chapter 18

Mark Hildebrand
Mail code 0202
Marine Biology Research Division
Scripps Institution of Oceanography
UCSD University of California
San Diego
9500 Gilman Drive
La Jolla, CA 92093-0202
USA
Fax: +1-858-5347313
E-mail: mhildebrand@ucsd.edu
Chapter 10

Willi Jahnen-Dechent
IZKF "BIOMAT"
RWTH Aachen
Pauwelsstraße 30
52074 Aachen
Germany
Fax: +49-241-80-82573
E-mail: willi.jahnen@rwth-aachen.de
Chapter 15

Christian Klein
School of Dental Medicine
Dept. of Operative Dentistry and
Periodontology
Osianderstr: 2-8
72076 Tübingen
Germany

Fax: +49-7071-29-5656
E-mail:
Christian.Klein@med.uni-tuebingen.de
Chapter 16

Nils Kröger
Institute for Biochemistry I
University of Regensburg
Universitaetsstraße 31
93053 Regensburg
Germany
Fax: +49-941-9432936
E-mail:
nils.kroeger@vkl.uni-regensburg.de
Chapter 9

Mary E. Marsh
Dept. of Basic Sciences
University of Texas Dental Branch
Health Science Center
6516 John Freeman Ave.
Houston, TX 77030
USA
Fax: +1-713-500-4500
E-mail: Mary.E.Marsh@uth.tmc.edu
Chapter 12

Tadashi Matsunaga
Dept. of Biotechnology
Tokyo University of Agriculture and Technology
2-24-16 Naka-cho, Koganei
Tokyo 184-8588
Japan
Fax: +81-42-385-7713
E-mail: tmatsuna@cc.tuat.ac.jp
Chapter 6

Paul Mulvaney
School of Chemistry
The University of Melbourne
Victoria 3010
Australia
Fax: +61-3-93475460
E-mail: mulvaney@unimelb.edu.au
Chapter 11

Teresa Nicolson
Oregon Hearing Research Center and Vollum Institute
Oregon Health & Science University
3181 SW Sam Jackson Pk. Rd.
Portland OR 97 239
USA
Fax: +1-503-494-2976
E-mail: nicolson.@ohsu.edu
Chapter 14

Dieter Oesterhelt
Max-Planck-Institute for Biochemistry
Dept. Membrane Biochemistry
Am Klopferspitz 18A
82152 Martinsried
Germany
Fax: +49-89-8578-3557
E-mail: oesterhe@biochem.mpg.de
Chapter 8

Stefanie Offermann
Centre de Recherche sur les Macromolécules Végétales
CERMAV-CNRS
Glycobiologie moléculaire
601 Rue de la Chimie
BP 53
38041 Grenoble Cedex 9
France
Fax: +33-(0)4-76-54-72-03
E-mail: stefanie.offermann@gmx.de
Chapter 8

Yoshiko Okamura
Dept. of Biotechnology
Tokyo University of Agriculture and Technology
2-24-16 Naka-cho, Koganei
Tokyo 184-8588
Japan
Fax: +81-42-385-7713
E-mail: yokamura@cc.tuat.ac.jp
Chapter 6

Katharina Reichenmiller
School of Dental Medicine

Dept. of Operative Dentistry and Periodontology
Osianderstasse 2-8
72076 Tübingen
Germany
Fax: +49-7071-29-5656
E-mail: kathrin.reichenmiller@med.uni-tübingen.de
Chapter 16

Ramon Rosselló-Mora
Grup d'Oceanaografia Interdisciplinar
Institut Mediterrani d'Estudis Avançats (CSIC-UIB)
C/Miquel Marqués 21
E-07190 Esporles
Mallorca
Spain
Fax: +34-971-611-761
E-mail: rossello-mora@uib.es
Chapter 3

Toshifumi Sakaguchi
Dept. Of Biotechnology
Tokyo University of Agriculture and Technology
2-24-16 Naka-cho, Koganei
Tokyo 184-8588
Japan
Fax: +81-42-385-7713
E-mail: sakaguch@cc.tuat.ac.jp
Chapter 6

Dirk Schüler
Max-Planck-Institute for Marine Microbiology
Celsiusstraße 1
28359 Bremen
Germany
Fax: +49-421-2028-580
E-mail: dschuele@mpi.bremen.de
Chapters 3 and 4

Christian Söllner
The Welcome Trust Sanger Institute
Welcome Trust Genome Campus
Hinxton, Cambridge, CB10 1SA
UK
E-mail: cs6@sanger.ac.uk
Chapter 14

Manfred Sumper
Lehrstuhl Biochemie I
University of Regensburg
Universitaetsstraße 31
93040 Regensburg
Germany
Fax: +49-941-9432936
E-mail: manfred.sumper@vkl.uni-regensburg.de
Chapter 9

Richard Wetherbee
School of Botany
The University of Melbourne
Victoria 3010
Australia
Fax: +61-3-9347-5460
E-mail: richardw@unimelb.edu.au
Chapter 11

Michael Winklhofer
Dept. of Earth and Environmental Science
Ludwig-Maximilians-University
Theresienstraße 41/IV
80333 München
Germany
Fax: +49-892180-4207
E-mail: michaelw@lmu.de
Chapter 7

Kornelius Zeth
Max-Planck-Institute for Biochemistry
Dept. of Membrane Biochemistry
Am Klopferspitz 18A
82152 Martinsried
Germany
Fax: +49-89-8578-2815
E-mail: zeth@biochem.mpg.de
Chapter 8

Abbreviations

AAS	atomic adsorption spectroscopy
ADP	adenosine diphosphate
ATCC	American Type Culture Collection
ATP	adenosine triphosphate
ATPase	adenosine triphosphatase
AFM	atomic force microscope
Bfr	bacterioferritin
BMP	bacterial magnetic particle
CA	carbonic anhydrase activity
CCM	carbon concentrating mechanism
CDF	cation diffusion facilitator
CEA	carcino-embryonal-antigen
CM	cytoplasmic membrane
CN	central nodule
CP	chloroplast
CV	coccolith vesicle
DEAE	diethylaminoethanol
DIC	dissolved inorganic carbon
DSi	dissolved silicon
DSM	Dt. Sammlung für Mikroorganismen
EDTA	ethylenediaminetetraacetic acid
ESI	energy spectroscopic imaging
EL	extracellular loops
ER	endoplasmatic reticulum
FAD	flavin adenine dinucleotide
FESEM	field emission scanning electron microscopy
FISH	fluorescence *in situ* hybridization
FMN	flavin mononucleotide
GA	N-acetylglucosamine
GFP	green fluorescent protein
GUT	grand unified theory
HRTEM	high resolution transmission electron microscopy
HPLC	high pressure liquid chromatography
ICS	intracellular carboxy segment
IgG	immunoglobulin G

IL	intracellular loops
INS	intracellular amino segment
kDa	kiloDalton
LPS	lipopolysaccharide
MA	N-acetyl muramic acid
MM	magnetosome membrane
MMP	many-celled magnetotactic procaryote
MRI	magnetic resonance imaging
MTB	magnetotactic bacteria
Myr	million years
NAD	nicotinamide adenine dinucleotide
NADH	nicotinamide adenine dinucleotide, reduced
NADPH	nicotinamide adenine dinucleotide phosphate, reduced
NMR	nuclear magnetic resonance
OA	ornithineamidelipid
OATZ	oxic–anoxic transition zone
ORF	open reading frame
OM	outer membrane
P	peptidoglycan layer
PC	phosphatidylcholine
PCR	polymerase chain reaction
PE	phosphatidylethanolamine
PET	positron emission tomography
PG	phosphatidylglycerol
PM	plasma membrane
R 123	Rhodamine 123
rRNA	ribosomal ribonucleic acid
SATA	succinimidyl-S-acethylthioacetat
SAED	selected area electron diffraction
SCID	severe combined immunodeficiency
SD	single-magnetic-domain
SDS	sodium dodecyl sulfate
SDS-PAGE	sodium dodecyl sulfate polyacrylamide gel electrophoresis
SDV	silica deposition vesicle
SEM	scanning electron microscopy
SER/THR	serine/threonine
SIT	silicic acid transporters
STEM	scanning transmission electron microscope
STV	silicon transport vesicle
TEM	transmission electron microscope
TEOS	tetraethyleneoxysilane
TMPD	tetramethyl-p-phenylenediamine
TPR	tetratricopeptide repeat
UTP	uridine triphosphate

1 Peptides, Pre-biotic Selection and Pre-biotic Vesicles

Edmund Bäuerlein

1.1 Peptides as Templates for Inorganic Nanoparticles: From Functional Groups to "Peptide Group Selectivity"

The "Combinatorial Phage Display Peptide Library" is the result of a gigantic random peptide synthesis initiative, based on molecular biology. In a special library [1], about one billion (10^9) peptides are present as combinations of 12 random amino acids. Each of these 12-amino-acid peptides is expressed as a fusion with the small, surface-displayed protein III of the bacteriophage M13. In addition, each phage molecule has five copies of protein III and, consequently, five identical peptides on its surface.

1.1.1 A Phage Display Peptide Library in "Regular Panning" for Mineral Binding and Synthesizing Peptides

This molecular biology approach became an important link to materials science, as it was not only used to select for peptides that bind specifically to inorganic materials – it was the brilliant idea of M. O. Stone that, vice versa, such peptides should also be capable to generate inorganic structures to which they had bound. The standard procedure [2a] describes a technique to select surface-specific peptides and to subsequently identify a subpopulation of silica-precipitating peptides from a larger pool of binders. This procedure, which includes multiple rounds of target binding, elution and amplification, was designated "biopanning". It is an additional advantage of this method that the low number of eluted peptide bacteriophages could be multiplied by infection of particular *Escherichia coli* host cells. It was then easy to sequence them because the DNA sequence of an individual peptide of the library is fused with that of the small surface-displayed protein III of the bacteriophage – a sequence which is well known and used as primer.

A comprehensive study was begun with peptide-mediated synthesis of a target silica. It was called biogenic, because the synthetic peptide R5, which contains 19 amino acid residues, was used [3]. It is the non-modified analog of the repeating sequence R5 in native silaffin-1A (natSil-1A) [4], a major organic component of the silica cell wall of the diatom *Cylindortheca fusiformis* which was recently described

Biomineralization: From Biology to Biotechnology and Medical Application, Second Edition. Edited by E. Bäuerlein

ISBN: 3-527-31065-7

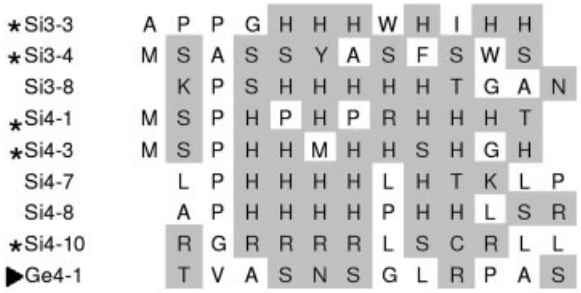

Figure 1.1 Multiple sequence alignment of silica-binding peptides obtained after the third and fourth rounds of panning. The various phage display peptides were plated on LB plates containing x-Gal and isopropyl-1-thio-*β*-D-galactopyranoside (IPTG). DNA was isolated from at least 10 independent blue plaques and sequenced [2]. Si3-4 was the fourth clone selected from the third round of panning. Amino acids with functional side chains that are able to interact with silica surface are shaded. (According to [2a], courtesy of M. O. Stone.)

by Kroeger et al. [4]. A network of silica spheres with a diameter of 400–600 nm was obtained when R5 peptide was incubated in freshly prepared orthosilic acid for 2–5 min at pH 7.5 and room temperature. The biosilica particles were subsequently washed several times to remove residual R5 peptide before use.

The phage display peptide library was now incubated with these particles. After three or four rounds of panning the sequence of the peptide, the peptide phage which remained bound to silica particles after stringent washing was determined. The multiple sequence alignments of such silica-specific peptides are shown in Fig. 1.1 [2a]. Binding of the phage peptides to the surface of silica particles was substantiated with a phage immunoassay and is presented in Fig. 1.2 [2a] using relative units. Si4-1 and Si4-10 apparently interacted more strongly with the silica particles, compared to the six other selected peptide phages.

The first, unprecedented step into materials production was now to examine the phage peptides, which were selected by their binding capacity on silica particles, for the formation of silica particles. They were incubated in a freshly prepared solution of orthosilic acid as described above for peptide R5. The amount of silica generated by phage peptides was quantified by the molybdate assay [5], as shown in Fig. 1.3. The highest activity was repeatedly observed with Si4-1. The phage peptides Si3-3, Si4-10, Ge4-1 and M13 showed only minor or no silica-precipitating activity.

This first experiment of phage peptide-mediated material formation resulted in the highest amounts of silica when three types of amino acid, i.e. hydroxyl- and imidazole-containing as well as of high cationic charge, were present in the peptides. Histidine and serine were found previously by Morse to be essential for catalysis by silicatein, a protein with enzymatic activity similar to human protease Cathepsin L. Silicateins were able to hydrolyze orthosilicic acid ester as tetraethoxysilane at neutral pH by simultaneous polycondensation to silica. Silicones were produced when methyl or phenyl triethoxysilanes were used as substrates [6].

With respect to the following experiments and results, it should be emphasized that here a subpopulation of phage peptides was obtained by standard panning

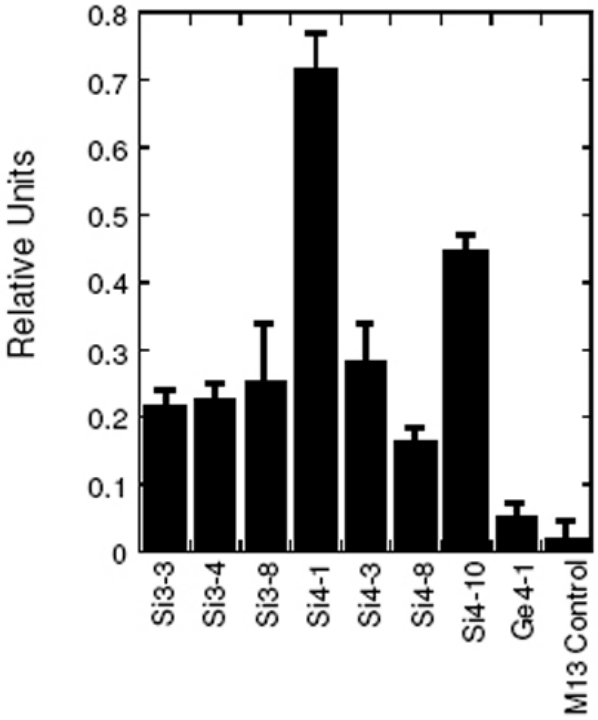

Figure 1.2 Binding of phage display peptides to silica by phage immunoassay. The binding of biotin-conjugated anti-Fd, an antibody raised against the pIII coat protein of M13 phage, was detected with the use of streptavidin–horseradish peroxidase. (According to [2a], courtesy of M. O. Stone.)

(later in Fig. 1.4 designated as ''regular panning'') which included amplification by infection of *E. coli* host cells with the selected phage peptides. This limited amplification [compared to the polymerase chain reaction (PCR), presented later] appears to preferentially result in peptides, which in terms of structure and possibly dynamics may be taken to be similar to active centers of enzymes [6], and, therefore, to act by definite residues in binding as well as in material production.

Such a similarity was supported by the first results of peptide-mediated synthesis and patterning of silver nanoparticles [2b]. These experiments were a kind of unexpected back reaction of Belcher's pioneering experiments with the ''Combinatorial Phage Display Peptide Library''. She used the library to identify peptides recognizing a range of semiconductor surfaces with high specificity, depending on the crystallographic orientation and composition of structurally similar materials (GaAs on silicon) [7]. Stone succeeded here in performing the back reaction – not the production of GaAs, but that of silver nanocrystals by a peptide of the phage display peptide library, which had been selected by regular panning (Fig. 1.4) [2b]. Only three different sequences, i.e. AG3, AG4 and AG5, of 30 independent assays were found

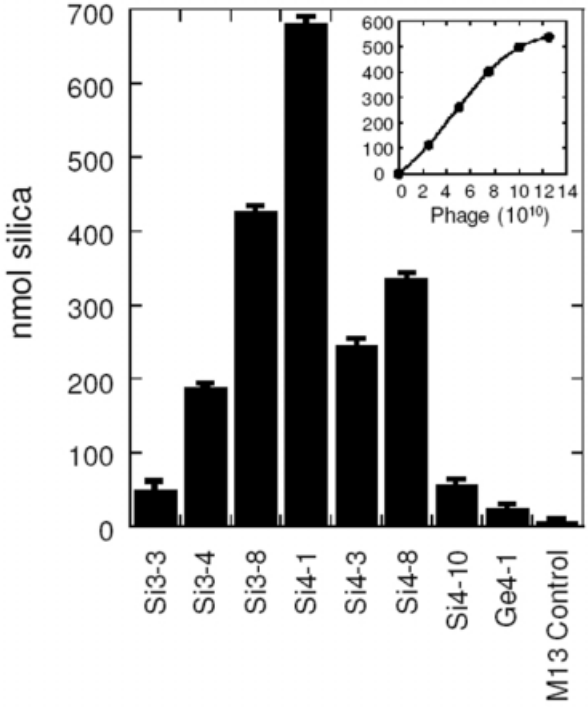

Figure 1.3 Silica condensation of the selected phage display peptides (clones). Equal amounts of phage particles (10^{11}) were incubated for 5 min in Tris-buffered saline (pH 7.5) with hydrolyzed tetramethyl orthosilicate. The silica precipitated was collected, washed and the amount of silica was measured with the spectrometric molybdate assay. The silica concentration obtained with R5 peptide (100 μg) was 1.05 μmol. The amount of silica precipitated is proportional to the amount of Si4-1 phage particles added (inset). (According to [2a], courtesy of M. O. Stone.)

in peptides which selectively bound to silver particles of a nano-sized activated powder (Table 1.1).

These silver-binding 12-amino-acid peptides contain preferentially prolines and hydroxyl amino acids:

AG3:	4 prolines	2 tyrosines	2 serines	
AG4:	2 prolines	2 tyrosines	3 serines	
AG5:	4 prolines	–	1 serine	2 threonine

For synthesis of silver nanoparticles, each of the three peptide phages was first incubated in a solution of silver nitrate for 24–48 h at room temperature. The reddish color of the solution and, after centrifugation, of the precipitate was observed using peptide phages AG3 and AG4, but not AG5. A characteristic surface plasmon resonance band about 440 nm was obtained in the ultraviolet-visible spectrum of the reddish solution, reflecting the size and shape distribution of the silver nanoparticles [2b].

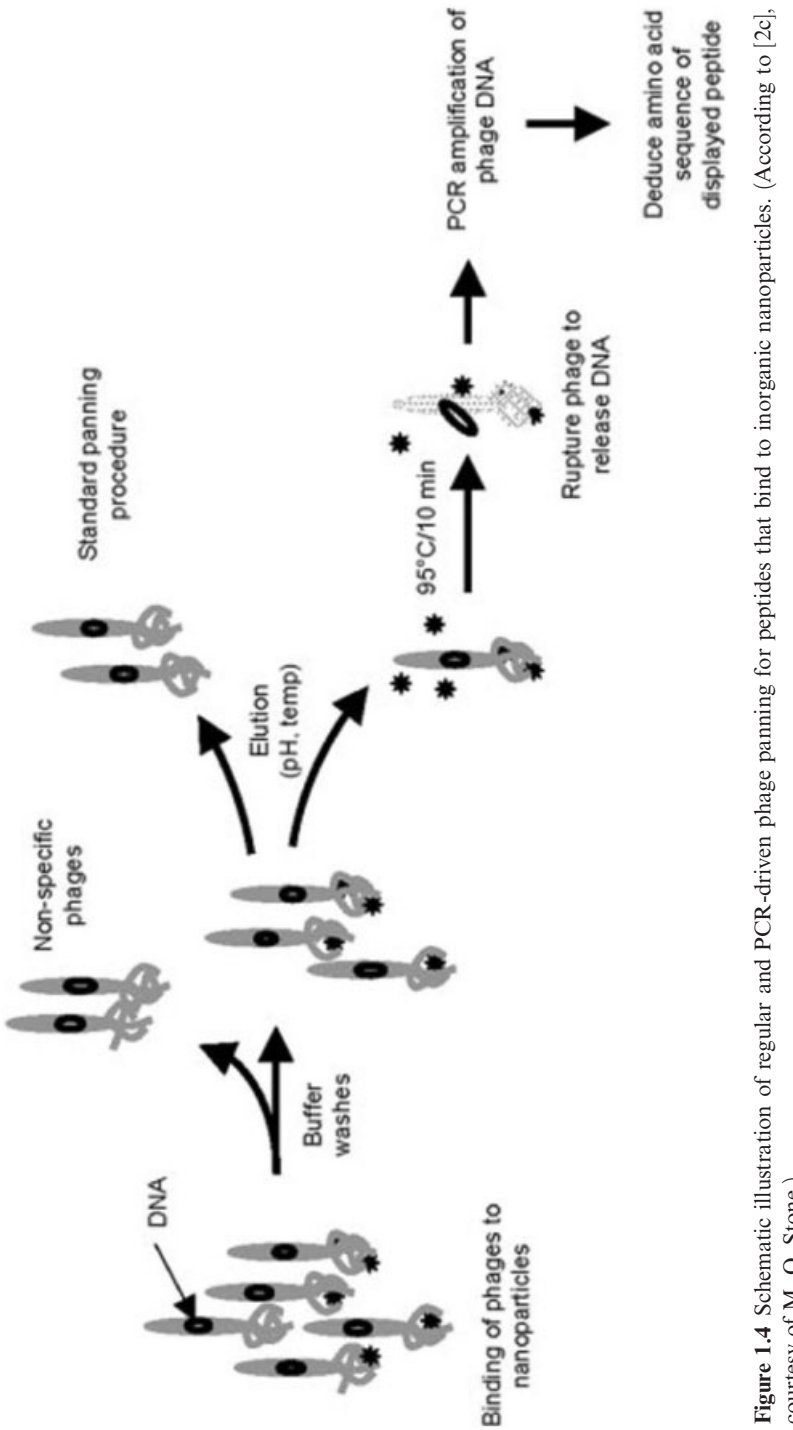

Figure 1.4 Schematic illustration of regular and PCR-driven phage panning for peptides that bind to inorganic nanoparticles. (According to [2c], courtesy of M. O. Stone.)

Table 1.1 Amino acid sequences and properties of the silver-selected peptides.

													Isoelectric pH (p*I*)[a]
AG3	A	Y	S	S	G	A	P	P	M	P	P	F	5.57
AG4	N	P	S	S	L	F	R	Y	L	P	S	D	6.09
AG5	S	L	A	T	Q	P	P	R	T	P	P	V	9.47
			●	●			●			★	●		

[a] p*I* calculated using p*I*/Mass program at www.expasy.ch.
Amino acids with functional side groups are shaded; ★, amino acids conserved in all three sequences; ●, amino acids conserved in two or the sequences.
According to [2b], courtesy of M. O. Stone

To rule out the possibility that the bacteriophage surface may provide an additional matrix for surface-bound peptides in this biomimetic synthesis, peptides were synthesized chemically based on the sequences of the peptide phages AG3, AG4 and AG5 (Table 1.1). In line with the corresponding peptide phages, both AG3 and AG4 peptide precipitated silver nanoparticles, and AG5 did not. It was assumed that the main difference between the activities of these three peptides may be the difference in the overall charge (Table 1.1). Silver nanoparticles synthesized by the AG4 synthetic peptide were analyzed by transmission electron microscopy (TEM). Hexagonal, spherical and triangular particles were discovered, which are crystals of a face-centered-cubic lattice structure corresponding to that of silver (Fig. 1.5).

1.1.2 A Phage Display Peptide Library in "PCR Panning" for Mineral Binding and Synthesizing Peptides

A surprisingly high number of silver-binding peptides was obtained when a new method, PCR-driven panning (Fig. 1.4), was used instead of regular phage panning for peptides to bind inorganic nanoparticles [2c]. PCR was introduced to check whether some peptide phages remained bound to silver nanoparticles *after* the acid elution procedure.

This could be indeed confirmed by the elaborated and easy PCR method. Fourteen new amino acid sequences of silver-binding peptides identified by PCR are shown in Table 1.2 in comparison with three sequences which were eluted previously by regular panning [2c]. Again, some of the peptides identified by the new method were synthesized chemically (Table 1.3). Out of those peptides, AG-P35 was compared with the synthetic AG4 peptide in terms of efficiency to reduce silver ions to metallic silver. AG-P35 generated small spherical silver nanoparticles 52 ± 13.2 nm in size (Fig. 1.6) [2c]. AG4, on the other hand, produced a variety of crystal morphologies 60–150 nm in size (Fig. 1.5) [2b].

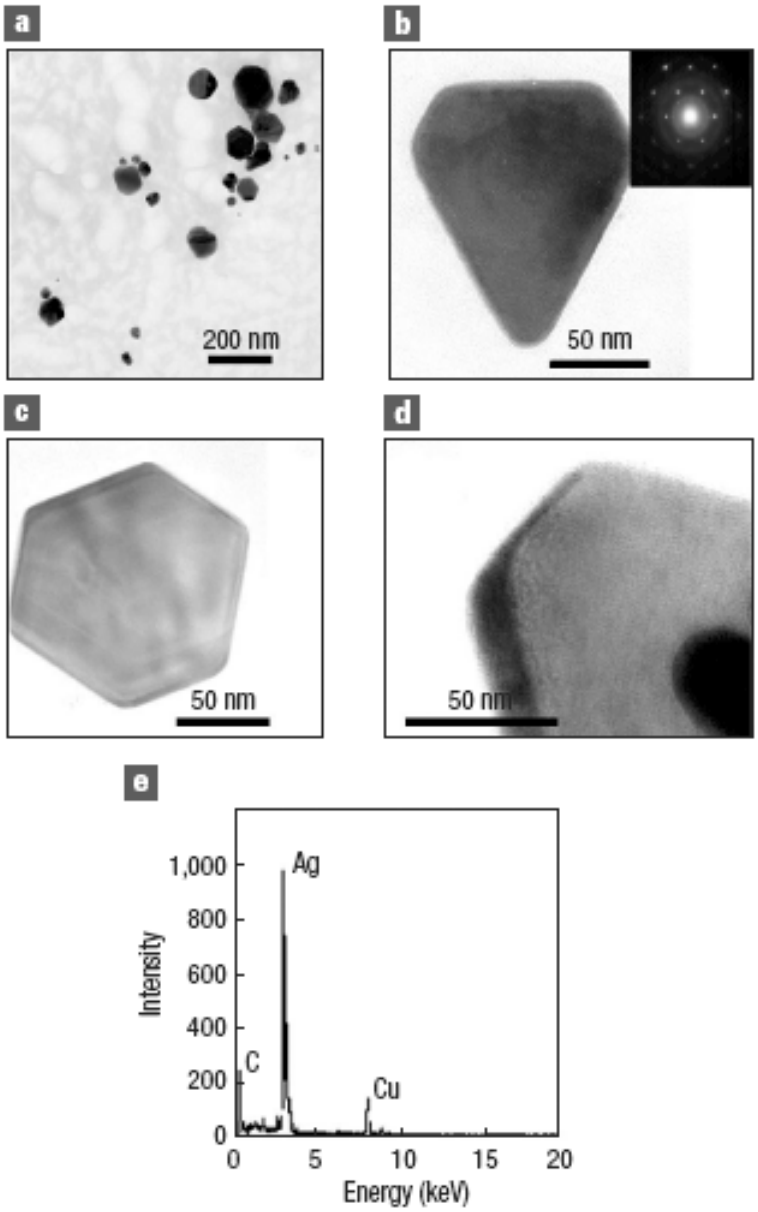

Figure 1.5 Characterization of biosynthetic silver nanoparticles. (a) A variety of crystals morphologies were obtained using AG4 peptide-phage. (b and c) The silver nanoparticles obtained using AG4 synthetic peptide. The inset in (b) shows the electron diffraction pattern obtained from the silver particle; the spot array is from the [111] beam direction, for a face-centered-cubic crystal. (d) Edge of the truncated triangle showing the thickness of the plate. (e) The energy dispersive X-ray spectrum for the crystals indicates elemental silver. The copper and carbon signals are caused by the grid used for TEM analysis. (According to [2b], courtesy of M. O. Stone.)

Table 1.2 Silver binding peptides.

PCR Method		Regular panning	
AG-P1	KFLQFVCLGVGP	AG3	AYSSGAPPMPPF
AG-P2	AVLMQKYHQLGP	AG4	NPSSLFRYLPSD
AG-P3	IRPAIHIIPISH	AG5	SLATQPPRTPPV
AG-P4	NVIRASPPDTSY		
AG-P5	LAMPNTQADAPF		
AG-P6	QQNVPASGTCSI		
AG-P10	NAMPGMVAWLCR		
AG-P11	HNTSPSPIILTP		
AG-P12	ASQTLLLPVPPL		
AG-P14	YNKDRYEMQAPP		
AG-P18	TLLLLAFVHTRH		
AG-P27	PWATAVSGCFAP		
AG-P28	SPLLYATTSNQS		
AG-P35	WSWRSPTPHWT		

According to [2c], courtesy of M. O. Stone

The number of peptide phages now binding to cobalt nanoparticles increased dramatically as a systematic study of the PCR method was performed. It allowed us to compare peptide sequences obtained before and after acid elution by the PCR method with peptide sequences obtained after four rounds of regular panning. Three sets of cobalt nanoparticles were investigated (Table 1.4):

Table 1.3 Peptides used in this study.

	Amino acid sequence	Isoelectric pH (p*I*)	Panning method
Silver-binding peptides			
AG-P3	IRPAIHIIPISH	9.7	PCR
AG-P4	NVIRASPPDTSY	5.8	PCR
AG-P5	LAMPNTQADAPF	3.8	PCR
AG-P28	SPLLYATTSNQS	5.2	PCR
AG-P35	WSWRSPTPHVVT	9.7	PCR
AG-4	NPSSLFRYLPSD	6.1	regular
Cobalt-binding peptides			
Co1-P1	HSVRWLLPGAHP	9.7	PCR
Co2-P2	KLHSSPHTLPVQ	8.6	PCR
Co1-P10	HYPTLPLGSSTT	6.7	PCR
Co1-P15	QYKHHPQKAAHI	9.7	PCR

According to [2c], courtesy of M. O. Stone

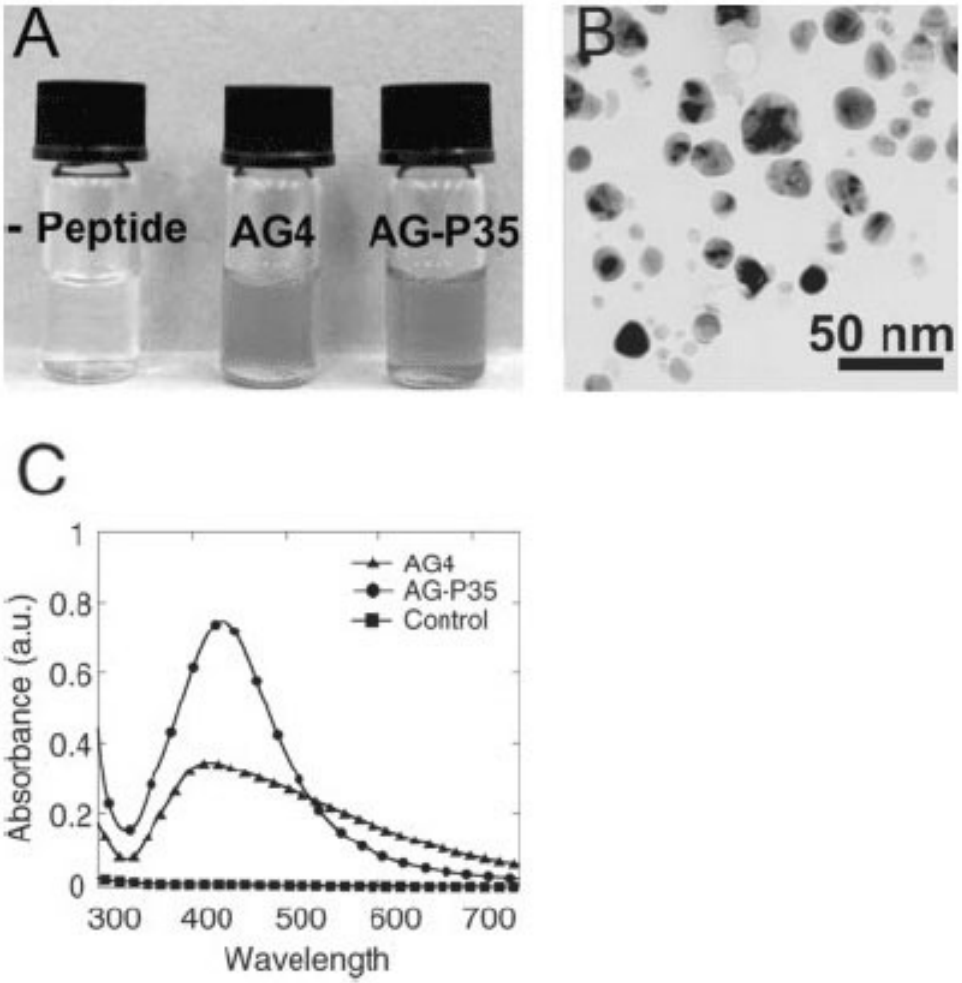

Figure 1.6 Synthesis of silver nanoparticles. (A) Incubation of peptides with 0.2 mM silver nitrate on the laboratory bench top for 24–48 h resulted in the formation of a yellow–red colored solution. Silver nitrate solution lacking peptide was colorless. (B) TEM analysis of AG-P35 synthesized nanoparticles. (C) Ultraviolet-visible spectra of the solutions shown in (A). (According to [2c], courtesy of M. O. Stone.)

Set I: Incubation with phage display peptide library, acid elution, PCR amplification reaction, sequencing.

Set II: Incubation with phage display peptide library, no acid elution, PCR amplification reaction, sequencing.

Set III: Incubation with phage display peptide library, acid elution, amplification and an additional three or four rounds of panning, DNA isolation from the phages, sequencing.

Table 1.4 Cobalt-binding peptides.

Eluted cobalt nanoparticles (Set I)	Uneluted cobalt nanoparticles (Set II)	Regular panning (Set III)
Co1-P1 HSVRWLLPGAHP	Co2-P4 HSVRWLLPGAHP	Co3-P12 GTSTFNSVPVRD
Co1-P2 HETNPPATIMPH	Co2-P3 SAPNLNALSAAS	Co3-P13 SAPNLNALSAAS
Co1-P3 WASAAWLVHSTI	Co2-P5 SVSVGMKPSPRP	Co3-P1 SVSVGMKPSPRP
Co1-P4 SPLQVLPYQGYV	Co2-P8 SPLQVLPYQGYV	Co3-P16 VPTNVQLQTPRS
Co1-P5 ESIPALAGLSDK	Co2-P1 SLTQTVTPWAFY	
Co1-P6 GVLNAAQTWALS	Co2-P7 TNLDDSYPLHHL	
Co1-P8 TPNSDALLTPAL	Co2-P6 TPNSDALLTPAL	
Co1-P10 HYPTLPLGSSTY	Co2-P12 HYPTLPLGSSTY	
Co1-P13 HAMRPQVHPNYA	Co2-P9 TQQTDSRPPVLL	
Co1-P15 QYKHHPQKAAHI	Co2-P14 QYKHHPQKAAHI	
Co1-P16 YGNQTPYWYPHR	Co2-P11 TFPSHLATSTQP	
Co1-P17 HPPTDGMVPSPP	Co2-P13 QNFLQVIRNAPR	
Co1-P18 TWQPFGMRPSDP	Co2-P2 KLHSSPHTPLVQ	
Co1-P21 TGDVSNNPNVTL	Co2-P17 QLLPLTPSLLQA	

According to [2c], courtesy of M. O. Stone

Three groups of sequences were detected in the sequences of the non-eluted nanoparticles (Set II): one group, but not all sequences, that was the same set of sequences as that from the eluded nanoparticles (Set I); a second group that was similar to the sequences obtained from the regular panning (Set III); and a third group of sequences that lacked both the two other groups. This difference may be explained by the probability that many amino acid sequences may not be detected by the regular panning method.

By comparing silver-binding (Table 1.2) with cobalt-binding peptides (Table 1.4), two results are remarkable:

(1) After *regular panning*, the typical (or specific) amino acids for binding and complex formation were absent in both cases. In these silver-binding peptides, cysteine (C) was absent that binds to silver and gold ions. The sequences of cobalt-binding peptides lacked histidine (H) and glutamic acid (E) – amino acids that are known to bind to cobalt.
(2) Using the *PCR method*, not only were these amino acids, known to be specific for binding, found in the sequences obtained, but also others which were also not present after the regular panning: glutamic acid (E), histidine (H), isoleucine (I) and tryptophan (W) in silver-binding peptides; and isoleucine (I), tryptophan (W) and tyrosine (Y) in cobalt-binding peptides.

Summarizing these experiments allows us to infer that several groups of peptides are able to bind tightly to metals. Their sequences are not restricted to those rare peptides with functional side-chains which are known to be specific for binding to silver or cobalt. It is evident that sequences even of several peptide groups are not

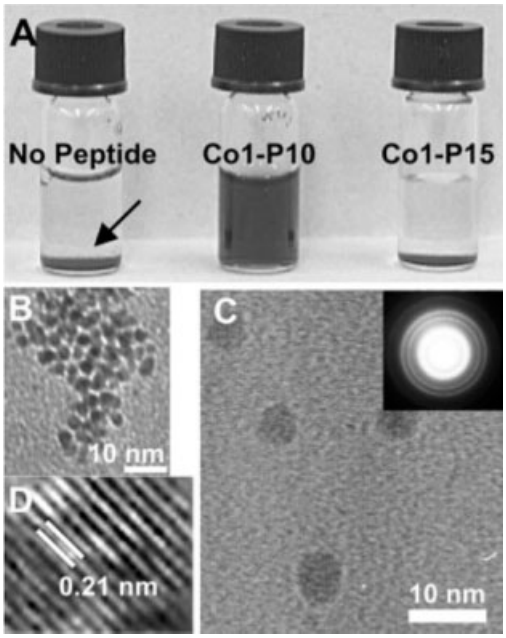

Figure 1.7 Synthesis of CoPt nanoparticles. (A) Solutions of CoPt nanoparticles. Dispersion of the Co1-P10 peptide stabilized CoPt nanoparticles, arrow indicates the accumulated precipitate at the bottom of the glass vials lacking peptide or in the presence of the Co1-P15 peptide. (B) TEM image of Co1-P10 synthesized CoPt nanoparticles. (C) TEM image of individual nanoparticles and the selected-area electron diffraction pattern (inset) of CoPt nanoparticles showing the rings corresponding to [110], [111] and [112] planes. (D) High-resolution TEM of a single CoPt nanoparticle showing the lattice fringes. (According to [2c], courtesy of M. O. Stone.)

random, because the experiments had begun with the 10^9 phage peptides of the library. That is what was designated ''Peptide Groups Selectivity'' in Section 1.1.

The most surprising experiment in biomineralization until now provides the synthesis of a CoPt alloy, mediated by cobalt-binding peptides. CoPt is a magnetic alloy, and a candidate for ultra-high-density magnetic recoding media because of its enhanced magnetic anisotropy and other peptides [8]. The peptides used in this study were synthesized chemically (Table 1.3). For the synthesis of CoPt nanoparticles one of the cobalt-binding peptides (Table 1.3) was added to a solution containing 1 mM ammonium tetrachloroplatinate and 1 mM cobalt acetate tetrahydrate at pH 7.5, and stored for 4 h to overnight at 4 °C. CoPt nanoparticles were obtained as well dispersed in the solution of the Co1-P10 peptide, which apparently stabilized the dispersion for a number of hours (Fig. 1.7), whereas a precipitate was observed without a peptide or with the Co1-P15 peptide. The Co1-P10 dispersion was analyzed by TEM. Nanocrystals of 3.5 ± 0.5 nm were detected and shown to be crystalline by high-resolution TEM (Fig. 1.7).

1.2 Hypothesis of "Pre-biotic Peptide Synthesis and Selection on Minerals"

What is the reason for the fact that, as a result of "PCR Panning", 23 peptides were selected from a random 12-amino-acid peptide library of 10^9 peptide phages which exhibited differing but high affinities for cobalt nanoparticles (Table 1.4)? One or a few peptides with specific functional groups might be expected for binding on mineral surfaces. However, faced with the 10^9 peptide phages used, it is clearly evident that even sequences of 23 compared to 10^9 of 12-amino-acid peptides cannot be regarded as random sequences. What reflects this selectivity – a quasi-specificity of 23 different sequences of 12-amino-acid peptides?

It alludes to an earlier, less-developed state of evolution. The author remembered a seminar in the department of his academic teacher, Theodor Wieland, in Frankfurt/Main about 40 years ago. Here, S. W. Fox had presented experiments which were thought to be steps into a "Molecular Evolution". In one of first model reactions [9], he introduced basalt as a mineral for thermal polymerization of amino acids. However, Fox was fascinated by the formation of protenoid microspheres, thought to be a model for protocells (for review, see [10]). Therefore, he deferred consideration of the numerous minerals existing in pre-biotic times that might be involved in the synthesis and binding of peptides.

It appears to be a clue to their selection that peptides were synthesized in pre-biotic times on numerous different minerals according to environmental conditions. Those peptides which were tightly bound to a mineral surface were very probably protected against rapid hydrolysis compared to peptides which remained in solution. [Tight binding of peptides to surfaces in inorganic materials was shown in experiments (see Sections 1.1.1 and 1.1.2) to compounds such as silica, and not only to metals such as silver and cobalt]. Moreover, selection in this way might be of importance to the fundamental processes of all polypeptides. However, how is such an evolution, such a "memory", transferred to the present day?

1.2.1 Pre-biotic Vesicles for Protection and Mobility

How are these peptides, tightly bound to micro- and nanoparticles, which should be ready for further interactions, preserved? To achieve this aim, the formation of fatty acid vesicles should be possible, which may envelop these micro- to nanoparticles. It was shown through various pre-biotic experiments that fatty acids may be generated in the primitive atmosphere and in solution [9]. In addition, fatty acids are able to form vesicles in a particular pH region (about pH 9), which equals the approximate pK of the acid in the bilayer [10]. Furthermore, Kempe and Kazmierczak proposed that biogenesis and early life on Earth may be favored by an alkaline ocean [11]. They studied Lake Van, Turkey, as a contemporary alkaline lake, a sample of which from 200 m depth had a pH of 9.87 and a low calcium level.

It is now assumed that calcium ions bind at alkaline pH 9 to carboxyl groups, at least to C-termini of the tightly bound peptides, as the initiation of bilayer forma-

tion. These fatty acid bilayers will be centered around loose aggregations of peptide-loaded micro- to nanoparticles of various minerals, because capryl and oleic acid had been reported by Luisi et al. to spontaneously form vesicles at about pH 9 [12]. Low calcium may be preferred now, because otherwise the cylindrical dimer structures of fatty acids will not be assembled. Such a dimer is a unit of the equimolar protonated form and the ionized form of the acid, stabilized by hydrogen bonding [13]. In addition, a rather broad size distribution of was obtained – up to giant vesicles with diameters of a few micrometers [12].

Selected peptides tightly bound to micro- to nano-sized mineral particles are now not only protected additionally by fatty acid vesicles, but also become mobile by water fluxes to areas of various new environmental conditions. Luisi et al. discovered a biosimilar property of fatty acid vesicles that was designated "autopoietic self reproduction". It is an increase of their population number due to a reaction which takes place within the spherical boundary of the vesicles themselves. Thus, the oleic acid vesicles catalyzed hydrolysis of oleic anhydride, which leads to an increase of surfactant molecules, and, as a consequence, growth *in both the size and number* of vesicles.

This property of fatty acid vesicles may open the way to distribute parts of the mineral particles, which are loosely aggregated, into various new vesicles. Anhydrides of fatty acids may be synthesized similarly to the peptides on minerals by heat.

Protection and mobility are very useful, but how may something like pores or channels for any limited exchange between inside and out, for change of pH, and release of the bound peptides originate?

1.2.2 How do Pores Originate?

Some bacteria are able to synthesize magnetite (Fe_3O_4) crystals of maximal magnetic moment, i.e. of a single magnetic domain. These magnetic crystals of 42–45 nm are enveloped by a phospholipid bilayer membrane, which is synthesized *de novo* in the cytoplasma of these magnetobacteria (for review, see [14]).

Magnetic particles appear to be very stable because they are found in ancient sediments of the oceans as well as in meteorites and in many rocks [14]. It is, therefore, probable that magnetic particles are widespread in the aggregation of micro- to nano-sized mineral particles, to which peptides are bound tightly. Recently, four small proteins could be isolated from magnetite crystals of *Magnetospirillum magneticum* AMB-1, when immersed 3 times in boiling 1 % SDS solution [15a]. These four are Mms5, Mms6, Mms7 and Mms13, which were shown by this procedure to be bound only on the surface of the magnetite crystal. The genes of homologous proteins were described previously in *Magnetospirillum gryphiswaldense* [15b], followed by the proteins, identified in proteomic analysis [15c] (see Chapters 4 and 6). Thus, the proteins, which are all coded in a magnetosome island, are not only localized in the magnetosome membrane.

Magnetic particles were proposed by Weaver to interrupt the barrier function of the cell membrane, instead of electroporation [17]. The energies of a hypothetical

process were considered that might result in the formation of hydrophilic pores by energy transfer from magnetic particles which interact with a magnetic field pulse. Experiments have not been performed to date and the analysis, therefore, predicts only that energies impose significant constraints. In pre-biotic times, pore formation by magnetic particles in possible magnetic fields of the Earth appears to be a very useful hypothesis, which will be developed in the future.

References

[1] New England Biolabs, Beverly, MA.
[2] (a) R. R. Naik, L. L. Brott, S. J. Clarson, M. O. Stone, *J. Nanosci. Nanotechnol.* **2000**, *2*, 95–100; (b) R. R. Naik, S. J. Stringer, G. Agarwal, S. E. Jones, M. O. Stone, *Nat. Mater.* **2002**, *1*, 169–172; (c) R. R. Naik, S. E. Jones, C. J. Murray, J. C. McAuliff, R. A. Vaia, M. O. Stone, *Adv. Funct. Mater.* **2004**, *14*, 25–30.
[3] N. Kroeger, R. Deutzmann, M. Sumper, *Science* **1999**, *286*, 1129–1132.
[4] N. Poulsen, M. Sumper, N. Kroeger, *Proc. Natl Acad. Sci. USA* **2003**, *100*, 12075–12080.
[5] R. K. Iler, *The Chemistry of Silica*, Wiley, New York, **1979**.
[6] (a) J. N. Cha, K. Shimizu, Y. Zhou, S. C. Christiansen, B. F. Chmelka, T. J. Deming, G. D. Stucky, D. E. Morse, *Proc. Natl Acad. Sci. USA* **1999**, *96*, 361–365; (b) Y. Zhou, K. Shimizu, I. N. Cha, G. D. Stucky, D. E. Morse, *Angew. Chem. Int. Ed.* **1999**, *38*, 779–782.
[7] S. R. Whaley, D. S. English, E. L. Hu, P. F. Barbara, A. M. Belcher, *Nature* **2000**, *405*, 665–668.
[8] T. Hyeon, *Chem. Commun.* **2003**, *1*, 927–931.
[9] (a) S. W. Fox, K. Dose (Eds), *Molecular Evolution and the Origin of Life*, revised edn. Marcel Dekker, New York, **1977**; (b) W. W. Leach, D. W. Nooner, J. Oro, *Origin of Life* **1978**, *8*, 113–122.
[10] (a) W. R. Hargreaves, D. W. Deamer, *Biochemistry* **1978**, *17*, 3759–3768; (b) D. P. Cistola, J. A. Hamilton, D. Jadeson, D. M. Small, *Biochemistry* **1988**, *27*, 1881–1888.
[11] S. Kempe, J. Kazmierczak, *Astrobiology* **2002**, *2*, 123–130.
[12] P. Walde, R. Wick, M. Fresta, A. Mangone, P. L. Luisi, *J. Am. Chem. Soc.* **1994**, *116*, 11649–11654.
[13] T. Haines, *Proc. Natl Acad. Sci. USA* **1983**, *80*, 160–164.
[14] E. Baeuerlein, *Ang. Chem.* **2003**, *42*, 614–641.
[15] (a) A. Arakaki, J. Webb, T. Matsunaga, *J. Biol. Chem.* **2003**, *278*, 8745–8750; (b) K. Grünberg, C. Waver, B. M. Tebo, D. Schüler, *Appl. Environ. Microbiol.* **2001**, *67*, 4573–4582; (c) K. Grünberg, E. C. Müller, A. Otto, R. Reszka, D. Linder, M. Kube, R. Reinhardt, D. Schüler, *Appl. Environ. Microbiol.* **2004**, *70*, 1040–1050.
[16] S. Schübbe, M. Kube, A. Scheffler, C. Wasser, U. Heyen, A. Meyerdirks, M. H. Madkour, F. Mayer, R. Reinhardt, D. Schüler, *J. Bacteriol.* **2003**, *185*, 5779–5790.
[17] T. E. Vaughan, J. C. Weaver, *Biophys. J.* **1996**, *71*, 616–622.

Magnetite (Fe_3O_4) and Greigite (Fe_3S_4)

Biomineralization: From Biology to Biotechnology and Medical Application,
Second Edition. Edited by E. Bäuerlein

ISBN: 3-527-31065-7

2 Magnetic Iron Oxide and Iron Sulfide Minerals within Microorganisms: Potential Biomarkers

Dennis A. Bazylinski and Richard B. Frankel

2.1 Introduction

A number of microorganisms are known to facilitate the deposition of minerals [1]. Mineral deposition by bacteria occurs by two generically different mechanisms [2]. In biologically induced mineralization, minerals form in the environment in an apparently uncontrolled manner from metabolites produced by the bacteria. The minerals formed and their properties depend on environmental conditions, and are generally indistinguishable from minerals formed inorganically under the same chemical conditions. In biologically controlled mineralization, minerals are deposited on or within organic matrices or vesicles inside the cell, allowing the organism to exert a high degree of control over the composition, size, habit and intracellular location of the minerals [3]. Because the intravesicular pH and Eh can be controlled by the organism, mineral formation is not as affected by external environmental parameters as in the biologically induced mode.

The biologically induced and biologically controlled deposition of magnetic iron minerals by bacteria has been recognized for some time. Dissimilatory iron-reducing bacteria [4] and dissimilatory sulfate-reducing bacteria [5] export ferrous ions and sulfide ions, respectively, into the environment, inducing the formation of a number of extracellular iron and sulfide minerals, including magnetic iron minerals such as magnetite (Fe_3O_4), greigite (Fe_3S_4) and pyrrhotite ($Fe_{1-x}S_x$) [5, 6]. These mineral particles are characterized by variable composition and crystallinity depending on environmental conditions, broad size distributions and lack of a consistent crystal habit [7]. On the other hand, magnetotactic bacteria [8] mineralize magnetosomes [9], which are nanometer-sized magnetite [10] or greigite [11] crystals in intracellular membrane vesicles [12], in a highly controlled manner. The mineral crystals are generally characterized by specific chemical compositions, high crystallinity, narrow size distributions and well-defined, consistent habits within each bacterial species or strain [13, 14].

In addition to magnetotactic bacteria, a number of eukaryotic microorganisms have been found to contain magnetosomes or magnetosome-like structures [15, 16]. In this chapter we will review the characteristics of magnetic minerals in magnetotactic bacteria and single-celled eukaryotes, and the role of the magnetic iron minerals in magnetotaxis. Molecular biological and biochemical aspects of magneto-

Biomineralization: From Biology to Biotechnology and Medical Application, Second Edition. Edited by E. Bäuerlein

ISBN: 3-527-31065-7

some formation in bacteria, as well as magnetite in higher organisms, will be discussed elsewhere in this volume.

2.2 Diversity of Magnetotactic Bacteria

Magnetotactic bacteria are a morphologically and physiologically diverse group of motile, Gram-negative prokaryotes, ubiquitous in aquatic environments [8, 13], that orient and migrate along magnetic field lines. They include coccoid, rod-shaped, vibrioid, spirilloid (helical) and even multicellular forms. Physiological forms include denitrifiers that are facultative anaerobes, obligate microaerophiles and anaerobic sulfate reducers [14]. Thus, there are likely many species of magnetotactic bacteria [17], although only several have been isolated in pure culture [13]. Each magnetotactic bacterium contains magnetosomes and iron can constitute as much as 3 % of the dry weight of the cells [18, 19]. The magnetosomes are generally arranged in one or more chains within the cell, aligned parallel to the axis of motility. Although most magnetotactic bacteria exclusively contain either magnetite or greigite magnetosomes, a large, rod-shaped marine bacterium has been found to contain both magnetite and greigite magnetosomes [20, 21]. More detailed discussion regarding the molecular diversity and phylogeny of the magnetotactic bacteria can be found in Chapter 3 this volume.

2.3 Ecology of Magnetotactic Bacteria

Magnetotactic bacteria are generally found in aquatic habitats that are close to neutrality in pH and not thermal, heavily polluted or well oxygenated [8]. They are cosmopolitan in distribution and occur in the highest numbers at the microaerobic zone, also known as the oxic–anoxic transition zone (OATZ) [13, 22]. In many freshwater habitats, the OATZ is located at the sediment water interface or just below it and the highest concentration of magnetotactic bacteria occur there [14]. In some brackish-to-marine chemically stratified systems, the OATZ in water depths of more than a few meters is found, or is seasonally located, in the water column as shown in Figure 2.1. The Pettaquamscutt Estuary (Narragansett Bay, RI, USA) [23] and Salt Pond (Woods Hole, MA, USA) [24] are examples of the latter situation. Hydrogen sulfide, produced by sulfate-reducing bacteria in the anaerobic zone and sediment, diffuses upward while oxygen diffuses downward from the surface resulting in a double, vertical, chemical concentration gradient (Figure 2.1) with a concomitant redox gradient. Typically, a pycnocline and thermocline are also associated with the OATZ in these situations which help to physically stabilize the chemical stratification.

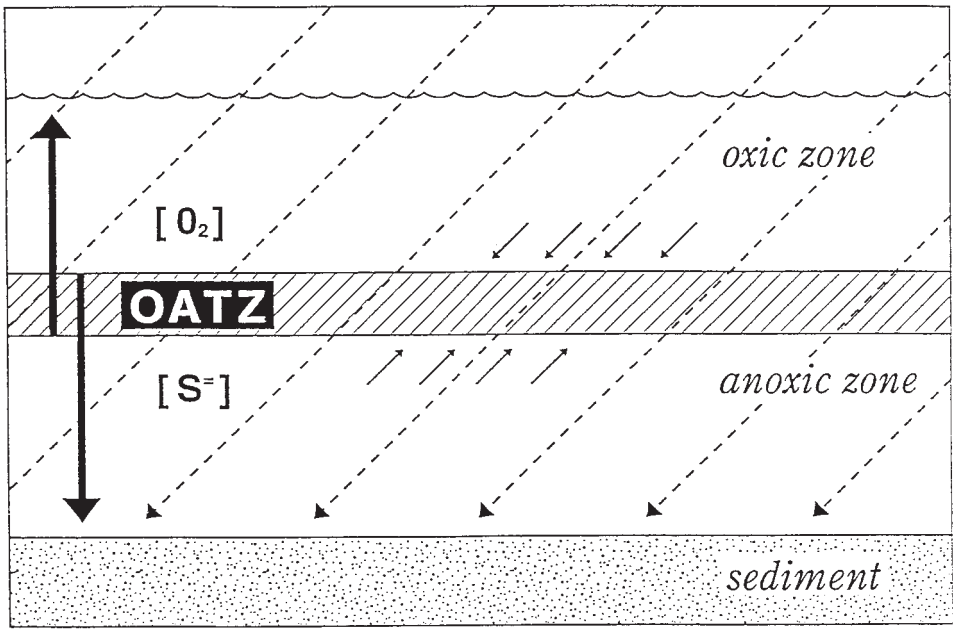

Figure 2.1 Schematic of the OATZ in the water column as typified by Salt Pond (Woods Hole, MA USA). Note the inverse double concentration gradients of oxygen ($[O_2]$) diffusing from the surface and sulfide ($[S^=]$) generated by sulfate-reducing bacteria in the anaerobic zone (vertical arrows). Magnetite-producing magnetotactic bacteria exist in their greatest numbers at the OATZ where microaerobic conditions predominate and greigite producers are found just below the OATZ where $S^=$ becomes detectable. When polar-magneto-aerotactic, magnetite-producing coccoid cells are above the OATZ in vertical concentration gradients of O_2 and $S^=$ (higher $[O_2]$ than optimal), they swim downward (small arrows above OATZ) along the inclined geomagnetic field lines (dashed lines). When they are below the OATZ (lower $[O_2]$ than optimal), they reverse direction (by reversing the direction of their flagellar motors) and swim upward (small arrows below the OATZ) along the inclined geomagnetic field lines. The direction of the flagellar rotation is coupled to an aerotactic sensory system that acts as a switch when cells are at a suboptimal position in the gradient as defined in the text. Magnetotactic spirilla (and other axial magneto-aerotactic microorganisms) align along the geomagnetic field lines and swim up and down relying on a temporal sensory mechanism of aerotaxis to find and maintain position at their optimal oxygen concentration at the OATZ.

A variety of magnetotactic bacteria are found at both the Pettaquamscutt Estuary and Salt Pond, stratified by depth [21]. Generally, the magnetite-producing bacteria prefer the OATZ proper (Figure 2.1) and behave as microaerophiles. Two strains of magnetotactic bacteria have been isolated from the Pettaquamscutt Estuary – a vibrio designated strain MV-2 [25, 26] and a coccus designated strain MC-1 [25, 27, 28]. Both strains grow as microaerophiles, although strain MV-2 can also grow anaerobically with nitrous oxide (N_2O) as a terminal electron acceptor. Other cultured magnetotactic bacterial strains, including the magnetotactic

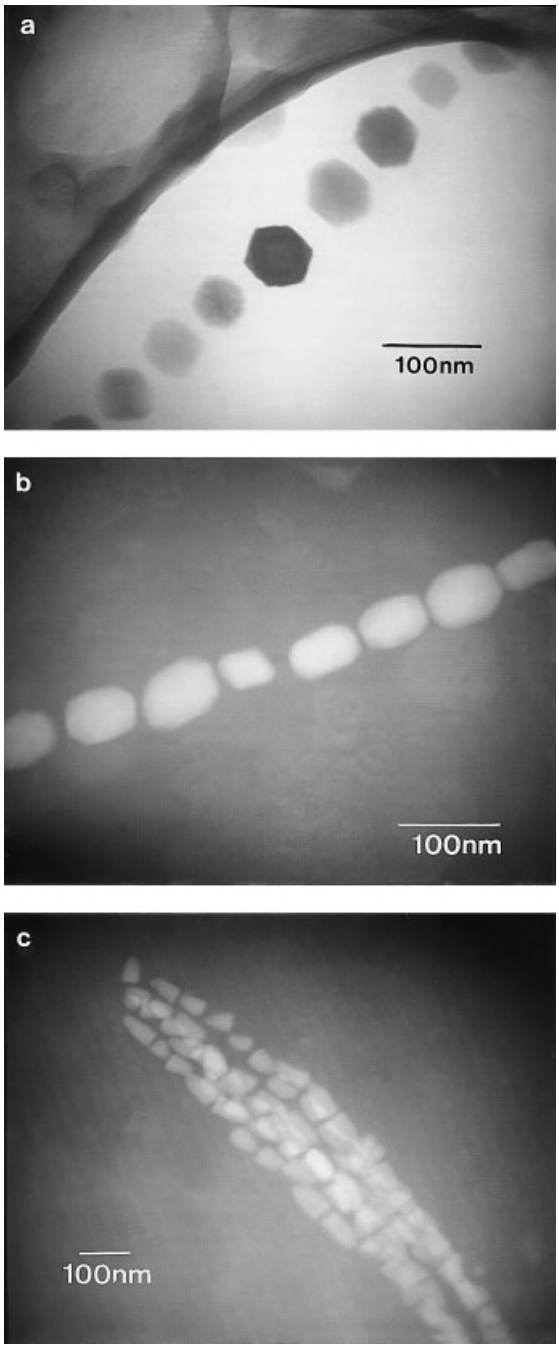

Figure 2.2 Morphologies of intracellular magnetite (Fe_3O_4) particles produced by magnetotactic bacteria collected from the OATZ of the Pettaquamscutt Estuary. (a) Bright-field scanning TEM (STEM) image of a chain of cubo-octahedra in cells of an unidentified rod-shaped bacterium, viewed along a [111] zone axis for which the particle projections appear hexagonal. (b) Dark-field STEM image of a chain of prismatic crystals within a cell of an unidentified marine vibrio, with parallelepipedal projections. (c) Dark-field STEM image of tooth-shaped (anisotropic) magnetosomes from an unidentified marine rod-shaped bacterium.

spirilla [29–33] and rods [34], are microaerophiles or anaerobes or both. The greigite-producing magnetotactic bacteria are likely anaerobes appearing to prefer the more sulfidic waters below the OATZ (Figure 2.1) where the oxygen concentration is zero [14, 21]. No magnetotactic bacterium with greigite magnetosomes has been grown in pure culture.

2.4 Magnetite Magnetosomes

The mineral composition of magnetite magnetosomes is specific in a given strain as shown by the fact that cells of several cultured strains continue to synthesize magnetite and not greigite even when hydrogen sulfide is present in the growth medium [26, 28]. Gorby [35] found that iron was not be replaced by other transition metal ions, including titanium, chromium, cobalt, copper, nickel, mercury and lead, in the magnetite crystals of *Magnetospirillum magnetotacticum* when cells were grown in the presence of these ions. Towe and Moench [36] reported very small amounts of titanium in the magnetite particles of an uncultured freshwater magnetotactic coccus, but this has not been confirmed by subsequent studies. Thus, the absence of transition metal ions other than iron is one of the hallmarks of magnetite magnetosomes.

Magnetite magnetosomes from a number of magnetotactic bacteria are shown in the electron micrographs in Figure 2.2. The habits of the magnetite crystals appear to be consistent within a given species or strain [26, 28], although some variations of shape and size can occur within single magnetosome chains [37]. The presence of smaller and more rounded crystals, common at one or both ends of the chains (Figure 2.3a) and interpreted as ''immature'' crystals, has been used as evidence that the magnetosome chain increases in size by the precipitation of new magnetosomes at the ends of the chain following cell division [3]. In addition to the roughly equidimensional crystal shapes seen in *M. magnetotacticum* and other freshwater magnetotactic spirilla (Figure 2.2a), several non-equidimensional shapes have been described in other species or strains [3, 38]. These include prismatic (Figure 2.2b) and tooth, bullet or arrowhead shapes (Figure 2.2c) [39–41]. Many crystals of these types have been studied by high-resolution transmission electron microscopy (HRTEM) and/or selected area electron diffraction (SAED), and idealized crystal habits based on simple forms, i.e. combinations of symmetry related crystal faces, have been proposed (Figure 2.4a–d) [3, 28]. It should be emphasized that both equidimensional and non-equidimensional crystals have the face-centered cubic structure of magnetite, as shown in the interplanar spacings and angles determined by HRTEM or SAED, but have different, species- or strain-specific, crystal habits.

Magnetite and greigite are in the Fd3m space group. Macroscopic crystals of magnetite display habits of the octahedral {111} form, more rarely dodecahedral {110} or cubic {100} forms [42]. The habit of the crystals in *M. magnetotacti-*

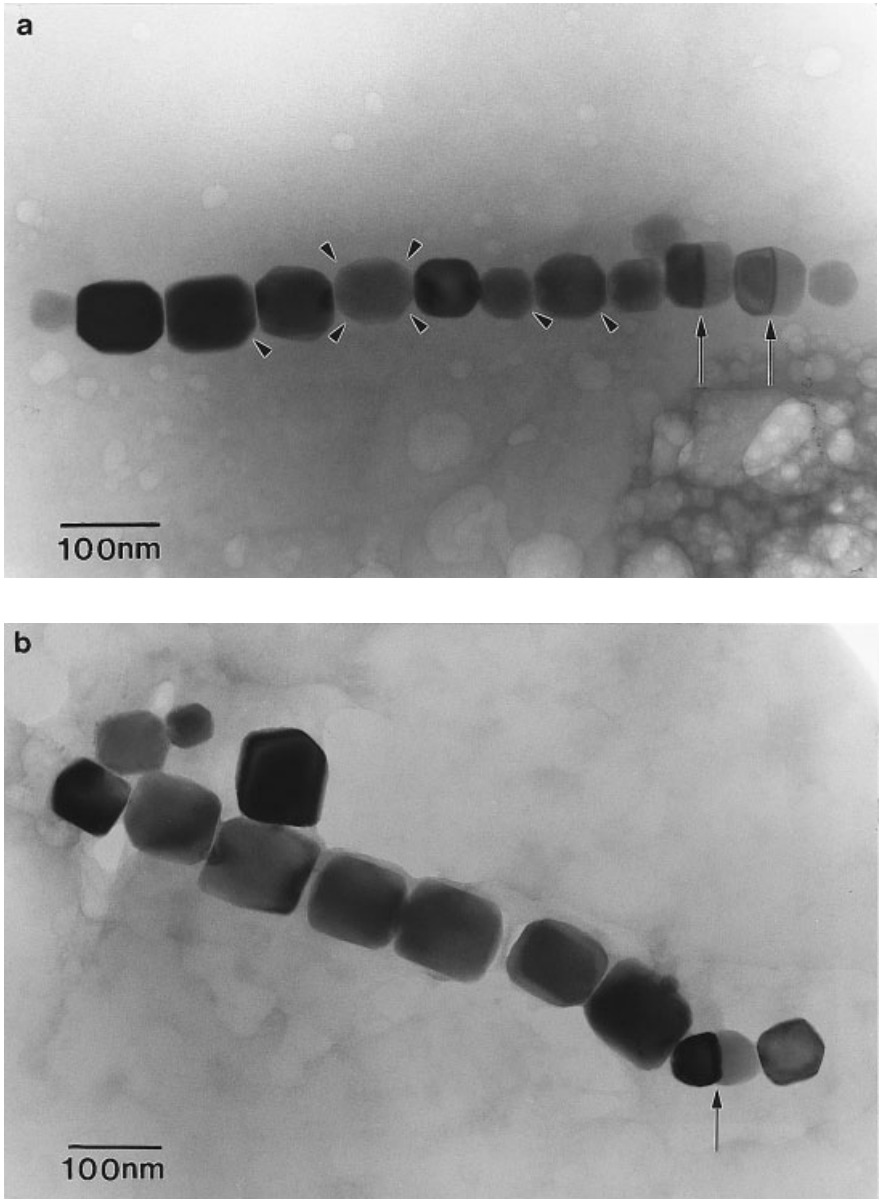

Figure 2.3 TEM image of magnetite magnetosome chains within cells of the magnetotactic coccus, strain MC-1, grown autotrophically (a) and heterotrophically (b). Note the presence of smaller, "immature" magnetite crystals at the ends of the chains [most obvious in (a)], the more pronounced truncations at the ends of the crystals in cells grown autotrophically in (a) indicated by the small arrows, and the twinned crystals in (a) and (b) indicated by the long arrows.

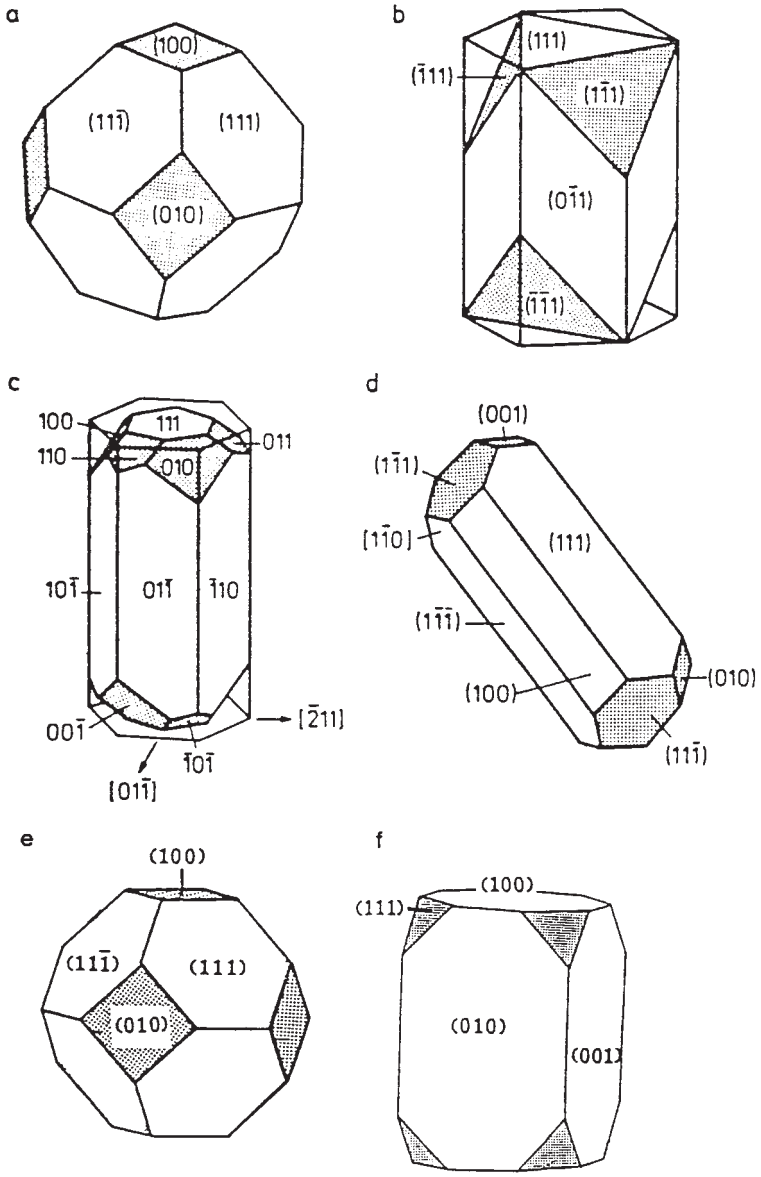

Figure 2.4 Idealized magnetite (a–d) and greigite (e–f) crystal morphologies derived from high-resolution TEM studies of magnetosomes from magnetotactic bacteria: (a and e) cubo-octahedra, (b and c) variations of pseudo-hexagonal prisms, (d) elongated cubo-octahedron and (f) elongated, truncated cube.

cum are cubo-octahedra (Figure 2.4a), composed of {100} + {111} forms [43], with equidimensional development of the six symmetry related faces of the {100} form and of the eight symmetry related faces of the {111} form. The habits of the non-equidimensional crystals, like those in strains MV-1 and MC-1, can be described as combinations of {100}, {111} and {110} forms [44]. In these cases, the six, eight and 12 symmetry related faces of the respective forms that constitute the habits do not develop equally. For example, crystals of both strains MV-1 (Figure 2.4b) [28] and MC-1 (Figure 2.4c) [26] have pseudo-prismatic habits elongated along a ⟨111⟩ axis, with six well-developed (110) faces parallel to the elongation axis and capped by (111) planes perpendicular to the elongation axis. In MV-1 crystals, the remaining six (111) faces form truncations of the end caps and the remaining six (110) faces are very small or missing [28]. In MC-1 crystals, the truncations at each end consist of three (100) faces alternating with three (110) faces. Thus, six (110) faces are larger and six are smaller, and six (111) faces are virtually absent in this habit. Only the six (100) faces are equidimensional [26]. The pseudo-prismatic motif of six elongated (110) faces capped by (111) faces with differing truncation planes appears to be the most common in magnetotactic bacteria with non-equidimensional magnetosome crystals.

The elongated, pseudo-prismatic habits, corresponding to the anisotropic development of symmetry-related faces, could occur either because of anisotropy in the growth environment (such as a concentration gradient) or anisotropy of the growth sites [3]. In the case of the non-equidimensional magnetosomes, the anisotropy of the environment could derive from an anisotropic flux of ions through the magnetosome membrane surrounding the crystal [12] or from anisotropic interactions of the magnetosome membrane with the growing crystal [3].

The most anisotropic habits are those of the tooth, bullet and arrowhead-shaped magnetite crystals. In one uncultured organism, small and large crystals have different habits, suggesting that growth occurs in two stages. The nascent crystals are cubo-octahedra which subsequently elongate along a [111] axis to form a pseudo-octahedral prism with alternating (110) and (100) faces capped by (111) faces (Figure 2.4d) [40, 41].

Culturing bacteria under very different growth conditions appears to have little or no effect on the overall crystal habit of magnetite crystals in magnetosomes. However, in one cultured bacterium, strain MC-1, the magnetite particles appear to have more pronounced truncations at the ends of these elongate crystals in cells grown autotrophically versus those grown heterotrophically (Figure 2.3a and b) [28]. As more cultures of magnetotactic bacteria become available, effects of growth conditions on magnetosome formation can be further studied.

Magnetosome magnetite crystals are typically 35–120 nm long [45]. Statistical analyses of crystal size distributions in cultured strains show narrow, asymmetric distributions and consistent width to length ratios within each strain [44]. Whereas the crystal size distributions of inorganic magnetite and magnetite resulting from dissimilatory iron reduction are typically log-normal [46], the shapes of the magnetosome crystal size distributions are asymmetric with a sharp high end cut-off, consistent with a transport-controlled Ostwald ripening process [47].

Twinned crystals are common in magnetotactic bacterially produced magnetites (around 10 %) with individuals related by rotations of 180° around the [111] direction parallel to the chain direction and with a common (111) contact plane (Figure 2.3a and b). Multiple twins are less common [44].

2.5 Greigite Magnetosomes

Although all freshwater magnetotactic bacteria have been found to mineralize magnetite magnetosomes, many marine, estuarine and salt marsh species produce magnetosomes with iron sulfide mineral crystals [11, 48, 49]. Bacteria with iron sulfide magnetosomes include a many-celled magnetotactic prokaryote (MMP) [25, 50, 51] and a variety of relatively large rod-shaped bacteria [50, 54]. The iron sulfide minerals are either greigite [11, 52, 53] or a mixture of greigite and transient non-magnetic iron sulfide phases that likely represent mineral precursors to greigite. These include non-magnetic mackinawite and likely a sphalerite-type cubic FeS [54, 55]. Based on TEM observations, electron diffraction and known iron sulfide chemistry [56, 57], the reaction scheme for greigite formation in the magnetotactic bacteria appears to be [54, 55]:

$$\text{cubic FeS} \rightarrow \text{mackinawite (tetragonal FeS)} \rightarrow \text{greigite } (Fe_3S_4)$$

Reports of iron pyrite [11] and pyrrhotite [49] in magnetotactic bacteria have not been confirmed. Interestingly, under the strongly reducing, sulfidic conditions at neutral pH in which the iron sulfide magnetotactic bacteria are found [21], greigite would be expected to transform into pyrite [57]. It is not known how the cells prevent this transformation, but probably involves control of the sulfide concentration in the cell and/or in the magnetosome vesicle. The size range of the greigite crystals in magnetotactic bacteria is similar to that observed for magnetite.

As with magnetite, several greigite crystal morphologies, composed primarily of {111} and {100} forms have been observed (Figure 2.4e and f) [53]. These include cubo-octahedral and pseudo-rectangular prismatic, as shown in Figure 2.4(e and f), and tooth-shaped [55]. Like that of their magnetite counterparts, the morphologies of the greigite particles in the rod-shaped bacteria are also apparently species- and/or strain-specific. In contrast to the rod-shaped bacteria, the MMP (Figure 2.5a) contains greigite crystals with a mixture of morphologies, including pleomorphic, pseudo-rectangular prismatic, tooth-shaped and cubo-octahedral [55]. Some of these particle morphologies are shown in Figure 2.5(b).

The mixed mineral, rod-shaped bacterium was found to contain magnetite magnetosomes with arrowhead-shaped crystals and rectangular prismatic crystals of greigite, co-organized within the same chains of magnetosomes (this organism usually contains two parallel chains of magnetosomes) as shown in Figure 2.6 [20, 21]. In addition to different, mineral-specific morphologies and sizes, the greigite and

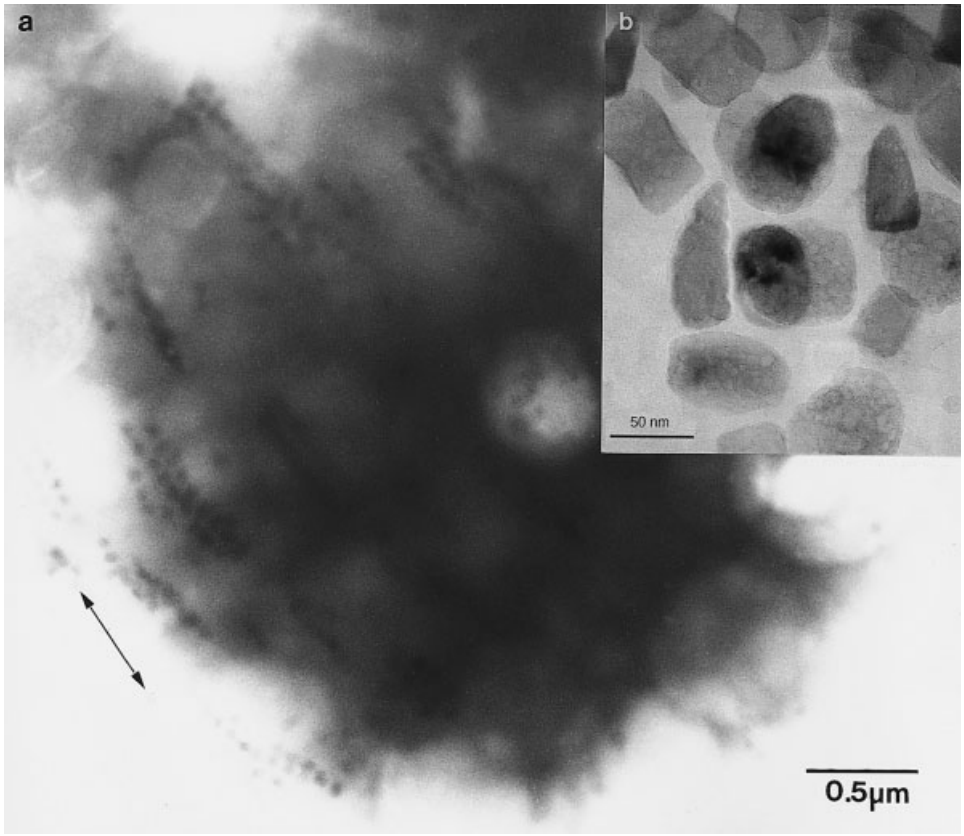

Figure 2.5 (a) TEM image of the MMP weakly stained with uranyl acetate showing that most of the magnetosome chains are oriented parallel to the axis designated by the double-ended arrow. (b, inset) TEM image of greigite particles within the MMP including tooth-shaped and rectangular prismatic crystals. [(b) Courtesy of M. Pósfai and P. R. Buseck.]

magnetite crystals have [100] and [111] crystal axes parallel to the chain direction, respectively. Both crystal morphologies and chain orientations have been found in organisms with single mineral component chains [3, 52, 53]. This suggests different biomineralization processes for the two minerals, possibly due to differences in the respective magnetosome membranes. Thus, it is likely that two separate sets of genes control the biomineralization of magnetite and greigite in this organism [21].

Significant amounts of copper, but not other transition metal, ions have been found in greigite magnetosomes of some magnetotactic bacteria [55, 58]. The amount of copper was variable from collection site to collection site. It was also variable from magnetosome to magnetosome within an individual cell, ranging in one case from about 0.1 to 10 at% relative to iron. This suggests that copper incorporation is a consequence of environmental conditions. The copper appeared in some cases to be mostly concentrated on the surface of the crystals [58]. These ob-

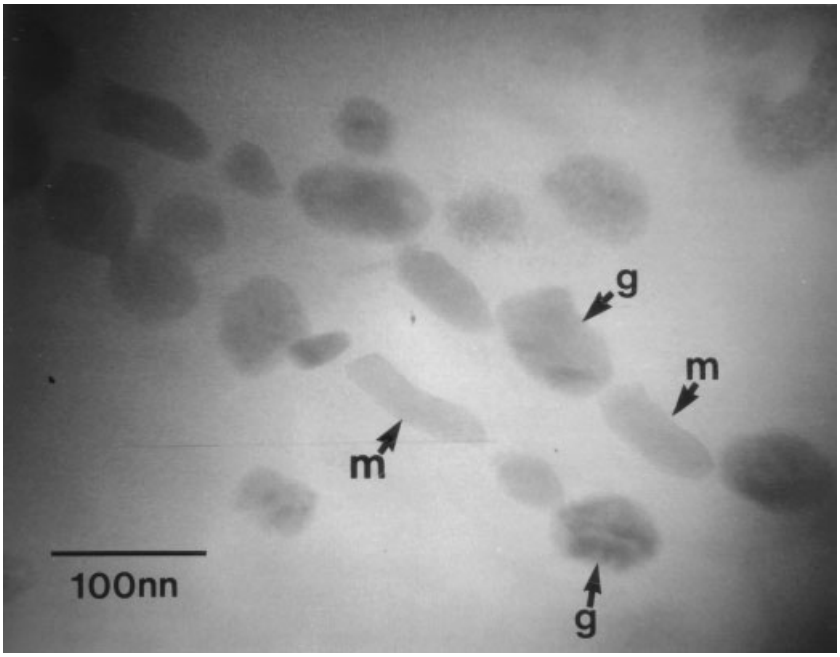

Figure 2.6 Bright-field STEM of tooth-shaped magnetite (m at arrows) and pleomorphic greigite (g at arrows) magnetosome crystals co-organized within the same chains in an uncultured magnetotactic bacterium collected from the OATZ of the Pettaquamscutt Estuary, RI.

servations indicate that mineralization in these organisms is more susceptible to chemical conditions in the external environment and suggest that the iron sulfide magnetosomes could function in transition metal detoxification.

The conversion of cubic FeS and mackinawite to greigite [54, 55] in iron sulfide magnetosomes involves changes in the stoichiometry of the magnetosome particle. Based on thermodynamic considerations, cubic FeS and mackinawite transform to greigite under strongly reducing sulfidic conditions at neutral pH [57]. Similar transformations occur inorganically in sediments in the same locales [59]. There is also the possibility that the rate of transformation, including suppression of transformation of greigite to pyrite, might be controlled by the cell.

2.6 Arrangement of Magnetosomes in Cells

In addition to controlled mineralization, magnetotactic bacteria control the placement of magnetosomes in the cell. The arrangement of magnetosomes in the cell, like the crystal habits of the magnetosome mineral particles themselves, also appears to be specific to a particular bacterial species and/or strain.

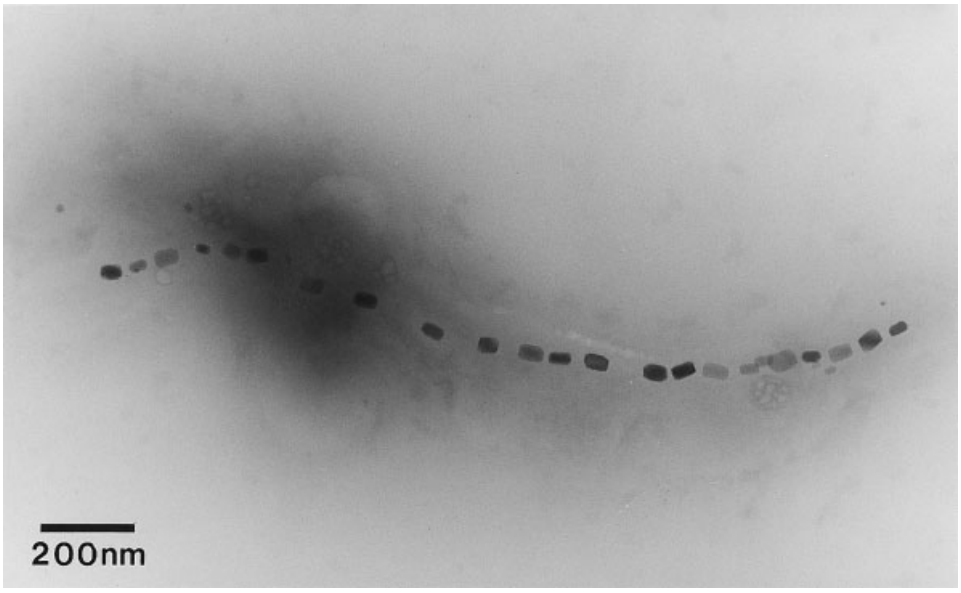

Figure 2.7 TEM image of an unstained cell of the marine, magnetotactic vibrio, strain MV-1, showing gaps between magnetosomes. Note that even with the relatively large gaps between some magnetosomes, there is a consistent orientation of each individual magnetosome along the direction of the magnetosome chain suggesting that the separated magnetosomes are co-organized with the others by a chain assembly process.

Typically, magnetosomes are organized into one or more chains with the particles arranged along the long axis of the cell (e.g. Figures 2.2 and 2.3). In most cases, magnetosomes are directly adjacent to one another, but in some bacteria, e.g. strain MV-1, large gaps can occur between magnetosomes (Figure 2.7) [21]. The magnetosomes appear to be fixed within the cell, generally adjacent to the cell membrane, by as yet unknown structural elements [21]. There is little evidence, however, that the membrane surrounding the individual magnetosome particles (i.e. the magnetosome membrane) is contiguous with the cell membrane.

Individual magnetite crystals are oriented within the chain with a crystal [111] axis parallel to the chain axis. For bacterial strains in which the magnetite crystals have elongated habits, the [111] axis parallel to the chain axis is also the axis of elongation of the crystals [3].

Several magnetotactic bacteria are known in which the magnetosomes are not arranged in chains. Some magnetite-producing cocci, including *Bilophococcus magnetotacticus*, do not construct magnetosome chains, but instead have a "clump" of magnetosomes at one end of the cell [60].

Most known, uncultured, greigite-producing, magnetotactic rod-shaped bacteria tend to synthesize multiple, usually two to four, parallel chains of magnetosomes

adjacent to one another that longitudinally traverse the cell. Unlike magnetite, greigite crystals are oriented with a [100] axis along the chain axis [53]. The iron sulfide magnetosomes in the MMP originally appeared in disrupted organisms to be positioned somewhat randomly in the constituent cells with some arranged in small chains. However, electron microscopy of intact organisms revealed that most magnetosomes exist in multiple chains which are for the most part aligned parallel to each other within each cell and between cells (Figure 2.5a). This consensus alignment of magnetosome chains results in a net magnetic dipole moment for the entire organism. Clumps of greigite magnetosomes have also been observed in some rod-shaped bacteria [52].

The *de novo* synthesis of non-magnetic, crystalline, iron sulfide precursors to greigite, cubic FeS and mackinawite (*vide supra*), aligned along the magnetosome chain indicates that chain formation and the orientation of the magnetosomes in the chain does not necessarily involve magnetic interactions.

2.7 Role of Magnetosomes and Magnetosome Chains in Magnetotaxis

The crystal size distributions for both magnetite and greigite magnetosomes peak within the permanent, single-magnetic-domain (SD) size range [45]. Magnetostatic interactions between the SD magnetosomes organized in a chain configuration cause the individual grain moments to orient parallel to each other along the chain direction. Thus, the chain has a permanent magnetic dipole approximately equal in magnitude to the sum of the individual magnetosome magnetic dipoles [61]. This has recently been demonstrated by electron holography of individual magnetotactic bacteria [62]. The permanent magnetic dipole of a cell is generally large enough so that its interaction with the geomagnetic field overcomes the thermal forces tending to randomize the orientation of the magnetic dipole in its aqueous surroundings [61]. Since the dipole is fixed in the cell, orientation of the dipole results in orientation of the cell. Magnetotaxis results as the oriented cell swims along magnetic field lines (**B**). The direction of migration along **B** is determined by the direction of flagellar rotation, which in turn is determined by the aerotactic response of the cell [27].

Some magnetotactic spirilla, such as *M. magnetotacticum*, swim parallel or antiparallel to **B** and form aerotactic bands [63] at a preferred oxygen concentration $[O_2]$ in oxygen gradient cultures or in suspensions of living cells. In a homogeneous medium, roughly equal numbers of cells swim in either direction along **B** [18, 63]. Most microaerophilic bacteria form aerotactic bands at a preferred or optimal $[O_2]$ where the proton motive force is maximal [64], using a temporal sensory mechanism [65] that samples the local environment as they swim and compares the present $[O_2]$ with that in the recent past. The change in $[O_2]$ with time determines the sense of

flagellar rotation [66]. The behavior of individual cells of *M. magnetotacticum* in aerotactic bands, termed axial magneto-aerotaxis, is consistent with the temporal sensory mechanism [27].

In contrast, the ubiquitous freshwater and marine, bilophotrichously flagellated (having two flagellar bundles on one hemisphere of the cell), magnetotactic cocci and some other magnetotactic strains swim persistently in a preferred direction relative to **B** when examined microscopically in wet mounts [8, 39, 67]. However, magnetotactic cocci in oxygen gradients can swim in both directions along **B** without turning around [27]. The cocci form microaerophilic, aerotactic bands and seek a preferred $[O_2]$ along the concentration gradient. However, while axial magneto-aerotaxis is consistent with the temporal sensory mechanism, the aerotactic behavior of the cocci is not. Instead their behavior is consistent with a two-state aerotactic sensory model in which the $[O_2]$ determines the sense of the flagellar rotation and hence the swimming direction relative to **B** [27]. This model, termed polar magneto-aerotaxis, accounts for the ability of the magnetotactic cocci to migrate to and maintain position at the preferred $[O_2]$ at the OATZ in chemically stratified, semi-anaerobic basins (Figure 2.1). An assay using chemical gradients in thin capillaries has been developed that distinguishes between axial and polar magneto-aerotaxis [68].

For both aerotactic mechanisms, migration along magnetic field lines reduces a three-dimensional search problem to a one-dimensional search problem. Thus, magnetotaxis is presumably advantageous to motile microorganisms in chemically-stratified locales because it increases the efficiency of finding and maintaining an optimal position in vertical concentration gradients, in this case, vertical oxygen gradients [69]. It is possible that there are other forms of magnetically assisted chemotaxis to molecules or ions other than oxygen, such as sulfide, or magnetically assisted redox or phototaxis in bacteria that inhabit the anaerobic zone below the OATZ.

Nevertheless, questions remain concerning the function of magnetotaxis. Many obligately microaerophilic bacteria find and maintain an optimal position at the OATZ without the help of magnetosomes, as do cultured non-magnetotactic mutants that do not make magnetosomes. Moreover, cultured magnetotactic bacteria form microaerophilic bands of cells in the absence of a magnetic field. Thus, it appears that the enormous iron uptake and magnetosome formation is somehow linked to cellular physiology and to other, as yet unknown, cellular functions.

2.8 Chemistry of Magnetosome Formation

Magnetite and greigite synthesis in magnetotactic bacteria begins with the uptake of iron. Because reduced Fe(II) is very soluble (up to 100 mM at neutral pH [70]), it is easily taken up by bacteria, usually by non-specific means. However, Fe(III) is extremely insoluble and many microbes synthesize and rely on low molecular weight

(below 1 kDa) iron chelators, called siderophores, which bind and solubilize Fe(III) for uptake [71]. These compounds are generally produced under iron-limited conditions and their synthesis repressed under high iron conditions. Although in many growth media used for cultivation of magnetotactic bacteria, iron is supplied as chelated Fe(III) (e.g. Fe(III)-quinate [18]), most of these media also contain chemical reducing agents (e.g. thioglycollate, ascorbic acid, etc.) potent enough to reduce Fe(III) to Fe(II) [18]. Thus both oxidized and reduced forms of iron are available to cells.

Several studies have focused on iron uptake in the magnetite-producing, freshwater, magnetotactic spirilla. A hydroxamate siderophore was found to be produced by cells of *M. magnetotacticum* grown under high but not under low iron conditions [72]. The siderophore production pattern here is the reverse of what is normally observed. Frankel et al. [73] originally assumed that iron uptake by this organism probably occurred via a non-specific transport system. Nakamura et al. [74] reported molecular evidence for the involvement of a periplasmic binding protein, sfuC, involved in the transport of iron by *M. magneticum* strain AMB-1. They did not detect siderophores in spent growth medium, although this species was recently found to produce both hydroxamate and phenolate siderophores [75]. Like cells of *M. magnetotacticum*, those of *M. magneticum* strain AMB-1 produce siderophores under growth conditions that would be considered to be at least iron-sufficient if not iron-rich for most prokaryotes. This unusual pattern of siderophore production could be explained by if iron is taken up by cells and rapidly converted to Fe_3O_4 that cannot be used by cells as a source of bioavailable iron. Thus, levels of iron available for growth likely decrease relatively quickly and the cells experience iron-limiting conditions stimulating siderophore production.

Schüler and Bäeuerlein [19] found that the major portion of iron for magnetite synthesis in *Magnetospirillum gryphiswaldense* was taken up as Fe(III) and that Fe(III) uptake is an energy-dependent process with Michaelis–Menten kinetics. This suggested that Fe(III) uptake by cells of *M. gryphiswaldense* involves a low-affinity, but high-velocity transport system [19]. Fe(II) was also taken up by cells by a slow, diffusion-like process. Schüler and Bäeuerlein also showed that magnetite formation was induced in non-magnetotactic cells by a low threshold oxygen concentration of about 2–7 μM (at 30 °C) and was tightly linked to Fe(III) uptake [19]. This finding is consistent with the results of Blakemore et al. [76] who found that microaerobic conditions and molecular O_2 were required for magnetite synthesis in *M. magnetotacticum.*

Frankel et al. [73] examined the nature and distribution of major iron compounds in *M. magnetotacticum* by using ^{57}Fe Mössbauer spectroscopy and proposed a model in which magnetite formation is preceded by formation of amorphous hydrous Fe(III) oxide in the magnetosome vesicles. Reduction of one third of the Fe(III) ions by electron transport into the vesicle or addition of Fe(II) results in the formation of magnetite. An amorphous electron-dense material was observed in magnetosomes by electron microscopy [3]. However, Schüler and Bäuerlein [77] showed that in cells of *M. gryphiswaldense*, Fe(III) is taken up and rapidly converted to magnetite without any apparent delay, suggesting that there is no signifi-

cant accumulation of a precursor to magnetite inside the cell at least under the conditions of the experiment which appeared optimal for magnetite production by that organism.

It is not known how the crystal habits and crystallographic orientation in the magnetosome chain is controlled, but is thought to involve specific proteins in the magnetosome membrane which both nucleate and constrain crystal growth [3].

2.9 Other Intracellular Iron Oxides and Sulfides in Bacteria

Iron-rich inclusions, other than magnetosomes, have also been observed in prokaryotic cells. Many bacteria have bacterioferritin to store intracellular iron [78]. The iron is sequestered in an 8-nm cavity in the protein as an amorphous hydrous iron phosphate (P/Fe $\sim$ 1) [79]. Some sulfate-reducing bacteria including *Desulfovibrio* and *Desulfotomaculum* species have been shown to produce intracellular electron-dense "particles" of an iron sulfide when grown in a medium containing high concentrations of iron (around 1 mM) [80]. The "particles" were arranged randomly in the cell and appeared to represent poorly ordered (amorphous) deposits of iron. In addition, the "particles" could not be separated from lysed cells using density gradient centrifugation. The function of these inclusions is unknown.

Magnetic iron oxide deposits other than magnetite magnetosomes have been identified and described in prokaryotic cells. Glasauer et al. [81] reported the presence of membrane-bounded iron oxide granules within cells of the dissimilatory iron-reducing bacterium *Shewanella putrifaciens* strain CN32 grown under an oxygen-free, H_2/Ar atmosphere with poorly crystalline, two-line ferrihydrite (a hydrous ferric oxide) as the electron acceptor (Figure 2.8). The granules appeared to be first formed near the cell membrane and then pushed into the cytoplasm. They were generally deposited at one or both ends of the cells. There was reasonable evidence from selected area electron diffraction determinations that the intracellular iron oxide particles might consist or partially consist of magnetite or maghemite (γ-Fe_2O_3) or both. Biologically induced magnetite crystals also formed extracellularly in the cultures.

There is another report of a magnetic, iron-rich, bacterial inclusion that may be an iron oxide. Vainshtein et al. [82] reported the presence of an intracellular magnet-sensitive inclusion in cells of the purple photosynthetic species, *Rhodopseudomonas palustris*, *R. rutilis* and *Ectothiorhodospira shaposhnikovii*, when grown with relatively high concentrations of iron. The inclusions were spherical particles containing an electron-transparent core surrounded with an electron-dense matrix. These particles could be separated from lysed cells and X-ray microanalysis showed that the inclusions are iron-rich, but do not contain sulfur. Interestingly, the inclusions, like magnetosomes, appear to form a chain or a "thread of beads" arranged along the long axis of the cell. The cells do show a magnetic response but are not necessarily magnetotactic. The authors speculate that these inclusions function similarly to the magnetosomes.

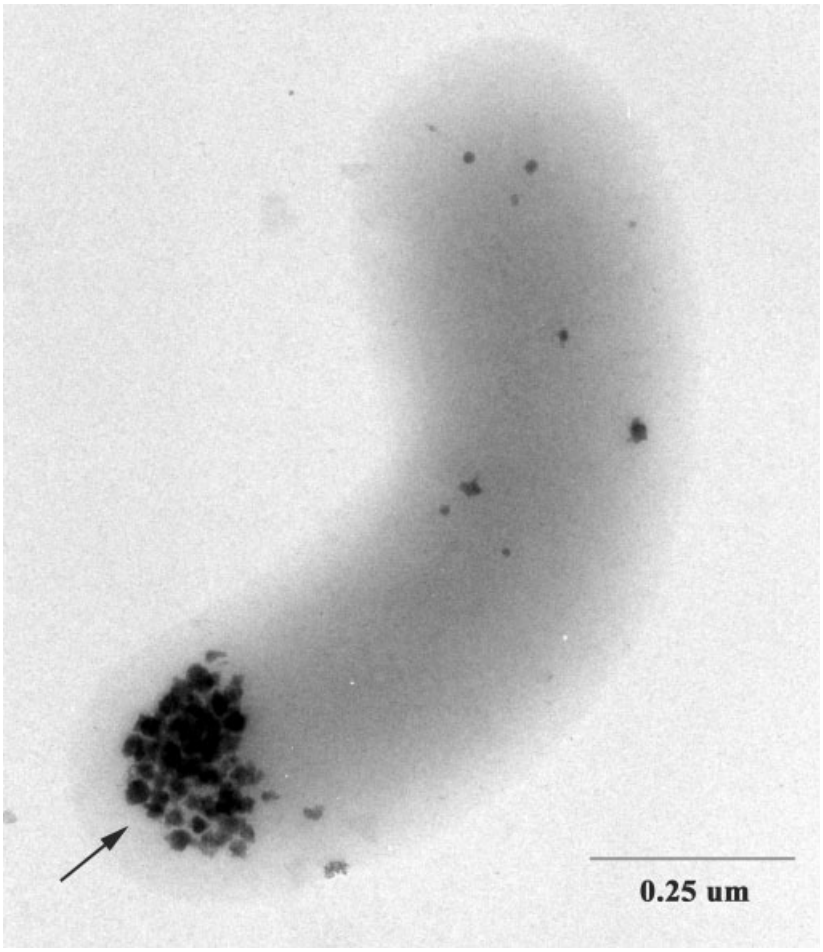

Figure 2.8 TEM of an unstained cell of *S. putrefaciens* strain CN32 grown under anaerobic conditions with hydrous ferric [Fe(III)] oxide (two-line ferrihydrite) as the terminal electron acceptor. This cell was removed from the culture after 14 days of incubation. The clump of intracellular iron-rich granules is shown at one end of the cell. (Courtesy of S. Glasauer.)

2.10 Magnetic Iron Oxides and Sulfides in Microorganisms other than Bacteria

Magnetosome or magnetosome-like magnetite particles have been observed in a number of Protistan species. They were first described in a Euglenoid alga in which several adjacent parallel chains of tooth-shaped magnetite particles are arranged in rows running down the length of the cell [15].

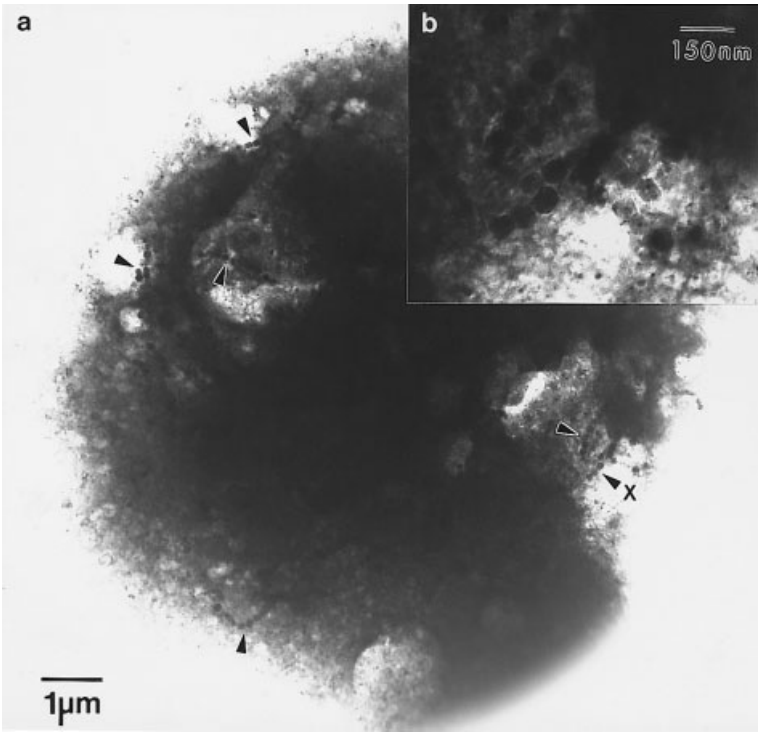

Figure 2.9 (a) Low-magnification TEM image of a magnetically responsive dinoflagellate showing numerous chains of magnetite crystals throughout the cell (at arrows). Because of the difficulty finding the particles in such a thick cell, a very high beam voltage was used which destroyed much of the cellular structure of the organism. (b, inset) High-magnification TEM image of magnetite crystals located at arrow labeled "X".

Populations of diverse, magnetically responsive protozoans have been found in the chemically stratified coastal pond, Salt Pond (Woods Hole, MA, USA; discussed earlier) [83]. These microorganisms included dinoflagellates, biflagellated Cryptomonads and a ciliate of the genus *Cyclidium*. Magnetite was identified as the mineral component in the dinoflagellate and a large Cryptomonad. Magnetite particles were arranged in chains arranged somewhat randomly within the cell and were about 55–75 nm in diameter (Figure 2.9). The particles were indistinguishable from those produced by some magnetotactic bacteria found at the site. Determination of the precise crystal habit of the particles was not possible due to the thickness of the protozoal cell. The mineral particles in other magnetically responsive protists were not identified so the possibility of greigite crystals in these microorganisms cannot be eliminated.

It is not known whether these protists biomineralize their magnetic particles or whether they ingest magnetotactic bacteria or their magnetosomes as they are released from lysing cells. It is known, however, that some species of protozoa ingest

iron particles, thereby becoming magnetic [84]. Iron is well recognized as a limiting factor in primary production in some oceanic areas and is often present in seawater in particulate and colloidal forms [85]. Barbeau et al. [85] showed that digestion of colloidal iron in the food vacuoles of protozoans during grazing of particulate and colloidal matter might generate more bioavailable iron for other species such as phytoplankton. In the case of Salt Pond, protists that ingest magnetotactic bacteria may play an important role in iron cycling by solubilizing iron in magnetosomes which might contribute to the high ferrous iron concentration at the OATZ and the high microbial cell concentrations there. Much more work is required to determine the biogeochemical roles these microorganisms play in iron cycling in chemically stratified and other aquatic habitats.

2.11 Biogenic Iron Oxides and Sulfides in Modern and Ancient Environments, their Presence in Higher Organisms, and their Use as Biomarkers

Nanophase magnetite grains have been recovered from a number of soils, freshwater sediments, and modern and ancient deep-sea sediments [86], and have been referred to as "magnetofossils" [87] (Figure 2.10). In some cases, they were identified as biogenic by their shape and size similarity to crystals in magnetotactic bacteria. Live bacteria were sometimes recovered along with the magnetite grains.

Magnetic effects have been reported in a number of higher organisms [88, 89]. For example, magnetite crystals with morphologies similar to those produced by the magnetotactic bacteria have been found in the ethmoid tissues of salmon [16] and in the human brain [90]. The fact that many higher creatures biomineralize SD crystals suggests the intriguing idea that that all these organisms share the same or similar set of genes responsible for magnetite biomineralization that would likely have originated in the magnetotactic bacteria. Thus, studying how magnetotactic bacteria biomineralize crystals of iron oxides and sulfides might have a significant scientific impact far beyond the studies of Microbiology and Geology.

2.11.1 Magnetosomes as Biomarkers for Life on Ancient Mars

A 2-kg carbonaceous stony meteorite, designated ALH84001, discovered in a glacial flow in the Allan Hills region of Antarctica in 1984 [91], was identified as a Martian meteorite by oxygen isotopic analysis in 1994. The bulk rock matrix, which constitutes around 98 % of the mass of ALH84001, crystallized 4.5 Ga (billion years) ago, comparable to the age of lunar rocks. It is the oldest of the more than 20 known Martian meteorites and the only one from the extant ancient Martian crust in the southern highlands of Mars, the region where there is evidence for the presence of liquid water in the past [92]. ALH84001 was ejected by an impact event

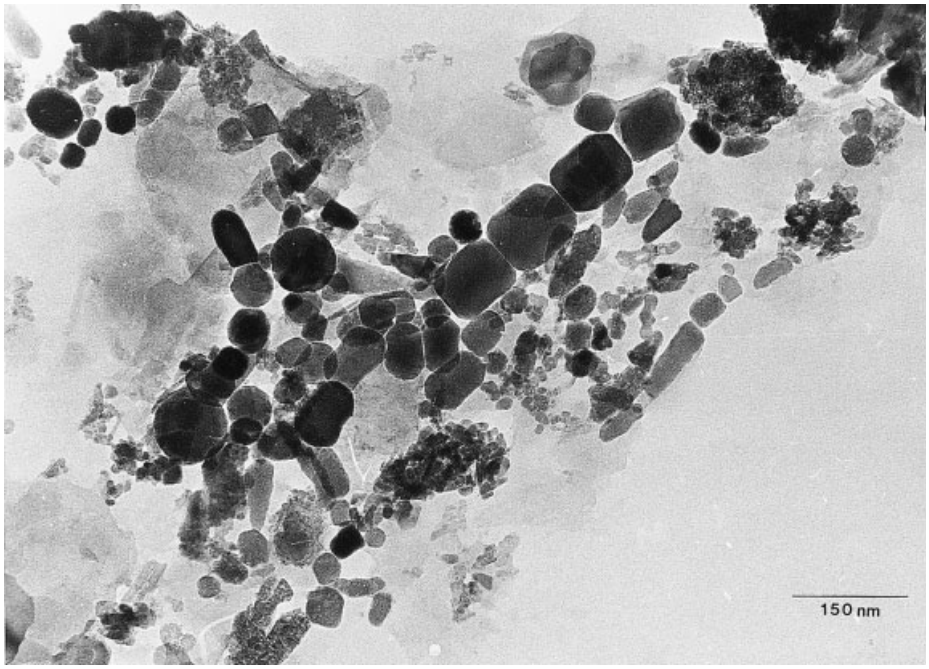

Figure 2.10 TEM image of "magnetofossils" in magnetically separated material from surface sediments collected from the Irish Sea. Cubo-octahedral, parallelepipedal and tooth-shaped magnetic crystals, presumably derived from magnetotactic bacteria, are clearly present. (Micrograph courtesy of Z. Gibbs-Eggar.)

from the surface of Mars about 16 million years ago and landed in Antarctica about 13 000 years ago.

In addition to the silicate rock matrix, the meteorite contains a number of secondary minerals including lenticular globules of chemically zoned calcium, magnesium and iron carbonates up to 250 μm in diameter in rock-matrix fractures. These globules formed about 3.9 Ga [93] and were subjected to several shock events after their formation, but prior to the ejection event [91].

In 1996, McKay et al. [94] reported four features associated with the carbonate globules that together comprise possible evidence for ancient life on Mars. These features are: (1) non-equilibrium distributions of iron, manganese, magnesium and calcium within the carbonate globules; (2) polycyclic aromatic hydrocarbons (PAHs) with a mass distribution unlike terrestrial PAHs or PAHs from other meteorites; (3) bacterium-shaped objects (BSOs) up to several hundred nanometers long that resemble fossilized terrestrial microorganisms; and (4) 10- to 100-nm magnetite, pyrrhotite and greigite crystals. These minerals were cited as evidence because of their similarity to biogenic magnetic minerals in terrestrial magnetotactic bacteria.

The ancient life on Mars hypothesis has been extensively challenged and alterna-

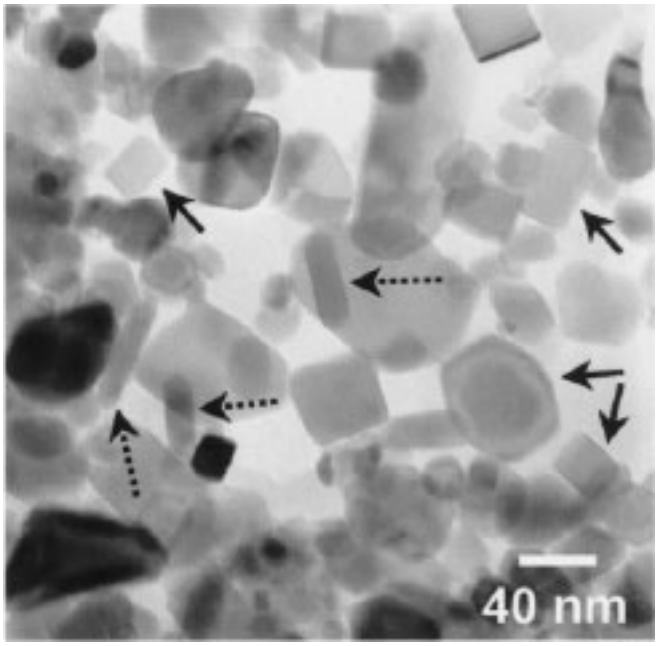

Figure 2.11 TEM of magnetite crystals from Martian meteorite ALH84001. Crystal morphologies include: irregular, cuboidal, tear-drop, rounded whiskers (dashed arrows) and elongated prisms (solid arrows) which have hexagonal or rectangular projections depending on the angle of stage rotation. (Micrograph courtesy of K. Thomas-Keprta.)

tive non-biological processes have been proposed for each of the four features cited by McKay et al. [94]. Here we review the current situation regarding the evidence for the biogenic origin of the magnetite crystals.

The magnetite crystals are primarily located in the rims of the carbonate globules. Transmission electron microscope studies of the crystals (*in situ* and removed from the carbonate matrix) have revealed a number of projected shapes [95–97] described as ribbon, whisker, quasi-rectangular and irregular (Figure 2.11). The irregular crystals have aluminum and titanium impurities [6], some of the ribbons and whiskers have screw dislocations [96, 97], and some of the whiskers are epitaxially associated with carbonate [95]. These features suggest non-biological, possibly high-temperature, origins. However, the crystals with quasi-rectangular projections, which constitute about 25 % of the total number of magnetite crystals, are reportedly chemically pure, elongated along a [111] axis and have projected hexagonal shapes when viewed along the elongation axis [96, 97]. It has been reported that these crystals are virtually identical to magnetite in the terrestrial magnetotactic bacteria [98, 99] and, moreover, crystals with these features have not been reported in any non-biological process [96]. Hence, the magnetite crystals in ALH84001 may be biogenic and therefore constitute evidence for life on ancient Mars.

2.11.2 The Biogenic Hypothesis

The biogenic hypothesis is based on independent studies by Thomas-Keprta et al. [96–98] and by Friedmann et al. [100]. Thomas-Keprta et al. [96–98] suggested six distinctive properties resulting from natural selection that taken together differentiate biogenic from abiogenic crystals of magnetite. Briefly these are: (1) narrow size range with a non-log-normal size distribution centered in the SD size range; (2) restricted width-to-length ratios optimized for maximum overlap with the SD size range of magnetite; (3) chemical purity; (4) very low density of crystal defects, with the exception of occasional twinning perpendicular to the [111] axis of elongation; (5) unusual, truncated, hexa-octahedral geometry described by the intersection of six {100} cubic faces, eight {111} octahedral faces and only six of the possible 12 dodecahedral {110} faces (i.e. those satisfying the relationship $\{110\} \cdot [111] = 0$); and (6) elongation along the [111] axis. Up to around 25 % of the magnetite crystals in the globular carbonate globules of ALH84001 reportedly display all six properties [96, 97]. The remaining roughly 75 % of the magnetite crystals lack sufficient characteristics to constrain their origin as either biogenic and/or inorganic. These magnetite crystals may have been formed by inorganic processes, including chemical precipitation from a hydrothermal fluid and/or allochtonous accumulation during carbonate formation.

On the other hand, electron holography studies have shown that magnetosome chains in some magnetotactic bacteria, e.g. *M. magnetotacticum*, with equidimensional, cubo-octahedral magnetite crystals have the same magnetic dipole per unit length as magnetosome chains in strain MV-1 with elongated, non-equidimensional magnetite crystals [62]. Thus, the evolutionary significance of the elongated habits is not obvious. Moreover, in strain MV-1 the relative sizes of the corner facets vary from crystal to crystal even in a single chain and many crystals have all 12 dodecahedral facets, although they are divided into two groups of six with respect to size [101]. Here, again, it is difficult to discern an evolutionary significance. Moreover, even if the ALH84001 and MV-1 magnetite crystals had identical habits, this in itself does not prove biogenic formation of the former crystals. Finally, it is interesting that among the 75 % of magnetite crystals judged to be non-biogenic, there are many with elongated habits [96]. This suggests that elongated habits may not be restricted to biogenic crystals.

Friedmann et al. [100] employed high-magnification, three-dimensional, backscattered, scanning electron microscopy (SEM-BSE), to ascertain the *in situ* arrangement of magnetite crystals embedded in the carbonate globules. They reported magnetite crystal chains and chain fragments, among masses of individual crystals, in the rim region of the carbonate globules. The crystal chains reportedly have uniform crystal size, uniform crystal shapes, gaps between crystals, orientation of elongated crystals along the chains and possible presence of fossilized organic material between crystals.

If correct, chains of magnetite crystals would be powerful evidence for biogenic formation, because chains of magnetite are a hallmark of terrestrial magnetotactic bacteria. However, the microanalytical methods used by Friedman et al. [100] to determine the chemical composition of the chain-forming particles did not have suf-

ficient resolution to verify that the individual crystals forming these chains were indeed magnetite. The spatial resolution also made it difficult to confirm the observations of crystal sizes, shapes and orientations [101].

2.11.3 The Non-biogenic Hypothesis

An alternative, non-biogenic, hypothesis is based on the low-temperature precipitation of carbonates [102] and subsequent thermal decomposition of iron-bearing carbonate to produce magnetite [103–105] with the implication that in ALH84001 such an event occurred through impact shock heating. Evidence for this process comes from the observation that in addition to magnetite, nano-dimensional periclase (MgO) crystals are also associated with the carbonate globules in ALH84001, particularly the magnesium-rich carbonate [104]. Both magnetite and periclase crystals are frequently associated with voids in the carbonate, suggesting a mineralization process in which CO_2 is released [104]. Some faceted magnetite and periclase crystals in carbonate are crystallographically oriented with respect to the carbonate crystal lattice [95, 104]. This is strong evidence that these magnetites formed abiogenically *in situ*. Golden et al. [105, 106] demonstrated that thermal decomposition of pure siderite [$FeCO_3$] above 450 °C results in magnetite crystals with a size range and projected shapes similar to those found in ALH84001. Some of these magnetite crystals are elongated along [111], as are the magnetite crystals in a number of magnetotactic bacteria, although there are some differences in the relative sizes of facets of the low index forms {100}, {110} and {111} [106].

On the other hand, paleomagnetic measurements [107–109] and inert gas measurements [110, 111] present evidence for little to no post-formation thermal processing of the carbonate globules necessary to produce magnetites. The paleomagnetic data show heterogeneous magnetization in the carbonates. This suggests that the carbonates were never heated above 80 °C, the experimentally measured superparamagnetic blocking temperature.

2.11.4 Iron Isotopic Fractionation

Although analyses of the sizes and shapes of fine-grained magnetite crystals as well as other characteristics might prove to be robust criteria, additional methods are required to distinguish between biogenic and non-biogenic, nanophase, magnetic iron minerals. Advances in multicollector, inductively coupled plasma, mass spectroscopy (MC-ICP-MS) have made it possible to detect variations in iron isotopic ratios ($^{56}Fe/^{54}Fe$) as low as 0.1 ‰ in samples as small as 1 ng of iron. Measurements by Walczyk and von Blanckenburg [112] have shown isotopic enrichment of ^{54}Fe relative to ^{56}Fe of the order of 2.6 ‰ in human blood compared to dietary iron, and up to 3 ‰ relative to inorganic iron. Mandernack et al. [113] found a temperature-dependent fractionation of oxygen isotopes in magnetite produced by *M. magnetotacticum* and strain MV-1 that closely matched that for extracellular magnetite produced by a bacterial consortium containing thermophilic iron-

reducing bacteria [114]. However, no detectable fractionation of iron isotopes was observed in the bacterial magnetite compared to the growth medium. In contrast, Beard et al. [115] found enrichment of ^{54}Fe compared to ^{56}Fe of the order of 1 ‰ in the soluble ferrous iron produced by a dissimilatory iron-reducing bacterium, *Shewanella algae*, growing with the iron oxide mineral ferrihydrite. How this isotopic fractionation is reflected in magnetite formed by this organism and other iron-reducing bacteria remains to be seen, but could provide a means for distinguishing biologically induced magnetite from abiotic magnetite. It should also be noted that studies Fe(II) oxidation consistently show a smaller isotopic fractionation for biotic oxidation (1.5–2.5 ‰) than for abiotic oxidation (3–4 ‰) [116]. Moreover, Witte et al. [117] conclude from iron isotope studies of biotically and abiotically precipitated iron oxides that it may not be possible to distinguish biogenic from non-biogenic iron oxides. Nevertheless, this technique holds great promise for future studies.

Acknowledgments

We thank M. Pósfai and P. R. Buseck for Figure 2.5(b), S. Glasauer for Figure 2.8, Z. Gibbs-Eggar for Figure 2.10, K. Thomas-Keprta for Figure 2.11, and P. R. Buseck, B. Devouard, K. W. Mandernack, M. Pósfai and D. Schüler for valuable discussions. D. A. B. acknowledges financial support from the US National Science Foundation (NSF) grant EAR-0311950 and the US National Aeronautics and Space Administration (NASA) Johnson Space Center grant NAG 9-1115.

References

[1] J. F. Banfield, K. H. Nealson (Eds), *Geomicrobiology: Interactions Between Microbes and Minerals*, Mineralogical Society of America, Washington, DC, **1997**.
[2] (a) H. A. Lowenstam, *Science* **1981**, *211*, 1126–1131; (b) H. A. Lowenstam, S. Weiner, *On Biomineralization*, Oxford University Press, New York, **1989**.
[3] S. Mann, R. B. Frankel, in *Biomineralization: Chemical and Biochemical Perspectives* (Eds S. Mann, J. Webb, R. J. P. Williams), VCH, Weinheim, **1989**, pp. 389–426.
[4] D. R. Lovley, *Microbiol. Rev.* **1991**, *55*, 259–287.
[5] D. T. Rickard, *Stockholm Contrib. Geol.* **1969**, *20*, 50–66.
[6] D. R. Lovley, in *Iron Biominerals* (Eds R. B. Frankel, R. P. Blakemore), Plenum Press, New York, **1990**, pp. 151–166.
[7] N. H. C. Sparks, S. Mann, D. A. Bazylinski, D. R. Lovley, H. W. Jannasch, R. B. Frankel, *Earth Planet. Sci. Lett.* **1990**, *98*, 14–22.
[8] R. P. Blakemore, *Annu. Rev. Microbiol.* **1982**, *36*, 217–238.
[9] D. L. Balkwill, D. Maratea, R. P. Blakemore, *J. Bacteriol.* **1980**, *141*, 1399–1408.
[10] R. B. Frankel, R. P. Blakemore, R. S. Wolfe, *Science* **1979**, *203*, 1355–1356.
[11] S. Mann, N. H. C. Sparks, R. B. Frankel, D. A. Bazylinski, H. W. Jannasch, *Nature* **1990**, *343*, 258–260.
[12] Y. A. Gorby, T. J. Beveridge, R. P. Blakemore, *J. Bacteriol.* **1988**, *170*, 834–841.

[13] D. A. Bazylinski, *ASM News* **1995**, *61*, 337–343.
[14] D. A. Bazylinski, B. M. Moscowitz, in *Geomicrobiology: Interactions Between Microbes and Minerals* (Eds J. F. Banfield, K. H. Nealson), Mineralogical Society of America, Washington, DC, **1997**, pp. 181–223.
[15] F. F. Torres de Araujo, M. A. Pires, R. B. Frankel, C. E. M. Bicudo, *Biophys. J.* **1986**, *50*, 385–378.
[16] S. Mann, N. H. C. Sparks, M. M. Walker, J. L. Kirschvink, *J. Exp. Biol.* **1988**, *140*, 35–49.
[17] S. Spring, R. Amann, W. Ludwig, K.-H. Schleifer, N. Petersen, *Syst. Appl. Microbiol.* **1992**, *15*, 116–122.
[18] R. P. Blakemore, D. Maratea, R. S. Wolfe, *J. Bacteriol.* **1979**, *140*, 720–729.
[19] D. Schüler, E. Bäeuerlein, *Arch. Microbiol.* **1996**, *166*, 301–307.
[20] D. A. Bazylinski, B. R. Heywood, S. Mann, R. B. Frankel, *Nature* **1993**, *366*, 218.
[21] D. A. Bazylinski, R. B. Frankel, B. R. Heywood, S. Mann, J. W. King, P. L. Donaghay, A. K. Hanson, *Appl. Environ. Microbiol.* **1995**, *61*, 232–3239.
[22] S. Spring, R. Amann, W. Ludwig, K.-H. Schleifer, H. van Gemerden, N. Petersen, *Appl. Environ. Microbiol.* **1993**, *59*, 2397–2403.
[23] P. L. Donaghay, H. M. Rines, J. M. Sieburth, *Arch. Hydrobiol. Beih. Ergebn. Limnol.* **1992**, *36*, 97–108.
[24] S. G. Wakeham, B. L. Howes, J. W. H. Dacey, R. P. Schwarzenbach, J. Zeyer, *Geochim. Cosmochim. Acta* **1987**, *51*, 1675–1684.
[25] E. F. DeLong, R. B. Frankel, D. A. Bazylinski, *Science* **1993**, *259*, 803–806.
[26] F. C. Meldrum, B. R. Heywood, S. Mann, R. B. Frankel, D. A. Bazylinski, *Proc. R. Soc. Lond. B* **1993**, *251*, 237–242.
[27] R. B. Frankel, D. A. Bazylinski, M. Johnson, B. L. Taylor, *Biophys. J.* **1997**, *73*, 994–1000.
[28] F. C. Meldrum, B. R. Heywood, S. Mann, R. B. Frankel, D. A. Bazylinski, *Proc. R. Soc. Lond. B* **1993**, *251*, 231–236.
[29] D. Maratea, R. P. Blakemore, *Int. J. Syst. Bacteriol.* **1981**, *31*, 452–455.
[30] K.-H. Schleifer, D. Schüler, S. Spring, M. Weizenegger, R. Amann, W. Ludwig, M. Kohler, *Syst. Appl. Microbiol.* **1991**, *14*, 379–385.
[31] T. Matsunaga, F. Tadokoro, N. Nakamura, *IEEE Trans. Magnetics* **1990**, *26*, 1557–1559.
[32] T. Matsunaga, T. Sakaguchi, F. Tadokoro, *Appl. Microbiol. Biotechnol.* **1991**, *35*, 651–655.
[33] D. Schüler, S. Spring, D. A. Bazylinski, *Syst. Appl. Microbiol.* **1999**, *22*, 366–471.
[34] T. Sakaguchi, J. G. Burgess, T. Matsunaga, *Nature* **1993**, *365*, 47–49.
[35] Y. A. Gorby, PhD thesis, University of New Hampshire, **1989**.
[36] K. M. Towe, T. T. Moench, *Earth Planet. Sci. Lett.* **1981**, *52*, 213–220.
[37] D. A. Bazylinski, A. J. Garratt-Reed, R. B. Frankel, *Microsc. Res. Tech.* **1994**, *27*, 389–401.
[38] T. Matsuda, J. Endo, N. Osakabe, A. Tonomura, T. Arii, *Nature* **1983**, *302*, 411–412.
[39] R. P. Blakemore, R. B. Frankel, A. J. Kalmijn, *Nature* **1980**, *236*, 384–385.
[40] S. Mann, N. H. C. Sparks, R. P. Blakemore, *Proc. R. Soc. Lond. B* **1987**, *231*, 469–476.
[41] S. Mann, N. H. C. Sparks, R. P. Blakemore, *Proc. R. Soc. Lond. B* **1987**, *231*, 477–487.
[42] C. Palache, H. Berman, C. Frondel, *Dana's System of Mineralogy*, Wiley, New York, **1944**.
[43] S. Mann, R. B. Frankel, R. P. Blakemore, *Nature* **1984**, *310*, 405–407.
[44] B. Devouard, M. Pósfai, X. Hua, D. A. Bazylinski, R. B. Frankel, P. R. Buseck, *Am. Mineral.* **1998**, *83*, 1387–1398.
[45] (a) B. M. Moskowitz, *Rev. Geophys. Suppl.* **1995**, 123–128; (b) M. Farina, B. Kachar, U. Lins, R. Broderick, H. Lins de Barros, *J. Microsc.* **1994**, *173*, 1–8.
[46] B. M. Moskowitz, R. B. Frankel, D. A. Bazylinski, H. W. Jannasch, D. R. Lovley, *Geophys. Res. Lett.* **1989**, *16*, 665–668.
[47] D. D. Eberl, V. A. Drits, J. Srodon, *Am. J. Sci.* **1998**, *298*, 499–533.
[48] D. A. Bazylinski, R. B. Frankel, A. J. Garratt-Reed, S. Mann, in *Iron Biominerals* (Eds R. B. Frankel, R. P. Blakemore), Plenum Press, New York, **1990**, pp. 239–255.
[49] M. Farina, D. M. S. Esquivel, H. G. P. Lins de Barros, *Nature* **1990**, *343*, 256–258.
[50] M. Farina, H. Lins de Barros, D. M. S. Esquivel, J. Danon, *Biol. Cell* **1983**, *48*, 85–88.
[51] F. G. Rogers, R. P. Blakemore, N. A. Blakemore, R. B. Frankel, D. A. Bazylinski, D. Maratea, C. Rogers, *Arch. Microbiol.* **1990**, *154*, 18–22.

[52] B. R. Heywood, D. A. Bazylinski, A. J. Garratt-Reed, S. Mann, R. B. Frankel, *Naturwiss.* **1990**, *77*, 536–538.
[53] B. R. Heywood, S. Mann, R. B. Frankel, in *Materials Synthesis Based on Biological Processes* (Eds M. Alpert, P. Calvert, R. B. Frankel, P. Rieke, D. Tirrell), Materials Research Society, Pittsburgh, PA, **1991**, pp. 93–108.
[54] M. Pósfai, P. R. Buseck, D. A. Bazylinski, R. B. Frankel, *Science* **1998**, *280*, 880–883.
[55] M. Pósfai, P. R. Buseck, D. A. Bazylinski, R. B. Frankel, *Am. Mineral.* **1998**, *83*, 1469–1481.
[56] R. A. Berner, *J. Geol.* **1964**, *72*, 293–306.
[57] R. A. Berner, *Am. J. Sci.* **1967**, *265*, 773–785.
[58] D. A. Bazylinski, A. J. Garratt-Reed, A. Abedi, R. B. Frankel, *Arch. Microbiol.* **1993**, *160*, 35–42.
[59] A. R. Lennie, S. A. T. Redfern, P. E. Champness, C. P. Stoddart, F. F. Schofield, D. J. Vaughn, *Am. Mineral.* **1997**, *82*, 302–309.
[60] (a) T. T. Moench, W. A. Konetzka, *Arch. Microbiol.* **1978**, *119*, 203–212; (b) T. T. Moench, *Antonie van Leeuwenhoek* **1988**, *54*, 483–496.
[61] R. B. Frankel, *Annu. Rev. Biophys. Bioeng.* **1984**, *13*, 85–103.
[62] R. E. Dunin-Borkowski, M. R. McCartney, R. B. Frankel, D. A. Bazylinski, M. Pósfai, P. R. Buseck, *Science* **1998**, *282*, 1868–1870.
[63] A. M. Spormann, R. S. Wolfe, *FEMS Lett.* **1984**, *22*, 171–177.
[64] I. B. Zhulin, V. A. Bespelov, M. S. Johnson, B. L. Taylor, *J. Bacteriol.* **1996**, *178*, 5199–5204.
[65] J. E. Segall, S. M. Block, H. C. Berg, *Proc. Natl Acad. Sci. USA* **1986**, *83*, 8987–8991.
[66] B. L. Taylor, *Trends Biochem. Sci.* **1983**, *8*, 438–441.
[67] R. P. Blakemore, *Science* **1975**, *190*, 377–379.
[68] R. B. Frankel, D. A. Bazylinski, D. Schüler, *Supramol. Sci.* **1998**, *5*, 383–390.
[69] R. B. Frankel, D. A. Bazylinski, *Hyperfine Interactions* **1994**, *90*, 135–142.
[70] J. B. Neilands, *Biol. Metals* **1984**, *4*, 1–6.
[71] M. L. Guerinot, *Annu. Rev. Microbiol.* **1994**, *48*, 743–772.
[72] L. C. Paoletti, R. P. Blakemore, *J. Bacteriol.* **1986**, *167*, 73–76.
[73] R. B. Frankel, G. C. Papaefthymiou, R. P. Blakemore, W. O'Brien, *Biochim. Biophys. Acta* **1983**, *763*, 147–159.
[74] C. Nakamura, T. Sakaguchi, S. Kudo, J. G. Burgess, K. Sode, T. Matsunaga, *Appl. Biochem. Biotechnol.* **1993**, *39/40*, 169–176.
[75] R. J. Calugay, H. Miyashita, Y. Okamura, T. Matsunaga, *FEMS Microbiol. Lett.* **2003**, *218*, 371–375.
[76] R. P. Blakemore, K. A. Short, D. A. Bazylinski, C. Rosenblatt, R. B. Frankel, *Gemicrobiol. J.* **1985**, *4*, 53–71.
[77] D. Schüler, E. Bäuerlein, *J. Bacteriol.* **1998**, *180*, 159–162.
[78] (a) E. I. Steifel, G. D. Watt, *Nature* **1979**, *279*, 81–83; (b) S. C. Andrews, J. B. C. Findlay, J. R. Guest, P. M. Harrison, J. N. Keen, J. M. A. Smith, *Biochim. Biophys. Acta* **1991**, *1078*, 111–116.
[79] G. D. Watt, R. B. Frankel, D. Jacobs, H. Heqing, G. C. Papaefthymiou, *Biochemistry* **1992**, *31*, 5672–5679.
[80] H. E. Jones, P. A. Trudinger, L. A. Chambers, N. A. Pyliotis, *Z. Allg. Mikrobiol.* **1976**, *16*, 425–435.
[81] S. Glasauer, S. Langley, T. J. Beveridge, *Science* **2001**, *295*, 117–119.
[82] M. Vainshtein, N. Suzina, V. Sorokin, *Syst. Appl. Microbiol.* **1997**, *20*, 182–186.
[83] D. A. Bazylinski, D. R. Schlezinger, B. H. Howes, R. B. Frankel, S. S. Epstein, *Chem. Geol.* **1999**, *169*, 319–328.
[84] J. L. Rifkin, R. Ballentine, *Trans. Am. Microsc. Soc.* **1976**, *95*, 189–197.
[85] K. Barbeau, J. W. Moffett, D. A. Caron, P. L. Croot, D. L. Erdner, *Nature* **1996**, *380*, 61–64.
[86] (a) N. Petersen, T. von Dobeneck, H. Vali, *Nature* **1986**, *320*, 611–615; (b) J. F. Stolz, S.-B. R. Chang, J. L. Kirschvink, *Nature* **1986**, *321*, 849–850; (c) S.-B. R. Chang, J. L. Kirschvink, *Annu. Rev. Earth Planet. Sci.* **1989**, *17*, 169–195; (d) J. Akai, S. Takaharu, S. Okusa, *J. Electron Microsc.* **1991**, *40*, 110–117.
[87] (a) J. L. Kirschvink, S.-B. R. Chang, *Geology* **1984**, *12*, 559–562; (b) S.-B. R. Chang, J. F. Stolz, J. L. Kirschvink, *Precambrian Res.* **1989**, *43*, 305–315.

[88] A. J. Kobayashi, J. L. Kirschvink, in *Electromagnetic Fields: Biological Interactions and Mechanisms. ACS Advances in Chemistry Series 250* (Ed. M. Blank), American Chemical Society, Washington, DC, **1995**, pp. 367–394.
[89] M. M. Walker, C. E. Diebel, C. V. Haugh, P. M. Pankhurst, J. C. Montgomery, *Nature* **1997**, *390*, 371–373.
[90] J. L. Kirschvink, A. Kobayashi-Kirschvink, B. J. Woodford, *Proc. Natl Acad. Sci. USA* **1992**, *89*, 7683–7687.
[91] A. H. Treiman, *Meteorit. Planet. Sci.* **1998**, *33*, 753–764.
[92] Rover Team, *Science* **1997**, *278*, 1765–1768.
[93] L. E. Borg, N. Connelly, L. E. Nyquist, C.-Y. Shih, H. Wiesmann, Y. Reese, *Science* **1999**, *286*, 90–94.
[94] D. S. McKay, E. K. Gibson, Jr, K. L.Thomas-Keprta, H. Vali, C. S. Romanek, S. J. Clemett, X. D. F. Chillier, C. R. Maechling, R. N. Zare, *Science* **1996**, *273*, 924–930.
[95] J. P. Bradley, H. Y. McSween, Jr, R. P. Harvey, *Meteorit. Planet. Sci.* **1998**, *33*, 765–773.
[96] K. L. Thomas-Keprta, D. A. Bazylinski, J. L. Kirschvink, S. J. Clemett, D. S. McKay, S. J. Wentworth, H. Vali, E. K. Gibson, Jr, C. S. Romanek, *Geochim. Cosmochim. Acta* **2000**, *64*, 4049–4081.
[97] K. L. Thomas-Keprta, S. J. Clemett, D. A. Bazylinski, J. L. Kirschvink, D. S. McKay, S. J. Wentworth, H. Vali, E. K. Gibson, Jr, M. F. McKay, C. S. Romanek, *Proc. Natl Acad. Sci. USA* **2001**, *98*, 2164–2169.
[98] K. L. Thomas-Keprta, S. J. Clemett, D. A. Bazylinski, J. L. Kirschvink, D. S. McKay, S. J. Wentworth, H. Vali, E. K. Gibson, Jr, C. S. Romanek, *Appl. Environ. Microbiol.* **2002**, *68*, 3663–3672.
[99] S. J. Clemett, K. L. Thomas-Keptra, J. Shimmin, M. Morphew, J. R. McIntosh, D. A. Bazylinski, J. L. Kirschvink, S. J. Wentworth, D. S. McKay, H. Vali, E. K. Gibson, Jr, C. S. Romanek, *Am. Mineral.* **2002**, *87*, 1727–1730.
[100] E. I. Friedmann, J. Wierzchos, C. Ascaso, M. Winklhofer, *Proc. Natl Acad. Sci. USA* **2001**, *98*, 2176–2181.
[101] P. R. Buseck, R. E. Dunin-Borkowski, B. Devouard, R. B. Frankel, M. R. McCartney, P. A. Midgley, M. Pósfai, M. Weyland, *Proc. Natl Acad. Sci. USA* **2001**, *98*, 13490–13495.
[102] D. C. Golden, D. W. Ming, C. S. Schwandt, R. V. Morris, S. V. Yang, G. E. Lofgren, *Meteorit. Planet. Sci.* **2000**, *35*, 457–465.
[103] E. R. D. Scott, *J. Geophys. Res.* **1999**, *104*, 3803–3813.
[104] D. J. Barber, E. R. D. Scott, *Proc. Natl Acad. Sci. USA* **2002**, *99*, 6556–6561.
[105] D. C. Golden, D. W. Ming, C. S. Schwandt, H. V. Lauer, R. A. Socki, *Am. Mineral.* **2001**, *8*, 370–375.
[106] D. C. Golden, D. W. Ming, R. V. Morris, A. J. Brearley, H. V. Lauer, Jr, A. H. Treiman, M. E. Zolensky, C. S. Schwandt, G. E. Lofgren, G. McKay, *Am. Mineral.* **2003**, submitted.
[107] J. L. Kirschvink, A. T. Maine, H. Vali, *Science* **1997**, *275*, 1629–1633.
[108] B. P. Weiss, J. L. Kirschvink, F. J. Baudenbacher, H. Vali, N. T. Peters, F. A. MacDonald, J. P. Wikswo, *Science* **2001**, *290*, 791–795.
[109] B. P. Weiss, H. Vali, F. J. Baudenbacher, J. L. Kirschvink, S. T. Stewart, D. L. Shuster, *Earth Planet. Sci. Lett.* **2002**, *201*, 449–464.
[110] D. D. Bogard, D. H. Garrison, *Meteorit. Planet. Sci.* **1999**, *34*, 451–473.
[111] B. P. Weiss, D. L. Shuster, S. T. Stewart, *Earth Planet. Sci. Lett.* **2002**, *201*, 465–472.
[112] T. Walczyk, F. von Blanckenburg, *Science* **2002**, *295*, 2065–2066.
[113] K. W. Mandernack, D. A. Bazylinski, W. C. Shanks, T. D. Bullen, *Science* **1999**, *285*, 1892–1896.
[114] C. Zhang, S. Liu, T. J. Phelps, D. R. Cole, J. Horita, S. M. Fortier, *Geochim. Cosmochim. Acta* **1997**, *61*, 4621–4632.
[115] B. L. Beard, C. M. Johnson, L. Cox, H. Sun, K. H. Nealson, C. Aguilar, *Science* **1999**, *285*, 1889–1892.
[116] K. W. Mandernack, N. Balci, K. Witte, B. Mayer, T. D. Bullen, W. C. Shanks, in *Geol. Soc. Am. Conf.*, Seattle, WA, November 2–5, **2003**, abstr. 110-7.
[117] K. Witte, K. W. Mandernack, T. D. Bullen, D. Emerson, N. Balci, W. C. Shanks, in *Geol. Soc. Am. Conf.*, Denver, CO, October 27–30, **2002**, abstr. 5-7.

3 Phylogeny and *In Situ* Identification of Magnetotactic Bacteria

Rudolf Amann, Ramon Rossello-Mora, Christine Flies and Dirk Schüler

3.1 Microbial Diversity and the Problem of Culturability

In the last decade molecular biological data have reinforced what is common knowledge to microbiologists – it is difficult to grow bacteria in pure culture! Some of those bacteria that are most conspicuous under the microscope have until now resisted all attempts of enrichment and cultivation. Among them are symbiotic prokaryotes like those chemolithoautotrophic bacteria found in marine invertebrates, the many bacteria and archaea dwelling in protozoa, slow-growing bacteria adapted to life in oligotrophic environments, and also magnetotactic bacteria [1]. The comparative analysis of bacterial 16S rRNA sequences directly retrieved from various environments by techniques pioneered by Woese [2] has proven that the about 5000 validly described bacterial species represent only a small part, likely less than 1 %, of the extant bacterial diversity [1, 3]. The combination of cultivation-independent rRNA gene retrieval, comparative sequence analysis and fluorescence *in situ* hybridization (FISH) has been shown to allow for phylogenetic affiliation and *in situ* identification of hitherto uncultured bacteria [4]. In this chapter we will review the application of this methodology to magnetotactic bacteria.

3.2 The rRNA Approach to Microbial Ecology and Evolution

The rRNA approach to microbial ecology and evolution was first described by a group of scientists including Norman Pace and David Stahl in 1986 [5]. It is based on the comparative sequence analysis of rRNA [2]. The different rRNA molecules, in bacteria the 5S, 16S and 23S rRNAs with approximate lengths of about 120, 1500 and 3000 nucleotides, are essential components of all ribosomes. These are the cellular protein factories present in every cell in high copy numbers. Their sequences are evolutionary quite conserved, but also contain regions in which changes accumulate more rapidly. Due to their ubiquity, conserved function and lack of lateral gene transfer, the longer 16S and 23S rRNA molecules, in particular, are ideal

Biomineralization: From Biology to Biotechnology and Medical Application, Second Edition. Edited by E. Bäuerlein

ISBN: 3-527-31065-7

chronometers for the reconstruction of bacterial evolution [2]. Furthermore, these two molecules contain highly conserved sites which allow their amplification from the rRNA genes present in environmental DNA by the polymerase chain reaction (PCR) [1, 3]. In the currently most widespread format, almost full-length 16S rRNA genes are amplified from conserved sites existing at the 5′ and 3′ ends of this molecule. The resulting mixed amplificates should reflect the natural bacterial community. It is subsequently ligated into a plasmid vector and cloned into *Escherichia coli* using standard molecular biology techniques. The cloning step allows segregation of the different fragments. This is necessary for the sequencing and in its effect is comparable to the segregation of individual strains by growth on agar plates.

In addition, denaturing gradient gel electrophoresis (DGGE) of PCR-amplified 16S rDNA fragments [6] was established as a less time-consuming alternative to the cloning step. DGGE permits the cultivation-independent analysis of the composition of complex microbial communities. The method allows the separation of double-stranded DNA fragments with identical lengths, but sequence heterogeneities, based on the different melting properties in polyacrylamide gels with a linearly increasing gradient of the DNA denaturants urea and formamide. After excision of bands and re-amplification, the DNA fragments can be sequenced. The 16S rRNA sequences thereby retrieved from environmental samples without cultivation of the original bacteria are then compared to large 16S rRNA sequence databases that contain more than 90 % of the 16S rRNA sequences of the hitherto cultured, validly described bacteria.

By comparative analyses, the closest known sequence can be identified and a 16S rRNA-based evolutionary tree can be reconstructed which either places the new sequence to a known phylogenetic group or on a new branch of the universal tree. The comparative analysis does, however, also allow the identification of sequence idiosyncrasies that, like a fingerprint, may serve for the identification of the new sequence. This sequence can then be the target for an oligonucleotide probe, which is a short, single-stranded piece of nucleic acid labeled with a marker molecule. Often a short oligonucleotide of 15–25 nucleotides is sufficient to discriminate by hybridization the 16S rRNA sequence retrieved from the environment from all other known sequences. The binding of a probe to a fully or partially complementary target is called hybridization. Under optimized conditions the hybridization is specific, meaning that the probe only binds to the target nucleic acid, but not to other (non-target) nucleic acids. The probes can be used to quantify the target nucleic acids in a mixture of environmental nucleic acids. In one particular technique, FISH, the nucleic acid probe is labeled with a fluorescent dye molecule and incubated with fixed, permeabilized environmental samples. During an incubation of one to several hours under defined conditions, the probes diffuse into the cells and bind specifically to their complementary target sites. Due to the fact that the 16S rRNA is quite abundant in bacterial cells, e.g. a rapidly growing *E. coli* cell contains about 70 000 copies of the molecule, even fluorescein-monolabeled oligonucleotides are sensitive enough to visualize individual bacterial cells by epifluorescence microscopy [1]. Using FISH, the 16S rRNA sequence retrieved from the environment is linked to defined cells, with a certain abundance, shape and spatial distribution. With this

so-called full cycle rRNA approach, bacteria can be phylogenetically affiliated and identified without prior cultivation.

3.3 Application of the rRNA Approach to Magnetotactic Bacteria

The potential of the rRNA approach for analysis of hitherto uncultured bacteria has also been demonstrated on various conspicuous bacteria, including magnetotactic bacteria. Although these have shapes and sizes typical of bacteria, they, if present, become conspicuous when live mounts of marine or freshwater surface sediments are exposed to changing magnetic fields. A fraction of cells decisively swims along the lines of the magnetic field and immediately follows any change in its orientation. Methods for their visualization and enrichment were developed after their discovery in 1975 by Blakemore [7]. When working with magnetotactic bacteria one has the unique advantage that they can be readily separated from sediment particles and other bacteria based on their magnetotaxis. However, of the many morphotypes detected, including spirilla, cocci, vibrios, ovoid, rod-shaped and even multicellular bacteria, only a few bacteria have been brought into pure culture (for review, see [8]). Some members of this interesting group of bacteria with their ferromagnetic crystalline inclusions were therefore investigated by the cultivation-independent rRNA approach. The main questions of interest were as follows. (1) Is the morphological diversity reflected in a diversity at the level of 16S rRNA? Here, the two alternative answers are that there exist only a few species of magnetotactic bacteria that have a variable morphology (pleomorphism) or that several species are hidden behind one common morphotype. (2) Are the magnetotactic bacteria forming a monophyletic group or are ferromagnetic crystalline inclusions found in different phylogenetic groups? (3) Has this specific trait developed once or independently several times during bacterial evolution?

3.4 The Genus *Magnetospirillum* Encompassing Culturable Magnetotactic Bacteria

It was the obvious starting point to determine the 16S rRNA sequences of the pure cultures available. Schleifer et al. [9] studied the two pure cultures available in 1991 and created the genus *Magnetospirillum* with the two species *Magnetospirillum magnetotacticum* (formerly *Aquaspirillum magnetotacticum* [10]) and *Magnetospirillum gryphiswaldense* [9]. In parallel, the sequence of *A. magnetotacticum* was determined by Eden et al. [11]. The 16S rRNA sequences of the two species affiliated them with

the α-proteobacteria, whereas the type species of the genus *Aquaspirillum* falls in the *β*-proteobacteria. *M. magnetotacticum* and *M. gryphiswaldense* strain MSR-1 share a similarity of 94.1 %, while the corresponding similarity values to the other proteobacterial sequences available at that time where between 84 and 89 %. The two culturable magnetospirilla have a very similar cell size (0.2–0.7 × 1–3 μm) and ultrastructure with respect to the arrangement (single chain of up to 60 magnetosomes), size (diameter approximately 40–45 nm) and cubo-octahedral crystal structure of magnetosomes as well as flagellation (single flagella at each pole). However, there are also differences such as oxidase and catalase activities that are found only in strain MSR-1, which has an increased oxygen tolerance. The mol% G + C content of MSR-1, originally reported to be 71 %, considerably higher than that of *M. magnetotacticum* (64.5 %) [9], was recently reexamined by a high-performance liquid chromatography-based technique and found to be 62.7 %, close to a new value for *M. magnetotacticum* of 63 % [12].

In 1993, Matsunaga's group [13] published the evolutionary relationships between the two facultatively anaerobic strains of magnetic spirilla (AMB-1 and MGT-1) and the genus *Magnetospirillum*. The 16S rRNAs of AMB-1 and MGT-1 share 98–99 % similarity with that of *M. magnetotacticum*, but only 95–96 % with that of *M. gryphiswaldense*. They clearly fall in the genus *Magnetospirillum* and their proximity to *M. magnetotacticum* at the 16S rRNA level does not exclude the placement of the strains AMB-1 and MGT-1 in this species. The authors also note that there are clearly two groups of magnetospirilla: the one around *M. magnetotacticum*, including MGT-1 and AMB-1, and the one with *M. gryphiswaldense* that are about as distant from each other as they are from some non-magnetotactic photo-organotrophic spirilla, e.g. *Phaeospirillum* (formerly *Rhodospirillum*) *fulvum* and *P. molischianum*.

Further diversity of magnetospirilla was recently revealed by a study of Schüler et al. [14] in which a new two-layer isolation medium with opposing oxygen and sulfide gradients was used for cultivation. Using this technique, seven strains of microaerophilic magnetotactic spirilla could be isolated from one freshwater pond in Iowa, USA. While the 16S rRNA sequences of five of the isolates (MSM-1, -6, -7, -8 and -9) were very similar to either *M. gryphiswaldense* or *M. magnetotacticum* (over 99.7 %), two (MSM-3 and -4) are likely to represent a third phylogenetic cluster and at least one additional species. Considerable diversity seems to exist within this genus of culturable magnetic bacteria. In a recent study, a number of novel magnetotactic spirilla strains were isolated from various freshwater habitats including a ditch and several ponds in Northern Germany [15]. Again, 16S rRNA analysis affiliated them all with the genus *Magnetospirillum*, with highest similarity to strain MSM-6. Interestingly, several recent reports described the isolation of bacteria which can be clearly identified as *Magnetospirillum* species by morphological, physiological and 16S rRNA sequence analysis, but which lack the capability to form magnetosomes ([16, 17] and others). It will be interesting to see if these non-magnetic "Magnetospirilla" are distinguished from their magnetic relatives by the absence of biomineralization genes, i.e. the magnetosome island [18].

Nevertheless, all isolates seem to represent only a minority of the magnetotactic population and are not abundant in the environment [19].

3.5 Phylogenetic Diversity and *In Situ* Identification of Uncultured Magnetotactic Cocci from Lake Chiemsee

The sequences of the two cultivated *Magnetospirillum* strains were subsequently compared to sequences originating from the upper sediment layers of Lake Chiemsee, a large, mesotrophic freshwater lake in Upper Bavaria, Germany [20]. The sediment was stored on a laboratory shelf protected from direct light for several weeks in a 30-l aquarium. At that time, high numbers of magnetotactic bacteria could be detected in wet mounts of subsamples taken right beneath the water–sediment interface. An enrichment was obtained based on magnetotactic swimming into sterile water or diluted agarose. It contained four distinct morphotypes: cocci, two big rods of distinct morphology (one slightly bent and therefore originally referred to as "big vibrio" [20]) and small vibrios. The 5′-end 16S rRNA gene fragments of about 800 nucleotides were PCR-amplified directly from the enriched cells without further DNA isolation and segregated by cloning. From the 54 clones analyzed, 21 different sequence types could be discriminated. Most of them grouped with 16S rRNA sequences of α-proteobacteria, several with other proteobacteria and one sequence, later shown not to originate from a magnetotactic bacterium, was found to be identical to the 16S rRNA of *Mycobacterium chitae*.

Three probes constructed complementary to signature regions of the most frequent α-proteobacterial sequences all bound to discrete subpopulations of the cocci which were accounting for about 50 % of all cells in the magnetotactic enrichment investigated. Simultaneous applications of two differentially labeled (red, green) probes for these magnetotactic cocci indicated differences in abundance and tactic behavior of the different populations. Genotype CS308 accounted for approximately 80 % of all magnetotactic cocci, and was therefore more frequent than the genotypes CS103 and CS310. Under the influence of a magnetic field, cells of genotype CS103 were predominantly entrapped nearest to the agarose solution–air interface.

Using comparative analysis, the partial 16S rRNA sequences of the three types of magnetotactic cocci were shown to be not closely related to any known sequence. The similarities were highest amongst each other but even there only moderate (89–93 %). The three newly retrieved sequences form a separate lineage of descent within the α-proteobacteria. Surprisingly, even though the genus *Magnetospirillum* also falls into this group, the magnetococci have more sequence similarity with other non-magnetic representatives of this α-proteobacteria than with the culturable magnetospirilla.

The study by Spring et al. [20] is interesting for several reasons. From a methodological point of view it was one of the first studies in which the problems of the rRNA approach became apparent. Even though three additional morphotypes were present in the enrichment, together accounting for about 50 % of all magnetotactic bacteria, their sequences were obviously not among those retrieved. This might have been caused by preferential PCR amplification of the partial 16S rRNA gene fragment of the magnetotactic cocci. Alternatively, since several non-

magnetotactic bacteria were also readily amplified in the experiment, the other magnetotactic bacteria might have been discriminated in any one of the following steps, i.e. cell lysis, DNA release, amplification and cloning. With regard to the diversity of magnetotactic bacteria, the discrimination of three genotypes within the magnetotactic cocci and the lack of binding of oligonucleotide probes for the cultivated magnetospirilla and the magnetotactic cocci to the other morphotypes indicated that the genotypic diversity of this bacterial group is higher than the morphological diversity. Furthermore, the first hints of a polyphyletic origin of the magnetotactic bacteria were obtained since the next known relatives of both the cultivated magnetospirilla and the Chiemsee magnetococci showed no magnetotaxis. Interestingly, even though the magnetotactic cocci are quite abundant in Lake Chiemsee and can be readily enriched from its sediment, they have until now resisted all attempts to bring them into pure culture (S. Spring, personal communication). This underlines the importance of cultivation-independent approaches in the study of magnetotactic bacteria.

3.6 The Magnetotactic Bacteria are Polyphyletic with Respect to their 16S rRNA

The magnetosomes of most magnetotactic bacteria contain only iron oxide particles, but some magnetotactic bacteria collected from sulfidic, brackish-to-marine aquatic habitats contain iron sulfide or both. DeLong et al. analyzed three magnetotactic bacteria of the magnetite or greigite type by the rRNA approach [21], and found the two isolates with the iron oxide magnetosomes, a magnetotactic coccus and a magnetotactic vibrio, to be affiliated with the α-proteobacteria. The coccus actually fell in the group of Chiemsee magnetococci, whereas the vibrio was closer to the magnetospirilla, even though based on different tree reconstructions it could not be finally shown whether it was closer to *Rhodospirillum rubrum* or to the genus *Magnetospirillum*. These findings were in line with those of Spring et al. [20]. The 16S rRNA sequence retrieved from an uncultured many-celled, magnetotactic prokaryote (MMP) with iron sulfide magnetosomes collected at various coastal sites in New England, however, was specifically related to the dissimilatory sulfate-reducing bacteria within the δ-proteobacteria. The closest relative is *Desulfosarcina variabilis* with a 16S rRNA similarity of 91 % [21]. This indicated a polyphyletic origin for magnetotactic bacteria. The authors also argue that their findings suggest that magnetotaxis based on iron oxide and iron sulfide magnetosomes evolved independently. They state that the biochemical basis for biomineralization and magnetosome formation for iron oxide-type and iron sulfide-type bacteria are likely fundamentally different, and speculate that in two independent phylogenetic groups of bacteria analogous solutions for the problem of effective cell positioning along physico-chemical gradients were found based on intracellular particles with permanent magnetic dipole moments [21].

3.7 "*Magnetobacterium bavaricum*"

The polyphyletic distribution of magnetotaxis in bacteria was further corroborated by the phylogenetic affiliation and *in situ* identification of the large rod-shaped magnetic bacterium from Lake Chiemsee sediment which was found to belong to a third independent lineage [22]. This bacterium was conspicuous because of its large size (5–10 μm long approximately 1.5 μm in diameter) and high number of magnetosomes. Up to 1000 hook-shaped magnetosomes with a length of 110–150 nm can be found in several chains. The large cells are Gram-negative and often contain sulfur globules. The cells are mobile due to one polar tuft of flagella. This morphotype, tentatively named "*M. bavaricum*", has so far only been enriched from the calcareous sediments of a few freshwater lakes in Upper Bavaria [23].

As is the case for many other magnetotactic bacteria, microbiologists were unable to grow this bacterium in pure culture until now. This morphotype was abundant in the magnetotactic enrichment investigated by Spring et al. previously [20], but its 16S rRNA sequence could not be retrieved in the presence of the magnetotactic cocci. "*M. bavaricum*" cells were therefore sorted from this enrichment by flow cytometry based on the high forward and sideward light scatter caused by the large cell size and the high amounts of magnetosomes. An almost full-length 16S rRNA sequence could be retrieved from the sorted cells that was proven by FISH to originate from "*M. bavaricum*" (Figure 3.1). Unlike the magnetotactic cocci, this conspicuous morphotype consisted of only one genotype which affiliated with neither the α- nor the δ-proteobacteria, but with a different line of descent, tentatively referred to as the *Nitrospira* phylum since it encompasses the cultured *Nitrospira moscovensis*. The 16S rRNA of "*M. bavaricum*" has less than 80 % similarities with any other known sequence of magnetotactic bacteria. The magnetosomes were shown to consist of the iron oxide magnetite (N. Petersen, personal communication), suggesting that there were also multiple phylogenetic origins for the iron oxide/magnetite-based magnetotaxis.

Recently, it was shown that the occurrence of magnetotactic bacteria from the *Nitrospira* phylum is apparently not restricted to Bavaria. A conspicuous magnetotactic rod (MHB-1) was magnetically collected from sediment of a lake nearby Bremen [15]. The magnetosomes from MHB-1 display the same bullet-shaped crystal morphology like those from "*M. bavaricum*" (Figure 3.2) and are aligned in multiple chains. However, unlike the latter organism, MHB-1 has less magnetosomes, which form a single bundle. 16S rRNA analysis revealed 94 % sequence similarity to "*M. bavaricum*" and cells hybridized with the FISH probe originally used for the identification of "*M. bavaricum*" [22], indicating that there exists morphological and phylogenetic diversity within this magnetotactic lineage.

"*M. bavaricum*" could be best enriched from a reddish brown layer at a depth of 5–8 mm below the sediment surface. Its abundance in the sediment was quantified by FISH and correlated to physico-chemical gradients determined with needle electrodes. Up to 7×10^5 mobile cells/cm^3 were present in the reddish-brown zone. This layer coincided with the microaerobic zone. No free sulfide above the detection limit of 10 μM could be detected using sulfide electrodes. However, sulfate-reducing

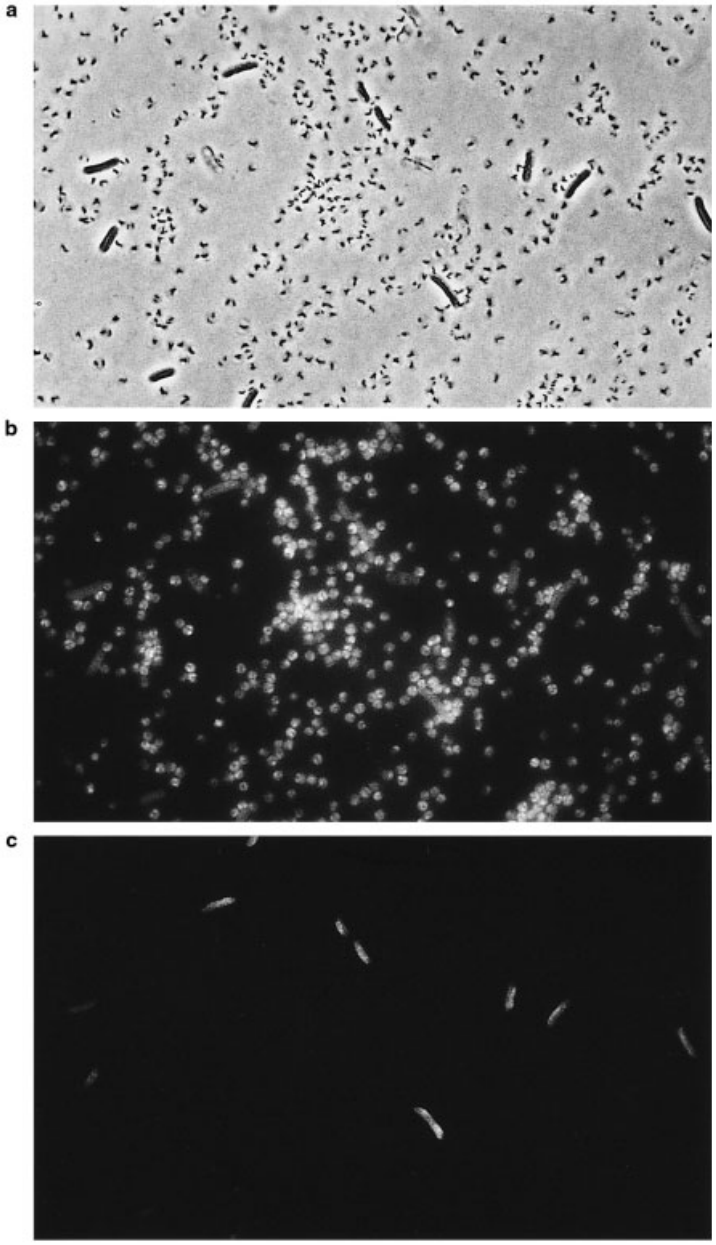

Figure 3.1 *In situ* identification of the hitherto uncultured "*M. bavaricum*" by FISH with a specific, 16S rRNA-targeted oligonucleotide probe [22]. (A) Phase contrast micrograph. (B) Visualization of hybridization of bacterial probe EUB338–fluorescein. (C) Selective visualization of "*M. bavaricum*" by a specific tetramethylrhodamine-labeled oligonucleotide probe. Identical microscopic fields are shown in (A)–(C).

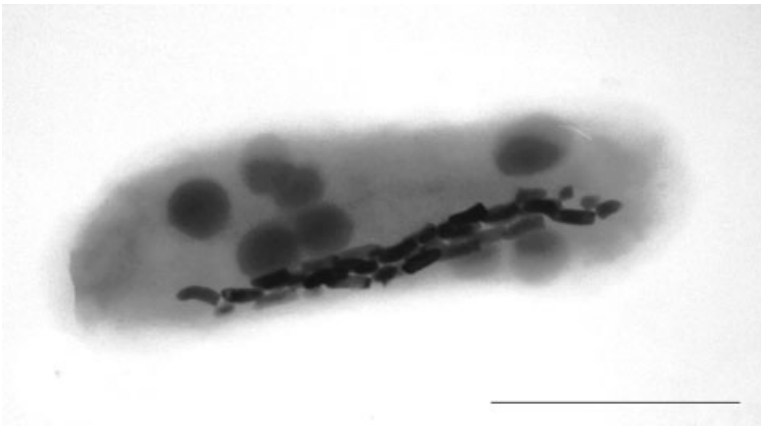

Figure 3.2 Transmission electron micrograph image of a novel magnetotactic rod of the *Nitrospira* phylum, which is closely related to "*M. bavaricum*". Bar = 0.7 μm.

bacteria were present in the microaerobic zone and the authors argue that low levels of sulfide might be continuously produced. They suggested that "*M. bavaricum*" has an iron-dependent method of energy conservation which depends on balanced gradients of oxygen and sulfide [22]. Based on its relative abundance of 0.64 ± 0.17 % and a large average cell volume of 25.8 ± 4.1 μm^3 it was estimated that "*M. bavaricum*" made up approximately 30 % of the bacterial biovolume in the reddish-brown zone. This demonstrates how hypotheses on the physiology and ecology of hitherto uncultured bacteria can be built based on the joint application of microscopic techniques, the rRNA approach and *in situ* characterization of the microhabitat of the bacterium of interest.

3.8 Further Diversity of Magnetotactic Bacteria

In the 1990s it became standard to infer evolutionary relationships of bacteria through phylogenetic analysis. In the following we will just quickly review further publications reporting 16S rRNA sequences from both cultured strains of magnetotactic bacteria and magnetic enrichments.

In 1994, Spring et al. used the cultivation-independent approach to retrieve another three partial and seven almost full-length 16S rRNA gene sequences from freshwater sediments of various sites in Germany [24]. Using FISH, all sequences were assigned to magnetotactic bacteria, nine to magnetotactic cocci and one to the second rod-shaped magnetotactic morphotype ("large vibrio") originally described in Lake Chiemsee [20]. The magnetotactic rod shared a 16S rRNA similarity of 90–92 % with the magnetotactic cocci, which among themselves mostly had

similarity values below 97 %. All sequences grouped with those earlier retrieved from the uncultured Chiemsee magnetotactic cocci [20]. The authors point out that the finding that most magnetotactic cocci have 16S rRNA similarities below 97 % has important taxonomic implications. In several studies on culturable bacteria it has been shown that a significant DNA–DNA relatedness that would justify assignment to one species exists only above 97 %. Therefore, upon isolation, the different magnetococci could be placed in different species. This work of Spring et al. [22] did not only corroborate that the diversity of magnetotactic cocci is fairly large, but it also showed that the ''Lake Chiemsee magnetococci'' branch does not exclusively consist of cocci. This once again demonstrates the limited value of cell morphology in bacterial systematics.

In 1995, Matsunaga's group published two reports related to the diversity and distribution of magnetotactic bacteria. In one, a PCR primer set specific for the 16S rRNA gene of the Lake Chiemsee magnetotactic cocci [20] was used to amplify DNA from magnetically isolated cocci. Comparative sequence analysis of the amplified 16S rDNA fragments proved their affiliation to the Lake Chiemsee magnetotactic cocci [25]. This demonstrated that this group of magnetotactic bacteria not only occurs in German sites, but also in Japan. The authors used the primer set to investigate the distribution of magnetotactic cocci in laboratory enrichments. 16S rRNA gene fragments of magnetotactic cocci were readily amplified from a water column above the sediment kept in an anoxic environment, but little was amplified from a water column kept in an oxic environment. The results suggest that the magnetotactic cocci found in the anoxic water column had migrated there from the sediment as a response to the micro-oxic or anoxic conditions or were present previously in a nonmagnetic form and had become magnetic due to the change in conditions. For instance, *M. gryphiswaldense* can grow aerobically, but produces magnetosomes only under micro-oxic or anoxic conditions (below 20 mbar O_2 [26]). Studies of their vertical distribution in freshwater sediments have indicated that most magnetotactic bacteria occur in a narrow layer in the suboxic zone, where dissolved iron is available [27].

In their second report, Matsunaga's group [28] described the phylogenetic analysis of a novel sulfate-reducing magnetic bacterium, RS-1. The almost full-length 16S rRNA gene of the pure culture was amplified and partially sequenced. The comparative sequence analysis placed it with the sulfate-reducing bacteria of the δ-proteobacteria within the genus *Desulfovibrio*. Interestingly, *Desulfovibrio magneticus* RS-1 was the first bacterium reported outside the α-proteobacteria that contains magnetite inclusions [29, 30]. It therefore disrupts the correlation between the α- and δ-proteobacterial magnetotactic bacteria and iron oxide (magnetite) and iron sulfide (greigite) magnetosomes, respectively, suggested by DeLong et al. [21].

This list of applications of the rRNA approach to the phylogeny and *in situ* identification of magnetotactic bacteria extends to a publication by Spring et al. [31] in 1998. In this study, natural enrichments of magnetic bacteria from the Itaipu lagoon near Rio de Janeiro in Brazil were analyzed. These were dominated by coccoid-to-ovoid morphotypes. Some of the cells produced unusually large magnetosomes that, with a length of 200 nm and a width of 160 nm, are almost twice as big as those found in other magnetotactic bacteria [32]. Partial sequencing of the 16S

rRNA genes revealed two clusters (Itaipu I and II) of closely related sequences within the lineage of magnetotactic cocci [20, 24, 25]. For a detailed phylogenetic analysis, several almost full-length 16S rRNA gene sequences were determined. A new methodology was applied in order to link at high resolution the ultrastructure of the enriched cells with their 16S rRNA sequence. Instead of light microscopic FISH with fluorescent oligonucleotide probes, *in situ* hybridizations with polynucleotide probes on ultra-thin section of embedded magnetotactic bacteria were examined by electron microscopy. One representative clone of each of the two closely related 16S rRNA clusters was used as a template for *in vitro* transcription of a 230-nucleotide variable region at the 5′ end of the 16S rRNA. The resulting RNA probe was labeled with digoxigenin- and fluorescein-labeled UTP during *in vitro* transcription. Bound polynucleotide probe was detected by incubation of the sections with gold-labeled antibodies specific for fluorescein or digoxigenin. The gold labels could then be detected by electron microscopy (Figure 3.3). For the first time, this enabled a detailed description of the morphological variety and ultrastructure of *in situ* identified, uncultured magnetic bacteria. Using this technique it was possible to link the presence of the unusually large magnetosomes in ovoid magnetotactic bacteria to the Itaipu I 16S rRNA type.

Cox et al. investigated the diversity of magnetotactic cocci in Baldwin Lake (Los Angeles) by restriction fragment length pattern (RFLP) analysis [33]. They found several 16S rRNA sequences, which had high similarities to known magnetotactic cocci from the database. In addition, they identified six sequences that formed a

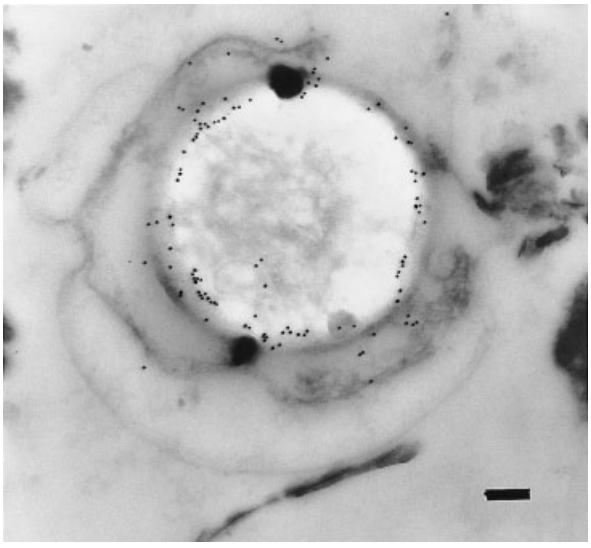

Figure 3.3 Electron micrograph of a hybridized thin section of magnetically enriched bacteria form the Itaipu lagoon (Rio de Janeiro, Brazil). Magnetosomes are visible as black inclusions. The digoxigenin-labeled polynucleotide probe mabrj58 specific for the morphotype Itaipu I was detected with anti-digoxigenin antibodies conjugated with 15-nm gold particles. Bar = 0.5 μm.

monophyletic cluster (ARB-1 cluster) related to, but distinct from, other magnetotactic bacteria (89 % similarity to the magnetotactic coccus CS92).

Recently, Flies et al. [15] have investigated the diversity of magnetotactic bacteria in various microcosms with freshwater and marine sediments from Germany and Sweden by DGGE and amplified ribosomal DNA restriction analysis (ARDRA) of the 16S rRNA genes. Initially, the sediments contained a highly diverse population of magnetotactic bacteria displaying a variety of different morphotypes. However, the magnetotactic population in the microcosms underwent a rapid succession, which usually resulted in the dominance of a magnetotactic coccus from the α-proteobacteria after several weeks of incubation.

While most 16S rRNA sequences from magnetotactic bacteria were identified after magnetic enrichment, two sequences putatively originating from marine magnetotactic bacteria were found without magnetic manipulation by Riemann et al., who investigated the bacterial community composition in the Arabian Sea by DGGE analysis [34]. Both sequences were nearly identical to each other and were closely related to an uncultivated magnetotactic coccus from a freshwater habitat (95 % similarity). This indicates that magnetotactic bacteria may also occur in the water column. Alternatively, these sequences may represent closely related non-magnetotactic species.

3.9 A Current View of the Phylogeny of Magnetotactic Bacteria

Our current view of the phylogeny of magnetotactic bacteria is shown in a 16S rRNA-based tree reconstruction in Figure 3.4. Magnetotactic bacteria can be found in the *Nitrospira* phylum and within the α- and δ-proteobacteria. Whereas the diversity in the *Nitrospira* branch of the magnetotactic bacteria consists only of the still uncultured "*M. bavaricum*" [22], the two proteobacterial branches are based on rRNA sequences of pure cultures and of still uncultured magnetotactic bacteria. Within the δ-proteobacteria there is the sequence of the pure culture *Desulfovibrio magneticus* RS-1 [25] and the sequence MMP [21] that was assigned to the hitherto uncultured multicellular magnetotactic prokaryote using the rRNA approach. The sequence of MMP is also the only sequence available of a magnetotactic bacterium with iron sulfide/greigite magnetosomes. The vast majority of currently known sequences of magnetotactic bacteria (over 90 % of those we found in the publicly available data bases) falls within the α-proteobacteria. Of this large diversity, only several members of the genus *Magnetospirillum*, the magnetic coccus MC-1 and the magnetic vibrio MV-1, have been cultured. In the last decade cultivation stagnated and only a few additional strains of magnetospirilla have been described [13, 14]. What was found in terms of new diversity over this period was mostly from uncultured magnetotactic bacteria. However, the new information obtained by the cultivation-independent approach since the phylogeny of magnetotactic bacteria was last reviewed by Spring and Schleifer in 1995 [19] is also limited. There

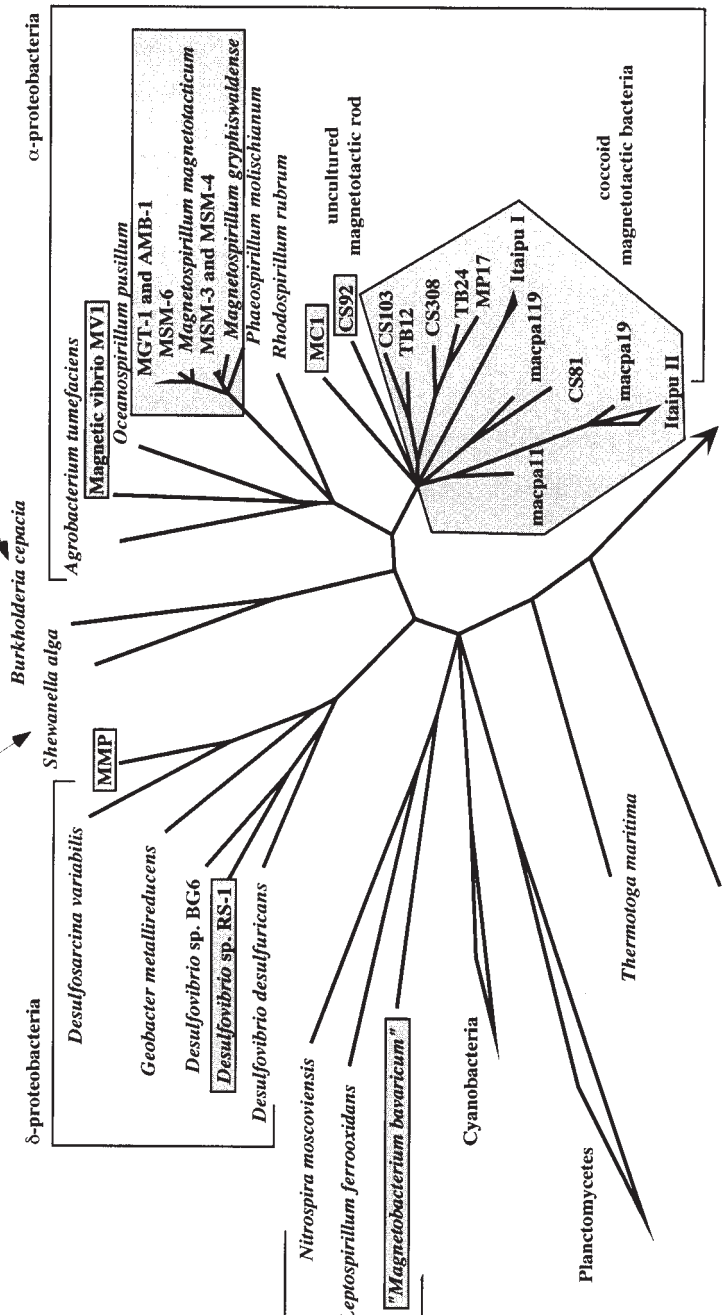

Figure 3.4 16S rRNA-based tree reconstruction showing the phylogeny of magnetotactic bacteria (grey). The tree is based on parsimony analyses and was corrected according to the results of maximum likelihood and neighbor joining methods using the ARB program package [35]. Multifurcations were drawn whenever branching orders were not stable [36]. The tree topology is based on almost full-length 16S rRNA sequences. The partial sequences of strains CS103, MC-1, MV-1, MMP and RS-1 have been added with the parsimony tool without allowing changes of the overall tree topology [35].

were only few new sequences affiliated with the already described branch of Lake Chiemsee magnetotactic cocci, for which the reports from Germany [20, 24], Japan [25] and Brazil [31] now suggest global distribution and considerable intragroup diversity.

What is the reason for this stagnation? One possibility is that the extant diversity of magnetotactic bacteria is by now fully described. The other possibility is that our methods are selective. We know this is true the cultivation methods, but it has to be realized that this is also true for the rRNA approach, especially if it starts from standard laboratory enrichments which themselves are selective. The methodology currently applied is biased towards motile, aero-tolerant bacteria, although the presence of atmospheric oxygen apparently did not affect the number of bacteria magnetically collected from anoxic sediment horizons [27]. New diversity might be detected if magnetotactic bacteria are directly retrieved from various habitats without prior storage of the sediments in the laboratory. Are there strictly anaerobic, nonmotile bacteria which form intracellular magnetosomes? In addition, primer sets other than the standard ''bacterial'' ones should be tested for 16S rRNA retrieval from magnetic enrichments. It is known that every primer set has preferences and the example of the discrimination of the ''*M. bavaricum*'' sequence against the magnetotactic cocci has been described before. In this case, it was only the large size and the extraordinary high magnetosome content that allowed further purification of the initial magnetotactic enrichment by flow cytometry. This is not possible for less conspicuous magnetotactic bacteria. Magnetotactic bacteria might occur in other bacterial lineages. It would also be interesting to check whether archaebacterial sequences can be sequenced from magnetotactic enrichments.

Future attempts to identify and characterize new magnetotactic bacteria should be undertaken. These should make use of the potential synergistic effects of cultivation-independent *in situ* and traditional cultivation approaches. If a cultured close relative can be identified in the 16S rRNA tree, then the affiliation of a ''new magnetic sequence'' may give important hints for its enrichment and cultivation. In addition, data on the *in situ* microhabitat of magnetotactic bacteria should be obtained and used for the formulation of suitable media.

In the last decade two of the three questions raised above have been answered. There exists a large diversity of magnetotactic bacteria that goes beyond that already indicated by the many morphotypes detected in the 1970s and 1980s, and the magnetotactic bacteria are polyphyletic. The third question, however, whether the biomineralization of magnetosomes or at least, for example, the intracellular formation of magnetite is monophyletic, is still open. It would be interesting to investigate by comparative analysis of the genes involved in magnetosome formation whether lateral gene transfer, e.g. from the α-proteobacterial magnetotactic bacteria to ''*M. bavaricum*'', contributed to the spreading of magnetite-based magnetotaxis or whether the mechanisms of magnetosome formation have developed independently in the different phylogenetic groups. Studies of this type will not necessarily rely on cultured strains since there is a rapidly increasing potential to directly retrieve form the environment and analyze large DNA fragments. If these fragments contain 16S rRNA genes or can be linked by overlaps to such fragments, environmental genomics allows for the comparative genome analysis of identified, uncul-

turable bacteria [35]. Recently, a substantial number of genes for magnetosome formation were identified (*mam* genes) which apparently are ubiquitously present in the genomes of all magnetotactic bacteria from the α-proteobacteria that have been analyzed so far [18]. Therefore, the cultivation-independent retrieval of genetic information directly from the environment should not be restricted to phylogenetic marker genes, but should be extended to those metabolic key genes. Magnetotactic bacteria can be easily collected by magnetic enrichment directly from environmental samples in high numbers and virtually free of contaminants. In addition, most, if not all, genes essential for magnetosome biomineralization are apparently clustered within a relatively small section of the chromosome as a genomic ''magnetosome island''. Thus, the future retrieval and analysis of large continuous sequences harboring these islands or even the analysis of the whole ''magnetotactic metagenome'' will be an extremely powerful approach to gain further insights in the genetic diversity of magnetosome biomineralization as well as a better understanding of the ecological interactions of these organisms. This might also lead to improved strategies for their isolation and cultivation.

Acknowledgments

The authors would like to thank Stefan Spring for critically reading earlier versions of this manuscript and for helpful discussions. The original research reviewed in this manuscript in which the authors were involved was supported by the Deutsche Forschungsgemeinschaft and by the Fonds der chemischen Industrie.

References

[1] R. I. Amann, W. Ludwig, K. H. Schleifer, *Microbiol. Rev.* **1995**, *59*, 143–169 and references therein.
[2] C. R. Woese, *Microbiol. Rev.* **1987**, *51*, 221–271.
[3] N. R. Pace, *Science* **1997**, *276*, 734–740 and references therein.
[4] R. Amann, N. Springer, W. Ludwig, H. D. Görtz, K. H. Schleifer, *Nature* **1991**, *351*, 161–164.
[5] G. J. Olsen, D. J. Lane, S. J. Giovannoni, N. R. Pace, D. A. Stahl, *Annu. Rev. Microbiol.* **1986**, *40*, 337–365.
[6] G. Muyzer, T. Brinkhoff, U. Nübel, C. Santegoeds, H. Schäfer, C. Wawer, in *Molecular Microbial Ecology Manual* (Eds A. D. L. Akkermans, J. D. van Elsas, F. J. de Bruijn), Kluwer, Dordrecht, **1998**, pp. 1–27.
[7] R. P. Blakemore, *Science* **1975**, *190*, 377–379.
[8] R. P. Blakemore, *Annu. Rev. Microbiol.* **1982**, *36*, 217–238.
[9] K. H. Schleifer, D. Schüler, S. Spring, M. Weizenegger, R. Amann, W. Ludwig, M. Köhler, *Syst. Appl. Microbiol.* **1991**, *14*, 379–385.
[10] R. P. Blakemore, D. Maratea, R. Wolfe, *J. Bacteriol.* **1979**, *140*, 720–729.
[11] P. A. Eden, T. M. Schmidt, R. P. Blakemore, N. R. Pace, *Int. J. Syst. Bacteriol.* **1991**, *41*, 324–325.

[12] T. Sakane, A. Yokota, *Syst. Appl. Microbiol.* **1994**, *17*, 128–134.
[13] J. G. Burgess, R. Kawaguchi, T. Sakaguchi, R. H. Thornhill, T. Matsunaga, *J. Bacteriol.* **1993**, *175*, 6689–6694.
[14] D. Schüler, S. Spring, D. Bazylinski, *Syst. Appl. Microbiol.* **1999**, *22*, 466–471.
[15] C. Flies, F. O. Glöckner, D. Schüler, in preparation.
[16] J. D. Coates, U. Michaelidou, R. A. Bruce, S. M. O'Connor, J. N. Crespi, L. A. Achenbach, *Appl. Environ. Microbiol.* **1999**, *65*, 5234–5241.
[17] Y. Shinoda, Y. Sakai, M. Ue, A. Hiraishi, N. Kato, *Appl. Environ. Microbiol.* **2000**, *66*, 1286–1291.
[18] S. Schübbe, M. Kube, A. Scheffel, C. Wawer, U. Heyen, A. Meyerdierks, M. Madkour, F. Mayer, R. Reinhardt, D. Schüler, *J. Bacteriol.* **2003**, *185*, 5779–5790.
[19] S. Spring, K. H. Schleifer, *Syst. Appl. Microbiol.* **1995**, *18*, 147–153.
[20] S. Spring, R. Arnann, W. Ludwig, K.-H. Schleifer, N. Petersen, *Syst. Appl. Microbiol.* **1992**, *15*, 116–122.
[21] E. F. DeLong, R. F. Frankel, D. A. Bazylinski, *Science* **1993**, *259*, 803–806.
[22] S. Spring, R. Amann, W. Ludwig, K. H. Schleifer, H. van Gemerden, N. Petersen, *Appl. Environ. Microbiol.* **1993**, *59*, 2397–2403.
[23] H. Vali, O. Förster, G. Amarantidis, N. Petersen, *Earth Planet. Sci. Lett.* **1987**, *86*, 389–426.
[24] S. Spring, R. Amann, W. Ludwig, K. H. Schleifer, D. Schüler, K. Poralla, N. Petersen, *Syst. Appl. Microbiol.* **1994**, *17*, 501–508.
[25] R. H. Thornhill, J. G. Burgess, T. Matsunaga, *Appl. Environ. Microbiol.* **1995**, *61*, 495–500.
[26] U. Heyen, D. Schüler, *Appl. Microbiol. Biotechnol.* **2003**, *61*, 536–44.
[27] C. Flies, K. Bosselmann, H. Jonkers, D. deBeer, M. Böttcher, D. Schüler, submitted.
[28] R. Kawaguchi, J. G. Burgess, T. Sakaguchi, H. Takeyama, R. H. Thornhill, T. Matsunaga, *FEMS Microbiol. Lett.* **1995**, *126*, 277–282.
[29] T. Sakaguchi, J. G. Burgess, T. Matsunaga, *Nature* **1993**, *365*, 47–49.
[30] T. Sakaguchi, A. Arakaki, T. Matsunaga, *Int. J. Syst. Evol. Microbiol.* **2002**, *52*, 215–221.
[31] S. Spring, U. Lins, R. Amann, K.-H. Schleifer, L. C. S. Ferreira, D. M. S. Esquivel, M. Farina, *Arch. Microbiol.* **1998**, *169*, 136–147.
[32] M. Farina, B. Kachar, U. Lins, R. Broderick, H. Lins de Barros, *J. Microsc.* **1994**, *173*, 1–8.
[33] L. Cox, R. Popa, D. Bazylinsky, B. Lanoil, S. Douglas, A. Belz, D. Engler, K. H. Nealson, *Geomicrobiol. J.* **2002**, *19*, 387–406.
[34] L. Riemann, G. F. Steward, L. B. Fandino, L. Campbell, M. R. Landry, F. Azam, *Deep-Sea Res. II Topical Studies Oceanogr.* **1999**, *46*, 1791–1811.
[35] W. Ludwig, O. Strunk, S. Klugbauer, N. Klugbauer, M. Weizenegger, J. Neumaier, M. Bachleitner, K.-H. Schleifer, *Electrophoresis* **1998**, *19*, 554–568.
[36] J. L. Stein, T. L. Marsh, K. Y. Wu, H. Shizuya, E. F. DeLong, *J. Bacteriol.* **1996**, *178*, 591–599.

4 Biochemical and Genetic Analysis of the Magnetosome Membrane in *Magnetospirillum gryphiswaldense*

Dirk Schüler

4.1 Introduction

Despite the impressive diversity of biomineralization processes, there are several fundamental principles governing the formation of inorganic materials in organisms [1]. One of those principles is the spatial control of nucleation and growth of inorganic crystals. In many organisms, this is achieved by the intracellular compartmentalization of biomineralization processes. Compartmentalization allows the biomineralization process to be strictly controlled through the chemical and spatial partitioning of the mineralization environment [2]. In magnetotactic bacteria (MTB), the biomineralization of magnetosomes is linked to the accumulation of substantial amounts of iron and the intracellular formation of an iron mineral within a special intracytoplasmic compartment, which is provided by the magnetosome membrane (MM).

4.2 The Biomineralization of Magnetite in MTB

Most MTB synthesize intracytoplasmic crystals of the ferrimagnetic iron mineral magnetite (Fe_3O_4). Unlike magnetite produced in inorganic systems, the magnetosome particles are characterized by nearly perfect crystallinity and narrow size distributions, which are within the magnetic single domain range (35–120 nm) [3]. While the size and habit of magnetic crystals are species-specific and uniform within a single cell, there is a considerable diversity of magnetosome morphologies found in different MTB (Figure 4.1).

The assimilation of iron for magnetite synthesis occurs very efficiently from low environmental concentrations. In *Magnetospirillum gryphiswaldense*, ferric iron is incorporated by a high-affinity uptake system, which is saturated at extracellular iron concentrations of 15–20 μM Fe [4]. Interestingly, the growth of a mutant which lost the ability to form magnetosomes was more sensitive to elevated concentrations of iron [5]. This might be indicative of a contribution of magnetite formation to iron homeostasis and detoxification of potentially harmful high intracellular

Biomineralization: From Biology to Biotechnology and Medical Application, Second Edition. Edited by E. Bäuerlein

ISBN: 3-527-31065-7

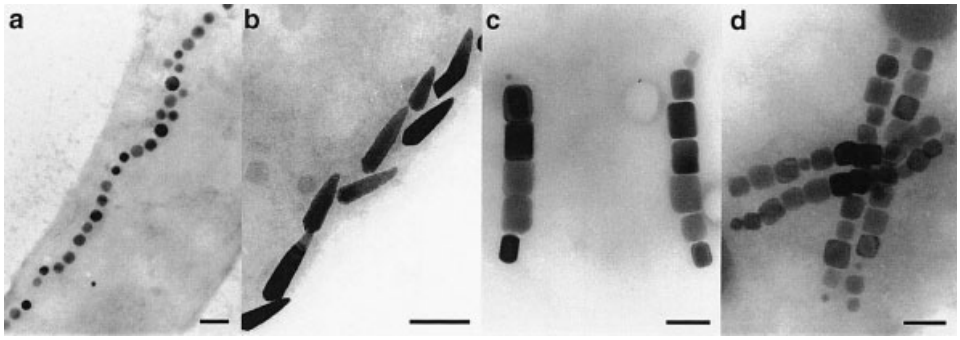

Figure 4.1 Crystal shapes and intracellular organization of magnetosomes found in various MTB. Shapes of magnetosomes include cubo-octahedral (a), bullet-shaped (b) and elongated prismatic (c and d) morphologies. The particles are arranged within the cell in one (a and b) or multiple (c and d) chains. Bar = 0.1 μm.

levels, similar, for instance, to the iron-storage proteins ferritin and bacterioferritin [6].

The number of magnetite particles per cell is variable depending on growth conditions. In addition to the availability of micromolar amounts of iron, microaerobic conditions are required for magnetite formation. Cells of *M. gryphiswaldense* are non-magnetic when grown under aerobic conditions, but start to produce Fe_3O_4 when the oxygen concentration is shifted below a threshold value of 20 mbar. There is a clear correlation of the increase in magnetosome content with decreasing extracellular oxygen concentration, with maximum magnetite synthesis occurring at 0.25 mbar O_2. Under those conditions, bacteria can synthesize up to 60 magnetosome particles per cell, which corresponds to an accumulation of iron up to 4 % of the total dry cellular weight [7, 8].

4.3 The MM is a Unique Structure in MTB

Compartmentalization through the formation of membrane vesicles enables the processes of magnetite mineralization to be regulated by biochemical pathways. The MM is likely the crucial component in the control of crystal growth, thereby providing spatial constraints for shaping of species-specific crystal morphologies. Magnetite formation requires the presence of mixed valence complexes in solution. Biomineralization of this material, therefore, requires precise regulation of both the redox potential and the pH. The growth of magnetite crystals is ultimately regulated by the uptake mechanisms and depends on a controlled flux of ions over the MM to provide a supersaturating iron concentration within the vesicle. Although

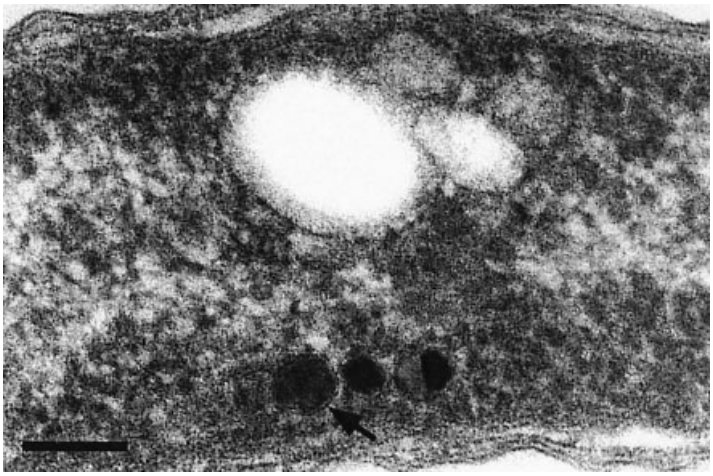

Figure 4.2 Electron micrograph of an ultrathin section of a *M. gryphiswaldense* cell. The arrow indicates the membrane surrounding each electron-dense particle. Bar = 0.1 μm.

their exact role has not been fully elucidated, it can be concluded that the constituents of the MM have specific functions in the transport and accumulation of iron, nucleation of crystallization, and redox and pH control [9, 10]. Thus, a detailed analysis of the MM is prerequisite for an understanding of magnetite biomineralization.

Balkwill et al. initially examined the ultrastructure of the magnetic spirillum *M.* (formerly *Aquaspirillum*) *magnetotacticum* strain MS-1 [11]. Individual magnetite crystals were found to be enveloped by a trilaminate structure, which has been referred to as a MM [9]. The overall composition of the MM did not appear to be significantly different in overall composition from other cell membranes. Neutral lipids, free fatty acids, glycolipids, sulfolipids and phospholipids were detected in the MM. Sodium dodecylsulfate–polyacrylamide gel electrophoresis (SDS–PAGE) revealed a complex protein pattern of the MM. While most proteins bands were shared between the MM and the outer or inner membrane, several proteins apparently were unique to the MM in *M. magnetotacticum* [9, 12].

A similar structure of a lipid bilayer membrane associated with proteins was found in magnetosomes of other cultivated magnetic spirilla including *M. gryphiswaldense* (Figure 4.2) [10] and *Magnetospirillum* sp. strain AMB-1 [13]. Although a detailed biochemical analysis of the MM in MTB other then Magnetospirilla has not yet been accomplished, electron microscopic studies in other cultivated and uncultivated MTB indicated similar structures surrounding the magnetite crystals [14, 15]. The preliminary genomic analysis of the magnetotactic coccus MC-1 revealed the presence of highly conserved genes, which had been previously identified to encode MM proteins in Magnetospirilla [16]. Thus, the presence of a MM seems to be a trait common to all MTB.

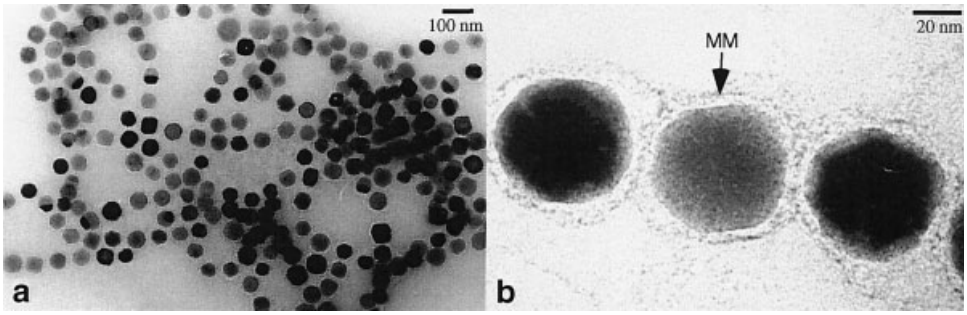

Figure 4.3 Transmission electron micrographs of purified magnetosomes from *M. gryphiswaldense*. (a) Due to the presence of the enveloping membrane that prevents agglomeration, isolated magnetosomes form stable suspensions. (b) High magnification of magnetite crystals that are enveloped by the MM, which is 8–12 nm thick.

4.4 Biochemical Analysis of the MM in *M. gryphiswaldense*

The magnetotactic bacterium *M. gryphiswaldense* can be readily cultivated to obtain ample material for biochemical analysis [8] and is genetically tractable [17]. In addition, sequence analysis of its genome is under way [5]. Therefore, this strain has recently emerged as a model for the investigation of magnetosome formation. Magnetosomes can be readily isolated and purified from disrupted cells by means of magnetic separation and ultracentrifugation (Figure 4.3), and the membrane can be solubilized by hot SDS treatment or organic solvents [16]. Isolated magnetosomes have a strong tendency to form chains, even after treatment with mild detergents, indicating that an interparticle connection mediated by MM components is involved in the organization of chains. A number of common fatty acids were identified in isolated magnetosomes of *M. gryphiswaldense* [18]. Phosphatidylethanolamin and phosphatidylglycerol were identified as the most abundant polar lipids, whereas ornithinamidlipid and an unidentified aminolipid are less abundant in the MM compared to the fraction of lipids from the outer and cytoplasmic membrane [18–20]. Analysis of the extracted membrane revealed that the magnetosome is associated with a highly specific and complex subset of proteins, which are present in various quantities. The amount of MM-bound polypeptides approximately represents 0.1 % of the total cellular protein [16]. Using various one- and two-dimensional electrophoresis methods in combination with N-terminal and mass spectrometric sequencing techniques, between 15 and 20 major polypeptides have been identified in the MM, several of them representing post-translational modifications of the same gene product (Figure 4.4). The different resistance of magnetosome proteins against proteases and detergents indicates that some proteins (e.g. MamC and MamF) are very tightly bound to the magnetosome crystals and/

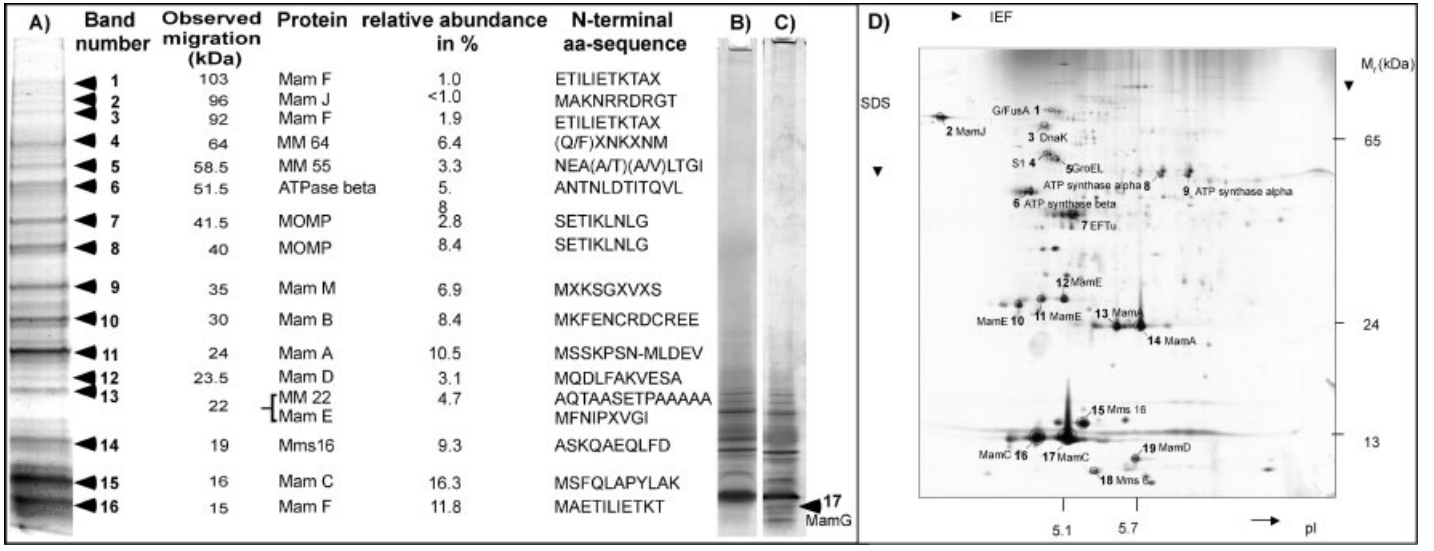

Figure 4.4 MM-associated proteins separated by one- and two-dimensional PAGE. (A) Summary of MMPs detected by Coomassie stain in one-dimensional SDS–PAGE (16 %). Proteins from indicated bands were identified by N-terminal amino acid analysis (Edman degradation). (B) Coomassie and (C) silver stained SDS–Tricine gels (16.5 %) of MM proteins. (D) Silver-stained two-dimensional PAGE of MM proteins from *M. gryphiswaldense*. Proteins from marked spots were identified by mass spectrometric sequencing. (Redrawn after [18].)

or embedded within the membrane. Others, e.g. MamA, seem to be loosely attached and can be selectively solubilized by mild detergents [18]. Several of the proteins contain covalently bound *c*-type heme as revealed by peroxidase staining. No glycoproteins, which are common constituents of other biomineralizing systems, have been detected so far.

4.5 Proteomic Analysis of Magnetosomes

Biochemical analysis in combination with reverse genetics and, most recently, the availability of substantial genome data have led to identification of the genes for all major MM proteins (MMPs) [5, 16, 18]. A number of minor constituents were occasionally found bound to isolated magnetosomes. Because they were mostly identified in small amounts and represent highly abundant cellular proteins, they most likely originate from contaminations during preparation, although it cannot be fully excluded that some of them, e.g. several detected ATPase subunits, might be *in vivo* associated with magnetosome function. The magnetosome subproteome of *M. gryphiswaldense* comprises 18 known MMPs (Table 4.1). Based on sequence analysis, most MMPs can be assigned to a number of characteristic protein families, which seem to be shared by all MTB.

4.5.1 Tetratricopeptide Repeat (TPR) Proteins

MamA, which has been also identified in the MM of other *Magnetospirillum* species [12], is an abundant protein of the MM and contains four to five copies of the TPR motif. TPR motifs, which have been identified in a growing number of proteins with diverse functions, are known to mediate protein–protein interactions [21]. It has therefore been speculated that MamA acts as a receptor in the MM interacting with cytoplasmic proteins or is involved in the assembly of multiprotein complexes within the MM [12, 22].

4.5.2 Cation Diffusion Facilitator (CDF) Proteins

Both MamB and MamM were identified as members of the CDF family of metal transporters, which comprises of proteins that function as efflux pumps of toxic divalent cations, such as zinc, cadmium, cobalt and other heavy metal ions. More specifically, MamB and MamM have greatest similarity to the CDF3 subfamily, which was postulated to comprise putative iron transporters [23]. It has been speculated that MamB and MamM are involved in the magnetosome-directed uptake of iron [16], and preliminary evidence obtained from mutant analysis seems to support this assumption (Schüler et al., unpublished).

Table 4.1 Characteristics of MMPs from *M. gryphiswaldense* (after [37])

Protein	Length (amino acids)	Deduced M_r (kDa)/p*I*	Blast homolog[a]	Characteristics	Putative function
MamA	217	24.01/5.64	MM2348 *M. mazei*	TPR motifs; relative abundance > 10 %	Protein–protein interaction
MamB	297	31.96/5.25	YdfM *B. subtilis*	CDF transporter	iron transport
MamC	125	12.40/4.88	–	relative abundance[b] > 16 %	unknown
MamD	314	30.20/9.68	–	Leu/Gly-rich motif	unknown
MamE	772	78.00/8.69	MLL5022 *R. loti*	PDZ domains; protease domain	serine protease
MamF	111	12.30/9.57	–	relative abundance > 15 %	unknown
MamG	84	7.70/9.28	–	Leu/Gly-rich motif	unknown
MamJ	466	48.51/3.80	–	Asp/Glu-rich repeats	unknown
MamM	318	34.50/5.82	BH 1238 *B. halodurans*	CDF transporter	unknown
MamN	437	46.14/6.70	TM0934 *T. maritima*	membrane protein	inorganic ion transport
MamO	632	65.40/6.51	CC1282 *C. crescentus*	PDZ domains; protease domain	serine protease
MamQ	272	30.00/8.48	LemA *T. maritima*	membrane protein	unknown
MamR	72	8.10/8.48	–	hydrophilic protein	unknown
MamS	180	18.71/7.02	–	membrane protein	unknown
MamT	174	18.88/10.05	–	heme binding	unknown
Mms6	136	14.26/9.79	–	Leu/Gly-rich motif	iron binding
Mms16	145	16.35/5.49	ApdA *R. rubrum*	weakly similar to phasins	activator PHB-depolymerase
MM22	196	20.00/7.14	*E. faecalis* V583	membrane protein	unknown

[a] Only hits with an *e* value < 0.01 are shown. Hits to other MTB are excluded.
[b] Relative abundances are with respect to the total amount of MM-associated protein.

4.5.3 HtrA-like Serine Proteases

MamE and MamO display sequence similarity to HtrA-like serine proteases. The *mamP* gene, encoding a further deduced protein with similarity to this family, is co-located with *mamE* and *mamO* within the same operon (see Section 4.6). HtrA-like proteins share a conserved trypsin-like protease domain and one or two PDZ domains. They act as molecular chaperones and heat-shock induced proteases, which degrade misfolded proteins in the periplasm [24]. It has been suggested that MamE and MamO are involved in magnetosome formation, perhaps by the processing, maturation and targeting of MMPs during MM assembly [16].

4.5.4 MTB-specific Protein Families

Most of the identified MMPs including, for example, the most abundant MM-associated proteins MamC and MamF, have no known homologues in organisms other than MTB and thus represent unique, MTB-specific protein families. One noticeable feature common to several of these proteins is the presence of repetitive motifs. Examples are found in MamD, Mms6 and MamG, which share conspicuous hydrophobic sequence motifs that are rich in repeated leucine and glycine residues. This motif displays an intriguing similarity to LG-rich repetitive sequences found in silk-like (fibroin) proteins [25], mollusk shell framework proteins [26] as well as elastins and cartilage proteins [27], which are known to have a remarkable tendency for self-aggregation and several of which are involved in other biomineralization processes. The Mms6 protein was described recently in *Magnetospirillum* strain AMB-1 as a tightly bound constituent of the MM, which exhibited iron-binding activity and had an effect on the morphology of growing magnetite crystals *in vitro* [28].

An additional sequence pattern with potential relevance for magnetite biomineralization is found in MamJ. MamJ, which displays extensive self-similarity, is particularly rich (18.7 %) in repeats of the acidic amino acid residues glutamate and aspartate. A number of additional conspicuous proteins with highly repetitive and/or acidic sequence motifs can be deduced from the genome assemblies of *M. gryphiswaldense* and other MTB. Clusters of acidic groups are commonly found in biomineralizing systems, such as in mollusk shells and others [2, 29]. Acidic groups have a strong affinity to metal ions and are known to be involved in the initiation of crystal nucleation by binding of metal ligands. MamJ and other acidic or repetitive proteins are therefore candidates for a function in magnetite biomineralization.

The closely related strains *Magnetospirillum* AMB-1 and *M. magnetotacticum* MS-1 produce magnetite crystals that are virtually identical with respect to their size, alignment and crystal morphologies. However, the biochemical analysis of the MM revealed divergent protein patterns of the MM between the three strains. Approximately 20–25 bands were identified in magnetosome preparations from MS-1 and AMB-1, respectively [18]. While the protein patterns of AMB-1 and MS-1 were similar to each other and shared a number of bands, their composition was clearly distinct from that of *M. gryphiswaldense* MSR-1 (Figure 4.5). The MpsA and MagA proteins were previously found associated with isolated magnetosomes in strain AMB-1 [13, 30]. Although equivalent genes are present in the genome of *M. gryphiswaldense*, they have not been detected as MM constituents of the latter organisms. Thus, it must be considered that neither MpsA and MagA are universal constituents of the MM. Alternatively, their co-purification with the magnetosomes may have been accidentally caused as a result of unspecific binding during preparation.

Mms16 has been detected in isolated magnetosomes of both *M. gryphiswaldense* and *Magnetospirillum* strain AMB-1. Because of its observed GTPase activity *in vitro*, it was suggested to be involved in the formation of MM vesicles [31]. However, it recently turned out that Mms16 has striking similarity to ApdA, an activator of polyhydroxybutyric acid (PHB) depolymerization in *R. rubrum* and Mms16 has been shown to substitute for ApdA function *in vitro* [32]. Hence, its function in

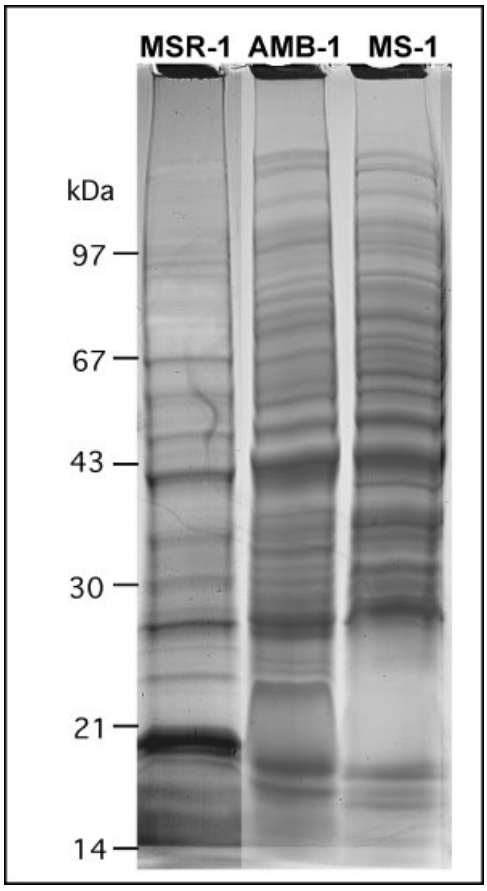

Figure 4.5 SDS–PAGE of MMPs from *M. gryphiswaldense* MSR-1, *Magnetospirillum* strain AMB-1 and *M. magnetotacticum* MS-1.

Magnetospirillum species seems to be independent of magnetosome formation and its *in vivo* association with the MM will require further clarification.

4.6 Genetic Organization of Magnetosome Genes

With the exception of *mm22* and *mms16*, all genes encoding MMPs are encoded within a single chromosomal region. This region representing a genomic ''magnetosome island'' could be functionally linked to magnetosome synthesis in a non-magnetic mutant strain harboring a large chromosomal deletion [5]. Magnetosome genes are co-located in three different operons, which are linked within less than 35 kb in the genome *of M. gryphiswaldense* (Figure 4.6).

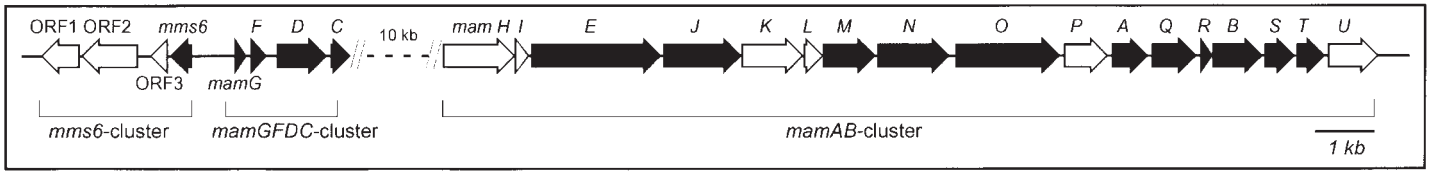

Figure 4.6 Organization of a region from the putative magnetosome island of *M. gryphiswaldense* comprising the entire *mms6*, *mamGFDC* and *mamAB* gene clusters. Black arrows indicate genes encoding identified MMPs. (Redrawn after [18].)

The *mamAB* cluster extends over 16.5 kb and comprises 17 consecutive, co-linear genes that were assigned *mamH–mamU* (*mam* for magnetosome membrane). As can be inferred from the available genome data of different MTB (http://www.jgi.doe.gov/tempweb/JGI_microbial/html/index.html), the gene order and amino acid sequences of the predicted Mam proteins are highly conserved in other MTB including *M. magnetotacticum* and the remotely related magnetic coccus strain MC-1 [16]. The 2.7 kb *mms6* operon (*mms* for magnetic particle membrane-specific protein [31]) comprising four genes is located 15 kb upstream from the left border of the *mamAB* cluster, and the *mamGFDC* operon is located 9.2 kb upstream of the *mamAB* cluster and extends over 2.1 kb. Remarkably, the regions within, adjacent and between these clusters contain many open reading frames, which have close homologs in the genomes of *M. magnetotacticum* MS-1 and strain MC-1, but yield no database hits to non-magnetic organisms. Hence, they can be considered MTB-specific and are likely to be involved in magnetosome formation. Other deduced gene products are predicted to have related functions based on sequence similarity to functionally characterized proteins, e.g. *mamK* of the *mamAB* cluster displays extensive similarity to a gene (*mreB*) encoding an actin-like cytoskeletal protein [33]. It has been speculated that MamK may be associated with the formation of a cytoskeletal ''superstructure'', which is involved in the positioning, anchoring and segregation of magnetosome chains [5].

A further intriguing feature of this region is the presence of numerous genes encoding mobile DNA elements such as insertion sequence elements and integrases. In total, these genes represent more than 14 % of the coding sequence. The presence of this high number of mobile elements may account for the observed genetic instability of this region under conditions of stationary growth [5]. In summary, all these features are strongly reminiscent of those described for genome islands in other bacteria. Genome islands usually comprise large genomic regions, which, for instance, are present as pathogenicity islands (PAIs) in the genomes of pathogenic strains, but absent from the genomes of non-pathogenic members of the same or related species [34]. They often encode ''accessory'' gene functions, are genetically unstable and can transfer horizontally. Thus, it seems that most of the gene functions required for magnetite synthesis are organized within a large genomic ''magnetosome island'', which may have been distributed by lateral gene transfer.

4.7 Conclusions and Outlook

Detailed knowledge of the biochemical composition of the MM as well as its structural analysis is the key for an understanding of bacterial magnetite biomineralization at the molecular level. Sequence analysis of the structural genes has already provided valuable insights into the genetic basis of magnetite synthesis. The identification of the major biochemical constituents together with the availability of techniques for genetic manipulation has set the stage for future functional and biomimetic analysis of the organic–inorganic interactions governed by the MM.

The formation of intracytoplasmic magnetosome vesicles is the result of a differentiation process that is poorly understood. Specifically, the question remains to be answered how such a macromolecular structure is assembled, and how are the MMPs expressed and targeted to their proper subcellular location. No sequence motifs or sorting signals universal to all MMPs have been identified. As a number of MMPs appear to be rather hydrophilic, binding of MMPs to the MM cannot be only by hydrophobic interactions, but for some proteins may involve protein–protein interactions or direct binding to the mineral surface of magnetite crystals. Interestingly, several MMPs contain PDZ and TPR domains, which are known to mediate protein–protein interactions, act as scaffolding proteins and typically coordinate the assembly of proteins into multisubunit complexes at particular subcellular locations [21, 35]. It could be envisioned that the organization around such a scaffold may allow the stable localization of interacting proteins during magnetosome assembly. Further experiments, such as *in situ* localization studies, are of importance to follow the expression and targeting of MMPs and the magnetosome assembly during growth. With the availability of *in vivo* genetic technology, experiments using gene fusions of MMPs coupled to green fluorescence protein (GFP), for example, appear to be a powerful tool to address these questions.

Because of their unique magnetic and crystalline properties, the biomineralization of magnetic nanoparticles is currently attracting growing interest from material scientists and biotechnologists for their potential use in numerous applications [36]. Thus, a biochemical and genetic understanding of magnetosome biomineralization will be of immediate relevance for technological applications, and could be used in the tailoring and engineering of magnetic nanoparticles with advanced properties.

Acknowledgments

I wish to acknowledge the continued collaboration and invaluable discussions with many colleagues. I am especially grateful to my co-workers and students of the Magneto-Lab at the Max Planck Institute for Marine Microbiology. Research in the author's lab is supported by the Max Planck Gesellschaft, the Deutsche Forschungsgemeinschaft and the *Biofuture* program of the German BMBF.

References

[1] H. A. Lowenstam, S. Weiner, *On Biomineralization*, Oxford University Press, Oxford, **1989**.
[2] E. Bäuerlein, *Angew. Chem. Int. Ed. Engl.* **2003**, *42*, 614–641.
[3] B. M. Moskowitz, *Rev. Geophys.* **1995**, *33*, 123–128.
[4] D. Schüler, E. Baeuerlein, *Arch. Microbiol.* **1996**, *166*, 301–307.
[5] S. Schübbe, M. Kube, A. Scheffel, C. Wawer, U. Heyen, A. Meyerdierks, M. Madkour, F. Mayer, R. Reinhardt, D. Schüler, *J. Bacteriol.* **2003**, *185*, 5779–5790.

[6] S. C. Andrews, A. K. Robinson, F. Rodriguez-Quinones, *FEMS Microbiol. Rev.* **2003**, *27*, 215–237.
[7] D. Schüler, E. Baeuerlein, *J. Bacteriol.* **1998**, *180*, 159–162.
[8] U. Heyen, D. Schüler, *Appl. Microbiol. Biotechnol.* **2003**, *61*, 536–544.
[9] Y. A. Gorby, T. J. Beveridge, R. P. Blakemore, *J. Bacteriol.* **1988**, *170*, 834–841.
[10] D. Schüler, *Int. Microbiol.* **2002**, *5*, 209–214.
[11] D. Balkwill, D. Maratea, R. Blakemore, *J. Bacteriol.* **1980**, *141*, 1399–1408.
[12] Y. Okuda, K. Denda, Y. Fukumori, *Gene.* **1996**, *171*, 99–102.
[13] C. Nakamura, J. Burgess, K. Sode, T. Matsunaga, *J. Biol. Chem.* **1995**, *270*, 28392–28396.
[14] D. A. Bazylinski, A. Garratt-Reed, R. B. Frankel, *Microsc. Res. Tech.* **1994**, *27*, 389–401.
[15] H. Vali, J. L. Kirschvink, in *Iron Biominerals* (Eds R. B. Frankel, R. P. Blakemore), Plenum Press, New York, **1991**, pp. 97–116.
[16] K. Grünberg, C. Wawer, B. M. Tebo, D. Schüler, *Appl. Environ. Microbiol.* **2001**, *67*, 4573–4582.
[17] D. Schultheiss, D. Schüler, *Arch. Microbiol.* **2003**, *179*, 89–94.
[18] K. Grünberg, E. C. Müller, A. Otto, R. Reszka, D. Linder, M. Kube, R. Reinhardt, D. Schüler, *Appl. Eviron. Microbiol.* **2004**, *70*, 1040–1050.
[19] M. Gassmann, Diplomarbeit, Tübingen/München, **1996**.
[20] E. Baeuerlein, in *Biomineralization* (Ed. E. Baeuerlein), Wiley-VCH, Weinheim, **2000**, pp. 61–79.
[21] G. L. Blatch, M. Lassle, *BioEssays* **1999**, *21*, 932–939.
[22] Y. Okuda, Y. Fukumori, *FEBS Lett.* **2001**, *491*, 169–173.
[23] D. H. Nies, *FEMS Microbiol. Rev.* **2003**, *27*, 313–339.
[24] T. Clausen, C. Southan, M. Ehrmann, *Mol. Cell* **2002**, *10*, 443–455.
[25] M. Zurovec, F. Sehnal, *J. Biol. Chem.* **2002**, *277*, 22639–22647.
[26] S. Sudo, T. Fujikawa, T. Nagakura, T. Ohkubo, K. Sakaguchi, M. Tanaka, K. Nakashima, T. Takahashi, *Nature* **1997**, *387*, 563–564.
[27] B. Bochicchio, A. Pepe, A. M. Tamburro, *Matrix Biol.* **2001**, *20*, 243–250.
[28] A. Arakaki, J. Webb, T. Matsunaga, *J. Biol. Chem.* **2003**, *278*, 8745–8750.
[29] B. A. Gotliv, L. Addadi, S. Weiner, *Chembiochem* **2003**, *4*, 522–529.
[30] T. Matsunaga, N. Tsujimura, H. Okamura, H. Takeyama, *Biochem. Biophys. Res. Commun.* **2000**, *268*, 932–937.
[31] Y. Okamura, H. Takeyama, T. Matsunaga, *J. Biol. Chem.* **2001**, *276*, 48183–48188.
[32] R. Handrick, S. Reinhardt, D. Schultheiss, T. Reichart, D. Schüler, D. Jendrossek, *J. Bacteriol.* **2004**, *186*, 2466–2475.
[33] L. J. Jones, R. Carballido-Lopez, J. Errington, *Cell* **2001**, *104*, 913–922.
[34] J. Hacker, J. B. Kaper, *Annu. Rev. Microbiol.* **2000**, *54*, 641–679.
[35] M. Sheng, C. Sala, *Annu. Rev. Neurosci* **2001**, *24*, 1–29.
[36] D. Schüler, R. B. Frankel, *Appl. Microbiol. Biotechnol.* **1999**, *52*, 464–473.
[37] D. Schüler, *Arch. Microbiol.* **2004**, *181*, 1–7.

5 Enzymes for Magnetite Synthesis in *Magnetospirillum magnetotacticum*

Yoshihiro Fukumori

5.1 Introduction

Magnetospirillum magnetotacticum, which was isolated from microaerobic freshwater sediments in 1979 by Blakemore et al. [1], possesses interesting particles called magnetosomes, with ferrimagnetic iron oxide magnetite crystals (Figure 5.1) [2]. By using the chained magnetosomes as a magnetic sensor, the bacterium orients itself along the lines of the Earth's magnetic field [3]. The magnetite crystal in the magnetosome occurs with almost the same size of 50–100 nm in the cytoplasm and enclosed by lipid bilayers with some characteristic proteins [4].

How does the bacterium synthesize the magnetite crystals and regulate the size at room temperature? Mann et al. [5] have reported the characterization of magnetic spinels prepared by two independent chemical methods. The first is based on the partial oxidation of Fe(II) solutions in the presence of nitrate at 100 °C and the second on the reaction of hydrated ferric oxide (ferrihydrite) with ferrous ions at room temperature and pH 7 [5]. Tamaura et al. [6] have also reported the chemical formation of magnetite by air oxidation of $Fe(OH)_2$ suspensions. The reaction proceeds in three stages: (1) formation of Fe(III) oxides and slower formation of Fe_3O_4; (2) rapid formation of Fe_3O_4; and (3) linear formation of Fe_3O_4. They also suggested that Fe(II) is oxidized on the surface of the solid phases during the course of air oxidation. On the other hand, Frankel et al. [2] proposed that *M. magnetotacticum* synthesizes magnetites in the following sequence: (1) iron uptake with a reduction of Fe(III) to Fe(II) in the transport process; (2) formation of low-density hydrous ferric oxide with re-oxidation of Fe(II); (3) formation of high-density hydrous ferric oxide (ferryhydrite) through the dehydration of low-density hydrous oxide; and (4) formation of magnetite by the partial reduction of iron and the further dehydration of ferryhydrite. However, these proposals demonstrate no enzymatic mechanisms of iron oxidation and reduction for magnetite synthesis in *M. magnetotacticum*. This chapter describes the purification and characterization of Fe(II)-nitrite oxidoreductase [7], NADH-Fe(III) oxidoreductase [8] and nitrate reductase [9] for magnetite synthesis, and discusses the mechanism of enzymatic synthesis of magnetite in *M. magnetotacticum* MS-1 (ATCC31632).

Biomineralization: From Biology to Biotechnology and Medical Application, Second Edition. Edited by E. Bäuerlein

ISBN: 3-527-31065-7

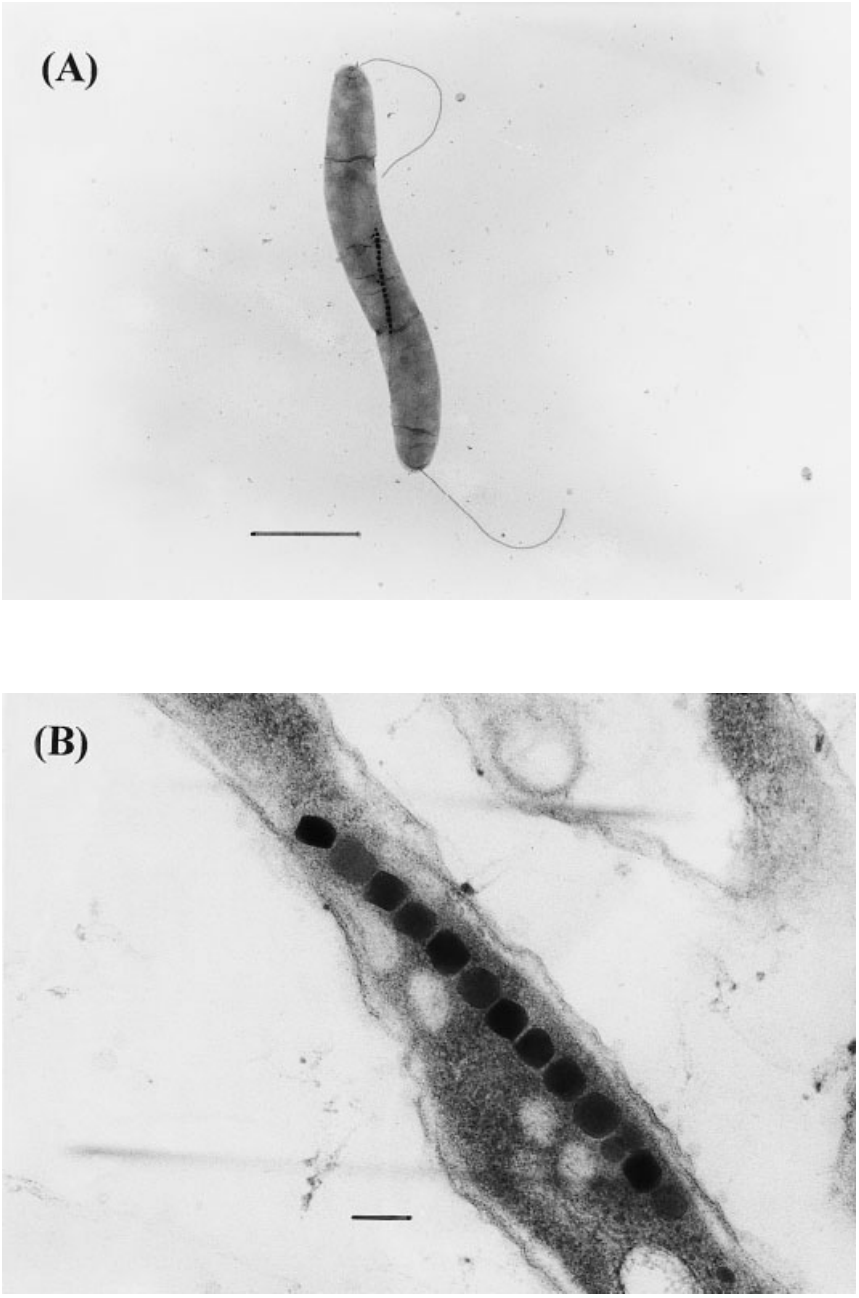

Figure 5.1 (A) Transmission electron micrograph of *M. magnetotacticum* MS-1 (ATCC31632). Electron-opaque spots in the middle of the cell are the magnetosomes. Single bipolar flagella are visible. Bar = 1 μm. (B) Thin section of *M. magnetotacticum*. Bar = 100 nm.

5.2 Ferric Iron Reduction in *M. magnetotacticum*

In general, the iron atom exists in its oxidized ferric state under aerobic conditions. A common strategy for bacteria to use in obtaining iron from their environment is to excrete siderophores, which bind and solubilize ferric iron. *M. magnetotacticum* uses a high-affinity siderophore system similar to that used by other Gram-negative organisms for iron acquisition [10]. For the iron held in the iron–siderophore complex to be used by the cell, it first must be removed from the siderophore. Current mechanisms envisioned for the removal of iron from siderophores include *in situ* reduction by ferric iron reductase [11], resulting in release of the ferrous iron. Reduction of Fe(III) to Fe(II) by ferric iron reductase is thought to be an obligatory step in iron uptake as well as the primary factor in making iron available for absorption by bacteria.

On the other hand, Nakamura et al. [12] have reported that *Magnetospirillum* sp. AMB-1 produces no siderophores and Schüler and Baeuerlein [13] have also reported that *Magnetospirillum gryphiswaldense* utilizes energy-dependent iron uptake, but not siderophore-like compounds. Although the uptake of iron in magnetic bacteria is still poorly understood, iron reduction must occur in the cell because magnetite is an oxide of mixed oxidation state, i.e. Fe(III) and Fe(II).

5.2.1 Localization and Purification of Iron Reductase from *M. magnetotacticum*

After *M. magnetotacticum* had been cultivated microaerobically in the chemically defined growth medium [1], the cells were suspended in 10 mM Tris–HCl buffer (pH 8.0) containing 0.75 M sucrose and incubated with EDTA plus lysozyme at 30 °C for 1 h. The suspension was centrifuged at 104 000 *g* for 30 min and the periplasmic fraction was retained as the supernatant. The precipitates obtained were resuspended in water at 4 °C and centrifuged at 104 000 *g* for 1 h. The supernatant was retained as the cytoplasmic fraction and the pellet was resuspended in 10 mM Tris–HCl buffer (pH 8.0), and utilized as the membrane fraction. The magnetosomes in the membrane fraction were removed with a magnet. Table 5.1 summarizes the localization of ferric iron reductase. Most of the ferric iron reductase is localized in the cytoplasm. The periplasmic fraction did not show any ferric iron reductase activity, although Paoletti and Blakemore [14] reported that the iron reductase activity in the cell-free extracts prepared from *M. magnetotacticum* was localized in the periplasmic space. On the other hand, the membranes retained about 30 % of the total activity detected in the cell-free extract. However, ferric iron reductase activity was not found in the membranes that had been washed with 0.3 M NaCl. Therefore, it seems likely that although the ferric iron reductase of *M. magnetotacticum* is a soluble enzyme, it may be loosely bound to the cytoplasmic face of the cytoplasmic membrane.

Table 5.1 Localization of ferric iron reductase in *M. magnetotacticum*

Fraction	Ferric iron reductase activity (nmol/min)	Nitrite reductase activity (μmol/min)	Malate dehydrogenase activity (μmol/min)
Periplasm	0	0.43	1.9
Cytoplasm	8.3	0	16.1
Membrane	3.6	ND[b]	ND[b]
Membrane[a]	0	ND[b]	ND[b]

The periplasm, cytoplasm, membrane and washed membrane were prepared by the method of [15]. The enzymatic activities were measured by the assay described by Noguchi et al. [9].
[a] Membranes were washed with 10 mM Tris–HCl buffer (pH 8.0), containing 0.3 M NaCl and centrifuged at 104 000 *g* for 1 h. The precipitate obtained was used as the washed membrane fraction.
[b] Not determined.

To purify the ferric iron reductase, the cells were broken with two passes through a French pressure cell at 1000 kgf/cm^2 and centrifuged at 10 000 *g* for 15 min. The supernatant was centrifuged at 104 000 *g* for 1.5 h and the resulting supernatant was fractionated with ammonium sulfate between 50 and 65 % saturation. The precipitate was suspended in 100 mM Tris–HCl buffer (pH 8.0) containing ammonium sulfate (30 % saturation) and the suspension was applied to a Butyl-Toyopearl column. The enzyme was eluted with a linear gradient of 30–10 % saturation of ammonium sulfate in 100 mM Tris–HCl buffer (pH 8.0) containing protease inhibitors. The active fractions were saturated with solid ammonium sulfate to 50 % and applied to a Sepharose CL-6B column that had been equilibrated with 50 % ammonium sulfate saturated buffer and eluted with a linear gradient of 50–25 % saturated ammonium sulfate buffer. The fractions showing ferric iron reductase activity were dialyzed against 50 mM sodium phosphate buffer (pH 7.0) containing 300 mM NaCl. The concentrated ferric iron reductase was further subjected to high-performance liquid chromatography and purified to an electrophoretically homogenous state. About 0.5 mg enzyme was purified from 40 *g* (wet weight) cells.

5.2.2 Characterization of *M. magnetotacticum* Ferric Iron Reductase

M. magnetotacticum ferric iron reductase is composed of a single subunit with a molecular mass of 36 kDa; the absorption spectrum of the purified enzyme shows an absorption peak at 280 nm, indicating that the enzyme has no prosthetic groups such as heme and flavin. However, it should be noted that the enzyme requires essentially FMN as an electron mediator from NADH to ferric iron. The activity in the presence of FAD is about 18 % of that in the presence of FMN and almost the same as that in the absence of the substrate, while other bacterial ferric iron reductases have been reported to be able to use FAD as an electron mediator. The K_m values for FMN, NADH and ferric citrate are 0.035, 1.3 and 15.5 μM, respectively. The V_{max} is about 0.87 s^{-1}.

The effects of $ZnSO_4$, $CaCl_2$, $MgSO_4$ and $MnCl_2$ on ferric iron reductase activity were examined. Zn^{2+} strongly inhibited the activity of the ferric iron reductase. The K_i values for Zn^{2+} were approximately 19.2 and 23.9 μM with respect to NADH and FMN, respectively. Other divalent cations had no effects on the enzymatic activity.

5.2.3 Function of Ferric Iron Reductase in *M. magnetotacticum*

Ferric iron reductases have been found in several other bacteria and are thought to be involved in many intracellular iron metabolism reactions. The ferric iron reductase of *M. magnetotacticum* has similar enzymatic and biochemical properties to those of *Rhodopseudomonas sphaeroides* [16] and *Azotobacter vinelandii* [17], suggesting that the enzyme has the same functions *in vivo*. However, *M. magnetotacticum* requires many more ferrous irons to synthesize magnetite than other heterotrophic bacteria. In fact, the magnetic cells of *M. magnetotacticum* contain 100 times as much iron as the heterotrophic bacteria [1]. Table 5.2 summarizes the effects of extracellular iron on ferric iron reductase activity of the soluble fraction and magnetite synthesis. The average number of particles per cell and ferric iron reductase activity of the soluble fraction decrease in parallel with the concentrations of ferric quinate in the medium. These results suggest that the iron reductase of *M. magnetotacticum* may participate in magnetite synthesis *in vivo*.

To demonstrate the participation of ferric iron reductase in magnetite synthesis, the effects of Zn^{2+} in the medium on magnetite synthesis were investigated by comparing the ferric iron reductase activity of the soluble fractions and the average numbers of magnetosomes in the cells, which were cultivated in the presence of various concentration of $ZnSO_4$. As shown in Figure 5.2, the bacterial growth was not affected by $ZnSO_4$, while the ferric iron reductase activity and the average number of magnetosomes decreased in parallel with the concentration of $ZnSO_4$ in the medium. Furthermore, the non-magnetic cells increased in parallel with the concentration of $ZnSO_4$ in the medium. In the cells grown in the presence of 75 μM $ZnSO_4$,

Table 5.2 Ferric iron reductase activity of the soluble fraction and the magnetosome numbers in a cell cultivated at various concentrations of Fe(III)-quinate

Fe(III)-quinate in the medium (μM)	Magnetosome numbers[a]	Iron reductase activity[b] (nmol Fe(II)-ferrozine formed/min/mg)
0	4.2	4.3
1	8.9	6.9
2.5	12	5.7
5	14	11.7
20	15	10.5

[a] Average magnetosome numbers were determined by counting electron-dense particles in the micrographs from a total of about 100 cells.
[b] The enzymatic activity was determined by the method described by Noguchi et al. [9].

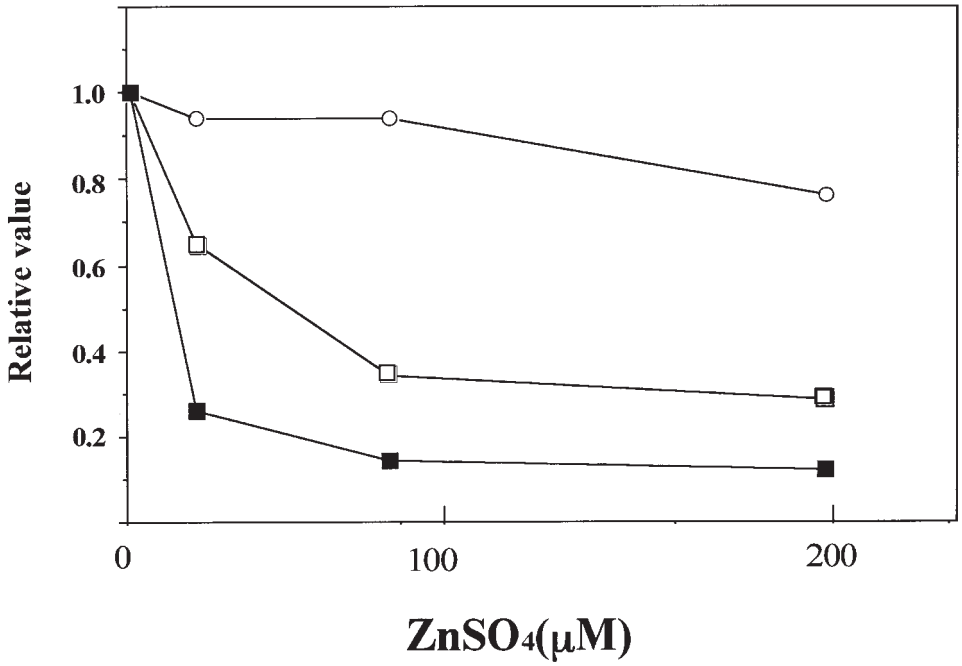

Figure 5.2 Effects of $ZnSO_4$ on growth, magnetosome numbers per cell and ferric iron reductase activity. *M. magnetotacticum* was cultivated in the medium supplemented with various concentrations of $ZnSO_4$. The growth (○) was determined by measuring the absorbance at 600 nm. The magnetosome numbers (□) were obtained by counting electron-dense particles in micrographs from a total of about 50 cells in each sample. The ferric iron reductase activity in the presence of Zn^{2+} (■) was determined by the method of [9].

about 48 % of cells did not have magnetic particles. These results strongly suggest that the ferric iron reductase plays a role in supplying ferrous iron to magnetite *in vivo*.

5.3 Ferrous Iron Oxidation in *M. magnetotacticum*

Blakemore et al. investigated the optimal growth conditions for magnetite synthesis by *M. magnetotacticum* and found that the bacterium produces much magnetite under microaerobic denitrifying conditions [18, 19]. The bacterium scarcely synthesizes magnetites under aerobic conditions and, furthermore, does not grow using nitrate respiration (denitrification) under strictly anaerobic conditions. Therefore, the bacterium can obtain the energy for life processes and synthesize magnetite by respiring with nitrate and oxygen as terminal electron acceptors simultaneously. Tamegai and Fukumori [20] have purified the *ccb*-type cytochrome *c* oxidase from

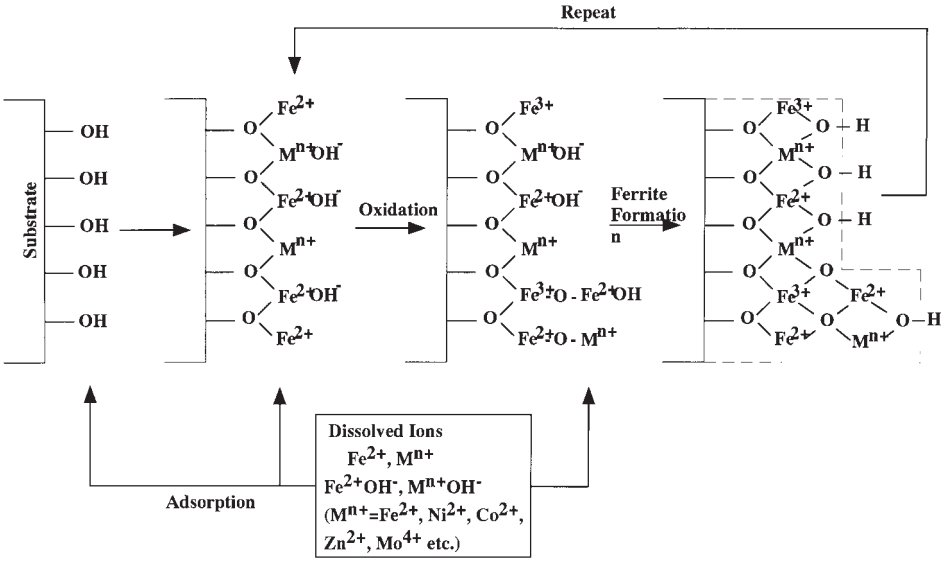

Figure 5.3 Principle of ferrite plating. A substrate with OH groups on its surface is immersed in a reaction solution containing Fe(II) and other metal ions. These ions are then adsorbed onto the surface mediated by the OH groups. When an oxidizing reagent such as $NaNO_2$ is introduced, some of the Fe(II) ions are oxidized to Fe(III), which causes a ferrite formation reaction [25].

M. magnetotacticum. The enzyme is very similar to those found in some microaerobic bacteria such as *Bradyrhizobium japonicum* [21] and *Rhodobacter sphaeroides* [22], and constitutively synthesized in both magnetic cells and non-magnetic cells [20]. Therefore, *M. magnetotacticum* appears to produce ATP with microaerobic respiration using the *ccb*-type cytochrome *c* oxidase, but not denitrification.

What is the function of denitrification in *M. magnetotacticum*? Denitrification involves four distinct enzyme systems – nitrate reductase, nitrite reductase, nitiric oxide reductase and nitrous oxide reductase – which catalyze the reaction, $NO_3 \Rightarrow NO_2 \Rightarrow NO \Rightarrow N_2O \Rightarrow N_2$ [23]. Abe and Tamaura [24, 25] have reported that nitrite can be used as an effective oxidizing reagent for the chemical synthesis of spinel-type ferrites in aqueous solution. Figure 5.3 shows the principles of magnetite synthesis by the ferrite-plating method developed by Egusa et al. [25]. A substrate with OH groups on its surface is immersed in a reaction solution containing ferrous ions. The ferrous ions are then adsorbed on the surface mediated by the OH groups. When an oxidizing reagent such as sodium nitrite is introduced at 70 °C, some of the ferrous ions are oxidized to ferric ions, which causes a magnetite formation reaction. In this model, nitrite functions as an oxidizing reagent for the chemical synthesis of magnetite, suggesting that a similar phenomenon, i.e. the enzymatic oxidation of ferrous iron by nitrite, might be occurring in *M. magnetotacticum*. Recently, we have purified cytochrome cd_1 (nitrite reductase) from *M. magnetotacticum* and found that the enzyme has high Fe(II)-nitrite oxidoreductase activity [7]. Blakemore et al. analyzed spectrophotometrically the cytochrome composition in

the soluble fractions and membranes prepared from *M. magnetotacticum* and found that cytochrome cd_1 was highly expressed in the denitrifying cells, which have large quantities of magnetites [26]. In this section, we describe the purification and novel enzymatic properties of cytochrome cd_1 from *M. magnetotacticum* and discuss the function of cytochrome cd_1 in magnetite synthesis.

5.3.1 Purification of *M. magnetotacticum* Cytochrome cd_1

The soluble fraction prepared from *M. magnetotacticum* was applied to a DEAE-Toyopearl column equilibrated with 10 mM Tris–HCl buffer (pH 8.0). The flow-through fraction was dialyzed against 10 mM sodium phosphate buffer (pH 6.5) for 12 h and the desalted solution was applied to a CM-Toyopearl column equilibrated with the same buffer used for dialysis. Cytochrome cd_1 was eluted with a linear gradient of 0–0.2 M NaCl in the same buffer. The fraction containing cytochrome cd_1 was subjected to gel filtration on a Sephacryl S-200 column equilibrated with 10 mM sodium phosphate buffer (pH 6.5) containing 0.2 M NaCl. The fraction containing cytochrome cd_1 was concentrated by ultrafiltration in an Amicon unit and used as the purified enzyme.

5.3.2 Spectral Properties and Molecular Features of *M. magnetotacticum* Cytochrome cd_1

The oxidized form of the purified cytochrome cd_1 had absorption peaks at 643, 409 and 280 nm (Figure 5.4). After reduction with sodium dithionite, the absorption peaks were observed at 663, 551, 522 and 418 nm. Although these spectral properties resemble those of *Pseudomonas aeruginosa* cytochrome cd_1, *M. magnetotacticum* cytochrome cd_1 showed some novel spectral features, different from those of other cytochrome cd_1. First, the α-peak attributed to heme *c* of *M. magnetotacticum* cytochrome cd_1 is symmetrical. The α-peak of the enzyme is not split at room temperature. Second, a prominent shoulder around 460 nm in the reduced form is not observed in *M. magnetotacticum* cytochrome cd_1. These spectral features suggest that the heme-binding environments of *M. magnetotacticum* cytochrome cd_1 may be different from those of other bacterial cytochrome cd_1.

The molecular mass of cytochrome cd_1 was determined to be about 133 000 on gel filtration. However, on sodium dodecylsulfate–polyacrylamide gel electrophoresis, the value was estimated to be about 54 000. These results suggest that the cytochrome cd_1 of *M. magnetotacticum* exists as a dimer.

5.3.3 Enzymatic Properties and Function of *M. magnetotacticum* Cytochrome cd_1

M. magnetotacticum cytochrome cd_1 showed *N*,*N*,*N*′,*N*′-tetramethyl-*p*-phenylenediamine (TMPD)-nitrite oxidoreductase activity. The V_{max} is 6.3 s^{-1} and the K_m

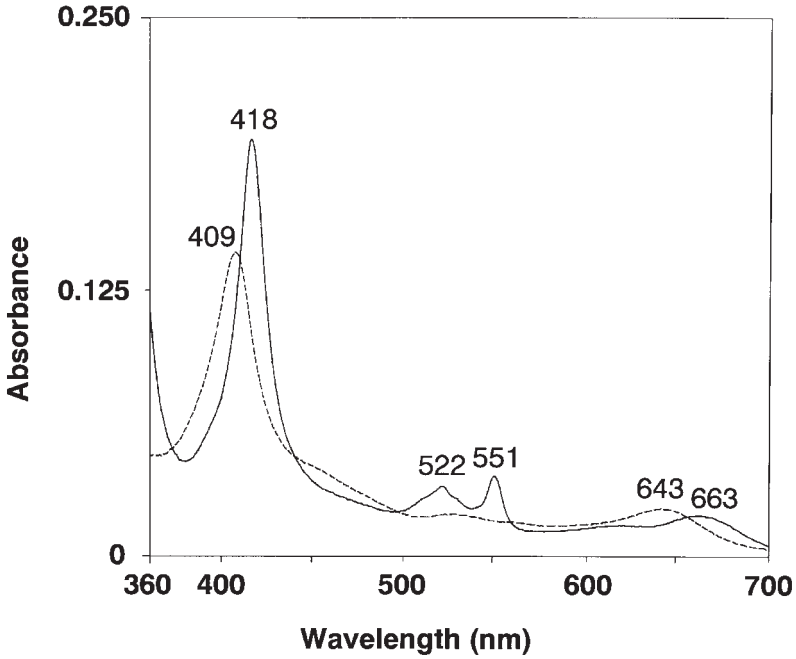

Figure 5.4 Absorption spectra of pure cytochrome cd_1 nitrite reductase from *M. magnetotacticum*. The oxidized form of the purified cytochrome cd_1 had absorption peaks at 643, 409 and 280 nm. After reduction with sodium dithionite, the absorption peaks were observed at 663, 551, 522 and 418 nm. Broken line, oxidized; full line, reduced with $Na_2S_2O_4$.

value for nitrite is 1.47 μM, while the V_{max} of *P. aeruginosa* cytochrome cd_1 is about 80 s^{-1}. Cytochrome cd_1 usually utilizes ferrocytochrome *c* as an electron donor *in vivo*. Although *M. magnetotacticum* has cytochrome *c*-550, which is homologous to cytochrome c_2 [27], the cytochrome cd_1 could not oxidize ferrocytochrome *c*-550 in the presence of nitrite. Furthermore, *M. magnetotacticum* cytochrome cd_1 was not equally induced in the magnetic cells and non-magnetic cells, even though both cells were grown under the same culture conditions. These results indicate that although *M. magnetotacticum* cytochrome cd_1 reduces nitrite to NO, the physiological function may not be closely related to the denitrifying respiratory chain.

On the other hand, Fe(II) is chemically oxidized with nitrite at pH 8, as previously reported by Moraghan and Buresh [28]. As shown in Figure 5.5, Fe(II) is chemically oxidized by nitrite under anaerobic conditions. However, Fe(II) is more rapidly oxidized by nitrite in the presence of *M. magnetotacticum* cytochrome cd_1. *P. aeruginosa* cytochrome cd_1, which showed much higher TMPD-nitrite oxidoreductase activity than *M. magnetotacticum* cytochrome cd_1, did not activate the oxidation of Fe(II).

Cytochromes cd_1 of denitrifying bacteria are considered to be localized in the periplasmic space or loosely bound to the cytoplasmic membrane. Recently, we

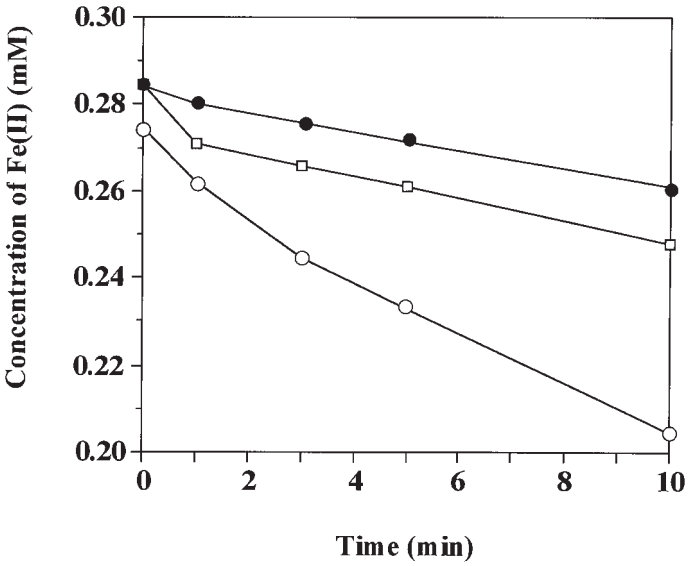

Figure 5.5 Enzymatic and chemical oxidation of Fe(II) in the presence of nitrite. The reaction mixture was assayed in 10 mM Tris–HCl buffer (pH 8.0) containing 0.6 μM cytochrome cd_1, D-glucose oxidase (2.4 U), catalase (60 U), 0.1 M glucose and 0.5 mM $FeSO_4$ in a total volume of 3 ml [7]. After the oxygen was removed by the action of the glucose/glucose oxidase/catalase system, 15 μl of 20 mM $NaNO_2$ was added at time zero to the reaction mixture. The following are indicated: the rate of Fe(II) oxidation in the absence of *M. magnetotacticum* and *P. aeruginosa* cytochrome cd_1 (●); the rate of Fe(II) oxidation in the presence of *M. magnetotacticum* cytochrome cd_1 (○); the rate of Fe(II) oxidation in the presence of *P. aeruginosa* cytochrome cd_1 (□).

have found that most *M. magnetotacticum* cytochrome cd_1 is localized in the periplasmic fraction [7]. Furthermore, some of these cytochromes were identified on the cytoplasmic membranes. Therefore, *M. magnetotacticum* cytochrome cd_1 seems to be situated on the periplasmic face of the cytoplasmic membrane. However, magnetosome vesicles are present in the cytoplasm, and the magnetosome membranes do not appear to be contiguous with the cytoplasmic membranes [4]. Therefore, to elucidate the involvement of cytochrome cd_1 in magnetite synthesis *in vivo*, the mechanism of the transport system of Fe(II) to the periplasmic space across the cytoplasmic membrane and the formation of magnetosome vesicles should be studied in future.

5.4 Nitrate Reductase of *M. magnetotacticum* MS-1

The nitrate reductase of *M. magnetotacticum* MS-1 is composed of 86- and 17-kDa subunits, and contains molybdenum, non-heme iron and heme *c* [9]. These properties are very similar to those of the periplasmic nitrate reductase found in *Paracoccus pantotrophus*. The *M. magnetotacticum nap* locus is clustered in seven open

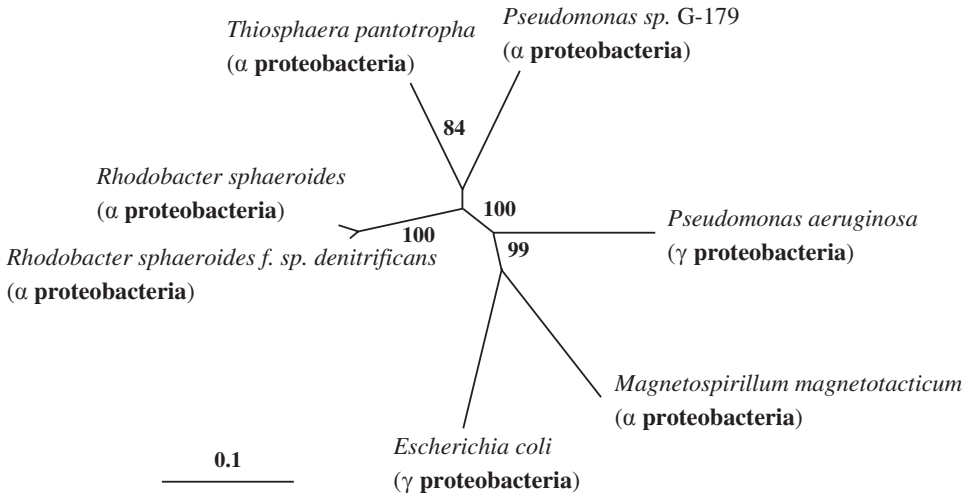

Figure 5.6 Phylogenetic tree of NapA. The 'out-group' was not defined. The tree was constructed with CLUSTAL W software using the neighbor-joining method. The figure represents bootstrap confidence percentages from 1000 bootstraps for grouping. The bar represents a distance of 0.1.

reading frames, *napFDAGHBC*. Figure 5.6 shows the phylogenetic tree of prokaryotic nitrate reductase NapA, suggesting a close relationship between *M. magnetotacticum nap* genes and *Escherichia coli nap* genes. It is of interest that α-proteobacteria possess a *napFDAGHBC*-type *nap* gene cluster.

The expression of the *E. coli* K-12 *napF* operon is atypically regulated via Fnr and NarP/NarL proteins. The 5′ end of the *napF* region of the *M. magnetotacticum nap* operon shows two binding sites of the putative transcriptional factors, Fnr and NarL/NarP proteins. Fnr protein is a global regulator that controls the transcription of genes whose functions facilitate adaptation to growth under oxygen-limiting conditions. On the other hand, NarL/NarP is a transmitter component of the two-component system, and controls gene expression in response to nitrate and nitrite. However, the putative NarL/NarP-binding site found in the upstream region of *M. magnetotacticum napF* is not located between the Fnr-binding site and the initiation site of *napF*, and, furthermore, is not organized as inverted repeats with 2-bp spacing. Therefore, it seems likely that expression of the genes encoding the periplasmic nitrate reductase of *M. magnetotacticum* is regulated by oxygen, but not nitrate/nitrite.

5.5 Structure and Function of the 22 kDa Protein Localized in the Magnetosome Membrane

The bacterium possesses a ''magnetosomes chain'', consisting of 10–30 magnetosomes. The magnetosome is composed of a single crystal of magnetite (Fe_3O_4)

which occurs in the cell with a diameter of 50–100 nm and enclosed by lipid membranes. Recently, we have found that a 22-kDa protein (MAM22) is localized in the magnetosomes prepared from *M. magnetotacticum* and is a new member of the tetratricopeptide repeat (TPR) protein family [29, 30]. Based on the consensus amino acid sequence pattern, MAM22 contains six tandemly arranged TPR units, although the first, second and last sequence have lower similarity to the consensus sequence pattern (Figure 5.7). In the case of MAM22, the TPR motifs occupy 90 % of the whole of MAM22.

The TPR motif was first identified as a tandemly repeated degenerate 34-amino-acid sequence in the cell division cycle genes [31, 32]. It is now realized that over 25 proteins are present, and organisms as diverse as bacteria and humans contain TPR motifs. In addition to cell cycle regulation, biological processes such as transcription control, mitochondrial and peroxisomal protein transport, neurogenesis, protein kinase inhibition, Rac-mediated activation of NADPH oxidase, and protein folding involve TPR motifs [33].

Recently, the crystal structure of the N-terminal TPR domain of a human Ser/Thr protein phosphatase, PP5, was reported [34]. The authors proposed a structural model for the tandemly arranged TPR motifs. According to this structural model, it was proposed that six TPR motifs containing MAM22 form the 6/7 turn of a superhelix. Furthermore, the top and outside of the superhelix consisted of negatively charged residues, the bottom of the superhelix consisted of positively charged residues and helix B of TPR1′ exposed to the outside and inside of the superhelix consisted of hydrophobic residues. Therefore, the inside of the superhelix interacts with a helix of other magnetosome proteins and MAM22 is localized on the magnetosome surface. Furthermore, the opposite charges of the top and bottom of MAM22 and/or hydrophobic residues of TPR1′ cause the interaction of MAM22 themselves.

The finding of a protein with TPR motifs in magnetosomes would provide important clues concerning the mechanism of magnetite synthesis and/or maintenance of the chain structure of magnetosomes in magnetotactic bacteria, although the elucidation of the mechanism would require detailed information about the structures of MAM22 and other magnetosome proteins such as MAM12 and MAM28. It should be studied in future, combining the construction of an MAM22-deficient mutant.

5.6 Proposed Mechanism of Magnetite Synthesis in *M. magnetotacticum*

Figure 5.8 shows a proposed mechanism for the enzymatic synthesis of magnetite in *M. magnetotacticum*. First, the bacterium takes up ferric quinate with a very poorly characterized system and transports it across the membrane into the cytoplasm. Once in the cell, Fe(III) is reduced by iron reductase, using NADH as the reducing power in the presence of FMN in the cytoplasm. The iron reductase of *M. magneto-*

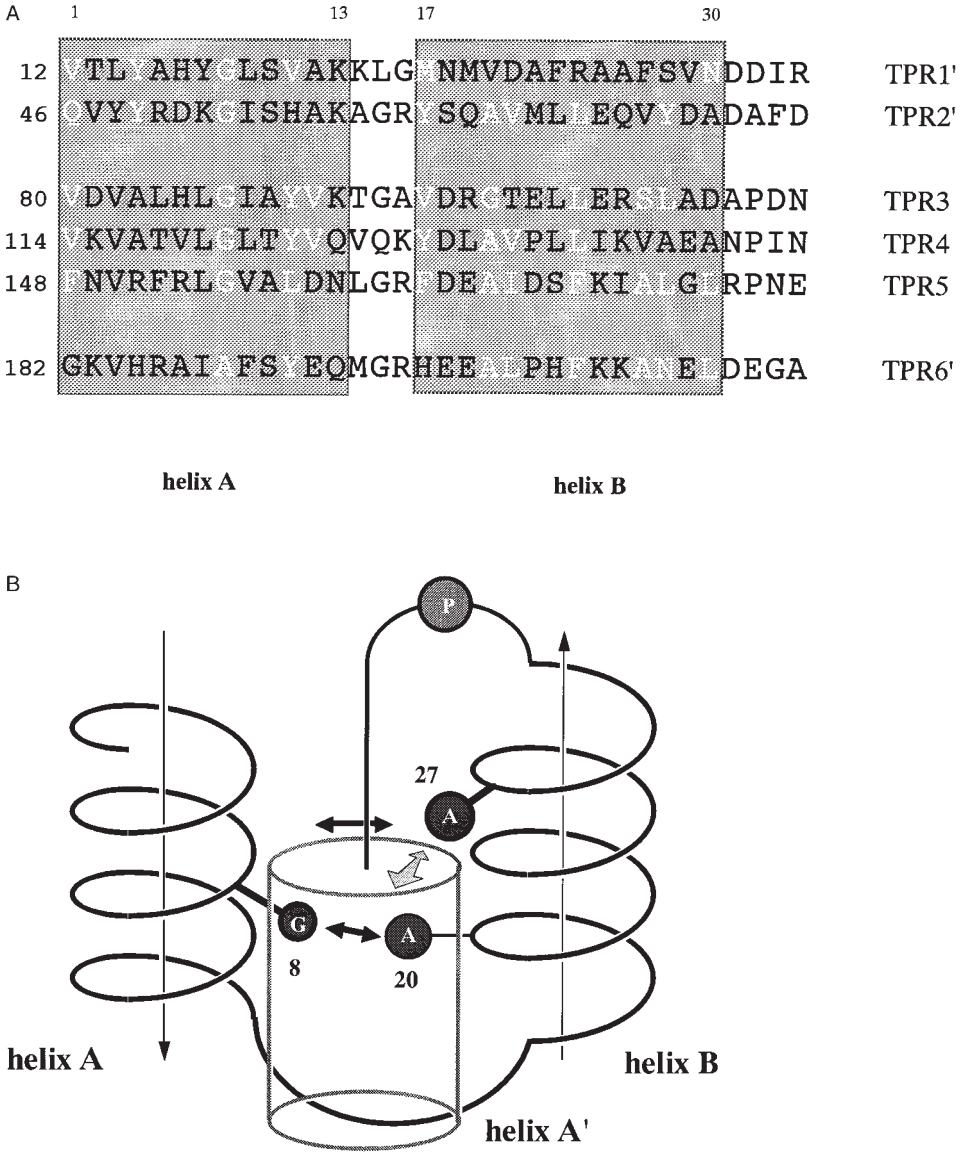

Figure 5.7 (A) Consensus sequence pattern of the TPR motif and six amino acid sequences of the TPR motif found in MAM22. The highly conserved large and small hydrophobic residues positioned among the TPR proteins are emphasized by white letters on the shaded background. The residues in the shaded box construct α-helix A and B, respectively. The number on the left of each sequence is the position of the first residue in the MAM22 sequence (GenBank accession no. D82942). (B) The structural model of the TPR motif. Residues 8 and 20 are located at the position of closest contact between the A and B α-helices of a TPR, whereas residue 27 on helix B is located at the interface of three helices [A, B and A′ (helix A of next TPR motif)] within a three-helix bundle.

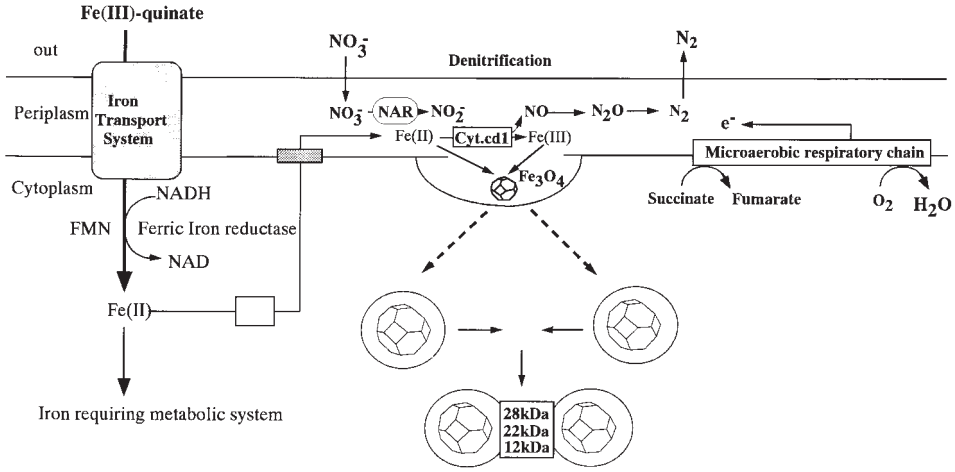

Figure 5.8 Proposed mechanism of magnetite synthesis and magnetosome formation in *M. magnetotacticum*. See the text for discussion.

tacticum appears to be an assimilatory enzyme, which has similar properties to those found in *R. sphaeroides* [16] and *A. vinelandii* [17]. The iron reductase is strongly inhibited by Zn^{2+} and the amounts of magnetite in the cell decrease proportionally to increasing concentrations of Zn^{2+} in the culture medium. Although the mechanisms of these inhibitory effects are still not clear, the iron reductase seems to be participating in magnetite synthesis in *M. magnetotacticum*.

M. magnetotacticum has a microaerobic respiratory chain [20]. Oxygen is essential for growth and is rapidly reduced to H_2O by cytochrome *c* oxidase [20]. It is therefore possible that most of the Fe(II) may be present as free ions at neutral pH even under microaerobic conditions. However, it is not clear whether or not Fe(II) is stored as intracellular iron-binding components.

In 1983, Abe et al. invented the ferrite plating technique [24]. The method enables crystalline ferrite films to be grown from an aqueous solution at 100 °C. The formation of Fe_3O_4 from an Fe(II) aqueous solution has two important steps: (1) oxidation of Fe(II) to Fe(III), forming γ-FeOOH and (2) adsorption of Fe(II) onto γ-FeOOH, which accompanies the spinel formation. Therefore, Fe(II) oxidation plays an essential role in the ferrite plating, for which $NaNO_2$ has been found to be the most expedient oxidizing reagent. As described in Section 7.3, the respiratory enzyme in denitrification, cytochrome cd_1, shows high Fe(II)-nitrite oxidoreductase activity. Furthermore, the enzyme is weakly bound to the cytoplasmic membrane in the periplasmic space. These results suggest that Fe(II) oxidation may occur on the cytoplasmic membrane surface, which might mimic the plate.

On the basis of high-resolution transmission electron microscopy and Mössbauer spectroscopy, many researchers have reported that the magnetite produced by *M. magnetotacticum* is a well-ordered, single-domain octahedral crystal [2, 35]. Therefore, the nucleation of magnetite occurs at one primary nucleation site, suggesting

the possibility that protein molecules, active in nucleation, are spatially organized at a unique site in the magnetosome membrane or cytoplasmic membrane. Furthermore, the nucleating proteins seem to have high affinity for Fe(II)/Fe(III). Recently, Arakaki et al. have proposed that the some proteins with low molecular weights are tightly bound to the magnetosomes prepared from *M. magneticum* strain AMB-1 and might be participated in the magnetite crystal formation [36]. The molecular mechanism of single magnetite crystal formation at room temperature will be a problem of central interest in *M. magnetotacticum*. Genetic systems in the bacterium have only recently begun, and little is known at the enzyme level. Improvement of genetic systems will be critical in learning about the regulatory mechanism of magnetite crystallization.

References

[1] R. P. Blakemore, D. Maratea, R. S. Wolfe, *J. Bacteriol.* **1979**, *140*, 720–729.
[2] R. B. Frankel, G. C. Papaefthymiou, R. P. Blakemore, W. O'Brien, *Biochim. Biophys. Acta* **1983**, *763*, 147–159.
[3] R. P. Blakemore, *Annu. Rev. Microbiol.* **1982**, *36*, 217–238.
[4] Y. A. Gorby, T. J. Beveridge, R. P. Blakemore, *J. Bacteriol.* **1988**, *170*, 834–841.
[5] S. Mann, N. H. C. Sparks, S. B. Couling, M. C. Larcombe, R. B. Frankel, *J. Chem. Soc., Faraday Trans.* **1989**, *85*, 3033–3044.
[6] Y. Tamaura, K. Ito, T. Katsura, *J. Chem. Soc., Dalton Trans.* **1983**, 189–194.
[7] T. Yamazaki, H. Oyanagi, T. Fujiwara, Y. Fukumori, *Eur. J. Biochem.* **1995**, *233*, 665–671.
[8] Y. Noguchi, T. Fujiwara, K. Yoshimatsu, Y. Fukumori, *J. Bacteriol.* **1999**, *181*, 2142–2147.
[9] A. Taoka, K. Yoshimatsu, M. Kanemori, Y. Fukmori, *Can. J. Microbiol.* **2003**, *49*, 197–206.
[10] L. C. Paoletti, R. P. Blakemore, *J. Bacteriol.* **1986**, *167*, 73–76.
[11] F. Halle, J.-M. Meyer, *Eur. J. Biochem.* **1992**, *209*, 621–627.
[12] C. Nakamura, T. Sakaguchi, S. Kudo, J. G. Burgess, K. Sode, T. Matsunaga, *Appl. Biochem. Biotechnol.* **1993**, *39/40*, 169–176.
[13] D. Schüler, E. Baeuerlein, *J. Bacteriol.* **1998**, *180*, 159–162.
[14] L. C. Paoletti, R. P. Blakemore, *Curr. Microbiol.* **1988**, *17*, 339–342.
[15] P. R. Alefounder, S. J. Ferguson, *Biochem. J.* **1980**, *192*, 231–240.
[16] M. D. Moody, H. A. Dailey, *J. Bacteriol.* **1985**, *163*, 1120–1125.
[17] M. Huyer, W. J. Page, *J. Bacteriol.* **1989**, *171*, 4031–4037.
[18] J. C. Escalante-Semerena, R. P. Blakemore, R. S. Wolfe, *Appl. Environ. Microbiol.* **1980**, *40*, 429–430.
[19] R. P. Blakemore, K. A. Short, D. A. Bazylinski, C. Rosenblatt, R. B. Frankel, *Geomicrobiol. J.* **1985**, *4*, 53–71.
[20] H. Tamegai, Y. Fukumori, *FEBS Lett.* **1994**, *347*, 22–26.
[21] O. Preisig, R. Zufferey, L. Thony-Meyer, C. A. Appleby, H. Hennecke, *J. Bacteriol.* **1996**, *178*, 1532–1538.
[22] J. A. Garcia-Horsman, E. Berry, J. P. Shapleigh, J. O. Alben, R. B. Gennis, *Biochemistry* **1994**, *33*, 3113–3119.
[23] W. G. Zumft, *Microbiol. Mol. Biol. Rev.* **1997**, *61*, 533–616.
[24] M. Abe, Y. Tamaura, *Jpn. J. Appl. Phys.* **1983**, *22*, L511.
[25] K. Egusa, K. Marugame, M. Abe, T. Itoh, in *Proc. 6th Int. Conf. on Ferrites (ICF-6)* (Eds T. Yamaguchi and M. Abe), Japan Society of Powder and Powder Metallurgy, Tokyo, **1992**, pp. 11–14.
[26] W. O'Brien, L. C. Paoletti, R. B. Blakemore, *Curr. Microbiol.* **1987**, *15*, 121–127.

[27] K. Yoshimatsu, T. Fujiwara, Y. Fukumori, *Arch. Microbiol.* **1995**, *163*, 400–406.
[28] J. T. Moraghan, R. J. Buresh, *Soil Sci. Soc. Am. J.* **1977**, *41*, 47–50.
[29] Y. Okuda, K. Denda, Y. Fukumori, *Gene* **1996**, *171*, 99–102.
[30] Y. Okuda, Y. Fukumori, *FEBS Lett.* **2001**, *491*, 169–173.
[31] R. S. Sikorski, M. S. Boguski, M. Goebl, P. Hieter, *Cell* **1990**, *60*, 307–317.
[32] T. Hirano, N. Kinoshita, K. Morikawa, M. Yamagata, *Cell* **1990**, *60*, 319–328.
[33] G. L. Blatch, M. Lassle, *BioEssays* **1999**, *21*, 932–939.
[34] A. K. Das, P. T. W. Cohen, D. Barford, *EMBO J.* **1998**, *17*, 1192–1199.
[35] S. Mann, R. B. Frankel, R. P. Blakemore, *Nature* **1984**, *310*, 405–407.
[36] A. Arakaki, J. Webb, T. Matsunaga, *J. Biol. Chem.* **2003**, *278*, 8745–8750.

6 Molecular and Biotechnological Aspects of Bacterial Magnetite

Tadashi Matsunaga, Toshifumi Sakaguchi and Yoshiko Okamura

6.1 Introduction

Magnetic bacteria synthesize intracellular magnetosomes consisting of magnetite (Fe_3O_4) or greigite (Fe_3S_4) that vary in from 50 to 100 nm. Magnetosomes are aligned in chains parallel to the cell axis, enabling the cell to migrate along the Earth's geomagnetic field lines and to maintain its position within the boundary of the oxic–anoxic transition zone (OATZ) [for review, see 1]. This magnetotaxis is associated with aerotactic sensory mechanisms [2]. However, facultative anaerobic *Magnetospirillum magneticum* AMB-1 and MGT-1 exhibit relatively less magnetotaxis. Thus, we refer to these strains as "magnetic" rather than magnetotactic. Magnetosomes are also referred to as bacterial magnetic particles (BMPs) to distinguish them from artificial magnetic particles (AMPs). The aggregation of BMPs can be easily dispersed in aqueous solutions compared to AMPs because of the enclosing membrane (Figure 6.1) [3]. In addition, the particle is the largest magnetic crystal that has a regular morphology within a single domain size. Therefore, BMPs have a vast potential for various technological applications, not only scientific interests. However, the molecular mechanism of magnetite biomineralization is poorly understood although iron oxide formation occurs widely in many organisms such as algae [4], chitons [5], honey bee [6, 7], yellowfin tuna [8], sockeye salmon [9, 10], etc. We are currently using *M. magneticum* AMB-1 (Figure 6.2A), for which gene transfer techniques have been developed [11], as a model organism in order to elucidate the molecular mechanisms of magnetite biomineralization. Here, we describe several findings and application studies for BMPs in *M. magneticum* AMB-1.

6.2 Isolation and Cultivation of Magnetic Bacteria

6.2.1 Pure Cultivation of Magnetic Bacteria

Since pure culture of *M. (Aquaspirillum) magnetotacticum* strain MS-1 was achieved in 1979 [12], the majority of magnetic bacteria have been found to be obligate microaerobic or anaerobic nitrate-reducing bacteria of the α-proteobacteria.

Biomineralization: From Biology to Biotechnology and Medical Application, Second Edition. Edited by E. Bäuerlein

ISBN: 3-527-31065-7

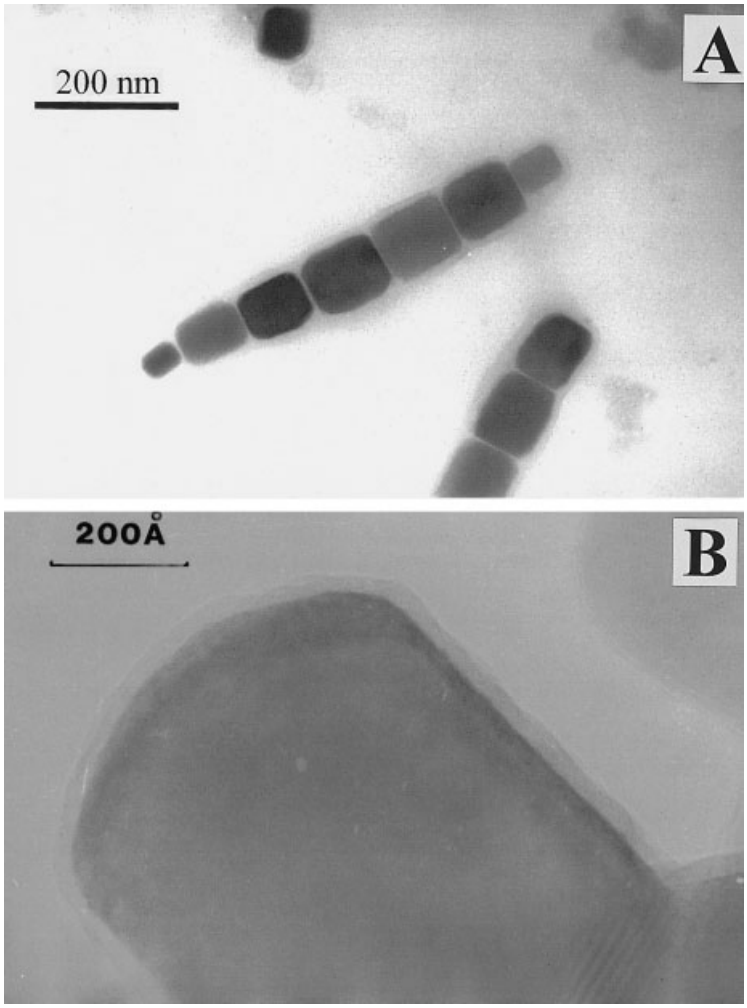

Figure 6.1 Transmission electron micrographs of BMPs. (A) BMPs extracted from magnetic bacteria by a French press, arranged in a chain. Average size of BMPs was 50–100 nm within the single-domain region. Bar = 200 nm. (B) Magnified picture of a single BMP. A thin organic membrane was observed covering the particle, with a thickness of about 3.5 nm. Bar = 200 Å.

They include an aerotolerant microaerophilic spirillum *M. gryphiswaldense* strain MSR-1 [13] and a microaerophilic coccus, strain MC-1 [14]. Three facultatively anaerobic vibrios, strains MV-1 [15], MV-2 and MV-4, are classed as γ-proteobacteria [16]. We have succeeded in isolating two facultatively anaerobic spirilla, *M. magneticum* strains AMB-1 [17, 18] and MGT-1 [3, 18, 19], and an obligate anaerobe, *Desulfovibrio magneticus* strain RS-1 [20, 21].

Many morphological types of magnetic bacteria have been found in natural aquatic environments [22, 23]; however, they cannot be cultured under artificial

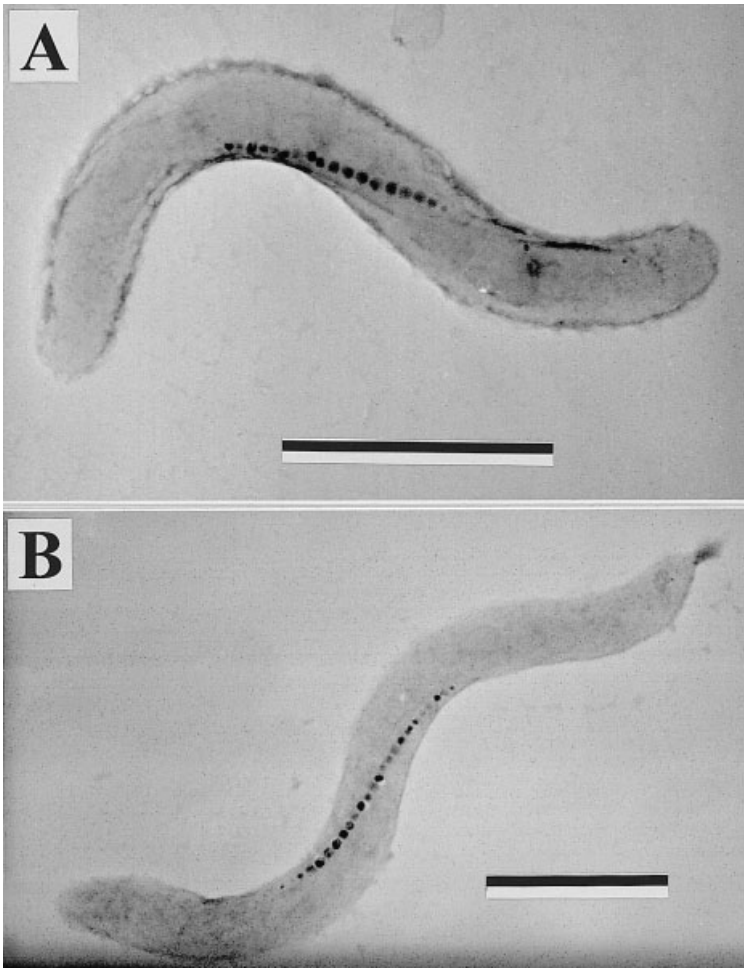

Figure 6.2 Transmission electron micrographs of magnetic bacteria, *Magnetospirillum* spp. strains AMB-1 (A) and MGT-1 (B). Cells were grown anaerobically in the growth medium [9]. Bar = 1.0 μm.

conditions. Therefore, new methods were necessary to obtain physiological information about non-cultured magnetic bacteria. Recent progress has been obtained in pure culture. Our isolated magnetic spirilla from freshwater sediment, *M. magneticum* strains AMB-1 and MGT-1 (Figure 6.2) are facultatively anaerobic denitrifiers that can grow well either aerobically or anaerobically by dissimilatory nitrate reduction. Cells of both strains have oxidase activity when they are grown in aerobic conditions. Although they are catalase negative, they are aerotolerants capable of forming colonies on solid agar medium without the addition of catalase. AMB-1 and MGT-1 can grow in free gaseous exchange with an air atmosphere under shak-

ing at 120 r.p.m. These characteristics against oxygen in AMB-1 and MGT-1 are different from that of an obligate microaerophile, *M. magnetotacticum* MS-1 [17, 18]. In addition, iron reduction involved in magnetite synthesis in *M. magnetotacticum* MS-1 was inhibited by azide, an inhibitor of the terminal electron acceptor of the respiratory chain [24]. On the other hand, iron reduction and BMP formation in *M. magneticum* AMB-1 under anaerobic condition were inhibited by dicumarol, a quinone inhibitor. Other inhibitors of respiration did not affect iron reduction [25]. It is apparent that there is a difference between AMB-1 and MS-1 in terms of the electron pathway for iron reduction in the respiratory chain. Furthermore, MS-1 requires oxygen respiration for iron oxidation involved in BMP synthesis [26], but this is not the case for AMB-1 [25].

AMB-1 and MGT-1 can grow aerobically and form colonies. In addition, the spiral morphology, cell size, ability for BMP production and crystal morphology of synthesized BMPs are similar between AMB-1 and MGT-1. However, both strains are regarded as distinct from each other because of their differences in carbon-source utilization. AMB-1 can use 12 carboxylic acids and MGT-1 can use 15 carboxylic acids when they are grown under anaerobic conditions [18]. Moreover, MGT-1 possesses a cryptic plasmid [27]. Our study on the evolutionary relationship among *Magnetospirillum* spp. based on 16S rDNA sequences indicates that AMB-1 and MGT-1 can be distinguished phylogenetically as different species in the genus [28].

6.2.2 Obligately Anaerobic Magnetic Bacteria

A novel sulfate-reducing magnetic bacterium, designated strain RS-1 was isolated [20] (Figure 6.3). RS-1 is also an obligate anaerobe capable of producing extracellular magnetic iron sulfides. The intracellular magnetite shows an irregular bullet-shaped morphology (Figure 6.4). This isolate illustrates a wider metabolic diversity of magnetic bacteria and suggests the presence of a novel mechanism of magnetite biomineralization. Phylogenetic analysis of RS-1, based on the 16S rDNA sequence, shows this bacterium to be a new bacterial species which is a member of δ-proteobacteria in the genus *Desulfovibrio* [29]. RS-1 was also described as a new species *D. magneticus* sp. nov. [21]. Genetic analysis of RS-1 is currently ongoing in order to elucidate the mechanism of magnetite formation.

6.2.3 Mass Cultivation of Magnetic Bacteria

In our early studies on the application of BMPs [30–32], fine biogenic magnetite had been obtained from enriched culture by the addition of nutrients such as nitrate and succinate into plastic containers containing sediments [32] or which were directly collected from natural sediment by harvesting [30]. Recently, pure cultivation of magnetic bacteria in defined medium has provided drastic progress on the application of BMPs. Mass cultivation of magnetic bacteria for BMP production is one of the most important biotechnological processes in the application of BMPs. Most

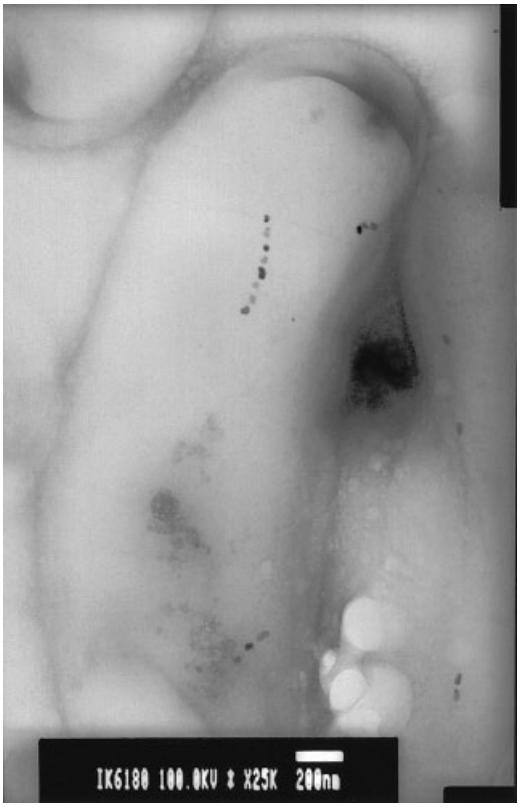

Figure 6.3 Transmission electron micrograph of a sulfate-reducing magnetic bacterium, strain RS-1. Bar = 200 nm.

of the magnetic bacteria isolated so far are difficult to grow in on a large scale due to their fastidious culture requirements. BMP production from aerotolerant magnetic bacteria, AMB-1 and MGT-1 has been achieved in mass-scale batch culture (in 1000 l using MGT-1 and AMB-1) [19] and by using a fed-batch culturing system (in a 4-l fermentor using AMB-1) [33]. In the mass-scale batch culture, the yield was about 2.6 mg of BMPs per liter of culture (i.e. a total of 2.6 g BMPs). In the fed-batch culturing system, feeding nitric acid and succinate, 1 l of AMB-1 culture could produce 4.5 mg BMPs from 0.34 g dry cells [33]. Moreover, ferrous sulfate and ferric gallate instead of ferric quinate, which is a conventionally used iron chelate, enhanced the BMP yield dramatically. The optimized conditions brought the cell density to 0.59 ± 0.03 g cell dry weight/l and BMP production to 14.8 ± 0.5 mg dry weight/l in fed-batch culture for 4 days [34]. Large-scale production of functionally active antibodies or enzymes expressed on BMP membranes is effectively accomplished by fed-batch culturing techniques [34]. Furthermore, a high-copy-number shuttle vector, pUMG, which is derived from a cryptic plasmid with high

Figure 6.4 Intracellular BMPs in RS-1 cells grown anaerobically under sulphate-reducing conditions, showing irregular (randomly bullet-shaped) morphology. The single cell has around 10–15 BMPs. Bar = 50 nm.

stability from another *Magnetospirillum* strain, MGT-1, was constructed [27]. Utilizing this high expression system in a large-scale culture, mass production of recombinant BMPs with highly expressed display proteins can be readily obtained.

6.3 Iron Uptake in *M. magneticum* AMB-1

A large amount of iron is required for BMP formation in magnetic bacteria. Because of the high concentration of iron to be assimilated, magnetic bacteria might possess an efficient iron transport system to avoid the generation of toxic radicals. Much effort has been devoted to the study of iron uptake in magnetic bacteria

under iron-sufficient conditions [12, 17], but under iron-deficient conditions this is virtually an unexplored field. The production and excretion of low-molecular-mass, high-affinity, Fe(III)-specific ligands induced under iron-deplete conditions has been reported in diverse groups of microorganisms. Detection of siderophores in magnetic bacteria was first reported in *M. magnetotacticum* MS-1 during normal cultivation condition containing 33 μM iron [35]. Another study was reported in *M. gryphyswaldense*, but no siderophores were detected in the iron-starved culture supernatants [36]. However, an energy-dependent Fe(III) uptake system was observed in *M. gryphyswaldense* [36]. This possibly corresponds to FhuB, which translocates iron–siderophore complexes into the cytoplasm.

In *M. magneticum* AMB-1, the siderophore production and iron concentration in the culture supernatants were monitored simultaneously [37]. When *M. magneticum* AMB-1 cells were inoculated in iron-sufficient medium, iron was rapidly assimilated, reaching levels comparable to those in iron-deficient cultures and thereby triggering siderophore production. These results might provide the answer for the unusual pattern of siderophore production observed in *M. magnetotacticum* MS-1 [35].

6.4 Genetic Analysis in *M. magneticum* AMB-1

The prerequisite for determining the mechanisms of magnetic particle biosynthesis is the isolation and characterization of the genes involved in the process. In order to isolate the genes, non-magnetic mutants were constructed by Tn5 or mini-Tn5 transposon mutagenesis [11, 38]. DNA sequences interrupted by transposons and their functions have been analyzed in numerous non-magnetic mutants that are defective in BMP formation.

6.4.1 Iron Transporter MagA

The *magA* gene, which shows homology to the Na^+/H^+ antiporter NapA from *Enterococcus hirae* [39], was isolated in *M. magneticum* AMB-1 through Tn5 transposon mutagenesis [40]. Intracellular localization of the MagA protein was examined using a MagA–luciferase fusion protein, and indicated that this protein is localized in both the cytoplasmic and BMP membranes [41]. Interestingly, MagA topology is inversely oriented between the cytoplasmic and the BMP membrane. MagA seems to function for iron efflux in the former and iron influx in the latter. The number of MagA molecules per magnetosome volume is much larger than per cell volume calculated from the total amount of expressed MagA [41]. This makes the quantity of effluxed iron by MagA on the cytoplasmic membrane negligible. The iron-uptake activity of MagA was determined using inverted vesicles prepared from fragmented membrane expressing MagA protein in *Escherichia coli*. Addition of ATP initiated

accumulation of ferrous ions in the vesicles. The ions were released by the addition of carbonyl cyanide *m*-chlorophenylhydrazone (CCCP), known as a protonophore [40]. This activity was also observed under an artificial proton gradient without ATP. These results suggests that MagA protein is a proton-driving $H^+/Fe(II)$ antiporter.

6.4.2 Aldehyde Ferredoxin Oxidoreductase (AOR)

Accurate oxidation–reduction systems are required for transition, storage and crystallization of large amounts of iron in magnetic bacteria. Ferric ions pass the cytoplasmic membrane and are released by siderophores. Ferric to ferrous conversion is required for iron to pass across the BMP membrane.

An AOR-deficient mutant of *M. magneticum* AMB-1, generated by mini-Tn5 transposon mutagenesis, was unable to synthesize BMP, however it remains an ability of iron accumulation [42]. Growth of this mutant was lower than in the wild-type under anaerobic conditions, but not under aerobic conditions. Although the specific function of AOR in BMP formation has not yet been determined, it is most probable that it contributes to iron reduction during nitrate respiration.

6.5 Protein Analysis in *M. magneticum* AMB-1

Proteins expressed on the BMP membrane play a direct role in regulating magnetite crystallization. Five proteins (Mms12, 16, 24, 67 and MpsA) specific to the BMP membrane of *M. magneticum* AMB-1 were reported [43, 44]. One of these is a 24-kDa protein, designated Mms24, that was observed in other *Magnetospirillum* species, and that corresponds to MAM22 in strain MS-1 [45] and MamA in MSR-1 [46]. In MS-1, 15- and 33-kDa specific proteins were observed [47], and MAM12, 22 and 28 were identified [45]. MamA, B, C, D and E were also identified as magnetosome membrane-specific in MSR-1 [46]. In our latest study, four proteins (Mms5, 6, 7 and 13) were found tightly bound to crystal magnetite [48]. These proteins specific to the BMP membrane from *M. magneticum* AMB-1 were characterized in order to clarify their function for BMP formation.

6.5.1 Magnetosome-specific GTPase Mms16

A 16-kDa protein designated Mms16 [49] was found to be the most abundantly expressed among the five proteins isolated from the BMP membrane of *M. magneticum* AMB-1 [43, 44]. Mms16 shows GTPase activity, and characteristics such as vesicle-specific and abundant in the components that are similar properties to eukaryotic small GTPases that control priming and trafficking of budding vesicles

[50, 51]. This finding led to the hypothesis that the BMP membrane is derived from the cytoplasmic membrane through an invagination process. GTPase inhibition experiments were conducted using aluminum fluoride (AlF_4^-), which is a commonly used inhibitor in vesicle formation [52, 53]. Although the AlF_4^- complex did not inhibit growth, cells lost magnetism as the concentration of AlF_4^- increased. Observation by electron microscopy revealed that cells grown with AlF_4^-contained interrupted chains of BMPs. The number of BMPs decreased compared with those in control cells [49]. These results suggest, at least, that GTPase activity is required for BMP synthesis.

6.5.2 Tightly Bound Protein to Magnetite Crystal, Mms6

Organic matrices contained in biominerals serve as templates as well as regulators for crystallization. These regulators might determine the size and shape of a BMP to maintain a single magnetic domain. During the search for such regulation factors for magnetic crystal formation, four proteins from *M. magneticum* AMB-1, tightly bound to the magnetite crystal, designated Mms5, 6, 7 and 13 were identified [48]. These proteins have the common sequence LGLGLGLGAWGP*XX*LG*XX*G-*X*AGA. Mms5 and Mms6 show no homologies with known functional proteins, but Mms7 is homologous to the C-terminal region of MamD and Mms13 to MamC in *M. gryphiswaldense* [46]. Mature Mms6 consists of a hydrophobic domain in the N-terminal region, predicted as the transmembrane region, and of a highly acidic domain, which is the C-terminal region. Amino acids containing hydroxyl groups were also observed. Furthermore, the region between the middle and C-terminal regions contain basic amino acids such as Lys, Tyr and Arg. These structural features were also observed in Mms5, 7 and 13. The hydrophilic domains in mineral-associated proteins capture metal ions [54, 55] or interact with the mineral phase [56].

Recombinant Mms6 corresponding to the mature protein was produced in *E. coli* and had radioactive iron-binding ability. This ability was blocked in both Mms6 and ferritin when 10 mM non-radioactive Fe^{3+} was added. Inhibition of binding of radioactive Fe^{3+} to Mms6, but not to ferritin, was observed in the presence of Ca^{2+} and Mg^{2+} [48]. The effect of Mms6 on crystal formation was observed during synthesis of artificial magnetite. The magnetic precipitates with Mms6 showed cuboidal morphology similar to *M. magneticum* AMB-1 BMPs with sizes ranging from 20 to 30 nm in diameter. The magnetic particles produced in the absence of Mms6 were non-homogeneous in size (1–100 nm in diameter) and shape. In addition, the observed needle-shaped crystals were similar to goethite (α-FeOOH). Electron diffraction analysis indicated that the black particles were composed mainly of magnetites (Fe_3O_4). These results suggest that magnetite crystallization is inorganically derived as demonstrated by Frankel et al. [57], but Mms6 directly binds ferric iron and regulates crystallization and morphology during magnetite formation. Mms5, 7 and 13 might also contribute to crystallization as these proteins also contain both hydrophilic and acidic regions.

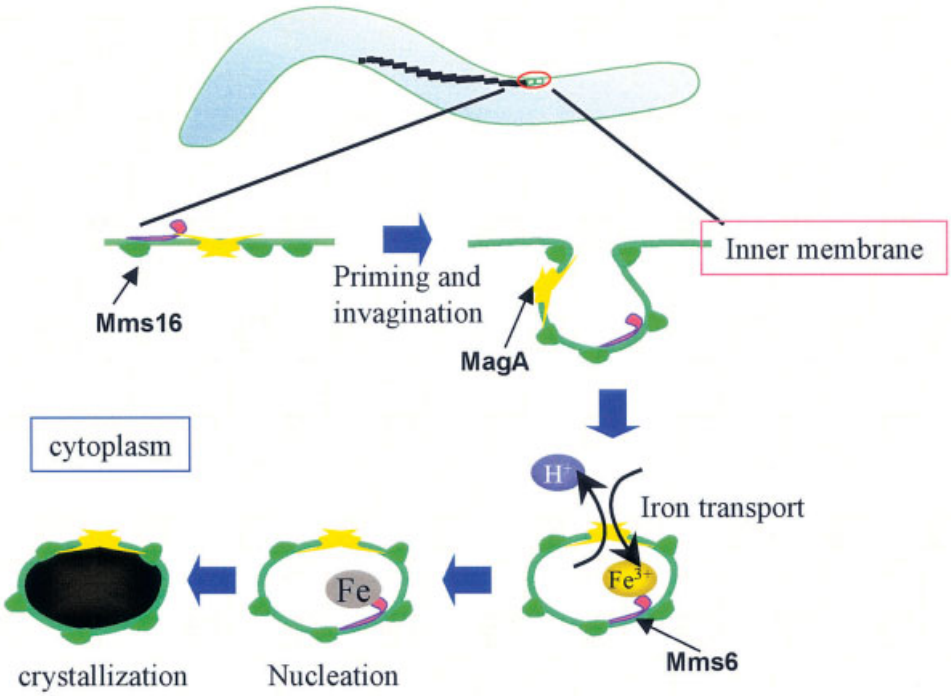

Figure 6.5 Hypothesized scheme of molecular mechanisms of BMP formation.

6.6 Hypothesis of a Molecular Mechanism of Magnetosome Formation

Taken together, the experimental data obtained from studies with *M. magneticum* AMB-1 allowed us to postulate that BMP formation is comprised of three major stages (Figure 6.5). The first stage entails the invagination of the cytoplasmic membrane primed by the GTPase and the vesicle formed serves as the precursor of the BMP membrane. Transmission electron microscopy of *M. magnetotacticum* MS-1 reveals that BMP envelopes appear before the crystallization of magnetite [47]. The second stage entails the accumulation of ferrous ions into the vesicles by the BMP transmembrane transporter MagA. External iron is internalized by transporters and siderophores, and internal iron is controlled strictly by an oxidation–reduction system. In the final stage, Mms6 triggers magnetite crystal nucleation and regulates morphology. Various proteins associated with the BMP membrane could play functional roles involved in magnetite generation. These include the accumulation of supersaturating iron concentrations, maintenance of reductive conditions and the oxidation of iron to induce mineralization, or the partial reduction and dehydration of ferrihydrite to magnetite.

6.7 Applications of Bacterial Magnetite

6.7.1 Magnetic Carriers for Immobilization of Molecules

Parallel to the study of the basic molecular mechanisms of BMP formation, the biotechnological applications of BMPs have also been investigated. BMPs, which are nanometer-sized, have a large surface area. This volume ratio is due to their small size and the BMP membrane interferes with aggregation of BMPs. So far, immobilized enzymes [58] and antibodies [59–61] have been utilized for sensing devices in biosensors, and DNA carriers have been used for gene transfer [62] and magnetic recovery of specific mRNA [63, 64]. The use of magnetic particles in immunoassays enables the separation of bound and free analytes by applying a magnetic field. For example, proteins can be attaching covalently to solid supports, such as magnetic particles, preventing desorption of antibodies during assaying. Because these particles disperse evenly throughout the reaction mixture, they allow rapid reaction kinetics without the need for continuous mixing or shaking, enable coupling antibodies and facilitating ease of use. Magnetic particles serve as both solid supports and a means of separation in the assay system. Highly sensitive immunoassay has been established through this technique. The utilization of BMPs as stable platforms has been reported for antibodies for efficient immunoassays [59–61, 65]. A good correlation is obtained between the luminescence intensity and mouse IgG concentration in the range of $1–10^5$ fg/ml. The minimum detectable concentration of IgG is 1 fg/ml (corresponding to 6.7 zmol = 4000 molecules as calculated from Avogadro's number) [65]. Various environmental pollutants including endocrine disruptors, alkylphenol ethoxylates (APEs), bisphenol A (BPA) and linear alkylbenzene sulfonates (LASs) were detectable using monoclonal antibodies immobilized on BMPs using an automated detection system [66].

High-performance DNA separation was achieved using BMP coated with 3-[2-(2-aminoethyl)-ethylamino]propyltrimethoxysilane (AEEA). The DNA-binding effi-

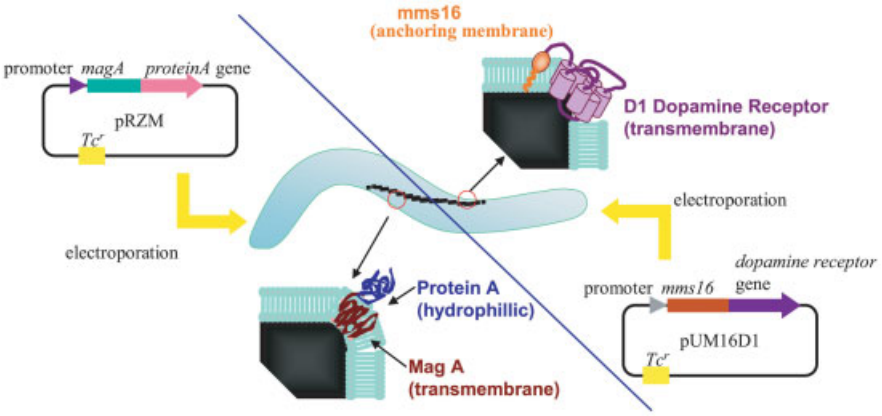

Figure 6.6 Molecular architecture for the display system on the surface of BMPs.

ciency increased with the number of amino groups present on the silane compounds and was 14-fold higher than with untreated magnetite [67]. Moreover, BMPs were modified using a polyamidoamine (PAMAM) dendrimer to increase the number of amino groups [68]. A PAMAM dendrimer forms a dense outer amine shell through a cascade type of polymer generation. The amine numbers double with every layer generated on the BMP surface. On the other hand, the number of amino groups generated on the same size artificial magnetic particle is 1/10th of that on the BMP at Generation 6. DNA recovery with 2 μg of dendrimer modified BMPs is about 6 times higher than with 2 μg of dendrimer-modified artificial magnetic particles [68].

6.7.2 High-throughput Genotyping using BMPs

A genotyping system using BMPs has been developed. For rapid and species discrimination of tuna (*Thunnus* spp.), a magnetic-capture hybridization technique employing BMPs was applied for the supervision of illegal fishing and trading irrespective of the decreasing stocks. Species-specific oligonucleotide probes designed based on the sequence of ATPase and cytochrome oxidase subunit III genes (ATCO fragment) were immobilized on BMPs via streptavidin–biotin conjugation and utilized for magnetic-capture hybridization with digoxigenin-labeled fragment amplified tuna ATCO fragments. There are five nominal species and one subspecies in large tunas of the genus *Thunnus* and all species were discriminated by this system [69].

Single nucleotide polymorphisms (SNPs) are the most common human genotype variation. Focused on aldehyde dehydrogenase 2 (ALDH2), a fluorescence-labeled probe immobilized on BMP could be available for discrimination of homozygous (normal and abnormal allele) and heterozygous genotypes [70].

6.7.3 Expression of Foreign Protein Displayed on BMP

Recently, a molecular architecture on the BMP surface display systems has been designed (Figure 6.6, see p. 101). MagA served as a workable anchor for the site-specific display of functional foreign proteins. Protein A was expressed on BMP membranes by the *protein A–magA* hybrid gene [71]. Using antibody-bound Protein A–BMP complexes, a rapid and highly sensitive diagnostic method has been developed for detecting human IgG (Figure 6.7) [72]. Although Protein A and the estrogen receptor hormone binding domain (ERHBD) are hydrophilic, MagA was found to be unsuitable as an anchor for displaying transmembrane proteins. Mms16 was used as an anchor fused with the G-protein-coupled receptor (GPCR) since it allows protein folding. Competition binding was undertaken for ligand detection. Fluorescence-labeled antagonists bind to the receptor and the addition of a competing agonist decreased the fluorescence. This confirmed that GPCR maintains its ligand-binding ability using Mms16 as an anchor. Moreover, this detection system is also able to quantify the amount of ligand. Seven-transmembrane

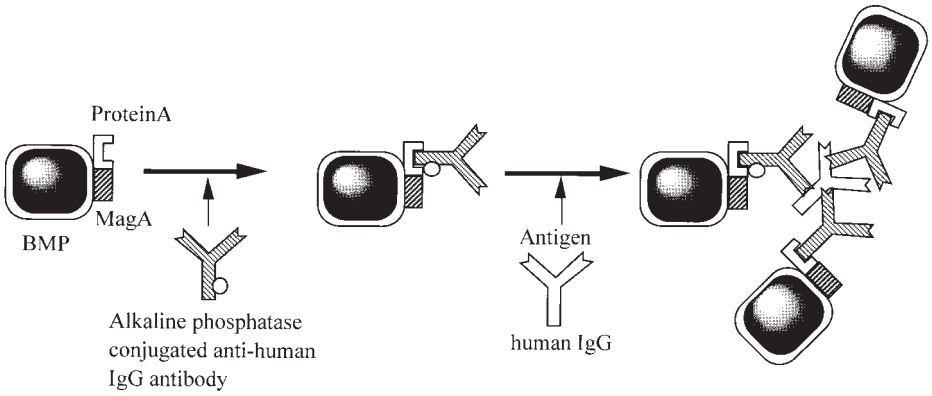

Figure 6.7 Homogenous chemiluminescence enzyme immunoassay using Protein A–BMP complexes. Alkaline phosphatase-conjugated anti-human IgG antibody was bound onto the BMPs (produced from pRZM-containing AMB-1 cells) based on the specific molecular recognition of the Z region of Protein A. These functional BMPs were used for the detection of human IgG at various concentrations. Luminescence intensity was measured in the supernatant after magnetic aggregation, due to the immunoreaction between the functional BMPs and human IgG.

receptors, GPCR are the most abundant class of receptors in mammalian biology. Operating by way of their linked signaling pathways, they participate in a myriad of biological processes. Because of their pivotal role in physiology, these receptors are the major focus of pharmaceutical drug development. In a conventional method, cloned GPCR gene is expressed in a high expression system and solubilized for purification. Unfolded GPCR is then reconstituted in liposomes. These complex procedures slow down the progress to further studies of these proteins. However, using the developed display system, convenient GPCR purification and analyses were achieved.

6.7.4 Fully Automated Immunoassay using Protein A–BMPs

Furthermore, fully automated immunoassay systems have been developed. An automated immunoassay system is equipped with a reaction station corresponding to a 96-well microtiter plate, tip track, multi-pipettes and magnetic separation apparatus (Figure 6.8). This fully automated sandwich immunoassay system was applied for determination of human insulin in serum using antibody–Protein A–BMP complexes and an alkaline phosphatase-conjugated secondary antibody. Dose–response curves were obtained from the luminescence intensity for human insulin concentrations in phosphate-buffered saline and serum. The detection limit was 2 μU/ml of human insulin, and a linear correlation between luminescence intensity and concentration was obtained over the range of 19–254 μU/ml [71]. In the measurement of endocrine disruptors, APE and LAS, all procedures were completed in 15 min, although typical plate methods took more than 2.5 h [66]. This method gave a wider

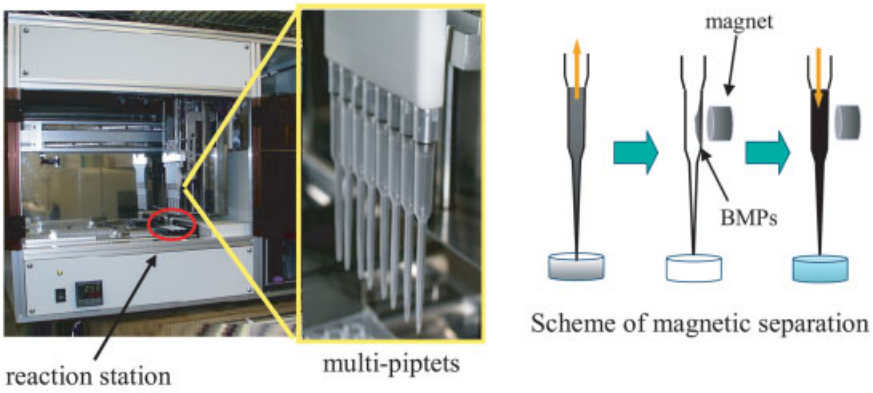

Figure 6.8 Fully automated system equipped with a magnetic separation unit.

range and lower detection limit than ELISA using the same antibodies for detection. Furthermore, detection limits of LAS and BPA were at similar levels compared with those of gas or liquid chromatography/mass spectroscopy.

References

[1] D. A. Bazylinski, *Int. Microbiol.* **1999**, *2*, 71–80.
[2] R. B. Frankel, D. A. Bazylinski, M. Johnson and B. L. Taylor, *Biophys. J.* **1997**, *73*, 994–1000.
[3] T. Matsunaga, *Trends Biotechnol.* **1991**, *9*, 91–95.
[4] F. F. Torres de Araujo, M. A. Pires, R. B. Frankel, C. E. M. Bicudo, *Biophys. J.* **1986**, *50*, 375–378.
[5] H. Lowenstam, *Geol. Soc. Am. Bull.* **1962**, *73*, 435–438.
[6] D. A. Kuterbach, B. Walcott, R. J. Reeder, R. B. Frankel, *Science* **1982**, *218*, 695–697.
[7] C.-Y. Hsu, C.-W. Li, *Science* **1994**, *256*, 95–96.
[8] M. M. Walker, J. L. Kirschvink, S.-B. R. Chang, A. E. Dizon, *Science* **1984**, *224*, 751–753.
[9] Y. Sakai, T. Tomiyama, M. Kato, M. Ogura, *IEEE Trans. Magnet*. **1990**, *26*, 1554–1556.
[10] S. Mann, N. H. C. Sparks, M. M. Walker, J. L. Kirschvink, *J. Exp. Biol.* **1988**, 35–49.
[11] T. Matsunaga, C. Nakamura, J. G. Burgess, K. Sode, *J. Bacteriol.* **1992**, *174*, 2748–2753.
[12] R. P. Blakemore, D. Maratea, R. S. Wolfe, *J. Bacteriol*. **1979**, *140*, 720–729.
[13] K. H. Schleifer, D. Schüler, S. Spring, M. Weizenegger, R. Amann, W. Ludwig, M. Köhler, *Syst. Appl. Microbiol.* **1991**, *14*, 379–385.
[14] F. C. Meldrum, S. Mann, B. R. Heywood, R. B. Frankel, D. A. Bazylinski, *Proc. R. Soc. Lond. B* **1993**, *251*, 231–236.
[15] D. A. Bazylinski, R. B. Frankel, H. W. Jannasch, *Nature* **1988**, *334*, 518–519.
[16] F. C. Meldrum, S. Mann, B. R. Heywood, R. B. Frankel, D. A. Bazylinski, *Proc. R. Soc. Lond. B* **1993**, *251*, 237–242.
[17] T. Matsunaga, T. Sakaguchi, F. Tadokoro, *Appl. Microbiol. Biotechnol*. **1991**, *35*, 651–655.
[18] T. Matsunaga, T. Sakaguchi, in *Ferrites: Proc. 6th Int. Conf. on Ferrites (ICF 6)*, Japan Society of Powder and Powder Metallurgy, Tokyo, **1992**, pp. 262–267.
[19] T. Matsunaga, F. Tadokoro, N. Nakamura, *IEEE Trans. Magnet*. **1990**, *26*, 1557–1559.

[20] T. Sakaguchi, J. G. Burgess, T. Matsunaga, *Nature* **1993**, *365*, 47–49.
[21] T. Sakaguchi, A. Arakaki, T. Matsunaga, *Int. J. Syst. Evol. Microbiol.* **2002**, *52*, 215–221.
[22] R. H. Thornhill, J. G. Burgess, T. Sakaguchi, T. Matsunaga, *FEMS Microbiol. Lett.* **1994**, *115*, 169–176.
[23] R. H. Thornhill, J. G. Burgess, T. Matsunaga, *Appl. Environ. Microbiol.* **1995**, *61*, 495–500.
[24] K. A. Short, R. P. Blakemore, *J. Bacteriol*. **1986**, *167*, 729–731.
[25] T. Matsunaga, N. Tsujimura, *Appl. Microbiol. Biotechnol*. **1993**, *39*, 368–371.
[26] W. F. Guerin, R. P. Blakemore, *Appl. Environ. Microbiol.* **1992**, *58*, 1102–1109.
[27] Y. Okamura, H. Takeyama, T. Sekine, T. Sakaguchi, A. T. Wahyudi, R. Sato, S. Kamiya, T. Matsunaga, *Appl. Environ. Microbiol.* **2003**, *69*, 4274–4277.
[28] J. G. Burgess, R. Kawaguchi, T. Sakaguchi, R. H. Thornhill, T. Matsunaga, *J. Bacteriol*. **1994**, *175*, 6689–6694.
[29] R. Kawaguchi, J. G. Burgess, T. Sakaguchi, H. Takeyama, R. H. Thornhill, T. Matsunaga, *FEMS Microbiol. Lett.* **1995**, *126*, 277–282.
[30] T. Matsunaga, S. Kamiya, *Appl. Microbiol. Biotechnol.* **1987**, *26*, 328–332.
[31] T. Matsunaga, S. Kamiya, in *Biomagnetism '87* (Eds K. Atsumi, M. Kotani, S. Ueno, T. Kalita, S. J. Williamsen), Tokyo Denki University Press, Tokyo, **1988**, pp. 410–413.
[32] T. Matsunaga, K. Hashimoto, N. Nakamura, K. Nakamura, S. Hashimoto, *Appl. Microbiol. Biotechnol*. **1989**, *31*, 401–405.
[33] T. Matsunaga, N. Tsujimura, S. Kamiya, *Biotechnol. Tech.* **1996**, *10*, 495–500.
[34] C.-D. Yang, H. Takeyama, T. Tanaka, T. Matsunaga, *Enz. Microb. Technol.* **2001**, *29*, 13–19.
[35] L. C. Paoletti, R. P. Blakemore, *J. Bacteriol.* **1986**, *167*, 73–76.
[36] D. Schuler, E. Baeuerlein, *Arch. Microbiol.* **1996**, *166*, 301–307.
[37] R. J. Calugay, H. Miyashita, Y. Okamura, T. Matsunaga, *FEMS Microbiol. Lett.* **2003**, *218*, 371–375.
[38] A. T. Wahyudi, H. Takeyama, T. Matsunaga, *Appl. Biochem. Biotechnol.* **2001**, *91–93*, 147–154.
[39] D. Strausak, M. Waser, M. Solioz, *J. Biol. Chem*. **1993**, *268*, 26334–26337.
[40] C. Nakamura, J. G. Buregess, K. Sode, T. Matsunaga, *J. Biol. Chem.* **1995**, *270*, 28392–28396.
[41] C. Nakamura, T. Kikuchi, J. G. Burgess, T. Matsunaga, *J. Biochem*. **1995**, *118*, 23–27.
[42] A. T. Wahyudi, H. Takeyama, Y. Okamura, Y. Fukuda, T. Matsunaga, *Biochem. Biophys. Res. Commun*. **2003**, *303*, 223–229.
[43] T. Matsunaga, N. Tsujimura, Y. Okamura, H. Takeyama, *Biochem. Biophys. Res. Commun*. **2000**, *268*, 932–937.
[44] Y. Okamura, H. Takeyama, T. Matsunaga, *Appl. Biochem. Biotechnol.* **2000**, *84–86*, 441–446.
[45] Y. Okuda, K. Denda, Y. Fukumori, *Gene* **1996**, *171*, 99–102.
[46] (a) K. Grunberg, C. Wawer, B. M. Tebo, D. Schuler, *Appl. Environ. Microbiol*. **2001**, *67*, 4573–4582; (b) S. Schübbe, M. Kube, A. Scheffel, C. Wawer, U. Heyen, A. Meyerdierks, M. H. Madkour, F. Mayer, R. Reinhardt, D. Schüler, *J. Bacteriol.* **1993**, *185*, 5779–5790.
[47] Y. A. Gorby, T. J. Beveridge, *J. Bacteriol*. **1988**, *170*, 834–841.
[48] A. Arakaki, J. Webb, T. Matsunaga, *J. Biol. Chem*. **2003**, *278*, 8745–8750.
[49] Y. Okamura, H. Takeyama, T. Matsunaga, *J. Biol. Chem*. **2001**, *276*, 48183–48188.
[50] S. L. Schmid, H. Damke, *FASEB J*. **1995**, *9*, 1445–1453.
[51] J. E. Rothman, *Protein Sci.* **1996**, *5*, 185–194.
[52] W. E. Balch, W. G. Dunphy, W. A. Braell, J. E. Rothman, *Cell* **1984**, *39*, 405–416.
[53] W. E. Balch, J. E. Rothman, *Arch. Biochem. Biophys*. **1985**, *240*, 413–425.
[54] S. J. Hattan, T. M. Laue, N. D. Chasteen, *J. Biol. Chem.* **2001**, *276*, 4461–4468.
[55] S. J. Lippard, J. M. Berg, in *Principles of Bioinorganic Chemistry*, University Science Books, Mill Valley, CA, **1994**, pp. 43–46.
[56] P. A. Raj, M. Johnsson, M. J. Levine, G. H. Nancollas, *J. Biol. Chem.* **1992**, *267*, 5968–5976.
[57] R. B. Frankel, G. G. Papaefthymiou, R. P. Blakemore, W. O'Brien, *Biochim. Biophys. Acta* **1983**, *763*, 147–159.
[58] T. Matsunaga, S. Kamiya, *Appl. Microbiol. Biotechnol.* **1987**, *26*, 328–332.
[59] N. Nakamura, K. Hashimoto, T. Matsunaga, *Anal. Chem.* **1991**, *63*, 268–272.
[60] N. Nakamura, J. G. Burgess, K. Yagiuda, S, Kudo, T. Sakaguchi, T. Matsunaga, *Anal. Chem*. **1993**, *65*, 2036–2039.

[61] N. Nakamura, T. Matsunaga, *Anal. Chim. Acta* **1993**, *281*, 585–589.
[62] H. Takeyama, A. Yamazawa, C. Nakamura, T. Matsunaga, *Biotechnol. Tech.* **1995**, *9*, 355–360.
[63] K. Sode, S. Kudo, T. Sakaguchi, N. Nakamura, T. Matsunaga, *Biotechnol. Tech.* **1993**, *7*, 688–694.
[64] T. Matsunaga, T. Sakaguchi, K. Sode, S. Kudo, N. Nakamura, in *Advanced Materials '93 II/A: Biomaterials, Organic and Intelligent Materials (Proc. 3rd IUMRS Int. Conf. Advanced Materials)* (Eds T. Nishi, K. Segawa, H. Hasegawa, I. Karube, T. Kajiyama, H. Aoki), Elsevier, Tokyo, **1994**, pp. 449–454.
[65] T. Matsunaga, M. Kawasaki, X. Yu, N. Tsujimura, N. Nakamura, *Anal. Chem*. **1996**, *68*, 3551–3554.
[66] T. Matsunaga, F. Ueki, K. Obata, H. Tajima, T. Tanaka, H. Takeyama, Y. Goda, S. Fujimoto, *Anal. Chim. Acta* **2003**, *475*, 75–83.
[67] B. Yoza, M. Matsumoto, T. Matsunaga, *J. Biotechnol*. **2002**, *94*, 217–224.
[68] B. Yoza, A. Arakaki, K. Maruyama, H. Takeyama, T. Matsunaga, *J. Biosci. Bioeng.* **2003**, *95*, 21–26.
[69] H. Takeyama, H. Tsuzuki, S. Chow, H. Nakayama, T. Matsunaga, *Mar. Biotech.* **2000**, *2*, 309–313.
[70] T. Yoshino, H. Takeyama, T. Matsunaga, *Electrochemistry* **2001**, *69*, 1008–1012.
[71] T. Matsunaga, R. Sato, S. Kamiya, T. Tanaka, H. Takeyama, *J. Magn. Magn. Mater*. **1999**, *194*, 126–131.
[72] T. Tanaka, T. Matsunaga, *Anal. Chem.* **2000**, *72*, 3518–3522.

7 Biogenic Magnetite as a Basis for Geomagnetic Field Perception in Animals

Michael Winklhofer

7.1 Introduction

How animals are capable of sensing the Earth's magnetic field is an outstanding problem in sensory physiology. After several decades of research into magnetic-field sensitivity in animals, it has only been in the last few years that candidate magnetoreceptors on which theoretical models can now be tested have been identified.

This chapter starts with a brief overview of the key observations that established the existence of a magnetic sense in animals, followed by a survey of the two most plausible hypotheses that have been put forward to explain the physical mechanisms underlying magnetic-field perception. In Section 7.3, the putative morphological correlate of a magnetoreceptor in homing pigeons is described in detail. Two biophysical models based on the histological findings are presented as to how a magnetic field stimulus can be transduced into a nerve signal. Section 7.4 presents a comparison between the candidate magnetoreceptor in pigeon and trout, as well as a discussion of open questions, such as the threshold sensitivity of receptor models and magnetite biosynthesis in vertebrates.

7.2 Facts and Hypotheses about Magnetoreception

7.2.1 Behavioral Evidence of Geomagnetic Field Sensitivity in Animals

Early observations on carrier pigeons showed that the Earth's magnetic field played a role in homing. Statistical analyses of pigeon races showed that homing performance was reduced during geomagnetically disturbed days [1]. In a later, more detailed study, which also included meteorological data, it was observed that magnetic fluctuations had an effect on homing speed only under poor weather conditions, but no effect in good weather [2]. Similar results were obtained previously by Keeton [3], who reported disorientation in pigeons that had magnets (coils) attached to their necks – birds that were released under overcast conditions were disturbed by the magnet, while it had no effect as long as the sun was visible. Thus, pigeons must have two independent navigation mechanisms – one based on the position of the

Biomineralization: From Biology to Biotechnology and Medical Application, Second Edition. Edited by E. Bäuerlein

ISBN: 3-527-31065-7

sun, the other on the local magnetic field. In the case that one mechanism should fail, there is still another one that can be relied upon.

While homing pigeons need to find their way back to their home loft over a relatively short distance (150–400 km), migratory birds fly over thousands of kilometers to their wintering grounds, following a fairly consistent bearing for several weeks. Although it had long been speculated that the Earth's magnetic field serves as a cue for migrants, it was only in the early 1970s that magnetic orientation could be demonstrated convincingly in behavioral experiments. Headings of caged migratory birds depended on the direction of the applied magnetic field [4]. Interestingly, the birds were only able to perceive the spatial orientation of the magnetic field lines, but not their polarity. Compared to the technical compass, the so-called inclination compass of birds is not based on North and South, but rather on "poleward" (the direction in which the field lines point to the ground) and "equatorward" (the direction in which they point upward). That way, the inclination compass is not affected by geomagnetic polarity reversals and thus seems to have an evolutionary advantage over a biological compass based on polarity, as observed in fish (e.g. salmon [5]). In the palaeomagnetic record over the last 5 million years, 20 polarity reversals are documented [6]. More importantly, however, a polarity reversal does not happen instantaneously, but takes some 5000 years, during which large directional fluctuations can occur [7]. Migrants would have to adapt to a changing magnetic field anyway, no matter if their compass is polarity based or not. Obviously, such field changes happen slowly enough to allow animals to adapt over generations. We would otherwise expect to observe species extinctions during polarity reversals, for which no palaeontological evidence exists.

Meanwhile, a magnetic compass sense has been demonstrated in some 50 species across all major groups, from invertebrates (mollusks, crustaceans, insects) to vertebrates (fish, amphibians, reptiles, birds, mammals), with migratory birds being the most thoroughly investigated group (for a complete reference until 1994, see [8]). Magnetic orientation therefore is a well-established phenomenon. When it comes to the underlying physical mechanisms, however, explanations are still hypothetical. The biophysical and neurophysiological principles of magnetic field reception are difficult to unravel for several reasons. To begin with, we are not capable of perceiving magnetic fields, at least not consciously. Thus, our knowledge is deduced mainly from behavioral experiments on animals under artificial magnetic fields. However, behavioral responses are a complex sum of neuronal processes, obscuring the primary processes in the receptors. Similarly, magnetic cues may serve as input for more than one sensory system and mediate more than one type of behavioral response [9]. Moreover, a magnetic field penetrates the whole body; hence, the magnetic sense could be located anywhere within the body and it is even possible that it is sensed over the whole body, e.g. through affecting bioelectric currents in the nervous system. On the other hand, gravity acts on the whole body, too, but is detected by specific sensory cells in the vestibular system. From that rationale, it is fair to assume that the magnetic field is detected and registered by specialized cells. Structural peculiarities of such receptors would provide us with important constraints on the possible physical mechanisms. However, magnetic sensory receptors have not been identified with certainty yet in any animal. Nevertheless, the geomagnetic field

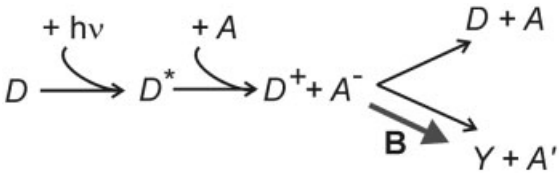

Figure 7.1 Reaction scheme for a possible photochemical compass mechanism in the retina [10, 11]. An electron donor molecule D (such as a photoactive pigment) absorbs a photon. An electron is transferred from the photoexcited state D^* to an acceptor molecule A to form a short-lived spin-correlated radical pair ($D^+ + A^-$). In a zero magnetic field, the radical pair will reform the precursor. In a finite magnetic field **B**, the radical pair will yield a product Y that is chemically different from D. The transition probability depends on the axial orientation of the magnetic field and its intensity.

is comparatively weak (50 μT) so that we can rule out a number of physically possible mechanisms that come into effect in strong magnetic fields only, e.g. diamagnetic anisotropy in biological membranes. The two most plausible hypothesis are examined below.

7.2.2 A Biochemical Compass Mechanism

Magnetic fields can influence biochemical reactions that involve transient spin-correlated radical pairs [10]. Although the strength of the magnetic interaction between the magnetic field and the transient state is much smaller than the randomizing thermal energy kT, the magnetic field can perturb a quantum-mechanical process, which may result in a reaction yield Y that is not produced if a magnetic field is absent (Figure 7.1). The probability of the yield Y depends on the direction and strength of the magnetic field [10]. The only required condition is that the transient state lives long enough (of the order of 0.1 μs) in order to be able to exchange magnetic energy with the geomagnetic field. Spin-correlated radical pairs can be generated by electron transfer from a photo-excited donor molecule D^* to an acceptor molecule A. Photoreceptors in the outer retina such as rhodopsin in the rods or color opsins in the cones are possible key proteins for a light-dependent magnetoreception mechanism. Since such a mechanism would be related to vision, affecting visual transduction pathways, the magnetic field would modulate visual patterns [11]. That way, the direction of the magnetic field could literally be seen.

In addition to the well-characterized photoreceptors for vision, a new class of photoreceptor molecules in the inner retina of vertebrates has recently been suggested as a basis for a biochemical compass [11] – cryptochromes, which are circadian photoreceptors [12]. Circadian rhythms are synchronized with light–dark cycles and can be influenced by an artificial magnetic field [13]. The electrical activity of the pineal organ of the guinea pig, which is involved in the regulation of the circadian rhythm, was affected by an Earth-strength magnetic field, too – in 15 of 71 cells, the firing rate was reduced by 50 % during magnetic field exposure. When

the magnetic field treatment was discontinued, the cells retained their diminished activity for up to 30 min [14].

Photoexcitation of cryptochromes is wavelength dependent – cryptochromes absorb green and blue light. Behavioral experiments have shown that pigeons and robins orient under green and blue light, while they are disoriented under red and yellow light [15]. The test birds may have been irritated by unnatural light conditions, although the fair agreement between theory and behavior suggests a possible link between magnetoreception and light reception, but not necessarily a link between magnetoreception and (color) vision. It needs to be emphasized that a possible magnetic effect on cryptochrome (as opposed to rhodopsin or photopsin) would *not* produce visual modulation patterns, but would rather influence the internal clock, e.g. by affecting the production of melatonin, a hormone that regulates sleep. However, it is not clear how the interaction of the magnetic field with a slow physiological process such as the internal clock would bring about an effect immediate enough to be utilized for magnetic sensory perception. As with other senses, the magnetic sense can be expected to function immediately with characteristic time scales below 1 s.

While a photochemical compass is at least a theoretically viable mechanism for detecting the axial direction of a magnetic field, the specific transducing processes and receptive structures are far from being understood. In particular, it is not clear if the mechanism is sensitive enough to resolve minute variations in magnetic field strength of the order of 70 nT as observed for pigeons [16]. It is possible that pigeons use a second compass based on a different physical mechanism. Similarly, animals that migrate at night or in the deep sea as well as subterranean animals like mole rats can evidently not utilize a photochemical compass. The magnetite hypothesis offers an alternative explanation.

7.2.3 The Magnetite Hypothesis

The magnetite hypothesis assumes that some specialized sensory cells contain accumulations of ferrimagnetic material, such as biogenic magnetite (γ-Fe_3O_4), through which the external magnetic field is coupled into the nervous system. In its simplest realization, the ferromagnetic material would act like a compass needle, being rotated into the direction of the magnetic field and thereby exerting a torque on the neighboring tissue. A torque produces mechanical deformation, which in combination with a mechanoreceptor like a Pacinian corpuscle can create a receptor potential and hence trigger a nerve signal. Such a torque mechanism is theoretically well understood [17] and of course plausible as it is already realized in magnetotactic bacteria [18], which can be considered as microscopic compass needles, swimming along magnetic field lines. What makes this hypothesis so attractive is the fact that magnetic single-domain (SD) crystals of magnetite have indeed been found in animal tissue and closely resemble bacterial magnetite crystals. The most impressive example in this context is magnetite crystals extracted from ethmoid tissue of the sockeye salmon, *Oncorhynchus nerka*, with grain sizes between 25 and 60 nm (mean 48 nm); the crystal morphology was described as cubo-octahedral [19]. Such

a narrow size range of grains is typical of biologically controlled mineralisation processes. Due to the extraction procedure, however, there was no information left on the *in situ* disposition of crystals and their histological context. Chains were observed in the magnetic extracts, but most likely are artifacts from the extraction procedure: ethmoid tissue was ground and dissolved, and the released magnetic particles centrifuged, washed, aggregated magnetically and resuspended ultrasonically [19]. Likewise, it is not known if the ethmoid tissue is involved in the magnetic sense of sockeye salmon. So far, however, chains of magnetite crystals have not been identified *in situ*.

The presence of SD magnetite in tissue does not automatically make a case for magnetite-based magnetoreception. SD magnetite been identified in radula teeth in recent chitons (Mollusca, Polyplacophora), where it forms denticle cappings [20]. Apart from being magnetic, magnetite is also quite hard (between calcite and quarz), thus allowing chitons to scrape encrusting algae from intertidal rocks without having their tooth cusps abraded. As an ore mineral, magnetite has a high density (5 g/cm^3), which can be utilized to design more sensitive gravity receptors than on the basis of calcium carbonate (3 g/cm^3), which otoconia in otolithic organs are normally made of. Indeed, magnetite particles in sand ingested by rays (guitarfish) were incorporated as otoconia in the vestibular organ, alongside calcitic otoconia [21]. Even though the magnetite particles are exogenous, they may well interact with the geomagnetic field and produce a mechanical torque on the sensory cells in the otolithic organs [22].

There may be additional physiological or metabolic functions of endogenously mineralized magnetite that have not been unearthed yet. Magnetite has been identified in the human brain, meninx [23] and hippocampus [24], as well as in the heart, spleen and liver [25]. Magnetite may therefore be an iron dump for the body, a by-product of iron metabolism or may even be diagnostic for uncontrolled metabolism in tumor cells. Magnetic remanence measurements on two mouse tumors have revealed large concentrations of ferromagnetic mineral, presumably magnetite [26]. Taken together, those findings suggest that a new approach is required to verify the magnetite hypothesis. First, magnetite (or some other ferrimagnetic) crystals have to be localized *in situ* in or next to nerve fibers which convey magnetic field-modulated impulses to the brain. Detection of magnetic remanence can only be taken as a first hint of where to search more closely. After describing the disposition of the crystals with respect to each other and to the cellular elements, a concrete biophysical model can be developed to the point of making quantitative predictions testable by experiment.

7.3 The Case for a Magnetoreceptor in Homing Pigeons

Recently, our interdisciplinary research group has managed to locate and identify a structural candidate for a magnetoreceptor in homing pigeons [27]. The putative magnetoreceptive structures are consistently found at six sites in the upper-beak

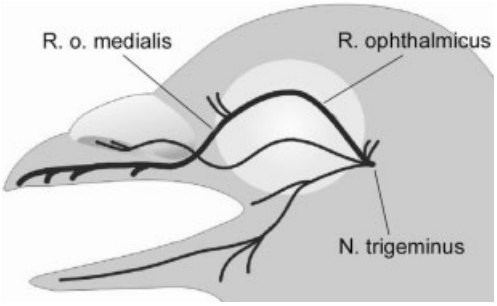

Figure 7.2 The ophthalmic branch of the trigeminal nerve in homing pigeons. The brain receives somatosensory input from the distal part of the beak skin by the median ophthalmic branch (R. o. medialis).

skin and contain clusters of ultrafine-grained magnetite crystals (grain sizes between 2 and 5 nm) [27, 28]. Importantly, the magnetite-bearing structures are innervated [29]. This has been the first study in which the subcellular organization and ultrastructure of a candidate magnetoreceptor has been characterized, and therefore is described here in more detail.

7.3.1 A New Methodological Approach to an Old Problem

A first hint about where to search for a magnetoreceptor in birds came from electrophysiological recordings showing that the ophthalmic nerve of the Bobolink (*Dolichonix oryzivorus*), a transequatorial migratory bird, is sensitive to small changes in the intensity of an applied magnetic field [30]. The ophthalmic branch of the trigeminus nerve (Figure 7.2) conveys the sensory input from the beak skin to the brain [31]. Preliminary magnetic measurements also pointed to ferromagnetic material present in the pigeon beak [27]. A series of tissue sections (10-μm thick) was stained with Prussian blue (PB, potassium hexacyanoferrate) to map enrichments of ferric iron [27–29]. Figure 7.3(A) shows a PB-stained section from the stratum laxum of the subcutaneous layer with intensive PB reaction. Some 20 tiny spherical PB reaction products (“granules”) are apparent, each roughly 1–2 μm in size. An antibody specific against avian neurofilament showed immunoreactivity in the streaks containing the PB-positive granules [29]. Counterstaining with Kernechtrot, specific for nuclei, did not show a reaction in the streaks; the streaks (5 μm width) turned out to be free nerve endings (FNE), i.e. bare dendrites as opposed to dendrites enclosed in a connective tissue capsule. The granules were only found in FNE, but not all FNE contained PB reaction products [29]. The ultrastructure of the granules was revealed by transmission electron microscopy (TEM) on adjacent sections that had not been subject to PB staining, as the PB reaction alters the chemical composition of the marked ferric iron compounds. A granule now appears as opaque patch of 1 μm diameter (Figure 7.3B), which under high magnification (Figure 7.3C) can be resolved into a cluster of extremely fine-grained particles (2–5 nm). Energy-

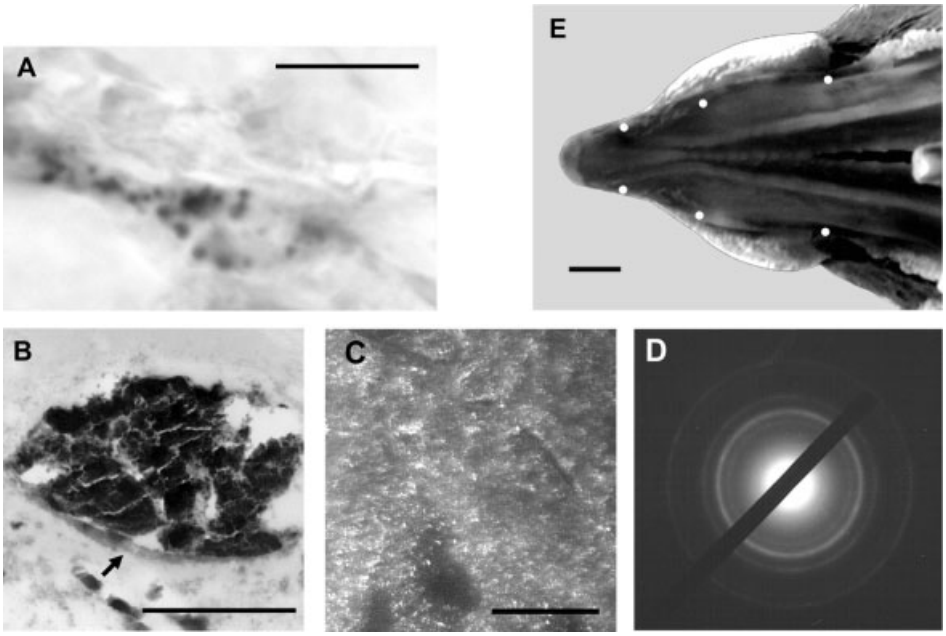

Figure 7.3 Clusters of ultrafine-grained magnetite in the upper beak of homing pigeons [27–29, 34]. (A) Light microscopic view of a tissue section stained with PB, specific for Fe(III). The PB reaction products, black granules between 1 and 2 μm in size, occur within free nerve endings. (B) Bright-field TEM image of a Fe(III)-rich granule. The electron-opaque granule is partly disrupted from sectioning. The arrow points to fibrous material, possibly encapsulating the granule. (C) Dark-field TEM image of the opaque granule in (b) at higher magnification. The bright dots are ultrafine-grained particles with grain sizes between 2 and 5 nm. (D) SAED pattern of the granule in (B). The diffraction pattern is diagnostic for magnetite. (E) Inside of the upper beak. The white dots indicate the six sites where candidate magnetoreceptors were found. Scale bars = 10 μm (A), 1 μm (B), 0.1 (C) μm and 2 mm (E).

dispersive X-ray analysis (EDXA) shows that iron is the dominant element in the clusters [27], and selected-area electron diffraction (SAED) demonstrates that the particles are crystalline and have a diffraction pattern consistent with nanocrystalline magnetite (Figure 7.3D). It is not possible to distinguish unequivocally between magnetite and maghemite (γ-Fe_2O_3), an oxidized form of magnetite, with the methods used. On the other hand, there is not enough material to be available to resolve this question by means of Mössbauer spectroscopy. Such a distinction is by no means crucial since nanocrystalline maghemite has magnetic properties very similar to nanocrystalline magnetite.

In a different study, conducted independently from ours, Williams and Wild [32] also found PB reaction products in the pigeon beak, innervated by ophthalmic nerve fibers. Unfortunately, they did not unearth the nature of the marked ferric iron compounds or resolve their ultrastructure. Intracellular ferric iron demonstrated by the PB stain may well be due to the iron storage complex hemosiderin,

which, however, is not ferrimagnetic and therefore no argument for a possible magnetoreceptor.

7.3.2 Interpretation in Terms of a Magnetoreceptor

FNE containing clusters of magnetite have consistently been observed at six different sites in the upper-beak skin, in all nine individuals where the entire upper-beak skin was analyzed (Figure 7.3E) [29]. This excellent reproducibility strongly suggests a biological function of the magnetite-containing structures.

Another crucial observation is that the magnetite clusters are located in FNE. FNE are bare dendrites ramifying from myelinated nerve fibers (axons) into the epidermis. Being unmyelinated and having no structural specialization, they detect temperature, pain and, more importantly, touch, i.e. they are sensitive to mechanical stimulation. At this point, it is necessary to take a closer look at the behavior of a cluster of nanocrystalline magnetite particles under a magnetic field.

7.3.3 Likely Mechanisms to Transduce a Magnetic Stimulus into a Nervous Signal

Due to their small grain size, the magnetic nanocrystals found in the pigeon beak cannot act as microscopic compass needles, but will be constantly buffeted by thermal fluctuations. Thus, while the individual crystals cannot carry a stable magnetization, a cluster of crystals does assume an induced magnetization in a magnetic field. Such a collective, statistical behavior is called superparamagnetism. Like a paramagnetic, it loses the magnetization once the field is switched off. The prefix "super" refers to the fact that such a collective has a surprisingly high susceptibility, i.e. even a field of low intensity can induce a large magnetization. Well-understood examples of superparamagnetic (SP) systems are technical ferrofluids, i.e. magnetic nanocrystals suspended in a carrier liquid. Such a suspension is both magnetic and fluid. More importantly, a droplet of a ferrofluid will deform in a magnetic field (Figure 7.4). Applied to SP clusters in FNE, this means that magnetic field-induced deformation can stimulate FNE to produce a nerve impulse [33]. Magnetic field-induced deformation is not restricted to SP clusters in which the particles are suspended in a liquid medium, but will also occur in SP clusters with particles embedded in a soft elastic matrix such as the cytoskeleton [28].

A second physical receptor model is based on magnetic interactions between clusters. As can be seen in Figure 7.3(A), roughly 20 clusters occur in one terminal, loosely arranged in a coherent elongated structure. A detailed analysis shows that the spacing between two adjacent clusters is roughly twice their diameter [34]. Thus, the clusters will interact magnetically, thereby attracting or repelling each other depending on the direction of the magnetic field with respect to the imaginary axis joining the clusters (Figure 7.5). Thus, mechanical forces arise that can stimulate the FNE.

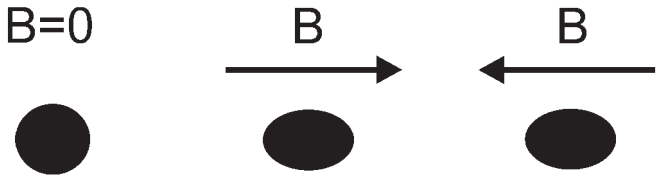

Figure 7.4 Deformation of a SP magnetite cluster in a magnetic field [33]. In zero field, the cluster has a spherical shape (left). A magnetic field **B** deforms the cluster into a prolate ellipsoid of revolution, whose long axis indicates the magnetic field direction (middle). When **B** has the opposite polarity, the cluster assumes the same shape. Only the axial direction of **B** can be registered, not its polarity. This behavior is in agreement with the inclination compass, which has been experimentally demonstrated in migratory birds and homing pigeons.

7.4 Discussion and Open Questions

Theoretical calculations show that the two mechanisms presented in Section 7.3 are viable when it comes to sensing the magnetic field direction [28, 33, 34]. From behavioral studies it has been inferred that pigeons can detect magnetic field variations as small as 0.1 % [16]. It is not clear if mechanical forces induced by small field variations are strong enough to stimulate FNE according to the theoretical models. A quantitative answer to this question requires numerical values of physical model parameters such as magnetic susceptibility of the SP clusters as well as viscosity and shear modulus of the medium containing the nanocrystals. Likewise, the threshold sensitivity of FNE to mechanical stimuli has to be determined. Still, FNE containing SP clusters are excellent structural candidates for a magnetoreceptor on which our theoretical models can be tested.

It is important to compare the candidate magnetoreceptor in pigeons with the one characterized in rainbow trout (*Oncorhynchus mykiss*) by Walker et al. [35]. Using electrophysiological recordings, they were able to identify single neurons in the superficial ophthalmic branch (ros V) of the trigeminal nerve that respond to changes in the intensity, but not the direction, of an imposed magnetic field. The ros V innervates the nose of the trout. To localize the magnetoreceptor in the nose, they used a staining technique to trace the magnetically responsive nerves back to the endings of the individual nerve cells. The candidate magnetoreceptor cells were eventually detected in the olfactory lamellae. Using confocal laser scanning microscopy (CLSM), TEM and EADX, they found iron-rich crystals (grain size 50 nm) in low volume concentrations, which by means of magnetic force microscopy (MFM) were later shown to have a permanent magnetism with magnetic properties similar to SD magnetite [36]. Surprisingly, the putative SD magnetite particles are located within a cell rather than in unmyelinated dendrites (FNE) or other mechanosensitive nerve structures. This raises questions about the possible transducer mechanism. It is not clear either if the magnetic particles are coupled to any potentially mechanosensitive elements and if they are arranged in the form of a chain or a cluster. Although MFM is a non-invasive technique, the magnetic gra-

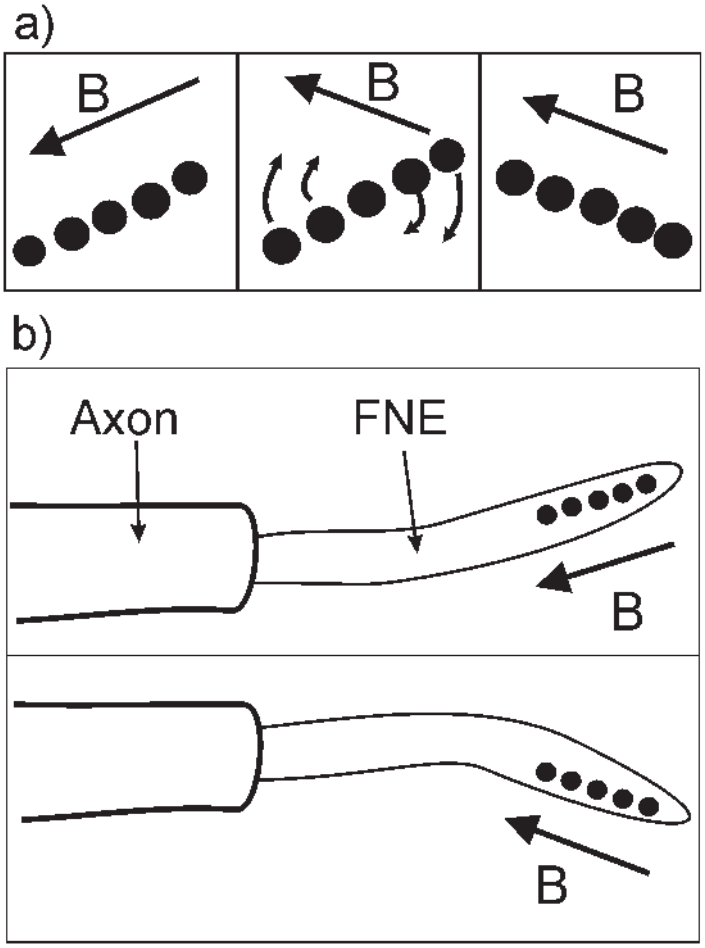

Figure 7.5 Magnetic field transduction based on a group of SP clusters as apparent in Figure 7.3(A). (a) Behavior of a chain of SP clusters in a magnetic field. In a magnetic field **B**, a group of clusters forms a chain aligned with the field (left). As the direction of **B** is changed, the old orientation of the chain becomes energetically unfavorable (middle) and the clusters will rearrange to form a chain aligned with the new field directions (right). (b) Possible transduction mechanism for a chain of SP clusters in a FNE. While the axon is surrounded by a myelin sheath and hence mechanically stiff, the FNE is unmyelinated and therefore flexible. The physical mechanism depicted in (a) will cause a torque, trying to bend the FNE in the field direction. FNE detect mechanical stimulation, and therefore are also suited to register magnetic field-induced mechanical deformation. Like the mechanism shown in Figure 7.4, this mechanism is independent of the polarity of the magnetic field.

dient force produced by the scanning tip can change the arrangement of the magnetic particles in the soft intracellular medium. Nevertheless, like the SP magnetite-containing FNE in the beak skin of pigeons, the SD magnetite-bearing cells in the nose of trout are excellent candidates for a magnetoreceptor, too.

A question so far unanswered concerns magnetite biomineralization in vertebrates. In the radula teeth of chitons (mollusks), iron oxyhydroxide ferrihydrite ($5Fe_2O_3 \cdot 9H_2O$) was identified as a precursor mineral to magnetite [37]. Using laser Raman spectroscopy, among other techniques, Brooker et al. [38] could demonstrate that ferrihydrite is the single main precursor of magnetite formation in chiton teeth and that iron mineralisation occurs simultaneously on two fronts.

Ferritin may be the key protein in magnetite biomineralization in vertebrates. Ferritins comprise a class of iron storage molecules ubiquitous among living systems. Each molecule of ferritin consists of 24 subunits which are assembled to form an approximately spherical cage-like structure of external diameter 12 nm; the cavity has a diameter of 8 nm [39]. Ferritin transforms highly toxic Fe(II) into the less toxic Fe(III) iron, to be sequestered in the cavity in the form of an iron mineral similar to ferrihydrite with varying amounts of phosphate incorporated [40]. Interestingly, the SP magnetite particles in homing pigeons have grain sizes below 8 nm and therefore may well have been originated in ferritin, with ferrihydrate as the precursor to magnetite. At this stage, this is just a working hypothesis, and further investigations are clearly warranted to elucidate the cellular and molecular pathways of magnetite biomineralization.

7.5 Conclusions

Not only has biogenic magnetite been found in magnetotactic bacteria, but also in several animals that use the Earth's magnetic field for orientation or navigation. This observation has led to the hypothesis that magnetite might play a key role in the magnetic sense of higher organisms, too. There have recently been two candidate magnetoreceptors described in homing pigeon [27–29, 34] and rainbow trout [35, 36]. Surprisingly, whilst both structural candidates contain magnetite and are innervated by the ophthalmic branch of the trigeminal nerve, the respective magnetite crystals have magnetic properties completely different to one another. This dissimilarity suggests that the magnetic sense in pigeons is based on a physical mechanism different to that which may be realized in trout. More research is needed to investigate the putative magnetosensory pathways and test models of transduction mechanisms.

References

[1] H. L. Yeagley, *J. App. Phys.* **1951**, *22*, 746–760.
[2] G. Schietecat, *Brieftaube* **1988**, *105*, 936–938 and 972–974.
[3] W. T. Keeton, *Proc. Natl Acad. Sci. USA* **1971**, *68*, 102–106.
[4] W. Wiltschko, R. Wiltschko, *Science* **1972**, *176*, 62–64.

[5] P. B. Taylor, *J. Fish Biol.* **1986**, *28*, 607–624.
[6] S. C. Cande, D. V. Kent, *J. Geophys. Res.* **1992**, *97*, 13917–13951.
[7] R. S. Coe, L. Hongre, G. A. Glatzmeier, *Phil. Trans. R. Soc. Lond.* **2000**, *358*, 1141–1170.
[8] R. Wiltschko, W. Wiltschko, *Magnetic Orientation in Animals*, Springer, Heidelberg, **1995**.
[9] (a) K. J. Lohmann, S. Johnsen, *Trends Neurosci.* **2000**, *23*, 153–159; (b) T. Ritz, D. H. Dommer, J. B. Phillips, *Neuron* **2002**, *34*, 503–506.
[10] (a) K. Schulten, in *Festkörperprobleme XXII – Advances in Solid State Physics* (Ed. P. Grosse), Vieweg, Braunschweig, **1982**, pp. 61–83; (b) R. S. Wadas, *Biomagnetism*, Ellis Horwood, Chichester, **1991**, pp. 38–47.
[11] T. Ritz, S. Adem, K. Schulten, *Biophys. J.* **2000**, *78*, 707–718.
[12] A. Sancar, *Annu. Rev. Biochem.* **2000**, *69*, 31–67.
[13] F. A. Brown, K. M. Sciw, *J. Interdiscipl. Cylce Res.* **1978**, *9*, 137–145.
[14] P. Semm, T. Schneider, L. Vollrath, *Nature* **1980**, *288*, 607–608.
[15] (a) R. Wilschko, W. Wiltschko, *Naturwissenschaften* **1998**, *85*, 164–167; (b) W. Wilschko, R. Wiltschko, *J. Comp. Physiol. A* **1999**, *184*, 295–299.
[16] W. T. Keeton, T. S. Larkin, D. M. Windsor, *J. Comp. Physiol.* **1974**, *95*, 95–103.
[17] E. D. Yorke, *J. Theor. Biol.* **1979**, *77*, 101–105.
[18] R. P. Blakemore, *Science* **1975**, *19*, 377–379.
[19] S. Mann, N. H. C. Sparks, M. M. Walker, J. L. Kirschvink, *J. Exp. Biol.* **1988**, *140*, 35–49.
[20] H. A. Lowenstam, *Bull. Geol. Soc. Am.* **1962**, *73*, 435–438.
[21] D. P. O'Leary, J. Vilches-Troya, R. F. Dunn, A. Campos-Munoz, *Experientia* **1981**, *37*, 86–88.
[22] (a) J. Vilches-Troya, R. F. Dunn, D. P. O'Leary, *J. Comp. Neurol.* **1984**, *226*, 489–494; (b) D. T. Edmonds, *Proc. R. Soc. Lond. B* **1992**, *249*, 27–31.
[23] J. L. Kirschvink, A. Kobayashi-Kirschvink, B. J. Woodford, *Proc. Natl Acad. Sci. USA* **1992**, *89*, 7683–7687.
[24] P. P. Schultheiss-Grassi, R. Wessiken, J. P. Dobson, *Biochim. Biophys. Acta* **1999**, *1426*, 212–216.
[25] P. P. Schultheiss-Grassi, J. P. Dobson, H. G. Wieser, N. Kuster, in *Electricity and Magnetism in Biology and Medicine* (Ed. S. Bersani), Plenum, New York, **1999**, 529–523.
[26] J. L. Kirschvink, F. L. Tabrah, S. Batkin, *J. Exp. Biol.* **1982**, *101*, 321–326.
[27] M. Hanzlik, C. Heunemann, E. Holtkamp-Rötzler, M. Winklhofer, N. Petersen, G. Fleissner, *BioMetals* **2000**, *13*, 325–331.
[28] M. Winklhofer, E. Holtkamp-Rötzler, M. Hanzlik, G. Fleissner, N. Petersen, *Eur. J. Miner.* **2001**, *13*, 659–669.
[29] G. Fleissner, E. Holtkamp-Rötzler, M. Hanzlik, M. Winklhofer, G. Fleissner, N. Petersen, W. Wiltschko, *J. Comp. Neurol.* **2003**, *458*, 350–360.
[30] P. Semm, R. C. Beason, *Brain Res. Bull.* **1990**, *25*, 735–740.
[31] A. Bubien-Waluszewska, in *The Cranial Nerves* (Eds A. S. King, J. McClelland), Academic Press, New York, **1981**, 385–438.
[32] M. N. Williams, J. M. Wild, *Brain Res.* **2001**, *889*, 243–246.
[33] V. P. Shcherbakov, M. Winklhofer, *Eur. Biophys. J.* **1999**, *28*, 380–392.
[34] A. F. Davila, G. Fleissner, M. Winklhofer, N. Petersen, *Phys. Chem. Earth* **2003**, *28*, 647–652.
[35] M. M. Walker, C. E. Diebel, C. Haugh, P. M. Pankhurst, J. C. Montgomery, C. R. Green, *Nature* **1997**, *390*, 371–376.
[36] C. E. Diebel, R. Proksch, C. R. Green, P. Neilson, M. M. Walker, *Nature* **2000**, *406*, 299–302.
[37] (a) K. M. Towe, H. A. Lowenstam, *J. Ultrastruct. Res.* **1967**, *17*, 1–13; (b) J. L. Kirschvink, H. A. Lowenstam, *Earth Planet. Sci. Lett.* **1979**; (c) K. S. Kim, D. J. Macey, J. Webb, S. Mann, *Proc. R. Soc. Lond B* **1989**, *237*, 335–346.
[38] L. R. Brooker, A. P. Lee, D. J. Macey, W. van Bronswijk, J. Webb, *Mar. Biol.* **2003**, *142*, 447–454.
[39] P. M. Harrison, P. Arosio, *Biochim. Biophys. Acta* **1996**, *1275*, 161–203.
[40] T. G. St Pierre, J. Webb, S. Mann, in *Biomineralization: Chemical and Biochemical Perspectives* (Eds S. Mann, J. Webb, R. J. P. Williams), VCH, Weinheim, **1989**, 295–344.

8 Iron-oxo Clusters and the Onset of Biomineralization on Protein Surfaces – Lessons from an Archaeal Ferritin

L.-O. Essen, S. Offermann, D. Oesterhelt and K. Zeth

8.1 Introduction

Iron is an essential cofactor of many enzymes, and participates in biological processes such as oxygen transport, electron transfer and enzymatic catalysis. Although iron is one of the most abundant elements of the Earth crust, its rather poor solubility in the oxidized Fe^{3+} state caused by the formation of insoluble Fe(III) oxides severely limits its bioavailability. Furthermore, due to the presence of molecular oxygen in the atmosphere, the highly soluble Fe^{2+} ions to which iron is reduced upon uptake into the cytosol may act as highly toxic species in aerobic organisms. Two major reactions with the radical-like Fe^{2+} ions are known to cause the formation of reactive oxygen species: Fe^{2+} can reduce molecular oxygen to the reactive superoxide anion radical (1), and it reacts in Fenton's reaction with peroxides and causes the generation of highly reactive hydroxyl radicals (2).

$$Fe^{2+} + O_2 \Leftrightarrow \lfloor Fe^{2+} \cdots O_2 \leftrightarrow Fe^{3+} \cdots O_2^{-\cdot} \rfloor \Leftrightarrow Fe^{3+} + O_2^{-\cdot} \quad (1)$$

$$Fe^{2+} + OOH^- \Leftrightarrow Fe^{2+} \cdots OOH^- \Leftrightarrow OH^- + Fe^{3+} \cdots O^- \Leftrightarrow OH^- + OH^{\cdot} + Fe^{3+} \quad (2)$$

Accordingly, the free Fe^{2+} concentrations are very low in the cytosol at about 10^{-8} M. The cytosolic iron is either associated as a cofactor with enzymes or stored in a bioavailable form by being internalized as the less-reactive Fe^{3+} ion in iron-complexing proteins. Most prominent among the storage proteins are the ferritins [1]. These proteins combine compact iron storage inside a voluminous nanocompartment with efficient iron release from these segregated compartments. The ferritins belong to a larger, all-α-helical superfamily of proteins which occurs throughout all kingdoms of life, including aerobic and anaerobic organisms. In members of the ferritin protein family, iron is taken up into the oligomeric protein shells as Fe^{2+} and oxidized therein to Fe^{3+} at ferroxidase centers (FOC) by molecular oxygen or H_2O_2. The almost insoluble Fe(III) oxides are then deposited in the nanocompartment of the ferritin oligomers as crystalline or amorphous ferrihydrite-like mineral cores [2]. Notably, redox-inert Fe^{3+} oxide that is bound to ferritins accounts for more than 90 % of the heme-independent iron storage.

Biomineralization: From Biology to Biotechnology and Medical Application, Second Edition. Edited by E. Bäuerlein

ISBN: 3-527-31065-7

In eukaryotes, 24-meric ferritins are the dominant iron storage proteins [3, 4]. In animals, they usually comprise two subunit types, H and L ($M_r \sim 20$ kDa, relative sequence identity around 55 %), which exert specialized functions in the co-assembled complexes. The H subunits comprise a di-iron FOC. In contrast, the L subunits apparently catalyze the nucleation of the iron oxide biomineral, because they comprise four glutamates along the inner surface of the protein shell instead of only two as in the H subunits. Interestingly, a structurally distinct protein family, the frataxins, was recently discovered in mitochondria which exhibits quite analogous iron-oxidizing and storage properties, and quaternary organizations as the ferritins. Upon iron binding these frataxins assemble in the mitochondrial matrix with up to 48 identical subunits of β-sandwich topology. These high-molecular-weight complexes of about 840 kDa mass have large storage capacities of about 2400 iron atoms per complex [5] so that storage presumably likewise occurs in the inner compartment of a hollow protein shell.

In eubacterial organisms, three ferritin-like protein subfamilies were found to promote iron storage. Heme-binding bacterioferritins [6] and heme-free ferritins share the same 24-meric architecture as their eukaryotic homologs (Fig. 8.1). In contrast, the ferritin-like members of the Dps subfamily (DNA-binding proteins from starved cells) have only half the size by forming dodecameric protein shells [7]. These Dps were originally described only to bind and to protect DNA under conditions of oxidative or nutritional stress [8]. However, Dps proteins have later been demonstrated to act as iron-storing and -releasing proteins [9] like the conventional 24-meric ferritins. It could also be shown that their protective activity stems mostly from the ability to sequester iron atoms under H_2O_2 consumption and to quench thereby hydroxyl radical formation by the Fenton reaction [10].

The mechanisms of iron uptake, oxidation, nucleation, storage and release have been studied in the past by a plethora of techniques. Identification and analysis of the mineral core was strongly enforced by X-ray and electron diffraction of single particles and the mineral phase. Accordingly, the composition of ferritin cores was revealed to be ferrihydrite with rather variable stoichiometries [2]. Due to the increased interest in ferritins for nanotechnological applications [11, 12], and the availability of advanced techniques like extended X-ray absorption fine structure (EXAFS), X-ray absorption near edge structure (XANES) and Mössbauer spectroscopy, iron cores formed inside ferritins under controlled *in vitro* conditions have been extensively characterized [13].

8.2 General Functional Properties of Dps-like Ferritins

Proteins of the Dps family were first discovered to protect genomic DNA of eubacterial organisms under conditions of oxidative stress [8, 14]. A direct interaction between DNA and Dps was later demonstrated by the Dps-mediated protection of DNA against degradation by various nucleases. However, the functions of members of the Dps subfamily can be more diverse than just DNA binding, because sev-

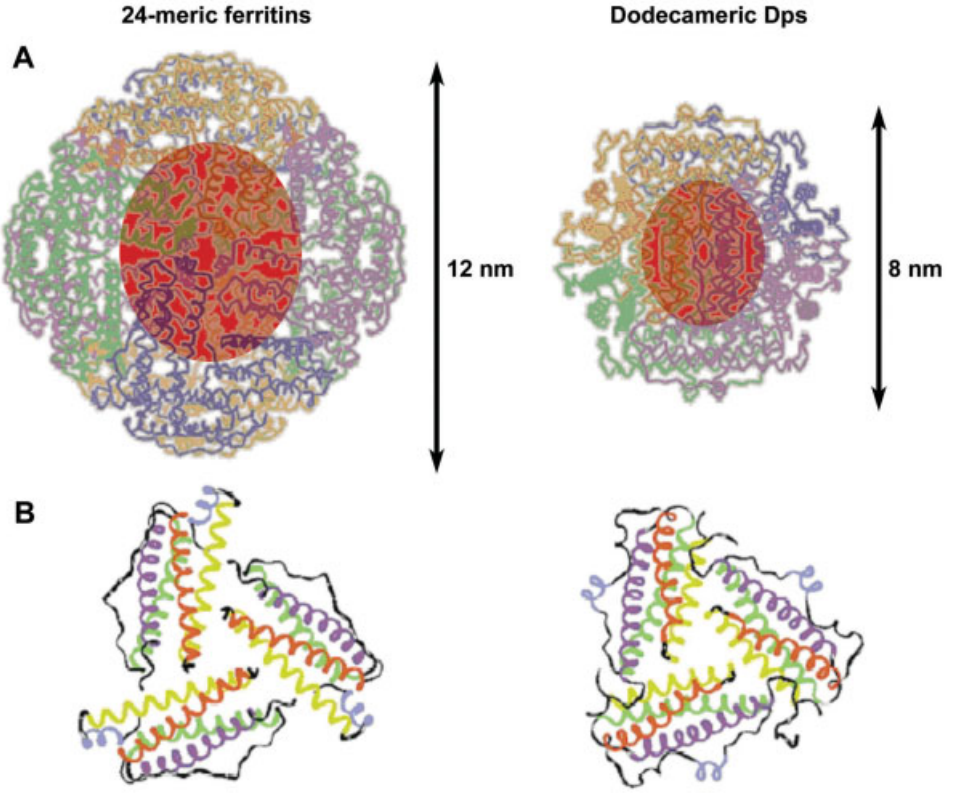

Figure 8.1 (A) Comparison of the quarternary structures of the 24-meric and dodecameric ferritins. The location of the mineral ferrihydrite core inside the protein shells is shown in brown. (B) Arrangement of protein subunits around the access channel of the three-fold symmetry axis. Parts reprinted with permission of Macmillan Magazines Ltd from [7].

eral members not only promote iron incorporation [9] like the 24-meric ferritins, but also act as immunogens and neutrophile activators [15] or even constituents of fine-tangled pili [16].

Currently, the Dps protein from *Escherichia coli* is the best-studied example in terms of structure [7] and function [8, 17, 18]. This protein was shown to act as a Fe^{2+}-binding and -storage protein where iron is most efficiently oxidized by H_2O_2 [18]. Upon oxidation of Fe^{2+} to Fe^{3+} an iron oxide core comprising around 500 atoms is formed inside the dodecameric protein shell (Fig. 8.1). This mineral core is similarly formed in the presence of O_2 as an electron acceptor, albeit at much slower rates than compared to the oxidant H_2O_2. The iron assembled within the crystalline core is reversibly bound and can be released *in vitro* by reducing agents like dithionite. These results and additional *in vitro* experiments based on DNA damage and DNA co-migration assays showed that the protective role of Dps is dual: (1) as an interaction partner with DNA, and (2) as an enzyme that detoxifies the combination of Fe^{2+} and H_2O_2 [18].

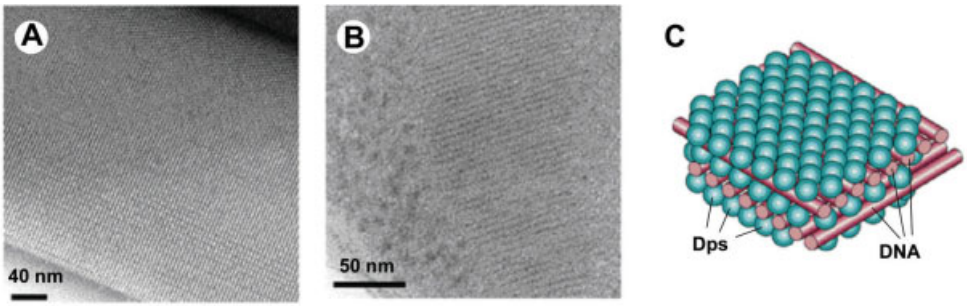

Figure 8.2 (A) *In vitro* assembled co-crystals of *E. coli* Dps and DNA. (B) *In vivo* formation of crystalline Dps/DNA-comprising phases inside the *E. coli* cytosol. (C) Model of the sandwich-like architecture of Dps–DNA co-crystals. Reprinted with permission of Macmillan Magazines Ltd from [21].

A physical interaction between the Dps from *E. coli* and genomic DNA has been demonstrated by electron microscopic analysis of tightly packed protein–DNA microcrystals [17, 19] which are either formed *in vivo* during cell starvation or *in vitro* after mixing the isolated components. While Dps alone forms two-dimensional, trigonal protein arrays, the addition of DNA greatly accelerates this co-crystallization process by growth into the third dimension (see Fig. 8.2). Interestingly the lattice spacing of the two-dimensional protein arrays is not significantly affected in the protein–DNA co-crystals. Consequently, a convincing model of alternating layers of protein and DNA could be proposed from the observed packing of Dps dodecamers inside three-dimensional Dps crystals without DNA ([20]; see also Fig. 8.2A and B). This sandwich-like mode of protein–DNA complex formation is apparently a physiologically relevant survival strategy as the overexpression of Dps in starved cells results in intracellular crystalline structures similar in spacing to the complexes observed *in vitro* (Fig. 8.2B). Like other stress proteins, Dps expression is only induced during cell starvation with up to 200 000 molecules per cell. The DNA–Dps co-crystallization process is additionally controlled by the concentration of divalent ions, which apparently has to pass a lower threshold during prolonged periods of starvation in order to promote bridging interactions between the Dps protein surface and DNA. On the other hand, the co-crystallization can be reversed if the concentration of divalent cations (Mg^{2+}, Fe^{2+}) increases again. Interestingly, these simple control mechanisms for Dps-mediated DNA condensation are sufficient to maintain genome function under stress conditions without the use of additional metabolic energy in terms of ATP [21].

8.3 General Structural Properties of Dps-like Ferritins

The first structural information for members of the Dps subfamily was derived from the crystal structure of Dps from *E. coli* [7]. Crystal structures of homologous pro-

teins from the Gram-positive bacteria *Listeria innocua* [22] and two *Bacillus* species [20, 23] were recently published, and display the same fold and quarternary arrangement. The isolated subunits represent essentially the fold of a four-helix bundle as observed for the mammalian ferritin homologs except of a short C-terminal helix that is missing in the Dps subfamily. Dps proteins assemble into dodecameric complexes of about 240 kDa molecular mass and cubic 23-symmetry so that six two-fold and four three-fold symmetry axes transverse the complex. Four pores penetrate the shell of the protein complex along the three-fold axes and thereby allow free access of ionic species to the inner compartment. The outer and inner diameters of the Dps complexes are 9 and 4.5 nm. In theory, the volume of the enclosed nanocompartment would be sufficient to store up to 2000 iron atoms as an amorphous ferrihydrite-like core, but such high iron loadings have never been reported. In addition to the conserved access channels, all crystal structures of eubacterial Dps proteins exhibit an interfacial iron-binding site that was assigned in Dps-like ferritins as the di-iron FOC for catalytic iron oxidation [20, 22].

8.4 Structural Aspects of a Dps-like Protein from a Halophilic Archaeon

Until recently, it was generally assumed that members of the Dps subfamily exclusively occur in eubacteria. The unexpected discovery of the Dps-like ortholog DpsA in the halophilic archaeon *Halobacterium salinarum* [24] showed that iron-binding members of the ferritin protein family may even occur in a few archaea, most likely due to horizontal gene transfer from a eubacterial organism.

The subsequently solved crystal structure of the dodecameric DpsA complex [25] showed that the overall architecture of this halophilic Dps protein resembles its eubacterial relatives. However, the crystallized halobacterial DpsA protein could be purified as an iron-comprising complex from the cytosol of *H. salinarum*. In its low-iron state (FEL), the presence of 16 iron-binding sites per protein complex was clearly confirmed by X-ray crystallography (see Fig. 8.3A). All iron-binding sites were located along the interior protein surface, of which 12 iron atoms were placed at the dimeric FOC and four on the trimeric subunit interfaces, the NII nucleation site.

DpsA of *H. salinarum* was previously shown to complex up to 100 iron atoms per dodecamer, which are at least partly constituents of larger ferric iron clusters according to electron paramagnetic resonance (EPR) spectroscopy [24]. Accordingly, in the high-iron state of DpsA (FEH) that was generated by incubation of DpsA crystals in the presence of iron [26], a total number of 110 irons per dodecameric complex could be structurally identified (Fig. 8.3B and C). These iron sites may be classified according to their locations and presumptive function in the DpsA ferritin complex (see Fig. 8.3C): the iron access routes (subsites T1–T3: $3 \times 12 = 36$), the FOCs (subsites F1–F3: 36), the nucleation centers NI along the two-fold axes (subsites N11–N13: 18) and, finally, the nucleation centers NII along the three-

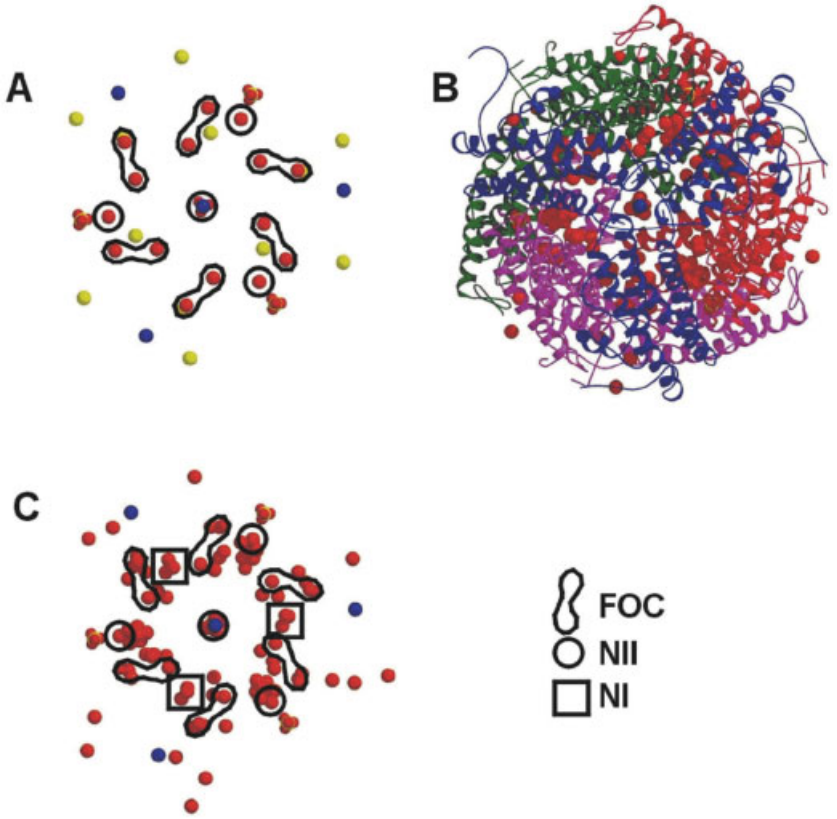

Figure 8.3 (A) The low-iron state FEL of DpsA from *H. salinarum* shown without the protein backbone. The iron-binding sites are rendered in brown, magnesium in grey, sodium in blue, and sulfate in yellow and red. The FOC and the nucleation centers I and II (NI and NII) are highlighted. (B) Ribbon model of the quaternary structure of the DpsA dodecamer as viewed along the three-fold axis [26]. (C) The high-iron state FEH of DpsA depicted in the same representation as (A).

fold axes (subsites N21–N25: 20). In the following, we present a short survey about the structural features of these highly diverse iron-binding sites, because the non-proteinaceous substructure of DpsA with its abundance of iron-binding sites is to our knowledge the most complete example among the ferritin-like proteins where pathways for iron conduction, oxidation and biomineralization may be directly derived from structural information.

8.4.1 Iron Access Route into DpsA

Structural differences between the meso- and halophilic homologs of the Dps subfamily occur mostly along the three-fold axes of the dodecamers. In the *L. innocua*

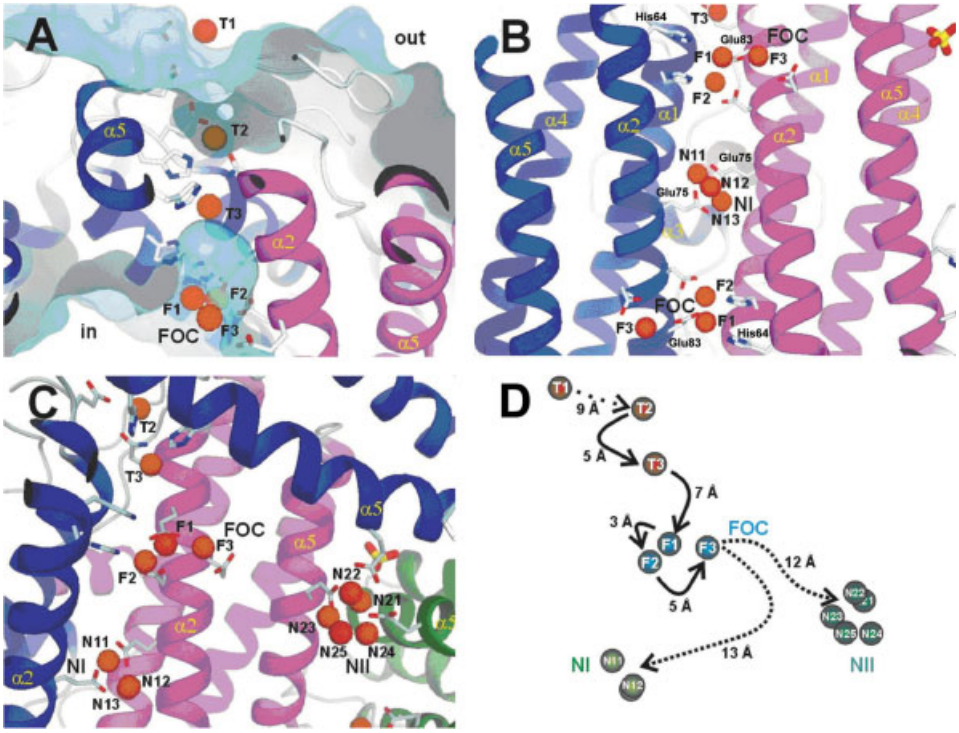

Figure 8.4 The iron-binding sites of the *H. salinarum* DpsA protein in its high-iron state FEH [26]. (A) Side view of the iron translocation channel with the initial iron-binding site (T1), and the subsequent iron-binding sites T2 and T3 which reside in the iron translocation channel. (B) The FOC as viewed along the two-fold axis. The helices, the three iron-binding subsites F1–F3 of the FOC and the nucleation center NI are depicted. (C) Overview of the FOC and the two nucleation centers, NI and NII. The nucleation center NI including the two symmetry-related iron atoms N11 and N12, and the symmetry-related liganding residues Glu72 and Glu75 are shown. (D) Possible routes of iron transfers the FOC to the NI and NII centers are highlighted. The distances between the iron sites and possible storage possibilities are indicated.

and *E. coli* Dps a hydrophilic, conserved pore of about 8 Å diameter runs between three symmetry-related subunits and is predominantly lined by acidic residues. In the halophilic DpsA dodecamer, this pore is plugged by a row of four residues, Glu141, His150, Arg153 and Glu154 [26]. Interestingly, the three-fold symmetry-related Glu154 residues serve as ligands of the NII nucleation center (see below, and Fig. 8.4C and 8.5A).

Compared to other structurally characterized 12-meric and 24-meric ferritins, the DpsA structure revealed a different pathway for iron binding and translocation [26]. At the outer protein surface an initial iron-binding site (T1) was found that is more than 20 Å distant from the catalytic FOC (Fig. 8.4A). This T1 site is close to the entrance of a water-filled pore leading to the inner compartment of the ferritin shell. A second site, T2, is buried inside the pore and 13 Å away from the FOC. A third

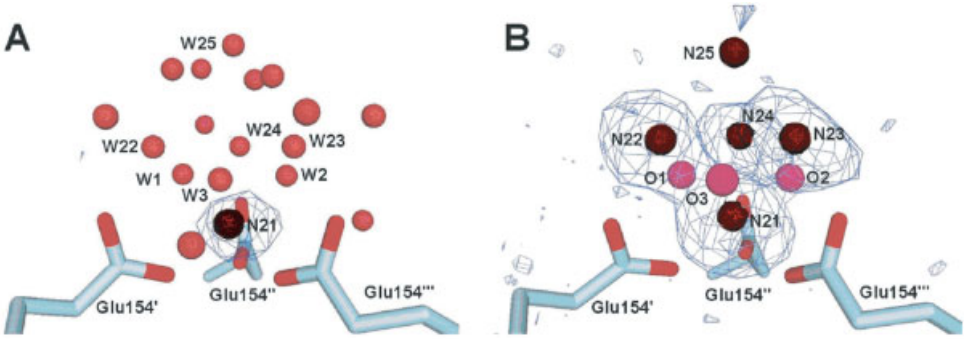

Figure 8.5 Iron coordination in the nucleation center NII of *H. salinarum* DpsA [26]. (A) View perpendicular to the three-fold axis on the nucleation center NII of the low-iron state FEL. The subsite N21 of the nucleation center NII is shown in brown; selected water molecules are depicted in red. Several solvent molecules form a crown-like structure around the N21 subsite; the labeling of these water molecules corresponds to the iron and oxygen atoms of the polynuclear iron cluster. (B) The polynuclear iron cluster in the NII center of the FEH structure. Anomalous difference Fourier maps (blue) were calculated at 2.2 Å and contoured at 3.2 σ to indicate the positions of individual iron atoms. Four strong (N21–N24) and one additional weak anomalous difference density peak (N25) were detected as constituents of a surface-bound pentanuclear iron cluster.

binding site, T3, is located about halfway between the T2 site that is liganded by residues of two adjacent monomers and the FOC. The distances between the four iron sites are all in the range of 5–9 Å (T1–T2: 9 Å; T2–T3: 5 Å; T3–F1: 7 Å, see Fig. 8.4A and C) and corroborate a model for the iron transport into the ferritin shell; thus, hydrated Fe^{2+} atoms are first bound to the outer surface of DpsA at the T1 site, and after that progressively guided through the pore via the T2 and T3 sites to the FOC. This pathway is obviously unique to DpsA, because in eubacterial Dps-like ferritins such a pathway would be sterically blocked by the protein shell. The diversion from the three-fold symmetric pores of mesophilic ferritins might be dictated by the hypersaline environment. First, due to the utilization of a non-symmetric protein interface for opening up access channels, the *H. salinarum* ferritin provides 12 entrance pores for iron instead of the four pores of the mesophilic Dps-like ferritins. The increased permeation of the DpsA protein shell might circumvent the problem that electrostatic guidance of iron ions as described for other ferritins is not feasible for a halophilic ferritin ortholog. In the cytosol of a haloarchaeal organism long-range electrostatic interactions are efficiently shielded by the almost saturated salt concentration of the cytosol (around 5 M KCl) so that local protein–iron interactions have to suffice for guiding the iron atoms into the inner compartment. Second, the involvement of histidine residues in the iron translocation pathway is also unique for DpsA, because other Dps orthologs mostly lack histidines in the iron access channels and along the inner protein surfaces. Here, the different coordination characteristics of iron and alkali irons presumably evoked the accumulation of histidines on the ferritin protein surfaces under the hypersaline environmental conditions: Fe^{3+} irons are known to coordinate to imidazole groups with similar dissociation constants (below 1 mM) as carboxylates, whereas potas-

sium ions only interact with the latter by forming ion pairs. Hence, the competition between iron and the highly abundant alkali ions for coordination to the ferritin shell might be better overcome by the more covalent and directional nature of complexation to histidine residues which are distributed along the inner and outer surfaces of *H. salinarum* DpsA.

8.4.2 The FOC

The ligands of the FOC are conserved throughout the Dps subfamily of ferritins, including the ferritin from *L. innocua* [22] and Dps from *E. coli* [7]. In the low-iron state structures of DpsA from *H. salinarum* [26] only a single iron atom (F1 subsite) is bound to the FOC. The F1 iron is coordinated in a hexagonally distorted manner to three conserved residues on the protein dimer interface. This geometry is similar to the FOCs found in the structures of Dps proteins from *L. innocua*, *Bacillus anthracis* and *E. coli* [13–15].

In the high-iron state structure FEH, two additional subsites F2 and F3 were detected at the FOC (Fig. 8.4B). The F2 subsite is 3.2 Å apart from F1, and the ion is coordinated to residues Glu83 and the His64 of the adjacent monomer. The distance between the F1 and F2 subsites apparently reflects the canonical distance of a Fe–O–Fe μ-oxo bond. Surprisingly, a third iron (F3) was found nearby at about 3.9 Å from F2 and 4.9 Å from F1. This F3 iron is coordinated to Glu80 and Glu83 of the same monomer. Interestingly, the F2 and F3 subsites are apparently only transiently occupied during the *in vitro* iron loading of DpsA [26], because these sites were absent in structures where DpsA crystals were soaked for longer than 2 h. Consequently, the F2 and F3 subsites might be only occupied by Fe^{2+} which is continuously oxidized to Fe^{3+} during the prolonged incubations in the presence of oxygen. While the F2 site can directly participate in the oxidation of hydrogen peroxide or oxygen, the functional role of the F3 subsite is still elusive. In the *E. coli* ferritin a third iron next to the di-iron FOC was shown to assist in the complete reduction of O_2 to water by which the generation of reactive oxygen species is avoided. Furthermore, the third site of the *E. coli* ferritin was also reported to stabilize the di-iron FOC such that the proportion of protein-bound iron was larger than in ferritins without this site [27]. Accordingly, the slowed incorporation of iron into iron cores was claimed to improve the bioavailability of iron in these microorganisms as compared to the rapidly biomineralizing mammalian ferritins.

In any case, if the oxidation of F2 and F3 site irons leads to Fe^{3+} ejection from the di- or tri-iron FOC these iron atoms would have to migrate about 12–13 Å to the closest NI or NII nucleation sites (Fig. 8.4C). The distance between the F3 subsite and the NII nucleation center might only be overcome by acidic intervening residues which are close to subsite F3 and the nucleation center NII, respectively.

8.4.3 The Nucleation Sites and Nanocluster Formation

Two acidic amino acids next to the two-fold symmetry axes of the dodecamer were supposed to form an iron core nucleation site along helix 2 (α2 in Fig. 8.4B) in the

ferritin from *L. innocua* [22]. It was further suggested that after oxidation at the ferroxidase site one Fe^{3+} is displaced by Fe^{2+} and migrates to the proposed helix 2-iron nucleation site. Interestingly, these residues are not conserved in DpsA [25]. As an alternative iron nucleation site the *H. salinarum* ferritin provides four acidic residues, Glu72 and Glu75, from two adjacent, two-fold-related monomers. Three iron peaks (N11–N13) were observed here in anomalous difference maps [26] of which two were directly coordinated to the protein (N11 and N13). Again, the ligands of these iron-binding sites were not conserved in other Dps-like ferritins. As the other polynuclear nucleation center (NII) is likewise not conserved, one may conclude that the mechanism earlier proposed by Ilari et al. [22] for iron accumulation in the *Listeria* ferritin is at least not applicable to the halophilic DpsA.

NII, the other novel iron nucleation center for the deposition of iron oxides, was observed below the inner surface of the *H. salinarum* ferritin (Fig. 8.4C and 8.5A). In the low-iron state of DpsA a single iron atom (subsite N21) has been found along the three-fold axis where it is prismatically coordinated to three symmetry-related Glu154 residues and three water molecules. This iron atom seems to serve as a seed atom for iron cluster formation (Fig. 8.5A), because in the high-iron state structure FEH this iron atom becomes part of a pentanuclear iron cluster [26]. In the FEH structure several water molecules which surround the N21 subsite are replaced by three-fold-symmetry-related iron atoms (Fig. 8.5B). Like the N21 iron, these additional iron atoms bind to Glu154, but coordinate to the other oxygen of the carboxylate function. Three water-derived ligands, presumably OH^- or O^{2-}, were observed as triply bridging ligands between N21 and pairs of the other subsites. Together with subsite N21, the additional iron subsites N22–N24 form a distorted tetrahedron with a distance of 3.1 Å to N21, 2.2 Å to the bridging oxygen atoms and 3.5 Å between each other (Fig. 8.5B).

The structure of the [4Fe–3O] cluster in the NII nucleation center clearly differs from the cubane-like [4Fe–4S] clusters found in many redox-active iron–sulfur proteins with iron–iron distances of around 2.8 Å. The [4Fe–3O] cluster resembles a site-differentiated cubane, although additional OH^-/O^{2-} ligands were not resolved as missing corners between the subsites N22 and N24 of the FEH structure. Such a geometry with widened iron-iron interatomic distances between the subsites N22–N24 is generally not found in protein structures that comprise [4Fe–4S] clusters. Likewise, the geometry of these [4Fe–3O] clusters is not found as the substructure of any other iron oxide/hydroxide minerals such as ferrihydrite, magnetite or lepidocreicite. Therefore, the unique arrangement of the iron atoms in the four subsites N21–N24 apparently only depends on the three-fold-symmetric protein environment.

One might postulate that the observed cluster in the NII site of the halophilic Dps protein might form some center for the early outgrowth of larger iron-oxo clusters. Indeed, the FEH structure showed a fifth iron-binding site (N25) with lower occupancy that protrudes further into the inner compartment of the DpsA protein shell [26]. This subsite is equidistant from the subsites N22–N24 (3.0 Å) and lacks any interactions with the protein. We speculated that the observed NII clusters may further increase in size upon prolonged incubations in the presence of iron. However, larger iron-oxo clusters or even nanocrystals inside the protein shell were not track-

able by X-ray crystallographic analysis after charging the DpsA crystals with iron for prolonged periods of time.

8.5 Biomineralization in 24-meric Ferritins

The 24-meric ferritins occur in the cytosol and mitochondria of eukaryotes as well as in many eubacteria. The doubled number of subunits as compared to the Dps subfamily implies an outer diameter of about 12 nm and a larger inner compartment of approximately 8 nm diameter (Fig. 8.1A). Consequently, the iron-loading capacity of these ferritins is higher than in the Dps subfamily with up to 4500 iron atoms per protein shell [1]. In contrast to the Dps subfamily, the catalytic FOC comprises only residues from one subunit. In cases where the ferritin protein shell is heterooligomeric, e.g. in the eubacterial bacterioferritins or the mammalian cytosolic ferritins, this function localizes with conserved residues only on a single subunit type [4].

The entry of iron into the inner compartment of the 24-meric ferritins with their characteristic cubic 432 symmetry has been subject of various studies (overview in [6]). In mammalian ferritins much evidence has been found that iron passage proceeds through the conserved access channels which cross the protein shell along the three-fold symmetry axes (see Fig. 8.1A and B). In addition, channels along the four-fold axes were recently postulated on the base of electrostatic calculations to form proton wires which facilitate proton efflux during the formation of ferrihydrite inside the protein shell [28]. Interestingly, in 24-meric ferritins of eubacterial origin like the heme-comprising bacterioferritins, an alternative to the three-fold-related iron passage pathways has been discovered where the channels transverse the protein subunits and end above the catalytic ferroxidase sites [29]. Thus, such a spatial coupling of iron transport and oxidation that has been discussed above in Section 8.4 for the dodecameric, halophilic DpsA [26] might be a widespread feature among prokaryotic ferritins.

The precise structure of the ferritin iron core is still a matter of debate [2, 13], although this biogenic mineral was early recognized as the hydrous ferric oxide ferrihydrite ([30]; bulk formula: $5Fe_2O_3 \cdot 9H_2O$). One complication is the chemical diversity observed for ferritin cores as reflected by varying iron:phosphate ratios (between 1.7 and 44) [2]. This heterogeneity presumably depends on the composition of the chemical environment from which the ferritins were isolated, because the mineral content of ferritin shells can be widely manipulated under *in vitro* conditions as demonstrated by the synthesis of ''magnetoferritins'' [31] and other artificially charged ferritins [32]. Likewise, the crystallinity is a function of the phosphate content with the highest crystalline order observed at low phosphate contents. Structurally, the ferritin cores apparently resemble the so-called six-line ferrihydrite whose major phase comprises octahedral iron atoms in hexagonal layers of oxygen atoms stacked according to the layer sequence ABAC [13]. However, further heterogeneity is also found for the iron oxide modifications, because in natural ferritin

preparations ultrastructural studies using electron nanodiffraction revealed minor populations of ferritin shells which comprise other biogenic iron oxide minerals like magnetite (Fe_3O_4) or hematite (α-Fe_2O_3) [13].

Biochemical studies on the bacterioferritins from *E. coli* and *Rhodobacter capsulatus* convincingly showed that the ferritins are not simple reaction vessels for the aggregation of iron hydroxide species, but provide peculiar nucleation sites along their inner protein surfaces, most likely along helix B. Here, mutants were generated which lost the ability to assemble to 24-meric protein shells, but still form stable dimers with ferroxidase activity [33]. These dimeric ferritin mutants were shown to catalyze the oxygen-dependent generation of polynuclear, antiferromagnetic clusters of Fe^{3+} ions which are tightly bound to the protein with nine Fe^{3+} ions (*E. coli*) and 16 Fe^{3+} ions (*R. capsulatus*) per dimer, respectively. Although no structural data currently exist about the geometries of these iron clusters, it is quite likely that their overall features resemble oxo-bridged iron clusters as demonstrated in the halophilic DpsA protein. Most likely, the contribution of the inner-surface carboxylates is not the simple provision of a sufficiently negatively charged microenvironment for biomineralization, but a specific involvement in the nucleation process and the early growth of polynuclear iron oxide species.

8.6 Ferrihydrite Formation in Ferritin and Ferritin-like Dps Proteins – A Masterplan for Biomineralization?

The X-ray crystallographic observation of a polynuclear iron oxide cluster inside a haloarchaeal ferritin shed some new light on potential pathways for biomineralization inside proteinaceous ferritin shells. Certainly, Fe^{2+} ions first have to diffuse towards the FOC after they have entered the inner compartment through pores in the protein shell. However, their further fate after oxidation to Fe^{3+} by molecular oxygen (24-meric ferritins) or H_2O_2 (12-meric ferritins) is still enigmatic. Three hypothetical scenarios might be put forward (Fig. 8.6).

In the first scenario (route I), hydrated Fe^{3+} ion species are directly ejected from the FOCs into the aqueous inner nanocompartment. Diffusion-controlled incorporation of Fe^{3+} ions into the surfaces of the ferrihydrite core might give rise to highly ordered mineral cores (Fig. 8.6, route I). The resulting biomineral might be still loosely attached to the negatively charged inner protein surface so that the transfer of the Fe^{3+} ion could occur rather locally. Prior nucleation of the ferrihydrite core might be simply catalyzed by the locally high concentration of Fe^{3+} ions which distribute as counter-cations along the negative protein surface as predicted by the Gouy–Chapman theory. Alternatively (route II), the growth of the biomineral core might proceed simultaneously at multiple sites from the inner protein surface. In such a pathway, free diffusion of Fe(III) oxide species between the ferroxidase site and the surface of the growing ferrihydrite mineral would be minimized. The outgrowth of polycrystalline or amorphous inorganic material from the periphery

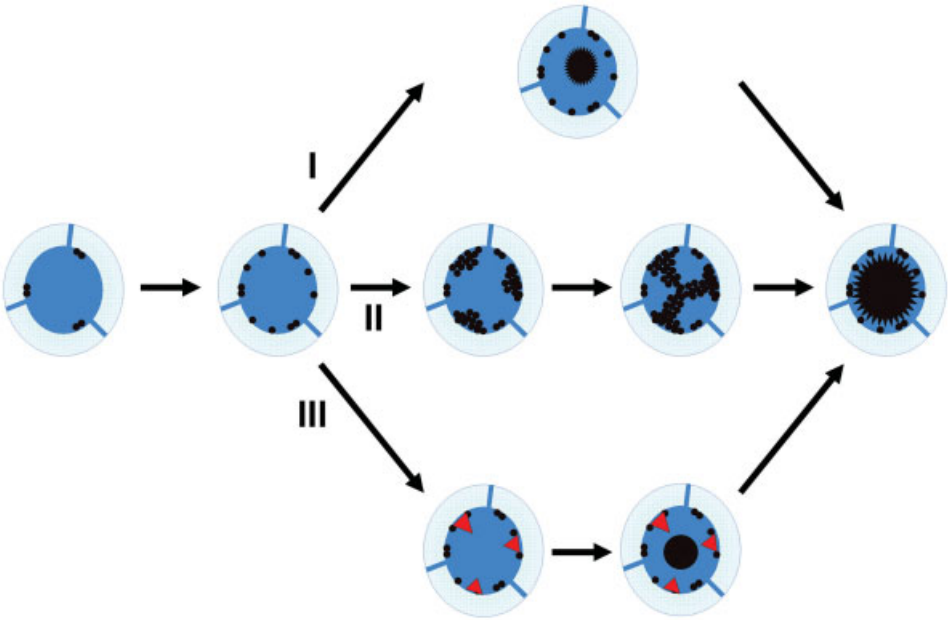

Figure 8.6 Hypothetical pathways of biomineralization in ferritins. In (I), an in–out mechanism is depicted where biomineral growth occurs diffusion-controlled from a crystalline nucleus. In (II), ferrihydrite aggregation proceeds according to an out–in mechanism from multiple centers along the inner protein surface. The pathway shown in (III) resembles the in–out mechanism, but postulates that ordered polynuclear clusters (red triangles) are first formed along the protein surface, released and merged with the growing nucleus.

instead from the center might depend on close spatial relationships between the catalytic FOCs and the iron access channels, because otherwise diffusion pathways to and from the catalytic centers might be easily blocked during biomineralization.

In the final scenario (route III), the Fe^{3+} species firstly participate in the formation of polynuclear iron oxide clusters which are tightly bound along the inner protein surface as found for the haloarchaeal ferritin [26]. As a net result, the incorporation of this iron into the growing mineral would be retarded. An advantage of this route might be that Fe^{3+} has transiently a better bioavailability, so if the cellular demand for iron increases again the reaction series could easily be reversed. Furthermore, rather whole polynuclear clusters and not single iron atom species might be ultimately incorporated into the growing biomineral core (Fig. 8.6, route III). Such an aggregation-based mechanism of nanocrystal growth was recently described for the biomineralization products of iron-oxidizing bacteria [34], where it is thought to lead to coarser, polycrystalline materials with a superior degree of reactivity. Interestingly, such polynuclear species do not play any role in the nonbiogenic formation of ferrihydrites. Here, only monomeric and, to a lesser, extent dimeric and trimeric iron oxide species accompany the precipitation of hydrous ferric oxides [35].

A surprising finding from the structure of the iron-rich, haloarchaeal DpsA ferritin is that the geometry of the polynuclear iron oxide cluster is highly distorted compared to other natural iron oxide minerals. Pre-alignment of ion-binding sites on protein templates with the crystal lattices of thereon growing biominerals was suggested to promote nucleation and biomineralization. A recent structure of the calcium-loaded osteocalcin [36] corroborated that notion by showing an almost perfect match between the five calcium ions bound to the flat protein surface and the prism face (100 plane) of the bone mineral hydroxyapatite. In that regard, the protein-controlled assembly of polynuclear iron oxide species with unique geometries might be a consequence of the highly polymorphic nature of hydrated iron oxides and could be relevant for other biogenic processes leading to iron oxide species like the magnetite nanocrystals which are found in many eubacterial and eukaryotic species (see Chapters 2, 4 and 7).

References

[1] P. M. Harrison, P. Arosio, *Biochim. Biophys. Acta* **1996**, *1275*, 161–203.
[2] N. D. Chasteen, P. M. Harrison, *J. Struct. Biol.* **1999**, *126*, 182–194.
[3] D. M. Lawson, P. J. Artymiuk, S. J. Yewdall, J. M. Smith, J. C. Livingstone, A. Treffry, A. Luzzago, S. Levi, P. Arosio, G. Cesareni, *Nature* **1991**, *349*, 541–544.
[4] P. D. Hempstead, S. J. Yewdall, A. R. Fernie, D. M. Lawson, P. J. Artymiuk, D. W. Rice, G. C. Ford, P. M. Harrison, *J. Mol. Biol.* **1997**, *268*, 424–448.
[5] O. Gakh, J. Adamec, A. M. Gacy, R. D. Twesten, W. G. Owen, G. Isaya, *Biochemistry* **2002**, *41*, 6798–6804.
[6] M. A. Carrondo, *EMBO J.* **2003**, *22*, 1959–1968.
[7] R. A. Grant, D. J. Filman, S. E. Finkel, R. Kolter, J. M. Hogle, *Nat. Struct. Biol.* **1998**, *5*, 294–303.
[8] M. Almiron, A. J. Link, D. Furlong, R. Kolter, *Genes Dev.* **1992**, *6*, 2646–2654.
[9] M. Bozzi, G. Mignogna, S. Stefanini, D. Barra, C. Longhi, P. Valenti, E. Chiancone, *J. Biol. Chem.* **1997**, *272*, 3259–3265.
[10] G. Zhao, P. Ceci, A. Ilari, L. Giangiacomo, T. M. Laue, E. Chiancone, N. D. Chasteen, *J. Biol. Chem.* **2002**, *277*, 27689–27696.
[11] I. Yamashita, *Thin Solid Films* **2000**, *393*, 12–18.
[12] M. Allen, D. Willits, J. Mosolf, M. Young, T. Douglas, *Adv. Mater.* **2002**, *14*, 1562–1565.
[13] J. M. Cowley, D. E. Janney, R. C. Gerkin, P. R. Buseck, *J. Struct. Biol.* **2000**, *131*, 210–216.
[14] A. Martinez, R. Kolter, *J. Bacteriol.* **1997**, *179*, 5188–5194.
[15] F. Tonello, W. G. Dundon, B. Satin, M. Molinari, G. Tognon, G. Grandi, G. Del Giudice, R. Rappuoli, C. Montecucco, *Mol. Microbiol.* **1999**, *34*, 238–246.
[16] R. J. Brentjens, M. Ketterer, M. A. Apicella, S. M. Spinola, *J. Bacteriol.* **1996**, *178*, 808–816.
[17] S. G. Wolf, D. Frenkiel, T. Arad, S. E. Finkel, R. Kolter, A. Minsky, *Nature* **1999**, *400*, 83–85.
[18] A. Ilari, P. Ceci, D. Ferrari, G. L. Rossi, E. Chiancone, *J. Biol. Chem.* **2002**, *277*, 37619–37623.
[19] D. Frenkiel-Krispin, S. Levin-Zaidman, E. Shimoni, S. G. Wolf, E. J. Wachtel, T. Arad, S. E. Finkel, R. Kolter, A. Minsky, *EMBO J.* **2001**, *20*, 1184–1191.
[20] B. Ren, G. Tibbelin, T. Kajino, O. Asami, R. Ladenstein, *J. Mol. Biol.* **2003**, *329*, 467–477.
[21] A. Minsky, E. Shimoni, D. Frenkiel-Krispin, *Nat. Rev. Mol. Cell. Biol.* **2002**, *3*, 50–60.
[22] A. Ilari, S. Stefanini, E. Chiancone, D. Tsernoglou, *Nat. Struct. Biol.* **2000**, *7*, 38–43.

[23] E. Papinutto, W. G. Dundon, N. Pitulis, R. Battistutta, C. Montecucco, G. Zanotti, *J. Biol. Chem.* **2002**, *277*, 15093–15098.
[24] S. Reindel, S. Anemüller, A. Sawaryn, B. F. Matzanke, *Biochem. Biophys. Acta* **2002**, *1598*, 140–146.
[25] S. Offermann, PhD thesis, Ludwig-Maximilians-University (Munich), **2003**.
[26] K. Zeth, S. Offermann, L.-O. Essen, D. Oesterhelt, *Proc. Natl Acad. Sci. USA*, in press.
[27] A. Treffry, Z. Zhao, M. A. Quail, J. R. Guest, P. M. Harrison, *FEBS Lett.* **1998**, *432*, 213–218.
[28] T. Takahashi, S. Kuyucak, *Biophys. J.* **2003**, *84*, 2256–2263.
[29] S. Macedo, C. V. Romao, E. Mitchell, P. M. Matias, M. Y. Liu, A. V. Xavier, J. LeGall, M. Teixeira, P. Lindley, M. A. Carrondo, *Nat. Struct. Biol.* **2003**, *10*, 285–290.
[30] P. M. Harrison, F. A. Fischbach, T. G. Hoy, G. H. Haggis, *Nature* **1967**, *216*, 1188–1190.
[31] F. C. Meldrum, B. R. Heywood, S. Mann, *Science* **1992**, *257*, 522–523.
[32] T. Douglas, D. P. E. Dickson, S. Betteridge, J. Charnock, C. D. Garner, S. Mann, *Science* **1995**, *269*, 54–57.
[33] S. A. Malone, A. Lewin, M. A. Kilic, D. A. Svistunenko, C. E. Cooper, M. T. Wilson, N. E. Le Brun, S. Spiro, G. R. Moore, *J. Am. Chem. Soc.* **2004**, *126*, 496–504.
[34] J. F. Banfield, S. A. Welch, H. Zhang, T. T. Ebert, R. L. Penn, *Science* **2000**, *289*, 751–754.
[35] U. Schwertmann, J. Friedl, H. Stanjek, *J. Coll. Interface Sci.* **1999**, *209*, 215–225.
[36] Q. Q. Hoang, F. Sicheri, A. J. Howard, D. S. C. Yang, *Nature* **2003**, *425*, 977–980.

Silica-hydrated SiO_2

Biomineralization: From Biology to Biotechnology and Medical Application,
Second Edition. Edited by E. Bäuerlein

ISBN: 3-527-31065-7

9 The Molecular Basis of Diatom Biosilica Formation

Nils Kröger and Manfred Sumper

9.1 Introduction

Diatoms (order *Bacillariophyceae*) are eukaryotic, unicellular algae that are ubiquitously present in almost every water habitat on Earth. In the oceans, diatoms often dominate phytoplankton blooms [1] and it is estimated that they are responsible for about 25 % of the net biological primary production on Earth [2]. The most striking feature of a diatom is the beautiful architecture of its cell wall, which is made of biosilica (Figure 9.1). Diatom biosilica is mainly composed of hydrated SiO_2 (silica) with a small proportion of associated organic macromolecules. X-ray diffraction analysis demonstrated diatom biosilica to be amorphous at the molecular scale [3], yet it contains highly symmetrical patterns in the nano- to micrometer range (biosilica nanopatterns) as is obvious from scanning electron microscopy (SEM) images (Figure 9.1). The biosilica nanopatterns are species-specific characteristics and are precisely reproduced during each cell division cycle, documenting a genetic control of this biomineralization process. Therefore, biogenesis of the diatom cell wall has been regarded as a paradigm for controlled production of nanostructured silica [4]. In the past, investigations on diatom cell wall biogenesis were mainly based on ultrastructural (electron microscopy) and physiological (silicic acid uptake studies) experiments. These investigations provided the first insights into the basic cell biological processes involved in biosilica formation [5] and revealed that silicic acid is actively taken up from the environment by specific transporter proteins located in the plasmamembrane [6]. However, the mechanism that controls the formation of the species-specific biosilica nanopatterns has remained enigmatic.

It has for a long time been speculated that the organic components of diatom biosilica are involved in silica deposition and nanopatterning [7–9]. However, further analysis of this process was hampered by the lack of both structural data of these organic molecules and a defined *in vitro* system to study their effect on silica formation. Only recently have proteins and other organic molecules from diatom biosilica been purified to homogeneity and extensively characterized regarding their chemical structures and silica formation properties. These data are summarized in the present review and discussed with respect to the role that these organic molecules may exert in biosilica morphogenesis.

Biomineralization: From Biology to Biotechnology and Medical Application, Second Edition. Edited by E. Bäuerlein

ISBN: 3-527-31065-7

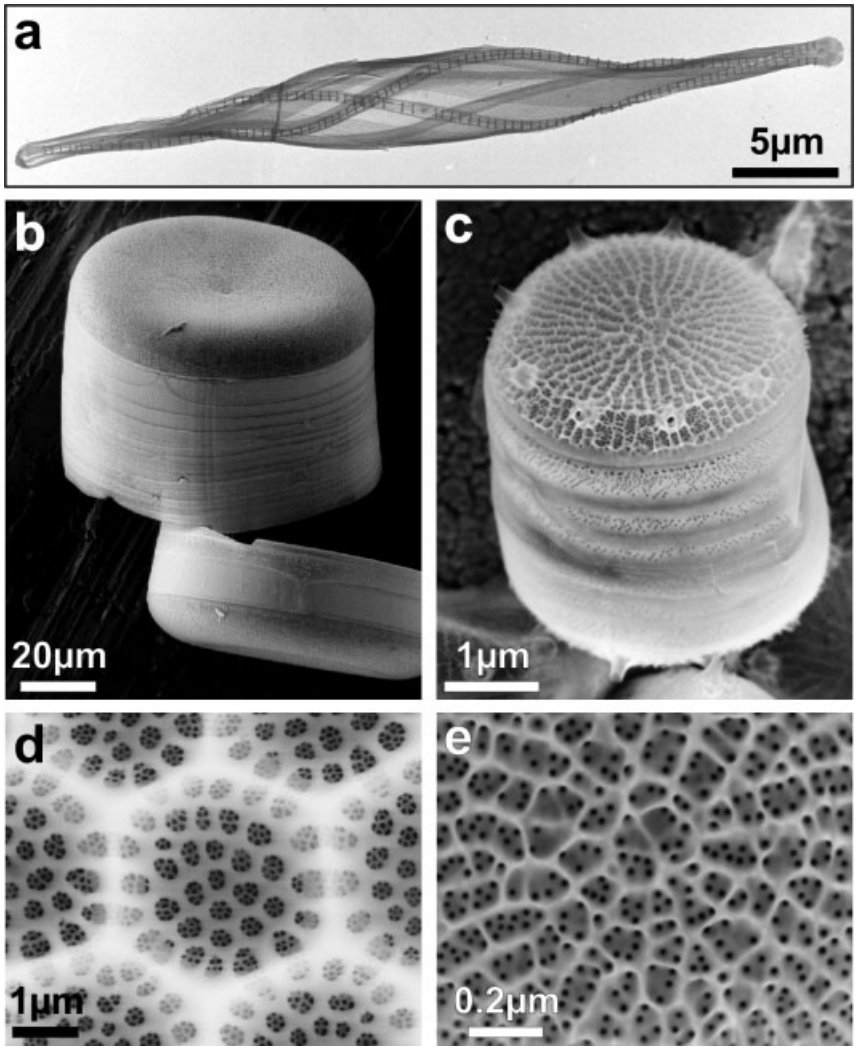

Figure 9.1 Structures of diatom cell walls. Electron microscopy images of isolated cell walls from different diatom species. (a) *Cylindrotheca fusiformis*, (b and d) *Coscinodiscus asteromphalus* and (c and e) *Thalassiosira pseudonana*.

9.2 The Diatom Cell Wall

The protoplast of a diatom cell is tightly enclosed by a cell wall (also termed frustule) that is constructed in a Petri dish-like fashion (Figure 9.2a). It contains a top

half (epitheca) that overlaps the slightly smaller bottom half (hypotheca). In most diatom species the structures of the hypotheca and epitheca are identical. Each theca is made up of a valve and several girdle bands that span the circumference of the cell. Both these theca elements are siliceous; however, it is the valve that displays the most elaborate morphological features, whereas the girdle bands are merely uniformly perforated. With respect to the symmetry of their frustules, diatoms are divided into two groups – the centrics and the pennates. Most pennates are bipolar symmetrical with the longitudinal axis running parallel to the plane of symmetry (Figure 9.1a). In contrast, the frustules of centric diatoms are usually radially symmetrical about an axis that passes through the center of the cell (Figure 9.1b and c). Some centric species, however, exhibit lower symmetries displaying triradiate or multiradiate morphologies. With respect to diatom evolution, centric cell walls are regarded to be more ancient since they appear first in the fossil record (about 200 million years ago). Therefore, it is hypothesized that the pennate morphology has evolved from a centric ancestor [10].

9.3 Diatom Cell Wall Biogenesis

The cellular events leading to the formation of a diatom cell wall have been extensively investigated by electron microscopic techniques. These studies lead to the important discovery that diatoms use a specialized intracellular compartment for biosilica production, termed the silica deposition vesicle (SDV). Studies on other silicifying protists have shown that the SDV is in fact not a specialty of diatoms, but rather represents a general organelle for silica biogenesis [11]. After completion of biosilica formation, the content of the SDV is transferred to the extracellular space by exocytosis (Figure 9.2b).

9.3.1 The SDV

Electron microscopic studies have clearly shown that the SDV represents a membrane-bound ''cellular reaction vessel'' that mediates biosilica morphogenesis. Therefore, a detailed analysis of the SDV components would be the most straightforward approach to study the biochemistry of biosilica nanopattern formation. Unfortunately, no method is available that allows isolation of the SDV and thus this approach has been so far impossible. The scarce information about the molecular properties of the SDV has been derived from indirect methods. In electron microscopic images of thin sections from diatom cells, the SDV membrane (silicalemma) appears as a typical lipid bilayer of 5–7 nm thickness. Results from fluorescence and electron microscopy show that Rhodamine 123 and DAMP [3-(2,4-dinitroanilino)-3′-amino-*N*-methyl-propyl-amine] accumulate within the SDV, indicating that an electrochemical potential exists across the silicalemma and that the SDV lumen exhibits an acidic pH [12, 13]. With respect to these properties,

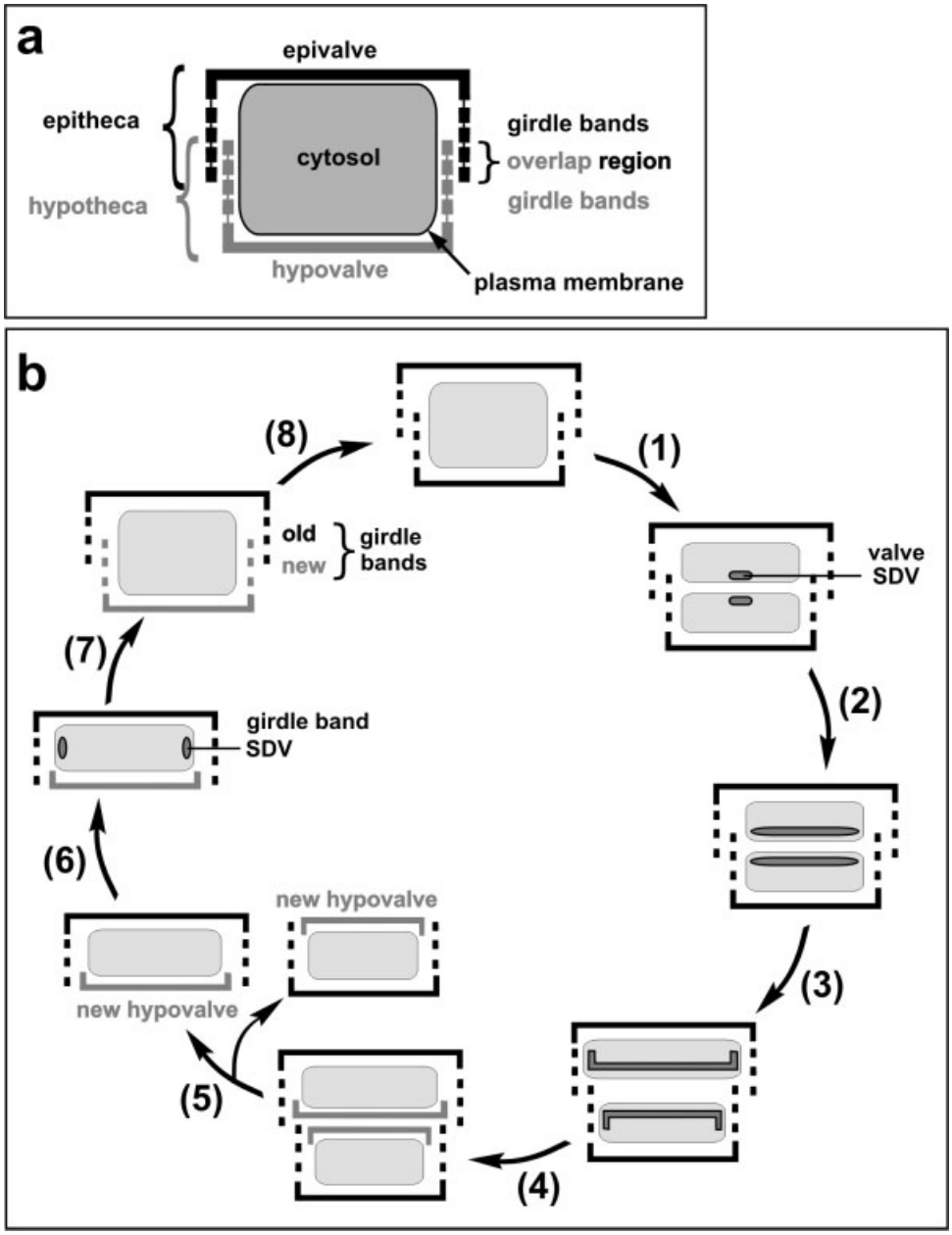

Figure 9.2 Construction and biogenesis of the diatom cell wall. Diatom cells are shown in cross-section (schematic). (a) Diatom cell wall structure. The cell wall is made up of two half shells, named the epitheca and hypotheca, which together fully enclose the protoplast. Each theca consists of a valve and one or more girdle bands that run laterally along the outline of the cell. The terminal

the SDV resembles the vacuoles and lysosomes of plant and animal cells. These compartments are connected to the Golgi apparatus of the cell by transport vesicles that deliver membrane and protein material. Likewise, it has been suggested that formation and expansion of the SDV is accomplished by the fusion of Golgi-derived vesicles. There are reports claiming the close association of small vesicles (16–100 nm) with the rim of the growing SDV [14], yet the origin of these vesicles is unclear. Therefore, SDV biogenesis and its relation to other endomembrane compartments is still under debate [5].

9.3.2 Silicic Acid Accumulation

Chemical analysis of diatom cell walls has shown that the inorganic component of biosilica represents almost pure hydrated silicon dioxide (silica) doped with small amounts of aluminum and iron [15]. The immediate precursor for biosilica formation inside the SDV is unknown, yet it is clear that monosilicic acid $Si(OH)_4$ represents the original source for silica formation. In natural water habitats monosilicic acid is available in concentrations between 1 and 100 μM [16]. It has been demonstrated that silicic acid uptake by diatoms requires active transport across the plasmamembrane and is mediated by Na^+-dependent transporter proteins [17]. Recently, a gene family encoding five transmembrane proteins (SIT1–SIT5) has been characterized from the diatom *Cylindrotheca fusiformis*. When heterologously expressed in *Xenopus* oocytes SIT1 was shown to mediate Na^+-dependent silicic acid uptake, indicating that the SIT proteins are responsible for monosilicic acid uptake into the diatom cell [18, 19; see Chapter 10 in this volume].

Diatom cell wall formation requires a large quantity of silicic acid to be transported and accumulated. For the diatoms *Thalassiosira weissflogii* and *Ethmodiscus* Castr., it has been calculated that the intracellular silicic acid concentration has to rise to concentrations between 10 and 100 mM during the diatom cell cycle to account for the production of the cell wall silica [20, 21]. At such a high concentration silicic acid is no longer stable under cellular pH conditions and would undergo spontaneous polycondensation (see Section 9.3.4). Therefore, the precise control of biosilica formation in diatoms requires the management of silicic acid uptake, intracellular storage and delivery to the SDV. It has been postulated that diatoms might have developed stable silicon complexes as intracellular storage and transport forms for silicic acid [22]. However, the chemical nature of these hypothetical silicic acid derivatives is unknown.

Figure 9.2 (*continued*)
girdle bands of each theca constitute the overlap region of the cell wall in which the slightly larger epitheca overlaps the hypotheca. (b) Diatom cell cycle. (1) Cytokinesis and formation of a valve SDV in each daughter protoplast. (2 and 3) Expansion of the SDV and formation of a new hypovalve within each SDV. (4) Exocytosis of SDV contents. (5) Separation of daughter cells. (6) Formation of the first girdle band SDV. (7) Consecutive formation and secretion of girdle bands. (8) DNA reduplication.

9.3.3 Silica Deposition

Regardless of the molecular nature of intracellular transport form of silicic acid, it is conceivable that monosilicic acid is liberated from the transport form once it has reached the SDV interior. Morse et al. [23, 24] have characterized a family of proteins (termed silicateins) from sponge biosilica that catalyze the hydrolysis of synthetic monosilicic acid esters. Silicatein-like proteins may also be present inside the diatom SDV, releasing monosilicic acid from putative transport complexes. If this scenario applies, silica deposition inside the SDV may simply be initiated by establishing a supersaturated concentration of silicic acid, which spontaneously undergoes auto-polycondensation eventually leading to silica deposition (see Section 9.3.4). Morphogenesis of diatom biosilica nanopatterns may then be achieved by either (1) a nanopatterned organic matrix within the SDV that determines the sites of silica deposition or (2) diffusion-limited deposition of silica particles. Both possibilities have been discussed in the literature. The theory of an organic matrix inside the SDV postulates that the diatom SDV contains organic macromolecules (proteins and polysaccharides) that spontaneously assemble into a regular pattern, serving as a template onto which silica is precipitated [25, 26]. According to this model, the diatom cell wall pattern would reflect the spatial arrangement of this putative matrix. In contrast, Gordon and Drum have developed an alternative theory [27]. These authors postulate that pattern formation is achieved by instabilities during diffusion-limited silica precipitation inside the SDV. Their scenario relinquishes the need for templating by an organic matrix. Using computer simulations, Gordon and Drum were able to demonstrate the formation of basic patterns of diatom cell walls simply by the diffusion-limited, irreversible adsorption of colloidal silica particles onto a nucleating center within the SDV. However, the authors also admit that there is the need for the presence of non-siliceous components controlling the kinetic parameters of biosilica formation to explain the creation of species-specific patterns and to account for the high rate of silica precipitation that is about 10^6 times faster compared to abiotic conditions.

9.3.4 Silica Chemistry

The inorganic chemistry of silicic acid polycondensation certainly represents an important parameter in diatom biosilica formation and is briefly summarized here [28].

An aqueous solution of monosilicic acid $Si(OH)_4$ is stable within the range of pH 2–9 as long as its concentration remains below 1 mM. At higher concentrations monosilicic acid spontaneously polymerizes by condensation to form dimers, trimers and higher molecular weight species of silicic acid (Figure 9.3a). The different oligosilicic acid species have a strong tendency to further polymerize in a way that a maximum of siloxane bonds (Si–O–Si) is produced with a minimum of uncondensed silanol groups (Si–OH) remaining. Therefore, highly branched polysilicic acid species predominate after the initial reaction phase. When monosilicic acid is used up, the polysilicic acids develop into larger spherical particles by Ostwald

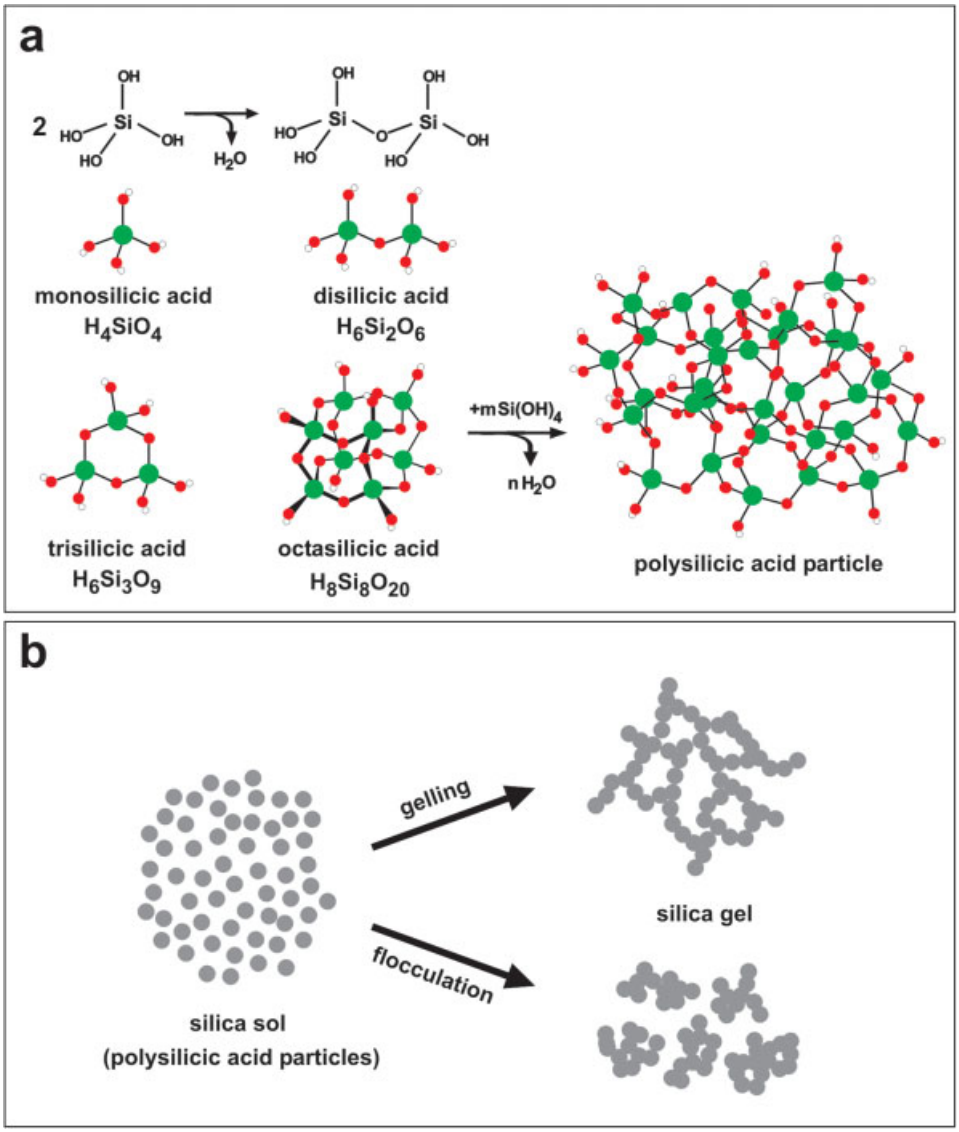

Figure 9.3 Silicic acid condensation and silica formation. (a) Condensation of monosilicic acid molecules yields disilicic acid, cyclic oligomers and subsequently highly condensed, spherical polysilicic acid particles. The Si–OH group is termed the silanol group. The Si–O–Si group is termed the siloxane group. (b) Formation of hard silica from a silica sol. Each sphere represents a polysilicic acid particle.

ripening. In this process, larger particles grow at the expense of smaller particles, because the latter have a higher solubility. The final particle size depends on the temperature and pH of the solution, and at ambient temperature ranges from 1 to 10 nm in diameter. These nanoscale polysilicic acid particles contain between 50 Si units in a 1-nm particle (molecular mass 3000 Da) and 50 000 Si units in a 10-nm particle (molecular mass 3.2×10^6 Da). Although such a polysilicic acid solution has a homogenous appearance, it is a colloidal system (termed silica sol) composed of a water phase and polysilicic acid particles. It depends on the pH of the solution and the presence of additional components, if the silica sol can form hard silica. Above pH 7 the silanol groups ($pK_s = 6.7$) of the polysilicic acid particles are considerably dissociated and repel each other due to their negative surface charges. Therefore, alkaline silica sols form stable solutions from which silica does not precipitate. In contrast, below pH 6, the polysilicic acid particles are almost uncharged and thus can collide with each other forming branched particle chains that are cross-linked by siloxane bonds. As a consequence, the molecular masses of the polysilicic acids increases, the sol becomes more and more viscous, and ultimately hardens as a transparent gel (gelling). This process is rather slow and may take several hours or even days. In contrast, when polycationic polymers (e.g. polyethyleneimine) are added to silica sols a silica precipitate rather than a silica gel is formed (flocculation) (Figure 9.3b). Flocculation occurs because polycationic polymers interconnect the sol particles by simultaneous interaction with the negative surface charges on adjacent particles. This creates localized, narrow-meshed networks of silica particles which are very different from the wide-meshed network that develops during gelling. Thus, flocculation leads to the formation of a hard, silica-enriched phase that rapidly (seconds to several minutes) precipitates from the less-dense, silica-depleted solution.

Apparently, diatom biosilica formation corresponds to silica flocculation rather than gelling, because numerous observations have been made in different diatom species that silica is initially laid down as tightly associated spheres of 10–100 nm diameter [29–32]. There have also been reports of the presence of fibrillar silica strands within developing SDVs [14, 33]. Such fibrils might actually be composed of linear rows of partially fused silica spheres.

9.4 Diatom Biosilica-associated Organic Components

Early studies on the amino acid composition of isolated diatom cell walls have led to the suggestion that proteins associated with diatom biosilica are generally rich in hydroxy amino acid and glycine residues [8, 9]. Furthermore, Nakajima and Volcani have isolated three unusual amino acids from diatom biosilica representing 3,4-dihydroxyproline, ε-*N*,*N*,*N*-trimethyl-δ-hydroxylysine and its phosphorylated derivative [7]. Volcani postulated that proteins composed of hydroxy amino acids, glycine, and the modified lysine and proline residues may be involved in diatom bi-

osilica formation by constituting an organic matrix within the SDV [26]. However, Volcani's group did not succeed in isolating the corresponding protein molecules and thus functional studies could not be performed.

Recently, several cell wall proteins from the diatom *C. fusiformis* have been isolated that exhibit unusual features and were shown to constitute three novel protein families (frustulins, pleuralins and silaffins) [34–38]. In addition, extremely long-chain polyamines (LCPA) have been characterized that are specifically associated with diatom biosilica [39]. Further studies revealed that frustulins and pleuralins are not involved in silica formation, because they become associated with the biosilica only after its deposition on the cell surface [40, 41]. In contrast, silaffins and LCPA appear to be directly involved in silica biogenesis since they exert a drastic influence on silica formation *in vitro*. In the following we summarize current knowledge about the structures and properties of silaffins and LCPA, and discuss their possible roles in diatom biosilica morphogenesis.

9.4.1 Chemical Structures of Silaffins and LCPA

Silaffins and LCPA are tightly associated with diatom biosilica, and can only be solubilized by complete removal of the silica. When anhydrous HF is used for silica dissolution, three polypeptides become solubilized exhibiting apparent masses of 17 (silaffin-2), 8 (silaffin-1B) and 4 kDa (silaffin-1A). In addition, the HF extract contains a smaller than 3.5 kDa non-protein component representing LCPA (Figure 9.4a). N-terminal amino acid sequencing of silaffins revealed a high degree of sequence homology between silaffin-1A and silaffin-1B. In both sequences, modified amino acid derivatives are present at positions 3 and 4. Only scarce sequence information was obtained by N-terminal sequencing of silaffin-2 since most Edman degradation cycles yielded unknown amino acid derivatives (Figure 9.4a). Information derived from the N-terminal sequence of silaffin-1B enabled the cloning of the corresponding sil-1 gene. The sil-1-encoded polypeptide (sil-1p) displays a modular primary structure that is composed of unique as well as repetitive sequence elements (Figure 9.4b and c). The N-terminus represents a typical signal peptide sequence (amino acids 1–19) that is followed by a highly negatively charged domain (amino acids 20–107). Starting from amino acid 108, the C-terminal part of sil-1p is composed of seven strongly basic repeat units. The first two repeat units R1 (amino acids 108–140) and R2 (amino acids 141–162) contain 33 and 22 amino acids, respectively. The remaining five repeat units (R3–R7) are slightly shorter, each being composed of 19 amino acid residues. The characteristic feature of each repeat unit is the presence of clusters of lysine and arginine residues that are connected by stretches containing hydroxy amino acids (serine, tyrosine) and glycine. Comparison of the sil-1p sequence with the peptide sequences of silaffins revealed the following key information about their chemical structures:

(1) The C-terminal part of sil-1p (repeat units R1–R7) becomes extensively proteolytically processed *in vivo* releasing each repeat unit as an individual peptide.

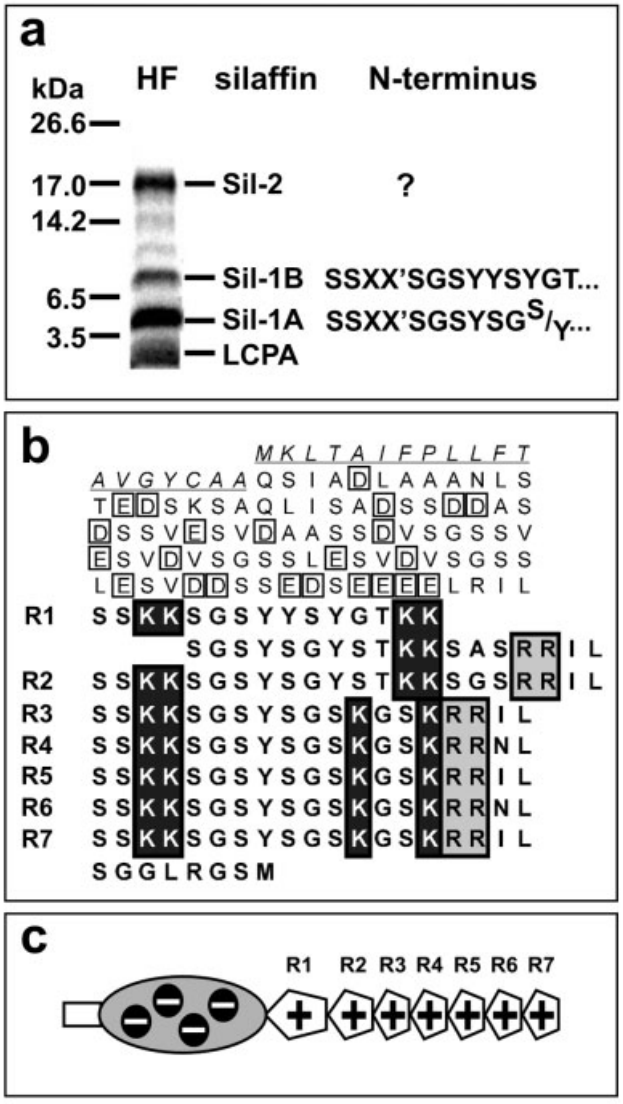

Figure 9.4 Silaffins. (a) Tricine/SDS–PAGE of the HF extract from *C. fusiformis* cell walls (HF). The positions, identity of silaffins and their corresponding N-terminal sequences are indicated on the right side of the lane, X and X′ represent modified lysines. (b) Amino acid sequence of sil-1p. The signal peptide is shown in italics and underlined. The N-terminal acidic domain is shown in normal letters. Aspartate and glutamate residues are boxed. The silaffin-generating C-terminal domain is shown in bold letters. Lysine and arginine residues are highlighted. R1–R7 indicate the repeating sequence elements within the C-terminal domain. (c) Schematic primary structure of sil-1p. The white box represents the signal peptide. The grey oval represents the negatively charged N-terminal domain. The silaffin-bearing part of sil-1p is shown as a row of pentagons. Each pentagon (R1–R7) corresponds to a sequence repeat as indicated in (b).

Silaffin-1B is derived from repeat unit R1, whereas silaffin-1A represents a mixture of the peptides derived from repeat units R2–R7. During proteolytic processing, the four C-terminal amino acid residues of each repeat unit are cleaved off generating identical 15 mer peptide sequences from R3 to R7. Thus, silaffin-1A represents a mixture of two peptide sequences, which were termed silaffin-$1A_1$ and silaffin-$1A_2$.

(2) All lysine residues in silaffin-$1A_1$, -$1A_2$ and -1B are modified.
(3) The "fate" of the acidic N-terminal half of sil-1p is unknown. Apparently, this peptide does not become incorporated into the cell wall.
(4) Silaffin-2 is not encoded by the sil-1 gene.

Silaffins have an extremely high content of hydroxy amino acids, which in many extracellular proteins are targets for post-translational modifications (e.g. carbohydrate and phosphate residues). Anhydrous HF, which was used for solubilization of silaffins, is known to cleave *O*-glycosidic and phosphate ester bonds, and thus silaffins may have become deglycosylated and dephosphorylated during HF extraction. To investigate this, silaffin extraction was performed by a gentler method using a slightly acidic, aqueous ammonium fluoride solution. When analyzed by sodium dodecylsulfate–polyacrylamide gel electrophoresis (SDS–PAGE), the apparent molecular masses of the ammonium fluoride-extracted silaffins are substantially larger compared to HF-extracted silaffins, indicating the presence of additional HF-labile modifications (Figure 9.5a). Since the gentle ammonium fluoride extraction method is likely to preserve the *in vivo* structure of silaffins, the ammonium fluoride-extracted silaffins were termed native silaffins (abbreviated natSil-1A,

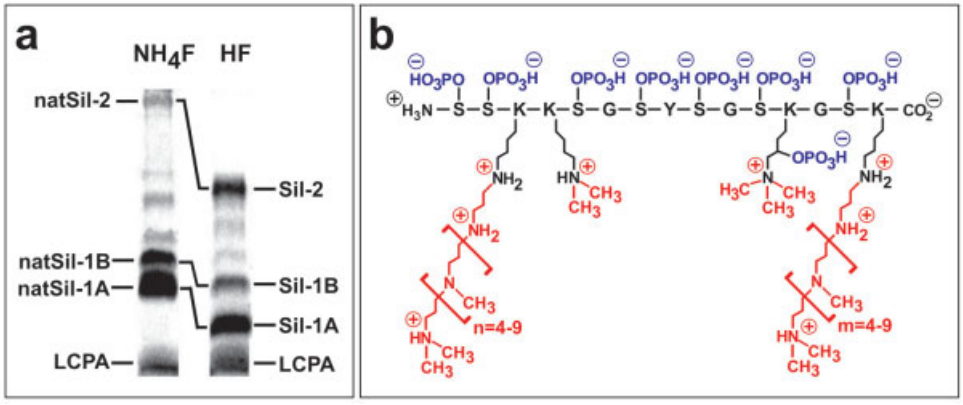

Figure 9.5 Native silaffins. (a) Comparison by Tricine/SDS–PAGE of ammonium fluoride extract (NH_4F) and HF extract (HF) from *C. fusiformis* cell walls. (b) Schematic chemical structure of natSil-$1A_1$. Post-translational modifications are depicted in color. The annotation of charges within the molecule is tentative for a solution around pH 5. Most likely, not all amino groups are protonated, because the basicity of amino groups is reduced due to mutual repulsion of the positive charges within the polyamine chain [45].

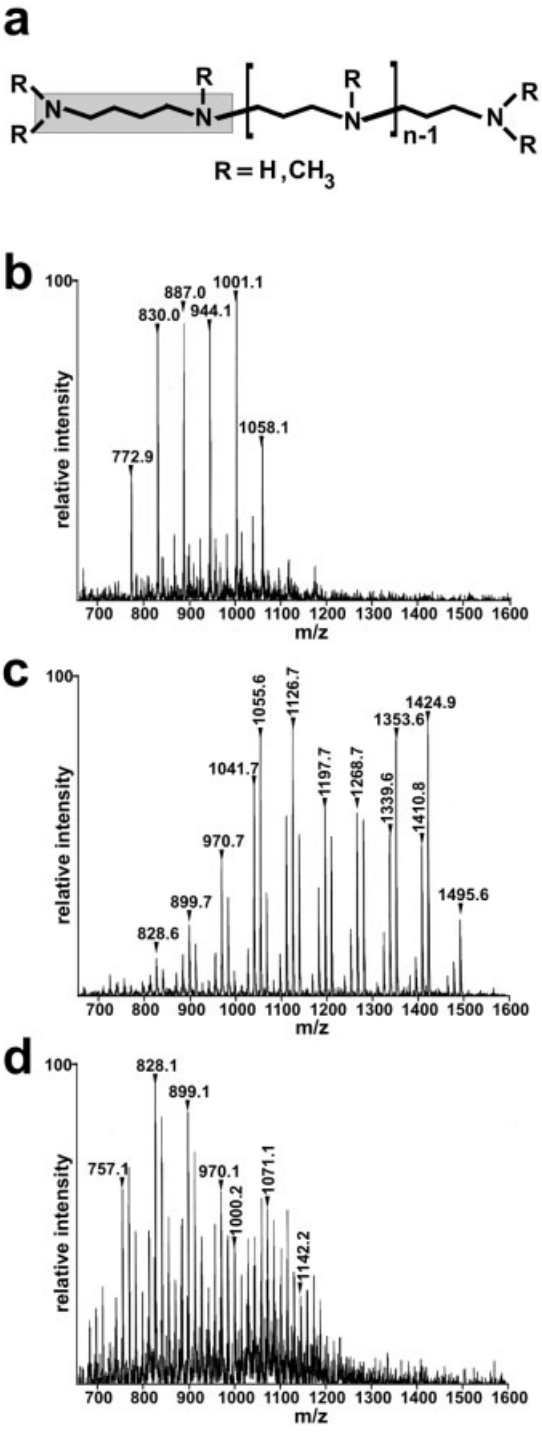

Figure 9.6 LCPA. (a) General, schematic chemical structure of LCPA. The gray box highlights the putrescine moiety. (b–d) Electrospray ionization tandem mass spectrometry (ESI-MS) analysis of purified LCPA from *C. fusifomis*, (b) *Chaetoceros didymum* (c) and *Nitzschia angularis* (d). Each peak represents a singly charged positive ion. Selected peaks are marked by their m/z values.

natSil-1B and natSil-2). Extensive biochemical analysis by peptide mapping, mass spectrometry and nuclear magnetic resonance (NMR) revealed the complete chemical structure of natSil-$1A_1$ (Figure 9.5b), which is representative of the structures of all sil-1p derived silaffins. Native silaffins carry an extremely high number of post-translational modifications with each lysine residue being *N*-alkylated and almost every hydroxy group carrying a phosphate residue. NatSil-$1A_1$ contains three different lysine residues representing ε-*N*,*N*-dimethyllysine (DML, position 4), phosphorylated ε-*N*,*N*,*N*-trimethylhydroxylysine (phospho-THL, position 13) and polyamine-modified lysines (positions 3 and 15). The latter modification is composed of a chain of six to 11 linearly linked propyleneimine units, in which each N atom except the one from the first unit is methylated. DML has been found in several other proteins (e.g. histones) and phospho-THL was previously isolated from diatom cell walls [7], yet natSil-$1A_1$ is the first peptide shown to contain a phospho-THL residue. Furthermore, the polyamine-modified lysines represent a novel type of amino acid modification that introduces a high number of both positive charges (protonated amino groups) and hydrophobic groups (propylene residues), and thus is likely to strongly influence the properties of silaffins (see Section 9.4.2).

Due of the lack of sequence information from natSil-2, it has not yet been possible to clone the corresponding gene. Therefore, only limited information about the chemical structure of natSil-2 has been so far obtained [38]. NatSil-2 is a phosphoprotein of 40 kDa apparent molecular mass exhibiting a highly complex molecular architecture, because it is also glycosylated and sulfated. The lysine modifications identified are DML, ε-*N*,*N*,*N*-trimethyllysine, THL and polyamine-modified lysines. The amino acid composition is again dominated by hydroxy amino acids (serine, threonine, hydroxyproline) and glycine, but the presence of significant amounts of methionine and leucine is a distinct feature of natSil-2. The polypeptide backbone is strongly basic due to the presence of the alkylated lysines, yet the polycationic charge is vastly overcompensated by the attachment of numerous phosphate, sulfate and glucuronic acid residues conferring a net polyanionic character on natSil-2. The phosphorylated amino acids identified are phosphoserine, phosphothreonine and, interestingly, phosphohydroxyproline, which has not yet been identified in any other biogenic protein.

LCPA exhibit identical apparent molecular masses when extracted by anhydrous HF and aqueous ammonium fluoride, respectively (Figure 9.5a), indicating that they carry no HF-sensitive modifications. Analysis by chemical derivatization and mass spectrometry revealed that LCPA consist of linear chains of N–C-linked propyleneimine units and thus are constructed in the same way as the polyamine-modified lysines from silaffins. However, in LCPA, the polyamine chain is attached to putrescine or a putrescine derivative rather than a polypeptide backbone (Figure 9.6a). LCPA are the longest polyamine chains found in nature, and each diatom is equipped with a species-specific set of LCPA exhibiting variations in chain length and methylation pattern (Figure 9.6b–d). In most diatom species, LCPA seem to be at least as abundant as silaffins and in diatoms of the genus *Coscinodiscus*, which completely lack silaffins, LCPA appear to be the main organic component associated with biosilica [42].

9.4.2 Silica Formation Activity of natSil-1A

The unique chemical structures of silaffins and their strong association with silica prompted the speculation that they may be involved in biosilica formation. Indeed, when natSil-1A is added to a slightly acidic silicic acid solution (pH 5.5), silica is rapidly precipitated within only a few minutes [43], whereas in the absence of silaffins the solution slowly hardens as a silical gel (see Section 9.3.4). Thus, natSil-1A greatly accelerates the polycondensation of silicic acid and acts as a flocculating agent. The following data demonstrate that the silica formation activity of natSil-1A is critically dependent on its post-translational modifications:

(1) Dephosphorylated natSil-1A (silaffin-1A) is unable to induce silica formation *in vitro* unless a sufficient concentration of inorganic phosphate is included in the assay (Figure 9.7a).
(2) In the presence of inorganic phosphate, silaffin-1A exhibits silica formation activity over a wide pH range down to pH 4.2. In contrast, the synthetic silaffin peptide pR5, which does not carry any amino acid modifications, exhibits silica formation activity only in the alkaline pH range (Figure 9.7b). Since the SDV of diatoms is an acidic compartment [13], it can be concluded that the lysine modifications of silaffins are essential for silica formation activity under physiological conditions.

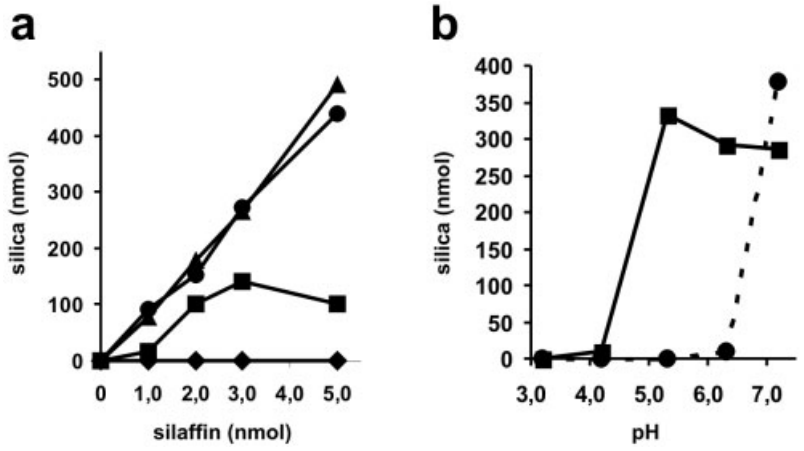

Figure 9.7 Silica precipitation activity of silaffins. The correlations between the amount of silaffin/peptide added to a buffered monosilicic acid solution and the amount of precipitated silica is shown. (a) Silica precipitation from a 100 mM silicic acid solution buffered by 50 mM sodium acetate, pH 5.5. Lines indicate silica precipitation using natSil-1A (circles), silaffin-1A (diamonds), silaffin-1A in the presence of 30 mM phosphate (triangles) and silaffin-1A in the presence of 3 mM phosphate (squares). (b) pH dependence of peptide-induced silica precipitation from a 100 mM silicic acid solution buffered by 100 mM sodium phosphate-citrate. The solid line shows the result for silaffin-1A, the dotted line represents the result for synthetic peptide pR5 (sequence: SSKKSGSYSGSKGSKRRIL). At each pH value the amount of peptide applied was 2.8 nmol.

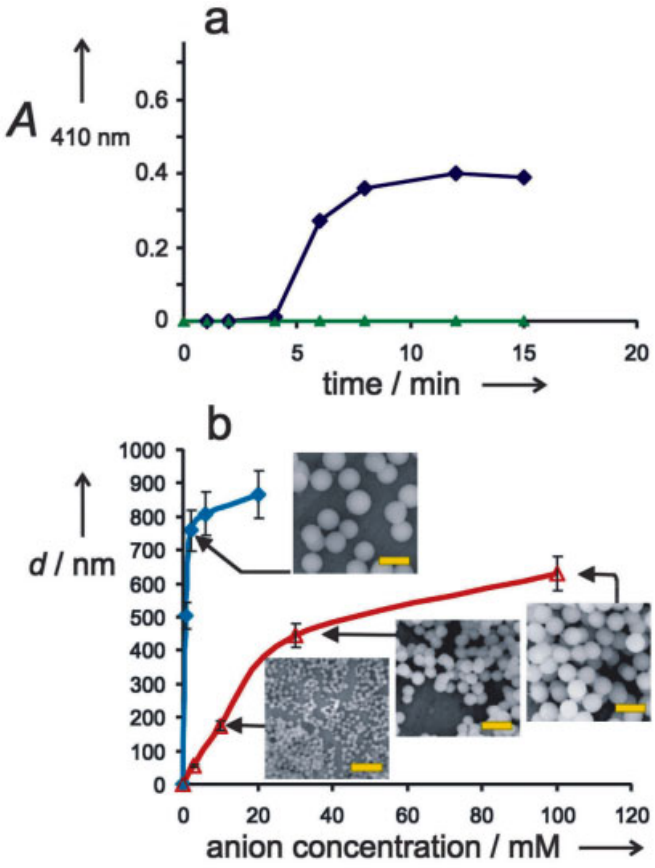

Figure 9.8 Characteristics of silica fabrication catalyzed by the polyamine/phosphate system. (a) Kinetics of silica precipitation. The incubation mixture contained 30 mM sodium phosphate pH 5.5, 0.2 mM polyamine and 40 mM mono/disilicic acid. The temperature was 25 °C. After the times indicated, aliquots (50 µl) were removed and centrifuged. Precipitated silica was dissolved in 2 M NaOH (5 min at 90 °C) and quantified by the molybdate method. An absorbance of 1.0 corresponded to 0.5 µmol SiO_2. Blue line, all components were mixed at $t = 0$ min. Green line, phosphate was replaced by 30 mM sodium acetate, pH 5.5. (b) Silica nanosphere diameters as a function of the multivalent anion concentration. Silica fabrication was performed in a 30 mM sodium acetate buffer, pH 5.5 as in (a) with increasing concentrations of multivalent anions. The reaction was allowed to proceed for 12 min. The resulting nanospheres were collected by centrifugation and analyzed by SEM. Response to orthophosphate and pyrophosphate is shown by the red and the blue line, respectively. Insets, SEM micrographs of the corresponding precipitates. Scale bars = 1 µm.

Insight into the mechanism of natSil-1A-mediated silica formation was gained by ^{31}P-NMR spectroscopy, which demonstrated that natSil-1A is not monomeric in solution, but forms supramolecular assemblies containing about 700 peptide molecules. The self-assembly is mediated by intermolecular interactions between the numerous positively and negatively charged groups of the zwitterionic natSil-1A

molecules [43]. Presumably, natSil-1A self-assembly is a prerequisite for silica formation, because such assemblies may provide a template for silicic acid polycondensation. This would explain the inability of silaffin-1A to promote silica precipitation in the absence of phosphate, because silaffin-1A molecules are highly positively charged and therefore would repel each other rather than forming supramolecular assemblies. The addition of phosphate anions restores the silica precipitation activity of silaffin-1A, presumably because phosphate anions serve as ionic cross-linkers promoting the aggregation of the polycationic silaffin-1A molecules.

Information regarding the function of the polyamine moieties of natSil-1A was obtained by the discovery that LCPA also exhibit silica formation activity in the presence of inorganic phosphate or other polyvalent anions (see Section 9.4.3). The kinetics and pH dependence of LCPA-induced silica formation are similar to the properties of natSil-1A, thus indicating that the interaction of natSil-1A with silicic acid molecules is mediated via the polyamine moieties. The mechanism of polyamine-mediated silica formation was further studied by investigating the aggregation behavior and silica formation properties of LCPA.

9.4.3 Silica Formation by LCPA

Recently, the function of phosphate anions in the polyamine-directed formation of silica nanospheres using the polyamines extracted from the cell wall of the diatom *Stephanopyxis turris* was studied [44]. These polyamines consist of 15–21 *N*-methylpropyleneimine repeated units attached to putrescine. The polyamines were able to precipitate silica nanospheres from a silicic acid solution after a few minutes even under acidic conditions (around pH 5). After a short lag phase, silica started to precipitate (Figure 9.8a, see p. 151, blue line). However, this precipitation was strictly dependent on the presence of phosphate. In the presence of acetate anions only (the buffer system), no precipitate at all was formed (Figure 9.8a, green line). Silica precipitation in the presence of increasing phosphate concentrations produced nanospheres with increasing diameters (Figure 9.8b, red line). It is the particle size of the silica nanospheres that is strictly controlled by the concentration of phosphate anions. Defined particle diameters between 30 and 700 nm could be obtained, and the resulting size distributions were close to monodisperse. Replacement of orthophosphate by pyrophosphate, an anion with a higher negative charge, exhibited a drastic effect. Control of nanosphere size distribution was exerted at anion concentrations nearly two orders of magnitude lower and the maximum sphere diameter was increased to about 1000 nm (Figure 9.8b, blue line). It is important to note that other multivalent anions (e.g. citrate and sulfate) are capable of producing silica precipitates as well, whereas monovalent anions such as chloride or acetate fail to do so.

Long-chain polyamines behave like amphiphilic substances, because they are extractable from an aqueous solution by chloroform:methanol (3:2, v/v). Possibly, these polyamines form aggregates in aqueous solution (microemulsions) with positively charged surfaces. If so, increasing concentrations of multivalent anions should promote higher order assemblies of the emulsion droplets. This assumption has been confirmed by NMR and dynamic light-scattering techniques. Microscopic

phase separation is necessary for the LCPA-induced silica precipitation from silicic acid-containing aqueous solutions. Silicic acid molecules may be adsorbed on and/or dissolved in the polyamine microdroplets, thereby forming a coacervate (formation of a "liquid precipitate") that hardens by silica formation. This mechanism is able to explain the observed correlation between phosphate anion concentration and the size of the silica nanospheres.

9.5 Model for LCPA-mediated Morphogenesis of Biosilica Nanopatterns

Diatoms of the genus *Coscinodiscus* exhibit extraordinarily intricate silica patterns including fine structures in the range 30–50 nm (Figure 9.1d). The valve structure can be interpreted as being composed of a hierarchy of self-similar hexagonal silica structures producing the complex, but highly symmetric, valve patterning. Surprisingly, HF extracts from these diatoms exhibit only LCPA and, in particular, lack silaffins. These observations stimulated a model of pattern formation that is exclusively based on the physicochemical properties of LCPA.

Based on the assumption that the LCPA phase separates within the SDV to form emulsions of microdroplets, it is possible to explain the observed stages of cell wall biogenesis in *Coscinodiscus* [42]. In a close-packed arrangement the microdroplets would form a hexagonal monolayer within the flat SDV. The contact sites between polyamine droplets and the aqueous phase that contains the hydrophilic silicic acid promote silicic acid polymerization (Figure 9.9a), and the precipitating silica necessarily creates a honeycomb-like framework. Silica formation consumes a defined fraction of the polyamine population by co-precipitation [37, 39]. This fact is assumed to cause a dispersion of the original organic droplets segregating smaller droplets (Figure 9.9b). Guided by the newly created water/polyamine interfaces, silicic acid continues to polymerize and precipitate, thereby consuming another fraction of the polyamine population. This, in turn, causes the remaining part of the original organic droplet to break up into a maximum number of smaller droplets, again creating new interfaces for silica deposition (Figure 9.9c). Iteration of this simple mechanism would create the nanopattern observed in *Coscinodiscus* valves.

Incorporating more recent experimental results into this model, the original size of phase-separated LCPA microdroplets might be controlled by a defined binary system polyamine/multivalent anion. In summary, LCPA (as well as silaffins) together with a polyanionic partner are assumed to undergo a phase separation process in the SDV that creates a pattern of areas promoting (or inhibiting) silica formation.

A number of diatom genera exhibit less symmetric biosilica nanopatterns (Figure 9.1e), which demands additional components that break up the inherently hexagonal arrangement of the proposed LCPA microdroplets. Presumably, this is achieved by the formation of an organic matrix composed of LCPA (or natSil-1A) and polyanionic silaffins (see below).

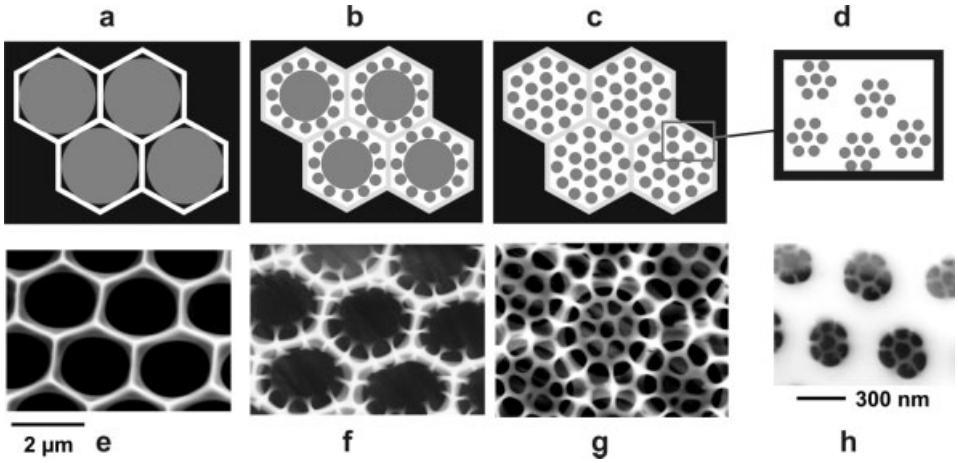

Figure 9.9 Schematic drawing of the templating mechanism by the phase separation model (a–d) and comparison with different stages of the cell wall biogenesis of *C. wailesii* (e–h). (a) The monolayer of polyamine-containing droplets in close-packed arrangement within the silica deposition vesicle guides silica deposition. (b and c) Consecutive segregations of smaller (about 300 nm) droplets open new routes for silica precipitation. (d) Dispersion of 300-nm droplets into 50-nm droplets guides the final stage of silica deposition. Silica precipitation only occurs within the water phase (white areas). The repeated phase separations produce a hierarchy of self-similar patterns. (e–h) SEM micrographs of valves *in statu nascendi* at the corresponding stages of development.

9.6 Silaffin-mediated Silica Morphogenesis

The influence of the supramolecular natSil-1A assemblies on silica morphogenesis *in vitro* was investigated in a time-resolved manner by SEM (Figure 9.10). The first silica structures were discernible 3.5 min after addition of silicic acid and appeared as extended flat networks of irregularly shaped, branched bands. Elemental analysis by energy-dispersive X-ray analysis demonstrated that these networks contain both silica and natSil-1A, and thus represent a silicified silaffin phase. This phase is not rigid, but rather flexible, since it becomes transformed into large spherical particles (diameter 400–700 nm) that again contain both silica and natSil-1A. These spheres, which are the end products of this amazing silica morphogenesis process, are certainly too large to be of biological relevance, since diatom biosilica is composed of particles that are only 10–100 nm in size [29–32]. However, the apparently plastic silaffin silica phase observed at the early stages of silica formation may represent the moldable biosilica material used to form the silica elements of *C. fusiformis*, which do not exhibit any patterning by nanosized pores.

Due to their very similar chemical structures, natSil-1B exhibits comparable silica formation properties as natSil-1A, generating large silica spheres when added to a silicic acid solution *in vitro*. Surprisingly, natSil-2 is incapable of forming silica

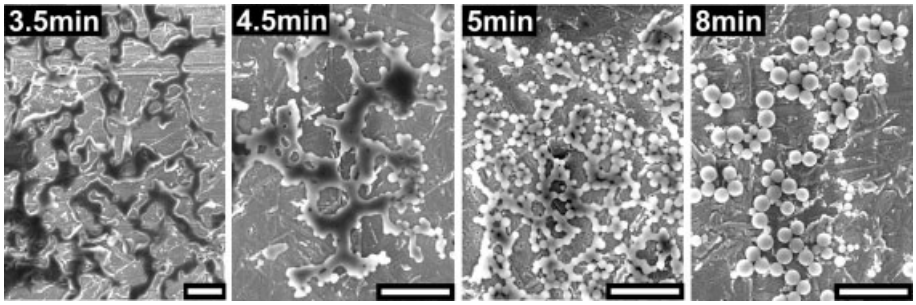

Figure 9.10 Analysis of natSil-1A-induced silica morphogenesis *in vitro*. SEM images of silica structures formed at indicated times after the addition of natSil-1A to a 100 mM monosilicic acid solution buffered at pH 5.5 (50 mM sodium acetate). Scale bars = 2 μm.

in vitro (Figure 9.11a, diamonds) although it contains the polyamine-modified lysines that confer silica formation activity to all natSil-1 derivatives (see Section 9.4.1). This apparent contradiction was resolved by the finding that the sulfate and carbohydrate groups in natSil-2 auto-inhibit the silica formation activities of the polyamine moieties [38]. Furthermore, natSil-2 acts as an inhibitor of natSil-1A-dependent silica formation (Figure 9.11a, circles) by interference with the self-

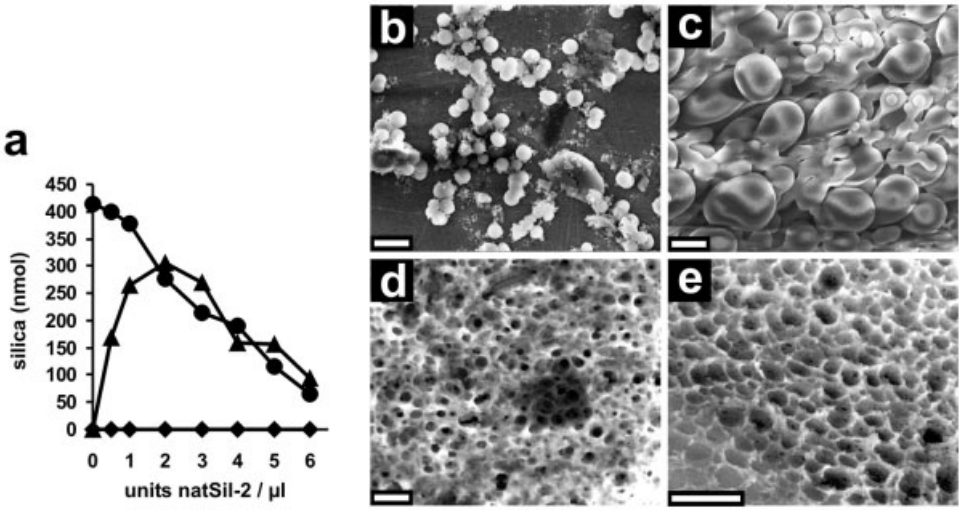

Figure 9.11 Influence of natSil-2 on silica formation. (a) Silica precipitation experiments were performed with pure natSil-2 (diamonds) and in the presence of 0.6 μg/μl LCPA (triangles) or 0.3 mM natSil-1A (circles), respectively (1 unit natSil-2 corresponds to 1 nmol protein-bound phosphate). (b–e) SEM analysis of silica precipitates formed by mixtures of natSil-1A and natSil-2: (b) 0.5 unit/μl natSil-2, 0.3 mM natSil-1A; (c) 5.0 unit/μl natSil-2, 0.3 mM natSil-1A; (d) 2.0 unit/μl natSil-2, 0.3 mM natSil-1A; (e) 1.6 unit/μl natSil-2, 0.2 mM natSil-1A.

assembly of natSil-1A molecules. However, natSil-2 does not exclusively act as an inhibitor of polyamine-dependent silica formation, because when combined with LCPA rapid silica precipitation occurs under conditions at which LCPA alone is unable to form silica (Figure 9.11a, triangles). Most probably, natSil-2 acts as a polyanion required for LCPA assembly. At higher concentrations, however, natSil-2 again exerts an inhibitory effect on LCPA-induced silica formation (Figure 9.11a, triangles). Due to these pleiotropic effects, natSil-2 may be regarded as a regulator of silica formation.

Although natSil-2 has no intrinsic silica formation ability, it is able to influence silica morphogenesis. This was demonstrated by SEM analysis of the silica precipitates formed by mixtures of natSil-2 and natSil-1A or LCPA, respectively. Figure 9.11(b–e) shows the silica structures that are produced at pH 5.5 by different natSil-1A/natSil-2 ratios, 10 min after the addition of silicic acid. At low and high natSil-2:natSil-1 concentration ratios, polydisperse silica spheres (diameter 100–1000 nm; Figure 9.11b) and large interconnected spherical or pear-shaped silica particles (Figure 9.11c), respectively, are obtained. At intermediate natSil-1A:natSil-2 ratios, the formation of silica particles becomes suppressed and porous silica blocks are formed (Figure 9.11d and e). Remarkably, the pore sizes are in the range of 100–1000 nm, which matches the characteristic size range of diatom biosilica nanopores. Similar structures can be generated using appropriate mixtures of LCPA and natSil-2. The fact that *C. fusiformis* biosilica lacks any nanopore patterning may thus be explained by the presence of extremes of natSil-1A (or LCPA):natSil-2 ratios within the SDV.

It has to be noted that natSil-2 molecules self-assemble into extremely large aggregates that are around 90 nm in diameter, but these are not dense enough to become pelleted by centrifugation. However, when natSil-2 and natSil-1A (or LCPA) are combined, a much denser, pelletable silaffin-phase (silaffin matrix) is created that can be readily separated from the aqueous phase by centrifugation [38]. It is likely that silicic acid becomes concentrated within the matrix by specific interaction with the long-chain polyamine moieties, thus increasing the rate of condensation reactions among the silicic acid molecules. Taken together, these results demonstrate that only two types of organic biomolecules are required to produce biologically relevant silica structures: polycationic molecules exhibiting silica forming activity (natSil-1A or LCPA) and polyanionic regulators.

Acknowledgments

We would like to thank our colleagues E. Brunner, R. Deutzmann and N. Poulsen for their contributions to the results presented in this review. This work was supported by the Deutsche Forschungsgemeinschaft (SFB521/A2) and the Fonds der Chemischen Industrie.

References

[1] V. Smetacek, *Nature* **1999**, *397*, 475–476.
[2] D. Werner, in *Biology of Diatoms, Botanical Monographs, Vol. 13* (Ed. D. Werner), Blackwell Scientific Publications, Oxford, **1977**, pp. 1–17.
[3] C. C. Perry, in *Biomineralization: Chemical and Biochemical Perspectives* (Eds S. Mann, J. Webb, R. J. P. Williams), VCH, Weinheim, **1989**, pp. 223–256.
[4] S. Mann, *Nature* **1993**, *365*, 499–505.
[5] J. Pickett-Heaps, A. M. M. Schmid, L. A. Edgar, in *Progress in Phycological Research, Vol. 7* (Eds F. E. Round, D. J. Chapman), Biopress, Bristol, **1990**, pp. 1–169.
[6] F. Azam, B. E. Volcani, in *Silicon and Siliceous Structures in Biological Systems* (Eds T. L. Simpson, B. E. Volcani), Springer, New York, **1981**, pp. 43–67.
[7] (a) T. Nakajima, B. E. Volcani, *Science* **1969**, *164*, 1400–1406; (b) T. Nakajima, B. E. Volcani, *Biochem. Biophys. Res. Commun.* **1970**, *39*, 28–33.
[8] R. Hecky, K. Mopper, P. Kilham, T. Degens, *Mar. Biol.* **1973**, *19*, 323–331.
[9] D. Swift, A. Wheeler, *J. Phycol.* **1992**, *28*, 202–209.
[10] W. H. C. F. Kooistra, M. De Stefano, D. G. Mann, L. K. Medlin, in *Progress in Molecular and Subcellular Biology, Vol. 33* (Ed. W. E. G. Müller), Springer, Berlin, **2003**, pp. 59–97.
[11] T. L. Simpson, B. E. Volcani, in *Silicon and Siliceous Structures in Biological Systems* (Eds T. L. Simpson, B. E. Volcani), Springer, New York, **1981**, pp. 3–12.
[12] C. W. Li, S. Chu, M. Lee, *Protoplasma* **1989**, *151*, 158–163.
[13] E. G. Vrieling, W. W. C. Gieskes, T. P. M. Beelen, *J. Phycol.* **1999**, *35*, 548–559.
[14] C. W. Li, B. E. Volcani, *Phil. Trans. R. Soc. Lond. B* **1984**, *304*, 519–528.
[15] J. C. Lewin, in *The Physiology and Biochemistry of Algae* (Ed. R. A. Lewin), Academic Press, New York, **1962**, pp. 445–455.
[16] P. Tréguer, D. M. Nelson, A. J. van Bennekom, D. J. DeMaster, A. Leynaert, B. Quéguiner, *Science* **1995**, *268*, 375–379.
[17] P. Bhattacharyya, B. E. Volcani, *Proc. Natl Acad. Sci. USA* **1980**, *77*, 6386–6390.
[18] M. Hildebrand, B. E. Volcani, W. Gassmann, J. I. Schroeder, *Nature* **1997**, *385*, 688–689.
[19] M. Hildebrand, K. Dahlin, B. E. Volcani, *Mol. Gen. Genet.* **1998**, *260*, 480–486.
[20] M. A. Brzezinski, D. J. Conley, *J. Phycol.* **1994**, *30*, 45–55.
[21] T. A. Villareal, L. Joseph, M. A. Brzezinski, R. F. Shipe, F. Lipschultz, M. A. Altabet, *J. Phycol.* **1999**, *35*, 896–902.
[22] C. W. Sullivan, in *Silicon Biochemistry (Ciba Foundation Symposium 121)*, Wiley, New York, **1986**, 59–89.
[23] K. Shimizu, J. Cha, G. Stucky, D. E. Morse, *Proc. Natl Acad. Sci. USA* **1998**, *95*, 6234–6238.
[24a] J. Cha, K. Shimizu, Y. Zhou, S. Christiansen, B. F. Chmelka, G. D. Stucky, D. E. Morse, *Proc. Natl Acad. Sci. USA* **1999**, *96*, 361–365.
[24b] K. Shimizu, D. E. Morse, in *Biomineralization: From Biology to Biotechnology and Medical Application* (Ed. E. Bauuerlein), Wiley-VCH, Weinheim, **2000**, pp. 207–220.
[25] D. H. Robinson, C. W. Sullivan, *Trends Biochem. Sci.* **1987**, *12*, 151–154.
[26] B. E. Volcani, in *Silicon and Siliceous Structures in Biological Systems* (Eds T. L. Simpson, B. E. Volcani), Springer, New York, **1981**, pp. 157–200.
[27] R. Gordon, R. W. Drum, *Int. Rev. Cytol.* **1994**, *150*, 243–372.
[28] R. Iler, in *The Chemistry of Silica*, Wiley, New York, **1979**, pp. 172–461.
[29] M. L. Chiappino, B. E. Volcani, *Protoplasma* **1977**, *93*, 205.
[30] A. M. M. Schmid, D. Schulz, *Protoplasma* **1979**, *100*, 267.
[31] S. A. Crawford, M. J. Higgins, P. Mulvaney, R. Wetherbee, *J. Phycol.* **2001**, *37*, 1.
[32] F. Noll, M. Sumper, N. Hampp, *Nano Lett.* **2002**, *2*, 91.
[33] J. Pickett-Heaps, D. Tippit, J. Andreozzi, *Biol. Cell.* **1979**, *35*, 199–206.
[34] N. Kröger, C. Bergsdorf, M. Sumper, *EMBO J.* **1994**, *13*, 4676–4683.
[35] N. Kröger, C. Bergsdorf, M. Sumper, *Eur. J. Biochem.* **1996**, *239*, 259–264.

[36] N. Kröger, G. Lehmann, R. Rachel, M. Sumper, *Eur. J. Biochem.* **1997**, *250*, 99–105.
[37] N. Kröger, R. Deutzmann, M. Sumper, *Science* **1999**, *286*, 1129–1132.
[38] N. Poulsen, M. Sumper, N. Kröger, *Proc. Natl Acad. Sci. USA* **2003**, *100*, 12075–12080.
[39] N. Kröger, C. Bergsdorf, R. Deutzmann, M. Sumper, N. Kröger, *Proc. Natl Acad. Sci. USA* **2000**, *97*, 14133–14138.
[40] W. H. van de Poll, E. G. Vrieling, W. W. C. Gieskes, *J. Phycol.* **1999**, *35*, 1044–1053.
[41] N. Kröger, R. Wetherbee, *Protist* **2000**, *151*, 263–273.
[42] M. Sumper, *Science* **2002**, *295*, 2430–2433.
[43] N. Kröger, S. Lorenz, E. Brunner, M. Sumper, *Science* **2002**, *298*, 584–586.
[44] M. Sumper, S. Lorenz, E. Brunner, *Angew. Chem. Int. Ed.* **2003**, *42*, 5192–5195.
[45] A. Bencini, A. Bianchi, E. Garcia-Espana, M. Micheloni, J. A. Ramirez, *Coord. Chem. Rev.* **1999**, *188*, 97–156.

10 Silicic Acid Transport and its Control During Cell Wall Silicification in Diatoms

Mark Hildebrand

10.1 Introduction

Perhaps the most outstanding examples of micro- and nanoscale structured materials in nature are the intricate and ornate silicified cell walls of diatoms. Although diatoms have been admired by microscopists for over 200 years, our understanding of the processes involved in making their cell walls is still very limited. With the application of electron microscopic and biochemical techniques, and more recently those of molecular biology, certain diatom species are being developed as model systems to study cellular silicon metabolism and silicified cell wall formation. Advances over the past decade hold the promise of beginning to unravel the molecular details controlling these processes [1–7].

Our own research has focused on applying molecular biological approaches to understand diatom cellular silicon metabolism. We isolated the first cDNA clones derived from silicon-responsive genes [8]. From these clones, we isolated, functionally identified and are continuing to characterize genes and proteins responsible for the transport of silicic acid into the diatom cell [5, 6]. The silicic acid transporters (SITs) were the first biological components shown to directly and specifically interact with silicon [5] and we hope to develop them as a model to understand how proteins in general may interact with silicon. More recently, we have investigated the relationship of intracellular silicon pools with transport and cell wall silica incorporation [9]. We and others have demonstrated a tight coupling between uptake and incorporation in some diatom species, and in these species shown that silicic acid uptake is actually regulated by incorporation [9–11]. Thus, the mineralization process and transport are intimately linked. Because of the chemistry of silicic acid [12] and the need to deliver correct amounts into the silica deposition vesicle (SDV) where silicification occurs, transport of silicon into the cell, through the cytoplasm and into the SDV are integral parts of the polymerization process. Therefore, a complete understanding of silicification cannot be gained without understanding silicic acid transport and its control. The purpose of this chapter is to develop this concept, present a review of our current understanding of silicic acid transport in the diatom and its relation to silicification of the cell wall, and identify areas for future research.

Biomineralization: From Biology to Biotechnology and Medical Application, Second Edition. Edited by E. Bäuerlein

ISBN: 3-527-31065-7

10.2 Overall Considerations for Silicic Acid Transport During Diatom Cell Wall Synthesis

The diatom cell wall, which is also called a frustule, can contain a substantial amount of silica. Measurements range from 7 to 1100 fmol per cell, depending on the species and environmental conditions [9, 13], comprising up to 50 % of the dry weight of the cell [14]. The silicified wall is formed after cytokinesis, but prior to cell separation [15], and so the daughter cells are still attached during cell wall synthesis (Figure 10.1). Silicification occurs within the silica deposition vesicle [16], which is enclosed by its own membrane (the silicalemma) and contained entirely within the plasma membrane of the cell (Figure 10.1). After deposition is complete, exocytosis of the SDV occurs [15] to become part of the new cell wall. Because the new walls form on adjacent faces within the two attached daughter cells, they are shielded from the external environment (Figure 10.1). This arrangement necessitates uptake of silicic acid from other parts of the cell which are in contact with the environment. Silicon must then be transported through the cytoplasm and into the SDV (Figure 10.1). The requirement for cytoplasmic transport has important consequences in the overall scheme of cellular silicon metabolism, because the cell must deal directly with the large amounts of silicic acid required for the cell wall. In many diatom species the wall is made in an hour or two, and in some much less [13]. The substantial amounts of silicon required within these short time periods results in a high concentration in the cytoplasm, where silicon must be prevented from autopolymerizing [12] before reaching the SDV. Thus, not only must cellular uptake be rigorously controlled to allow enough silicon for the wall, yet preventing excess, but intracellular transport must be adapted to maintain silicon in a soluble form. At the same time, the intracellular transport mechanism must deliver and release silicic acid into the SDV in a carefully controlled manner.

10.3 The Solution Chemistry of Silicon

The solution chemistry of silicon is complex, but has been thoroughly described in the monograph by Iler [12]. Because of its complexity, and the fact that different silicon compounds may be present at different steps in cellular transport and deposition, some description may be useful. The term "silicon" not only refers to the element, but is used as a generic term when the specific form of a silicon compound is unknown [17]. The predominant form of silicon in aqueous solution at low concentrations is silicic acid, $Si(OH)_4$. This is a weak acid with a pK_a of 9.8 for the formation of $SiO(OH)_3^-$. By increasing the concentration in solutions of $pH < 9$, or decreasing the pH of a saturated solution, silicic acid will autopolymerize to form amorphous silica [12]. Polymerization occurs through stabilized intermediates, forming polysilicic acids, then colloidal silica particles of discrete sizes and, finally,

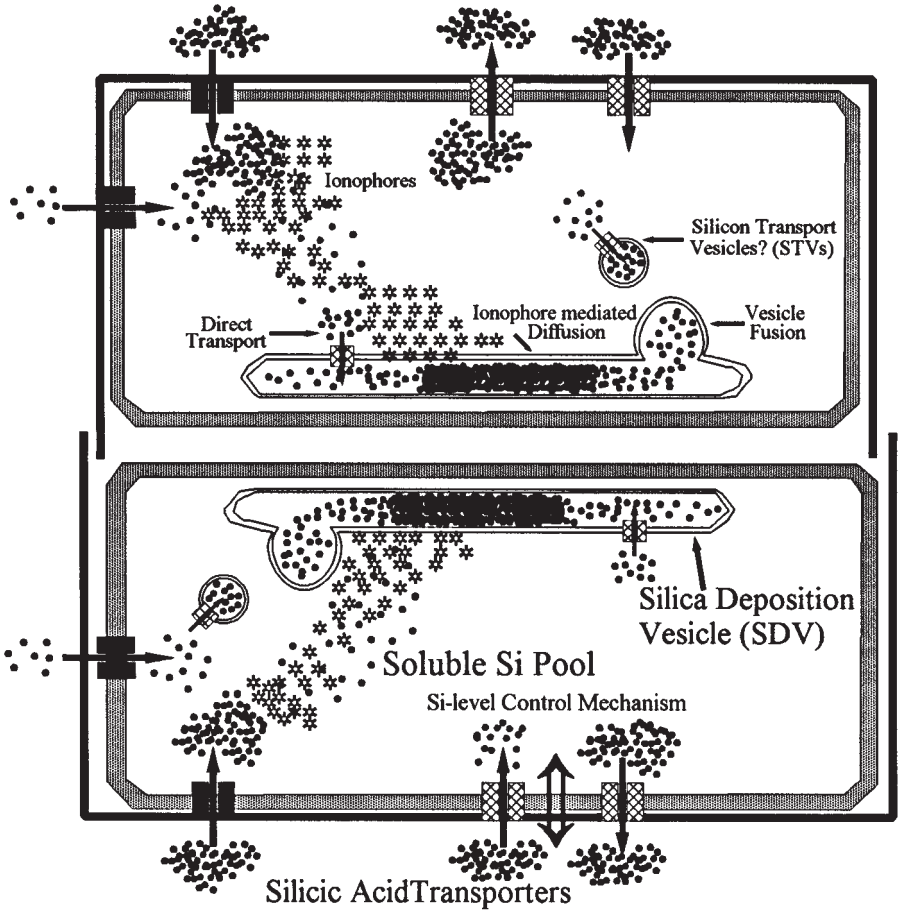

Figure 10.1 Features of silicic acid uptake, intracellular transport and deposition in a dividing diatom cell, depicting two daughter cells after cytokinesis still within the silicified walls of the mother cell during cell wall synthesis. Dark outer lines represent the silicified walls of the mother cell, large rectangles just inside with shaded borders represent the plasma membrane of each daughter cell. Other components are labeled. Dark dots represent silicic acid. The lower daughter cell illustrates three major components of transport and silicification: the silicic acid transporters, the soluble silicon pool and the silica deposition vesicle. Different transporters may have differing affinity or capacity for transport (compare extreme left with lower left). As part of the cell's silicon level control mechanism, the transporters can both take up and efflux silicic acid (bottom right of center). The upper daughter cell illustrates three possible means of intracellular transport: direct transport by intracellularly localized silicic acid transport proteins, ionophore-mediated transport by silicate ionophoretic activities and transport via silicon transport vesicles, which can fuse with the SDV.

depending on the pH, either a three-dimensional silica gel network or a sol [12, 18]. The solubility of silica is 1.7–2.5 mM over a broad range of pH values below 10 [12]. Although silicon is the second most abundant element in the Earth's crust, and is therefore plentiful, its availability for biological use is limited by its solubility

in water. In fact, the growth of marine diatoms can so deplete surface waters of silicon that their further proliferation is prevented [19]. Prior to the evolution of siliceous plankton, oceanic silicic acid concentrations were near saturation [20], but now the global ocean average is 70 μM and usually much less in surface waters [21]. $Si(OH)_4$ comprises about 97 % of the dissolved silicon in seawater and $SiO(OH)_3^-$ most of the remaining 3 % [22]. Silicon in the aqueous environment is referred to as dissolved silicon (DSi), or in relation to the cell, extracellular or external silicon. Silicon in the diatom cell wall is amorphous silica and silicon in intracellular pools is called intracellular soluble silicon.

10.4 Characterization of Diatom Silicic Acid Transport

The first demonstrations of silicon uptake by diatoms were by Lewin [23, 24]. The first kinetic measurements of uptake, demonstrating active silicon transport, were by Paasche [25] and Azam et al. [26]. Numerous studies [25–31] have shown that the specific rate of uptake follows Michaelis–Menten or Monod [32] saturation functions, indicating that transport is carrier mediated. Kinetic parameters for silicon uptake have been measured in many diatom species, and K_s values range from 0.2 to 7.7 μM, with V_{max} values of 1.2–950 fmol/cell/h [33].

Studies using the diatom *Phaeodactylum tricornutum* suggested that the ionized form of silicic acid [$SiO(OH)_3^-$] was the chemical form of silicon transported [34], but work [35] on three different diatom species has indicated that undissociated silicic acid [$Si(OH)_4$] was the transported form. Controls using *P. tricornutum* showed variable results, sometimes implicating silicic acid and sometimes the anion as the form transported [35]. The unique response of *P. tricornutum* may be related to its habitat, which can be in conditions of high pH where the anion is more prevalent [35]. Silicic acid transport is coupled to sodium in marine diatoms [31], and apparently coupled to sodium and perhaps potassium in freshwater species [29], although at much lower ionic strength. Thus transport in marine species has the characteristics of a sodium/silicic acid symporter [5, 31]. Indirect evidence suggests that transport is electrogenic and that the $Si(OH)_4$:Na^+ ratio is 1:1 [31]. Metabolic energy is required for uptake [26] and silicic acid transport is inhibited by sulfhydryl blocking reagents [21, 29]. Germanium (germanic acid) and silicic acid are competitive inhibitors for uptake of each other [26, 36], which has led to the use of ^{68}Ge as a radiotracer analog of silicon [36].

Three different modes of silicic acid uptake have been defined in diatoms: (1) surge uptake, (2) internally controlled uptake and (3) externally controlled uptake [10]. Surge uptake occurs upon silicon replenishment of silicate-starved cells, when intracellular silicon pools are depleted and the concentration gradient into the cell is maximum. Uptake rates are at a maximum during surge uptake. In internally controlled uptake, rates are controlled by the rate of utilization of silicon for cell wall deposition [9, 10]. When extracellular concentrations drop to very low levels, externally controlled uptake occurs, where rates are a function of decreasing substrate concentration [10].

Sullivan [30] showed that silicic acid uptake in diatoms did not occur continuously throughout the cell cycle, but in synchronized cultures of *Navicula pelliculosa* was induced just prior to cell wall synthesis. Sullivan [30] also showed that uptake was highly induced during silicate starvation, then decreased 2 h after silicate replenishment and was completely repressed after 4 h. He showed that cells took up enough silicon sometime between 1 and 2 h to allow complete cell wall synthesis and division [30]. Induction of transport was dependent upon protein synthesis [30]. Inhibition of protein synthesis paralleled the natural decrease in activity and the timing of this suggested that the protein involved was turned over rapidly [30]. V_{max} and K_s values for uptake changed over the course of the cell cycle, indicating changes in the number and affinity of transport sites [30]. This was the first clear indication that silicic acid transport was controlled during cell wall formation and during the cell cycle, and that this occurred by the synthesis and degradation of a specific transporter protein.

10.5 Molecular Characterization of the Silicic Acid Transport System

The cDNA libraries that we generated from *Cylindrotheca fusiformis* [8] were derived from genes turned on or off between conditions of silicate starvation and 1 h after silicate replenishment in synchronized cultures. These conditions were similar to those in Sullivan's study [30], when silicic acid transport activity was induced and repressed. Therefore, it seemed reasonable that the libraries might contain a copy of a silicic acid transporter gene. We screened clones for expression of their corresponding mRNAs during the cell cycle and in response to silicate starvation and replenishment, and identified several that responded in accord with Sullivan's data. We initially isolated six of these clones and found that they had identical sequences (but differed in length), encoding proteins predicted to be rich in hydrophobic amino acids. After obtaining a full-length copy and determining the complete sequence, an open reading frame of 548 amino acids was identified, with what were predicted to be 12 hydrophobic stretches of amino acids indicative of membrane-spanning segments [5]. The encoded protein also had a long hydrophilic C-terminal region [5]. Multi-membrane-spanning segments are characteristic of transport proteins [37, 38]. Because of this feature and the expression response of the gene, we thought it possible that the clone might encode a silicic acid transporter.

The function of the protein encoded by the cDNA was tested directly by microinjecting RNA transcribed *in vitro* from the clone into *Xenopus laevis* oocytes and monitoring uptake. We showed that injected oocytes gained the ability to take up ^{68}Ge from the medium [5] and that uptake was dependent on factors that would control the expression levels of the protein (Hildebrand, unpublished). Competition experiments using unlabeled silicic acid demonstrated that the cloned protein was a specific silicic acid/germanic acid transporter [5]. Transport in oocytes was sodium-dependent and sensitive to the sulfhydryl blocker *N*-ethyl malemide [5 and unpub-

lished] as observed in diatoms [29, 31]. These results [5] directly demonstrated that the clone encoded a silicic acid transporter, which we called *SIT1* (*Si*licic acid *T*ransporter *1*).

Using the *SIT1* cDNA as a probe, we identified multiple hybridizing bands in digests of *C. fusiformis* genomic DNA [6], suggesting the presence of a gene family. A total of five different types of *SIT* gene were isolated from *C. fusiformis* and sequenced and each type was correlated to a hybridizing band [6]. The predicted amino acid sequences of the five SITs are presented in Figure 10.2. The SITs have no identified homologs and thus represent a new class of transporter, although they contain most of a signature sequence (AX_3LX_3GR) for sodium symporters [38, 39] at residues 216–225 (Figure 10.2). Although originally thought to have 12 membrane-spanning segments [5], two new predictive programs [40] suggest that only 10 are present (Figures 10.2 and 10.3) and agree on the location of each. A revised topological model of the SITs is presented in Figure 10.3. The N- and C-termini are predicted to be located in the cytoplasm (Figure 10.3), which has been shown directly in other even-numbered multi-transmembrane segment transporters [41]. The transmembrane domain must be where silicic acid passes through the membrane, and is highly conserved (87–99 % amino acid identity) comparing the five SITs (Figure 10.2A and B). The C-terminal domain is less conserved (39–67 %) and has a high probability of forming a coiled-coil structure [6], suggesting that this portion of the transporters interacts with other proteins. In other transporters, the C-terminus can be involved in regulating the activity of transport, in controlling conformational changes in the protein and in some cases in differential intracellular targeting [42–48]. By analogy, the C-terminus of the SITs is likely to be important in controlling their activity or intracellular location and the lower degree of conservation in this region suggests that these parameters will vary in the different SITs.

SIT gene mRNA expression was induced 4-fold just prior to cell wall synthesis in *C. fusiformis* [6] and the overall pattern of expression correlated with silicic acid transport activity during cell wall synthesis in *N. pelliculosa* [30], quickly reaching high levels prior to maximum silica deposition and then decreasing rapidly. An increase in silicic acid uptake lagged between 20 and 40 min after induction of the genes (Hildebrand, unpublished), which was probably due to the time required for *SIT* mRNA to be translated and the protein to reach the plasma membrane. Although the pattern of mRNA expression of four of the genes (*SIT2–5*) was almost identical, levels differed by 24-fold. The pattern differed for *SIT1*. Thus, the transporters were required in different amounts during cell wall synthesis, suggesting that they played specific roles in the overall process of transport. These results indicated that transcriptional control was a major component in the regulation of silicic acid transport, but the coiled-coil structures at the C-termini suggested that transport was also controlled via protein–protein interactions.

From the sequence and expression analysis data, and based on the precedence of other transporters [43, 44, 46, 47] and the documented changes in K_s and V_{max} during diatom cell wall synthesis [30], we proposed [6] that the different forms of SITs have differing affinity and capacity for transport (K_s and V_{max} values) or different intracellular localization (Figure 10.1). We believe that the regulated expression and possibly localization of the SITs, as well as control at the protein level, are

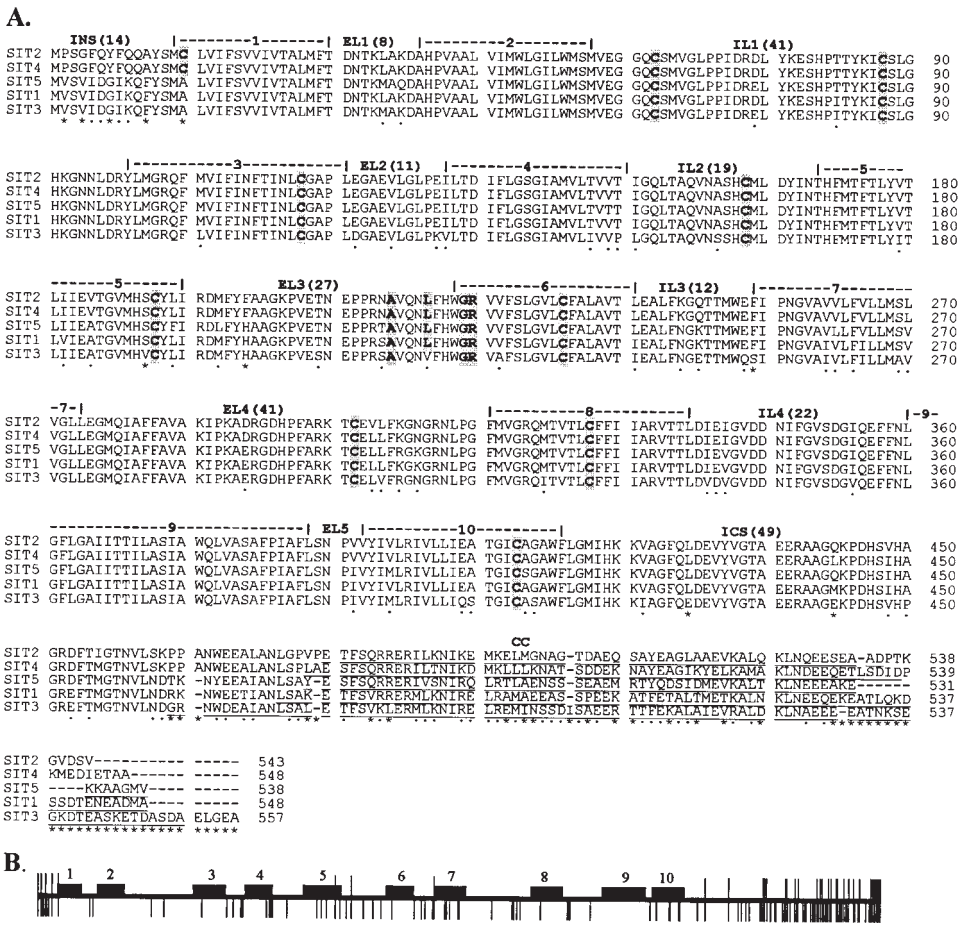

Figure 10.2 Comparison of silicic acid transporter sequences from *C. fusiformis*. (A) Predicted amino acid sequences from the five *SIT* genes were aligned using the MAP program [49]. Sequences are identified on the left and the amino acid residue number is given on the right. Gaps in the sequences are placed every 15 residues to aid in determining residue number, dashes (–) facilitate maximal alignment. Below the sequences, an asterisk (*) represents a non-conservative replacement in at least one of the sequences, a dot (.) is a conservative replacement and no symbol indicates identity in all of the sequences. The locations of potential membrane-spanning segments [40] are numbered (1–10) and delineated by brackets above the sequences. Between these segments are intra- and extracellular loops (IL and EL, respectively) numbered according to order, and in parentheses are the number of amino acids in each loop. INS is an intracellular amino segment and ICS is an intracellular carboxy segment, with parentheses indicating the number of residues in each. Underlined residues in the C-terminal regions have a high probability of forming coiled coils (CC), as determined by the COILS program [50] using a window of 28 residues. Cysteine residues are highlighted, as well as conserved residues in a portion of a signature sequence for sodium-coupled symporters [37, 38] at residues 216–225 (AX_3LX_3GR). (B) Schematic diagram of the amino acid conservation pattern in the five *C. fusiformis* SIT sequences. The thick horizontal line represents the coding region. The dark blocks above the thick line represent the location of transmembrane segments, numbered consecutively. Thinner vertical lines below the thick line locate a conservative amino acid replacement in at least one of the sequences and vertical lines spanning the thick line locate non-conserved residues in at least one of the sequences.

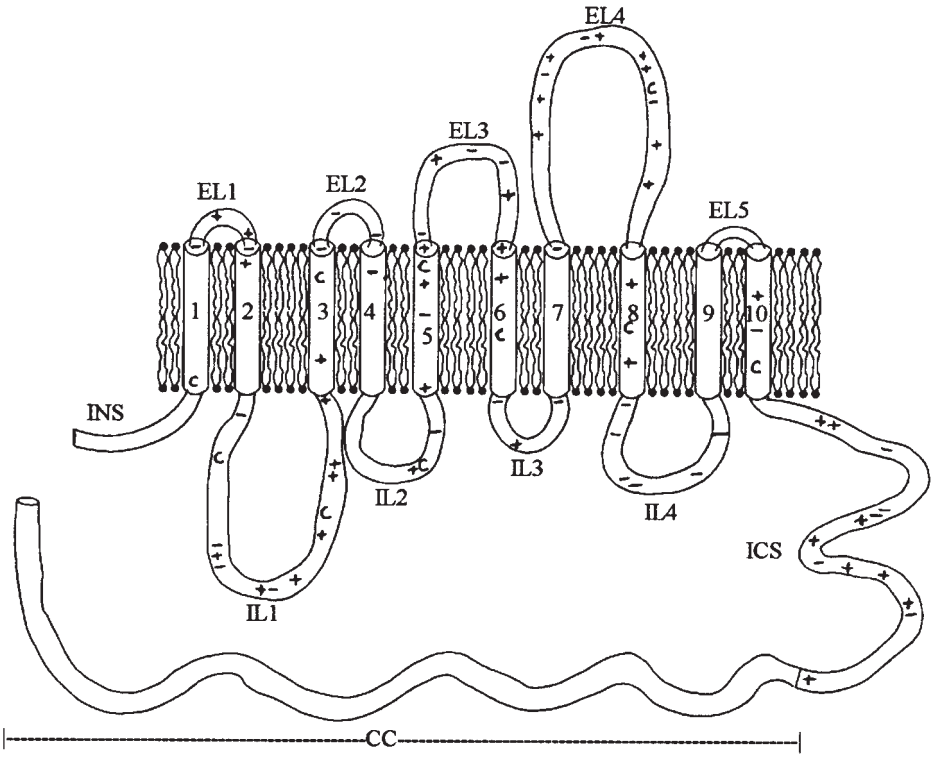

Figure 10.3 Topological model of *C. fusiformis* silicic acid transporters, depicting an extended model of the SITs, based on SIT4, residing in a lipid bilayer membrane. Bottom would be intracellular. Membrane-spanning segments are shown as tubes (1–10), which are connected by intracellular (IL) and extracellular (EL) loops. The intracellular amino segment (INS) and intracellular carboxy segment (ICS), as well as the coiled-coil region (CC) are shown. Pluses (+) and minuses (−) locate positively and negatively charged amino acids, and C locates cysteine residues. The location of charged amino acids is not presented in the coiled-coil region because of substantial variation within the five SITs.

key factors in the overall control of silicic acid uptake in diatoms. Hybridization experiments showed that multiple *SIT* gene copies were present in all diatom species tested [6], suggesting that similar mechanisms may operate.

10.6 Intracellular Silicon Pools

Intracellular pools of soluble silicon in diatoms were first identified by Werner [51]. Studies since then have shown that pool silicon can account for a sizable fraction (up to 50 %) of the total cellular silicon in some species under certain conditions

[9, 11, 33]. The actual concentration of intracellular soluble silicon depends upon measurement of intracellular water volume, which has resulted in some discrepancies. Pool concentrations (assuming monosilicic acid) of 438–680 mM in *N. pelliculosa* were reported by Sullivan [52]. However, cell water (by weight) was estimated as 20 % and recent measurements suggested a value of 85 % for this species [9]. New direct measurements of cell water volume and intracellular silicic acid [9] were in accord with an appropriate adjustment of Sullivan's data, indicating that intracellular concentrations ranged between 58 and 162 mM in this species. Comparison of several diatom species using direct determination of intracellular water volume indicated that pool concentrations (assuming monosilicic acid dispersed equally throughout the cell) ranged from 19 to 340 mM [9]. All results [9, 11, 52, 53] have indicated that diatoms can maintain extremely high intracellular concentrations of soluble silicon, well above saturation for silica solubility [12].

An important question is how can such high intracellular concentrations be maintained? An extremely high silicon concentration gradient from inside to outside the cell has been identified [9, 52], which is consistent with intracellular silicon having a different chemical form than extracellular, or being bound or sequestered by some means. Azam et al. [26] and Sullivan [52] suggested that partially polymerized or colloidal silica, or organosilicon compounds, could account for high pool levels. However, intracellular concentrations are so high in most species [9] that maintenance of lower molecular weight polysilicic acids should not be possible without some mechanism of stabilization. Substantial amounts of colloidal silica are also not likely because this would be detrimental to the integrity of cellular membranes [12]. Measurement of molybdate-reactive silicon from sonicated *Thalassiosira weissflogii* cells suggested that the predominant form was mono- or disilicic acid [53]. The results of Blank et al. [54] also indicated that most intracellular silicon was molybdate-reactive in the first hour after silicate addition to starved *Navicula saprophilia*, but from 1 to 6 h the fraction of molybdate-reactive silicon decreased. If the measured form of silicon was truly monomeric silicic acid in the cell, then because of the high concentration [9] it would have to be maintained by interaction with other cellular components. However, one must consider that in the molybdate assay intracellular contents are substantially diluted and in some cases heated to 100 °C [9, 53, 54], which may dissolve polymerized forms of silicic acid into molybdate-reactive monomers [12]. More substantial evidence that suggested an association of silicon with organic material or proteins was obtained by Werner [51] and Azam et al. [26], who found that 80 % of the pool of soluble silicon in *Nitzschia alba* was precipitable with trichloroacetic acid. Thus, pool silicon could be maintained in soluble form at high concentrations by organic silicon-binding components in the cell. An alternative mechanism proposed that silicon was sequestered in specialized vesicles with conditions in the lumen conducive to maintaining solubility [55, 56]. However, there was no evidence that these intracellular vesicles contained silicon and, even if they did, they would also have to have organosilicon complexes or extremely high pHs to maintain it in a soluble form. In summary, it has not been unambiguously shown what form of silicic acid is present in intracellular pools, which may in part be due to the complexity of silicic acid solution chemistry [12]. However, it is probably safe to say that pool silicon consists of mono- or lower-

molecular-weight polysilicic acids, maintained in soluble form by complexation with organic material [26, 51, 56], or perhaps sequestration [55, 56].

Pool sizes differ in different diatom species, part of which may be due to the relative timing of silicic acid uptake and silica incorporation into the frustule. In many species, uptake and deposition are almost simultaneous, resulting in a relatively small soluble pool of silicon, but in others uptake and deposition are temporally uncoupled, allowing the accumulation of sizable pools [11]. *T. weissflogii* can accumulate intracellular soluble silicon sufficient for the synthesis of an entire cell wall [53, 57]. Even in species where pools remain small, levels are above saturation for silica solubility [9]. Pool sizes vary within a species [9, 30, 53]; in *C. fusiformis* pool levels changed in a regular manner during the course of cell wall synthesis [9].

10.7 The Relationship of Intracellular Pools and Incorporation to Uptake

In diatom species where uptake and incorporation were coupled temporally, transport was regulated by the intracellular utilization of silicon, which presumably was the rate of silica incorporation into the wall [10]. We recently showed directly that uptake was controlled by incorporation in *C. fusiformis* [9]. Germanium is a specific inhibitor of diatom cell wall silica incorporation [58] and a competitive inhibitor of silicic acid uptake [26]. In *C. fusiformis* cultures growing in medium with a Ge:Si ratio of 0.1:1, cell wall incorporation was inhibited to 22–25 % of the control [9, 59], but according to the K_i value determined in another diatom species, silicic acid transport would not have been appreciably directly inhibited [26, 60]. We showed, however, that uptake was inhibited by blocking incorporation with germanium and the level of inhibition was identical for both processes, indicating that they were coupled [9]. Thus, in some, and perhaps most [11] diatom species, not only is there a close coupling between the timing of silica incorporation and silicic acid uptake, but incorporation actually exerts control over uptake [9, 10]. In other words, rather than silicic acid being pumped into the cell and driving the silicification process, silicic acid is drawn into the cell upon demand. This would allow the cell to take up enough silicic acid at a given time, but not an excess, keeping intracellular pools to a minimum.

The control of uptake by incorporation was proposed to occur by a mechanism involving intracellular soluble pools, whereby pools were assumed to increase to maximum levels and then feedback to control transport [10]. However, in *C. fusiformis*, soluble pools did not have to increase to maximum levels before uptake was controlled [9]. In fact, soluble pool levels changed only gradually over long time periods and did not transiently expand to accommodate uptake (except under certain conditions of surge uptake). This suggested that other cellular factors were involved in the mechanism controlling transport. We proposed that soluble pool levels were determined by the capacity of intracellular silicon-binding components [9]. We

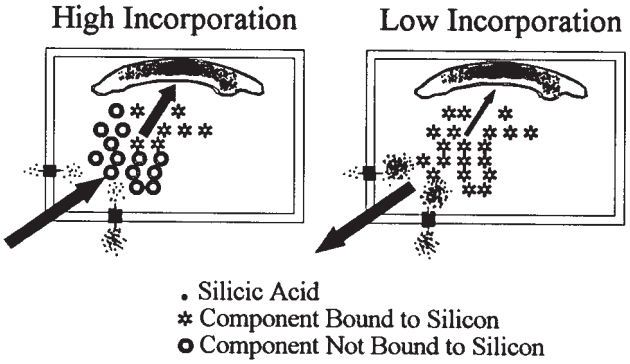

Figure 10.4 Model for control of silicic acid uptake by cell wall silica incorporation through the intermediary of intracellular silicon-binding components. Large rectangles represent diatom cells. Arrows spanning the left side of cells represent net uptake or efflux (left cell and right cell, respectively) of silicic acid under conditions of high and low silica incorporation into the cell wall. The structures at inside top of cells represent silica deposition vesicles; arrows pointing at these denote the relative rate of cell wall incorporation.

do not know what these components are and use the term "binding" only to indicate some means of maintaining silicon in a soluble form. However, the proposed mechanism should work regardless of how this is accomplished. More or less of the silicon-binding components could be present, explaining the observed range of pool levels over long time periods, but at a given time, soluble pool sizes would be determined by the amount of binding component. We proposed that transport was controlled by the relative amounts of bound and unbound silicon [9]. When unbound silicon-binding component was in excess, uptake would be favored, and with excess unbound silicon, uptake would be inhibited or efflux induced (Figure 10.4). Incorporation could control uptake by drawing silicic acid from the intracellular pool, altering the ratio of bound to unbound silicon (Figure 10.4). The driving force for efflux could be the unbound silicic acid concentration gradient from inside to outside the cell.

This mechanism is consistent with data measuring silicic acid efflux from diatom cells [26, 29]. Efflux did not occur in the absence of external silicate [29], indicating that the cell has some means of preventing this, perhaps by binding or sequestering all intracellular silicic acid. Consistent with this, intracellular pools were not depleted even upon prolonged silicate starvation [9, 53]. Increasing amounts of external silicate up to a saturating level actually increased efflux [29]. An explanation for this is that surge uptake should be higher with increasing external silicon (due to the higher concentration gradient into the cell) and the greater intracellular excess at higher external silicon should result in more efflux. These data [29] are consistent with our hypothesis [9], in that they suggest that intracellular levels are maintained by silicon-binding components and that efflux results from a transient imbalance when the level of transport exceeds the capacity of these components.

Because of the requirement to control the silicic acid concentration in the cytoplasm to prevent autopolymerization, we propose that silicon-binding components

are part of an intracellular silicon-level control mechanism operating in the diatom (Figure 10.4). This mechanism senses the amount of silicon required for deposition, and through the silicon-binding components links this to the uptake process (Figure 10.4). Because the C-terminal portions of the SITs are very likely to interact with other proteins [6], and the C-termini of other transporters can regulate activity [43, 61], it may be that the control mechanism operates at this step through proteins that bind to and affect the activity of the SITs (Figure 10.1).

10.8 Intracellular Transport of Silicon

The mechanisms of intracellular silicon transport and transport into the SDV (Section 10.9) are very poorly understood. Silicon is found in all major cellular organelles in the diatom [62] and surprisingly in many organelles in rat tissue cells [63]. A direct comparison of levels in all organelles was not possible, but silicon was particularly abundant in the mitochondria and chloroplasts of the diatom (the SDV could not be isolated), and nucleus, microsomes and mitochondria in rat liver cells [62, 63]. Lipid bilayer membranes are almost impermeable to $Si(OH)_4$ [12], so the presence of silicon in organelles must be due to a transport process. If intracellular transport involved silicic acid transport proteins, then a specific form of SIT would have to be located in each major organelle, not only in the diatom, but in rat tissue cells as well. Unless each organelle has a specific use for silicon, this is unlikely. The available data [62, 63] suggest a general intracellular transport mechanism without specific targeting to a particular location.

Silicate ionophoretic activities, enabling the transport of silicic (and germanic) acid across lipid bilayers and bulk organic phases, have been isolated from *N. alba* [64]. The ionophoretic activities were induced 6-fold in silicate-starved cultures, suggesting that they were directly linked to cellular silicon metabolism [64]. Bhattacharyya and Volcani [64] proposed that intracellular transport could occur by ionophore-mediated diffusion, which would be consistent with silicon's presence in all organelles or at least within organellar membranes [62]. They proposed that, through binding, these ionophoretic activities could also be involved in maintaining high intracellular levels of unpolymerized silicic acid [64]. These activities differed from classical ionophores in that they apparently bound two different ions, silicon and sodium, and required both to translocate across an organic layer [64]. The ionophores were isolated by organic extraction and therefore they should preferentially partition into cellular lipid membranes. It is possible that in the cell they translocate silicic acid by binding and releasing on either side of a membrane. What then would prevent them from transporting silicic acid through the plasma membrane out of the cell, which would be favorable due to the high concentration gradient in this direction? Perhaps because the Na^+ concentration gradient is opposite and the ionophore binds Na^+, this may favor an inward facing orientation, preventing silicic acid efflux. In intracellular organelles or vesicles, binding and release of silicic acid by the ionophore may be facilitated by conditions (Na^+, pH or other factors) on

one or other side of the membrane. The structures of these ionophoretic activities were not determined, although it was suggested that they contained vicinal hydroxyl groups [64]. If one ionophore per silicon was required, their synthesis may be energetically expensive to the cell. However, the fact that silicon is found in many organelles in rat tissue cells suggests that the activities responsible are derived from compounds normally present in all cells. For example, catechols readily bind and dissolve silica [12], and catecholamines such as epinephrine and derivatives are components of normal cellular metabolism. Perhaps in the diatom these types of compounds have been adapted or modified, including amplifying their levels, for use in intracellular silicon transport. Desired properties of these compounds would be specific binding, but with not too high a binding constant, because silicic acid would have to be eventually released for polymerization.

An alternative hypothesis regarding intracellular transport is that it could occur by the movement of vesicles in which silicic acid has been sequestered [55, 65]. Small vesicles, called silicon transport vesicles (STVs) by Schmid and Schulz [55], have been identified near actively silicifying portions of the SDV in several electron micrographic studies [55, 66, 67]. These vesicles have been seen to fuse with the SDV and the size of the vesicles matched reasonably well with the size of silica particles adding to the growing frustule [55]. Presumably, these vesicles would be transported through the cell along microtubule networks. There are some considerations in regard to this hypothesis. Most important is that these vesicles have not been directly shown to contain silicon, either in soluble or polymerized form. This should be possible by X-ray microprobe analysis [63]. Also, the identification of specific silicic acid transport proteins [5, 6] precludes the uptake of silicic acid by binding at the plasma membrane and vesicle invagination, so silicic acid pumped into the cytoplasm by the SITs would then have to be transported into the vesicles. This could be feasible, because both plasma membrane and vesicular localization of transporters occur [47]. To maintain silicic acid solubility in the lumen of the vesicles, they would either have to contain silicic acid-binding components and/or maintain a very high pH. However, a low pH has been found in the SDV [7], which should not be the case if appreciable amounts of high pH vesicular contents were being continuously released into it. If silicon-binding components in the vesicles were released into the SDV, these might also interfere with polymerization. An alternative hypothesis regarding the STVs is that they do not specifically deliver silicon, but rather provide a way of adding large amounts of membranous material (along with proteins and other components) during rapid expansion of the SDV [66] and that the silica particles identified in the SDV result from the colloidal growth [18] of silica. Thus, it is unclear at present what the potential contribution of STVs to the maintenance of soluble pools and intracellular transport is.

There may be other as yet unidentified cellular components involved in maintenance of pools and intracellular transport. Proteins that could bind multiple silicic acids would be energy efficient for the cell to produce, and there is ample evidence for the involvement of proteins in binding and sequestration of other ions such as Ca^{2+} [68].

Most of the evidence to date is consistent with an ionophoretic or organic silicon-binding component being responsible for maintenance of intracellular soluble pools

and intracellular transport. However, because these compounds have been insufficiently characterized and not enough work has been done on the alternatives, we are still ignorant of the actual mechanisms.

10.9 Transport into the Silica Deposition Vesicle

The possibility that silica deposition and transport are coupled in some diatom species has been discussed above. In addition, there is a mass transport effect on the extent of silicification, which is determined by the extracellular silicon concentration. It has been shown that diatom frustules are more heavily silicified with higher extracellular silicon [9, 25, 69] and under conditions of silicon limitation, frustules are thinner and siliceous spines (if normally present) are smaller or absent [13, 70].

The molecular details of the formation of silicified structures in the SDV are not well known. How silicon is transported into the SDV is also unclear and understanding this depends upon understanding the intracellular transport mechanism, about which we have little hard evidence. Thus, we can currently only present speculative possibilities, which hopefully will guide future research in these areas.

As far as the possibility of direct transport of silicic acid into the SDV by the SITs is concerned, it should be possible to test this by determining the intracellular location of the SITs using specific antibody probes. If the SITs are involved in intracellular transport, they would have to pump in the reverse direction compared with plasma membrane localized forms, which could occur because transporters can work in both directions, although it is not presently clear what the driving force for intracellular transport would be. Although vesicle fusion with the SDV has been directly demonstrated [55, 66, 67], as discussed, the presence of silicon in these vesicles needs to be substantiated and there are other considerations as described. There are several favorable observations regarding the ionophore-mediated transport hypothesis. The cationic, lipophilic dye Rhodamine 123 (R123) accumulates in electronegative intracellular compartments such as the mitochondria [71]. It also accumulates in the SDV in diatoms, where it is incorporated into actively polymerizing silica [72] and can actually be used to quantitatively monitor silica incorporation [57]. R123 transport into mitochondria is independent of ΔpH, but dependent on the transmembrane potential [73]. The compound electrophoretically moves across the mitochondrial membrane and the concentration ratio inside:out is 4000:1 [73]. Thus, intracompartmental electronegativity can provide a highly efficient mechanism for concentrating compounds. Perhaps such a mechanism works for silicate ionophores in the SDV and mitochondria. This would imply that the ionophores were positively charged and lipophilic, the latter of which we know is true and the former of which has not been tested [64]. In this hypothesis, if electronegativity concentrated silicic acid in an organelle, what then would prevent silica polymerization in certain organelles and promote polymerization in the SDV? Perhaps the SDV has specific intralumenal chemical conditions and/or specific proteins or carbohydrates not found in other organelles that promote the release of silicon

from organic transporting components and polymerization. It could be that the acidic environment identified in the SDV [7] favors the dissociation of organosilicon complexes, whereas in the slightly basic pH of the mitochondria [74] this may not be favored. By itself, this may not explain why silicic acid is not released in other acidic organelles, where at high enough concentrations the pH would promote polymerization [12]. Perhaps proteins are also involved. Models proposing a templating or polymerization-enhancing role of SDV proteins in diatoms have been described [75]. The identification of proteins occluded within the silica of a sponge spicule that have templating and polymerization-enhancing activity *in vitro* [76, 77 and Chapter 14], indicates that polymerization is mediated by these proteins *in vivo*. Interestingly, not only was silicic acid a substrate for the sponge proteins, but also silicon-organic (silsesquioxanes) derivatives normally requiring extremes of pH for polymerization [77]. It is tempting to see this as an analogy to a silicic acid–ionophore conjugate in the SDV, in that SDV proteins may catalyze the release of silicic acid from the ionophores and polymerization. Alternatively, removal of silicic acid from the intralumenal SDV solution by the polymerization process may drive the release of silicic acid from an organic complex. Proteins occluded within diatom silica have been identified [1, 3, 5, 78] and the recently characterized polycationic polypeptides known as silaffins [5] promoted condensation of uncomplexed silicic acid under acidic conditions, which would be inconsistent with the latter hypothesis for silicic acid release.

10.10 Summary

In this chapter we have developed the concept that cell wall silicification in diatoms is an integrated process. Not only silica polymerization, but silicic acid uptake, maintenance of intracellular silicon pools, intracellular transport and release into the SDV are essential for the formation of the cell wall. Indeed, in the model we have developed, intracellular silicon-binding components may play a pivotal role in the process because they would not only maintain silicon in soluble form, but would be part of the mechanism of controlling intracellular levels, be responsible for the coupling between deposition and uptake, and deliver silicic acid to and into the SDV for polymerization.

Although the model is consistent with the available data, studies on many aspects of silicic acid transport and deposition are clearly limited and more investigation is required. We are now poised to pursue an in-depth study of the mechanism and control of silicic acid uptake by the SITs. Having cloned these genes enables us to manipulate them *in vitro* and analyze them after reintroduction into the diatom [79] or into a heterologous host such as yeast. By comparing SIT gene sequences in different diatom species [6], we can identify regions containing amino acids that are essential for transport. Using site-directed mutagenesis, we can directly test the role of conserved amino acids in transporter function and the control of transport activity by the C-terminus. Because we believe that proteins interacting with the C-

terminus of the SITs are part of the intracellular sensing and control mechanism, isolating and characterizing these proteins may bring us one step further towards understanding how this mechanism works.

It is not clear what maintains silicon in soluble form at high concentrations in the cytoplasm nor what the mechanism of intracellular transport is. The silicate ionophoretic activities [64] may be the most promising candidates for being involved in these processes, and should be reisolated and characterized in detail. To evaluate the validity of the STV hypothesis [55], the contents of these vesicles need to be identified and their movements in the cell tracked. Approaches aimed at identifying other silicon-binding components may also be useful.

These investigations are not only important in understanding the cellular and molecular biology of silicification in the diatom, but may have applications in *in vitro* chemical or materials syntheses. The efficiency of biological processing of silicon undoubtedly stems from the specific molecular interaction between cellular components and silicon. Understanding the nature of these interactions at the molecular level could provide insight into how to control or optimize chemical reactions. Controlling the transport of silicic acid across lipid bilayers or bulk organic layers may have direct application in chemical or materials syntheses. By developing purification schemes for the SITs and understanding how their activity is controlled, perhaps these could be used to deliver specific amounts of silicic acid into or out of lipid bilayer systems. Ionophoretic activities could be used for transport across both lipid bilayers and bulk organic layers [64]. Biology has had billions of years to develop and refine sophisticated mechanisms for controlling chemistry, including spatial and temporal control of reactions, and an understanding of the biological control of silicon chemistry is likely to be extremely beneficial.

Acknowledgments

We are grateful for support over the years from Ethyl Corp. and Whitby Research, the Kellogg Family of La Jolla, CA, Dow Corning Corp., and the US Army Research Office.

References

[1] N. Kröger, C. Bergsdorf, M. Sumper, *EMBO J.* **1994**, *13*, 4676–4683.
[2] N. Kröger, C. Bergsdorf, M. Sumper, *Eur. J. Biochem.* **1996**, *239*, 259–264.
[3] N. Kröger, G. Lehmann, R. Rachel, M. Sumper, *Eur. J. Biochem.* **1997**, *250*, 99–105.
[4] N. Kröger, R. Duetzmann, M. Sumper, *Science* **1999**, *286*, 1129–1132.
[5] M. Hildebrand, B. E. Volcani, W. Gassmann, J. I. Schroeder, *Nature* **1997**, *385*, 688–689.
[6] M. Hildebrand, K. Dahlin, B. E. Volcani, *Mol. Gen. Genet.* **1998**, *260*, 480–486.
[7] E. G. Vrieling, W. W. C. Gieskes, T. P. M. Beelen, *J. Phycol.* **1999**, *35*, 548–559.

[8] M. Hildebrand, D. R. Higgins, K. Busser, B. E. Volcani, *Gene* **1993**, *132*, 213–218.
[9] M. Hildebrand, submitted.
[10] (a) H. L. Conway, P. J. Harrison, C. O. Davis, *Mar. Biol.* **1976**, *35*, 187–199; (b) H. L. Conway, P. J. Harrison, *Mar. Biol.* **1977**, *43*, 33–43.
[11] S. W. Chisholm, F. Azam, R. W. Eppley, *Limnol. Oceanogr.* **1978**, *23*, 518–529.
[12] R. K. Iler, *The Chemistry of Silica: Solubility, Polymerization, Colloid and Surface Properties, and Biochemistry*, Wiley, New York, **1979**.
[13] M. A. Brzezinski, R. J. Olson, S. W. Chisholm, *Mar. Ecol. Prog. Ser.* **1990**, *67*, 83–96.
[14] J. C. Lewin, R. R. L. Guillard, *Annu. Rev. Microbiol.* **1963**, *17*, 373–414.
[15] J. D. Pickett-Heaps, A.-M. M. Schmid, L. A. Edgar, in *Progress in Phycological Research, Vol 7.* (Eds F. E. Round and D. J. Chapman), Biopress, Bristol, **1990**, pp. 2–168.
[16] R. W. Drum, H. S. Pankratz, *J. Ultrastruct. Res.* **1964**, *10*, 217–223.
[17] T. L. Simpson, B. E. Volcani (Eds) *Silicon and Siliceous Structures in Biological Systems*, Springer, New York, **1981**, p. 6.
[18] R. G. Greer, in *Scanning Electron Microscopy, Part I, Proceedings of the 4th Annual Scanning Electron Microscopy Symposium*, IIT Research Institute, Chicago, IL, **1971**, pp. 153–160.
[19] (a) J. J. Goering, D. M. Nelson, J. A. Carter, *Deep-Sea Res.* **1973**, *20*, 777–789; (b) F. Azam, S. W. Chisholm, *Limnol. Oceanogr.* **1976**, *21*, 427–435; (c) M. A. Brzezinski, D. M. Nelson, *Deep-Sea Res.* **1989**, *36*, 1009–1030.
[20] H. D. Holland, *The Chemical Evolution of the Oceans*, Princeton University Press, Princeton, NJ, **1984**.
[21] T. Tréguer, D. M. Nelson, A. J. Van Bennekom, A. Leynaert, B. Queguiner, *Science* **1995**, *268*, 375–379.
[22] (a) N. Ingri, in *Biochemistry of Silicon and Related Problems.* (Eds G. Bendz and I. Lindqvist), Plenum Press, New York, **1978**, pp. 3–51; (b) W. Stumm, J. J. Morgan, *Aquatic Chemistry*, Wiley Interscience, New York, **1970**.
[23] J. C. Lewin, *J. Gen. Physiol.* **1954**, *37*, 589–599.
[24] J. C. Lewin, *J. Gen. Physiol.* **1955**, *39*, 1–10.
[25] E. Paasche, *Mar. Biol.* **1973**, *19*, 262–269.
[26] F. Azam, B. B. Hemmingsen, B. E. Volcani, *Arch. Microbiol.* **1974**, *97*, 103–114.
[27] D. M. Nelson, J. J. Goering, S. S. Kilham, R. R. L. Guillard, *J. Phycol.* **1976**, *12*, 246–252.
[28] S. S. Kilham, C. L. Kott, D. Tilman, *J. Great Lakes Res.* **1977**, *3*, 93–99.
[29] C. W. Sullivan, *J. Phycol.* **1976**, *12*, 390–396.
[30] C. W. Sullivan, *J. Phycol.* **1977**, *13*, 86–91.
[31] P. Bhattacharyya, B. E. Volcani, *Proc. Natl Acad. Sci. USA* **1980**, *77*, 6386–6390.
[32] J. Monod, *Annu. Rev. Microbiol.* **1942**, *3*, 3–71.
[33] V. Martin-Jezequel, M. Hildebrand, M. Brzezinski, *J. Phycol.* **2000**, *36*, 821–840.
[34] G. F. Riedel, D. M. Nelson, *J. Phycol.* **1985**, *21*, 168–171.
[35] Y. Del Amo, M. A. Brzezinski, *J. Phycol.* **1999**, *35*, 1162–1170.
[36] (a) F. Azam, *Planta* **1974**, *121*, 205–212; (b) F. Azam, B. E. Volcani, *Arch. Microbiol.* **1974**, *101*, 1–8.
[37] M. A. Hediger, *J. Exp. Biol.* **1994**, *196*, 15–49.
[38] J. Reizer, A. Reizer, M. J. Saier, Jr, *Biochim. Biophys. Acta* **1994**, *1197*, 133–166.
[39] Y. Deguchi, I. Yamoto, Y. Anraku, *J. Biol. Chem.* **1990**, *265*, 21704–21708.
[40] (a) T. Hirokawa, S. Boon-Chieng, S. Mitaku, *Bioinformatics* **1998**, *14*, 378–379; (b) TMpred, Baylor College of Medicine Protein Secondary Structure Prediction, Web address: http://dot.imgen.bcm.tmc.edu:9331/seq-search/struc-predict.html.
[41] (a) A. Davies, K. Meeran, M. T. Cairns, S. T. Baldwin, *J. Biol. Chem.* **1987**, *262*, 9347–9352; (b) R. Seckler, J. K. Wright, P. Overath, *J. Biol. Chem.* **1983**, *258*, 10817–10820.
[42] T. Caspari, R. Stadler, N. Sauer, W. Tanner, *J. Biol. Chem.* **1994**, *269*, 3498–3502.
[43] A. D. Due, Q. Zhinchao, J. M. Thomas, A. Buchs, A. C. Powers, J. M. May, *Biochemistry* **1995**, *34*, 5462–5471.
[44] G. D. Holman, S. W. Cushman, *BioEssays* **1994**, *16*, 753–759.
[45] H. Katagiri, T. Asano, H. Ishihara, K. Tsukuda, J.-L. Lin, K. Inukai, M. Kikuchi, Y. Yazaki, Y. Oka, *J. Biol. Chem.* **1992**, *267*, 22550–22555.

[46] Y. Oka, T. Asano, Y. Shibasaki, J.-L. Lin, K. Tsukuda, H. Katagiri, Y. Akanuma, F. Takaku, *Nature* **1990**, *345*, 550–553.
[47] K. J. Verhey, S. F. Hausforff, M. J. Birnbaum, *J. Cell Biol.* **1993**, *123*, 137–147.
[48] K. J. Verhey, J. I. Yeh, M. J. Birnbaum, *J. Cell Biol.* **1995**, *130*, 1071–1079.
[49] K. C. Worley, R. Smith, B. Weise, P. Culpepper, *Genome Res.* **1996**, *6*, 454–462.
[50] A. Lupas, M. Van Dyke, J. Stock, *Science* **1991**, *252*, 1162–1164.
[51] D. Werner, *Arch. Mikrobiol.* **1966**, *55*, 278–308.
[52] C. W. Sullivan, *J. Phycol.* **1979**, *15*, 210–216.
[53] B. J. Binder, S. W. Chisholm, *Mar. Biol. Lett.* **1980**, *1*, 205–212.
[54] G. S. Blank, D. H. Robinson, C. W. Sullivan, *J. Phycol.* **1986**, *22*, 382–389.
[55] A.-M. Schmid, D. Schulz, *Protoplasma* **1979**, *100*, 267–288.
[56] C. W. Sullivan, in *Silicon Biochemistry*, Wiley, Chichester, **1986**, pp. 59–89.
[57] M. A. Brzezinski, D. J. Conley, *J. Phycol.* **1994**, *30*, 45–55.
[58] J. Lewin, *Phycologia* **1966**, *6*, 1–12.
[59] W. M. Darley, B. E. Volcani, *Exp. Cell Res.* **1969**, *58*, 334–342.
[60] F. Azam, B. E. Volcani, in *Silicon and Siliceous Structures in Biological Systems* (Eds T. L. Simpson and B. E. Volcani), Springer, New York, **1981**, pp. 43–67.
[61] E. Carafoli, *FASEB J.* **1994**, *8*, 993–1002.
[62] C. W. Mehard, C. W. Sullivan, F. Azam, B. E. Volcani, *J. Physiol.* **1974**, *30*, 265–272.
[63] C. W. Mehard, B. E. Volcani, *Cell Tissue Res.* **1976**, *166*, 255–263.
[64] P. Bhattacharyya, B. E. Volcani, *Biochem. Biophys. Res. Commun.* **1983**, *114*, 365–372.
[65] M. Lee, C.-W. Li, *Bot. Bull. Acad. Sin.* **1992**, *33*, 317–325.
[66] C.-W. Li, B. E. Volcani, *Phil. Trans. R. Soc. Lond. B* **1984**, *304*, 519–528.
[67] (a) C.-W. Li, B. E. Volcani, *Protoplasma* **1985**, *124*, 10–29; (b) D. Schulz, G. Drebes, H. Lehmann, R. Jank-Ladwig, *Eur. J. Cell Biol.* **1984**, *33*, 43–51.
[68] (a) R. Spencer, M. Charman, P. Wilson, D. E. M. Lawson, *Nature* **1976**, *263*, 161–163; (b) S. S. Jande, S. Tolnai, D. E. M. Lawson, *Nature* **1981**, *294*, 765–767; (c) J. H. Henson, D. A. Begg, S. M. Beaulieu, D. J. Fishkind, E. M. Bonder, M. Terasaki, D. Lebeche, B. Kaminer, *J. Cell Biol.* **1989**, *109*, 149–161.
[69] (a) D. Tilman, S. Soltau-Kilham, *J. Phycol.* **1976**, *12*, 375–383; (b) P. J. Harrison, H. L. Conway, R. W. Holmes, C. O. Davis, *Mar. Biol.* **1977**, *43*, 19–31.
[70] (a) E. Paasche, *J. Exp. Mar. Biol. Ecol.* **1975**, *19*, 117–126; (b) C. O. Davis, *J. Phycol.* **1976**, *12*, 291–300; (c) P. J. Harrison, H. L. Conway, R. C. Dugdale, *Mar. Biol.* **1976**, *35*, 177–186.
[71] L. V. Johnson, M. L. Walsh, L. B. Chen, *Proc. Natl Acad. Sci. USA* **1980**, *77*, 990–994.
[72] C.-W. Li, S. Chu, M. Lee, *Protoplasma* **1989**, *151*, 158–163.
[73] R. K. Emaus, R. Grunwald, J. J. Lemasters, *Biochim. Biophys. Acta* **1986**, *850*, 436–448.
[74] J. Llopis, J. M. McCaffery, A. Miyawaki, M. G. Farquhar, Y. Tsien, *Proc. Natl Acad. Sci. USA* **1998**, *95*, 6803–6808.
[75] (a) R. E. Hecky, K. Mopper, P. Kilham, E. T. Degens, *Mar. Biol.* **1973**, *19*, 323–331; (b) K. D. Lobel, J. K. West, L. L. Hench, *Mar. Biol.* **1996**, *126*, 353–360.
[76] K. Shimizu, J. Cha, G. D. Stucky, D. E. Morse, *Proc. Natl Acad. Sci. USA* **1998**, *95*, 6234–6238.
[77] J. N. Cha, K. Shimizu, Y. Zhou, S. C. Christiansen, B. F. Chmelka, G. D. Stucky, D. E. Morse, *Proc. Natl Acad. Sci. USA* **1999**, *96*, 361–365.
[78] D. M. Swift, A. P. Wheeler, *J. Phycol.* **1992**, *28*, 202–209.
[79] (a) T. G. Dunahay, E. E. Jarvis, P. G. Roessler, *J. Phycol.* **1995**, *31*, 1004–1012; (b) K. E. Apt, P. G. Kroth-Pancic, A. R. Grossman, *Mol. Gen. Genet.* **1996**, *252*, 572–579; (c) H. Fischer, I. Robl, M. Sumper, N. Kröger, *J. Phycol.* **1999**, *35*, 113–120.

11 The Nanostructure and Development of Diatom Biosilica

Richard Wetherbee, Simon Crawford and Paul Mulvaney

11.1 Introduction

The degree of complexity and hierarchical structure displayed by biomineralized composites has never been matched in artificial materials, as a diverse range of biological organisms possess mechanisms for the nanofabrication of ornately sculptured silicates under ambient conditions and at near-neutral pH [1, 2]. The success of biological systems in processing silica must result from specific interactions between the silica and the associated biomolecules produced by the cells. Templating molecules exist in nanogram or smaller concentrations within the complex organic–inorganic matrix of a range of biologically mineralized composites [3–6] and there is now evidence that a similar template may exist during the development of diatom biosilica [7]. However, the identity and location of the organic–inorganic interface that chemically and spatially directs the polymerization of silica in diatoms is largely unknown. In addition, there remain enormous ambiguities and mysteries about the mechanisms used by diatoms to absorb silicon, and then to process and template siliceous structures with such speed and precision. In this chapter we summarize the state of our knowledge on the development and nanostructure of diatom biosilica.

11.2 General Features of the Diatom "Glass House"

The diatoms from the algal class Bacillariophyceae (Heterokontophyta) are microscopic, unicellular protists that are major primary producers in most marine and freshwater habitats. Diatoms are immediately recognizable due to the presence of a highly ornate, silicified cell wall. Called a frustule, the morphology of the ''glass house'' is species-specific, and comprised of both silicified components and a range of organic layers and casings. A number of reviews cover the ultrastructure and cell biology of diatom wall formation in great detail [8–10], and we only summarize some of these features below. In addition, Chapters 9 and 10 of this volume are de-

Biomineralization: From Biology to Biotechnology and Medical Application, Second Edition. Edited by E. Bäuerlein

ISBN: 3-527-31065-7

voted to various aspects of diatom wall biogenesis, and many of the issues involved with diatom wall formation and silicification are discussed here.

The diatom frustule consists of two halves that typically overlap much like a Petri dish, a larger epitheca and a marginally smaller hypotheca (Figure 11.1). Each theca consists of a highly patterned valve plus one or more girdle bands that run around the circumference of the cell. The silicified valves and accompanying girdle bands are precisely attached to one another by organic layers (or adhesives) to form each theca. In addition, the silicified components are also associated with a range of organic casings that function in a variety of ways, including protection from desilicification [8–10]. As living cells must constantly interact with their environment, the valves and, to a lesser degree, girdle bands are formed with a myriad of openings (pores, slits, etc.) that facilitate such exchanges (Figures 11.1–11.10) [8, 9]. These openings are not randomly oriented but, together with other sculptured features of the valve, typically display a complex pattern and symmetry that is the basis of their taxonomy. Two major groups of diatoms are discerned: the radially symmetric "centric" diatoms and the bilaterally symmetric "pennate" diatoms.

The biogenesis and silicification of individual valves and girdle bands occurs within a single silica deposition vesicle (SDV) which is surrounded by a distinct membrane, the silicalemma [9]. The complex environment of the SDV determines the nanostructure and nanofabrication of diatom biosilica, and is discussed in more detail below.

11.3 The Chemistry of Biosilica Formation

Biomineralization studies seek to explore the mechanisms by which soft molecular structures such as surfactants and organic polymers (e.g. proteins, polysaccharides, glycoproteins) are able to template and direct the crystal growth or precipitation of "harder" inorganic minerals such as $CaCO_3$ and silica. The major problem with silica is the fact that it is comparatively inert chemically. Silicon forms few bonds with elements other than oxygen and direct Si–C bonds are unusual in the natural world. Hence, a method of sequestering silicon has remained largely undetermined. There are several points of chemical interest in the sequence of events required for the formation of diatom biosilica within a cytoplasmic SDV.

Firstly, the silica walls appear to be assembled from colloidal silica [11–13], although evidence suggests that diatoms do not directly transport colloidal silica, but use monomeric silica as a substrate [14–16] and then "gel" it within the SDV.

The exact nature and location of the organic–inorganic interface within the SDV is unknown, although a "matrix" material has been hypothesized to be involved in both the morphogenesis and silicification of the sculptured walls [7, 17].

It is not known how well the pH, salt and metal ion concentrations, can be regulated within the SDV, as a means of controlling the silica nucleation and growth processes.

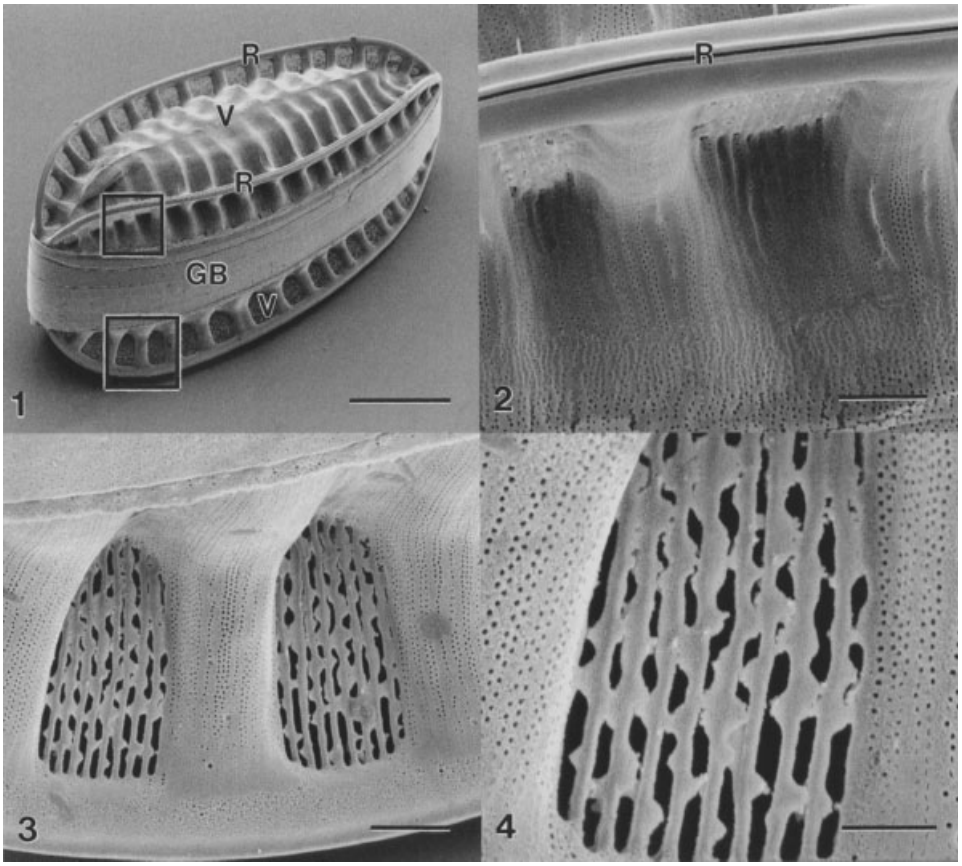

Figures 11.1–11.6 Field emission scanning electron microscope (FESEM) images illustrating the ornate morphology of the silicified frustule of *Surirella* sp. Figure 11.1 depicts a whole cell, illustrating basic diatom structure with two valves (V) joined by girdle bands (GB). In this species each valve has two raphes (R). Scale bar = 20 μm. Figures 11.2–11.4 show higher magnification images of the boxed regions of the cell shown in Figure 11.1. The major structural features of the valves are a result of macromorphogenesis, such as the raphe fissure shown in Figure 11.2. The tiny pores and some of the additional detail seen in Figures 11.4–11.6 probably results from micromorphogenesis. Scale bars = 2 μm for Figures 11.2, 11.3 and 11.5; 1 μm for Figure 11.4; 500 nm for Figure 11.6.

11.3.1 Parameters Affecting Silicon and Silicification

Sillén et al. [18] carried out potentiometric titrations of silicate ion in the early 1960s as part of their research into global weathering and pH control through geochemical processes. Much of their data was assimilated and analysed by Baes and Mesmer in their classic text, *Hydrolysis of Cations* [19]. More recently, Sjoberg et al. [20, 21] have remeasured the hydrolysis constants of Si(IV) in water at high NaCl con-

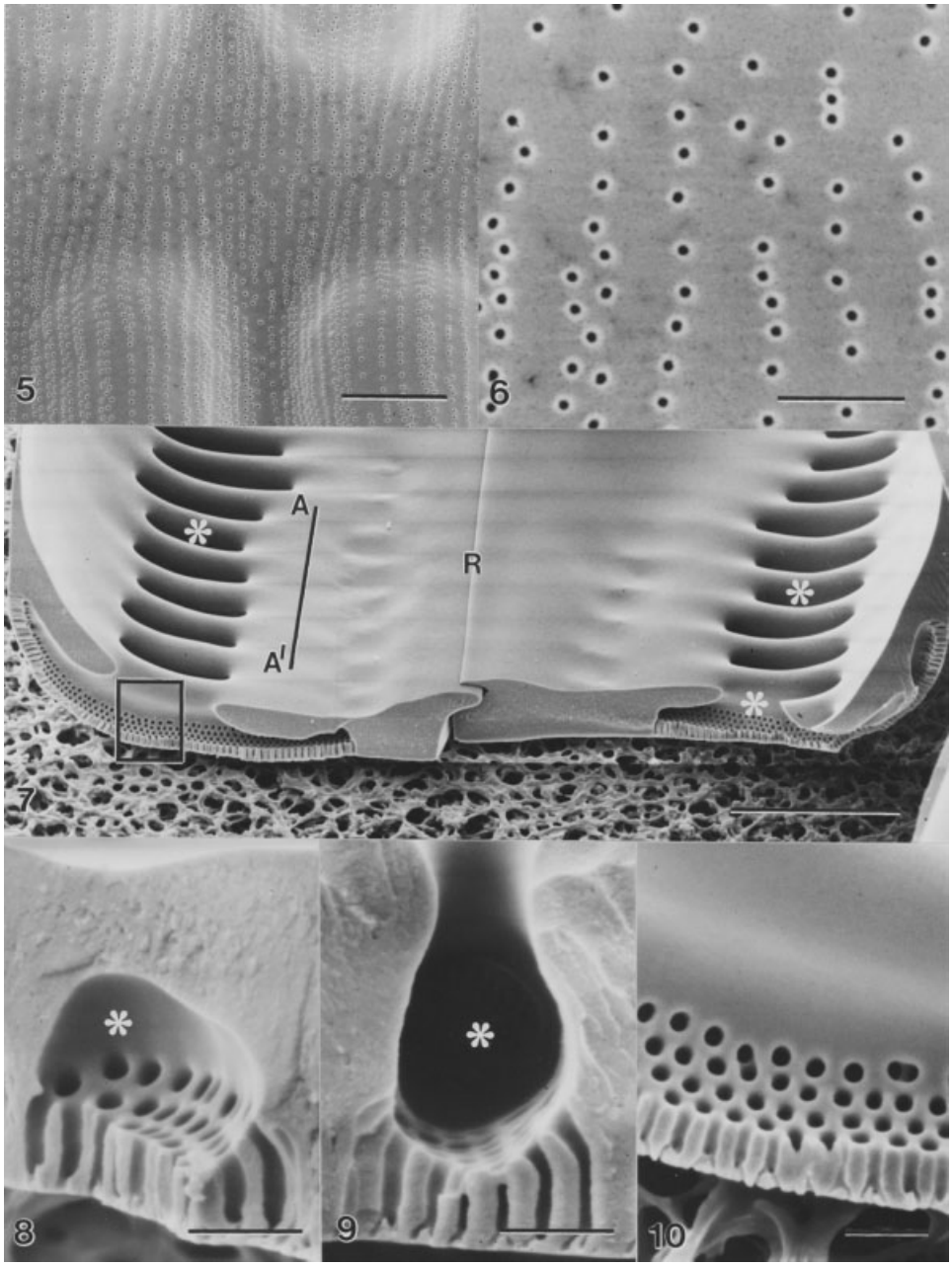

Figures 11.7–11.10 FESEM images of *Pinnularia* sp. Figure 11.7 shows a fractured valve in cross-section and viewed on the cytoplasmic surface, while the enclosed chambers seen in Figures 11.8 and 11.9 (asterisk) would result from a fracture along the AA′ axis seen in Figure 11.7. Figure 11.10 is a high magnification image of the boxed region in Figure 11.7. Note the results of molded macromorphogenesis including the raphe (R) in Figure 11.7 and the larger chambers (asterisks) in Figures 11.7–11.9. In Figures 11.8–11.10, the tiny pores organized in precise arrays result from micromorphogenesis. Scale bars = 5 μm for Figure 11.7; 500 nm for Figures 11.8–11.10.

centrations to mimic seawater. It is important to recognize that the speciation of silicon, like other species in solution, is determined firstly by resolving whether the solution is saturated or not with respect to the element. This is determined by the equilibrium:

$$SiO_2(s) + 2H_2O \Leftrightarrow Si(OH)_4(aq.) \quad K_{s10} \tag{1}$$

For quartz, $\log K_{s10} = -4.00$ (6 p.p.m.), whereas for amorphous silica $\log K_{s10} = -3.0$ to -2.7, about 10 times higher. Note that the silicic acid molecule has not been formally isolated; its existence has been inferred on the basis of nuclear magnetic resonance (NMR) spectroscopy, titration data and molybdate complexation. In view of the prolific abundance of sand, one can assume that marine waters close to land are saturated with respect to silicate ion. Hence at all times the $Si(OH)_4$ concentration is about 6 p.p.m. In laboratories the silicate ion concentration may be artificially reduced by keeping the diatoms in polythene bottles rather than glass vessels. Sufficient silicate will leach out of most commercial glasses within several hours when in contact with water at pH > 9.

Under these saturated conditions, the concentration of $Si(OH)_4$ is always given by Eq. (1). Depending on pH, electrolyte and chelate concentrations, the silicic acid will dissociate into a number of ions and oligomers. All the earlier researchers seem to concur that at low [Si], the hydrolysis of silicon is simple and involves only monomeric silicon species. The two important ionization equilibria are:

$$Si(OH)_4 + H_2O \Leftrightarrow SiO(OH)_3^- + H^+ \qquad \log K_{11} = -9.86 \tag{2}$$

At 0.5 M $NaClO_4$, this is lowered slightly to $\log Q_{11} = -9.46$, where the change to Q indicates the use of a supporting electrolyte to maintain constant activity coefficients. The second deprotonation has the following equilibrium constant:

$$Si(OH)_4 \Leftrightarrow SiO_2(OH)_2^{2-} + 2H^+ \qquad \log K_{12} = -22.92 \tag{3}$$

This species is only significant above pH 12 and can be ignored in studies of biosilica uptake. The total silicon dissolved in solution, Si_T is hence the sum of the individual concentrations:

$$Si_T = [Si(OH)_4] + [SiO(OH)_3^-] = [Si(OH)_4]^*\{1 + K_{11}/[H^+]\} \tag{4}$$

The speciation versus pH diagram for 10 μM Si(IV) is shown in Figure 11.11(a). Note that at pH 8, $Si(OH)_4$ accounts for over 90 % of the silicon in solution. At higher silicon concentrations or under conditions of supersaturation, polymers form. The stability constants for the two most well-established polymers have been measured to be:

$$4Si(OH)_4 \Leftrightarrow Si_4O_6(OH)_6^{2-} + 2H^+ + 4H_2O \qquad \log K_{12} = -13.44 \tag{5}$$

$$4Si(OH)_4 \Leftrightarrow Si_4O_8(OH)_4^{4-} + 4H^+ + 4H_2O \qquad \log K_{12} = -35.80 \tag{6}$$

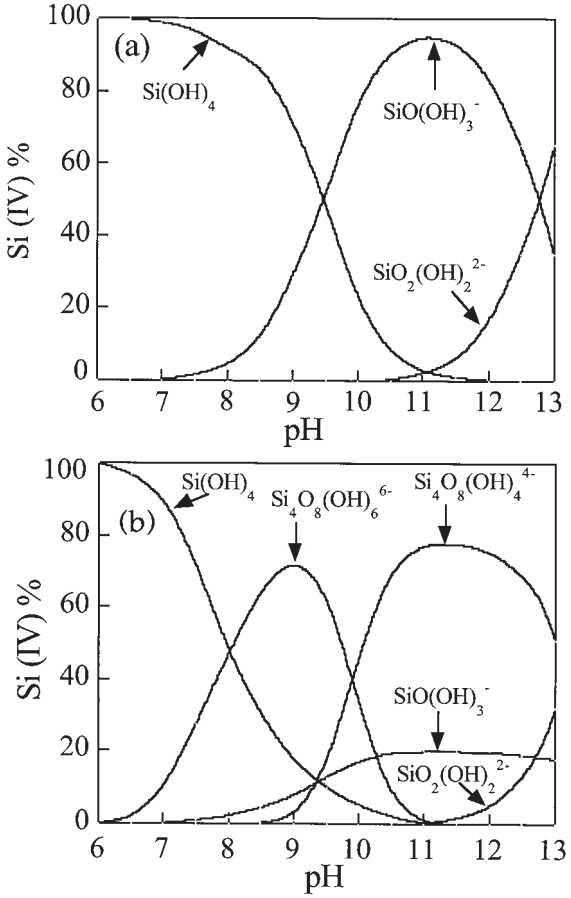

Figure 11.11 (a) Distribution of silicate species at an ionic strength of $I = 3$ m and 25 °C, for solutions containing 10 μM Si(IV). (b) Distribution of silicate species at an ionic strength of $I = 3$ m and 25 °C, for solutions containing 0.1 M Si(IV). The silicate species below pH 10 are supersaturated with respect to silica formation.

In natural waters, the silicon levels are low enough to preclude significant amounts of polynuclear species, and at pH 6–9, such species are only metastable anyway and will condense to form colloidal silica. The speciation diagram for Si(IV) at 0.1 M is shown in Figure 11.11(b). Note that below pH 10, the calculated concentrations are non-equilibrium values. Silica is thermodynamically favoured below pH 10 at 0.1 M Si(IV).

11.3.2 Hypothetical Effects of Chelating Agents on Silica Deposition

The above calculations fail to take into account the role of complexation and chelation by ligands, biomolecules and templating molecules that might exist in organ-

isms, such as within the cytoplasm and SDV of diatoms. Thus, normal chemistry fails to predict the nucleation conditions for silica precisely when it is needed most. Without tabulated values of the binding constants of amino acids, proteins, proteoglycans, sugars and membrane surfactants to silicate ions under various pH regimes, it is impossible to calculate the actual silicate concentration within the diatom nor can we be sure about the conditions needed for supersaturation. Ligands that form soluble silicates will increase the amount of total dissolved silica and make precipitation more difficult. Conversely, cations that can form very insoluble complexes, e.g. Ca or Mg, can render silica less soluble in water and assist deposition in biological systems.

The difficulties of interpretation can be highlighted by considering the binding of a silicate substrate to a hypothetical biomolecule or transporter. We will assume that the silicate is bound through an amine functional group on the biomolecule, which we will denote by NH_2R. First, the biomolecule could be aiding deposition by formation of *soluble* amino-silicates which are used to help build up a high, local concentration of silicate ions within the SDV. By simple modulation of the pH, it could release the silicate ion, which would then rapidly precipitate within the confines of the SDV.

Scheme 1:

$$\begin{aligned} &Si(OH)_4\ (\text{low},\ \text{CP}) + NH_2\text{–R}\ (\text{transporter}) \\ &\quad \Leftrightarrow Si(OH)_3NH\text{–R}\ (\text{high},\ \text{SDV}) + H_2O \end{aligned} \tag{7}$$

This equation denotes silicates being coerced into SDVs by complexation with transporter amines. CP refers to the cytoplasm, and low and high refer to relative silicate concentrations.

$$Si(OH)_3NH\text{–R} + H_2O + H^+ \Leftrightarrow Si(OH)_4\ (\text{high},\ \text{SDV}) + NH_3\text{–R}^+ \tag{8}$$

(pH lowered in SDV from 9 to 7; the amine protonates and releases silicic acid)

$$Si(OH)_4\ (\text{high},\ \text{SDV}) \Leftrightarrow SiO_2 + H_2O \tag{9}$$

(supersaturated silica precipitates)

Scheme 2:

Alternatively, the biomolecule could form a very *insoluble* complex with silicate ions, lowering its solubility within the SDV. This could be used to spatially direct nucleation. In this case, a transporter brings silicate ions to the SDV. As the concentration increases, nucleation on the silicalemma occurs:

$$\begin{aligned} &Si(OH)_4\ (\text{high},\ \text{SDV}) + NH_2\text{–R}\ (\text{template director molecule}) \\ &\quad \Leftrightarrow Si(OH)_3NH\text{–R}\ (\text{insoluble},\ \text{SDV wall}) + H_2O \end{aligned} \tag{10}$$

Spatial localization of a polyamine on the inner surface of the silicalemma and facing the SDV lumen, for example, could allow it to direct silicate nucleation. In this case, silicate ion is simply transported at high flux into the SDV. Precipitation of the least-soluble silicate is thermodynamically favored. If the solubility of the biosilicate complex is less than that of pure, colloidal biosilica, it will precipitate preferentially. This keeps the total silicate ion concentration below the threshold for silica nucleation and ensures homogeneous growth of the templated nuclei. Thereafter, the SDV silicate ions will condense onto the nascent silica surfaces. Hence, complexation of silicate by biomolecules can be utilized in several ways to serve biomineralization processes.

11.3.3 Silica Chemistry in Seawater

The uptake of silica as part of diatom valve/girdle band formation occurs at pH values in the range 6–9. At these pH values, the dominant monomers are $Si(OH)_4$ and $SiO(OH)_3^-$.

It is important to note that only monomers are significant even in alkaline solution and that these two species successfully account for silicon speciation from pH 7 to 10.5. Hence, under conditions where the sodium silicate concentration is kept below 100 μM, no insoluble silica exists and biogenic uptake must involve sequestration of one of these monomers.

The high sodium ion concentrations in seawater could, in principle, complicate the equilibria by formation of sodium silicate complexes. However, Sjoberg et al. [20, 21] find these can be neglected at low [Si] and at up to 0.5 M NaCl. Their values for Eq. (11) suggest that sodium binding is not important, although sodium levels may be critical in gel and colloid formation.

$$Na^+ + SiO(OH)_3^- \Leftrightarrow NaSiO(OH)_3 \qquad K = 0.37\ M^{-1} \tag{11}$$

The solubility of Si(IV) increases from $K_{s10} = 10^{-2.74}$ to $10^{-2.64}$ as the temperature is varied from 25 up to 35 °C and hence in normal marine environments there is no strong effect of temperature on the bioavailability of silicon.

11.4 Silica Uptake by Diatoms

Recent work has shown that the silica walls of diatoms consist of colloidal aggregates, gelled to form porous, non-crystalline layers [13]. This suggests that diatoms may in fact take silica up in monomeric form or even directly as a colloid building block. At least three factors dictate against this latter mechanism. First, the larger size makes intercellular and intracellular transport difficult. Second, mechanisms for biologically selecting colloidal particles and binding them would be difficult. Third, the concentration of ''active'' particles capable of being taken up is capricious, being controlled by solution phase kinetic factors, ionic strength, complexation, li-

gand concentrations, etc., and pH fluctuations [22]. Finally, silica growth is observed even when no insoluble silica is present in solution!

The rates of silica valve growth are so fast that normal diffusion is not considered adequate and "active" transport of silica in some form is necessary [14, 15] to provide the flux of silicon to the SDV for deposition. For the reasons outlined above, it seems likely that active transport is used to transfer silica monomers into the diatom and to the SDV. Colloidal silica could then be generated by controlled polymerization of silica monomer within the confines of the SDV, using pH, chelators and alkali metal ion concentrations to modulate gelation and colloid growth processes.

The rate of growth of diatoms appears to be incredibly fast, and hence many authors refer to the miracle of "active" transport. If convection is assumed to be low, the maximum rate at which silicon monomers could be taken up from the solution by the growing diatom is fixed by diffusion. We can estimate this "diffusion-limited" rate of growth as follows. The diffusive flux to a single diatom is given by:

$$J_{\text{diff}} = \frac{4\pi a D}{10^3}[\text{Si}]_\infty \text{ mol/s} \tag{12}$$

where a is the diatom radius, D the silicate ion diffusion coefficient and $[\text{Si}]_\infty$ is the bulk solution silicate concentration. Taking the diatom to be a 5 μm radius sphere with a silica shell thickness of 2 μm and taking $D \sim 10^{-5}$ cm^2/s for the $Si(OH)_4$ diffusion coefficient, yields a value of about $J_{\text{diff}} \sim 5 \times 10^{-16}$ mol/s. We have assumed a silica monomer concentration of just 10 μM. The total volume of silica required for the shell described is 4×10^{-10} cm^3. Hydrated silica has a molar volume of about $V_m = 35$ cm^3/mol, so the number of moles of silica needed to be absorbed by the diatom is roughly 1×10^{-11} mol. The time to accrue this silica under optimal conditions is hence:

$$\begin{aligned} t_{\text{growth}} &= \text{moles required/diffusive flux} = 1 \times 10^{-11}/5 \times 10^{-16} \\ &= 2 \times 10^4 \text{ s} \end{aligned} \tag{13}$$

If the silica concentration were 100 times higher at 1 mM, this would reduce to just 200 s! Based on these figures it is easy to see that provided diatoms are able to effectively sequester silicon by surface complexation and to actively transport it into the cytoplasm, there is little difficulty in explaining the growth of diatoms on a time scale of minutes to hours. In fact, Sullivan has estimated that total soluble silica concentrations inside the diatom lie in the range 450–700 nM [23, 24], which is very high. This suggests that uptake of silicon by the diatom is very efficient and the rate of growth could be pushed towards the diffusion-limited rate.

11.5 Nanostructure of Diatom Biosilica

Early structural evidence suggested that the silica valves/girdle bands had a nanostructure resembling globular particles and they appeared to be constructed of col-

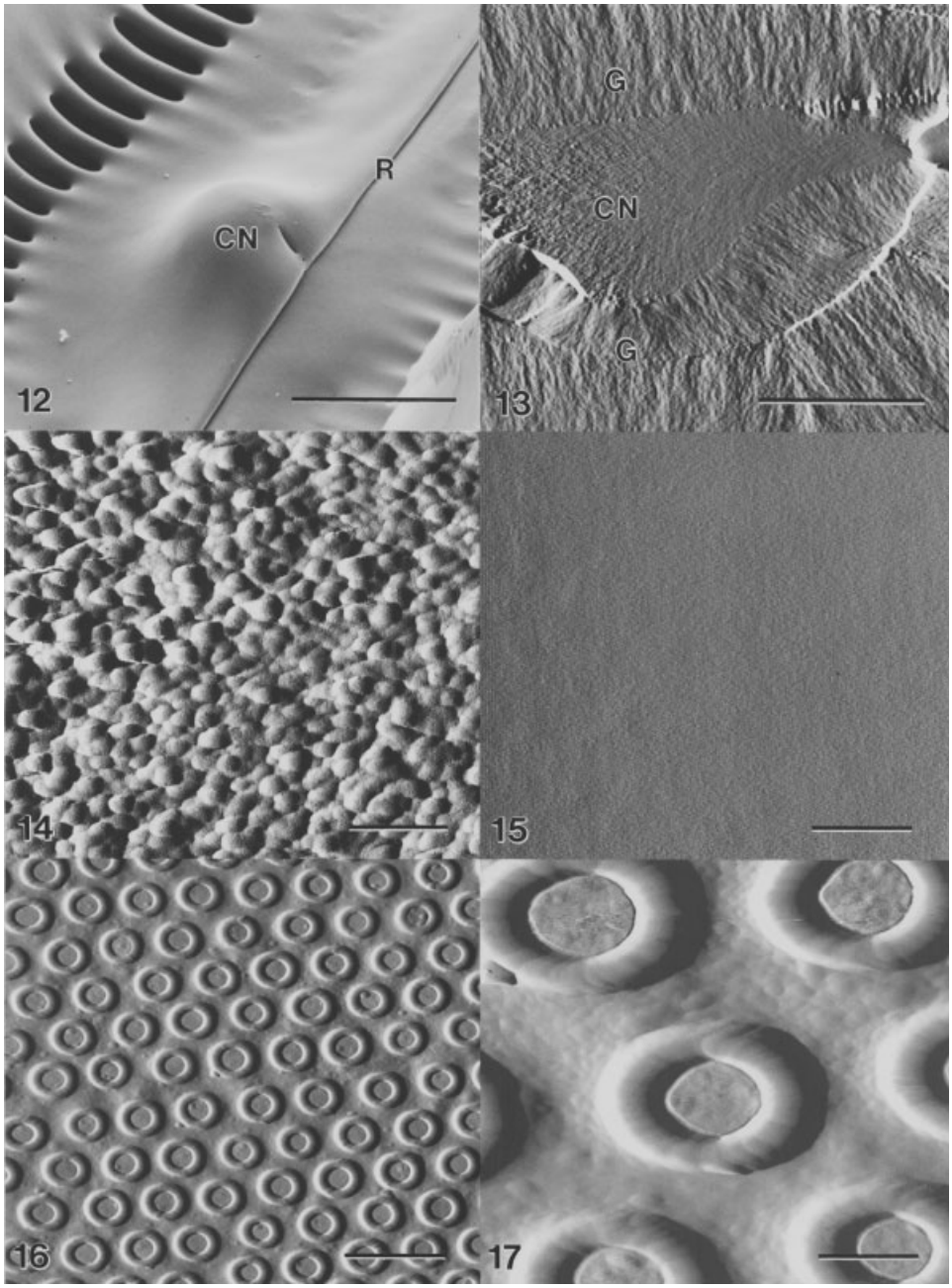

Figure 11.12 FESEM image of the internal valve surface of *Pinnularia* sp. showing the raphe fissure (R) and central nodule (CN). Scale bar = 5 μm.

loidal silica [11, 12]. Our own atomic force microscopy data fully support this result, i.e. that the walls show globular silica in cross-section (Figures 11.12–11.14, 11.16 and 11.17). However, it is interesting that the surface of many frustule components can be perfectly smooth (e.g. Figure 11.15), while other surface images reveal the globular silica. This in turn raises the question whether diatoms are able to manipulate colloidal silica and whether they take up colloidal silica directly. Two factors dictate against the direct uptake of colloidal material. The first is simply that diatoms can grow even under conditions of strongly undersaturated silicon, e.g. at micromolar concentrations, albeit it more slowly. As highlighted above, under these conditions, only monomeric silicon species exist in solution, as determined from Figure 11.11. The second fact is that oligomeric silica exists in a range of sizes from 0.5 to 4 nm in diameter. In this size regime, it redissolves rapidly, undergoes Ostwald ripening, and the particle size is strongly affected by both pH and electrolyte levels. It seems unlikely that active uptake via a membrane transporter species would be reliable if the speciation is so prone to size fluctuations. Growth would technically only be possible in saturated silica solutions, which would be a colossal disadvantage to the diatom. It seems more likely that the colloidal silica that is observed in cell walls is a product of internal morphogenic processes.

A number of key papers have been published in this area. By monitoring the uptake kinetics via radiolabeling, it has recently been shown that the most likely species to be the active substrate for transport is $Si(OH)_4$. Again growth was observed at silicon levels down to 15 μM, well below the level where any colloidal silica could be present. This implies that at some point during internal transport, or directly within SDVs, the silicon is then assembled into colloidal particles for incorporation into the growing valve. Hildebrand et al. [14] have now identified a protein which they claim is the active silicon transporter that brings $Si(OH)_4$ [16] into the cell cytoplasm. It is not clear whether the same transporter or a relative is then responsible for transfer of silicon to the SDV and ''developing'' wall. This cytoplasmic transport issue has not been directly addressed as yet and is discussed in detail in Chapter 9 of this volume.

Figures 11.13–11.17 AFM images. Figure 11.13 is an AFM image of the *Pinnularia* valve in cross-section, mounted in epoxy glue (G) and fractured through the region of the central nodule (CN) by a technique described by Egerton-Warburton et al. [29]. Figure 11.14 shows a high-resolution AFM image of the *Pinnularia* valve in cross-section revealing the globular particle structure. Figure 11.15 is an AFM image of the internal surface of the valve seen in Figure 11.12 and reveals a perfectly smooth surface where the particulate structure is no longer observed. Figures 11.16 and 11.17 are AFM images of the outer valve surface of the centric diatom *Coscinodiscus* sp. showing larger pores that result from macromorphogenesis. The surface of this species is not smooth as seen in Figure 11.15, but Figure 11.17 reveals that the globular particulate structure can be seen in high magnification. Scale bars = 5 μm for Figure 11.13; 2 μm for Figure 11.16; 500 nm for Figures 11.14, 11.15 and 11.17.

11.6 Development of Diatom Biosilica within a Confined Space – Silica Deposition Vesicles (SDVs)

The intricate and highly patterned valves of diatoms are species-specific and therefore genetically determined, although alterations to the chemical composition and thickness of valves can be induced by the cell's environment [9]. All of this information must impact on the SDVs, which seemingly regulate all aspects of valve/girdle band nanofabrication. Two primary hypotheses have been proposed to explain the processes of diatom wall morphogenesis within SDVs. The first is that patterning and silicification are nucleated and controlled simply by the physicochemical environment, and constraints provided by the SDV and the silicalemma [25, 26]. According to this hypothesis, cytoplasmic components imprint on the outer surface of the silicalemma to mold and shape the wall, followed by autopolycondensation of silica within the SDV [26]. These cytoplasmic molding processes are referred to as macromorphogenesis [9, 27] and have been observed during the expansion of the SDV in a range of diatoms. A highly patterned arrangement of organelles (e.g. mitochondria, endoplasmic reticulum, ''spacer vesicles'') as well as cytoskeletal components (e.g. microtubules and microtubule-associated molecules and complexes) become closely associated with the silicalemma, restricting SDV expansion to form structural features such as pores, slits and chambers of various size and shape. The larger compartments seen in Figures 11.1–11.3 and 11.7–11.10 are examples of macromorphogenesis, including the slit-like raphe (Figure 11.2) that is responsible for diatom adhesion and motility. The exact way in which molding occurs is not known and it is also possible that silica deposition is selectively controlled within the SDV by cytoplasmic components interacting through the silicalemma. Therefore, the macromorphology of the enclosed, developing valve may be affected in a number of ways.

There is extensive evidence in support of SDV molding during valve formation, but far less information about events that occur within the silicalemma. It has been postulated that silicification and fine patterning may be induced by the presence of an organic matrix or template located within the SDV [7, 9, 17]. Presumably, this template could be attached to the inner surface of the silicalemma, within the SDV lumen or both. If organic matrix material exists within the SDV lumen, it may exist embedded or encased within the globular silica particles, as surface strands or coatings surrounding the colloidal silica, or both. The processes isolated to the inner silicalemma have been referred to as ''membrane-mediated morphogenesis'' [9, 27], while we use the term micromorphogenesis to refer to all processes that occur within the SDV lumen, including those generated from the silicalemma. The tiny pores that often dominate the valves, and occasionally the girdle bands, of several diatoms illustrate a structure that must result from a form of micromorphogenesis (Figures 11.3–11.6, 11.8–11.10). In *Pinnularia*, Pickett-Heaps et al. [28] showed that the highly patterned, tiny pores of the valve (Figures 11.7–11.10) were not surrounded by the silica membrane during their formation, but arose within the lumen during valve development. We assume here that the pore openings must have re-

sulted from a template on the inner surface of the expanding silicalemma, blocking silicification at those points, or perhaps by the precise deposition of an organic component that prevents mineralization. Alternatively, it is possible that a cytoplasmic component acts through the silicalemma via a transmembrane connector (i.e. macromorphogenesis). Another example of micromorphogenesis might be the perfectly flat surfaces of some silica components (Figures 11.12 and 11.15), which may result from a specific molecule (or template) that only exists on the inner surface of the SDV at the completion of valve formation. If micromorphogenesis is the mechanism, it must be possible to identify and characterize the responsible molecules.

It should be noted that no organic component has thus far been localized within the developing SDVs of diatoms, although there are many hypotheses about their existence [9, 27]. A protective coating of organic material is known to encase the mature silicified components of the frustule, although there is no evidence at present that these coatings are synthesized within the SDV or that they are in any way involved in morphogenesis or silicification. If present, embedded matrix molecules might be isolated from mature walls. Although this approach has resulted in the characterization of a number of wall-associated proteins (i.e. frustulins and HEP proteins) [30–32], these proteins have been localized to the surface of the silicified wall components and not within developing SDVs. It appears that the frustulins and HEP proteins are unlikely to be involved in mineralization or morphogenesis. However, in the closely related chrysophycean alga *Mallomonas*, we have shown a protein and glycoprotein to be localized to the mature silicified scales and bristles and within their developing SDVs [33], suggesting that similar organic molecules will be found within diatom SDVs as well. The recent discovery of silaffins isolated from diatom biosilica [7] indicates that an organic template may have a role in diatom wall silicification. However, the silaffins have yet to be formally localized to the SDV, although they have very interesting properties, as demonstrated by their ability to generate silica spheres of uniform morphology when added to a solution of silicic acid.

In many organisms, interactions between an organic matrix and mineral results in the controlled nucleation, growth and final morphology of the biomineralized structure [34], and such mechanisms have been shown to operate during biosilicification in molluscs and sponges [3, 34, 35]. Biochemical and molecular analyses of materials isolated from demineralized diatom frustules provide the only evidence to date for an organic matrix or template [7, 17, 24, 35–37 (note, concentration units are incorrect in 24, p. 151)], and these studies indicate the presence of proteins and/or polysaccharides associated with the frustule. In most cases the organic coverings could not have been totally removed from the silicified components with the extraction conditions used and the resulting ''matrix'' material was undoubtedly contaminated with these surface materials. Regardless, the published data provide no basis from which to infer mechanisms of morphogenesis and silicification in diatoms.

11.7 Transport of Silica to the SDV

Reimann [11] and later Dawson [12] both suggested that the silica is transferred into the SDV by fusion of smaller vesicles containing either colloidal or polymeric silica. Once within the SDV that directs silica deposition, the major biomineralization events take place. Some of the critical observations are as follows:

(1) Silica deposition stops after the silicalemma is lost – hence, the particular environment offered by the SDV is critical. After the new valve is secreted onto the cell surface, silica dissolution becomes possible. However, this is offset by the presence of an organic coating that inhibits chemical dissolution. This layer is apparently 8–10 nm thick and of unknown origin [9].
(2) The SDV expands as the silica wall grows, so the growing silica surface is always in the same environment with respect to any organic component. This may be essential to ensuring consistent deposition.
(3) Various studies have reported silica spheres to be present in the nanostructure of diatom biosilica [25, 37, 38]. The spheres are usually 10–50 nm in size, but are mostly 30–50 nm. Many appear to be aggregates of smaller spheres and occasionally some are up to 200 nm.
(4) These spheres have been found also in early walls with smaller sizes of 3–20 and 40–50 nm. The implication is that the smaller particles are primary particles [12]. In some cases, the spheres appear to be organized into regular arrays.
(5) According to Schmid and Schulz [25], all silica grows by accretion of silica spheres, which become compacted with age. Schmid [38] had earlier found that the younger growing zone consisted of a loose assemblage of small silica spheres, and the older zone was compacted. They claimed that there was a clear younger/older zone visible in the walls. Subsequently they also presented evidence for the silica spheres originating in 30–40 nm cytoplasmic vesicles [25]. Leaching with SDS or acid was used to support the presence of silica in these extraneous vesicles. Finally, they also suggested that a second type of silica was involved in filling in the spaces [25].

Once again, this data comes from microscopic images of diatom thin sections, and information on the chemistry and the chemical environment of the SDV is sparse. If silicate ion is accumulated against the natural concentration in solution, this requires energy. In principle, deposition of silica is only thermodynamically feasible once it reaches saturation levels of 6 p.p.m. within the SDV. However, precipitation is possible at lower concentrations if it occurs via precipitation of insoluble metal silicates [39] or as an organic chelated complex (e.g. an amino acid–silicate). The evidence from elemental composition is that the walls are predominantly amorphous silica, so the precipitation through reaction with Mg (or Ca, Fe, Al, Mn) within the SDV via:

$$Ca^{2+} + SiO(OH)_3^- \Rightarrow CaSiO_3 + H_2O + H^+ \quad (14)$$

does not seem plausible at this time. If the valve is more or less silica then, at the time of nucleation and growth, the local silicate concentration must exceed its solubility at that intracellular pH value. Silicate deposition can be accelerated by decreasing the overall solubility of silicate ions by acidifying the SDV in the region of valve growth:

$$SiO(OH)_3^- + H^+ \Rightarrow SiO_2 + 2H_2O \tag{15}$$

From Figure 11.11(a and b), we see that below pH 6 the only species in solution is silicic acid with a solubility of 6 p.p.m. The major question is then how to rationalize the fact that the diatom walls are clearly made up of globular particles in cross-section (Figures 11.12–11.14) and are not molecularly smooth as would be predicted if they were assembled from $Si(OH)_4$ by a molecular accretion process.

The monodispersity of the globular particles suggests a mechanism that is independent of the vagaries of nucleation and is controlled. This would be more easily explained by concentration of the silica in a spatially and chemically controlled microenvironment such as SDVs. The prerequisites appear to be:

(1) The cell needs to prevent random precipitation of silica within the cytoplasm.
(2) The Si(IV) must at some point exceed 3–4 mM if it is to precipitate.
(3) The pH must be kept reasonably low to ensure rapid polymerization and nucleation/growth.
(4) It needs to be moved to the walls without redissolving in low [Si] environments.

The actual morphology of the silica is influenced by pH and pNa. At high pH, surface charge causes the silicate ions to condense as colloidal spheres, whereas at intermediate pH, where the surface charge is lower, cross-linking of silicate polymers to form networks and gels occurs via siloxane formation:

$$SiOH + SiO^- \Rightarrow Si{-}O{-}Si + OH^- \tag{16}$$

The necessity for anionic surface sites, which facilitate nucleophilic attack of the hydroxylated silicon by the negative charge on the ionized silicon requires $4 < pH < 9$. Above pH 9, the silicate solubility increases due to formation of anionic complexes and the reaction in Eq. (16) tends to run to the left, i.e. there are increasing rates of silica dissolution and uncontrolled reprecipitation. If the Na or K level is high, gelation occurs. Consequently, the ideal conditions for silica deposition as globular particles or colloidal silica are low pH and low alkali metal concentrations. Vrieling et al. [40] have recently reported that the SDV is acidic, which they established via fluorescence experiments with a pH-dependent fluorophore.

As valve formation is completed, it appears they may undergo some further cross-linking and ripening, which leads in some species to incredibly smooth silica surfaces (Figure 11.15). This could be rationalized by simple control of pNa levels and by Ostwald ripening. Once the initial silica globules are deposited, addition of

Na or acid to the SDV will drive silica gelation and lead naturally to the pores being filled. In addition, transition metals will react with silicate within the valves to form insoluble silicates.

11.8 Micromorphogenesis and an Organic Matrix?

The question remains as to whether the diatom valve is assembled from colloidal silica, which is itself constructed from monomers within vesicles, or does the globular particle structure come about as a result of rapid deposition of monomers by a template-directing organic matrix? The final answer here is likely to depend on the nature of the biomineralizing matrix (e.g. proteins?). Two templating candidates have recently appeared for two different types of silicified structure. Shimizu et al. [4] have isolated a protease from sponge spicules (silicatein) where the active site contains a serine. It is proposed that this hydroxyl-containing amino acid "participates in the organization of silicic acid precursors" [4]. This supports a computer model based on hydroxyl chelation [41].

Perhaps a more chemically satisfactory candidate has now been isolated from a diatom [7]. This polycationic peptide directs silica formation via pendant polyamines that are grafted biochemically onto a protein backbone. This molecule drastically alters the rates of silicate precipitation. Importantly, these results correlate strongly with the known catalytic effects of polyamines on sodium silicate nucleation [42–44]. Such amines would lower the solubility of silicate ion, provide a template for nucleation and would control the silica colloid size within the SDV. In fact, we may argue that the globular particles of silica observed by AFM, and transmission and scanning electron microscopy reflect the chain lengths of the polyamines used to direct silica deposition. However, once again, at this stage the silaffins have yet to be formally localized to the SDV and growing walls.

11.9 Conclusions

Ultimately, it seems obvious that if active transport is capable of sequestering monomeric silica in one of its pH-dependent forms, and transferring it through the plasma membrane and into the SDV, then such molecules or enzymes may also be able to directly cement each monomer into the growing valve. The active transport molecule/enzyme can be guided into position via membrane proteins. However, ultimately the cross-linking of the silica monomer to the nascent wall is governed by silica chemistry. Thus strong limits on pH and salt are still necessary. Conversely, the deposition may simply be due to the excess monomer concentration within the SDV due to the active transport enzyme causing accumulation of silicic acid that then deposits into the silicalemma-lined mold. In either case, identification

of the active moieties responsible for silica complexation is vital for further elucidation of the mechanisms of silicification by diatoms.

Acknowledgments

R. W. thanks the Office for Naval Research (USA) and all three authors thank the Australian Research Council for financial support.

References

[1] S. Mann, *Nature* **1993**, *365*, 499–505.
[2] S. Oliver, A. Kupermann, N. Coombs, A. Lough, G. A. Ozin, *Nature* **1995**, *378*, 47–50.
[3] J. N. Cha, K. Shimizu, Y. Zhou, S. C. Christiansen, B. F. Chmelka, G. D. Stucky, D. E. Morse, *Proc. Natl Acad. Sci. USA* **1999**, *96*, 361–365.
[4] K. Shimizu, J. N. Cha, G. D. Stucky, D. E. Morse, *Proc. Natl Acad. Sci. USA* **1998**, *95*, 6234–6238.
[5] A. M. Belcher, X. H. Wu, R. J. Christensen, P. K. Hansma, G. D. Stucky, D. E. Morse, *Nature* **1996**, *381*, 56–58.
[6] H. A. Lowenstam, S. Weiner, *On Biomineralization*, Oxford University Press, New York, **1989**.
[7] N. Kröger, R. Deutzmann, M. Sumper, *Science* **1999**, *286*, 1129–1132.
[8] F. Round, R. Crawford, D. Mann, *The Diatoms. Biology and Morphology of the Genera*, Cambridge University Press, Cambridge, **1990**, pp. 1–129.
[9] J. D. Pickett-Heaps, A.-M. M. Schmid, L. A. Edgar, in *Progress in Phycological Research, Vol 7* (Eds F. E. Round and D. J. Chapman), Biopress, Bristol, **1990**, pp. 2–168.
[10] N. Kröger, M. Sumper, *Protist* **1998**, *149*, 213–219.
[11] B. E. F. Reimann, J. C. Lewin, B. E. Volcani, *J. Phycol.* **1966**, *2*, 74–84.
[12] P. Dawson, *J. Phycol.* **1973**, *9*, 353–365.
[13] E. G. Vrieling, T. P. M. Beelen, R. A. van Santen, W. W. C. Gieskes, *J. Phycol.* **2000**, *36*, 146–159.
[14] M. Hildebrand, B. E. Volcani, W. Gassmann, J. I. Schroeder, *Nature* **1997**, *385*, 688–689.
[15] M. Hildebrand, K. Dahlin, B. E. Volcani, *Mol. Gen. Genet.* **1998**, *260*, 480–486.
[16] Y. Del Amo, M. A. Brzezinski, *J. Phycol.* **1999**, *35*, 1162–1170.
[17] D. M. Swift, A. P. Wheeler, *J. Phycol.* **1992**, *28*, 202–209.
[18] L. G. Sillén, in *Oceanography* (Ed. M. Sears), American Association for Advancement of Science, Washington, DC, **1961**.
[19] C. F. Baes, R. E. Mesmer, *The Hydrolysis of Cations*, Robert Krieger, Malabar, FL, **1986**.
[20] S. Sjöberg, Y. Hägglund, A. Nordin, N. Ingri, *Mar. Chem.* **1983**, *13*, 35–44.
[21] S. Sjöberg, A. Nordin, N. Ingri, *Mar. Chem.* **1981**, *10*, 521–532.
[22] R. K. Iler, *The Chemistry of Silica: Solubility, Polymerization, Colloid and Surface Properties, and Biochemistry*, Wiley, New York, **1979**.
[23] C. W. Sullivan, *J. Phycol.* **1976**, *12*, 390–396.
[24] D. H. Robinson, C. W. Sullivan, *Trends Biochem. Sci.* **1987**, *12*, 151–154.
[25] A.-M. Schmid, D. Schulz, *Protoplasma* **1979**, *100*, 267–288.
[26] S. Mann, in *Biomineralization in Lower Plants and Animals* (Eds B. S. C. Leadbeater and R. Riding), Clarendon Press, Oxford, **1986**, pp. 39–54.

[27] A.-M. M. Schmid, *Protoplasma* **1994**, *181*, 43–60.
[28] J. D. Pickett-Heaps, D. H. Tippit, F. A. Andreozzi, *Biologie Cellulaire*, **1979**, *35*, 199–206.
[29] L. M. Egerton-Warburton, S. T. Huntington, P. Mulvaney, B. J. Griffin, R. Wetherbee, *Protoplasma* **1998**, *204*, 34–37.
[30] N. Kröger, C. Bergsdorf, M. Sumper, *EMBO J.* **1994**, *13*, 4676–4683.
[31] N. Kröger, C. Bergsdorf, M. Sumper, *Eur. J. Biochem.* **1996**, *239*, 259–264.
[32] N. Kröger, G. Lehmann, R. Rachel, M. Sumper, *Eur. J. Biochem.* **1997**, *250*, 99–105.
[33] (a) M. Ludwig, J. L. Lind, E. A. Miller, R. Wetherbee, *Planta* **1996**, *199*, 219–228; (b) T. F. Schultz, L. M. Egerton-Warburton, S. Crawford, R. Wetherbee, *Protist* **2001**, *152*, 315–327.
[34] H. A. Lowenstam, *Science* **1981**, *211*, 1126–1131.
[35] T. L. Simpson, B. E. Volcani (Eds), *Silicon and Siliceous Structures in Biological Systems*, Springer, New York, **1981**, p. 6.
[36] R. E. Hecky, K. Mopper, P. Kilham, E. T. Degens, *Mar. Biol.* **1973**, *19*, 323–331.
[37] B. E.Volcani, in *Silicon and Siliceous Structures in Biological Systems* (Eds T. L. Simpson and B. E. Volcani), Springer, New York, **1981**, pp. 157–200.
[38] A. M. Schmid, *Nova Hedwigia* **1976**, *28*, 309–351.
[39] W. Stumm, J. J. Morgan, *Aquatic Chemistry*, Wiley-Interscience, New York, **1970**.
[40] E. G. Vrieling, W. W. C. Gieskes, T. P. Beelen, *J. Phycol.* **1999**, *35*, 548–559.
[41] K. D. Lobel, J. K. West, L. L. Hench, *Mar. Biol.* **1996**, *126*, 353–360.
[42] G. M. Lindquist, R. A. Stratton, *J. Coll. Interface Sci.* **1976**, *55*, 45–59.
[43] T. Mizutani, H. Nagase, N. Fujiwara, H. Ogoshi, *Bull. Chem. Soc. Jpn* **1998**, *71*, 2017–2022.
[44] T. Mizutani, H. Nagase, H. Ogoshi, *Chem. Lett.* **1998**, 133–134.

Calciumcarbonates

Biomineralization: From Biology to Biotechnology and Medical Application,
Second Edition. Edited by E. Bäuerlein

ISBN: 3-527-31065-7

12 Biomineralization in Coccolithophores

Mary E. Marsh

12.1 Introduction

Biomineralization in coccolithophores is a phenomenon of global importance. The appearance of coccolithophores and foraminifera – calcareous nanoplankton – in the late Triassic marked the onset of calcium carbonate sedimentation in the deep ocean, a process thought to stabilizes the carbon cycle today [1]. The massive chalk and limestone deposits formed from the calcitic scales of coccolithophores are a dramatic testament to their impact on the structure and composition of the lithosphere. Coccolithophores as calcite ($CaCO_3$)-secreting phytoplankton also impact the atmosphere by consuming CO_2 during photosynthesis and generating CO_2 during calcification [2]. In today's oceans, coccolithophores are the major produces of pelagic $CaCO_3$ and CO_2 (Eq. 1), yet the biology and regulation of coccolithophore calcification is still poorly understood.

$$Ca^{2+} + 2HCO_3^- \leftrightarrow CaCO_3 + CO_2 + H_2O \quad (1)$$

The coccolithophores are a clade within the division Haptophyta – a phylogenetic group of unicellular predominantly marine phytoflagellates [3–6] descended from a red alga–protozoan chimera formed about 1.2 billion years ago [7, 8]. The coccolithophores are distinguished from other haptophytes by their production of an outer covering of calcitic scales known as coccoliths (Figure 12.1) during at least one stage of their life history. Coccolithophores first appear in the geological record in the late Triassic and attain their maximum abundance and diversity in the late Cretaceous (references in Young et al. [9]). Most species became extinct at the Cretaceous/Tertiary boundary [10] and new species subsequently emerged. Although there are numerous extant coccolithophores, biomineralization studies have necessarily been limited to species that are easily maintained in laboratory culture – *Pleurochrysis carterae*, *Emiliania huxleyi* and, to a lesser extent *Coccolithus pelagicus*. *Pleurochrysis* and *Coccolithus* are costal and subpolar genera, respectively. *Emiliania huxleyi* is the most abundant and cosmopolitan species today, and forms vast coastal and mid ocean blooms.

$CaCO_3$ formation in coccolithophores is regulated by processes that control ion accumulation, calcite nucleation and crystal growth. Ion accumulation refers to

Biomineralization: From Biology to Biotechnology and Medical Application, Second Edition. Edited by E. Bäuerlein

ISBN: 3-527-31065-7

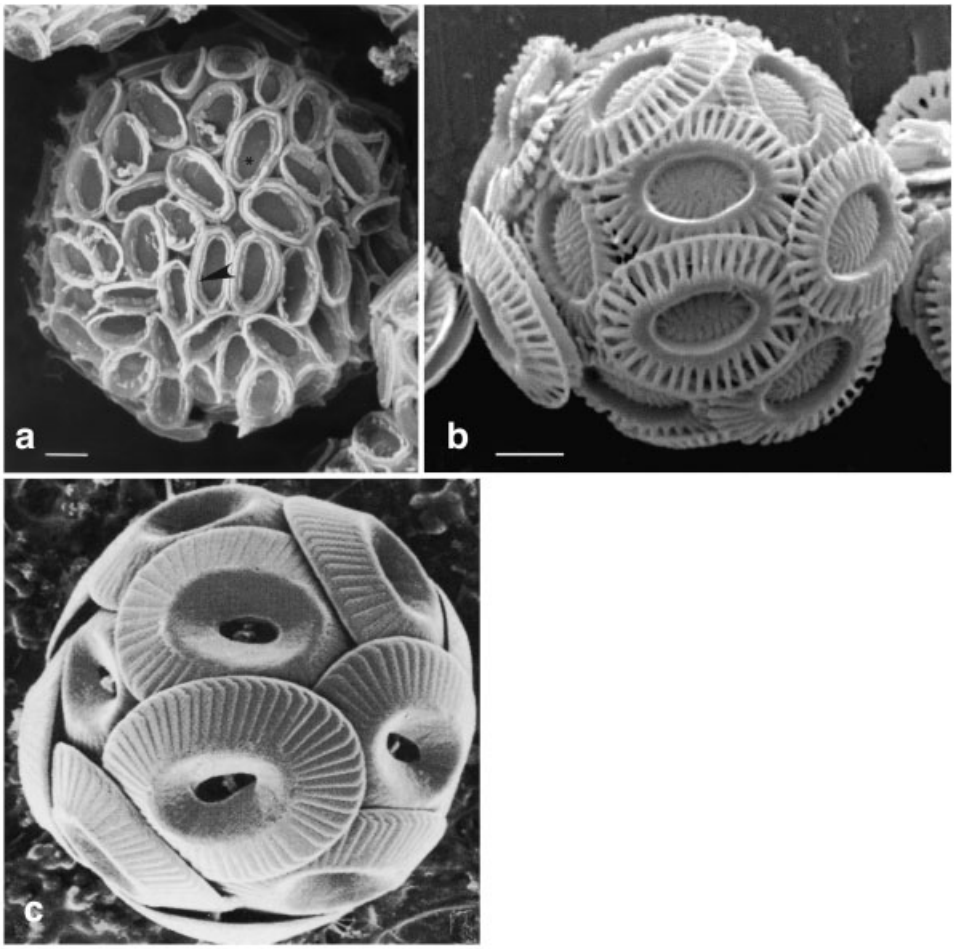

Figure 12.1 Scanning electron micrographs of coccolithophores. (a) *Pleurochrysis carterae* (reproduced from Marsh [13]). The mineralized rims (arrow head) and organic base plates (×) of the coccoliths are indicated. (b) *Emiliania huxleyi*. (c) *Coccolithus pelagicus* (image by S. Nishida). Bar = 1.0 μm.

processes which generate and maintain a medium supersaturated with respect to $CaCO_3$ at mineralizing foci throughout calcite nucleation and crystal growth; it includes temporally and spatially controlled mechanisms for amassing calcium and bicarbonate ions and removing hydrogen ions. Nucleation refers to all processes and factors other than ion accumulation that determine the rate and site of calcite nucleation, and the crystallographic orientation of the initial mineral phase. Growth includes all processes subsequent to nucleation that regulate crystal growth and morphology.

The remainder of this chapter describes the molecular, cellular and structural aspects of coccolith formation in *Pleurochrysis*, *Emiliania* and *Coccolithus* as it is pres-

ently understood. The calcifying function of acidic polysaccharides and large molecular aggregates is addressed by comparing their expression in wild-type cells, poorly calcifying mutants and naturally occurring non-calcifying morphotypes. Finally, the impact of biomineralization on the Quaternary pCO_2 flux and global climate is explored in relationship to coccolithophore phase transitions between calcifying and non-calcifying (or poorly calcifying) morphotypes.

12.2 Heterococcolith-bearing Morphotypes

12.2.1 Coccolith Structure

Coccoliths are composed of $CaCO_3$ crystals attached to an underlying oval-shaped organic base plate (Figure 12.2) and are classified as heterococcoliths or holococcoliths based on calcite crystal morphology. Heterococcolith crystals have intricate complex shapes that are species specific and not observed in inorganically formed mineral (Figures 12.1–12.4). The *Pleurochrysis*, *Emiliania* and *Coccolithus* heterococcoliths are known as placoliths because their crystals form parallel double disks which radiate from the coccolith rim [11]. The double disks are actually a ring of single interlocking crystals with alternating radial (R) and vertical (V) orientation – a structure that may be common to heterococcoliths in general [12]. V and R refer to the alignment of the crystallographic *c*-axes of the crystal units with respect to the coccolith plane. The parallel disks are known as the distal and proximal shield

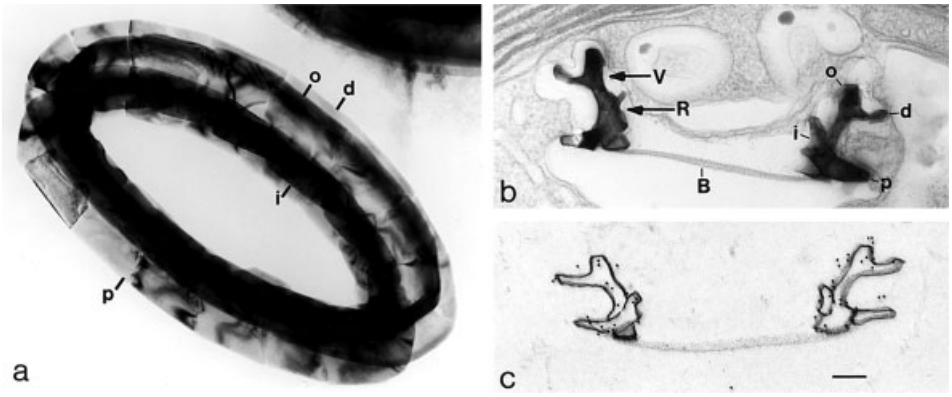

Figure 12.2 Transmission electron micrographs (TEM) of *Pleurochrysis* coccoliths. (a) Mature coccolith inclined about 30° to the plane of the page. (b) Thin section of mature coccolith seen in cross-section just prior to secretion into the coccosphere. The V and R crystal units are located on the rim of the base plate (B). (c) Similar to (b) except the coccolith is demineralized to show the organic coat surrounding the mature crystals. The distal shield (d), proximal shield (p), inner tube (i) and outer tube (o) elements of the mineral ring are indicated. Bar = 0.1 μm. (Reproduced from Marsh [13].)

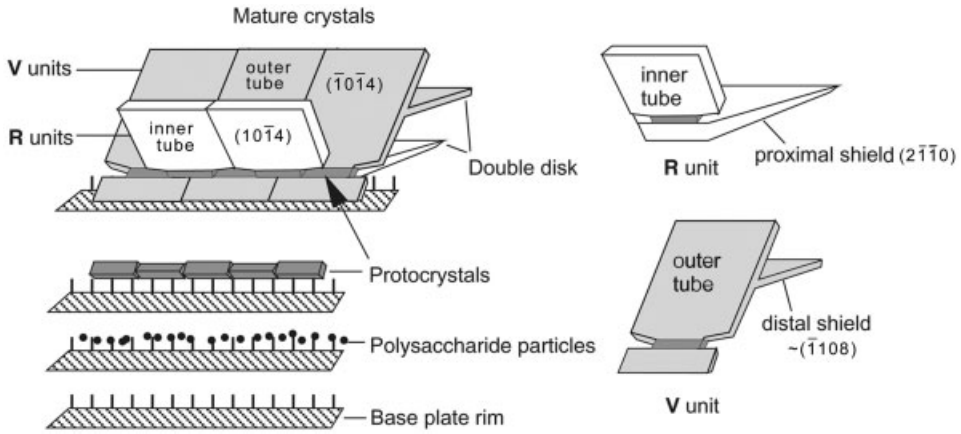

Figure 12.3 Schematic showing the stages of *Pleurochrysis* coccolith mineralization on the base plate rim as viewed from the interior of the coccolith. The 20-nm polysaccharide particles (coccolithosomes) are replaced by a ring of protocrystals. In wild-type cells, the protocrystals develop into mature interlocking V and R units. The protocrystals become the waists of the mature crystals. For simplicity the crystal tube and shield elements are depicted as thin plates. The proximal and distal shield elements form the double disk. (Reproduced from Marsh et al. [23].)

elements, and the vertical or subvertical structures linking the shields are known as tube elements [11] (Figures 12.2–12.4).

In *Pleurochrysis* the mineral ring has four plate-like elements (Figures 12.2 and 12.3): the distal shield and outer tube elements form the V unit, and the proximal shield and inner tube elements form the R units [13]. The plate-like surfaces of both tube elements correspond to the common (10$\bar{1}$4) rhombohedral faces of calcite and the plates of the proximal shield element are prismatic (2$\bar{1}\bar{1}$0) faces. The plates of the distal shield element are rather curved (Figure 12.2b and c) and their orientation does not correspond to a favorable calcite face; however, for convenience, they are described as approximately ($\bar{1}$108) faces – faces which rarely, if ever, develop in inorganic sources of calcite.

In *Emiliania* coccoliths (Figure 12.4), the proximal and distal shield elements and the inner and outer tube elements are all derived from the R units [14–16]. In this species, the vestigial V units are only observed in very immature coccoliths as they are rapidly overgrown by the massive R units [12]. As observed in *Pleurochrysis*, the plate-like surfaces of the proximal shield elements correspond to (2$\bar{1}\bar{1}$0) faces [15].

12.2.2 Heterococcolith Formation

12.2.2.1 Ion Accumulation

Heterococcolith mineralization occurs on the rim of a preformed organic base plate in a specialized Golgi-derived structure known as the coccolith vesicle (Figures 12.5

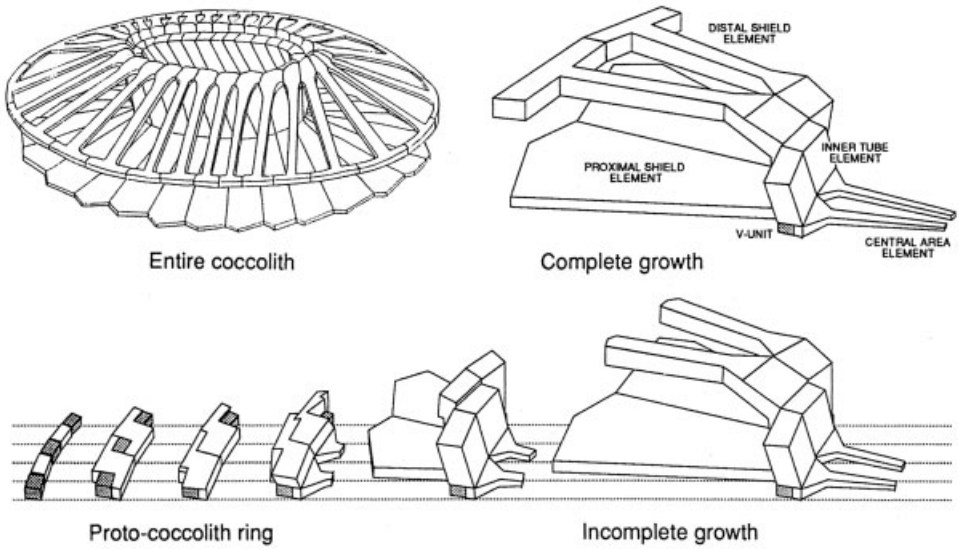

Figure 12.4 Schematic showing the stages of *Emiliania* coccolith mineralization. The V units of the protococcolith ring (shaded) are rapidly overgrown by the R units, which ultimately form both shield and tube elements of the mature coccolith. (Reprinted by permission from *Nature* [12] © 1992 Macmillan Magazines Ltd.)

and 12.6). After completion of the base plate in *Emiliania*, a labyrinthine membrane system known as a reticular body develops at the distal surface of the coccolith vesicle [17] and is present throughout the mineral deposition process (Figure 12.6). The reticular body has a large membranous surface area surrounding a small internal volume. Although its precise functions are unclear, its design is beautifully suited to the rapid transport of large quantities of mineral ions into a small confined volume – the large membrane surface could accommodate vast numbers of calcium and perhaps bicarbonate ion pumps – hence providing and maintaining a supersaturated solution of mineral ions during calcite nucleation and growth. Transport enzymes associated with coccolith vesicle membranes are discussed in Chapter 13 of this volume.

The *Pleurochrysis* coccolith vesicle does not develop a reticular body; instead it contains large numbers of 20-nm particles known as coccolithosomes [18], which are complexes of calcium ions and the acidic polysaccharides PS1 and PS2 [19–21] (Figure 12.5). The polysaccharides effectively buffer the calcium ion concentration in the coccolith vesicle by providing a large reservoir of loosely bound calcium [21]. PS1 is a polyuronide with a glucuronic:galacturonic acid ratio of 1:3 and contains small amounts of uncharged glycosyl residues (Table 12.1). PS2 is the more abundant polysaccharide and has an unusual structure, a repeating sequence consisting of D-glucuronic, *meso*-tartaric and glyoxylic acid residues (Figure 12.7). With a net ionic charge of -4 per repeating unit, PS2 has the highest calcium-binding capacity of any known mineral-associated polyanion. Chemically induced mutants

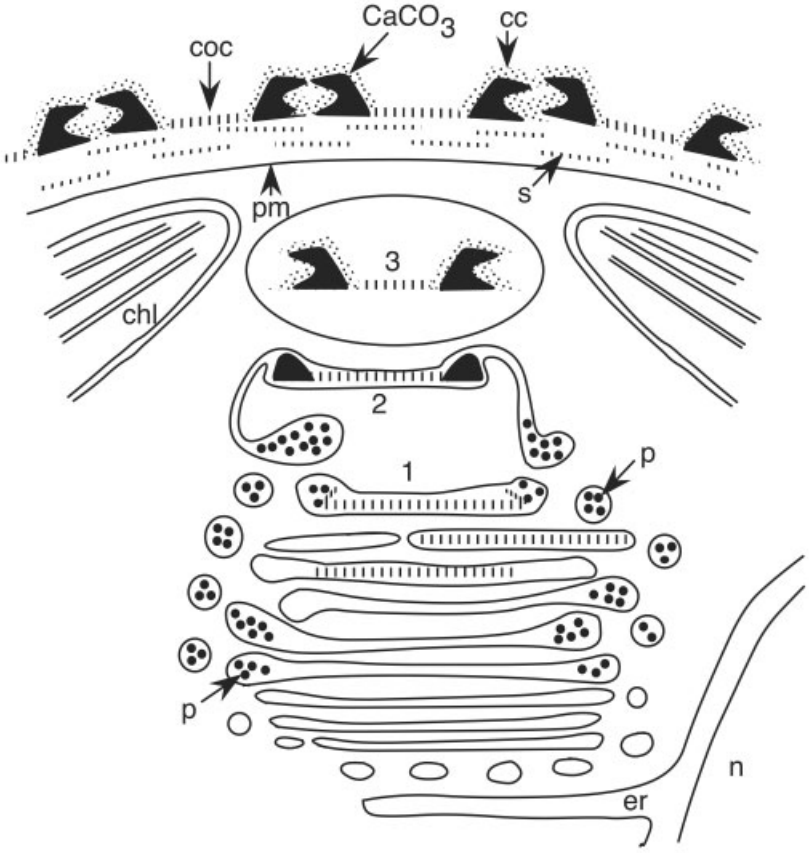

Figure 12.5 Model of coccolith formation in the *Pleurochrysis* Golgi system. The coccolith vesicle is shown before (1) during (2), and after (3) mineral deposition. Ca–PS1/PS2 complexes (coccolithosomes) are synthesized in medial Golgi cisternae. They are organized in discrete particles (p) before and during mineral deposition (1 and 2) and in amorphous crystal coats (cc) after mineralization ceases (3 and coccosphere). Coccolith bases (hatch marks), coccoliths (coc), unmineralized scales (s), chloroplast (chl), endoplasmic reticulum (er), nucleus (n), plasma membrane (pm). (Reproduced from Marsh [21].)

and spontaneously occurring variants of *Pleurochrysis*, which do not express PS2, have a $CaCO_3$ content only 5 % of that in wild-type cells [22] (see Figures 12.10b and 12.11b). Cells lacking PS2 are probably incapable of maintaining a concentration of calcium ions high enough to sustain calcite nucleation and growth.

In both *Pleurochrysis* and *Emiliania*, termination of mineralization coincides with a pronounced swelling of the coccolith vesicle (Figures 12.5 and 12.6). The huge influx of fluid probably quenches mineral deposition by rapidly lowering the calcium carbonate ion product. In *Emiliania*, the end of mineralization also coincides with the dissociation of the reticular body, while in *Pleurochrysis*, the end of calcite growth is accompanied by the dissociation of the coccolithosomes and the forma-

Table 12.1 Composition of *Pleurochrysis* polysaccharides expressed as mole ratios.

Residue	PS1	PS2	PS3
Glucuronic acid	0.30	1.04	0.16
Galacturonic acid	1.00	0.10	1.00
Galactose	0.050		
Rhamnose	0.035		
Arabinose	0.10		
Tartaric acid		1.00	
Glyoxylic acid		1.01	
Mannose			0.53
Xylose			0.09
SO_4	trace		0.27

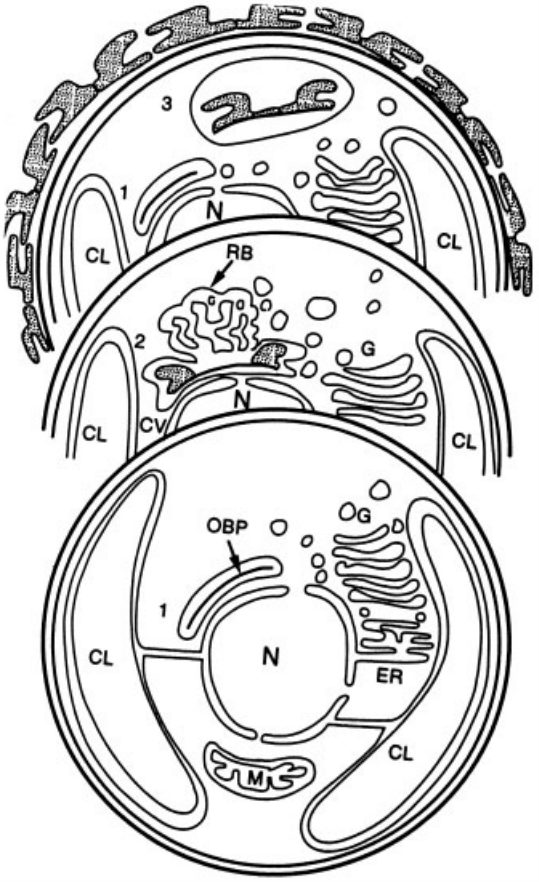

Figure 12.6 Schematic representation of *Emiliania* cells showing three stages (1–3) of coccolith formation. Upper cell also shows extracellular coccoliths. Chloroplast (Cl), nucleus (N), mitochondrion (M), endoplasmic reticulum (ER), Golgi apparatus (G), organic base plate (OBP), calcifying vesicle (CV), reticular body (RB). (Reproduced from de Vrind-de Jong and de Vrind [61].)

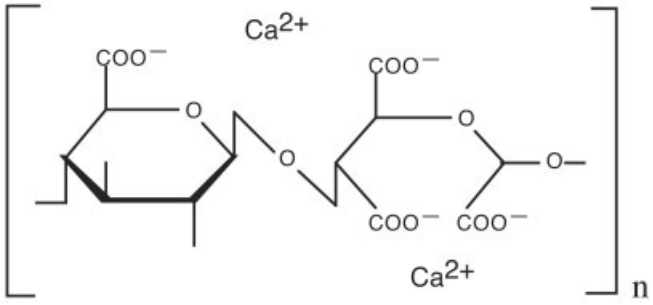

Figure 12.7 The calcium salt of PS2. PS2 derived from the CCMP 645 strain of *P. carterae* is a linear polysaccharide with a repeating unit consisting of D-glucuronic, *meso*-tartaric and glyoxylic acid residues [20]. PS2 fractions obtained from other strains may have different compositions [62, 63]. In one strain the β-linked D-glucuronic acid is replaced by its C5 epimer α-linked L-iduronic acid (N. Ozaki, personal communication). The major function of PS2 appears to be its ability to buffer the calcium ion concentration in the mineralizing vesicle. Hence, the important aspect of PS2 structure may be the presence of many low-affinity calcium-binding sites, while the stereochemistry of the binding sites may have less impact on the glycan's function.

tion of a polysaccharide coat on the mineral surface. The *Emiliania* crystals also acquire a polysaccharide coat, but of different composition. The crystal coats in both species may inhibit further crystal growth.

12.2.2.2 Calcite Nucleation

Calcite nucleation occurs exclusively on or near the rim of the coccolith base plate in both *Pleurochrysis* and *Emiliania*. Just prior to mineralization in *Pleurochrysis*, clusters of coccolithosomes and a narrow band of organic material known as the coccolith ribbon appear on the distal rim of the base plate (Figure 12.8) [13]. Subsequently small crystals form within the coccolithosome clusters and in contact with the coccolith ribbon. A complete closed ring of small crystallites (the protococcolith ring) develops about the rim with the crystallites having alternately R and V orientation with respect to their crystallographic *c*-axes (Figure 12.9a). *Pleurochrysis* mutants and variants which do not express PS2 – the major coccolithosome component – produce few crystal (Figure 12.11b), indicating that PS2 is important for efficient crystal nucleation. Nucleation may be inhibited in cells lacking PS2 simply because the calcium carbonate ion product in the coccolith vesicle is too low (see above) and not because of any structural modification to the nucleation site occasioned by the absence of PS2, i.e. the coccolithosomes may be localized on the coccolith rim in wild-type *Pleurochrysis* cells only to insure a sufficiently high calcium ion concentration during calcite nucleation. The fact that *Emiliania* nucleates calcite without expressing PS2 – or any analogous polyanion – supports this view.

In *Pleurochrysis*, the coccolith ribbon tethers the initial crystallites to the base plate and is the probable site of calcite nucleation. Although a coccolith ribbon has not been directly observed in other genera, Young et al. [12] proposed a model

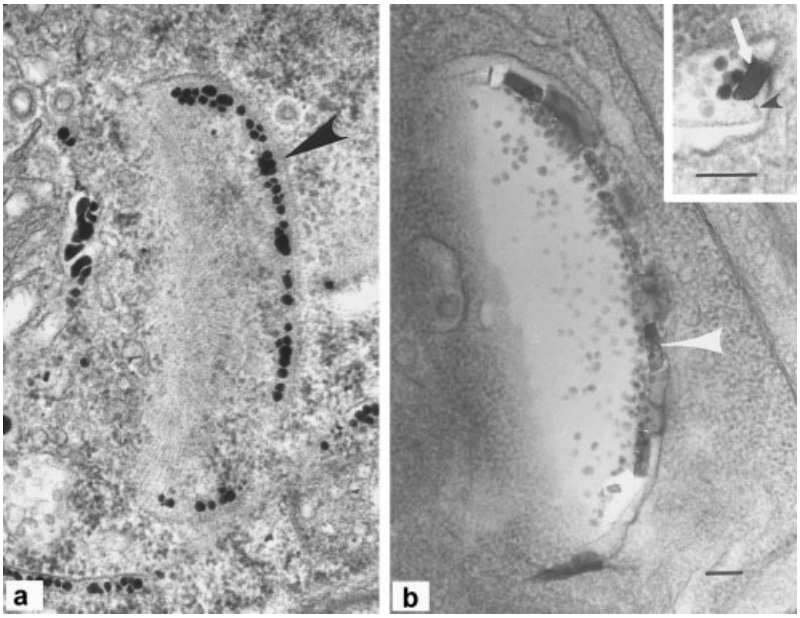

Figure 12.8 Grazing sections showing successive early stages of *Pleurochrysis* coccolith rim mineralization. (a) Base plate with dense calcium/polysaccharide particles (coccolithosomes) associated with the rim (arrowhead). (b) Base plate with a ring of small rectangular crystals among the polysaccharide particles on the rim (arrowhead). Unstained section. (Inset) Cross-section showing a small crystal (arrow) above the base plate apparently attached to the coccolith ribbon (arrowhead). Bars = 0.1 μm. (Reproduced from Marsh [13].)

for alternate V and R unit nucleation based on a folded ribbon-like structure that is applicable to placoliths in general. Multiple folds normal to the coccolith rim [12] or a single fold parallel to the rim [13] would produce nucleation sites with similar structures but different orientations on either side of the fold. This arrangement permits the nucleation of crystals in two different orientations from the same crystallographic face – the face most compatible with the nucleation site. Since the *Pleurochrysis* crystals are bound to the coccolith ribbon on $(10\bar{1}4)$ faces, the ribbon is the most likely nucleation site, but the possibility that the crystallites are nucleated elsewhere and subsequently bound to the ribbon cannot be ruled out.

12.2.2.3 Crystal Growth

The development of mature rim elements from the simple crystallites of the protococcolith ring has recently been described for *Pleurochrysis* coccoliths [13]. The earliest habits observed for both V and R units correspond to rectangular parallelepipeds (Figures 12.9a). Outgrowth from the initial V unit begins by expansion of a $(10\bar{1}4)$ face that forms the plate-like surface of the outer tube element (Figure 12.9b, inset). Outgrowth from the initial R unit produces a double parallelogram structure

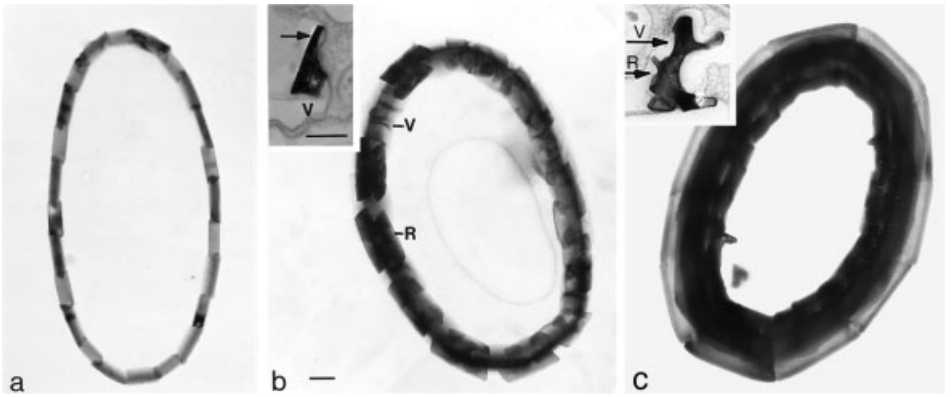

Figure 12.9 Isolated *Pleurochrysis* coccoliths illustrating stages of rim development. (a) Protococcolith. It has a ring of 24 small crystals in the shape of rectangular parallelepipeds. The crystals have alternating V and R unit orientations. (b) Immature coccolith at a later stage of development. The R units have double parallelogram structures as observed in projection which will develop into the inner tube and proximal shield elements. (Inset) Cross-sectioned coccolith of similar stage showing an immature V unit on the rim. The $(10\bar{1}4)$ plate – the outer tube element (arrow) – has emerged from the initially rectangular-shaped crystal. The distal shield element of the V unit has not yet appeared. (c) Mature coccolith. (Inset) Cross-sectioned mature coccolith showing fully formed V and R units. (Reproduced from Marsh [13].) TEM micrographs. Bars = 0.1 μm.

when viewed in projection perpendicular to the coccolith plane (Figure 12.9b). The outer parallelogram develops into the proximal shield element and the inner tube element develops from the inner parallelogram. Finally, the distal shield element (approximately $(\bar{1}108)$ plate) emerges from the V element completing the parallel double-disk structure characteristic of the mature coccolith (Figure 12.9c inset).

The development of $\{10\bar{1}4\}$ faces is not uncommon in inorganic sources of calcite, but the development of plate-like protrusions – like the tube elements of *Pleurochrysis* crystals – as opposed to rhombohedral forms is indicative of directional growth in response to outside pressure. The spatial constraints imposed by the framework of the surrounding coccolith vesicle must limit crystal growth to specific directions. Cellular filaments that might control the shape of the coccolith vesicle have not yet been identified. Crystal growth and vesicle deformation are probably concerted processes with each process influencing the other.

A sulfated galacturonomannan known as PS3 (Table 12.1) has been localized in the *Pleurochrysis* coccolith vesicle at the interface between the developing calcite crystals and the vesicle membrane [20, 23]. In chemically induced mutants which do not express PS3, mineralization ceases after the formation of the protococcolith ring (Figures 12.10c and 12.11c) [23], demonstrating that PS3 is part of the machinery which regulates crystal growth and morphology. The putative role of PS3 in vesicle membrane deformation and crystal growth depends on whether the membrane is distorted by action at its cytoplasmic or lumenal surface. If the force originates in the cytoplasm, then PS3 may have a signaling function, linking calcite deposition with the recruitment of cytoplasmic filaments. If the membrane is displaced by a

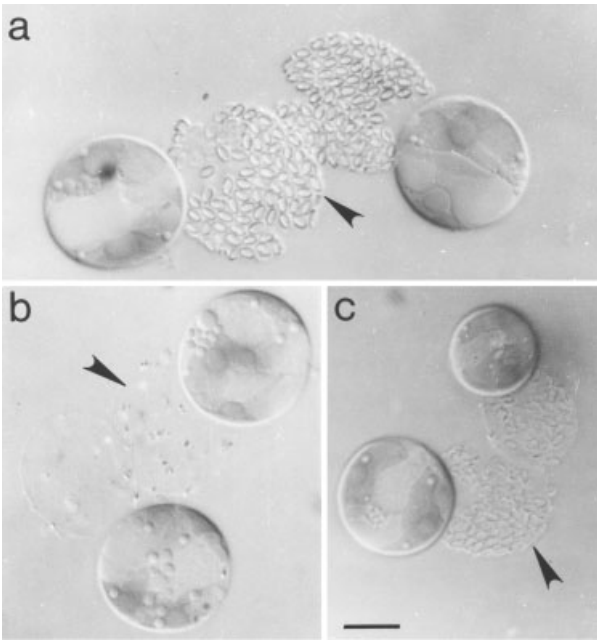

Figure 12.10 Nomarski photomicrographs of *Pleurochrysis* cells and their coccospheres (arrow heads) which were shed during microscopy. (a) The coccosphere of the wild-type cell is composed of oval-shaped refractile structures representing the calcite rims of the coccoliths. (b) The coccospheres of the *ps2*$^{-}$ cells (no synthesis of PS2) contain little refractile material. (c) The protococcoliths of the *ps3*$^{-}$ cells (no PS3 synthesis) are barely discernible as their calcite rims are quite narrow in comparison to the wild-type rim. Bar = 5 μm. ((a) and (b) reproduced from Marsh and Dickinson [22].)

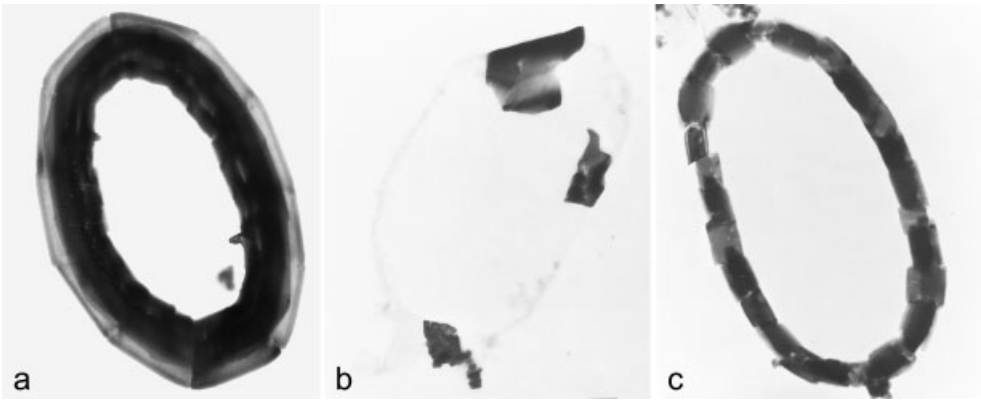

Figure 12.11 *Pleurochrysis* wild-type and mutant coccoliths. (a) Wild-type coccolith. (b) Coccolith of *ps2*$^{-}$ mutant. A few rim elements of variable size are observed. (Reproduced from Marsh and Dickinson [22].) (c) Protococcolith of *ps3*$^{-}$ mutant. Complete rims with immature parallelepiped-shaped crystals are observed. TEM micrographs.

pushing action on its lumenal surface, then polymerization of PS3 into a filamentous structure (alone or in conjunction with other lumenal molecules) may be a force-generating process [23].

Emiliania also expresses a sulfated galacturonomannan known as the coccolith polysaccharide (CP) localized in the coccolith vesicle [24]. The compositions of CP and *Pleurochrysis* PS3 are similar, suggesting that galacturonomannans or analogous molecules may have similar crystal-shaping functions in many, if not all, coccolithophore species that develop morphologically complex rim elements [23, 25].

12.3 Non-calcifying Morphotypes

12.3.1 *Pleurochrysis*

In addition to the unicellular coccolith-bearing forms described above, *Pleurochrysis* also has a filamentous non-calcifying phase [26–29] which is haploid with respect to calcifying cells [30]. The filaments release unmineralized swarmers, which fuse and evolve into coccolith-bearing cells [26, 31]. Filamentous forms appear in aging stationary phase cultures and then disappear when diluted into fresh medium, suggesting that nutrient limitation favors formation and propagation of the haploid stage, while nutrient-replete medium favors the formation and propagation of the diploid coccolith-bearing phase. However some filamentous colonies – isolated from *Pleurochrysis* strain CCMP 645 – have not reverted to the calcifying morphotype despite propagation in nutrient replete medium for over 6 years (Marsh, unpublished). Hence, unrecognized *Pleurochrysis* populations may exist in natural communities in stable filamentous stages.

Unicellular non-calcified *Pleurochrysis* morphotypes occur sporadically at low frequency in CCMP 645 cultures, but revert rather rapidly to the calcified state. An interesting variant is the $ps2^{-}$ cell described above – it does not express PS2, produces few calcite crystals and has the same ploidy as the calcifying morphotype [22]. Other non-calcifying morphotypes include a variant which does not form organic base plates and variants which fail to calcify for unknown reasons (Marsh, unpublished). Apparently *Pleurochrysis* can exist in either a calcified or non-calcified state, with the calcified form favored under standard culture conditions (18 °C in F2 medium [32]); however, non-calcifying phases of *Pleurochrysis* may occupy important niches in the natural phytoplankton communities of the world ocean.

12.3.2 *Emiliania*

Motile non-calcifying scale-bearing cells (S-cells) arise spontaneously in calcifying cultures of many *Emiliania* strains [33, 34]. The S-cells are haploid with respect to

calcifying cells [35] and may serve as gametes [36], although meiosis and sexual fusion have not been observed. Environmental conditions and nutrient status favoring the appearance of S-cells are not understood. In a recent study, Laguna et al. [37] induced calcifying cells to transform into small non-calcifying haploids by plating strain CCMP 1516 on solid medium. The small haploids in turn gave rise to calcifying cells when transferred to liquid medium, suggesting that medium viscosity may trigger phase transition in some strains. The haploids of the Laguna study [37] are much smaller than the S-cell haploids described earlier [34] and may represent a distinct life-cycle stage.

Non-motile, non-calcified morphotypes (N-cells) commonly arise in *Emiliania* cultures; the transition from calcifying cell to N-cell is favored by nitrogen- and phosphorous-rich media [33]. N-cells – for which the DNA content has been measured – have the same ploidy as calcifying cells [35, 38]. When *Emiliania* is held in long-term culture, the entire population frequently shifts from a calcifying cell to an N-cell morphotype, whereas spontaneous transition of an N-cell culture to the calcifying morphotype has not been reported except for strain F61. F61 expresses the N-cell morphotype in phosphate-limiting medium; when the phosphate is exhausted, the cells cease dividing and begin to calcify [33, 39]. Hence, it is reasonable to suppose that other N-cell populations are capable of switching to a calcifying morphotype if presented with the appropriate trigger. Non-calcifying *Emiliania* morphotypes may occupy important niches in natural phytoplankton communities.

12.4 Holococcolith-bearing Morphotypes

Many species have two coccolith-bearing life-cycle phases, with one phase expressing heterococcoliths and the other phase expressing holococcoliths [40, 41]. Heterococcolith crystals have large intricate complex shapes that are species specific and not observed in inorganic sources of calcite. In contrast, holococcolith crystals have small simple rhombohedral or prismatic habits characteristic of inorganically formed calcite (Figure 12.12b). Holococcolith/heterococcolith phase shifts were first observed in cultures of *Coccolithus pelagicus* [42]. Now a number of species capable of expressing both phases have been identified in natural populations through discovery of individual organisms in phase transition (Figure 12.12c), where the coccosphere of the emerging phase underlies the coccosphere of the initial phase. Environmental forces that trigger phase transition are unknown, although there is a tendency for the holococcolith form to occur higher in the water column than the corresponding heterococcolith form [40].

In *Coccolithus*, the heterococcoliths are calcified within the coccolith vesicle as described above before discharge into the coccosphere, while the holococcoliths are secreted into the coccosphere as organic scales and then calcified extracellularly

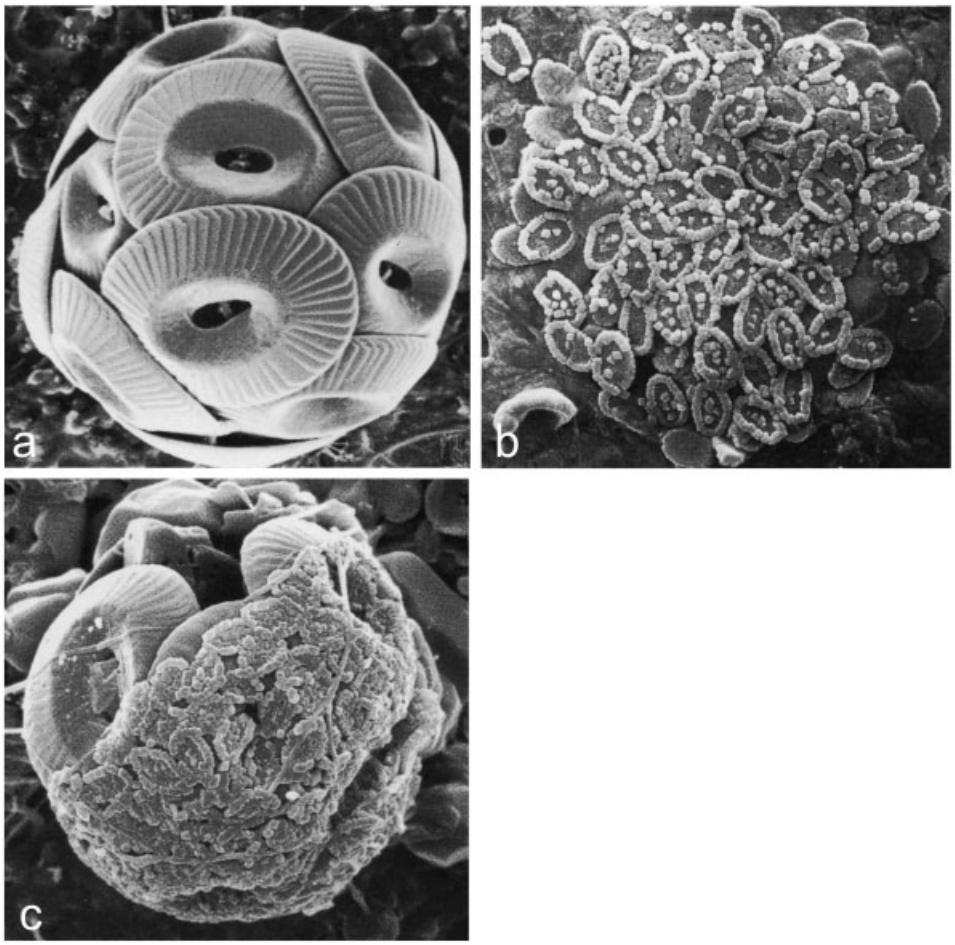

Figure 12.12 Life history stages of *Coccolithus pelagicus*. (a) Heterococcolith stage (image by S. Nishida). (b) Holococcolith stage (image by C. Samtleben). (c) Cell is transition from holococcolith to heterococcolith stage (image by C. Samtleben).

[43, 44]. The holococcolith phase is haploid with respect to the heterococcolith phase [45].

Emiliania and *Pleurochrysis* holococcolith morphotypes have not been observed, probably because they lack a mechanism for extracellular calcification of the organic scales secreted by the haploid stage. The common occurrence of haploid holococcolith forms in many genera supports the notion that *Emiliania* and *Pleurochrysis* non-mineralized haploid forms may also be prevalent in natural communities, but remain unrecognized as they are not easily distinguished from other species that comprise the non-calcifying flagellated and colonial plankton population.

12.5 Coccolithophore Calcification and the Ocean Carbon Cycle

Analysis of air bubbles trapped in Antarctic ice show a tight correlation between atmospheric pCO_2 and sea surface temperature over the past 400 000 years. pCO_2 is 30 % lower during glacial periods than during pre-anthropogenic interglacial times, suggesting that pCO_2 is a driver or amplifier of glacial cycles, which in turn are linked to orbital (Milankovitch) periodicity [46]. Although the process by which Quaternary pCO_2 levels are regulated is still unknown, it is generally accepted that the ocean is the only reservoir capable of absorbing atmospheric pCO_2 changes over time scales recorded in ice cores [47]. Until recently the huge carbon pool in the lithosphere turned over too slowly to seriously impact glacial cycles [48]. However, lithospheric carbon is today being dumped into the atmosphere by the extraction and burning of fossil fuels.

CO_2 is partitioned between the atmosphere and ocean via the biological CO_2 and carbonate pumps, and through ocean circulation with the exchange of carbon between deep and surface waters. Atmospheric and surface water pCO_2 are in dynamic equilibrium; thus processes which draw CO_2 from surface to deeper waters, also draw CO_2 from atmosphere to ocean.

Diatoms, dinoflagellates and coccolithophores are the major primary producers in today's ocean. They decrease pCO_2 in the upper euphotoic zone through photosynthetic fixation of CO_2 into organic molecules (Eq. 2), most of which remineralizes (reverse of Eq. 2), releasing CO_2 at a deeper level as the plankton and plankton-derived debris sink through the water column. This process – known as the biological CO_2 pump – pumps CO_2 from surface to deeper water, decreasing atmospheric pCO_2.

$$CO_2 + H_2O \leftrightarrow CH_2O + O_2 \tag{2}$$

Coccolithophores and planktonic foraminifera increase the pCO_2 of surface water and atmosphere by formation of $CaCO_3$ scales and shells, respectively (Eq. 1). This process is the biological carbonate pump; it decreases surface alkalinity (roughly the sum of carbonate and bicarbonate ion concentrations) and drives CO_2 into the atmosphere. Some of the $CaCO_3$ redissolves in the water column or upper sediments (reverse of Eq. 1) and the remainder is preserved in deep sediments [49].

As the flux of organic carbon C_o relative to $CaCO_3$ ($C_o/CaCO_3$) leaving the upper ocean for deeper waters increases, the pCO_2 of surface water decreases and atmospheric CO_2 is drawn into the ocean. A glacial increase in photosynthesis and/or decrease in calcite production may explain the lower pCO_2 of the glacial atmosphere. The "alkalinity theory" postulates that $CaCO_3$ production decreases during glacial periods and rebounds during interglacial times [50], and is consistent with paleo-pH data which indicate that the glacial ocean was significantly more basic than it is today [51].

The contribution of coccolithophores to the pelagic $CaCO_3$ flux ranges from less than 20 % to over 90 % depending on season and geographical location [52–56]. Hence, a significant increase or decrease in coccolith production would over time contribute significantly to increases or decreases, respectively, in atmospheric pCO_2. Variation in coccolithophore $CaCO_3$ formation can occur through (1) variation in coccolithophore numbers, and (2) transition of coccolithophores between calcifying and non-calcifying states.

Models capable of generating Quaternary pCO_2 fluctuations incorporate parameters based on putative changes in ocean circulation, variations in total primary productivity and/or variations in coccolithophore numbers relative to other phytoplankton groups (notably diatoms). Glacial increases in SiO_2-forming diatoms relative to $CaCO_3$-forming coccolithophores have been modeled by providing the glacial ocean with an elevated level of dissolved silica, an element required for diatom growth [47]; however, a similar result can be achieved by shifting significant numbers of coccolithophores into non-calcifying states during glacial periods. A major goal of biomineralization studies is to understand how $CaCO_3$ production varies naturally within coccolithophore populations and to determine how environmental forces affect the variation.

12.6 Future Prospects

Ocean climate models are limited by the inability to temporally and spatially parameterize significant biological activities such as the rates of $CaCO_3$ production [47]. Coccolithophore populations are limited in size by nutrient supply, competition with non-calcifying taxa and other environmental variables. However, the level of $CaCO_3$ production within a coccolithophore population may be regulated through reversible transitions between calcifying and non-calcifying morphotypes. Studies of coccolithophore distribution throughout the expanse and depth of the ocean are providing better insight into environmental influences on planktonic community composition; however, studies of environmental effects on coccolithophore life history stages are almost non-existent. The function of calcified scales in coccolithophores is poorly understood [57], making it difficult to predict environmental conditions which would favor the growth and expansion of the calcified morphotype over a non-calcified phase. Additionally, epigenetic mechanisms – other than meiosis/syngamy – utilized by coccolithophores to switch between non-calcifying/calcifying forms are unknown. The presence of calcified scales has been, with few exceptions, the sole criterion used to identify coccolithophores in environmental and sediment trap studies as non-calcified coccolithophores are almost impossible to identify by microscopy alone. As a consequence the presence, the species and the numbers of non-calcified coccolithophores in natural phytoplankton communities – today and in the past – are essentially unknown. Campbell et al. [58] using immunochemistry identified non-coccolith-bearing *Emiliania*a cells in Atlantic and Pacific Ocean plankton communities, but their numbers relative to the calcified form were

not reported. Moon et al. [59, 60] found haptophyte 18S rDNA sequences in a picoplankton community in the equatorial Pacific Ocean that are closely related to coccolithophore rDNA, but since the DNA was derived from an environmental assemblage, the haptophyte sequences could not be matched to a particular cell morphology. In order to establish the presence of non-calcifying coccolithophore phases in natural communities, it will be necessary to correlate coccolithophore-specific DNA sequences with a non-coccolith-bearing morphology.

An ocean-wide expansion of non-calcifying coccolithophores with a concomitant reduction in the coccolith-bearing population would decrease atmospheric pCO_2 by decreasing $CaCO_3$ production, while expansion of the calcifying population at the expense of the non-calcified phase would increase $CaCO_3$ production and atmospheric pCO_2. Consequently phase shifting cycles in coccolithophores – if induced by environmental consequences of Milankovitch orbital cycles – may drive or amplify the Quaternary fluctuations in atmospheric pCO_2.

A greater insight into coccolithophore biology is needed to address the organism's environmental impact. It should be possible to identify other molecular elements in addition to the acidic polysaccharides and organic base plates that are critical to the expression of a calcified morphotype by comparing gene expression in calcifying versus non-calcifying phases – or heterococcolith versus holococcolith – bearing phases since the latter does not calcify through the intracellular pathway. The sequencing of the *Emiliania* genome now underway (T. Wahlund, personal communication) should facilitate identification of genes encoding proteins with a calcifying function. Finally, the cellular and environmental pathways for regulation of morphotype switching and stability must be explored and understood both in culture and the ocean.

Acknowledgments

Work in the author's laboratory was supported by grants from the US Office of Naval Research and the Fundamental Space Biology Program of the US National Aeronautics and Space Administration (NAG2-1498).

References

[1] A. J. Ridgwell, M. J. Kennedy, K. Caldeira, *Science* **2003**, *302*, 859–862.
[2] P. Westbroek, C. W. Brown, J. van Bleijswijk, C. Brownlee, G. J. Brummer, M. Conte, J. Egge, E. Fernandez, R. Jordan, M. Knappertsbusch, J. Stefels, M. Veldhuis, P. van der Wal, J. Young, *Global and Planetary Change* **1993**, *8*, 27–46.
[3] T. Cavalier-Smith, in *The Chromophyte Algae: Problems and Perspectives* (Eds. J. C. Green, B. S. C. Leadbeater, W. L. Diover), Clarendon Press, Oxford, **1989**, pp. 381–407.

[4] R. W. Jordan, J. C. Green, *J. Mar. Biol. Ass. UK* **1994**, *74*, 194–174.
[5] B. Edvardsen, W. Eikrem, J. C. Green, R. A. Andersen, S. Y. Moon-van der Staay, L. K. Medlin, *Phycologia* **2000**, *39*, 19–35.
[6] S. Fujiwara, M. Tsuzuki, M. Kawachi, N. Minaka, I. Inouye, *J. Phycol.* **2001**, *37*, 121–129.
[7] T. Cavalier-Smith, in *Progress in Phycological Research, Vol. 4* (Eds. F. E. Round, D. J. Chapman), Biopress, Bristol, **1986**, pp. 309–347.
[8] H. S. Yoon, J. D. Hackett, G. Pinto, D. Bhattacharya, *Proc. Natl Acad. Sci. USA* **2002**, *99*, 15507–15512.
[9] J. R. Young, P. R. Brown, J. A. Burnett, in *The Haptophyte Algae* (Eds. J. C. Green, B. S. C. Leadbeater), Clarendon Press, Oxford, **1994**, pp. 379–392.
[10] A. Hallam, K. Perch-Nielsen, *Tectonophysics* **1990**, *171*, 347–57.
[11] J. R. Young, J. A. Bergen, P. R. Bown, J. A. Burnett, A. Fiorentino, R. W. Jordan, A. Kleijne, B. E. Van Niel, A. J. Ton Romein, K. Von Salis K, *Palaeontol.* **1997**, *40*, 875–912.
[12] J. R. Young, J. M. Didymus, P. R. Bown, B. Prins, S. Mann, *Nature* **1992**, *356*, 516–518.
[13] M. E. Marsh, *Protoplasma* **1999**, *207*, 54–66.
[14] N. Watabe, *Calcif. Tissue Res.* **1967**, *1*, 114–121.
[15] S. Mann, N. H. C. Sparks, *Proc. R. Soc. Lond. B* **1988**, *234*, 441–453.
[16] S. A. Davis, J. R. Young, S. Mann, *Botanica Marina* **1995**, *38*, 493–497.
[17] D. Klaveness, *Protistologica* **1972**, *8*, 355–346.
[18] D. E. Outka, D. C. Williams, *J. Protozool.* **1971**, *18*, 285–297.
[19] P. van der Wal, E. W. de Jong, P. Westbroek, W. C. de Bruijin, in *Environmental Biogeochemistry, Vol. 35* (Ed. R. Hallberg), Swedish Research Council, Stockholm, **1983**, pp. 251–258.
[20] M. E. Marsh, D. K. Chang, G. C. King, *J. Biol. Chem.* **1992**, *267*, 20507–20512.
[21] M. E. Marsh, *Protoplasma* **1994**, *177*, 108–122.
[22] M. E. Marsh, D. P. Dickinson, *Protoplasma* **1997**, *199*, 9–17.
[23] M. E. Marsh, A. L. Ridall, P. Azadi, P. J. Duke, *J. Struct. Biol.* **2002**, *139*, 39–45.
[24] P. R. van Emberg, E. W. de Vrind-de Jong, W. T. Daems, *J. Ultrastruct. Mol. Struct. Res.* **1986**, *94*, 246–259.
[25] A. M. J. Fichtinger-Schepman, J. P. Kamerling, C. Versluis, J. F. G. Vliegenthart, *Carbohydrate Res.* **1981**, *93*, 105–123.
[26] H. A. von Stosch, in *Vegatative Fortpflanzung, Parthenogenese und Apogamie bei Algen, Encyclopedia of Plant Physiology, Vol. 18* (Ed. W. Ruhland), Springer, Berlin, **1967**, pp. 646–656.
[27] B. S. C. Leadbeater, *Br. Phycol. J.* **1970**, *5*, 57–69.
[28] B. S. C. Leadbeater, *Ann. Bot.* **1971**, *35*, 429–439.
[29] R. N. Pienaar, in *Coccolithophores* (Eds. M. Winter, W. G. Seisser), Cambridge University Press, Cambridge, **1994**, pp. 13–37.
[30] D. G. Rayns, *J. Mar. Biol. Ass. UK* **1962**, *4*, 481–484.
[31] P. Gayral, J. Fresnel, *Protistologica* **1983**, *19*, 245–361.
[32] R. R. L. Guillard, in *Culture of Marine Invertebrate Animals* (Eds. W. L. Smith, M. H. Chanley), Plenum, New York, **1975**, pp. 29–60.
[33] E. Paasche, *Phycologia* **2002**, *40*, 503–529.
[34] D. Klaveness, E. Paasche, *Arch. Mikrobiol.* **1971**, *75*, 382–385.
[35] J. C. Green, P. A. Course, G. A. Tarran, *J. Mar. Syst.* **1996**, *9*, 33–44.
[36] D. Klaveness, *Br. Phycol. J.* **1972**, *7*, 309–318.
[37] R. Laguna, J. Romo, B. A. Read, T. M. Wahlund, *Appl. Environ. Microbiol.* **2001**, *67*, 3824–3831.
[38] E. Paasche, D. Klaveness, *Arch. Mikrobiol.* **1970**, *73*, 143–152.
[39] E. Paasche, *Eu. J. Phycol.* **1998**, *33*, 33–42.
[40] L. Cros, A. Kleijne, A. Zeltnes, C. Billard, J. R. Young, *Mar. Micropaleontol.* **2000**, *39*, 1–34.
[41] M. Geisen, C. Billard, A. T. C. Broerse, L. Cros, I. Probert, J. R. Young, *Eur. J. Phycol.* **2002**, *37*, 531–550.
[42] M. Parke, I. Adams, *J. Mar. Biol. Ass. UK* **1960**, *39*, 263–274.
[43] I. Manton, G. F. Leedale, *J. Mar. Biol. Ass. UK* **1969**, *49*, 1–16.
[44] J. D. Rowson, B. S. C. Leadbeater, J. C. Green, *Br. Phycol. J.* **1986**, *21*, 359–370.
[45] A. Houdan, C. Billard, D. Marie, F. Not, A. G. Sáez, J. R. Young, I. Probert, *Systematics and Biodiversity* **2004**, *1*, 453–465.

[46] J. R. Petit, J. Jouzel, N. I. Raynaud, N. I. Barkov, J. M. Barnola, I. Basile, M. Bender, J. Chappellaz, M. Davis, G. Delaygue, M. Delmotte, V. M. Kotlyakov, M. Legrand, V. Y. Lipenkov, C. Lorius, C. Pepin, C. Ritz, E. Saltzman, M. Stievenard, *Nature* **1999**, *399*, 429–436.
[47] D. Archer, A. Winguth, D. Lea, N. Mahowald, *Rev. Geophys.* **2000**, *38*, 159–189.
[48] R. A. Berner, A. C. Lasaga, R. M. Garrels, *Am. J. Sci.* **1983**, *283*, 641–683.
[49] J. D. Milliman, *Global Biogeochem. Cycles* **1993**, *7*, 927–957.
[50] D. E. Archer, E. Maier-Reimer, *Nature* **1994**, *367*, 260–264.
[51] A. Sanyal, G. Hemming, G. Hansen, W. Broecker, *Nature* **1995**, *373*, 234–237.
[52] K. Takahashi, in *The Haptophyte Algae* (Eds. J. C. Green, B. S. C. Leadbeater), Clarendon Press, Oxford, **1994**, pp. 335–350.
[53] J. C. Steinmetz, in *Coccolithophores* (Eds. A. Winter, W. G. Siesser), Cambridge University Press, Cambridge, **1994**, pp. 179–197.
[54] A. T. C. Broerse, P. Ziveri, J. E. van Hinte, S. Honjo, *Deep-Sea Res. II* **2000**, *47*, 1877–1905.
[55] Y. Tanaka, H. Kawahata, *Marine Micropaleontol.* **2001**, *43*, 273–384.
[56] C. Sprengel, K. H. Baumann, J. Henderiks, R. Henrich, S. Neuer, *Deep-Sea Res. II* **2002**, *49*, 3577–3598.
[57] J. R. Young, in *Coccolithophores* (Eds. M. Winter, W. G. Seisser), University Press, Cambridge, **1994**, pp. 63–82.
[58] L. Campbell, L. P. Shapiro, E. Haugen, *J. Plankton Res.* **1994**, *16*, 35–51.
[59] S. Y. Moon-van der Staary, G. W. M. van der Staay, L. Guillou, C. Herve, L. K. Medlin, D. Vaulot, *Limnol. Oceanogr.* **2000**, *45*, 98–109.
[60] S. Y. Moon-van der Staary, R. de Wachter, D. Vaulot, *Nature* **2001**, *409*, 607–610.
[61] E. W. de Vrind-de Jong, J. P. M. de Vrind, in *Geomicrobiology: Interactions between Microbes and Minerals* (Eds. J. F. Banfield, K. H. Nealson), Mineralogical Society of America, Washington, DC, **1997**, pp. 267–307.
[62] N. Ozaki, S. Sakuda, H. Nagasawa, *Biosci. Biotechnol. Biochem.* **2001**, *65*, 2330–2333.
[63] N. Ozaki, M. Okazaki, T. Kogure, S. Sakuda, H. Nagasawa, *Thalassas* **2004**, *20*, 59–68.

13 The Proton Pump of the Calcifying Vesicle of the Coccolithophore, *Pleurochrysis*

Elma L. González

13.1 Introduction

Many organisms are capable of calcification, but only a few organisms calcify in a subcellular compartment. Even fewer organisms are genetically capable of controlling the morphology of their calcified products. There are hundreds of species of coccolithophores whose specific designations are primarily based on the morphology of their coccoliths – the modular mineralized plates that make up the outer cell covering (coccosphere). The utility of the mineral morphs for taxonomic identification suggests two things – that the process of coccolith production is stable and highly replicable, and that the morphology of the complex structures is under genetic control. Furthermore, we can postulate that the key processes that lead to the specific shapes of each coccolith are operating at the level of the coccolith vesicle – where calcium carbonate is deposited on the organic base plates that are elaborated by the Golgi apparatus [1]. These topics are further elaborated in Chapter 12 of this volume.

Coccolithophore mineralization is the end result of a series of steps that include (1) ion accumulation in the coccolith vesicle, (2) calcite nucleation, (3) crystal growth and (4) exocytosis [2]. The presumption is that all of these steps are directed by elements within the coccolith vesicle or associated with it (e.g. cytoskeletal elements).

Our work on the coccolith vesicle has led us to focus on the proton pump vacuolar (V)-ATPase and its possible role during mineralization [2]. In particular, one aspect of subcellular mineralization that is worthy of attention is the fate of protons released during the calcification reaction in the confined space of the coccolith vesicle. Because the calcification reaction is acidotic (acidogenic), it is logical to assume that as the mineral is formed in the vesicle, the acidity produced by the reaction, $HCO_3^- + Ca^{2+} \rightarrow CaCO_3 + H^+$, must be removed. It has been suggested that the protons from calcification are an essential feature of the carbon concentrating mechanism (CCM) of the coccolithophores and it has also been suggested that protons from calcification also play a role in nutrient uptake [3]. If these hypotheses are correct, one may further hypothesize a relationship between calcification and photosynthesis (via the CCM) and calcification and stress (induced by oligotrophic conditions). It is thus probable that the coccolith proton pump is a central feature of the ecophysiology of the coccolithophore.

Biomineralization: From Biology to Biotechnology and Medical Application, Second Edition. Edited by E. Bäuerlein

ISBN: 3-527-31065-7

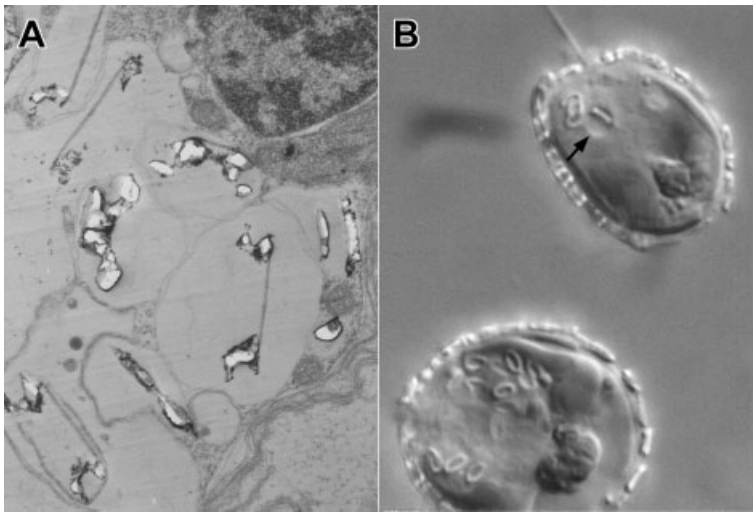

Figure 13.1 Micrographs depicting subcellular development of coccoliths in the coccolith vesicle of *Pleurochrysis*. (A). Electron microscope image of a cell grown under conditions that inhibit exocytosis of completed coccoliths. (B). Light micrograph showing living cells with forming coccoliths. Arrow points to an expanded vesicle containing a completed coccolith.

13.2 The Coccolith Vesicle

The coccolith vesicle is differentiated from the trans-most Golgi cisternae. In *Pleurochrysis*, the Golgi is responsible for synthesizing and assembling the complex polysaccharides that make up the organic base-plates upon which calcium carbonate crystals are nucleated [1, 4]. Under certain conditions, it is possible to observe many coccolith vesicles in electron microscope and light micrographs at various stages of completion (Figure 13.1). When such cells are fractionated, the isolated cell fractions are highly enriched for membrane-delimited (stained by NBD-ceramide, a membrane intercalating fluorochrome) structures and, upon examination by Nomarski optics, also reveal the expected tridimensional, sculptured features of an enclosed coccolith [5] (Figure 13.2), confirming identity of the isolated structures with the coccolith-producing compartment in the cell. The isolated vesicle fractions also exhibit V-ATPase activity as will be discussed in the next section.

13.3 The V-ATPase Enzyme Complex and Immunolocalization

The localization of the V-ATPase has been confirmed by means of immunolocalization using a homologous, monospecific antibody. This antibody was raised against

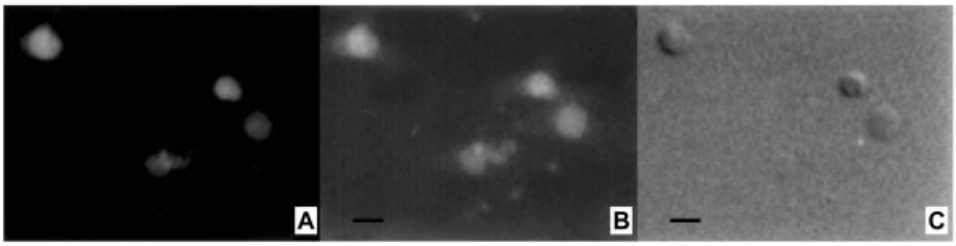

Figure 13.2 Isolated coccolith vesicles visualized by epifluorescence microscopy. The aldehyde-fixed vesicles were doubly labeled by (A) anti-VAP (subunit *c*) and a TRITC-labeled secondary antibody, and (B) NBD-ceramide. (C) The same vesicles in (A) and (B) are shown under Nomarski optics. Reproduced from [13] by permission of the *Journal of Phycology*.

a peptide generated *in vitro* from the amino acid sequence deduced from a cDNA clone, encoding subunit *c* of the V-ATPase, isolated from a *Pleurochrysis* cDNA library [5, 6].

The isolated vesicle membranes were also analyzed on sodium dodecylsulfate–polyacrylamide gels. Approximately 20 relatively abundant polypeptides have been detected [3a]. These analyses showed a distribution and complexity of polypeptides consistent with the presence of the V-ATPase complex [3a]. Although not all of the known V-ATPase polypeptides have been identified in these preparations, many of them have apparent molecular weights that closely match the principal subunits, of both the V_1 (A–E) and V_o (a and c) domains of the ATPase [7]. The polypeptide with an apparent M_r of 59 kDa corresponds to the 60-kDa subunit B since it specifically reacts with the 2E7 monoclonal antibody raised against subunit B, the ATP-binding subunit, of oat roots [8] (Figure 13.3). Immunofluorescence microscopy also shows that this antibody reacts with the membrane of aldehyde-fixed, isolated coccolith vesicles (Figure 13.4).

The V-ATPase subunit *c* of the V_o domain, also known as the "16-kDa proteolipid" [9], has also been identified in the coccolith vesicle preparations [5]. However, the subunit *c* of *Pleurochrysis* has an apparent M_r of 24 kDa [5, 6]. This is a larger molecular mass than would be expected from the coding sequence of the corresponding cDNA (16.2 kDa), suggesting that the polypeptide is modified post-translationally [5]. In *Pleurochrysis*, the gene encoding subunit *c* is present as a single genomic copy [5].

The V-ATPase complex has been the subject of much work across a wide range of plant and animal species [7]. The observed subunit composition has varied between 12 and 13 subunits in the organisms examined [7, 10]. The actual number of subunits in the coccolithophorid V-ATPase complex has not been determined.

13.4 Proton Transport

Wholly intracellular calcification is rare among organisms, and is particularly interesting because it permits precise control over mineralization chemistry and litho-

Figure 13.3 Immunoblot of coccolith vesicle membrane polypeptides. One polypeptide, M_r 59 kDa, in membrane preparations from Golgi (G) and coccolith vesicle (CV) cross-reacted with the 2E7 monoclonal anti-subunit B from oat, but not to chloroplast (CP) membranes. Modified from [13].

morphogenesis [4]. However, although calcification is a source of protons, the coccolithophorid cell must maintain a defined, alkaline microenvironment sufficient to permit crystal nucleation, growth and the integrity of fully mineralized calcium carbonate until eventual exocytosis. It is evident that these conditions are met since the organism exhibits a high rate of calcite production and excretion (20–40 pg/cell/day) [11] and one may, therefore, infer that the resulting protons are neutralized or secreted from the calcifying (coccolith) vesicle. Various mechanisms have been proposed, but the situation is still not fully resolved.

We have examined the activities of the principal organelle fractions in the presence of inhibitors and other pharmacological agents to assess organelle-specific diversity of the ATPase activities including V-, P- and F-type enzymes [12]. In all cells, the ubiquitous transport of either protons or calcium is made possible by genetically and structurally distinct ATP-dependent enzymes [12].

The *Pleurochrysis* plasma membrane (PM) demonstrates a P-type, calcium-stimulated ATPase that has very different inhibitor sensitivity from that of the coccolith vesicle, V-type enzyme [13]. The isolated PM is capable of ATP-dependent ^{45}Ca transport that is sensitive to well-characterized inhibitors of P-type ATPase [13]. In contrast, the coccolith vesicle membrane shows a V-type ATPase activity [13]. The V-ATPase is also present on the Golgi, which is not unexpected since the coccolith vesicle is derived from the trans-Golgi [1, 13].

We have examined isolated coccolith vesicle preparations for proton- and

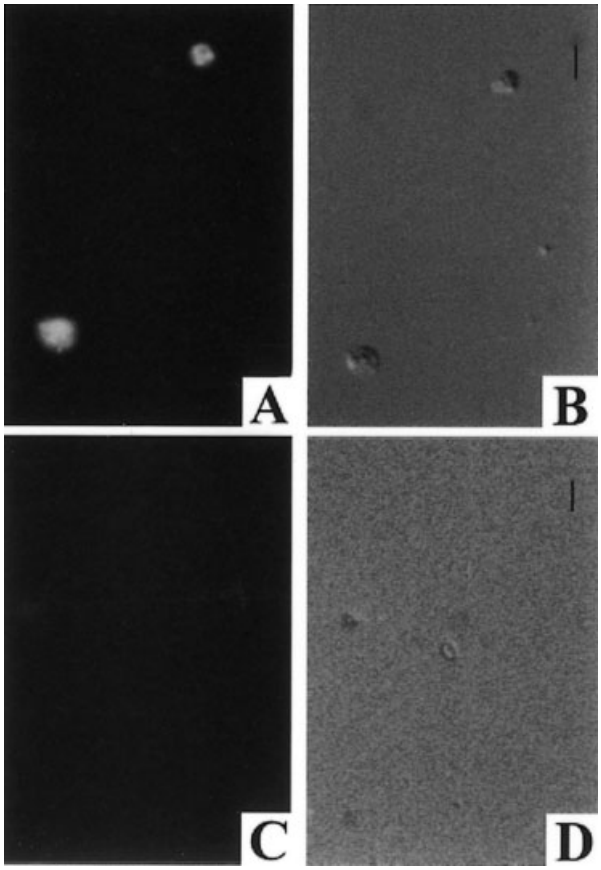

Figure 13.4 Immunofluorescence microscopy of coccolith vesicles. Isolated, aldehyde-fixed vesicles were exposed to the 2E7 monoclonal (see Figure 13.3) and secondary antibody labeled with FITC fluorochrome. (A and B) Vesicles exposed to the 2E7 monoclonal viewed with epifluorescence (A) and Nomarski optics (B). (C and D) Vesicles exposed to non-immune ascites fluid: epifluorescence (C) and Nomarski (D). Bar = 1 μM.

calcium-pumping activities. Purified coccolith vesicles are capable of ATP-dependent proton transport (Figure 13.5). Proton pumping on the coccolith vesicle is inhibited by nitrate, but not vanadate, which is consistent with a V-type activity as compared to the P-type activity present on the PM [13]. In contrast to the PM, $^{45}Ca^{2+}$ transport across the coccolith vesicle membrane was not observed, although the coccolith vesicle binds Ca^{2+} with high affinity and such a high background may mask low levels of transport activity [13].

Despite the presence of the V-ATPase on the coccolith vesicle membrane, its contribution to proton secretion has not been fully explained. Subunit *c* of the V-ATPase is a highly conserved polypeptide with a high degree of similarity to, for example, the higher plant tonoplast ATPases [6, 14]. Thus, by analogy to those

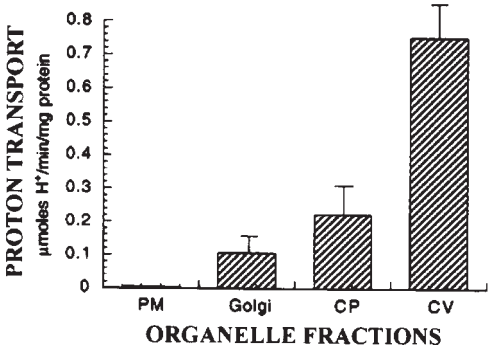

Figure 13.5 ATP-dependent proton-pumping, specific activity in organelle fractions. Organelles were isolated in sucrose gradients. These activities were sensitive to nitrate and insensitive to vanadate. PM, plasma membrane; CP, chloroplast; CV, coccolith vesicle. Reproduced from [13] by permission of the *Journal of Phycology*.

known enzymes, the orientation of the holoenzyme in the *Pleurochrysis* coccolith vesicle membrane appears to be typical for V-ATPases of the endomembrane system. In other words, its orientation indicates that protons are pumped *into* the vesicle. A possible explanation for this situation may lie with an, as yet, unidentified membrane complex that could act as a potential ion exchanger across the coccolith vesicle membrane. Antiporters, working in concert with a V-ATPase, have been described in organisms where luminal spaces sequester ions by exchanging protons. The midgut of *Manduca* is an example where highly conserved V-ATPase and an ion antiporter maintain a highly alkaline pH [15]. Moreover, the vacuolar membrane of *Mesenbryanthemum crystallinum*, a halophyte with inducible crassulacean acid metabolism, exhibits a proton-pumping ATPase and a separately inducible ion/proton antiporter that act in concert to achieve high levels of Na^+ ion concentrations within the tonoplast (vacuole) [16].

13.5 Conditions for Expression of Subunit *c*

Although the coccolithophores are generally adapted for life under oligotrophic conditions, extremely low nutrient levels are probably stressors [3]. In a recent review of the literature on plant V-ATPases, Dietz et al. found that the expression of V-ATPase enzymes correlates with a wide range of stressing conditions and hypothesized that the enzyme must have adaptive value under such conditions [17]. Thus, it is reasonable to hypothesize a correlation between V-ATPase and nutrient limitation.

We have examined the expression of subunit *c* in cells grown in batch cultures that are initially depleted of the specific nutrient and have subsequently been al-

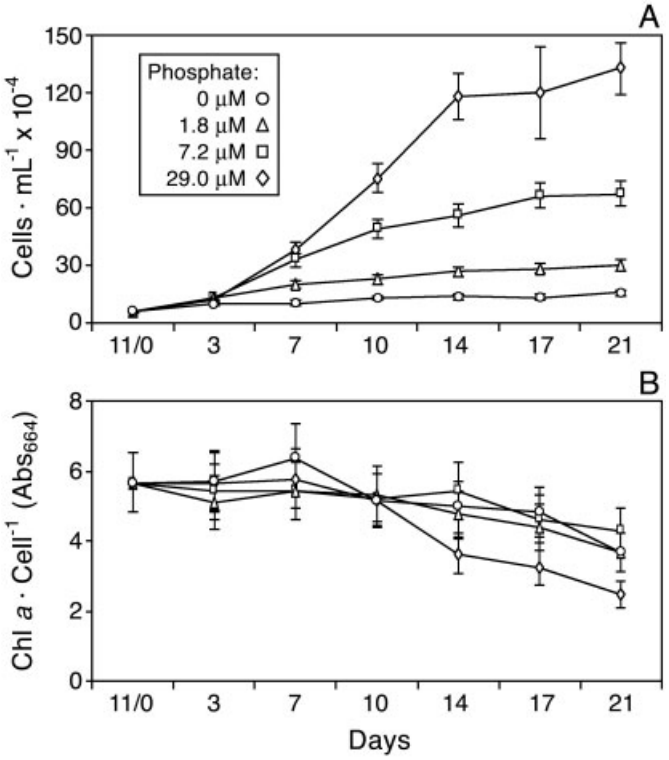

Figure 13.6 Effects of phosphate addition to P-starved cells. (A) Cell density (cells/ml). (B) Chl *a* per cell ($A_{604} \times 10^6$). Cells were starved for 11 days and subsequently brought up to 29, 7.2, 1.8 or 0 µM P and sampled for 21 days. Error bars represent SD for triplicate cultures. Reproduced from [18] by permission of the *Journal of Phycology*.

lowed to recover in fresh medium replenished by additions of the nutrient at several concentrations [18]. In this way, replicate cultures that are initially nutrient-depleted at time zero can be followed for up to 21 days as they respond to the continued absence of nutrient, or to added nutrient (in a concentration series, Figure 13.6). This experimental design permits analysis of gene expression as the cultures are, in due course, exposed to severe limitation (at time 0) to recovery and, eventually, again to limiting conditions (especially for those cultures that begin recovery at the lower nutrient levels). Corstjens and González [18] followed the expression of subunit *c* mRNA by using semi-quantitative reverse transcriptase polymerase chain reaction (RT-PCR) and comparing the specific synthesis of subunit *c* mRNA against the synthesis of PCNA (proliferating cell nuclear antigen) mRNA. The expression of PCNA, a component of the RNA polymerase, is directly correlated to the rate of cell division in *Pleurochrysis* [19]. The assumption made is that cells that are dividing rapidly are probably not nutrient limited (i.e. not stressed). This assumption remains to be tested since there has been no work to establish ''stress'' parameters for

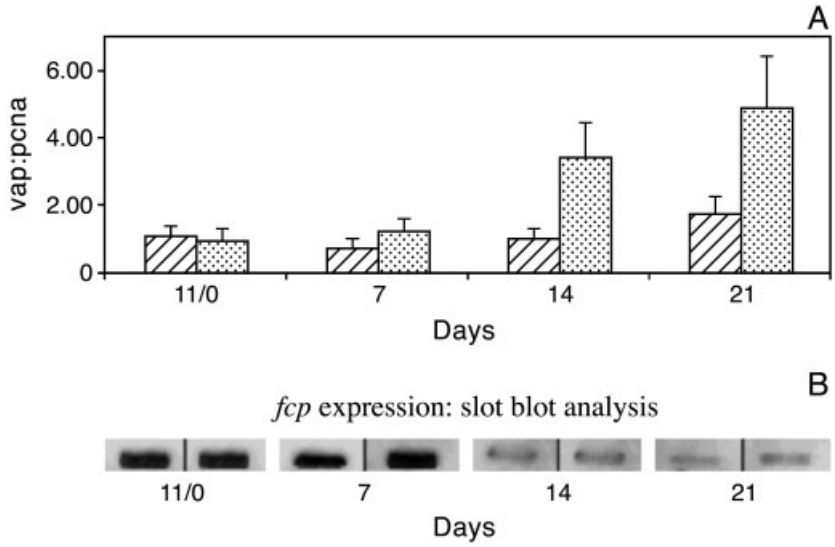

Figure 13.7 Effects of phosphate addition on the expression of RNA in P-starved cells. (A) Expression of *vap* (subunit c) and *pcna* (RT-PCR). (B) Expression of *fcp* (slot-blot analysis). Striped bars represent results obtained with cells recovering in 290 μM P: dotted bars, 7.2 μM P. Error bars are SD from triplicate cultures. Reproduced from [18] by permission of the *Journal of Phycology*.

the coccolithophorids. In the depletion experiments, cell counts and chlorophyll *a* per cell values were monitored across time. Sampling points were carefully selected to compare nutrient-replete to -depleted cells. In these experiments, the synthesis of subunit *c* mRNA relative to PCNA mRNA was highest when cells were experiencing nutrient depletion (Figure 13.7). This was true whether the depleted nutrient was nitrogen or phosphorus [18]. Although, the experiments did not unequivocally demonstrate subunit *c* induction, they clearly demonstrated that subunit *c* expression was not a characteristic of nutrient replete, rapidly dividing cells.

Interestingly, low nutrient conditions also enhance calcification in *Pleurochrysis* and *Emiliania* species (Figure 13.8) [20]. Such observations are consistent with the proposed roles of the coccolith vesicle ATPase during calcification [13]. Furthermore, they also suggest the possibility that enhanced calcification is a coccolithophore stress response. Although there are few published reports on the stress responses of the coccolithophores [21], such information is essential to an understanding of the ecophysiology of coccolithophores. In particular, it is important that we understand the essential relationships between the organisms' physiology, including mineralization, and their response to environmental changes. These questions have motivated us (Kaufman and Gonzalez, unpublished) to examine the stress responses of *Emiliania*. In preliminary experiments, we have detected differential expression of a heat-shock protein (HSP) in *Emiliania huxleyi*: at least one of the HSPs is enhanced at low nutrient levels. The HSPs are characteristic molecular indicators of stress in many different organisms [22]. These studies are ongoing.

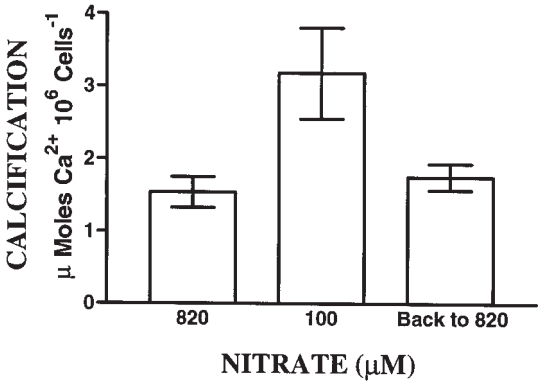

Figure 13.8 Nutrient levels affect calcification. Cells were grown for 7 days at high nitrate (820 μM) and replicates assayed for total calcium. The remainder of the cells was then transferred to low nitrate (100 μM) for 7 days and replicates taken for total calcium assay. Remaining cells were finally returned to high nitrate (820 μM) for a further 7 days and re-assayed. (Calcite in internal, external and free coccoliths was solubilized and calcium determined with the BAPTA assay [25].)

13.6 Calcification and Photosynthesis

The important features of the generic CCM described by Badger [23] are found in the coccolithophores. In the coccolithophores, protons from calcification are thought to be an essential element of a CCM [3, 24, 25]. As discussed earlier, the source of protons is calcification in the coccolith vesicle. A second important and necessary element for a CCM is the presence of carbonic anhydrase in the chloroplast stroma [24, 25]. While the linkage between calcification and photosynthesis has been debated in the literature [26, 27], the reliance of photosynthesis on the activity of a chloroplastic carbonic anhydrase has been supported by a number of studies [23, 25].

13.7 Carbonic Anhydrase

A fairly wide range of photoautotrophs, including the marine microalgae, have been shown to depend upon a set of proteins/enzymes that permit accumulation of inorganic carbon (C_i) at the active site of ribulose bisphosphate carboxylase/oxygenase (rubisco). These CCMs require the participation of carbonic anhydrase (CA) and ion transporters at the PM, chloroplast membrane and possibly thylakoid membranes [23]. In the marine microalgae, an active CCM permits the chloroplast to attain rates of photosynthesis higher than those predicted at the low levels of dissolved CO_2 in seawater [23, 28]. Marine microalgae are believed to take up dis-

solved inorganic carbon, either CO_2, if it is available, or HCO_3^-, and transport it across the chloroplast membrane where it is converted back to CO_2. Such tight coupling of enzymatic action in a confined space is believed to allow higher carboxylation efficiencies [23, 25]. This model is supported by results on cyanobacteria [29], diatoms [30], *Chlamydomonas* [31] and coccolithophores [24, 25, 28]. The principal points that support this model in the coccolithophores are the presence of CA in the chloroplasts of *Pleurochrysis* [24] and *Emiliania* [32], and physiological studies on *Emiliania* [33]. The possible role of membrane transporters in the coccolithophore PM or chloroplast membranes has not been investigated.

An important consequence of carbon flux mediated by a CCM is the presumptive proton competition between the thylakoid e^- transport and the higher demand imposed by carbonic anhydrase as it dehydrates HCO_3^- [34]. Some studies suggest that CA is located in the chloroplast stroma, while others find CA, along with rubisco, as a component of the chloroplast's pyrenoid [31]. In either case, CA activity should result in a greater proton deficit in the chloroplast stroma.

In the coccolithophorids, it has been shown that bicarbonate is the substrate of calcification and it has also been argued that bicarbonate is the sole source of CO_2 for photosynthesis [25, 27]. Although there has been much discussion regarding C_i interconversions at the periplasm and across the cytosol, utilization of bicarbonate is made possible by carbonic anhydrase in the chloroplast [23]. According to this view, not only is the concentration of CO_2 at the active site of rubisco enhanced, reducing the oxygenase activity, but the "solid-state" arrangement of enzymes (CA and rubisco) in the pyrenoid would result in greater efficiency of C_i utilization because CO_2 generation would occur in close proximity to the carboxylation site of rubisco and reduce the opportunity for loss of CO_2 because of leakage from the chloroplast. Buitenhuis et al. [25] have shown that utilization of CO_2 from bicarbonate is highly efficient. In the context of an alkaline ocean, any source of protons made available to the cytosol may offer a selective advantage. The synergy of the acidotic calcification reaction coupled with the proton pumping V-ATPase may offer such an advantage.

13.8 Is there a Connection between Calcification and Stress?

It was mentioned earlier that the V-ATPases have been implicated in stress responses [17]. It is interesting to note that coccolithophores under low nutrient conditions undertake enhanced calcification [18, 20]. It is possible to hypothesize that under nutrient limitation where cells are no longer dividing, yet photosynthetically active, a proton gradient (from enhanced calcification) may facilitate a nutrient exchange across the plasma membrane [3]. This hypothesis predicts a more active proton pump on the coccolith vesicle, and is consistent with the higher expression of subunit *c* (as compared to the cell division marker, PCNA) *and* the higher calcification rates observed for both *Pleurochrysis* and *Emiliania* under the same conditions (Figure 13.6) [20].

13.9 Summary

The rarity of subcellular calcification among eukaryotes suggests that the coccolithophorids have uniquely evolved a typical eukaryotic vacuole to a coccolith vesicle capable of calcification. A highly conserved V-Type ATPase, with proton-pumping activity, has been demonstrated on isolated coccolith vesicle membranes. The proton-pumping ATPase is an essential component that links the calcification reaction to photosynthesis by participating in the removal of protons from the calcifying vesicle and allowing for the generation of CO_2 (from HCO_3^-) within the chloroplast. There is a correlation between calcification and nutrient depletion, and this suggests that the proton pump is also the logical component needed to move protons from calcification for nutrient uptake (mediated by proton exchange). These roles of the proton-pumping V-ATPase have important consequences for the survival of the coccolithophores as they have adapted to life in an alkaline, nutrient-poor environment. A fascinating question is whether changing conditions, leading to lower pH and higher nutrient levels, may reduce the adaptive value of calcification [34]. Despite some progress, we still have a long way to go to fully understand the cellular and biochemical processes that underlie the unique ability of the coccolithophores for calcification.

Acknowledgments

The Office of Naval Research, Department of Defense, USA supported work in the author's laboratory.

References

[1] (a) D. E. Outka, D. C. Williams, *J. Protozool.* **1971**, *18*, 285–297; (b) M. R. Brown, *Portugaliae Acta Biol.* **1974**, *95*, 369–384; (c) P. van der Wal, E. W. de Jong, P. Westbroekk, W. C. de Bruijn, A. A. Mulder-Stapel, *J. Ultrastruc. Res.* **1983**, *85*, 139–158.
[2] D. K. Kwon, E. L. González, *J. Phycol.* **1994**, *30*, 689–695.
[3] (a) E. L. González, in *Biomineralization* (Ed. E. Baeuerlein), Wiley-VCH, Weinheim, **2000**, pp. 269–282; (b) T. A. McConnaughey, J. F. Whelan, *Earth Sci. Rev.* **1997**, *42*, 95–117.
[4] (a) M. E. Marsh, *Protoplasma* **1994**, *177*, 108–122; (b) M. E. Marsh, *Protoplasma* **1996**, *190*, 181–188.
[5] P. L. A. M. Corstjens, Y. Araki, E. L. González, *J. Phycol.* **2001**, *37*, 71–78.
[6] P. L. A. M. Corstjens, Y. Araki, P. Westbroek, E. L. González, *Plant Physiol.* **1996**, *111*, 652.
[7] M. E. Finbow, M. A. Harrison, *Biochem. J.* **1997**, *324*, 697–712.
[8] J. M. Ward, A. Reinders, H.-T. Hsu, H. Sze, *Plant Physiol.* **1992**, *99*, 161–169.
[9] M. Mandel, Y. Moriyama, J. D. Hulmes, Y.-C. E. Pan, H. Nelson, N. Nelson, *Proc. Natl Acad. Sci. USA* **1988**, *85*, 5521–5524.

[10] H. Sze, J. M. Ward, S. Lai, *J. Bioenerg. Biomembr.* **1992**, *24*, 371–381.
[11] W. M. Balch, P. M. Holligan, K. A. Kilpatrick, *Continental Shelf Res.* **1992**, *12*, 1353–1374.
[12] P. L. Pedersen, E. Carafoli, *Trends Biochem. Sci.* **1987**, *12*, 146–150.
[13] (a) Y. Araki, E. L. González, *J. Phycol.* **1998**, *34*, 79–88; (b) Y. Araki, PhD thesis, University of California, Los Angeles, **1997**.
[14] J. Nelson, N. Nelson, *FEBS Lett.* **1989**, *247*, 147–153.
[15] J. A. T. Dow, *J. Exp. Biol.* **1992**, *172*, 355–375.
[16] (a) M. S. Tsiantis, D. M. Bartholomew, J. A. C. Smith, *Plant J.* **1996**, *9*, 729–736; (b) B. J. Barkla, L. Zingarelli, E. Blumwald, J. A. C. Smith, *Plant Physiol.* **1995**, *109*, 549–556.
[17] K. J. Dietz, N. Tavakoli, C. Kluge, T. Mimura, S. S. Sharma, G. C. Harris, A. N. Chardonnens, D. Golldack, *J. Exp. Bot.*, **2001**, *52*, 267–302.
[18] P. L. A. M. Corstjens, E. L. González, *J. Phycol.* **2003**, *40*, 82–87.
[19] S. Lin, P. L. A. M. Corstjens, *J. Phycol.* **2002**, *38*, 164–173.
[20] E. Paasche, S. Brubak, *Phycologia* **1994**, *33*, 324–330.
[21] S. T. Dhyrman, B. Palenik, *J. Plankton Res.* **2003**, *25*, 1215–1225.
[22] A. Grover, *Cell Stress and Chaperones* **2002**, *7*, 1–5.
[23] M. Badger, *Photosynthesis Res.* **2003**, *77*, 83–94.
[24] O. Quiroga, E. L. González, *J. Phycol.* **1993**, *29*, 321–324.
[25] E. T. Buitenhuis, H. J. W. de Baar, M. J. W. Velduis, *J. Phycol.* **1999**, *35*, 949–959.
[26] A. A. Israel, E. L. González, *Mar. Ecol. Prog. Ser.* **1996**, *137*, 243–250.
[27] C. S. Sikes, R. D. Roer, K. M. Wilbur, *Limnol. Oceanogr.* **1980**, *25*, 248–261.
[28] (a) M. Badger, D. T. Hanson, G. D. Price, *Funct. Plant Biol.* **2002**, *29*, 161–173; (b) G. D. Price, D. Sultemeyer, B. Klughammer, M. Ludwig, M. R. Badger, *Can. J. Bot.* **1998**, *76*, 973–1002.
[29] (a) M. Badger, G. D. Price, *Annu. Rev. Plant Physiol. Plant Mol. Biol.* **1994**, *45*, 369–392; (b) F. M. M. Morel, E. H. Cox, A. M. L. Kraepiel, T. W. Lane, A. J. Mulligan, I. Schaperdoth, J. R. Reinfelder, P. D. Tortell, *Funct. Plant Biol.* **2002**, *29*, 301–308.
[30] (a) J. V. Moroney, H. D. Husic, N. E. Tolbert, *Plant Physiol.* **1985**, *79*, 177–183; (b) J. V. Moroney, S. G. Bartlett, G. Samuelsson, *Plant Cell Environ.* **2001**, *24*, 141–153.
[31] N. A. Nimer, M. D. Iglesias-Rodriguez, M. J. Merrett, *J. Phycol.* **1997**, *33*, 625– 631.
[32] (a) N. A. Nimer, M. J. Merrett, *New Phytol.* **1992**, *121*, 173–177; (b) N. A. Nimer, C. Brownlee, M. J. Merrett, *Mar. Ecol. Prog. Ser.* **1994**, *109*, 257–262; (c) N. A. Nimer, M. J. Merrett, C. Brownlee, *J. Phycol.* **1996**, *32*, 813–818.
[33] J. A. Raven, *Plant Cell Environ.* **1997**, *20*, 147–154.
[34] M. D. Iglesias-Rodriguez, C. W. Brown, S. C. Doney, J. Kleypas, D. Kolber, Z. Kolber, P. K. Hayes, P. G. Falkowski, *Global Biogeochem. Cyc.* **2002**, *16*, 1100.

14 The Zebrafish as a Genetic Model to Study Otolith Formation

C. Söllner and T. Nicolson

14.1 Introduction

Fish move and orient themselves in three dimensions. Like other vertebrate organisms, they use gravitational and visual clues for spatial orientation and postural control. In order to register gravity and linear accelerations, and transform them into electrical signals, fish have developed a detection system consisting of three components within the inner ear, i.e. dense calcium carbonate crystals ($CaCO_3$) representing an inertial mass, an underlying sensory unit consisting of hair cells and a gelatinous membrane that connects the crystals with the sensory epithelium. In zebrafish (*Danio rerio*) and all bony fishes, the acellular crystalline mineral deposits are called otoliths (literally, "ear stones"). They are composites of inorganic and organic components [1, 2]. Tiny calcium carbonate crystallites are associated with an organic fibrous matrix, indicating that seeding and growth of these crystals are under genetic control. The molecular mechanisms involved in the regulation of the mineral deposition and the morphogenesis of otoliths are just now becoming clearer. One model organism, the zebrafish, has become particularly useful. Otoliths in zebrafish larvae are highly accessible, providing the rare opportunity to study the complex interactions between matrix proteins and inorganic crystals *in vivo*. The zebrafish is a well-established vertebrate model system that offers the possibility to identify genes involved in the biogenesis of otoliths by means of forward and reverse genetic approaches. In addition, techniques are established to study loss-of-function phenotypes, and the pattern of gene expression and localization of proteins within the organism.

In the first part of this chapter we describe the function and formation of the otoliths in wild-type zebrafish, and then focus on genetic and biochemical approaches which have led to the identification of several key molecules involved in otolith formation.

14.2 Otoliths and Otoconia

In 4-day-old zebrafish larvae, the ear (Figure 14.1) consists of five interconnected chambers, the utricle, saccule and three semicircular canals. Each chamber contains

Biomineralization: From Biology to Biotechnology and Medical Application, Second Edition. Edited by E. Bäuerlein

ISBN: 3-527-31065-7

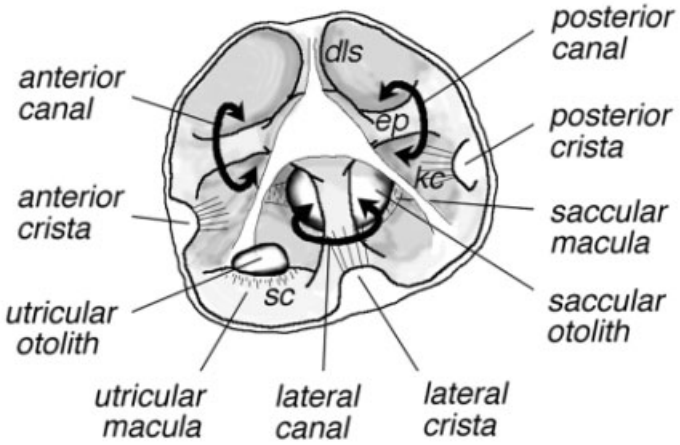

Figure 14.1 Schematic diagram of the structural features of an ear from a 4-day-old zebrafish. At this stage of development, the ear is already functional. Abbreviations: dls, dorsolateral septum; ep, epithelial projections; kc, kinocilia; sc, stereociliary bundles. (Reproduced with permission from [39].)

a sensory epithelium of sensory hair cells and supporting cells. The task of the semicircular canals is to register rotational acceleration in the three principal planes. The utricle and saccule are involved in the detection of linear acceleration, gravity and sound [3, 4]. Their sensory patches are called maculae. Each macula is associated with an otolith (Figure 14.2a). The otolithic membrane is in direct contact with apical protrusions of the hair cells – the stereociliary bundles. Mechanical deflection of these bundles is thought to open transduction channels located near the tips of each stereocilium. Opening of transduction channels then leads to cell depolarization and subsequently triggers the release of neurotransmitters [5]. The mass load of the otoliths increases the sensitivity of the detection system. Mammals also have calcium carbonate crystals associated with the sensory epithelium of their vestibular macular organs. These crystal structures are homologous to fish otoliths. Due to their number and size, they are called otoconia (Figure 14.2b), which literally means "ear dust". A major difference between otoliths and otoconia is that otoliths display a daily growth pattern [6], whereas the barrel-shaped otoconia are essentially inert and undergo little changes. In addition to otoliths and otoconia, vertebrates have several mineralized tissues like teeth, bones and scales, but only the otoliths and otoconia are composed of calcium carbonate. Primitive jawless fish use calcium phosphate as the mineral component of the otoliths. However, in the course of vertebrate evolution, there was a clear trend towards the use of calcium carbonate. The otoliths of fish are predominantly composed of the calcium carbonate polymorph aragonite. In rare cases, vaterite is also present. In contrast, mammals use the most stable and less dense calcium carbonate polymorph calcite in their otoconia. A possible explanation for the preference of calcium carbonate instead of calcium phosphate could be the ability to exert a separate homeostatic control on the biominerals present in the ear.

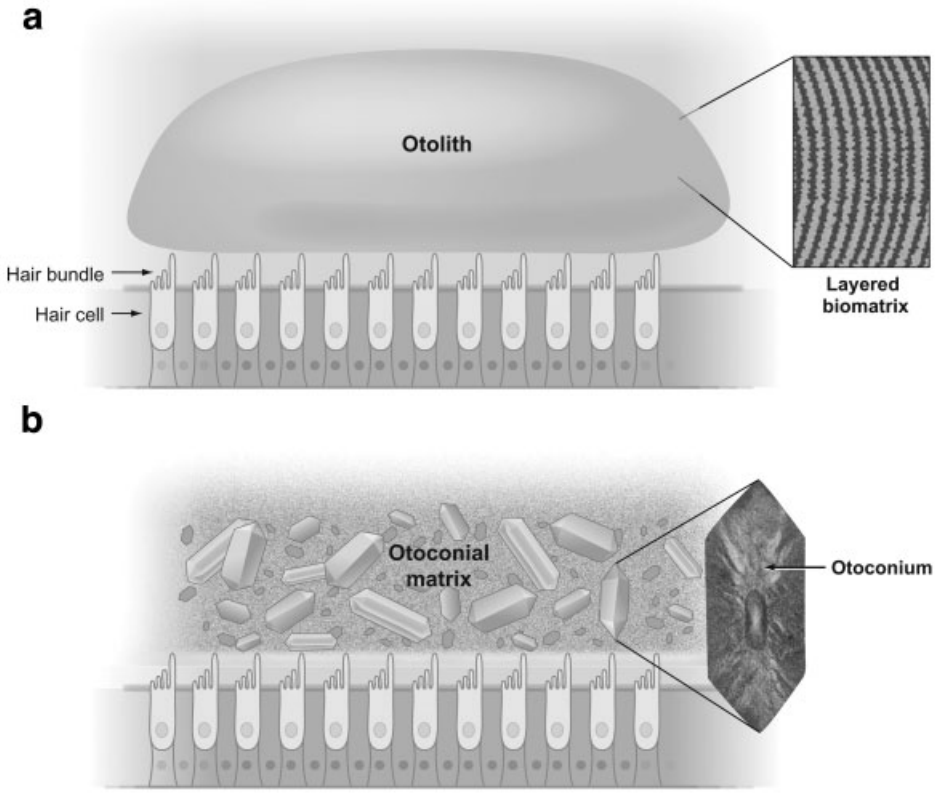

Figure 14.2 Comparison of the inner ear sensory detection systems associated with calcium carbonate crystals. Otoliths in fish (a) and otoconiain mammals (b). The cross-sections indicate the composite nature of these crystals. (Reproduced with permission from [40].)

14.3 Characterization of Otolith Development in Wild-type Zebrafish

The zebrafish is an ideal organism to study otolith development. External fertilization offers the possibility to study all stages of development. In addition, zebrafish embryos are optically transparent, facilitating the study of the structures of the inner ear by means of a dissecting microscope.

The assembly of the otoliths is an extracellular process that takes place in the endolymphatic fluid present in the lumen of the inner ear. In contrast to vertebrate bones, teeth or molluscan shells, the inner ear epithelium is not in direct contact with the region of calcification. Moreover, the endolymphatic fluid has an anti-calcifying activity [1]. This unusual extracellular fluid is characterized by an alkaline pH, a high concentration of potassium ions and saturated levels of the calcium car-

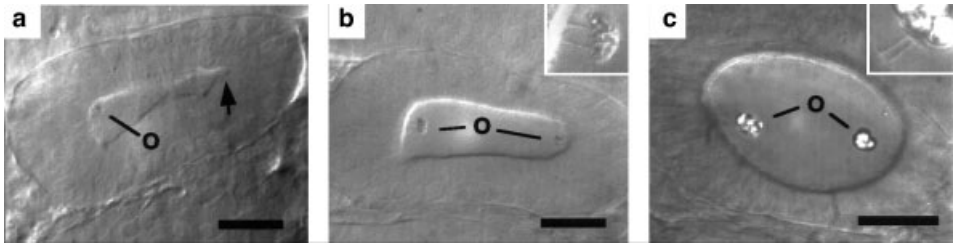

Figure 14.3 Histological analysis of early otolith development in live zebrafish embryos. (a) At 18.5 h.p.f., the otic vesicle is in the process of expanding. The anterior otolith (O) is already present. (b) The ear at 21.5 h.p.f. The posterior otolith begins to form. The inset shows a higher magnification of the anterior part of the otic vesicle. Both kinocilia of the tether cells connected with the otolith are visible. (c) The ear at 24 h.p.f. Both otoliths have a crystalline appearance. Bar = 25 μm. (Reproduced and modified from [10] with permission.)

bonate precursor ions Ca^{2+} and HCO_3^- [7]. Carbonic anhydrase (CA) appears to be involved in the creation and maintenance of the endolymphatic composition by catalyzing CO_2 to HCO_3^- and by removing hydrogen ions from the endolymph [8].

During early development, the otic placode becomes visible around 15 h postfertilization (h.p.f.). Shortly thereafter, by a process of cavitation, the placode transforms into an otic vesicle [9]. Otolith formation begins between 18 and 18.5 h.p.f. [10]. At this stage, the otic vesicle is composed of epithelial cells surrounding a lumen filled with endolymphatic fluid (Figure 14.3a). Two tether cells located at the anterior and posterior regions of the otic vesicle represent an exception. Tether cells have long kinocilia on their apical surface projecting into the lumen of the ear (Figure 14.3b, inset). These cilia serve as an anchor for otolith development (Figure 14.3c). Many free-moving otolith precursor or seeding particles are present in the lumen of the ear at this stage. They are, at least in part, composed of glycogen [11] and attach to the tips of the kinocilia. Repetitive aggregation of these spherical particles (spherules) leads to the formation of globules (Figure 14.4a). Some electron-dense spherules do not fuse and instead remain located in the middle of the otolith. They form the nucleus of the otolith (Figure 14.4b) [10]. In addition to the kinocilia of the tether cells, another population of cilia is involved in the early steps of otolith formation. These are motile cilia located at the surface of many epithelial cells of the otic vesicle. These cilia beat rapidly, ensuring the even distribution and prevent premature aggregation of otolith seeding particles [10]. The otolith seeding particles and the motile cilia disappear around 24 h.p.f. when each otolith has a diameter of approximately 7–8 μm. This first step of otolith formation takes place before the ear becomes functional. During the second phase of otolith development, the anterior and posterior otoliths start to differ in size and shape, and acquire distinctive morphologies. The second phase of otolith formation is characterized by a 90 % decrease of the growth rate [10]. In transmission electron microscopy (TEM) micrographs of otoliths derived from 5-day-old zebrafish larvae, a nucleus composed of densely stained spherules surrounded by succeeding rings of organic matrix is visible (Figure 14.4c). The organic matrix is a complex network of proteins, glycopro-

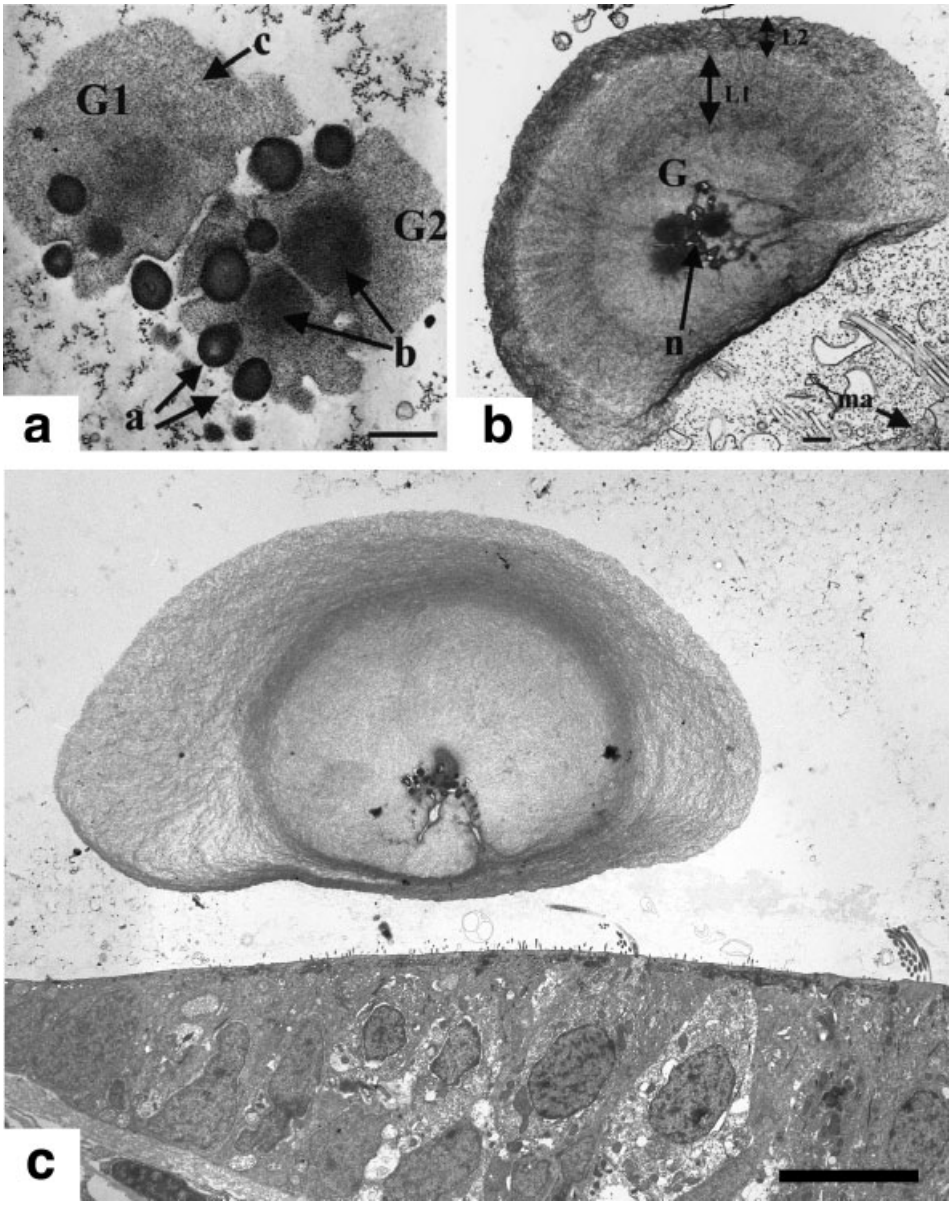

Figure 14.4 TEM micrographs showing sections through otoliths at several stages of development. (a) At 23 h.p.f., electron-dense spherules marked with 'a' are depicted during the process of attaching to the periphery of the otolith. These spherules gradually start to transform into globules (G1 and G2) indicated by 'b' and 'c'. (b) TEM section through a 50-h.p.f. otolith. In the center of the otolith, electron-dense spherules forming the nucleus (n) of the otolith are visible. At this stage, the fused globules (G) are surrounded by two radial layers (L1 and L2). (c) Transverse TEM section through an utricular otolith from a 5-day-old larva. Bars = 0.5 (a), 1.0 (b) and 10 μm (c). [(a) and (b) are reproduced with permission from [10], (c) is courtesy of C. Seiler.]

teins and collagens [1]. The soluble matrix is very rich in acidic macromolecules. However, most of the mass is composed of mineral. Polycrystalline calcium carbonate with the crystal lattice of aragonite comprises 90–95 % of the otolithic mass [12, 13]. At the electron microscopic level, distinct zones are visible, consisting mainly of polycrystalline calcium carbonate and organic matrix that has higher electron density (Figure 14.4c). These different zones are arranged in daily growth increments [6] and can be used for age determination. Borelli et al. [14] showed that there are indeed daily variations in the concentrations of calcification factors in trout endolymph that could account for the formation of bilayered rings during day and night periods. The concentration of organic matrix precursors is very high at dusk, whereas the levels of CO_3^{2-} and Ca^{2+} reach their maximum at dawn. In older zebrafish (around day 12), an additional third otolith located in the developing lagena starts to form, most likely by a process also involving otolith precursor particles [15].

14.4 Zebrafish Mutants with Defects in Otolith Formation

The study of zebrafish otolith mutants will yield valuable insights into otolith biogenesis. Mutants can be generated by either forward or reverse genetic approaches. A forward genetic approach involves the induction of random mutations, followed by the selection of the mutants and cloning of the affected genes. Thus far, many zebrafish mutants have been identified with defects in otolith formation. Large-scale screens carried out in Tübingen and Boston identified a group of recessive mutants with defects in otolith development but unaffected ear morphology [16, 17]. These otolith mutants can be assigned to four different groups. The mutants of the one group, *einstein* and *menhir*, have only one otolith in their ear at all stages. *half stoned*, *stein und bein* and *what's up* belong to another group of mutants, which initially have no or tiny otoliths, but some of the homozygous mutant larvae develop a single or two small otoliths later on. Homozygous *keinstein* and *backstroke* mutants display the most severe phenotype, lacking otoliths at all stages. In *rolling stones* mutants, the otoliths are normal in size, but they are not correctly anchored, indicating that a protein essential for attaching the otoliths to the kinocilia of the tether cells or to the otolithic membrane is affected. Many of these mutants also display a behavioral phenotype: they fail to maintain balance and hence swim in circles or sideways.

In addition to the above mutants, other mutants with smaller otoliths or in which the otolith phenotype is a secondary defect have been identified [16, 17]. Riley and Grunwald described a dominant, semi-lethal zebrafish mutation named *monolith* [18]. Fish carrying this mutation are not able to form the anterior (utricular) otolith. All other structures of the inner ear including the posterior (saccular) otolith have normal morphology in *monolith* mutant embryos. The dispersal of otolith precursor particles in the lumen of the otic vesicle is also normal. About one-fourth of the homozygous and more than half of the heterozygous mutant larvae start to form

an anterior otolith between 6 and 10 days post-fertilization (d.p.f.). These larvae survive to adulthood; however, adult mutants still have smaller utricular otoliths. By transplanting totipotent cells from wild-type embryos into *monolith* mutants, Riley and Grunwald demonstrated that small numbers of wild-type supporting cells present in a mutant host utriculus are able to rescue the phenotype. This elegantly illustrates that supporting cells play a direct role in the generation of otoliths. This mutant also shows that the formation of the anterior otolith is controlled in a different way than the posterior otolith. Moreover, the utricular otolith is necessary and sufficient for vestibular function in zebrafish [15].

In zebrafish *mind bomb* mutants, a ubiquitin ligase is affected [19]. The mutation causes failure in lateral inhibition, resulting in patterning defects of the hindbrain and the absence of supporting cells in sensory patches in the ear. These mutants are still able to develop small yet irregularly shaped otoliths [20]. This phenotype clearly shows that the supporting cells are not the only cell type delivering materials into the otic lumen necessary for otolith formation. It also suggests that hair cells are required for this process, as the structure of *mind bomb* otoliths is very similar to wild-type otoliths at the electron microscope level [20].

14.5 Zebrafish Genes Having a Direct Role in Otolith Formation

The *starmaker* gene [21] was identified due to weak similarities at the protein level with the human *DSPP* gene, which is involved in teeth formation and in rare cases is also associated with deafness [22, 23]. Both proteins are very acidic, and share long repetitive stretches consisting mainly of aspartic acids and serines. The *starmaker* gene is expressed at high levels in the otic placode and otic vesicle (see Figure 14.6a). Later, the expression becomes restricted predominantly to the sensory patches associated with otoliths. Using a reverse genetic approach, with morpholino oligonucleotide-mediated targeted gene knock-down, it was shown that the *starmaker* gene is an essential regulator of the otolithic shape [21]. Antisense oligonucleotides block efficient translation or splicing of the targeted mRNA. Down-regulation of the Starmaker protein levels causes a dramatic concentration-dependent change in otolith shape (Figure 14.5). In morpholino-injected fish, the otoliths lost their round, ovoid form at low doses (Figure 14.5b). Higher doses of the morpholino caused the formation of star shaped otoliths (Figure 14.5c). Nearly complete loss of *starmaker* activity gave rise to otoliths resembling chunks of pure crystalline calcium carbonate (Figure 14.5d). Synchrotron X-ray diffraction experiments showed that this change in otolith shape goes hand in hand with a change of the size and polymorph of the calcium carbonate crystals. Tiny aragonite crystallites normally present in wild-type otoliths changed into larger crystals in the star-like otoliths. Upon complete reduction of gene activity, a switch to large crystals with the lattice of calcite was observed. Immunolocalization experiments using an antibody directed against the C-terminal end of Starmaker showed that cells of the sen-

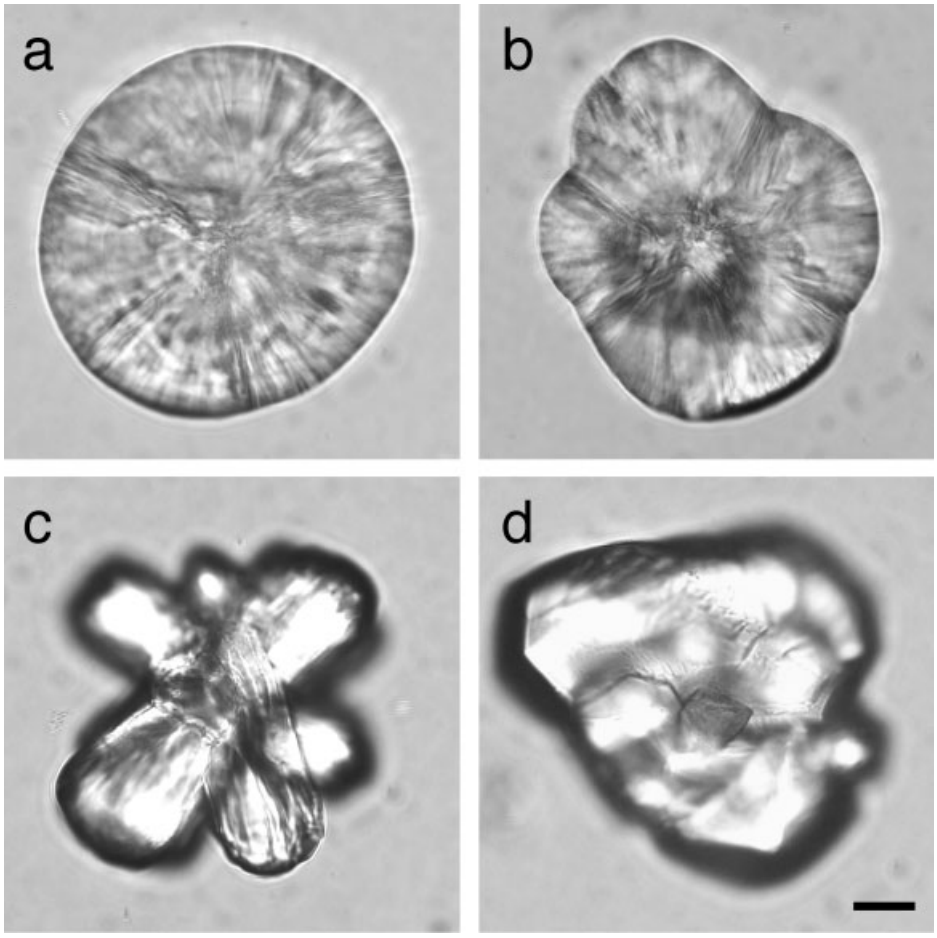

Figure 14.5 Otoliths derived from 7-day-old zebrafish. (a) Smooth ovoid otolith from a wild-type zebrafish. (b) Otolith with slight indentations caused by minor reduction of Starmaker protein levels. (c) Star-shaped otolith obtained by stronger reduction of the Starmaker levels. (d) Otolith resembling an inorganic crystal derived from a zebrafish where the Starmaker protein was absent. Bar = 10 μm.

sory epithelium secrete the protein into the lumen of the ear. In the first phase of otolith formation, the protein associates with the otolithic seeding particles present in the lumen of the ear (Figure 14.6b). Starmaker also remains associated with the growing otoliths during the second phase of otolith formation. Ultrathin cross-sections of otoliths from 5-day-old larvae labeled with anti-Starmaker antibody show that the Starmaker protein is a component of the organic matrix of the otoliths (Figure 14.6c). The immunolocalization results suggest that a change in the endolymph composition of the ear as seen in mice with mutations in the *Pendrin* gene [24] was not responsible for the observed phenotype. The results of the reverse

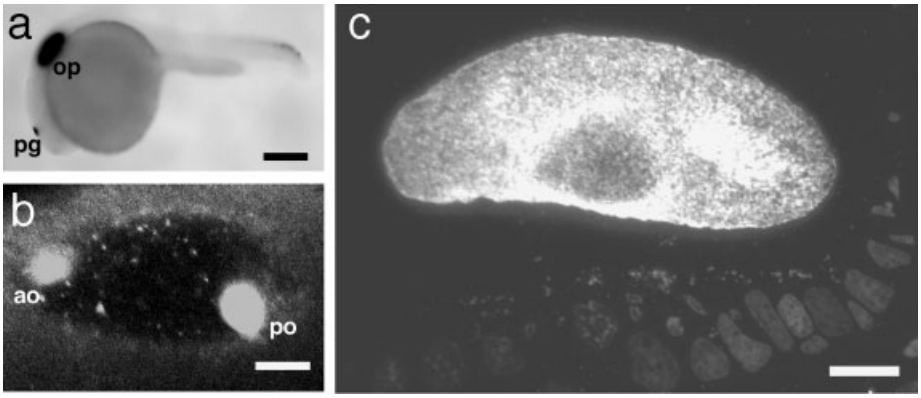

Figure 14.6 Expression of the *starmaker* mRNA and immunofluorescent localization of the Starmaker protein. (a) *In situ* hybridization in a 24-h.p.f. zebrafish embryo shows that the *starmaker* message is very strongly expressed in the otic vesicle. Additional labeling is visible in the pineal organ of the brain and in the posterior tail region. (b) In 24-h.p.f. zebrafish embryos, an antibody directed against the Starmaker protein recognizes developing otoliths and otolithic seeding particles floating in the cavity of the ear. (c) Starmaker protein is part of the otolithic matrix, as seen in ultrathin sections. In addition, Starmaker-positive vesicles are present in the apical region of underlying sensory epithelial cells. Bars = 35 (a) and 12 μm (b and c). Abbreviations: ao, anterior otolith; op, otic placode; pg, pineal gland; po, posterior otolith.

genetic study with *starmaker* indicate that a single protein can select for the nucleation of the calcium carbonate polymorph aragonite and can control crystal growth. Particular features of the Starmaker protein may explain the molecular mechanisms favoring the nucleation of aragonite. The predicted β-strand region consisting of alternating aspartic acids and serines may provide a surface that resembles the surface of calcium carbonate with the crystal lattice of aragonite. The inhibition of crystal growth is most likely achieved by direct recognition and binding between the surface of the crystal and the Starmaker protein. Inhibition of crystal growth ensures that the otoliths are composite structures consisting of innumerous crystallites embedded in an organic matrix.

Mutations in the *otopetrin-1* gene in mouse have been shown to be associated with the lack of otoconia [25]. A candidate gene approach revealed that a mutation in the orthologous gene in zebrafish is responsible for the *backstroke* phenotype characterized by the lack of otoliths at all stages [16 and unpublished data]. In zebrafish, the *otopetrin-1* mRNA is specifically expressed in the otic placode and otic vesicle. At later stages (4 d.p.f.), the message is restricted to the sensory hair cells of the ear and the lateral line system. The protein encoded by the *otopetrin-1* gene is predicted to have ten transmembrane domains (Figure 14.7a), suggesting a function as a receptor, channel or transporter. The missense mutation present in *backstroke* causes an amino acid exchange that leads to the prediction of two additional transmembrane domains. These additional transmembrane domains may severely affect the function of the protein. In mice, the Otopetrin-1 protein localizes

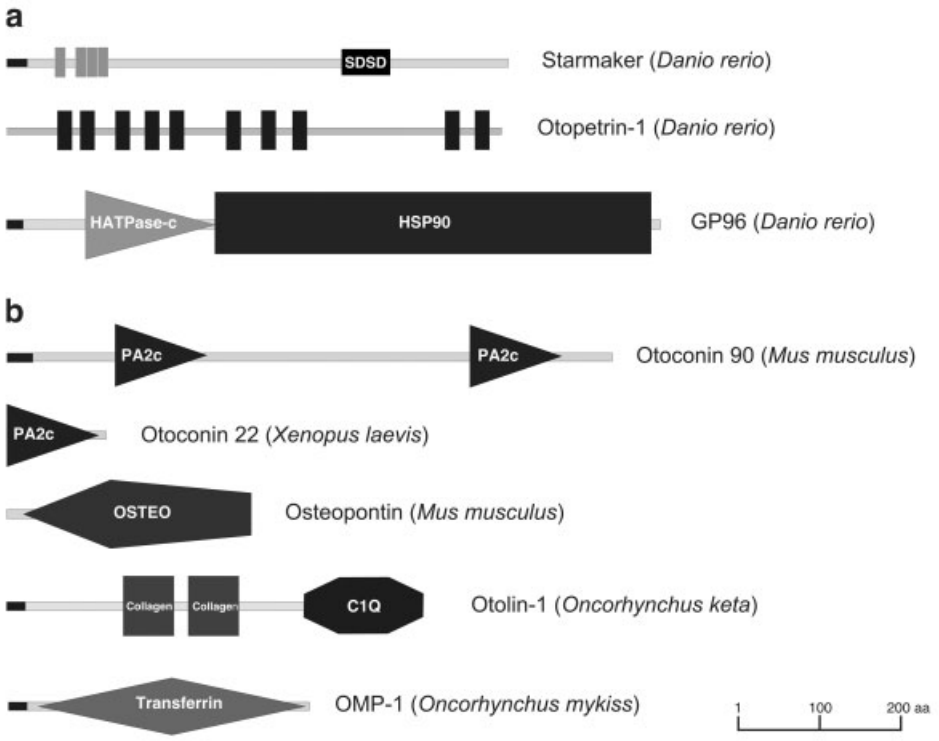

Figure 14.7 Domain structure of proteins required for otolith or otoconia development. (a) The functions of Starmaker, an extremely acidic protein with four internal repeats of unknown function, and a stretch of alternating serines (S) and aspartic acids (D), Otopetrin-1, a protein with 10 transmembrane domains, and the heatshock protein GP96 have been studied either by knock-down or by forward genetics. (b) Proteins that are associated with otoliths and/or otoconia. Several are components of the otolithic organic matrix.

to the otolithic membrane, suggesting that it has a direct function in otolith formation [25]. Immunoreactivity with the antibody directed against the Starmaker protein in *backstroke* mutants revealed that a subset of epithelial cells of the otic vesicle fail to secrete Starmaker protein into the lumen of the ear. Instead, the Starmaker protein accumulated in these cells, suggesting that Otopetrin-1 is involved in protein trafficking of the Starmaker protein. Using the same antibody in the *keinstein* mutants, another zebrafish mutant that lacks otoliths, revealed a different defect. The Starmaker protein is secreted in the lumen of the ear but is not associated with otolithic seeding particles (unpublished observations).

GP96, an endoplasmatic reticulum chaperone protein (Figure 14.7a), is necessary for otolith formation in zebrafish [26]. Chaperones ensure the correct assembly and folding of newly synthesized proteins. GP96 mRNA is expressed in a specific pattern during zebrafish embryogenesis including the otic placode and otic vesicle.

Sumanas et al. showed that morpholino mediated knock-down of GP96 results in a specific defect – the inability of otolith precursor particles to adhere to the kinocilia of the tether cells. Instead, the otolith seeding particles fuse and often form a single large or irregularly formed otolith. These clumpy otoliths remain unanchored in most, but not all cases. Interestingly, the observed phenotype caused by knock-down of GP96 is reminiscent of the phenotypes described for the zebrafish *einstein*, *menhir* and *monolith* mutants. It is evident that GP96 is not a direct component of the otoliths, leading Sumanas et al. to speculate that it could be involved in the processing of integrins, a family of transmembrane glycoproteins involved in adhesion and signaling. Integrin $\alpha_8\beta_1$ has been shown to be required for stereocilia maturation in sensory hair cells [27] and to bind to the Osteopontin protein [28], a protein that is associated with rodent otoconia. Interactions between Osteopontin and Integrin $\alpha_8\beta_1$ may be a possible mechanism for attachment of otolith precursor particles to the kinocilia of the tether cells.

14.6 Proteins Reported to be Associated with Otoliths or Otoconia

By biochemical extraction approaches or immunolocalization experiments, several proteins have been identified that are associated with the organic matrix of otoconia or otoliths in a variety of species. Otoconins, ear-specific glycoproteins, are a part of the organic matrix of calcitic (Otoconin-90/95), aragonic (Otoconin-22) and vateritic (Otoconin-55) otoconia [29, 30]. They all possess one or two most likely non-functional domains related to the secretory phospholipase A2 (PLA2) (Figure 14.7b). PLA2 enzymes are normally involved in membrane trafficking. Otoconin-90 is expressed only in the non-sensory epithelia of maculae in mice [31, 32]. Verpy et al. proposed that the PLA2 domains of Otoconin-95 interact with membranes of the pre-otoconia [32].

Osteopontin, a secreted phosphorylated glycoprotein (Figure 14.7b) not specific to mineralized tissues, has also been identified in otoconia [33]. *Osteopontin* mRNA was detected in sensory hair cells. Primary Osteopontin is a component of the extracellular matrix (ECM) associated with bone and cartilage [34], and appears to be involved in the regulation of bone and teeth biomineralization [35].

Otolin-1, a collagen-like protein (Figure 14.7b), has been extracted from decalcified salmon otoliths [36]. It is related to type VIII and X collagens that form a three-dimensional meshwork. Immunocytochemistry showed that it is produced by cells located at the periphery of the sensory epithelium, and is part of the otolithic matrix and the gelatinous layer of the otolithic membrane [37]. The authors [36] speculate that Otolin-1 may serve as a nucleator of crystallization or provide a surface for interaction with other otolithic matrix proteins [36]. It is noteworthy that collagens are also involved in the formation of bones and teeth. In contrast to Otolin-1,

the collagens involved in bone and dentin formation belong to the group of fibrillar collagens.

Otolith matrix protein-1 (OMP-1) is a non-acidic glycoprotein (Figure 14.7b) that was found in rainbow trout otoliths [38]. OMP-1 contains a transferrin domain. Transferrin domains are known to be involved in iron binding and presumably control the level of free iron in biological fluids. OMP-1 is a component of the otolithic organic matrix and is secreted from non-sensory squamous epithelial cells into the lumen of the ear [37].

Mutations in the above genes have not been reported. The orthologous genes in zebrafish therefore represent ideal candidates for a reverse genetic approach. In addition, the genes encoding components of otoconia and otoliths are excellent candidate genes for the zebrafish otolith mutants.

14.7 Conclusions

Taken together, the results from studies in zebrafish and studies in other fish species and mammals provide a more comprehensive picture of otolith or otoconia formation. During the first phase of otolith development, the presence of glycogenous otolithic seeding particles is crucial for the formation of the otoliths. Prior to the attachment of these seeding particles to the kinocilia of the tether cells, matrix proteins involved in otolith formation are already associated with seeding particles (Figure 14.5b). These otolithic seeding particles probably provide the correct microenvironments for the process of calcium carbonate nucleation. Either the seeding particles themselves or matrix proteins associated with the particles such as collagens or acidic proteins like Starmaker may facilitate this process.

Many different cell types of the ear participate in delivering material to the site of otolith biogenesis (Figure 14.8). Hair cells and supporting cells of the sensory epithelium secrete Starmaker protein into the lumen of the ear. The otoconins appear to be synthesized and secreted by cells not associated with the sensory epithelium. Otopetrin-1 in zebrafish is predominantly expressed in hair cells.

The study of the Starmaker protein function and distribution implies a model for sculpting inorganic crystals and determine their shape. Starmaker controls the structure and composition of the mineral component of the otolith and is therefore a key regulator of the otolithic shape. Higher levels of Starmaker protein present at the base of the otolith facing the neurosensory epithelium than at the distal side may account for the flat bottom shape of the otoliths. Indeed, Borelli et al. showed that there is a spatial gradient of proteins in the endolymph of macular ear chambers [1]. The concentration of proteins is higher at the side facing the macula than at the distal region of the ear chamber.

Further characterization of loss-of-function phenotypes and molecular interactions of the proteins, which have been reported to be associated with otoliths or otoconia, will provide a more complete model of otolith formation.

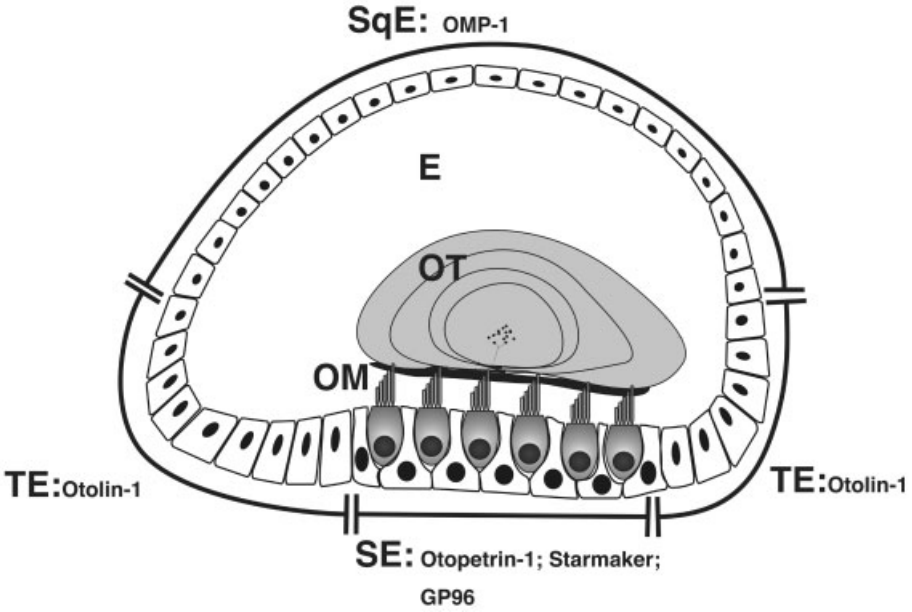

Figure 14.8 Schematic diagram of a cross-section through a fish utricle illustrating the epithelia involved in the secretion of proteins required for otolith biogenesis. OMP-1 is expressed in non-sensory epithelium (SqE). Cells of the transitional epithelium (TE), adjacent to the sensory epithelium, express Otolin-1. Otopetrin-1, Starmaker and GP96 are expressed in cells of the sensory epithelium. Abbreviations: E, endolymph; OM, otolithic membrane; OT, otolith; SE, sensory epithelium; SqE, squamous epithelium; TE, transitional epithelium.

Acknowledgments

We would like to thank E. Busch-Nentwich and C. Seiler for helpful suggestions on the manuscript.

References

[1] G. Borelli, N. Mayer-Gostan, H. De Pontual, G. Boeuf, P. Payan, *Calcif. Tissue Int.* **2001**, *69*, 356.
[2] S. E. Campana, *Mar. Ecol. Prog. Ser.* **1999**, *188*, 263.
[3] R. R. Fay, *Science* **1984**, *225*, 951.
[4] A. Popper, C. Platt, in *The Physiology of Fishes* (Ed. D. H. Evans), CRC Press, Boca Raton, FL, **1993**, pp. 99–136.
[5] A. J. Hudspeth, P. G. Gillespie, *Neuron* **1994**, *12*, 1.

[6] G. Pannella, *Science* **1971**, *173*, 1124.
[7] P. Payan, H. Kossmann, A. Watrin, N. Mayer-Gostan, G. Boeuf, *J. Exp. Biol.* **1997**, *200*, 1905.
[8] H. Tohse, H. Ando, Y. Mugiya, *Comp. Biochem. Physiol. A Mol. Integr. Physiol.* **2004**, *137*, 87.
[9] C. Haddon, J. Lewis, *J. Comp. Neurol.* **1996**, *365*, 113.
[10] B. B. Riley, C. Zhu, C. Janetopoulos, K. J. Aufderheide, *Dev. Biol.* **1997**, *191*, 191.
[11] M. Pisam, C. Jammet, D. Laurent, *Cell Tissue Res.* **2002**, *310*, 163.
[12] D. Carlström, *Biol. Bull. Mar. Biol. Lab. Woods Hole* **1963**, *125*, 441.
[13] E. T. Degens, W. G. Deuser, R. L. Haedrich, *Mar. Biol.* **1969**, *2*, 105.
[14] G. Borelli, M. E. Guibbolini, N. Mayer-Gostan, F. Priouzeau, H. De Pontual, D. Allemand, S. Puverel, E. Tambutte, P. Payan, *J. Exp. Biol.* **2003**, *206*, 2685.
[15] B. B. Riley, S. J. Moorman, *J. Neurobiol.* **2000**, *43*, 329.
[16] T. T. Whitfield, M. Granato, F. J. van Eeden, U. Schach, M. Brand, M. Furutani-Seiki, P. Haffter, M. Hammerschmidt, C. P. Heisenberg, Y. J. Jiang, D. A. Kane, R. N. Kelsh, M. C. Mullins, J. Odenthal, C. Nüsslein-Volhard, *Development* **1996**, *123*, 241.
[17] J. Malicki, A. F. Schier, L. Solnica-Krezel, D. L. Stemple, S. C. Neuhauss, D. Y. Stainier, S. Abdelilah, Z. Rangini, F. Zwartkruis, W. Driever, *Development* **1996**, *123*, 275.
[18] B. B. Riley, D. J. Grunwald, *Dev. Biol.* **1996**, *179*, 427.
[19] M. Itoh, C. H. Kim, G. Palardy, T. Oda, Y. J. Jiang, D. Maust, S. Y. Yeo, K. Lorick, G. J. Wright, L. Ariza-McNaughton, A. M. Weissman, J. Lewis, S. C. Chandrasekharappa, A. B. Chitnis, *Dev. Cell* **2003**, *4*, 67.
[20] C. Haddon, C. Mowbray, T. Whitfield, D. Jones, S. Gschmeissner, J. Lewis, *J. Neurocytol.* **1999**, *28*, 837.
[21] C. Söllner, M. Burghammer, E. Busch-Nentwich, J. Berger, H. Schwarz, C. Riekel, T. Nicolson, *Science* **2003**, *302*, 282.
[22] S. Xiao, C. Yu, X. Chou, W. Yuan, Y. Wang, L. Bu, G. Fu, M. Qian, J. Yang, Y. Shi, L. Hu, B. Han, Z. Wang, W. Huang, J. Liu, Z. Chen, G. Zhao, X. Kong, *Nat. Genet.* **2001**, *27*, 201.
[23] X. Zhang, J. Zhao, C. Li, S. Gao, C. Qiu, P. Liu, G. Wu, B. Qiang, W. H. Lo, Y. Shen, *Nat. Genet.* **2001**, *27*, 151.
[24] L. A. Everett, I. A. Belyantseva, K. Noben-Trauth, R. Cantos, A. Chen, S. I. Thakkar, S. L. Hoogstraten-Miller, B. Kachar, D. K. Wu, E. D. Green, *Hum. Mol. Genet.* **2001**, *10*, 153.
[25] B. Hurle, E. Ignatova, S. M. Massironi, T. Mashimo, X. Rios, I. Thalmann, R. Thalmann, D. M. Ornitz, *Hum. Mol. Genet.* **2003**, *12*, 777.
[26] S. Sumanas, J. D. Larson, M. Miller Bever, *Dev. Biol.* **2003**, *261*, 443.
[27] A. Littlewood Evans, U. Muller, *Nat. Genet.* **2000**, *24*, 424.
[28] S. Denda, L. F. Reichardt, U. Muller, *Mol. Biol. Cell* **1998**, *9*, 1425.
[29] K. G. Pote, M. D. Ross, *Comp. Biochem. Physiol. B* **1991**, *98*, 287.
[30] K. G. Pote, C. R. Hauer, H. Michel, J. Shabanowitz, D. F. Hunt, R. H. Kretsinger, *Biochemistry* **1993**, *32*, 5017.
[31] Y. Wang, P. E. Kowalski, I. Thalmann, D. M. Ornitz, D. L. Mager, R. Thalmann, *Proc. Natl Acad. Sci. USA* **1998**, *95*, 15345.
[32] E. Verpy, M. Leibovici, C. Petit, *Proc. Natl Acad. Sci. USA* **1999**, *96*, 529.
[33] T. Takemura, M. Sakagami, T. Nakase, T. Kubo, Y. Kitamura, S. Nomura, *Hear. Res.* **1994**, *79*, 99.
[34] D. T. Denhardt, X. Guo, *FASEB J.* **1993**, *7*, 1475.
[35] C. M. Giachelli, S. Steitz, *Matrix Biol.* **2000**, *19*, 615.
[36] E. Murayama, Y. Takagi, T. Ohira, J. G. Davis, M. I. Greene, H. Nagasawa, *Eur. J. Biochem.* **2002**, *269*, 688.
[37] E. Murayama, Y. Takagi, H. Nagasawa, *Histochem. Cell Biol.* **2004**, *121*, 155–166.
[38] E. Murayama, A. Okuno, T. Ohira, Y. Takagi, H. Nagasawa, *Comp. Biochem. Physiol. B Biochem. Mol. Biol.* **2000**, *126*, 511.
[39] T. T. Whitfield, B. B. Riley, M. Y. Chiang, B. Phillips, *Dev. Dyn.* **2002**, *223*, 427.
[40] D. M. Fekete, *Science* **2003**, *302*, 241.

Calciumphosphates

Biomineralization: From Biology to Biotechnology and Medical Application,
Second Edition. Edited by E. Bäuerlein

ISBN: 3-527-31065-7

15 Lot's Wife's Problem Revisited: How We Prevent Pathological Calcification

Willi Jahnen-Dechent

15.1 A Short History of Calcification Inhibition

Biomineralization is first documented in the Precambrian invertebrate *Cloudina* [1] and may well have evolved as a protective mechanism against calcification. Considering that the Cambrian sea was extremely mineral-rich, and inarguably caused the build-up of both massive geological and biogenic mineral deposits, it is tempting to speculate that early biomineralizing organisms tried to escape mineralization and hence enmuring by precipitating salts. A basic anti-calcifying strategy of secreting mucoid, charged polymers (carbohydrate, protein) was developed [2]. Together with the mineral this organic matrix comprised a first form of "biomineral". This strategy is conserved in today's shell-forming marine life [3], which may still be struggling not do be immobilized by a mineral crust. Once the encrusting problem was solved by developing a regulated crust called a "shell" this became an evolutionary advantage against predators.

Shells of mollusks and the "exoskeleton" of crustaceans were carried along when these animals left the ocean to colonize the land. Cellular metabolism is critically dependent on calcium as a counter ion, a stabilizer of proteins and nucleic acids, and indeed an important intracellular (second) messenger. In higher organisms, calcium is essential for neuromuscular stimulation, and for the stability of tissues in general and tightness of epithelial cell junctions in particular. Phosphate, on the other hand, is indispensable for making DNA and RNA, i.e. maintaining the genetic code, for energy metabolism, and also for critical switching of cell signals, which rely on phosphate tags attached to sugars, proteins and lipids. Unfortunately, calcium and phosphate tend to form highly insoluble salts, and precipitate at the extracellular concentration required for intracellular function. Thus, most extracellular fluids are "metastable" regarding the solubility of these ions. Incomplete as this quick rundown of biomineralization history may be, it illustrates one important point. Cellular metabolism evolved at a time when extracellular mineral abounded. From that time onward cells needed relatively high extracellular calcium and phosphate to function properly. The relative lack of these minerals in the immediate environment of land-dwelling creatures was compensated by mechanisms collecting minerals from the environment and preventing their loss. One important function of the skeleton in vertebrates is to maintain extracellular calcium homeostasis. While this keeps cells "happy", it causes the exact same problem to the, say, the

Biomineralization: From Biology to Biotechnology and Medical Application, Second Edition. Edited by E. Bäuerlein

ISBN: 3-527-31065-7

innards of a typical vertebrate animal that prompted its Cambrian ancestors to "invent" biomineralization in the first place, i.e. prevention of unwanted mineralization by the extracellular fluid. This short history of biomineralization illustrates that the efficient inhibition of unwanted mineralization is a logical consequence of relying on minerals for cell function. A solution to this problem is, therefore, critically important for survival.

Exactly how much of a problem is the supersaturation of extracellular solutions like blood in vertebrates? The stability of a solute system is described by the thermodynamical solubility product. Solubility products are listed in compendia of chemistry, but we will soon learn that the figures are of limited predictive value for our purpose. As an example, we will try to predict the stability of an aqueous calcium phosphate solution in a real-life biological system like blood from the thermodynamical solubility product of synthetic hydroxyapatite [$Ca_5(PO_4)_3(OH)$, $\sim 10^{-53}$ M^{-9}]. To this end we will first enter the combined blood serum ion concentrations into the equation:

$$K_{SP} = [Ca^{2+}]^5 \times [PO_4{}^{3-}]^3 \times [OH^-] \tag{1}$$

Applying the serum concentrations for $[Ca^{2+}]$, $[P_i]$ and $[OH^-]$ to Eq. (1) we will arrive at a calculated product of 5.47×10^{-31}:

$$K_{SP} = (1.2 \times 10^{-3})^5 \times (1.3 \times 10^{-3})^3 \times 10^{-7} = 5.47 \times 10^{-31}\ M^9 \tag{2}$$

This suggests that we all live 22 orders of magnitude beyond the chemical equilibrium! In view of this discrepancy of solubility product and actual extracellular concentrations of calcium and phosphate ions, we all suffer what has been aptly called "Lot's wife's problem", the imminent danger of turning into a pillar of salt [4]. However, simply taking serum ion concentrations is incorrect because only a small portion of $[P_i]$ (less than 0.01 %) will actually exist in the $[PO_4{}^{3-}]$ form at neutral pH. Furthermore, the presence in serum of additional electrolytes (NaCl) and ions that destabilize nascent apatite crystals (Mg^{2+}, $HCO_3{}^-$) diminishes the difference in solution products. Regardless of the exact contribution of these factors, they cannot fully account for the 22 orders of magnitude gap. For practical purposes, therefore, we resort to a simplified version of the solubility product, the so-called ion product, which is routinely used in clinical chemistry as a predictor of calcification risk. Laboratory experience suggests that at physiological pH, ionic strength (mainly NaCl) and body temperature, solutions with a $[Ca^{2+}] \times [P_i]$ ion product equal or greater than 6×10^{-6} M^2 will spontaneously precipitate. Normal serum is a metastable solution in that the ion product ranges from 1.3×10^{-6} M^2 in human adults to 2.6×10^{-6} M^2 in newborns. Small rodent serum ion products have been measured slightly higher at 4×10^{-6} M^2 (adult rat), but still fall within the region of metastability.

Carbonate-substituted apatite of variable stoichiometry and morphology will eventually form at most calcification sites in vertebrates, because at neutral pH and body temperature it is the thermodynamically most stable of all possible

$Ca^{2+} \times P_i$ compounds. Even chemically pure hydroxyapatite (HAP) has a fairly complex crystal unit cell of 18 ions $Ca_{10}(PO_4)_6(OH)_2$. It is almost inconceivable that these ions will spontaneously assemble into a correct crystallographic unit merely through diffusion and collision in solution. Biogenic apatite is formed through a series of increasingly complex $[Ca^{2+}] \times [P_i]$ compounds that assemble on their respective precursor. These precursors include dicalcium phosphate dihydrate (DCPD), $Ca(HPO_4)\cdot 2H_2O$; octacalcium phosphate (OCP), $Ca_8H_2(PO_4)_6$; amorphous calcium phosphate (ACP), $Ca_9(PO_4)_6$(var.); and HAP $Ca_5(PO_4)_3OH$. In addition, the biogenic formation of apatite is greatly facilitated by a process called heterogeneous nucleation – the formation of crystals on an organic template. Purified collagen serves as an excellent template and will calcify at $[Ca^{2+}] \times [P_i]$ products as low as 1.3×10^{-6} M^2. This is well below 6×10^{-6} M^2, the level required for spontaneous, homogeneous nucleation. This brings us back to the question why not all collagen-containing tissues calcify and, indeed, why the extracellular fluid does not calcify. Obviously potent inhibitors of spontaneous calcification must exist.

15.2 Osteogenesis and Bone Mineralization versus Calcification

Mineralization is usually restricted to bones and teeth in vertebrates. However, bone formation (osteogenesis) can also occur outside the skeleton. This so-called ectopic (out of place) ossification happens when precursor cells inappropriately receive signals to develop into mature bone cells, to synthesize extracellular matrix (ECM) and to create a specialized environment favoring mineralization. In one of the most extreme examples of ectopic bone formation, *fibrodysplasia ossificans progressiva*, inflammatory cells produce bone morphogenetic protein-4 (BMP-4) and thus stimulate their immediate tissue-resident stem cells to transform muscle into bone [5]. Ultimately this results in a ''skeleton outside the skeleton'' as depicted in Figure 15.1(A and B).

Ectopic activation of osteogenesis also contributes to the calcification of blood vessels, calcifying atherosclerosis [6], the leading cause of death and disability in developed countries [7]. This link of bone biology and atherosclerosis has grown so strong that many researchers hypothesize that calcification in the body may always be preceded by osteogenesis [8–10]. The calcifying entities in bone mineralization called matrix vesicles [11] (spherical structures in bone and cartilage where mineralization is believed to start) and the calcifying apoptotic bodies (blebs of dying smooth muscle cells in atherosclerosis) are strikingly similar, thus corroborating this view [12]. However, there are differences [13]. In addition, calcification disease usually progresses slowly. In contrast, osteogenesis has evolved to form complex mineralized tissues – bones and teeth – in a relatively short period of time. Osteogenesis requires that bone progenitor cell migrate to the sites of bone formation,

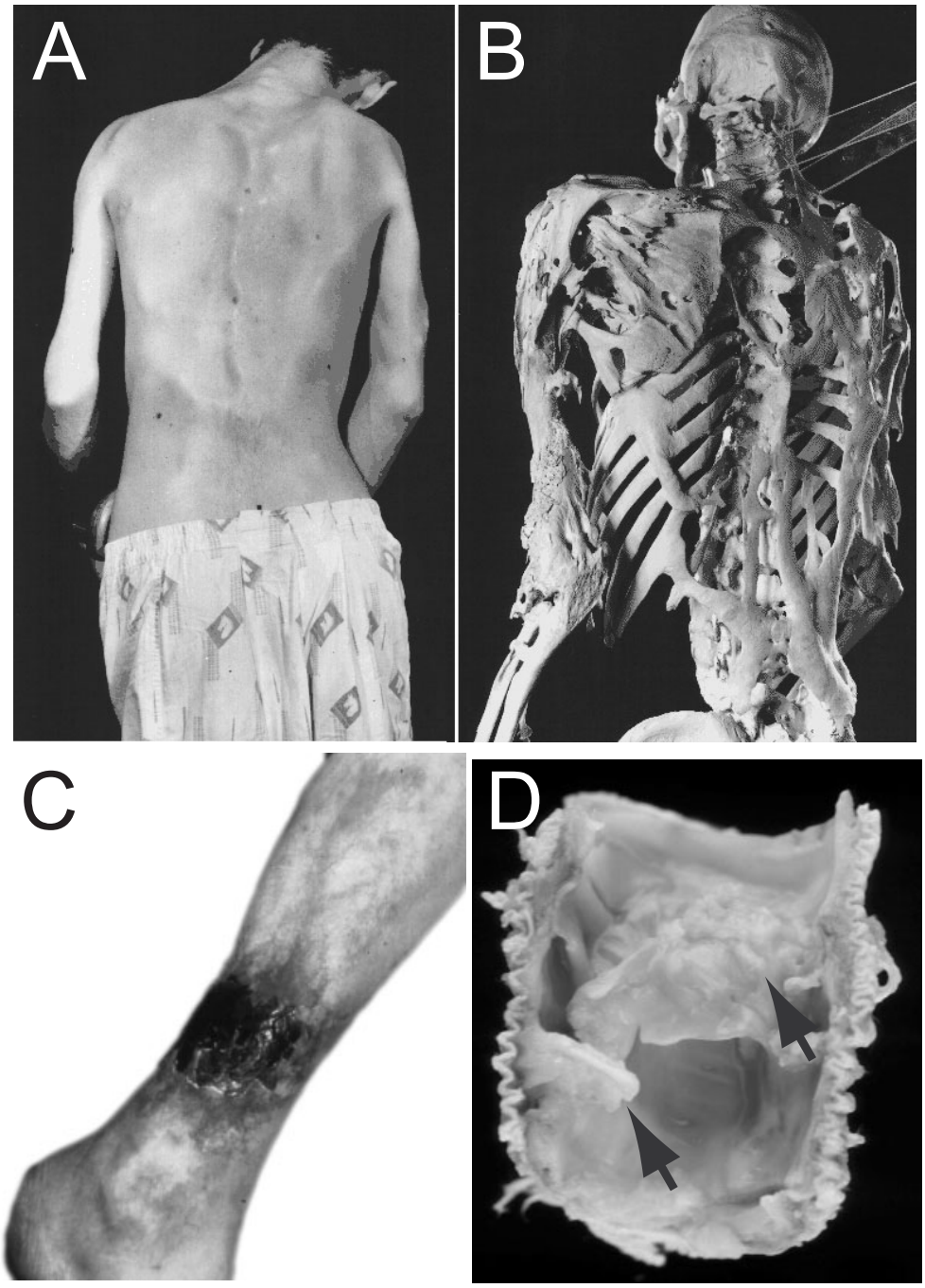
A
B
C
D

proliferate and differentiate into chondrocytes, osteoblasts and osteoclasts. Blueprints of the bones are first laid down by cartilage-forming cells (chondrocytes) that are subsequently replaced by bone-forming cells (osteoblasts). The process is called endochondral (out of cartilage) ossification and allows growth of the skeleton. Osteoid is then formed as the bone ECM, which will eventually mineralize. It contains collagen and non-collagen proteins, presumably regulating the mineralization of the organic matrix [14, 15]. Matrix mineralization is the very final step of osteogenesis. This entire developmental sequence including mineralization is completed within less than 2 weeks in mice. In contrast, a widely adopted model of atherosclerosis in mice, the apolipoprotein E-deficient mouse, takes months to develop atherosclerosis [16]. Bone formation continues throughout adolescence. Several rounds of remodeling of primary bone by osteoblasts and osteoclasts (bone-resorbing cells) are required before a skeleton reaches its final size. Even in the adult state, bone is continuously remodeled by osteoblasts and osteoclasts. Every step in this orchestrated organ development requires that complex genetic programs are started, regulated and eventually stopped by interdependent genes [17]. The observation that several bone marker proteins are also expressed in cells near calcification sites outside the skeleton [8, 9, 18], especially in calcifying smooth muscle cells, has prompted the view that unwanted calcification is essentially a consequence of the fact that the entire bone formation program is inappropriately started in cells not meant to calcify [19, 20]. It is, however, controversial whether calcification is the cause or a consequence of the ectopic expression of an osteoblastic phenotype. *In vitro* evidence from studies with cultured cells shows that high extracellular calcium [21], high extracellular phosphate [10] and an elastin-deficient ECM [22] can induce cellular phenomena reminiscent of extracellular calcification in fibroblasts, smooth muscle cells and retinal pigmented epithelial cells. The differentiation of precursor cells into atherosclerotic plaque-forming and calcifying cells is indeed considered an important step in the pathology of atherosclerosis and vascular calcification [9, 23]. Local factors present in inflamed tissue, matrical lipidic debris (see below) and initially small calcium phosphate deposits may drive the differentiation of precursor cells into osteoblastic cells, which will stabilize this bone-like compartment and thus establish a vicious circle.

Figure 15.1 (A and B) Clinical appearance and skeleton of a man with *fibrodysplasia ossificans progressiva*. The rigid posture in this 25-year-old man was due to calcification of the spine, shoulders and elbows (ankylosis). He died of pneumonia at the age of 40 years. Major muscles were turned into plates of bone contouring the skin over the back and arms (A), and can be seen directly on the skeleton (B). Courtesy of the Mütter Museum, College of Physicians of Philadelphia. (C) Ulcerous skin lesion in calciphylaxis. In this disease, patients calcify small subdermal vessels to the point of complete obstruction. As a result, the surrounding tissue dies and disintegrates. Secondary infections of the skin lesions are associated with a mortality of up to 80 %. (D) Calcified prosthetic aorta made of Dacron®. Calcification of this vascular prosthesis completely obstructed the vessel lumen and required revision operation and replacement. (C and D) Photographs courtesy of the Institute of Pathology, University of Aachen.

15.3 Calcification Disease

Pathologic calcification can thus occur before and after osteogenesis. Old pathology wisdom reminds us of the prominent role electron microscopy has played in the elucidation of calcification mechanisms. Feroce Ghadially brings back to all of us who are "blissfully ignorant of past history" some very basic facts of cellular calcification [24]. In particular, he points out that most cells shed "matrical lipidic debris", which are processes breaking off and drifting into the ECM. Large amounts of these cell remnants are formed following tissue insult and the ensuing increased remodeling activity. Matrical lipidic debris readily calcifies. Figure 15.1(C and D) illustrates two examples of this so-called dystrophic calcification in the human body. Figure 15.1(C) shows the leg of a patient suffering from calciphylaxis (nephropathy associated arteriolopathy). In this rare, but serious, calcification disease [25] calcified concrements precipitate inside the lumen of small blood vessels. Surrounding tissues starve and die. The necrotic tissue is prone to serious bacterial infections, which are lethal in 80 % of the calciphylaxis patients. Figure 15.1(D) illustrates yet another example of "boneless calcification" – calcification of a synthetic blood vessel prosthesis made of Dacron®. In general, calcification is a major problem of implants like bioartificial heart valves or vessel prostheses [26]. Material surfaces of artificial implants tend to calcify because the synthetic materials they are made of have no secretory epithelia and, hence, no natural protection against calcification. Calcification is known to be a major shortcoming of bioartificial heart valves [27].

15.4 Regulation of Calcification

Figure 15.2 summarizes recognized pro- and anti-calcifying principles. High extracellular calcium and phosphate concentrations drive calcification along following the chemical equilibrium. So do lipid-containing matrical remnants [24] or apoptotic or matrix vesicles, or other calcifiable cell remnants present in necrotic tissue (dead cells). The ECM itself is readily calcifiable in bone osteoid, but inhibits calcification in any other body location, presumably because of the presence of highly charged matrix components. Low-molecular-weight inhibitors of calcification include magnesium, inorganic pyrophosphate [28] and its synthetic derivatives bisphosphonates [29]. High-molecular-weight inhibitors include glycoproteins, phosphoproteins, γ-carboxyl glutamic acid containing proteins (GLA proteins) as well as ECM proteoglycans and hyaluronans.

Extracellular calcium is tightly regulated in blood serum in mammals through a concerted effort of the gut, kidney and bone, with the parathyroid gland as the master regulator. Mild forms of calcification can be caused by continuously feeding a diet rich in lactose and calcium (milk alkaline diet), thus over-exaggerating the nutritional composition of mothers' milk, a natural diet with the highest calcium

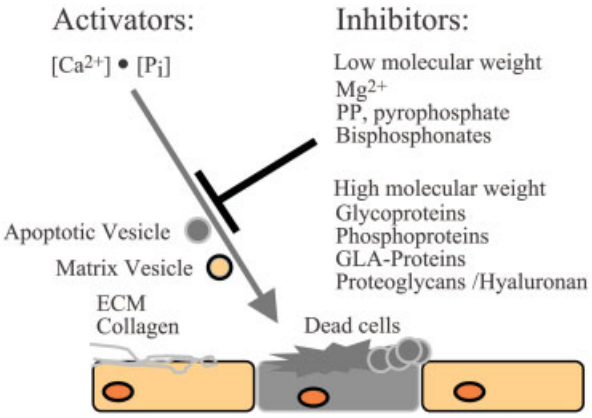

Figure 15.2 Activating and inhibiting principles in mammalian calcification. High calcium and phosphate serum concentration caused by metabolic disease or by kidney disease form a high Ca × P product facilitating calcification. Matrical lipidic vesicles of remodeling cells [24], matrix vesicles of cartilage and bone-forming cells, and apoptotic vesicles of dying cells strongly enhance calcification [13]. Hence, both bone osteoid and apoptotic vesicles of damaged and dying cells readily calcify. Low-molecular-weight inhibitors (Mg^{2+}, intracellular and extracellular PP and their synthetic derivatives, bisphosphonates) interfere with mineral formation at the level of crystal morphology. High-molecular-weight inhibitors can interfere with calcification at the level of mineral formation, stability, dissolution and removal by phagocytosis (remodeling). Depending on their expression pattern in the body, inhibitors can be tissue-restricted or systemic.

content. A more drastic form of calcification can be induced in certain strains of mice by withholding dietary magnesium, damaging tissue, e.g. with a cold probe [30], or poisoning animals with exceedingly high doses of the calciotropic hormone, vitamin D [31]. A "natural" version of this latter treatment occurs in cattle feeding on yellow oat grass (*Trisetum flavescencs*), a foodstock rich in vitamin D metabolites [32]. In the 1970s, the disease enzootic calcinonosis was described as an endemic condition in cattle of Southern Bavaria causing calcification of the vasculature, lung, kidney, knee joints and reproductive organs. Similar diseases are known around the world as "Enteque seco" in Argentina and Brazil, "Manchester wasting disease" in Jamaica or "Naalehu disease" in Hawaii. This form of generalized soft tissue calcification illustrates the pivotal role of $1,25(OH)_2$-vitamin D_3 (calcitriol) in extracellular calcium homeostasis of mammals which is illustrated in Figure 15.3 (see p. 254).

Parathyroid hormone (PTH) and calcitriol [$1,25(OH)_2D_3$] are key regulators of extracellular calcium transport and mobilization. A calcium-sensing receptor senses the concentration of extracellular calcium and triggers a regulating cascade involved in extracellular calcium homeostasis [33]. Serum usually contains 2.5 mM total calcium. Only free ionic calcium (around 1.25 mM) is biologically active and signals back to the calcium sensing receptor in the parathyroid and the kidney tubules. Calcium complexed to proteins (1 mM) or phosphate or hydrogen carbonate (0.25 mM total) serves as a buffer reservoir. Blood pH changes greatly affect the

buffering capacity of albumin the major ionized calcium binding protein in blood. Low serum calcium triggers the release of PTH, which stimulates mobilization of calcium from the bone, retention in the kidney and increased uptake through the gut. This is mediated by the PTH-stimulated synthesis of $1,25(OH)_2D_3$ in the kidney. Subsequently $1,25(OH)_2D_3$ stimulates the synthesis of calcium binding and intracellular transport proteins, calbindins, in the gut [34]. Phosphate uptake in the gut is likewise increased by vitamin $1,25(OH)_2D_3$. In addition, low serum phosphate stimulates the synthesis of $1,25(OH)_2D_3$ in the kidney through "phosphatonins", a group of signaling proteins including fibroblast growth factor, FGF23 and secreted Frizzled-related peptide, sFRP [35]. Concomitantly, phosphatonins activate a sodium-dependent phosphate transporter in kidney epithelial cells mediating the re-uptake of phosphate in the kidney tubuli. Dysfunction of this transporter is associated with low serum calcium, hypophosphatemia, and defective bone mineralization, osteomalacia.

Disturbance of every single key regulator of the extracellular calcium regulatory network can cause severe pathological calcification. Dialysis patients are particularly vulnerable to calcification because they have no functioning kidneys. Kidneys are however, critically involved in the control of mineral homeostasis at the level of PTH, vitamin D_3, phosphatonins and calcium, as well as phosphate transporters [36].

Most of the calcium available for precipitation circulates in the blood. Classic experiments of Blumenthal et al. have shown that blood serum contains potent inhibitors of spontaneous calcium salt precipitation [37]. Serum proteins mediating this precipitation inhibition were identified by testing *in vitro* their ability to inhibit the spontaneous formation of calcium salt precipitates from supersaturated ion solutions or by binding to solid-phase calcium apatite. This research revealed candidate inhibitor proteins including bulk serum proteins like albumin [38] and apatite-binding proteins in serum [39]. The apatite-binding proteins are often generic carrier proteins. Apart from their affinity to calcium apatite, they also bind several more ligands including lipids, proteases, growth factors and ECM. Therefore, it is hard to decide if the inhibition of calcium salt precipitation *in vitro* is fortuitous and due to bulk binding or whether it represents a true physiological function of a given protein. Whether or not a protein fulfills a protective role against unwanted calcification *in vivo* was for a long time impossible to determine due to the lack of genetic mutants. With the advent of gene-targeting technology, however, this function can be tested in mutant mice. Gene knockout models with pathological calcification are listed in Table 15.1. We tentatively grouped genes according to their point of interference with calcification.

The first group of gene products affects cell stability and survival. Deletion of the gene for desmin is associated with severe cardiomyopathy and cardiac calcification. Mice lacking the glycosidase I protein family member *klotho* suffer from premature ageing, pulmonary emphysema with increased cell death with associated alveolar calcification [40]. Both mouse models illustrate the importance of necrosis in calcification. In the *klotho* knockout mice a 5-fold increase in serum calcitriol was recently reported. Therefore klotho may also function as a negative regulator of vitamin D production [41]. We would predict that genes involved in cell survival or apoptosis

Table 15.1 Genes which have been associated with calcification in mutant mice.

Group	Gene	Level of interference	Mouse mutant	Calcification phenotype	Reference
1	Klotho	cell integrity, age promoting	*klotho*$^{-/-}$	lung (accelerated ageing in general)	40
	Desmin	cytoskeleton stability	*desmin*$^{-/-}$	cardiac, septum and right ventricle wall	99
2	Osteoprotegerin	osteogenesis, remodeling	*Opg*$^{-/-}$	vascular, associated with osteoporosis	100
	Smad6/Madh6	osteogenesis	Madh6-mutant	aorta	101
3	MGP	mineral, remodeling	*Mgp*$^{-/-}$	aorta media, arterial, valves, cartilage	57, 102
	Osteopontin	mineral, remodeling	*Opn*$^{-/-}$	implant calcification, compound phenotype with *Mgp*$^{-/-}$	46, 103
4	Carbonic anhydrase II	mineral, pH and ion activity	*Car2*$^{-/-}$	small arteries, osteopetrosis, renal tubular	53
5	ENPP1, PC-1, nucleotide PP	mineral, PP production	*ttw, tip-toe walking*	articular cartilage, arteries	63
	Ank	mineral, PP transport	*Ank, ankylosis spondylitis*	articular joints	62
	TNAP, TNSAP; tissue non-specific alkaline phosphatase	mineral, failure to cleave/ inactivate PP	*Tnap*$^{-/-}$	CPPD deposition in articular cartilage, bone hypomineralization	64, 66
6	α_2-HS glycoprotein/fetuin-A	mineral, solubilization transport (remodeling?)	*Ahsg*$^{-/-}$	generalized and systemic, interstitial and intravascular	56, 79

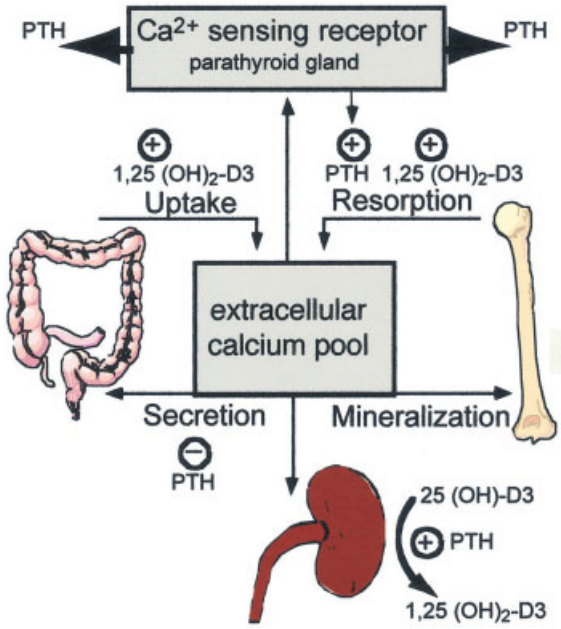

Figure 15.3 Simplified scheme of mammalian extracellular calcium homeostasis. In the gut, calcium intake is effected by calcium-binding proteins, calbindins, mediating epithelial transport to the blood. Excess calcium is secreted into feces (gut) or urine (kidney). PTH inhibits calcium secretion. In healthy subjects, high serum calcium (and phosphate) enhances physiological bone mineralization. The extracellular calcium pool (blood and extracellular fluids) calcium concentration is monitored by a calcium-sensing receptor in the parathyroid gland. Low serum calcium triggers the release of PTH, which stimulates bone resorption, renal calcium re-uptake in the kidney tubules and the synthesis of calcitriol [$1,25(OH)_2D_3$] in the kidney. $1,25(OH)_2$ stimulates both bone resorption and synthesis of calbindins, and hence calcium uptake in the gut. Note that the kidney is involved at almost every step of this regulatory loop. Therefore, patients with renal failure (no functioning kidneys or no kidneys at all) run an extremely high risk of vascular and soft tissue calcification. In addition, their bone tissue becomes unresponsive to bone-forming stimuli (adynamic bone disease) associated with excess soft tissue calcification.

could generally be involved in the development of dystrophic calcification when their activity or lack thereof causes necrosis.

As stated before, several bone-related genes play a role in calcification. Examples of this second group of genes are the genes *Smad6*, mother against decapentaplegic homolog 6, and *Opg*, osteoprotegerin, which are involved in both osteoblast and osteoclast signaling, and therefore in bone remodeling. Smad6 is an intracellular inhibitor of BMP signaling. In the absence of Smad6, BMP signaling in the heart leads to aortic and cardiac calcification. Opg is a decoy receptor for OPGL, osteoprotegerin ligand/RANKL, receptor activator of NF-κB ligand. RANKL is a potent differentiation and survival factor for osteoclasts [42] and a disturbance of the Opg/RANKL balance is associated with osteoporosis and vascular calcification

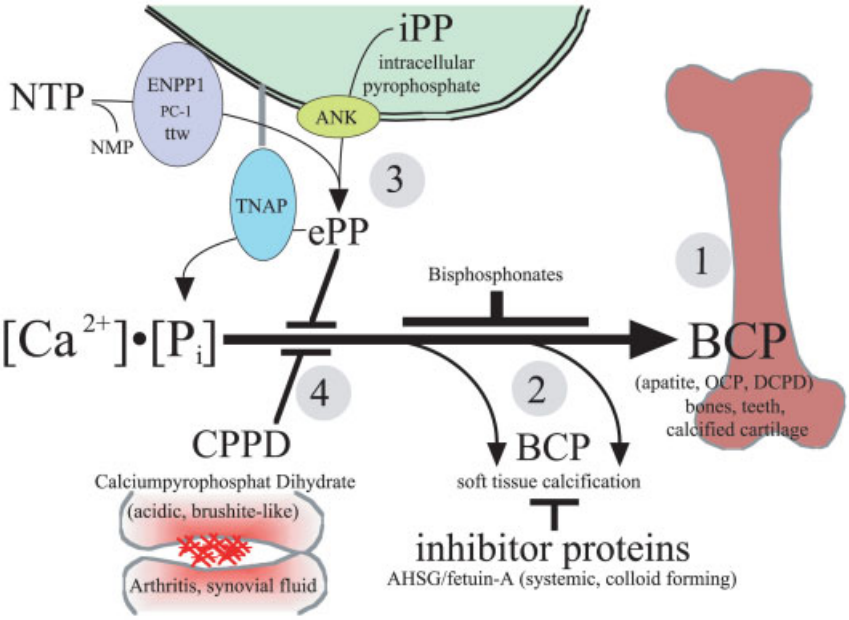

Figure 15.4 Calcium phosphates in mammals. Physiological mineralization of bones and teeth (reaction 1) yields mainly basic calcium phosphates, BCPs including carbonated, substituted apatite, OCP, DCPD and amorphous calcium phosphates. Soft tissue calcification including renal calcification and abdominal (peritoneal) calcification as well as atherosclerotic plaque calcification likewise contain BCP. Deposition of calcified remnants is inhibited by the systemic inhibitor protein Ahsg/fetuin-A and possibly other systemic or tissue restricted inhibitors. ePP is an extremely efficient inhibitor of BCP formation in articular joints and in the spinal canal, and possibly also in the general circulation. ePP originates from intracellular organic phosphate metabolites and is transported outside the cell by the PP transporter, ANK. The ectoenzyme nucleotide pyrophosphatase/phosphotransferase 1 (ENPP1, PC-1) catalyzes the formation of ePP from nucleotides. Both ENPP1 and ANK thus maintain ePP levels, and mutations or deletions of these genes cause BCP calcification due to the lack of ePP as an inhibitor. TNAP cleaves ePP into phosphate. TNAP deficiency is associated with hypophosphatasia and osteomalacia, a bone mineralization defect syndrome. Excess ePP in articular joints can cause CPPD disease, the deposition of an acidic brushite-like calcium phosphate, calcium PP dihydrate, in the articular cartilage.

[42]. Once again it should be pointed out that bone-related genes cause calcification by recapitulating osteogenic development. The question is still pending as to what activates these genes in precursor cells and turns the affected tissues into bone-like calcified tissues. For a more comprehensive listing of bone-related genes and their putative role in calcification, the reader is referred to a recent review [6].

Group 3 genes code for non-collagenous bone proteins presumably involved in bone remodeling [14]. A role in bone turnover was confirmed in knockout mice lacking *On*, osteonectin/SPARC/BM-40 [43]. Osteonectin-deficient mice developed profound osteopenia, but no ectopic calcification. Mice lacking the non-collagenous bone Gla protein *Oc*, osteocalcin, had slightly increased bone density, but also no

ectopic calcification. However, a third non-collagenous bone protein *Opn*, osteopontin, seems to form a link betweeen bone biology and immunology [44]. Osteopontin inhibits calcification *in vitro*, but unchallenged $Opn^{-/-}$ mice do not calcify [45]. However, implanted biomaterials calcify more readily in $Opn^{-/-}$ mice than in wild-type mice. Interestingly, Opn promotes regression of calcification by inducing expression of carbonic anhydrase II (*Car2*) in monocytic cells [46], suggesting a role for *Car2* in calcification as well (see below). Osteopontin is a pro-inflammatory cytokine and macrophage chemoattractant [47, 48] involved in many inflammatory diseases including atherosclerosis [16], PTH-induced osteoporosis [49], collagen-induced arthritis [50] and multiple sclerosis [48]. These results were obtained with *Opn*-deficient mice maintained on a hybrid genetic background. Some of the result were called into question by a recent study using a new *Opn*-deficient mouse strain on a defined genetic background [51]. Nevertheless, *Opn* has a clear and important role in bone formation and inflammatory processes [44]. In atherosclerosis, *Opn* proved pro- [52] or anti-atherosclerotic [16] depending on the mouse model employed. In both instances, however, macrophages were activated by osteopontin. Osteopontin's role in calcification may therefore be both at the level of direct interference with mineral formation and in stimulating phagocytic cells to clear calcified remnants.

Group 4 genes code for transporters or ion channels involved in pH and mineral homeostasis. As stated above, carbonic anhydrase II is involved in the *Opn*-stimulated dissolution of calcified deposits [46]. *Car2* participates in proton secretion by phagocytic cells, which promotes acidification of the extracellular milieu and hence apatite dissolution. Unsurprisingly, the lack of carbonic anhydrase II in $Car2^{-/-}$ mice by itself is associated with calcification of small arteries, nephrocalcinosis and osteoporosis [53]. *Car2* is critically important for the regulation of local pH and mineral ion activity [54], and its total lack cannot be compensated for in all tissues. Both conditions greatly influence mineralization and mineral dissolution. Theoretically, any major disturbance in calcium or phosphate transport leading to elevated $Ca \times P_i$ products in cells and tissues could cause calcification. Idiopathic hypercalciuria is the most common kidney stone risk factor, and evidence in humans and in a rat model indicates that hypercalciuria is a complex, polygenic trait. Candidate genes for idiopathic hypercalciuria include the renal sodium dependent phosphate transporter (NPC) and chloride channels [55]. The sodium dependent phosphate co-transporter Pit-1 (Glvr-1) was already shown to contribute to phosphate induced calcification of vascular smooth muscle cells and calcification could be prevented by the specific NPC inhibitor, phosphonoformic acid [10].

Group 5 gene products directly interfere with mineral formation and stability. The reactions of these chemical inhibitors of calcification are illustrated in Figure 15.4. As shown in reaction 1, physiological bone minerals form from Ca^{2+} and inorganic phosphate, P_i. They comprise mainly basic calcium phosphates (BCP), apatite, OCP, DCPD and ACP, because these are most stable at physiological pH and body temperature. A similar reaction can take place in the general circulation and in the extracellular fluid of soft tissues. In healthy animals reaction 2 is strongly inhibited by circulating inhibitors like Ahsg [56] or by tissue-specific inhibitors like matrix Gla protein (MGP) [57] – two glycoproteins that will be discussed below in more detail.

Several lines of evidence suggest that a simple inorganic compound, pyrophosphate (PP) is an extremely efficient inhibitor of BCP formation in the way depicted in reaction 3. PP is an established inhibitor of biological calcification [28]. Its chemical structure inspired the development of synthetic calcification inhibitors, bisphosphonates [58], which have been developed into potent drugs preventing mineral loss in osteoporosis [29]. Work reviewed in detail elsewhere [20, 59] demonstrates that reduced production of extracellular (ePP) or insufficient transport of intracellular (iPP) into the extracellular milieu are both associated with excessive calcification of articular joints or spinal canal. More specifically, deletion of the gene for ENPP1 (ecto nucleotide PP/phosphodiesterase), also known as PC-1 (plasma cell protein 1) [60] is associated with a phenotype similar to the mouse mutant *ttw* (*tip-toe walking*). These mice suffer from arthritis, calcification and stiffening of articular cartilage, which prevents articulation of the joints and normal walking. In humans, mutations in ENPP1 are associated with idiopathic infantile arterial calcification [61]. The importance of ePP is further illustrated by the mouse mutant *ank/ank* [62]. The *ank* mice have a truncation mutation in the gene for a membrane-associated PP transporter. This genetic defect is associated with myopathy and calcification similar to the ENPP/PC-1-deficient phenotype [63].

Further evidence for the importance of ePP in the prevention of calcification comes from knockout mice lacking tissue non-specific alkaline phosphatase (TNAP). This enzyme cleaves and inactivates ePP in the bone. TNAP deficiency is associated with a complex phenotype. As would be expected in the presence of excess ePP, the bones of TNAP-deficient mice suffer from osteomalacia, a hypomineralization defect, [64] as well as from hypophosphatasia [65]. In addition, lack of TNAP promotes the deposition in articular and meniscal cartilage of excess ePP as an acidic calcium phosphate, calcium PP dihydrate (CPPD) depicted in reaction 4. Thus, TNAP deficiency in humans, like in mice [66], is associated with CPPD disease, a syndrome of osteomalacia, pseudo gout and articular chondrocalcinosis [59, 67].

One mutant mouse strain mentioned earlier carries a targeted deletion of the gene for MGP [57], a protein originally isolated from bone organic matrix [68]. Mice lacking MGP die within the first 2 months post-natal due to calcification of the main aortic trunk and surrounding connective tissue. The same tissues also produce most MGP in early post-natal live [57]. Therefore, MGP is considered a *bona fide* inhibitor of calcification in these tissues. MGP is poorly soluble and is a prototypic matrix-bound or tissue-restricted protein inhibitor of unwanted calcification. None of the proteins mentioned so far are expressed throughout the body like a systemic inhibitor of calcification should be. However, as stated earlier, free soluble inhibitors must exist on theoretical grounds to prevent calcification of the extracellular fluid itself.

15.5 α_2-HS Glycoprotein/Fetuin-A is a Systemic Inhibitor of Unwanted Calcification

Work from our laboratory has shown that α_2-HS glycoprotein/fetuin-A (genetic symbol *Ahsg* or *Fetua*), a serum protein, lends itself to this function. The name α_2-

HS glycoprotein refers to the fact that this protein migrates with the α_2 fraction of serum proteins upon traditional cellulose acetate paper based electrophoresis. Furthermore, it reminds us of the two co-discoverers of this protein in humans [69] – Heremans [70] and Schmid [71]. In the 1980s, a relationship was noticed between human α_2-HS glycoprotein and bovine fetuin, the major globulin of fetal calf serum [72]. It was soon established that α_2-HS/fetuin proteins are liver-derived, highly soluble and abundant serum glycoproteins present in all extracellular fluids, including blood, lymph and cerebrospinal fluid [73]. Bone tissue fractionation with guanidine hydrochloride and EDTA [15, 74] and immunochemistry [75] showed that fetuin is highly concentrated in the mineralized bone matrix. This seems paradoxical considering that Ahsg is an efficient inhibitor of calcification both *in vitro* and *in vivo*. We will see in a detailed description of the inhibitory mechanism that the inhibition of calcification is transient and that Ahsg remains tightly associated with the mineral phase after precipitation has eventually occurred.

Bovine fetuin-A was described in 1944 by Pedersen as fetuin (derived from the latin word *fetus*), the most abundant globular serum protein in fetal calf serum [72]. After the discovery of a second fetuin, fetuin-B, the protein originally named fetuin was renamed fetuin-A [76]. Fetuin-A and the human species homolog α_2-Heremans and Schmid glycoprotein (α_2-HS glycoprotein/Ahsg) are major serum proteins in mammals, including cattle, sheep, pig and goat, as well as in humans and rodents [77]. Fetuins belong to the cystatin superfamily of cysteine protease inhibitors, which encompass a series of closely related liver-derived serum proteins. Further members of this superfamily sharing cystatin-like domains are kininogens and histidine-rich glycoproteins [78]. Ahsg has been implicated in several diverse functions, including osteogenesis and bone resorption [79], regulation of insulin activity [80], hepatocyte growth factor activity [81], response to systemic inflammation [82], and inhibition of unwanted mineralization [56, 83, 84]. These seemingly diverse functions may well be redundant or interdependent. They bear witness of the fact that fetuins are multi-ligand binding proteins that potentially interfere with any biochemical pathway whose components they can bind and sequester. Whether or not this is physiologically relevant can be tested in a mouse animal model that we have generated [56, 85]. This animal model unambiguously demonstrated that the inhibition of unwanted calcification is one major biological function of Ahsg.

Affinity depletion experiments demonstrated that in human serum Ahsg contributed about half to one-third of a 10-fold redundancy of total serum to inhibit the spontaneous precipitation of apatite from supersaturated solutions of calcium and phosphate [83]. These findings were fully confirmed when sera from Ahsg-deficient mice were analyzed in a precipitation inhibition assay [85]. Apart from this partial lack of precipitation inhibition, the Ahsg-deficient mice on a mixed C57Bl/6-129 genetic background displayed only a mild calcification phenotype. The lack of generalized ectopic mineralization in Ahsg-deficient mice was somewhat anticipated, because Ahsg only accounted for a fraction of the inhibition of apatite precipitation observed with total serum of normal mice. Reversing this argument, combining the Ahsg knockout with genetic strains of mice which are naturally prone to calcification like the strain DBA/2 [86] should exacerbate the mild calcification phenotype

Figure 15.5 Whole-body radiographs of wild-type and Ahsg/fetuin-A deficient male DBA/2 mice. The bright spots in the $Ahsg^{-/-}$ mouse are calcified lesions present in subcutaneous fat, and especially in the tongue, lung, myocard, kidney and reproductive organs. The lesions are generally non-inflammatory. This phenotype is associated with a reduced lifespan and fertility. The mice can live well into adulthood, but stop breeding at an age of about 6 months.

observed in the original Ahsg-deficient mice. Furthermore, severe induced hypercalcemia in these animals should overwhelm the residual inhibition of BCP precipitation and should therefore result in severe calcification. Both experiments were met with the expected outcome, i.e. severe, systemic calcification in Ahsg-deficient mice [56], as depicted in Figure 15.5.

Mice treated in the ways described above suffered systemic calcification affecting major organs, including the kidney, myocard, lung and skin. The animals closely resembled uremia-associated arteriolopathy/calciphylaxis with its clinical hallmarks [56]. This drastic phenotypic expression of Ahsg deficiency also reduced breeding performance and life expectancy. Taken together, we demonstrated by reverse genetics in mice that the serum protein α_2-HS glycoprotein/fetuin-A is a systemic inhibitor of ectopic calcification.

Is Ahsg deficiency also important in human pathology? To this end we performed a clinical study in uremic and healthy subjects, and showed that lack of Ahsg correlates with the severity of calcification, and indeed is a statistically highly significant predictor of short-term morbidity and mortality in uremic patients [87]. Regardless of the precise molecular mechanism, it is important to state that, unlike established inhibitors of ectopic calcification, Ahsg acts systemically, not locally. This suggests that raising Ahsg concentrations in the circulation may be one reasonable approach to prevent ectopic calcification accompanying various diseases.

15.6 How does Inhibition of Calcification Work?

Ahsg/fetuin-A is easily purified and can be obtained in large quantities for structure function analyses. Important parts of the three-dimensional structure can be modeled after the known structure of chicken egg white cystatin [88]. Taken together, this offered an excellent opportunity to study the mechanism of calcification inhibition by a mammalian protein. Using dynamic light scattering and transmission electron microscopy we showed that Ahsg solubilizes apatite as a colloid [84]. This was reminiscent of how apolipoproteins ensheath and thereby solubilize insoluble lipids like cholesterol. In analogy to the lipoprotein particles of varying buoyant density (high-density, low-density, very-low density lipoproteins, etc.) formed by apolipoproteins and lipids, we called the calcium and phosphate-containing Ahsg colloid a *calciprotein particle* (CPP). An important feature of the inhibition is the fact that CPPs are only transiently soluble for up to 36 h at body temperature. The mineral phase of CPPs is initially amorphous and non-diffractive. Within 24 h the CPPs undergo a marked morphological transformation from rounded nanospheres with a diameter of around 50 nm to larger, irregular and progressively more crystalline appearance and sizes up to several hundred nanometers (Figure 15.6). It is important to remember that Ahsg binds calcium phosphate. Bovine fetuin-A calcium binding is rather poor with a K_d of 0.95×10^{-4} M [89]. Even if three calcium-binding sites exist, Ahsg/fetuin-A (10 μM serum concentration) would only cause a minute change in serum calcium concentration (2.5 mM). Therefore, albumin (1 mM serum

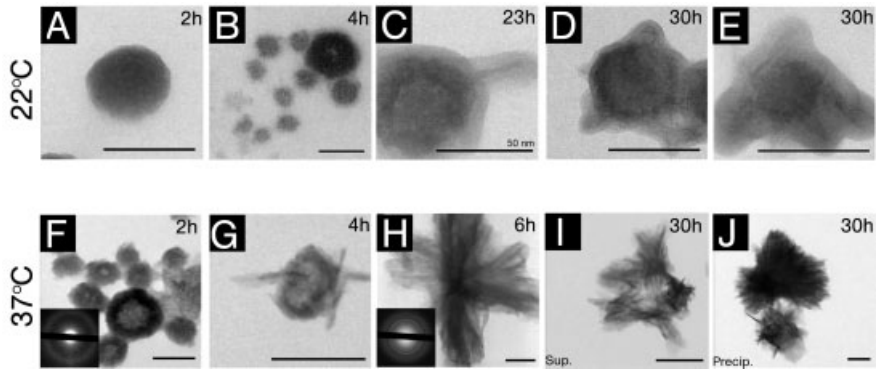

Figure 15.6 Electron micrographs of CPPs – colloidal spheres containing calcium, phosphate and Ahsg/fetuin-A. Growth and transformation of soluble CPPs. The inhibition of BCP precipitation by Ahsg is achieved by the formation of soluble colloidal complexes containing calcium, phosphate and Ahsg. The CPPs have a diameter of 30–150 nm (A, B and F). Diffraction analysis indicated the temperature- and time-dependent transition of amorphous into crystalline BCP precipitate (inserts in F and H). Radial growth of crystalline needles on the surface of the particles after 23 h at 22 °C (C) or after 4 h at 37 °C (G). After 30 h at 37 °C, crystalline but soluble needles were found in the supernatant. (I) Electron-dense crystals accumulated in the precipitate (J). Scale bar = 100 nm, if not depicted otherwise. Reproduced from [84] with permission.

concentration) should be considered the major binding protein for ionized calcium and Ahsg/fetuin-A is a highly effective scavenger of BCP, which precipitates in the absence of this protein [56].

Can we watch this inhibitory mechanism in action in living animals? So far we failed to isolate CPP-like structures from the blood of mice, probably because the removal of CPPs from the circulation is extremely fast and efficient. Experiments conducted in rats come to the rescue, however. Treatment of baby rats with high doses of the bisphosphonate etidronate, with overdoses of calcitriol or with RANKL, all caused acute and severe hypercalcemia, raising total serum calcium from a normal of around 2.5 up to 10 mM [90]. Almost all of the surplus calcium was sequestered in a high-molecular-weight complex of calcium, phosphate and fetuin-A. Small amounts of MGP and prothrombin were also present in this complex. The complex originated in bone and the amount of complex circulating in serum correlated with arterial calcification [91]. These studies corroborated that Ahsg/fetuin-A is the major protein component in a high-molecular-weight complex, which is very likely identical to CPP. Therefore, Ahsg may stabilize CPP and hence insoluble calcium phosphates as colloids *in vivo* similar to what we observed *in vitro* [83, 84].

15.7 What Happens to the CPPs?

So far, we have discussed the evidence that Ahsg is an important inhibitor of unwanted calcification *in vivo*. In addition, we have presented functional data suggesting that the precipitation of calcium phosphates is transiently prevented by the formation of soluble colloids consisting of Ahsg, calcium and phosphate. In analogy to the well-established lipoprotein particles we termed these colloids CPP (Figure 15.7). This leaves us with the question of where and how the CPPs are normally eliminated, and indeed how mineral is removed in the body. The efficient recycling and cellular catabolism of calcified remnants and CPPs is equally important as extracellular calcium homeostasis (Figure 15.3) and the stabilization of calcium phosphate as a colloid (Figure 15.6), because this process completes the extracellular calcium phosphate cycle and thus prevents build-up of unwanted calcification. Established mechanisms capable of removing calcium phosphate crystals are phagocytosis and acidification [92]. An obvious candidate organ for the removal from the circulation of particulate matter like cell remnants, molecular aggregates and likely also of ‘‘mineral dirt’’ is the so-called reticuloendothelial system (RES). This network of phagocytic cells encompasses endothelial cells and macrophages in the liver, spleen and bone marrow. It is likely that CPPs are phagocytosed and thereby recycled in this compartment (Figure 15.8). Do fetuins play a role in this context as well? Several reports throughout the literature indeed suggest that Ahsg has opsonizing properties, and promotes the phagocytosis of DNA and latex particles [93]. It is striking that the removal of calcified remnants like bone turnover is usually non-inflammatory. Even the large calcareous deposits of *Ahsg* knockout mice show no

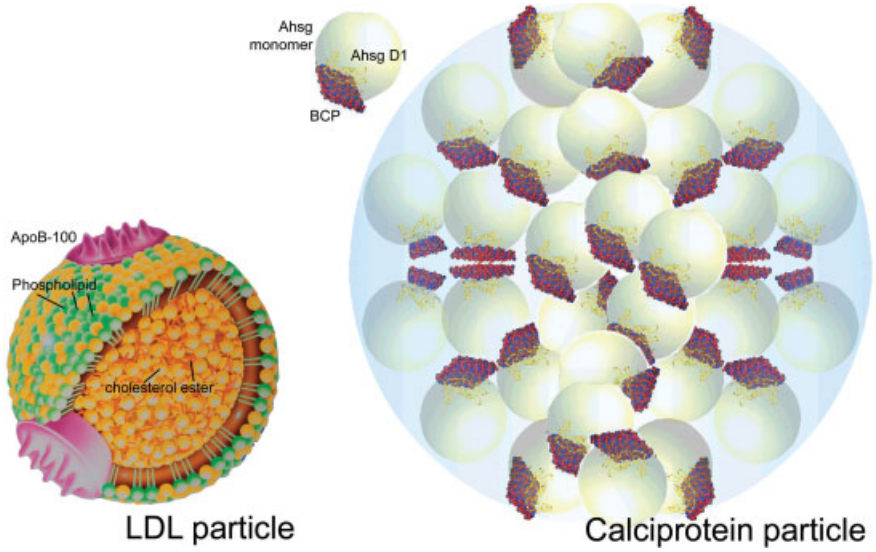

Figure 15.7 Hypothetical models of a low-density lipoprotein particle (LDL) and a CPP. LDL is about 22 nm in diameter, and contains many esterified cholesterol molecules in the hydrophobic core, cholesterol, phospholipids and few apolipoprotein B-100 molecules (513 kDa) in the hydrophilic coat. A CPP contains up to 100 globular Ahsg molecules (52 kDa) with the cystatin-like domain D1 juxtaposed to nine apatite unit cells (BSP). Note that nine apatite unit cells arranged in a lattice of 3×3 closely match this number as well as the surface area of the extended β-sheet in Ahsg domain D1, which is drawn to scale. Modified after [84]. LDL particle modified after [104].

signs of inflammatory cell infiltrates. Is this suppression of inflammation possibly also mediated by fetuin and possibly other mineral binding proteins? In the case of fetuin the answer may be yes. Fetuin coating may well render phagocytosed material non-inflammatory by carrying along the anti-inflammatory polyanions like spermine [82, 94] and the anti-inflammatory cytokine transforming growth factor-β [79, 95]. The combination of tight mineral binding and stabilization in calciprotein particles, the opsonizing and phagocytosis-promoting properties, and the anti-inflammatory activity make fetuin an ideal bridging molecule for the efficient and harmless uptake of mineral debris from tissue and circulation. Such debris will form due to short-term fluctuations in mineral homeostasis or in the course of normal tissue remodeling during development or following a tissue insult. *Ahsg* knockout mice will be a valuable tool in identifying the pathways of this mineral debridement. Indeed we expect the revelation of basic regulatory mechanisms of mineralization, and their integration into the general tissue and organ formation and remodeling landscape which is effective throughout life [96]. Basis biological phenomena like this are best studied in simple model organisms. Recently, an Ahsg/fetuin-A like molecule was shown in the carp to inhibit nephrosin, a matrix metalloproteinase belonging to the astacin protein familiy [97]. The presence of fetuin-like molecules in the zebrafish genome database holds promise that fetuin biology may be studied in this model organism. This little fish has already helped biomineralization researchers to identify molecules involved in gravitation perception

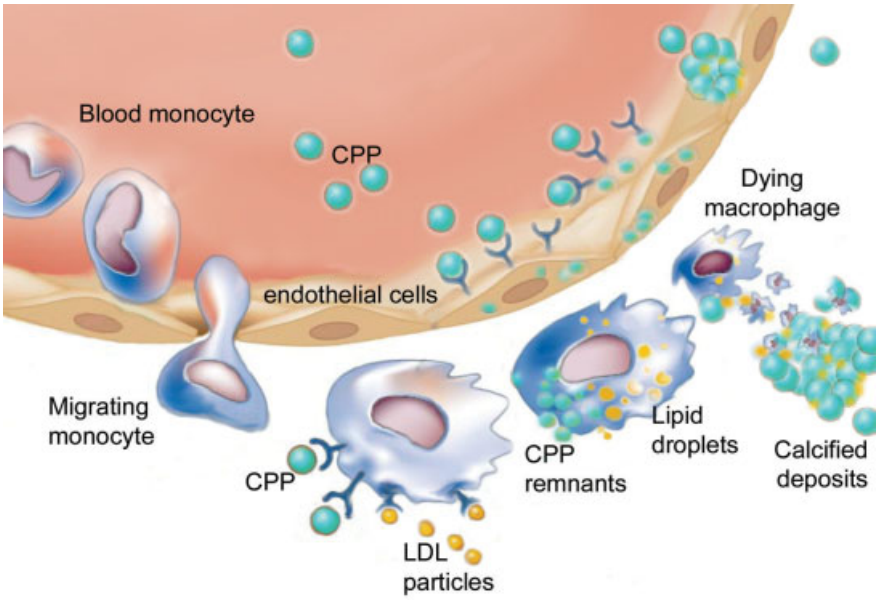

Figure 15.8 Hypothetical pathway of removal of CPP from circulation by endothelial cells and tissue resident phagocytes. In healthy individuals, CPP may form spontaneously in small numbers or may occur as a spill-over into blood of bone catabolism. When mineral homeostasis is severely disturbed, e.g. in dialysis patients, bouts of hypercalcemia and hyperphosphatemia will result in the formation of high numbers of CPP. Ahsg/Fetuin-A will be consumed in the process. CPP in the interstitial space will be phagocytosed by macrophages as depicted or by any other phagocytosing tissue resident cell type. In hyperlipidemia, excess lipoprotein (LDL) will concur and be cleared through similar pathways. Too much CPP remnants in combination with lipid droplets may overwhelm the clearing capacity of the RES system phagocytes and perhaps the lymphatic system, and may result in apoptosis and deposition of calcified apoptotic cell remnants also rich in lipid. Ahsg/fetuin-A stabilizes CPP in circulation and mediates their efficient uptake by phagocytes. This latter function remains to be experimentally verified. Note that many "inhibitors of calcification" activate monocytes/macrophages and stimulate phagocytosis (see Table 15.1, group 3), and therefore stimulation of calcified remnant removal may be equally important like inhibition of precipitation. Modified after [105].

by otoliths [98]. An entire chapter dealing with zebrafish genetics and mineralization in this book on biomineralization is therefore both timely and rewarding (see Chapter 14). It will be interesting to learn what the fish teach us about the role of fetuins and other calcification inhibitors in vertebrate mineral formation and turnover.

References

[1] J. L. Kirschvink, J. W. Hagadorn, in *Biomineralization* (Ed. E. Baeuerlein), Wiley-VCH, Weinheim, **2000**, pp. 139–149.

[2] F. Marin, M. Smith, Y. Isa, G. Muyzer, P. Westbroek, *Proc. Natl Acad. Sci. USA* **1996**, *93*, 1554–1559.
[3] F. Marin, P. Corstjens, B. De Gaulejac, E. De Vrind-De Jong, P. Westbroek, *J. Biol. Chem.* **2000**, *275*, 20667–20675.
[4] W. F. Neuman, in *Fundamental and Clinical Bone Physiology* (Ed. M. R. Urist), Lippincott, Philadelphia, PA, **1980**, pp. 83–107.
[5] A. B. Shafritz, E. M. Shore, F. H. Gannon, M. A. Zasloff, R. Taub, M. Muenke, F. S. Kaplan, *N. Engl. J. Med.* **1996**, *335*, 555–561.
[6] T. M. Doherty, K. Asotra, L. A. Fitzpatrick, J. H. Qiao, D. J. Wilkin, R. C. Detrano, C. R. Dunstan, P. K. Shah, T. B. Rajavashisth, *Proc. Natl Acad. Sci. USA* **2003**, *100*, 11201–11206.
[7] M. Ezzati, S. V. Hoorn, A. Rodgers, A. D. Lopez, C. D. Mathers, C. J. Murray, *Lancet* **2003**, *362*, 271–280.
[8] C. R. Dhore, J. P. Cleutjens, E. Lutgens, K. B. Cleutjens, P. P. Geusens, P. J. Kitslaar, J. H. Tordoir, H. M. Spronk, C. Vermeer, M. J. Daemen, *Arterioscler. Thromb. Vasc. Biol.* **2001**, *21*, 1998–2003.
[9] C. M. Shanahan, D. Proudfoot, K. L. Tyson, N. R. Cary, M. Edmonds, P. L. Weissberg, *Z. Kardiol.* **2000**, *89 (Suppl. 2)*, 63–68.
[10] C. M. Giachelli, *J. Am. Soc. Nephrol.* **2003**, *14*, S300–S304.
[11] T. Kirsch, H. D. Nah, I. M. Shapiro, M. Pacifici, *J. Cell Biol.* **1997**, *137*, 1149–1160.
[12] K. Johnson, K. Pritzker, J. Goding, R. Terkeltaub, *J. Rheumatol.* **2001**, *28*, 2681–2691.
[13] T. Kirsch, W. Wang, D. Pfander, *J. Bone Miner. Res.* **2003**, *18*, 1872–1881.
[14] H. I. Roach, *Cell Biol. Int.* **1994**, *18*, 617–628.
[15] J. D. Termine, *Ciba Found. Symp.* **1988**, *136*, 178–202.
[16] Y. Matsui, S. R. Rittling, H. Okamoto, M. Inobe, N. Jia, T. Shimizu, M. Akino, T. Sugawara, J. Morimoto, C. Kimura, S. Kon, D. Denhardt, A. Kitabatake, T. Uede, *Arterioscler. Thromb. Vasc. Biol.* **2003**, *23*, 1029–1034.
[17] G. Karsenty, *Nature* **2003**, *423*, 316–318.
[18] (a) A. Bini, K. G. Mann, B. J. Kudryk, F. J. Schoen, *Arterioscler. Thromb. Vasc. Biol.* **1999**, *19*, 1852–1861; (b) S. A. Steitz, M. Y. Speer, G. Curinga, H. Y. Yang, P. Haynes, R. Aebersold, T. Schinke, G. Karsenty, C. M. Giachelli, *Circ. Res.* **2001**, *89*, 1147–1154.
[19] L. L. Demer, *Circulation.* **1997**, *95*, 297–298.
[20] F. Rutsch, R. Terkeltaub, *Curr. Opin. Rheumatol.* **2003**, *15*, 302–310.
[21] P. B. Halverson, A. Greene, H. S. Cheung, *Osteoarthritis Cartilage* **1998**, *6*, 324–329.
[22] H. Sugitani, H. Wachi, H. Murata, F. Sato, R. P. Mecham, Y. Seyama, *J. Atheroscler. Thromb.* **2003**, *10*, 48–56.
[23] (a) L. Hegyi, F. H. Gannon, D. L. Glaser, E. M. Shore, F. S. Kaplan, C. M. Shanahan, *J. Pathol.* **2003**, *201*, 141–148; (b) T. M. Doherty, P. K. Shah, T. B. Rajavashisth, *FASEB J.* **2003**, *17*, 592–597.
[24] F. N. Ghadially, *Ultrastruct. Pathol.* **2001**, *25*, 243–267.
[25] A. Fine, J. Zacharias, *Kidney. Int.* **2002**, *61*, 2210–2217.
[26] F. J. Schoen, R. J. Levy, *J. Biomed. Mater. Res.* **1999**, *47*, 439–465.
[27] C. H. Lee, N. Vyavahare, R. Zand, H. Kruth, F. J. Schoen, R. Bianco, R. J. Levy, *J. Biomed. Mater. Res.* **1998**, *42*, 30–37.
[28] J. L. Meyer, *Arch. Biochem. Biophys.* **1984**, *231*, 1–8.
[29] R. G. Russell, M. J. Rogers, J. C. Frith, S. P. Luckman, F. P. Coxon, H. L. Benford, P. I. Croucher, C. Shipman, H. A. Fleisch, *J. Bone Miner. Res.* **1999**, *14 (Suppl. 2)*, 53–65.
[30] S. R. Brunnert, S. Shi, B. Chang, *Genomics* **1999**, *59*, 105–107.
[31] S. Miller, E. Vernon-Roberts, J. Mcclure, *J. Pathol.* **1984**, *142*, 7–13.
[32] M. Wolf, G. Dirksen, *Dtsch. Tierärztl. Wschr.* **1976**, *83*, 391–430.
[33] E. M. Brown, P. M. Vassilev, S. C. Hebert, *Cell* **1995**, *83*, 679–682.
[34] S. Christakos, F. Barletta, M. Huening, P. Dhawan, Y. Liu, A. Porta, X. Peng, *J. Cell Biochem.* **2003**, *88*, 238–244.
[35] (a) S. C. Schiavi, R. Kumar, *Kidney Int.* **2004**, *65*, 1–14; (b) L. D. Quarles, *J. Clin. Invest.* **2003**, *112*, 642–646.
[36] T. B. Drueke, *Nephrol. Dial. Transplant.* **2002**, *17*, 330–331.

[37] N. C. Blumenthal, *Clin. Orthop.* **1989**, *247*, 279–289.
[38] J. Garnett, P. Dieppe, *Biochem. J.* **1990**, *266*, 863–868.
[39] R. A. Terkeltaub, D. A. Santoro, G. Mandel, N. Mandel, *Arthritis Rheum.* **1988**, *31*, 1081–1089.
[40] T. Suga, M. Kurabayashi, Y. Sando, Y. Ohyama, T. Maeno, Y. Maeno, H. Aizawa, Y. Matsumura, T. Kuwaki, O. M. Kuro, Y. Nabeshima, R. Nagai, *Am. J. Respir. Cell Mol. Biol.* **2000**, *22*, 26–33.
[41] H. Tsujikawa, Y. Kurotaki, T. Fujimori, K. Fukuda, Y. Nabeshima, *Mol. Endocrinol.* **2003**, *17*, 2393–2403.
[42] A. M. Sattler, M. Schoppet, J. R. Schaefer, L. C. Hofbauer, *Calcif. Tissue Int.* **2004**, *74*, 103–106.
[43] A. M. Delany, M. Amling, M. Priemel, C. Howe, R. Baron, E. Canalis, *J. Clin. Invest.* **2000**, *105*, 915–923.
[44] E. M. Gravallese, *J. Clin. Invest.* **2003**, *112*, 147–149.
[45] S. R. Rittling, D. T. Denhardt, *Exp. Nephrol.* **1999**, *7*, 103–113.
[46] S. A. Steitz, M. Y. Speer, M. D. Mckee, L. Liaw, M. Almeida, H. Yang, C. M. Giachelli, *Am. J. Pathol.* **2002**, *161*, 2035–2046.
[47] R. P. Wuthrich, X. Fan, T. Ritthaler, V. Sibalic, D. J. Yu, J. Loffing, B. Kaissling, *Autoimmunity* **1998**, *28*, 139–150.
[48] D. Chabas, S. E. Baranzini, D. Mitchell, C. C. Bernard, S. R. Rittling, D. T. Denhardt, R. A. Sobel, C. Lock, M. Karpuj, R. Pedotti, R. Heller, J. R. Oksenberg, L. Steinman, *Science* **2001**, *294*, 1731–1735.
[49] H. Ihara, D. T. Denhardt, K. Furuya, T. Yamashita, Y. Muguruma, K. Tsuji, K. A. Hruska, K. Higashio, S. Enomoto, A. Nifuji, S. R. Rittling, M. Noda, *J. Biol. Chem.* **2001**, *276*, 13065–13071.
[50] K. Yumoto, M. Ishijima, S. R. Rittling, K. Tsuji, Y. Tsuchiya, S. Kon, A. Nifuji, T. Uede, D. T. Denhardt, M. Noda, *Proc. Natl Acad. Sci. USA* **2002**, *99*, 4556–4561.
[51] T. Blom, A. Franzen, D. Heinegard, R. Holmdahl, *Science* **2003**, *299*, 1845; author reply 1845.
[52] S. Chiba, H. Okamoto, S. Kon, C. Kimura, M. Murakami, M. Inobe, Y. Matsui, T. Sugawara, T. Shimizu, T. Uede, A. Kitabatake, *Heart Vessels* **2002**, *16*, 111–117.
[53] S. S. Spicer, S. E. Lewis, R. E. Tashian, B. A. Schulte, *Am. J. Pathol.* **1989**, *134*, 947–954.
[54] (a) T. H. Maren, *Physiol. Rev.* **1967**, *47*, 595–781; (b) E. R. Swenson, *Comp. Biochem. Physiol. A Mol. Integr. Physiol.* **2003**, *136*, 229–241.
[55] S. J. Scheinman, *Semin. Nephrol.* **1999**, *19*, 381–388.
[56] C. Schäfer, A. Heiss, A. Schwarz, R. Westenfeld, M. Ketteler, J. Floege, W. Müller-Esterl, T. Schinke, W. Jahnen-Dechent, *J. Clin. Invest.* **2003**, *112*, 357–366.
[57] G. Luo, P. Ducy, M. D. Mckee, G. J. Pinero, E. Loyer, R. R. Behringer, G. Karsenty, *Nature* **1997**, *386*, 78–81.
[58] H. Fleisch, R. G. Russell, *J. Dent. Res.* **1972**, *51*, 324–332.
[59] R. A. Terkeltaub, *Am. J. Physiol. Cell Physiol.* **2001**, *281*, C1–C11.
[60] L. Hessle, K. A. Johnson, H. C. Anderson, S. Narisawa, A. Sali, J. W. Goding, R. Terkeltaub, J. L. Millan, *Proc. Natl Acad. Sci. USA* **2002**.
[61] F. Rutsch, N. Ruf, S. Vaingankar, M. R. Toliat, A. Suk, W. Hohne, G. Schauer, M. Lehmann, T. Roscioli, D. Schnabel, J. T. Epplen, A. Knisely, A. Superti-Furga, J. Mcgill, M. Filippone, A. R. Sinaiko, H. Vallance, B. Hinrichs, W. Smith, M. Ferre, R. Terkeltaub, P. Nurnberg, *Nat. Genet.* **2003**, *34*, 379–381.
[62] A. M. Ho, M. D. Johnson, D. M. Kingsley, *Science* **2000**, *289*, 265–270.
[63] A. Okawa, I. Nakamura, S. Goto, H. Moriya, Y. Nakamura, S. Ikegawa, *Nat. Genet.* **1998**, *19*, 271–273.
[64] W. Tesch, T. Vandenbos, P. Roschgr, N. Fratzl-Zelman, K. Klaushofer, W. Beertsen, P. Fratzl, *J. Bone Miner. Res.* **2003**, *18*, 117–125.
[65] S. Narisawa, N. Frohlander, J. L. Millan, *Dev. Dyn.* **1997**, *208*, 432–446.
[66] K. N. Fedde, L. Blair, J. Silverstein, S. P. Coburn, L. M. Ryan, R. S. Weinstein, K. Waymire, S. Narisawa, J. L. Millan, G. R. Macgregor, M. P. Whyte, *J. Bone Miner. Res.* **1999**, *14*, 2015–2026.

[67] M. P. Whyte, *Endocr. Rev.* **1994**, *15*, 439–461.
[68] P. A. Price, M. R. Urist, Y. Otawara, *Biochem. Biophys. Res. Commun.* **1983**, *117*, 765–771.
[69] H. E. Schultze, K. Heide, H. Haupt, *Naturwissenschaften* **1962**, *49*, 15–17.
[70] J. F. Heremans, *Les Globulines Sériques du Système Gamma*, Arscia, Brussels, **1960**.
[71] K. Schmid, W. Bürgi, *Biochim. Biophys. Acta* **1961**, *47*, 440–453.
[72] K. O. Pedersen, *Nature* **1944**, *154*, 575.
[73] K. M. Dziegielewska, W. M. Brown, *Fetuin*, Springer, Heidelberg, **1995**.
[74] K. M. Conn, J. D. Termine, *Bone.* **1985**, *6*, 33–36.
[75] M. D. Mckee, A. Nanci, *Microsc. Res. Tech.* **1995**, *31*, 44–62.
[76] E. Olivier, E. Soury, P. Ruminy, A. Husson, F. Parmentier, M. Daveau, J. P. Salier, *Biochem. J.* **2000**, *350*, 589–597.
[77] K. M. Dziegielewska, W. M. Brown, C. C. Gould, N. Matthews, J. E. C. Sedgwick, N. R. Saunders, *J. Comp. Physiol. B* **1992**, *162*, 168–171.
[78] (a) P. P. Cheung, L. A. Cannizzaro, R. W. Colman, *Cytogenet. Cell Genet.* **1992**, *59*, 24–26; (b) B. C. Hennis, R. R. Frants, E. Bakker, R. H. Vossen, E. W. Van Der Poort, L. A. Blonden, S. Cox, P. M. Khan, N. K. Spurr, C. Kluft, *Genomics* **1994**, *19*, 195–197.
[79] M. Szweras, D. Liu, E. A. Partridge, J. Pawling, B. Sukhu, C. Clokie, W. Jahnen-Dechent, H. C. Tenenbaum, C. J. Swallow, M. D. Grynpas, J. W. Dennis, *J. Biol. Chem.* **2002**, *277*, 19991–19997.
[80] S. T. Mathews, G. P. Singh, M. Ranalletta, V. J. Cintron, X. Qiang, A. S. Goustin, K. L. Jen, M. J. Charron, W. Jahnen-Dechent, G. Grunberger, *Diabetes* **2002**, *51*, 2450–2458.
[81] T. Ohnishi, O. Nakamura, N. Arakaki, Y. Daikuhara, *Eur. J. Biochem.* **1997**, *243*, 753–761.
[82] M. Ombrellino, H. Wang, H. Yang, M. Zhang, J. Vishnubhakat, A. Frazier, L. A. Scher, S. G. Friedman, K. J. Tracey, *Shock* **2001**, *15*, 181–185.
[83] T. Schinke, C. Amendt, A. Trindl, O. Pöschke, W. Müller-Esterl, W. Jahnen-Dechent, *J. Biol. Chem.* **1996**, *271*, 20789–20796.
[84] A. Heiss, A. Du Chesne, B. Denecke, J. Grötzinger, K. Yamamoto, T. Renné, W. Jahnen-Dechent, *J. Biol. Chem.* **2003**, *278*, 13333–13341.
[85] W. Jahnen-Dechent, T. Schinke, A. Trindl, W. Müller-Esterl, F. Sablitzky, S. Kaiser, M. Blessing, *J. Biol. Chem.* **1997**, *272*, 31496–31503.
[86] F. A. Van Den Broek, R. Bakker, M. Den Bieman, A. X. Fielmich-Bouwman, A. G. Lemmens, H. A. Van Lith, I. Nissen, J. M. Ritskes-Hoitinga, G. Van Tintelen, L. F. Van Zutphen, *Biochem. Biophys. Res. Commun.* **1998**, *253*, 204–208.
[87] M. Ketteler, P. Bongartz, R. Westenfeld, J. Wildberger, A. Mahnken, R. Böhm, T. Metzger, C. Wanner, W. Jahnen-Dechent, J. Floege, *Lancet* **2003**, *361*, 827–833.
[88] W. Bode, R. Engh, D. Musil, U. Thiele, R. Huber, A. Karshikov, J. Brzin, J. Kos, V. Turk, *EMBO. J.* **1988**, *7*, 2593–2599.
[89] M. Suzuki, H. Shimokawa, Y. Takagi, S. Sasaki, *J. Exp. Zool.* **1994**, *270*, 501–507.
[90] P. A. Price, G. R. Thomas, A. W. Pardini, W. F. Figueira, J. M. Caputo, M. K. Williamson, *J. Biol. Chem.* **2002**, *277*, 3926–3934.
[91] (a) P. A. Price, M. K. Williamson, T. M. T. Nguyen, T. N. Than, *J. Biol. Chem.* **2004**, *279*, 1594–1600; (b) P. A. Price, J. M. Caputo, M. K. Williamson, *J. Bone Miner. Res.* **2002**, *17*, 1171–1179; (c) P. A. Price, J. E. Lim, *J. Biol. Chem.* **2003**, *278*, 22144–22152; (d) P. A. Price, T. M. Nguyen, M. K. Williamson, *J. Biol. Chem.* **2003**, *278*, 22153–22160.
[92] (a) M. D. Fallon, S. L. Teitelbaum, A. J. Kahn, *Lab. Invest.* **1983**, *49*, 159–164; (b) S. A. Nesbitt, M. A. Horton, *Science* **1997**, *276*, 266–269; (c) J. Salo, P. Lehenkari, M. Mulari, K. Metsikko, H. K. Vaananen, *Science* **1997**, *276*, 270–273.
[93] (a) J. G. Lewis, C. M. Andre, *Immunology* **1980**, *39*, 317–322; (b) J. G. Lewis, C. M. Andre, *Immunology* **1981**, *42*, 481–487; (c) L. Thiele, J. E. Diederichs, R. Reszka, H. P. Merkle, E. Walter, *Biomaterials* **2003**, *24*, 1409–1418; (d) H. P. Jersmann, I. Dransfield, S. P. Hart, *Clin. Sci. (Lond.)* **2003**, *105*, 273–278.
[94] H. Wang, M. Zhang, M. Bianchi, B. Sherry, A. Sama, K. J. Tracey, *Proc. Natl Acad. Sci. USA* **1998**, *95*, 14429–14434.
[95] M. Demetriou, C. Binkert, B. Sukhu, H. C. Tenenbaum, J. W. Dennis, *J. Biol. Chem.* **1996**, *271*, 12755–12761.

[96] (a) J. Savill, V. Fadok, *Nature* **2000**, *407*, 784–788; (b) P. M. Henson, D. L. Bratton, V. A. Fadok, *Curr. Biol.* **2001**, *11*, R795–805.
[97] P. L. Tsai, C. H. Chen, C. J. Huang, C. M. Chou, G. D. Chang, *J. Biol. Chem.* **2004**.
[98] C. Söllner, M. Burghammer, E. Busch-Nentwich, J. Berger, H. Schwarz, C. Riekel, T. Nicolson, *Science* **2003**, *302*, 282–286.
[99] L. Thornell, L. Carlsson, Z. Li, M. Mericskay, D. Paulin, *J. Mol. Cell. Cardiol.* **1997**, *29*, 2107–2124.
[100] N. Bucay, I. Sarosi, C. R. Dunstan, S. Morony, J. Tarpley, C. Capparelli, S. Scully, H. L. Tan, W. Xu, D. L. Lacey, W. J. Boyle, W. S. Simonet, *Genes Dev.* **1998**, *12*, 1260–1268.
[101] K. M. Galvin, M. J. Donovan, C. A. Lynch, R. I. Meyer, R. J. Paul, J. N. Lorenz, V. Fairchild-Huntress, K. L. Dixon, J. H. Dunmore, M. A. Gimbrone, Jr, D. Falb, D. Huszar, *Nat. Genet.* **2000**, *24*, 171–174.
[102] A. F. Zebboudj, M. Imura, K. Bostrom, *J. Biol. Chem.* **2002**, *277*, 4388–4394.
[103] M. Y. Speer, M. D. Mckee, R. E. Guldberg, L. Liaw, H. Y. Yang, E. Tung, G. Karsenty, C. M. Giachelli, *J. Exp. Med.* **2002**, *196*, 1047–1055.
[104] D. Steinberg, *Nat. Med.* **2002**, *8*, 1211–1217.
[105] P. Libby, *Nature* **2002**, *420*, 868–874.

16 Aspects of Dentinogenesis: A Model for Biomineralization

Katharina Reichenmiller and Christian Klein

16.1 Introduction

In the tooth, three types of biominerals are united in one system on a hydroxyapatite base. Only the combination of these three dental hard tissues [enamel (being the hardest and showing the highest mineralization), dentin and cementum] ensures that the tooth as a system can function for a time span of about seven decades. The top layer of the crown area consists of enamel and the outer layer of the root area is the cementum. Cementum and alveolar bone are connected by fibers that physiologically reinforce the tooth in its socket. Dentin occurs both underneath the enamel and cement (Fig. 16.1A). Innervated soft tissue (the pulp) makes up the inside of a tooth. At present, the role played by dental soft tissue is not completely understood. However, in animal experiments it was shown that neuronal signals trigger differentiation of odontoblast-like cells and in the process hard substance neogenesis is induced [1, 2]. This is an important prerequisite of dentinogenesis as a model for biomineralization: the development of hard substance can take place in the pulp throughout the life of a tooth and thus a functioning, albeit limited, cellular reaction is possible to external influences like trauma, attrition, abrasion, caries or other means.

16.2 Basic Odontogenesis

Determination and, therefore, positioning of dental hard substance-forming tissue precede the actual formation and development of dental hard substances in the framework of embryologic development (Fig. 16.2A–C). In humans, the responsible processes start 28–40 days after ovulation with the thickening of the oral epithelium, later evolving into the so-called dental lamina, caused by subepithelial ectomesenchyme in the area of the oral cavity space. The subepithelial ectomesenchyme is recruited from cells that migrated into the oral cavity originally stemming from the neural groove. Starting from this dental ridge, the earliest stage of dental buds, compact epithelial buds (*bud stage*), form between week 7 and 10. Through

Biomineralization: From Biology to Biotechnology and Medical Application, Second Edition. Edited by E. Bäuerlein

ISBN: 3-527-31065-7

Figure 16.1 (A) Histological section through a human tooth [dentin (D), pulp (P), cementum (C)]. Through decalcification of the preparation, the highly mineralized enamel is no longer present.

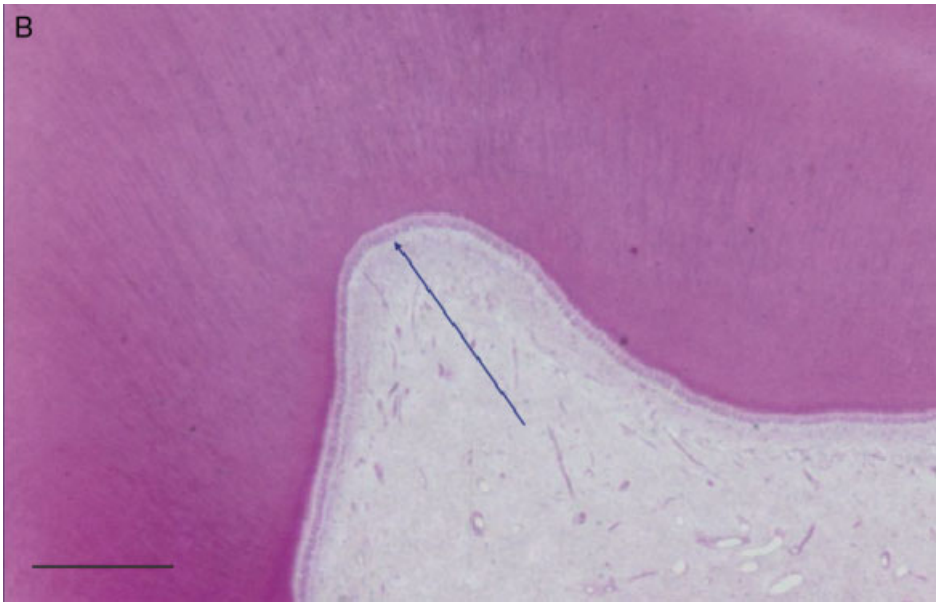

Figure 16.1 (B) Magnified section from (A) (blue frame) to depict the odontoblast layer (blue arrow); bar = 1 mm. 16.1(A) + (B), courtesy of Claus Löst.

proliferation of the bud margins as well as by differentiation of cells, the so-called *cap stage* is reached (week 8–10). The tooth germ enters the *bell stage* which marks the completion of this development and thus the end of the proliferation phase. The germs of the anterior deciduous teeth reach this stage between week 12 and 16, and the posterior teeth normally between the week 15 and 21 after ovulation. During the bell stage, the dental papilla which is surrounded by the bell-shaped dental organ made up from ectomesenchymale tissue, can be differentiated from the dental follicle. The dental organ is located at the dental germ. The dental organ is differentiated into outer and inner dental epithelium, the stratum intermedium, and the enamel pulp, also called the stratum reticulum. The outer dental epithelium is the outer boundary and devolves into the inner dental epithelium at the margin of the ''bell'' (the so-called *cervical loop*). The inner dental epithelium forms the inner surface of the bell and is divided from the dental papilla by a basal membrane. On top of the single layer of cells from the inner dental epithelium, from which ameloblasts differentiate, rests the three- to four-layered stratum reticulum. The internal space of the dental organ is taken up by the stratum reticulum, whose star-shaped cells are imbedded in a mucopolysaccharide-enriched intercellular area. The basal membrane of the inner dental epithelium is the mold of the dentin and represents the future enamel–cement junction. Additional induction for differentiation of odontoblasts and ameloblasts (enamel and dentin-forming cells) takes place along that line. Thus, the dental papilla causes the differentiation of the inner dental epithelium. This again induces the formation and alignment of odontoblasts on the basal membrane of the inner dental epithelium, and the formation of primary dentin. As soon as the first layer of primary dentin becomes the basis for forming enamel, the differentiation of the inner dental epithelium from pre-ameloblasts to ameloblasts is induced (Fig. 16.2D–G). The above-described differentiation comprises chronological as well as spatial proceedings. This process starts with a relatively small bell shape in the small area where the mineralization of the cusps is going to start and the dental pulp is going to be. The small bell shape gets bigger and bigger through proliferation in the area of the cervical loop – while enamel and dentin is already deposited – until the form has reached the final size of the future dentinal core [3–5].

16.3 Dentinogenesis

There are several different forms of dentin. Classification is according to stages of development, and is recorded as primary, secondary and tertiary dentin. Primary dentin has the largest quantity and is formed until the growth of the root has been completed. After that, secondary dentin is formed physiological, but in much lesser quantities. Certain stimuli cause the growth of tertiary dentin (Fig. 16.3) [6–9].

Classification can also be achieved by the mechanism of formation. The inner enamel epithelium influences the differentiation of ectomesenchymal cells in the dental papilla. The cells closest to the inner enamel membrane align themselves on the tooth bell and polarize, lose their ability to divide, and form a junctional com-

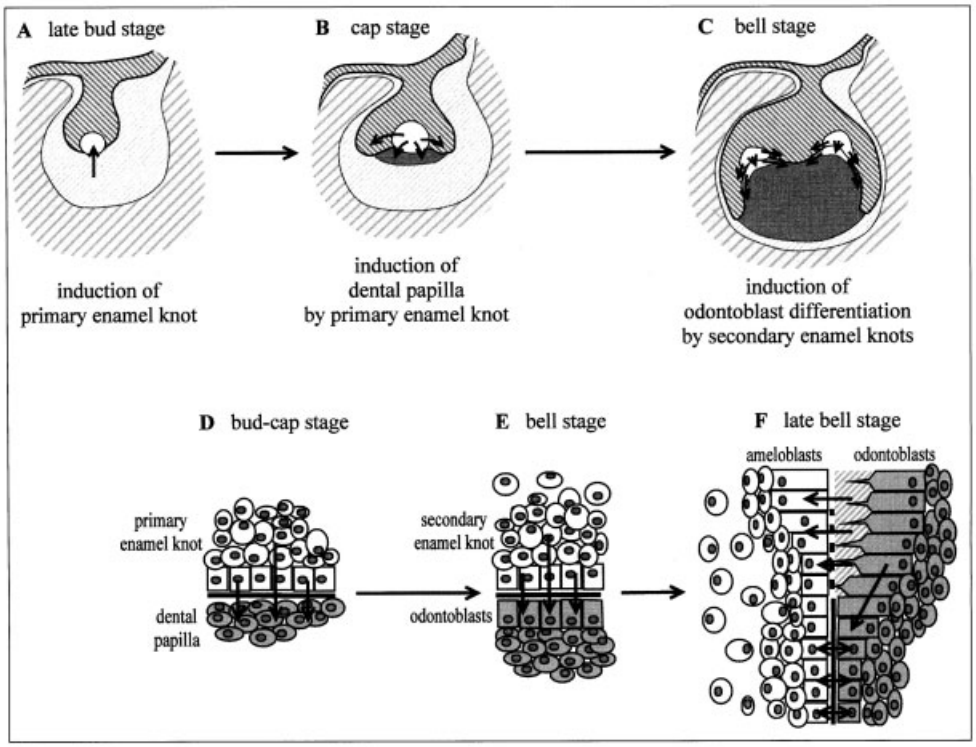

Figure 16.2 Schematic presentation of the association of enamel knot signaling with morphogenesis and odontoblast differentiation. (A) During the bud stage, the condensed odontogenic mesenchyme induces the formation of the primary enamel knot at the tip of the epithelium. (B) During the cap stage, the enamel knot expresses signaling molecules, which regulate the formation of the dental papilla and growth of the cervical loops of the epithelium. (C) During the bell stage, signals from the secondary enamel knots regulate the formation of cusps and may induce the initiation of terminal differentiation of odontoblasts. Differentiation proceeds toward the intercuspal areas and cervical loops. (D) Closer view of (B) shows the induction of dental papilla cells in the dental mesenchyme underlying the primary enamel knot. (E) Closer view of the cusp tip at the time of secondary enamel knot formation (stage slightly preceding that in C) shows the induction of odontoblast differentiation in the dental papilla cells underlying the secondary enamel knot. (F) Closer view of the odontoblast differentiation proceeding at the slope of the cusp (region of the vertical arrow in the left cusp in C). After initiation of odontoblast differentiation at the cusp tip, the differentiation signals may come from the epithelium in which the expression of several enamel knot signals are spreading (arrows from left to right) and/or the signals may be relayed by differentiating odontoblasts (vertical arrow). The odontoblasts secrete dentin and induce the terminal differentiation of ameloblasts (arrows from right to left). Reproduction from [24], with permission.

Figure 16.3 Histological section through a human tooth. Tertiary dentin (T) stimulated by caries. Inflamed pulp tissue (P), dentin (D) (bar = 500 μm). Courtesy of Claus Löst.

plex. These pre-odontoblasts already start to excrete a dentin matrix pre-form consisting of type I and type III collagen, fibronectin, and glycosaminoglycans. The dentin layer these pre-odontoblasts secrete directly at the dentin–enamel junction has a thickness of about 10–30 μm and, once mineralization is completed, is called the mantle dentin. It is distinguished from the circumpulpal dentin, which is formed by differentiated odontoblasts [3–6, 10–12].

A differentiated odontoblast is a polar cell 40–50 μm long with a diameter of 7 μm. Its characteristic form is a strong, distal cytoplasmatic process showing a distinguished microtubuli system. This process remains intact in length even during the retraction of the odontoblasts from the cement–enamel junction and is characteristic for dentin (Fig. 16.4). The pre-dentin secreted from odontoblasts consists of type I collagen fibers, glycoproteins and glycosaminoglycans. This pre-dentin still has to mature to a dentin matrix capable of mineralization. Therefore, there is a space of 5–20 μm between the front lines of odontoblasts and mineralization. At a later time, the centers of mineralization become confluent and this is where mineralization starts. It is assumed that mineralization occurs by matrix vesicles. The particular sequences and feedback mechanisms are also not known. The above-mentioned portion of circumpulpal dentin is called *intertubulary dentin* [7, 10, 11, 13–20].

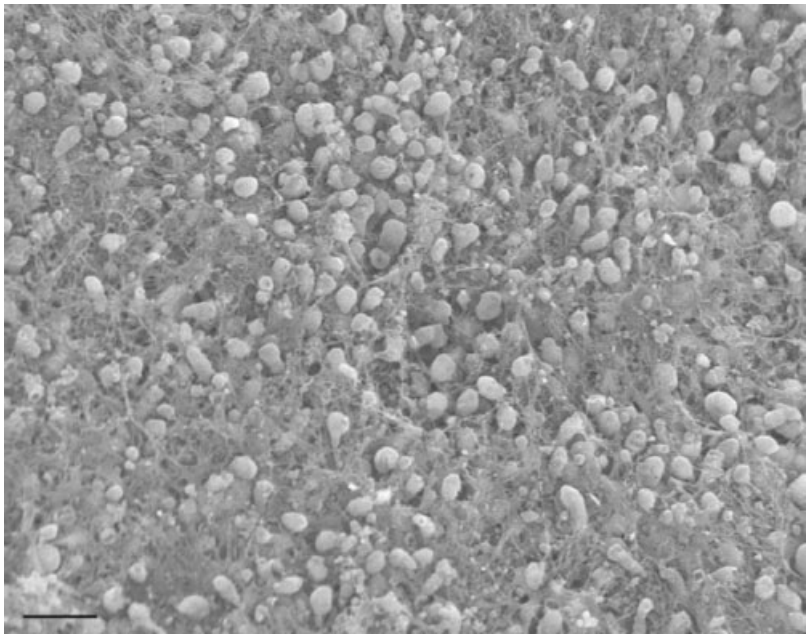

Figure 16.4 Odontoblasts at the pulp–dentin junction after removal of the pulp. The odontoblasts get caught at the dentin tubules with their processes (bar = 20 μm).

Intertubulary dentin is distinguished from *peritubulary dentin*. The latter is formed by secretion of a matrix consisting of mucopolysaccharides in the space resulting from a reduction in the diameter of the odontoblast process. However, no collagen fibers are secreted. The following peritubulary dentin is more higher mineralized than intertubulary dentin with its composition containing 50 % fibers. Formation of peritubulary dentin is a life-long process and is even increased by external stimuli. This can lead to a complete macroscopic obturation of the dentinal tubuli [7, 16, 17, 20].

Dentin with a weight proportion of about 10 % water and 20 % inorganic matrix consisting predominantly of collagen fibers shows less mineralization than enamel. The hydroxylapatite crystals are smaller and, therefore, dentin clearly shows a lower hardness than enamel, but a higher hardness than cement and bone. The presence of fibers makes dentin clearly more elastic.

Dentin mineralization takes place differently. The extracellular matrix of preodontoblasts is a pre-form of the dentin matrix which then mineralizes into the so-called mantle dentin. Differentiated odontoblasts form pre-dentin. The confluence of varying mineralized areas causes intertubulary dentin to be formed. However, differentiated odontoblasts also deposit dentin in the dentinal tubules, i.e. the peri-

tubulary dentin. Intertubulary and peritubulary dentin together are called *circumpulpal dentin*.

Different mineralization processes take place during tooth development. Furthermore, the tooth is a functioning system of dental hard and soft tissues. Since there are no extensive restructuring and decomposition processes after tooth development is completed, no "disruptive factors" need to be considered. Therefore, dentinogenesis is a very suitable model system for biomineralization processes.

Non-collagenous proteins play a crucial role in dentin formation, most of all the dentinsialophosphoprotein (DSPP) [21].

16.4 Pre-conditions for Dentinogenesis as Model for Biomineralization Processes

One pre-condition is that odontoblasts never lose their ability to form dentin. Odontoblasts are located at the dentin/pulp border in the tooth in the form of an odontoblast layer (Fig. 16.1B and 4). They do not perish during the eruption of the tooth like ameloblasts. Dentin regularly formed after dentition is called secondary dentin; dentin formed by an outside stimuli is called tertiary dentin (Fig. 16.3). Another pre-condition is that odontoblasts can differentiate from undifferentiated mesenchymal cells of the pulp. Perished odontoblasts can so be replaced, which makes the examination of mineralization processes on cultivated pulp cells possible. This cultivation process should be adapted to the physiological conditions as much as possible.

Dentin formation as a model has several advantages:

- Clear morphology of the teeth.
- No decomposition or conversion processes in dentin.
- No contamination with other tissues.
- Odontoblasts and their undifferentiated progenitor cells can be isolated in their pure form.

In the meantime the immuno-histochemical evidence could be established that the cultivated cells are indeed odontoblast-like cells.

16.5 Methods and Results

We used primary cultures of human pulp-derived fibroblasts (HPF). The HPF were derived from pulp tissue of freshly extracted and caries-free human third molars

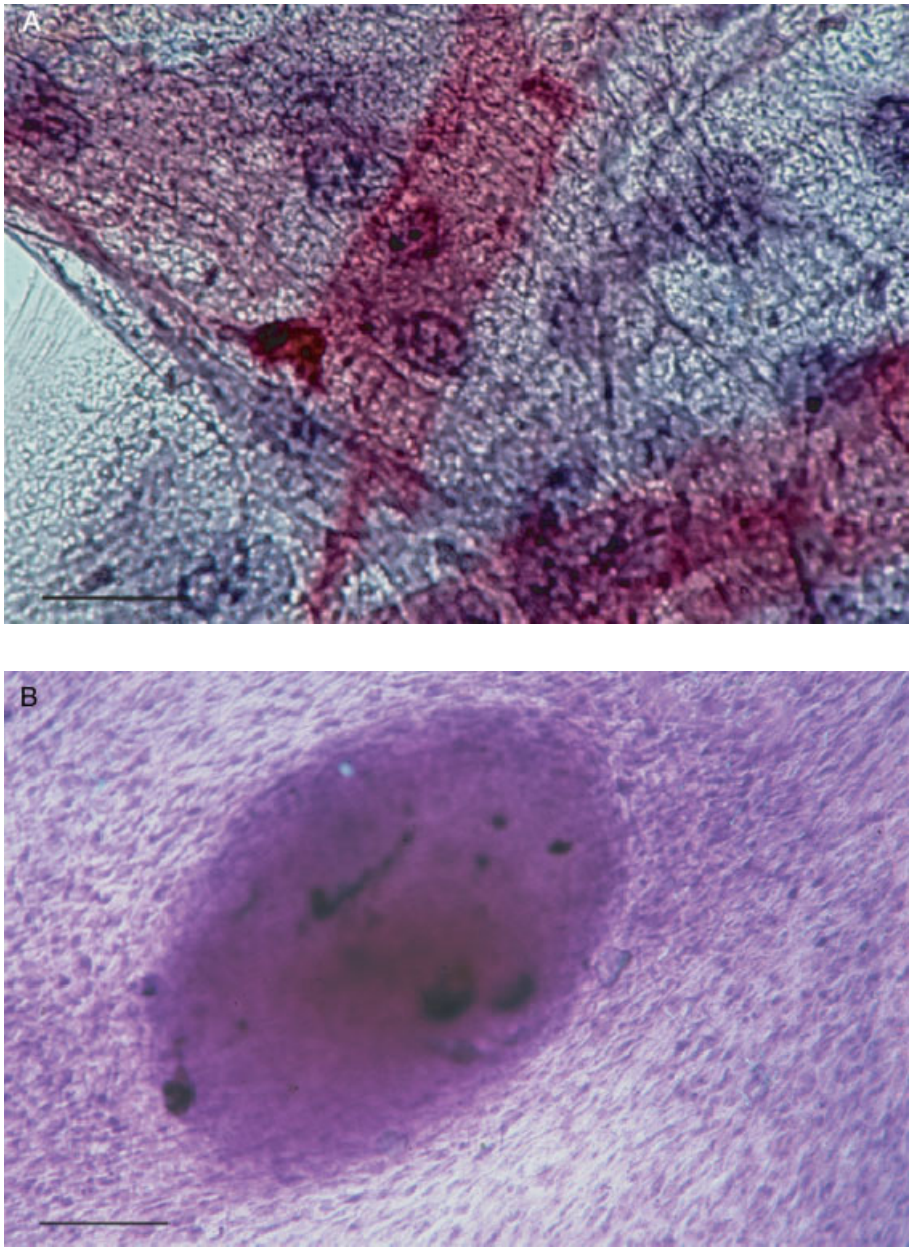

Figure 16.5 (A) Odontoblast-like cell, alkaline phosphatase expression and typical morphology. Alkaline phosphatase is shown as red. Alkaline phosphatase was verified topographically in the cells by histochemical staining (bar = 10 μm). (B) Mineralized nodule of odontoblast-like cells on Thermanox after a cultivation period of 5 weeks. High alkaline phosphatase activity (red) detectable in the nodule (bar = 150 μm).

Figure 16.6 Clinical picture of lower anterior teeth with presence of Dentinogenesis imperfecta. Malfunctioning dentine formation resulted in anomalous enamel.

from apparently healthy male donors, aged 14–22 years. Indication for their extraction was given on the basis of clinical findings. Consent for further use of the molars was obtained from each donor and was approved by the local ethics committee.

After extraction, the teeth were transferred into Dulbecco's modified Eagle's medium (DMEM), to which 100 IU/ml penicillin, 100 mg/ml streptomycin, 15 % fetal calf serum, 1 IU/ml mycostatin and 25 mg/ml gentamicin were added (all purchased from Gibco Life Technologies, Paisley, UK). The teeth were stored in the culture medium at 4 °C until further use within 2 h after extraction. Tissue was removed out of the tooth with a root canal instrument under sterile conditions, cut into 1-mm^3 pieces and transferred to 25-cm^2 tissue culture flasks (Costar, Cambridge, MA). Then, 4 ml of the culture medium was added and the tissue particles cultured in a CO_2 incubator (5 % CO_2, 37 °C). After 7 days, the medium was replaced by a modified medium that contained no mycostatin and no gentamicin. Within approximately 21 days, spindle-shaped pulp fibroblasts (HPF) had grown out from the tissue. After reaching confluence, the HPF monolayer was harvested with trypsin and passaged.

In transfer phase (T) 3 they are placed into a special, commercially obtainable three-dimensional continuous flow cell culture system (Minucells and Minutissue, Bad Abbach, Germany) which meets physiological conditions. Different, even three-dimensional support materials may be used depending on the aim of the study. Cells proliferate and differentiate differently on differing support material. Three-dimensional nodules are formed, showing the very high activity of alkaline

A

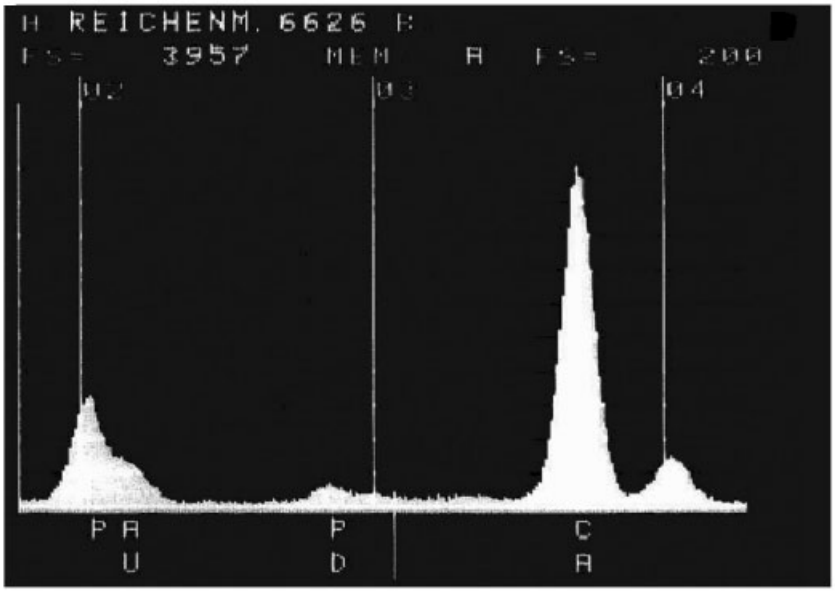

B

Figure 16.7 (A) SEM representation of a mineral formed by odontoblast-like cells on Thermanox after a cultivation period of 5 weeks. (B) EDX analysis of the mineral shown in (A) shows the presence of calcium and phosphate.

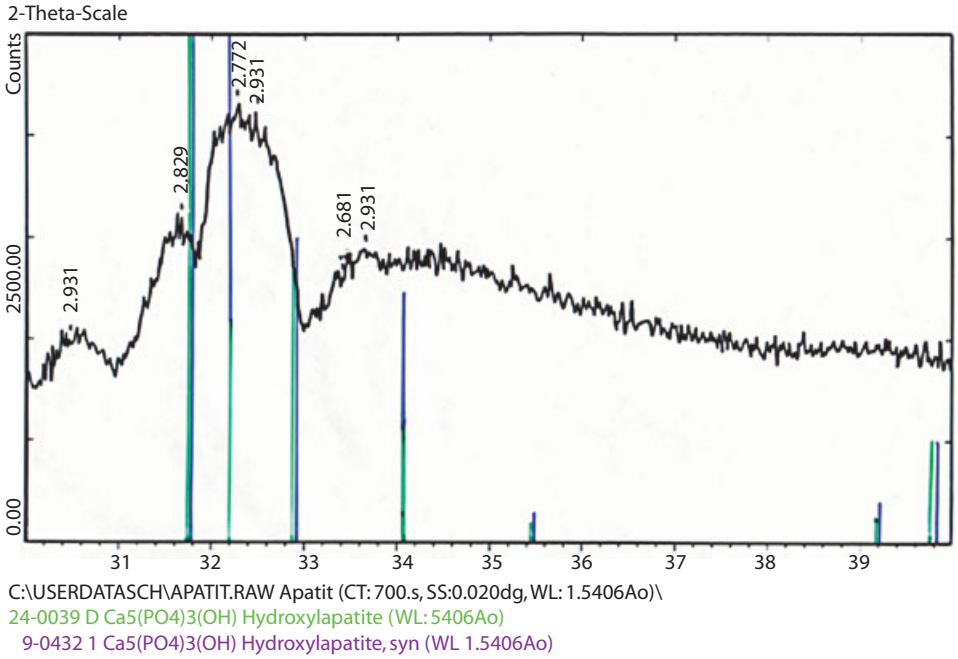

Figure 16.7 (C) X-ray diffractometry of the mineralization formed on odontoblast-like cells after a cultivation period of 5 weeks on Thermanox displays hydroxylapatite.

phosphatase (Fig. 16.5). Alkaline phosphatase expression is one classical parameter for cell differentiation to hard substance-forming cells. Seen from an immunohistochemical view, the pattern of expression is similar to that of odontoblast-like cells, which means it is also comparable to bone metabolism. The DSPP plays a crucial role in the verification of specific dentin-forming, odontoblast-like cells. If it is missing during tooth development, defects in dentinogenesis can be observed (Dentinogenesis imperfecta) (Fig. 16.6) [21]. This is much more expressed by odontoblasts than by osteoblasts. When cells are being cultivated as described above, the creation of calcium phosphate can be observed by scanning electron microscopy (SEM) and energy dispersive X-ray analysis (EDX) (Fig. 16.7A and B). After a culture is sustained for about 4 weeks, apatite can be verified by X-ray diffractometry as the specific final product of the cells (Fig. 16.7C).

The expression of DSPP by cultivated HPF has been verified by immunohistochemistry (Fig. 16.8) as well as by quantitative real-time polymerase chain reaction.

This shows that these cells can differentiate to odontoblast-like cells. There are similarities and differences between odontoblasts that specify either bone or dentin. It is assumed that the non-collagenous proteins are responsible, e.g. their charge may be responsible for different mineralization processes and structures.

Whenever human dental pulp stem cells (DPSCs) are used, they form ectopic

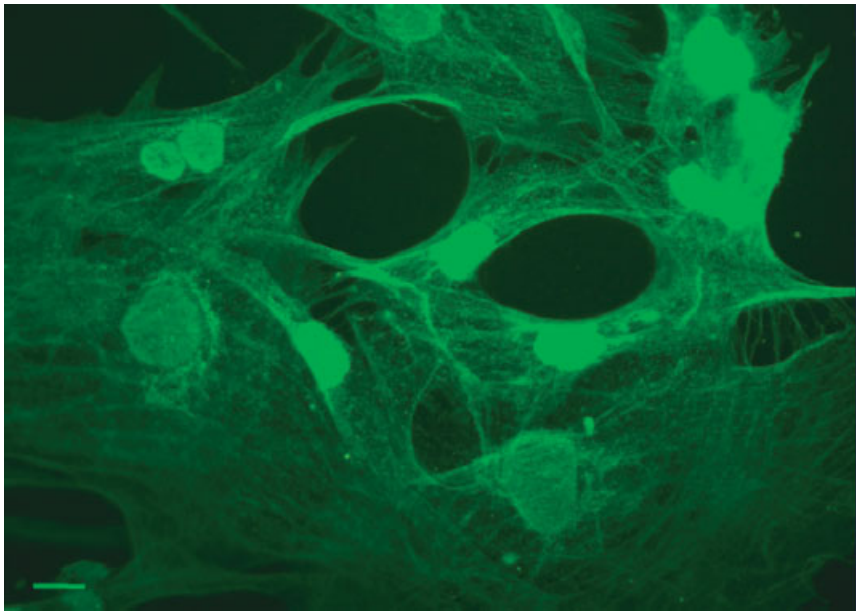

Figure 16.8 Immunohistochemical verification of the expression of DSPP by cultivated HPF after a cultivation period of three weeks on Thermanox (resin support material). (bar = 25 μm.)

dentin and associated pulp tissue *in vivo* [22]. DPSCs are similar to the cells described in this chapter. Stromal-like cells were re-established in culture from primary DPSCs transplants and re-transplanted into immunocompromised mice to generate a dentin pulp-like tissue. DPSCs possess stem cell-like qualities, including self-renewal capabilities [22].

Human exfoliated deciduous teeth (SHED) contain multipotent stem cells. SHED were identified to be a population of highly proliferative, clonogenic cells capable of differentiating into a variety of cell types including neural cells, adipocytes and odontoblasts: exfoliated teeth may be an unexpected unique resource for tissue engineering [23].

Acknowledgments

I would like to thank Claus Löst for supporting our work, E. Baeuerlein for inspiring such interesting discussions and Larry W. Fisher (National Institute of Health, Bethesda, MD) for providing the DSPP antibody. This work was supported by the Deutsche Forschungsgemeinschaft (DFG) SPP 1117, RE-1562-2.

References

[1] M. R. Byers, M. V. Narhi, *Crit. Rev. Oral. Biol. Med.* **1999**, *10*, 4–39.
[2] H. D. Rodd, F. M. Boissonade, *J. Anat.* **2003**, *202*, 195–203.
[3] G.-H. Schuhmacher, H. Schmidt, H. Börning, W. Richter, Entwicklung der Zähne, in *Anatomie und Biochemie der Zähne* (Eds G.-H. Schuhmacher, H. Schmidt, H. Börning, W. Richter), Gustav Fischer Verlag, Stuttgart, **1990**, pp. 55–155.
[4] J. V. Ruch, H. Lesot, C. Begue-Kirn, *Int. J. Dev. Biol.* **1995**, *39*, 51–68.
[5] J. V. Ruch, *Biochem. Cell Biol.* **1998**, *76*, 923–938.
[6] D. Tziafas, *Int. Endod. J.* **1994**, *27*, 61–74.
[7] A. J. Smith, N. Cassidy, H. Perry, C. Begue-Kirn, J. V. Ruch, H. Lesot, *Int. J. Dev. Biol.* **1995**, *39*, 273–280.
[8] D. Tziafas, *J. Dev. Biol.* **1995**, *39*, 281–290.
[9] A. J. Smith, H. Lesot, *Crit. Rev. Oral. Biol. Med.* **2001**, *12*, 425–437.
[10] A. Linde, T. Lundgren, *Int. J. Dev. Biol.* **1995**, *39*, 213–222.
[11] T. Sasaki, P. R. Garant, *Anat. Rec.* **1996**, *245*, 235–249.
[12] H. E. Schroeder, Dentinogenesis und Dentin, in *Orale Strukturbiologie* (Ed. H. E. Schroeder), Thieme, Stuttgart, **2000**, pp. 85–123.
[13] M. Goldberg, M. Takagi, *Histochem. J.* **1993**, *25*, 781–806.
[14] W. T. Butler, *Connect. Tissue Res.* **1995**, *33*, 59–65.
[15] W. T. Butler, H. Ritchie, *Int. J. Dev. Biol.* **1995**, *39*, 169–179.
[16] M. Goldberg, J. J. Lasfargues, *J. Dent. Res.* **1995**, *23*, 15–20.
[17] M. Goldberg, D. Septier, S. Lecolle, H. Chardin, M. A. Quintana, A. C. Acevedo, G. Gafni, D. Dillouya, L. Vermelin, B. Thonemann, G. Schmalz, P. Bissila-Mapahou, J. P. Carreau, *Int. J. Dev. Biol.* **1995**, *39*, 93–110.
[18] M. Goldberg, D. Septier, S. Lecolle, L. Vermelin, P. Bissila-Mapahou, J. P. Carreau, A. Gritli, A. Bloch-Zupan, *Connect. Tissue Res.* **1995**, *33*, 105–114.
[19] W. T. Butler, *Eur. J. Oral Sci.* **1998**, *106*, 204–210.
[20] I. A. Mjor, O. B. Sveen, K. J. Heyeraas, *Quintessence Int.* **2001**, *32*, 427–446.
[21] M. MacDougall, D. Simmons, X. Luan, J. Nydegger, J. Feng, T. T. Gu, *J. Biol. Chem.* **1997**, *272*, 835–842.
[22] S. Gronthos, J. Brahim, W. Li, L. W. Fisher, N. Cherman, A. Boyde, P. DenBesten, P. Gehron, S. Robey, S. Shi, *J. Dent. Res.* **2002**, *81*, 531–535.
[23] M. Miura, S. Gronthos, M. Zhao, B. Lu, L. W. Fisher, S. Gehron, P. Robey, S. Shi, *Proc. Natl Acad. Sci. USA* **2003**, *100*, 5807–5812.
[24] I. Thessleff, S. Keränen, J. Jernvall, *Adv. Dent. Res.* **2001**, *15*, 8–13.

17 The Zebrafish as a Model for Studying Skeletal Development

Shao Jun Du and Yutaka Haga

17.1 Introduction

The skeleton is a specialized tissue that, together with cartilage, makes up the skeletal system that confers multiple mechanical and biological functions, such as providing a support site for muscle attachment, protecting vital organs (e.g. brain) or cells (e.g. bone marrow) and serving as a reserve of ions [1]. The important function of bone can be easily recognized in day-to-day life, where millions of people suffer from bone disease such as osteoporosis, that is, in part, caused by an imbalance between bone formation and bone resorption [2]. A better understanding of the regulation of bone formation will provide important insights into the molecular mechanisms of bone disease and give rise to novel strategies for new drug design. Zebrafish have become an excellent model for systematic screening for mutations affecting different aspects of embryonic development including bone formation. Many of the point mutations that were created in fish more closely resemble human skeletal dysplasias. This chapter describes the embryonic origins and molecular regulation of bone formation in zebrafish. This review is primarily focused on recent studies that have taken advantage of the simple embryology and genetic tractability of zebrafish to dissect the cellular and molecular mechanisms underlying osteogenesis.

17.2 Skeleton Development and Patterning in Vertebrates

The vertebrate skeleton develops from cells of three embryonic lineages, i.e. the neural crest, somitic mesoderm and lateral plate [3–5]. Mesenchymal cells in the neural crest give rise to the craniofacial skeleton and branchial arches. Cells in the sclerotome of the somite form the axial skeleton and the tetrapod limb skeleton arises from cells of the lateral plate mesoderm. The earliest event in bone formation is migration of mesenchymal cells to specified locations where they form densely packed cell condensations. This process, called skeletal morphogenesis, controls the size, shape, number and arrangement of bones. Once patterning of a given skeletal element is achieved, mesenchymal cells in this element will undergo osteogene-

Biomineralization: From Biology to Biotechnology and Medical Application, Second Edition. Edited by E. Bäuerlein

ISBN: 3-527-31065-7

sis to form bones. There are two modes of bone formation. In one mode, mesenchymal cells differentiate directly into osteoblasts in a process called intramembranous ossification. This type of osteogenesis occurs primarily in the bones of the skull. In another mode, mesenchymal cells in the patterned skeletal element first differentiate into chondrocytes, the cell type specific to cartilage. The cartilaginous template is eventually replaced by bone containing osteoblasts and osteoclasts. The osteoblasts secrete bone matrix that is ossified to become bone. This process of bone formation is called endochondral ossification. These two types of bone formation are found in all vertebrates. In fish, the skeletal elements of the fin rays, the lepidotrichia, have a dermal origin. It is in contrast to endochondral bones of girdles or of the limb segments in tetrapods. Lepidotrichial ontogenesis occurs by direct mineralization of a collagenous matrix without passage through a cartilaginous precursor [6, 7].

17.3 Zebrafish as a Model for Studying Skeletal Development

In the past, most of our knowledge on bone formation was gained from clinical studies. However, recently, many important insights into bone formation have come from studies of animal models, including chicks and genetically modified mice. These studies have provided fundamental information about growth factors [e.g. bone morphogenetic proteins (BMPs)] and transcription factors (e.g. Cbfa1) that regulate growth and differentiation of chondroblasts and osteoblasts [8–10]. Models for human skeletal dysplasias have been created in mice by gene knockout. It is apparent that most of the regulatory factors or pathways that control bone formation are highly conserved in vertebrates during evolution and signaling molecules required for embryonic skeletal development are also important for adult homeostasis. The gene knockout approach is most useful for studying diseases resulting from loss of gene functions. At times, mouse models of null mutations do not quite resemble the mutations in human skeletal dyplasias because the human disorders are often caused by missense mutations. Subsequently, in recent years, there has been increasing interest in using new approaches and new animal models for studying skeletal development.

Zebrafish (*Danio rerio*) have become an important model for developmental studies, because zebrafish have several advantages compared with other model systems. Zebrafish are a small freshwater cyprinid native to southeastern Asia [11]. Their rapid development, short generation time and embryonic transparency make them a very attractive system for genetic studies of development. In addition, the easy accessibility of zebrafish embryos for direct observation of the development process, and their suitability for systematic mutagenesis further facilitate genetic screening to identify genes regulating the development of various tissues and organs, including the skeletal system [12–14]. The genetic approach has been shown to be very powerful and productive. In the past few years, several hundred zebrafish

mutants have been generated, which possess developmental defects in various tissues or cell types in early embryonic stages [15, 16]. Together, the recent advances in systematic genetic analysis and the Zebrafish Genome Project have facilitated the discovery of many genetic programs controlling development and other fundamental physiologic processes. As a result, zebrafish have moved to the forefront as a vertebrate model system. Also see Chapter 14 for a review of zebrafish as a genetic model to study otolith formation.

17.4 Methods for Visualizing Bones in Zebrafish

The success of any genetic screen depends largely on the application of an easy and effective screening method to identify interesting mutants. The ability to observe early development *in vitro* and to identify morphological abnormalities under a stereomicroscope have made the initial screening highly productive in zebrafish. Thousands of mutants have been generated [15, 16]. Most of the mutants were, however, identified based on phenotypes that could be easily distinguished under a dissecting microscope. This screening method has obvious limitations for tissues that develop internally and cannot be observed easily, such as the skeletal system. Alternative screening approaches include staining with specific dyes [17–20] and even X-rays have been applied to search for zebrafish mutants with abnormal bone structures [21].

Large numbers of interesting mutants have been identified using the classical Alcian blue or Alizarin red staining. Alcian blue stains chondrocytes (Figure 17.1), whereas Alizarin red labels mineralized bone matrix (Figure 17.2A), the earliest sign of ossification. However, these methods possess a number of drawbacks. For example, staining methods require the use of fixed embryos. In addition, the staining procedure is long and can take a few days. Therefore, the development of a simple and sensitive method to visualize the skeletal structure in live fish embryos is desirable for large-scale systematic screening of mutations that affect bone development. In order to develop a method for visualizing skeletal structures in zebrafish embryos that would be suitable for screening skeletal mutants, we investigated the use of the fluorescent chromophore calcein ($C_{30}H_{26}N_2O_{13}$), which binds specifically to calcium in calcified skeletal structures [22]. Because the skeletal system is comprised of calcified structures, calcein has been used to label bone structures and to study bone growth [10]. Calcein has been used in fish as a non-specific marking compound, where calcein marks in the rays have successfully been produced by immersion of Atlantic salmon *Salmo salar* [23] and rainbow trout [24]. In comparison to Alcian blue or Alizarin red, calcein staining has several advantages. First, calcein staining is quick and simple. The procedure can be performed on live zebrafish embryos and can be completed in approximately 20 min. Second, calcein staining is a more sensitive and inclusive method for visualizing skeletal structures in zebrafish embryos. It labels both cartilage and ossified bone (Figures 17.1 and 17.2). This method has great potential in future screening for skeletal mutants.

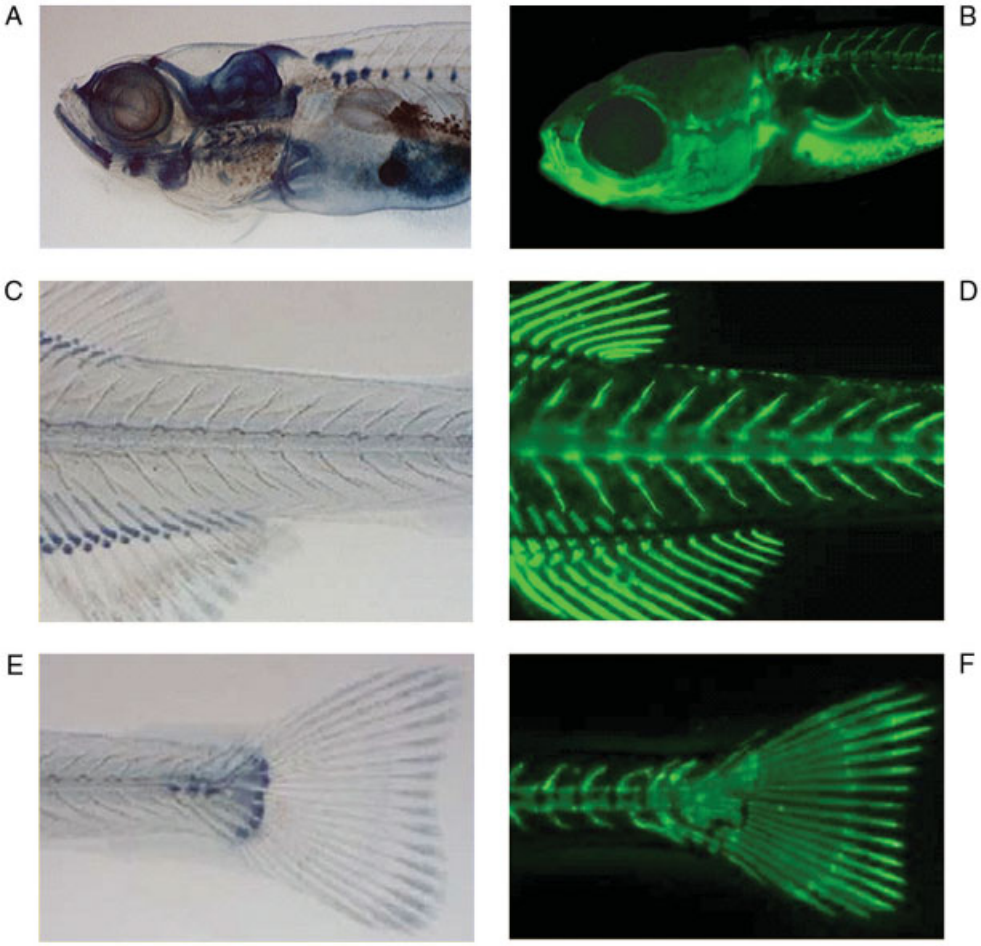

Figure 17.1 Visualization of skeletal structures in zebrafish larvae by Alcian Blue and calcein staining. (A, C and E) Alcian Blue staining in the head, trunk and tail regions of a 23 days post-fertilization (d.p.f) embryo. (B, D and F) Calcein labeling of calcified structures in the head, trunk and tail regions of a 23 d.p.f. embryo.

17.5 Bone Development in Zebrafish Embryos

The development of the head and axial skeleton has been closely examined in zebrafish embryos and larvae using various staining methods (Figure 17.3). It was found that the development of the skeletal structure appears in a progressive fashion from head to tail. Skeletal structures in the head (i.e. the skull and pharyngeal cartilages) develop first [20, 22, 25, 26], followed by the axial skeleton in the trunk [22, 27, 28]. This is followed by the caudal, dorsal, anal and paired fins [28, 29].

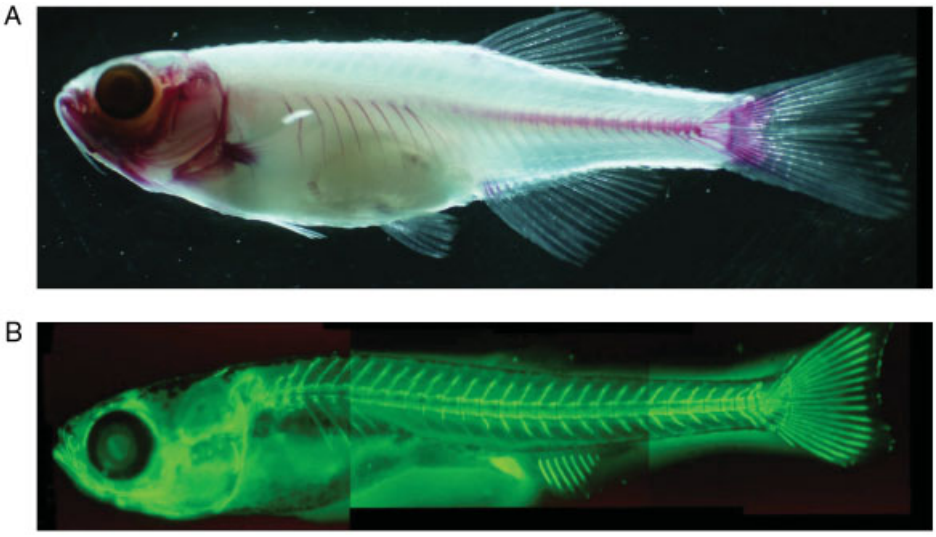

Figure 17.2 Visualization of skeletal structures in zebrafish larvae by Alizarin red and calcein staining. (A) Alizarin red staining of skeleton in a 45 d.p.f. zebrafish larvae. (B) Calcein labeling of skeleton in a 23 d.p.f. zebrafish larvae.

17.5.1 Development of the Head Skeleton

The formation of the vertebrate skull has a pivotal role in evolution. Because mineralized bones fossilize readily, we have gained a substantial understanding of how the head skeleton has evolved during evolution. In contrast to the trunk skeleton,

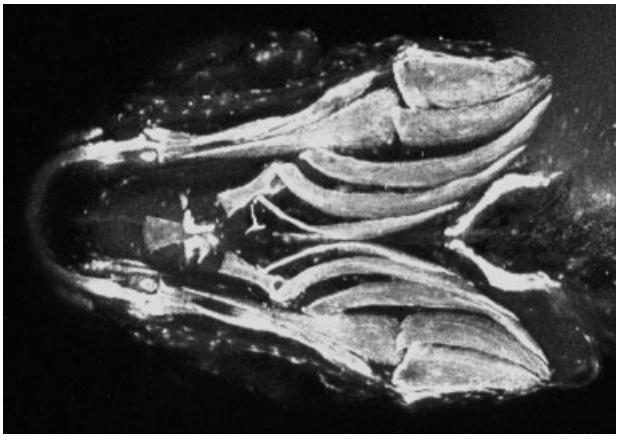

Figure 17.3 Visualization of calcified head skeletal structures in zebrafish larvae by calcein staining. Ventral view of the head skeleton of a zebrafish larvae at 20 d.p.f.

the craniofacial and jaw skeleton is composed of an often bewildering assortment of cartilage and bones that have been highly modified during evolution. The development of the head skeleton has been extensively studied in several animal models. Despite the complex head skeletal structures among the vertebrates, there appears to be conserved mechanisms that control the developmental process. Current developmental genetic analyses are providing new insight on how skeletal development is regulated and how the processes have evolved [30, 31].

The head skeleton in zebrafish larvae is relatively simple and composed primarily of cartilages. These cartilages consist of two prominent types of cells – chondrocytes and perichondrial cells [31]. As in other vertebrates, the cartilaginous head skeleton has two major divisions – the neurocranium, protecting brain and sensory organs, and the pharyngeal arches, supporting the feeding and gill-breathing structures. There are seven pharyngeal arches in zebrafish. The first and second pharyngeal arches give rise to the lower jaw (mandibular) or basihyal (hyoid), respectively, whereas the remaining five pharyngeal arches are gill-bearing arches, also known as branchial arches. The pharyngeal arches are a highly organized structure with dorsal–ventral and anterior–posterior patterns.

The development of the skeleton in the skull has been well-documented in a large numbers of vertebrate species. Lineage studies have defined the origins of the zebrafish cranial skeleton at the single-cell level [32]. As in other vertebrates, the neurocranium that protects the brain and sensory organs of the head is generated from both the neural crest and mesoderm. The pharyngeal skeleton including the jaw and the branchial arches is solely derived from neural crest cells [32–35].

17.5.1.1 Jaw and Branchial Arch Mutants in Zebrafish

Systematic screening has been performed to identify mutants with developmental defects in the jaw and the pharyngeal arches. Large numbers of mutants have been identified [17–19]. The known mutants fall among at least 30 genes. These mutants affect distinct aspects of craniofacial development, and include defects in the specification of craniofacial skeleton elements, differentiation and morphogenesis of cartilage, and organization of head skeletal elements. For example, genes that are responsible for mutants such as *hammerhead*, *jellyfish* and *knorrig* are required for cartilage differentiation and growth. In *hammerhead*, the mesoderm-derived cartilages are reduced, whereas *jellyfish* mutant larvae are characterized by a severe reduction of all cartilaginous elements [17, 18]. In *knorrig* mutant embryos, tumor-like outgrowths of chondrocytes occur along the edges of all cartilaginous elements [17, 18]. In other types of mutants, the craniofacial defects appear to be restricted to specific arches or defined regions in the arch. Mutations in four genes (*schmerle*, *sucker*, *hoover* and *sturgeon*) show specific defects in the first two arches and leave the more posterior pharyngeal arches largely unaffected [17, 18]. In the *lockjaw* mutant, the hyoid arch is strongly reduced and subsets of branchial arches do not develop [17]. Together, these data indicate that some of these genes have a general effect on head cartilage formation, while others have a specific effect on head skeletal patterning.

17.5.1.2 Molecular Characterization of Jaw and Branchial Arch Mutants

A number of genes responsible for craniofacial mutants have been mapped and cloned. Knight et al. [36] showed that the craniofacial mutant *lockjaw* disrupts the zebrafish homolog of *tfap2a* gene that encodes a transcription factor of the activator protein 2 (AP2) family. Zebrafish *tfap2a* is expressed in the pre-migratory neural crest. It is required for the survival of the neural crest migrating from the hindbrain and spinal cord. Increased apoptosis is found in the cranial region of *lockjaw* at early segmentation stages [36, 37]. In addition of being important for pharyngeal arches, *tfap2a* is also required for the formation of subsets of neural crest-derived cell types including sensory neurons and pigment cells [36, 38]. The *lockjaw*/*tfap2* mutant phenotype is similar to the *Tcfap2a* mutant mice that have craniofacial, neural tube, body wall, limb and eye defects [39–41]. These data suggest that Tfap2a has highly conserved and multi-faceted roles in vertebrate development with many implications for human craniofacial and deafness syndromes [36, 38].

Recent studies by Yan et al. [42] have shown that two alleles of *jellyfish* contain mutations in the *sox9a* gene, one of the two orthologs of the human transcription factor SOX9. Sox9a is expressed in pharyngeal arches and neurocranium in zebrafish embryos [43]. Zebrafish *jellyfish* mutants show craniofacial defects and lack cartilage elements of the neurocranium, pharyngeal arches and pectoral girdle similar to human with campomelic dysplasia [42, 44]. The *jellyfish* mutant embryos lack the organized stacking of chondrocytes and proper shaping of individual cartilages [42]. Molecular analysis using markers indicates that neural crest specification and migration is normal in *jellyfish* mutants. Pharyngeal arch condensation, however, appears to be affected. These studies demonstrate that Sox9a is essential for both morphogenesis of condensations and cartilage differentiation.

Recent studies by Kimmel et al. [45, 46] have demonstrated that the zebrafish jaw mutant *sucker* carries mutations in the gene *endothelin 1* (*edn1*), which encodes a secreted peptide. Consistent with the specific defects in the first (mandibular) and second (hyoid) pharyngeal arch of the zebrafish *sucker* mutant, *edn1* is expressed in these pharyngeal arch primordia [45, 47]. Genetic analyses suggest that two Edn1 downstream targets, the basic helix-loop-helix (bHLH) transcription factor Hand2 and the homeobox transcription factor Bapx1, may mediate the function of Edn1 in patterning ventral pharyngeal cartilage and the jaw joint [47]. Bapx1 expression in the intermediate domain, which later marks the jaw joint in zebrafish, requires Edn1 function [47]. In mice, targeted inactivation of the Edn1 receptor, EdnrA, produces a similar phenotype as Edn1 inactivation, i.e. loss of the mandible and severe malformations of other pharyngeal skeletal elements [48]. Pharmacological inactivation of EdnrA disrupts lower jaw formation in chick embryos [49]. Thus, Edn1/EdnrA signaling is required for lower jaw formation in vertebrates.

Another interesting mutant, *van gogh* (*vgo*), characterized by defects in the ear, pharyngeal arches and associated structures, has been recently mapped and cloned. Piotrowski et al. [50] showed that *vgo* is caused by a mutation in *tbx1*, a member of the large family of *t-box* genes. *Tbx1* acts directly in a cell autonomous manner to control the development of pharyngeal mesoderm and indirectly in neural crest-

derived cartilages [50]. There appears to be regulatory interactions between *vgo*, *edn1* and *hand2* in the control of pharyngeal arch development [50]. The phenotypes of *vgo* mutants bears striking resemblance to humans affected with DiGeorge syndrome. Individuals with DiGeorge syndrome are characterized by craniofacial defects, aortic arch malformation and hearing loss [51]. Tbx1 has been suggested to be a major contributor to the defects in DiGeorge syndrome in humans. The zebrafish *vgo* mutants thus provide a potentially useful model system for understanding the etiology of DiGeorge syndrome.

17.5.1.3 Signaling Molecules in Head Skeleton Patterning

Patterning genes are largely responsible for directing cells to the proper locations. Most of these genes encode signaling molecules involve in cell-to-cell communication and intracellular signaling, and transcription factors such as Homeobox and *pax* genes. These patterning genes establish a regulatory circuit that imparts information about identity and spatial position to migrating cells. Several classes of signaling molecules involved in neural crest specification and differentiation have been implicated in controlling head skeleton formation. *Wnt-11*, for example, encodes *silberblick* (*slb*) [52]. *slb* mutants show developmental defects in the basiocranial cartilage [31]. In addition, several other midline mutants resulted from mutations in the transforming growth factor (TGF)-β, Hedgehog and fibroblast growth factor (FGF) signaling pathways also exhibit skeletal defects in the head [31]. The type I TGF-β family member receptor Alk8 which acts in the BMP signaling is required for neural crest cell formation and development of pharyngeal arch cartilages in zebrafish [53]. The zebrafish mutant *laf*, which shows pharyngeal mesodermal defects, carries mutations in Alk8 [53–55]. Inhibiting FGF receptor activity or blocking FGF3 or FGF8 expression results in complete or near-complete loss of neurocranial cartilage [56, 57]. FGF and BMP signals repress the expression of Bapx1 in the mandibular mesenchyme and control the position of the developing jaw joint [58]. These data suggest that BMP and FGF are important signal molecules in patterning the pharyngeal arches.

17.5.1.4 Hox Genes in Anterior–Posterior Patterning of the Head Skeleton

Hox code may be involved in anterior–posterior patterning of head skeleton elements. Molecular analyses reveal that the same nested expression patterns of the homeobox genes that regulate skeletal patterning in birds and mammals also participate in zebrafish head morphogenesis [59–62]. As might be suspected from such conserved patterns of gene expression, mutations in mice and zebrafish homeobox genes produced similar phenotypes. Mutation of *lazarus*/*pbx4*, encoding a *hox* gene partner, and disruption of *valentino*/*kreisler*, a *hox* gene regulator, produce anterior–posterior axis disruptions of pharyngeal cartilages [63–65]. In *valentino* mutants, an ectopic cartilage resembling the small interhyal cartilage characteristic of the second arch is found in the third arch [66]. The duplication of the small cartilages in *valentino*/*kreisler* mutants correlates closely with changes in *hox* gene expression. In both fish and mice, loss of *valentino*/*kreisler* function results in the

ectopic expression in the third arch of *hox* genes normally expressed in the second arch. Mutations in *hox* genes themselves have yet to be analyzed in zebrafish. Targeted mutagenesis of Hoxa2 in the mouse shows a crucial role for this gene in patterning along the anterior–posterior axis [67]. Hoxa2 is expressed in the second arch, but not in the mandibular pharyngeal segment. A knockdown in zebrafish Hox2 function produces defects in the second pharyngeal arch, where ventral skeletal elements were replaced by duplicated first arch structures [68], analogous to the mouse HoxA2 mutant phenotype [67]. Together, these data suggest that the *hox* genes function as selector genes in anterior–posterior patterning of the pharyngeal arches.

17.5.2 Development and Patterning of the Axial Skeleton

The axial skeleton in zebrafish includes the vertebral column and associated median (unpaired) fins [28]. The vertebral column is composed of an alternating pattern of vertebral bodies and intervertebral discs [69]. The vertebral body consists of centrum, neural arches and spines, haemal arches and spines, and ventral (pleural) ribs [28]. The medial fins include the dorsal, ventral (anal) and caudal fins.

17.5.2.1 Development of the Vertebral Skeleton

The axial skeleton is derived from the sclerotome, a mesenchymal cell population that occupies the ventromedial region of the somite. In zebrafish, sclerotome cells constitute only a small proportion of the somite located at the anterior region of the ventromedial somite [70]. These cells express a zebrafish homolog of *Drosophila twist* [70]. Sclerotome cells migrate to surround the axial midline structures (the notochord) and differentiate as cartilage and bone [70]. An ultrastructural study by transmission electron microscopy (TEM) shows that each vertebra consists of a core of notochord cells surrounded by a sheath of bone. Compared with other vertebrates, some teleosts, including zebrafish, are unique in having bone that lacks osteocytes embedded in the matrix [71].

Fleming et al. [69] found that vertebral bodies (centra) in zebrafish larvae arise by secretion of bone matrix from the notochord rather than somites. Centra do not form via a cartilage intermediate stage nor do they contain osteoblasts. This is very similar to osteogenesis of vertebral bone in Japanese medaka (*Oryzias latipes*). Ekanayake and Hall [72, 73] showed that vertebral bone is devoid of cells embedded in the matrix throughout development. Cells that secrete bone matrix do not become trapped in their own secretion. Instead, they always remain as a surface layer over the outer surface of the bone. Bone is only deposited by osteoblasts lining the outer surface of the bone – no deposition of bone takes place on the inner surface [72, 73]. Moreover, in later stages of osteogenesis, matrix-producing cells secrete matrix only toward the already-deposited bone. This polarized matrix secretion allows the osteoblasts to always stay on the bone surface and never to become trapped in the matrix as osteocytes [73].

17.5.2.2 Regulation of Segmented Vertebral Patterning

The vertebral column is the defining feature of vertebrates. The vertebral column is segmented and composed of an alternating pattern of vertebral bodies (centra) and intervertebral disks [69]. The ossification process of vertebrae progresses from the anterior to posterior regions in a segmented fashion as the zebrafish embryos develop (Figure 17.4). Within each vertebrae, the ossification process initiates at the boundary of each muscle segment (Figure 17.4) and then expands in both directions. As embryonic development progresses, the neural and haemal arches appear in the dorsal and ventral sides of the vertebrae, respectively (Figure 17.4).

The segmented vertebral column shows a tight correlation with the muscle segments. It was noted over a century ago that vertebrae are displaced by half a segment relative to muscle segments [74]. Despite the importance of the vertebral column in defining the overall vertebrate body plan, very little is known about the genetic and cellular interactions that control vertebral segmentation [27]. It has been suggested by the ''resegmentation'' model that vertebral periodicity originates from the segmented somites. The ''resegmentation'' model suggests that a single vertebra forms from the recombination of the anterior and posterior halves of two adjacent sclerotomes on both sides of the embryos.

The ''resegmentation'' model is being challenged by new studies in zebrafish. Recent lineage analyses in zebrafish embryos have shown that cells from one half-sclerotome can contribute to two consecutive vertebrae, rather than only to one vertebrae as predicted by the ''resegmentation'' model [27]. Moreover, Fleming et al. [69] found that vertebral bodies (centra) in zebrafish larvae are formed by secretion of bone matrix from the notochord rather than somites, suggesting that the notochord plays a key, perhaps ancient, role in the segmental patterning of vertebrae.

By advantageously using the available zebrafish mutants with segmental defects in somites, several investigators have analyzed the skeletal development in the *fused somites* (*fss*) mutant. They found that in *fss* mutants, the haemal and neural arches grow in an irregular fashion [69, 75]. The development of the centrum, however, appears relatively normal [69, 75]. These findings indicate that the somite is not critically involved in establishing the segmentation of the vertebral column. Although these studies indicate the importance of the notochord in vertebral segmentation, they also raise questions about whether the notochord is segmented at the molecular level and the nature of the molecular mechanism underlying the notochord segmentation. Interestingly, *hox* gene expression reveals regionalization along the anterioposterior axis of the zebrafish notochord, suggesting that Hox code might be involved in the notochord segmentation [27].

17.5.2.3 Development of Neural Arches, Haemal Arches and Spines

The neural arches form from either cartilage (endochondral) or membrane bone precursors, depending on their position along the vertebral column [28]. Most haemal arches develop from ventrally projecting, bilaterally paired, membranous ossification. Haemal spines develop as a result of continued membranous ossification of

haemal arches. The haemal arches and spines of preural vertebrae (caudal vertebrae anterior to the urostyle), however, are derived from cartilage. The haemal spines elongate by means of continued cartilage growth, and they later ossify [28].

17.5.2.4 Molecular Regulation of Axial Skeleton Formation and Patterning

Extensive signaling events are required for sclerotome specification and differentiation. Two families of proteins, i.e. the Hedgehog and BMP families, play key roles in these processes. *Hedgehog* (*hh*) was first identified in *Drosophila* as being required for normal patterning of embryonic segments and imaginal disks [76]. Hedgehogs are secreted proteins that function through the membrane receptors Patched and Smoothened, and several downstream intracellular components including Fused, Costal-2, protein kinase A (PKA) and Glis/Ci [77–79]. Molecular cloning has revealed that there are multiple members of the Hh family in vertebrates and they are expressed in several tissues such as notochord, floor plate and limb bud. Sonic hedgehog (Shh) expressed in notochord is crucial for sclerotome development, as Shh mutant mice lack a vertebral column and form only a few rudimentary rib cartilages [80]. Genetic data also supports a crucial role for Gli2 and Gli3 in mediating Shh-dependent sclerotome induction and formation of the axial skeleton. Impaired endochondral bone development and osteopenia is observed in Gli2-deficient mice [81]. Compound *gli2* and *gli3* double mutants exhibit more severe defects than either single mutant, indicating some overlapping functions in skeletogenesis [82, 83].

Hhs are not only important for sclerotome induction during early embryogenesis, they also play a role in chondrocytes proliferation and differentiation during bone growth. Indian hedgehog (Ihh) signaling is directly required for the osteoblast lineage in the endochondral skeleton [84]. The best-defined regulatory circuit involves the Ihh and parathyroid hormone-related protein (PTHrP). Secreted by prehypertrophic chondrocytes, Ihh promotes chondrocyte proliferation and activates a negative feedback loop mediated by PTHrP [85, 86]. These data clearly demonstrate that Hhs play a critical role in sclerotome induction and subsequent chondrocyte differentiation during mouse development and growth. The functions of Hhs in fish skeleton formation have yet to be determined. The major obstacle is that the zebrafish mutants with defective Hh signaling are embryonic lethal prior to the formation of the axial skeleton, thus preventing the use of Hh mutants in studying skeletal defects in fish. Instead, Hh signaling has been found to be essential for slow muscle development in zebrafish [87–90].

BMPs are another family of signaling molecules that play important roles in bone formation. As their names imply, BMPs were originally identified as factors capable of inducing bone *de novo* when implanted ectopically *in vivo* [91]. Several BMPs are expressed by chondrocytes and the perichondrium during normal development [92]. BMPs stimulate mesenchymal cells to differentiate into chondrocytes and osteoblasts, which deposit bone matrix. Inactivation of BMP genes causes skeletal malformation in mice [8]. The activities of BMPs are controlled by inhibitors from three BMP binding proteins: short gastrulation/chordin, Noggin and Cerberus [93].

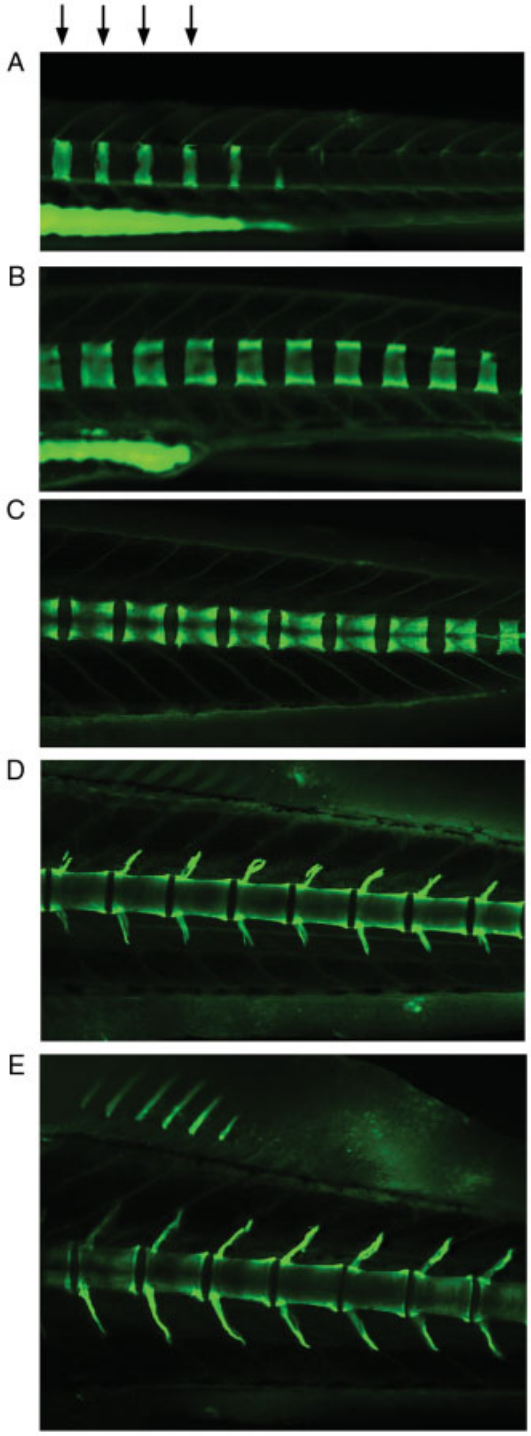

Figure 17.4 Visualization of developmental process of axial skeleton in developing zebrafish embryos. Calcification of vertebrae progress in a segmented fashion from the anterior to posterior regions. Axial skeleton revealed by calcein staining in the trunk region of zebrafish larvae at different developmental stages; (A) 11, (B) 13, (C) 15, (D) 18 and (E) 21 d.p.f. Arrows indicate the calcification initiation site of the vertebrae, which commences at the boundaries of each muscle segment.

Noggin and Chordin were found to inhibit the activity of BMPs by preventing interaction with their BMP receptors [94, 95]. Noggin mutant mice lack joints, but also exhibit hyperplastic cartilage and defective cartilage maturation [96]. Blocking BMP function by Noggin is thus thought to prevent osteogenesis at sites of joint formation [96]. Expression of Gremlin (a BMP antagonist) in limb bud mesenchyme is required for maintenance of Shh and FGF signals during limb patterning [97], suggesting a tight interaction between BMP and Hh in controlling skeletal formation.

A direct role of BMPs in fish formation remains to be established. Several mutant lines with mutations in the BMP signaling pathways have been identified [98, 99]. Because BMPs are also involved in early dorsoventral patterning of the embryos, these mutants, including *swirl* (*swr*), *somitabun* (*sbn*), *piggytail* (*pyy*), *minifin* (*mfn*) and *lost-a-fin* (*laf*), show strong dorsalized phenotype. Therefore, studies of zebrafish mutants with defective BMP signaling have not provided significant informative on BMP functions in bone development because of inherent complications such as early lethality. However, Fisher and Halpern [21] provide evidence that skeletal development is regulated by Chordin through its ability to block BMP activity. These investigators show that patterning in the zebrafish axial skeleton requires early Chordin function [21]. Chordin mutants have defects in tail vertebrae, including incomplete neural and haemal arches, absent or abnormal spinous processes, and anteriorly directed processes fused with those of adjacent vertebrae [21]. At present, it is not entirely clear whether the caudal skeletal defects of mutant adults reflect the early requirement for Chordin at gastrulation or, alternatively, a later requirement for Chordin in bone morphogenesis. Two pieces of evidence support a direct role of Chordin in osteogenesis. First, Chordin is expressed by cells surrounding several cartilages [21]. Second, Chordin proteins could persist in a stable compound with BMP and the action of Tolloid may release active BMPs from the complexes at a later stage of skeletogenesis [100, 101]. It has been shown that mutants of the zebrafish Tolloid homolog [102] have abnormally thickened vertebral spinous processes, as well as an altered number and shape of bones in the anal and dorsal fin endoskeletons [21].

17.5.3 Fin Development in Zebrafish

17.5.3.1 Development of Median Fins

The three median fins (dorsal, ventral and caudal) are formed in different temporal patterns. The caudal fin is the first to develop. It is followed by the anal and, finally, the dorsal fin. The dorsal and anal fins consist of endoskeleton supports, or radials, and exoskeleton supports, or fin rays. The endoskeletons are formed by endochondral ossification of cartilaginous radials. Ossification of the radials proceeds proximally and distally from the middle of the radial [28]. The caudal fin also contains both endoskeleton and exoskeleton development. The endoskeleton is mainly composed of five hypurals that are expanded and laterally flattened haemal arches and

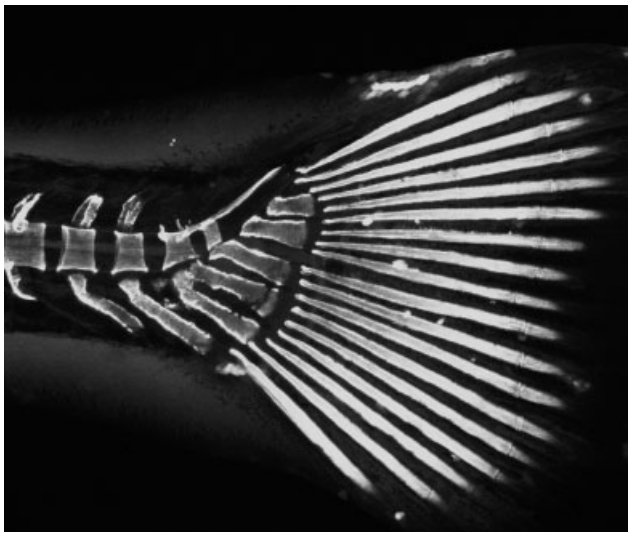

Figure 17.5 Visualization of calcified skeletal structures in the caudal fin of zebrafish larvae by calcein staining. Side view of the entire caudal fin including endoskeleton and exoskeleton (fin ray) of a 20 d.p.f. zebrafish larvae.

spines that serve as attachments for the caudal fin rays (Figure 17.5). In addition, the parhypural, the haemal and neural arches and spines of the second and third preural vertebrae also contribute to the endoskeleton of the caudal fin [28]. As with the endoskeletons of the dorsal and anal fins, the endoskeletons of the caudal fin are also formed by endochondral ossification. In contrast to the endoskeletons, the exoskeletons are dermal skeleton that is generated by direct ossification of collagenous matrix without going through a cartilaginous step.

17.5.3.2 Development of Paired Fins

It has been noted over a century ago that there is considerable homology between the bones of fish paired fins and tetrapod limbs [103]. The paired fins consist of pelvic and pectoral fins [29]. Because of these similarities, the fish pectoral and pelvic fins have been suggested to be homologous to the tetrapod forelimb and hindlimb, respectively. Several pieces of evidence support this idea. First, gene expression studies have demonstrated that Shh and En-1 are expressed at equivalent positions in zebrafish fin buds [104–107] and tetrapod limb buds [108]. The Shh expression in pectoral fin buds is consistent with a role in mediating the activity of a structure analogous to the zone of polarizing activity (ZPA) that is critical for limb patterning in tetrapods [104, 108–110]. Second, although fish pectoral fins and tetrapod forelimbs differ with respect to the somite level from which they arise from, their position is consistent with respect to the level of Hox gene expression along the anterior–posterior axis. For example, fish pectoral fins and mammalian forelimb

buds are found at the most anterior expression region of Hoxc-6, the position of the first thoracic vertebra [62, 111–113]. While the specific homologies between the proximal elements (endoskeleton) of the fish paired fins and the limbs are readily supported, little evidence exists to support the homologies proposed between the autopod of the limb (the hand or foot at the distal end) and fish fin ray (exoskeleton). Based on the patterns of *hox* gene expression, Sordino et al. [105] have concluded that a structural equivalent of the tetrapod autopod is absent in the zebrafish. This idea is consistent with the different developmental origins of fin ray and limb. The skeletal elements of the fin rays, the lepidotrichia, have a dermal origin. It is in contrast to endochondral bones of girdles or of the limb segments in tetrapods. Fin rays ossify by direct mineralization of a collagenous matrix without cartilaginous precursors [6, 7].

17.5.3.3 Molecular Regulation of Fin Formation

The molecular regulation of fin development has been studied via several approaches. Genetic screening in zebrafish has identified a total of 108 mutations affecting fin formation in both median and paired fins in zebrafish embryos and larvae [114]. These mutations apparently result in degeneration of fins and fin folds. Interestingly, in mutants of one of these genes, *dackel* (*dak*), pectoral fin buds form initially, but later the fin epithelium fails to expand. *In situ* hybridization of *dak* mutants shows that the signaling molecule Shh is initially expressed at low levels in *dak* pectoral fins and later disappears from *dak* fins [114]. Presumably, the *dak* mutation disrupts the Shh signaling pathway, which results in pectoral fin defects similar to the limb defects shown for Shh mutants in mice [80]. Grandel et al. [115] show that *dak* acts in the ectoderm of the zebrafish pectoral fin bud to maintain apical ectoderm ridge (AER) signaling.

In addition to mutants with fin defects in embryos, several mutations specifically affecting the development of the adult fin have also been identified [114, 116]. Two mutants, *longfin* (*lof*) and *another longfin* (*alf*), have generally longer fins. In contrast, *Stein und bein* (*sub*) has reduced dorsal and pelvic fins, whereas *finless* (*fls*) and *wanda* (*wan*) mutants affect all adult fins [114]. *Short fin* (*sof*) mutants have 'normal' fins and fin rays that are approximately half the size of typical zebrafish fins [116]. At least one of the fin mutants has been mapped and cloned. Lesions in connexin 43 (the protein subunits of gap junctions) are linked to the *short fin* phenotype, suggesting a role for gap junction in fin growth (Kathy Ioine, Lehigh University, personal communication).

Interestingly, in some of the fin mutants, developmental defects are also observed in other tissues. Several mutants (*hammerhead*, *pekinese*, *head on*, *jellyfish* and *shallow chin*) have been identified where outgrowth of both pectoral fins and branchial arches is reduced [114]. These genes are probably required for proper cartilage differentiation [18, 114].

Another approach to the study of fin development is the analysis of fin regeneration [117]. Zebrafish caudal fins can regenerate rapidly after amputation. Analysis of fin regeneration is not only informative in its own right, but may also

provide information pertaining to earlier morphogenetic events [118]. The regeneration processes are reminiscent of those occurring during larval stages, including re-expression of developmental genes [119]. Laforest et al. [120] demonstrated that Hedgehog and BMP signals are involved in patterning zebrafish dermal fin rays. Ectopic expression of Shh or BMP2 in the blastema induced excess bone deposition and altered patterning of the regenerate [118]. The effects of Shh ectopic expression could be antagonized by ectopic expression of chordin [118]. Retinoic acid is another important factor that control fin formation and regeneration. Global exposure of fish embryos to retinoic acid disrupted the formation and regeneration of caudal fins [121, 122]. Retinoic acid may act by downregulating the expression of *Shh*, *ptc1* and *bmp2* [120]. Retinoic acid response element has been identified in the 5′-flanking sequence of *shh* gene [123].

17.6 Other New Aspects in Fish Skeleton Development

17.6.1 New Screening Method for Mutants with Skeletal Defects in Adult Zebrafish

The ability to identify morphological abnormalities in zebrafish embryos under a stereomicroscope have made the initial screening of the mutants that affect early development highly productive. However, these studies failed to identify mutants that affect the formation of the axial skeleton. This is largely due to the fact that complete maturation of the skeleton is a relatively late event in zebrafish development [124]. Juvenile fish are fully mobile and sexually mature before the skeleton is fully mineralized. Using radiography, Fisher et al. [124] have undertaken a mutagenesis screen for skeletal dysplasia in adult zebrafish to detect abnormalities in skeletal anatomy and bone morphology. They have isolated a dominant mutant, *chihuahua*, which show a general defect in bone growth. Heterozygous *chihuahua* mutants have phenotypic similarities to human osteogenesis imperfecta. Both are dominantly acting mutations that allow normal cartilage formation, but result in a general defect in bone growth. Uneven mineralization of growing bone and fragile bones with frequent fractures are characteristic of *chihuahua* heterozygous mutants. Molecular characterization revealed that *chihuahua* carries a glycine to aspartic acid mutation in the Gly–X–Y triplet repeat in the type I collagen I(a) chain, a genetic mutation also responsible for the vast majority of human osteogenesis imperfecta [124].

17.6.2 Use of the Transgenic Approach to Analyze BMP Function in Bone Development

Bone morphogenetic proteins and their antagonists such as Noggin play important roles in recruiting mesenchymal precursor cells into condensations and modulating

bone formation. In addition to having a role in bone development, BMPs are key signaling molecules in establishing the dorso-ventral patterning during early embryogenesis [98, 99]. Zebrafish mutants with BMP signaling defects are severely dorsalized and are embryonic lethal, which prevents using them for bone developmental studies. To analyze the role of BMP in bone development in zebrafish, we ectopically expressed BMP and BMP-like proteins in the notochord of zebrafish embryos by DNA injection using a notochord-specific promoter [22, 125]. Ectopic expression of BMP proteins in notochord cells of zebrafish embryos disturbs the development of the vertebral column and haemal arch projections [22]. These data indicate that BMP may to play a role in development of the axial skeleton in zebrafish. This transient expression approach is applicable to analyzing the functions of other signaling molecules that may play a role in controlling skeletal formation in zebrafish.

17.6.3 Zebrafish as a Model for Bone Deformity induced by Teratogenic Chemicals

Toxic pollutants including pesticides and industrial organic chemicals are widespread contaminants of the marine environment. It is becoming increasingly evident that some of these chemical pollutants could disrupt the normal development, growth and reproduction of animals and humans. The effects of these chemical pollutants on embryogenesis are especially alarming because embryos are very sensitive to environmental changes and the disruption of normal developmental processes could lead to birth defects.

Fish have served as useful sentinels to detect environmental hazards, and as efficient and cost-effective model systems for toxicology and risk assessment [126]. The toxic effects of several classes of chemicals including heavy metals, pesticides, herbicides and organic chemicals have been tested on fish [126, 127]. Some of these chemicals cause skeletal defects in fish. For example, exogenous retinoic acid treatment of fish embryos induced jaw deformity and developmental defects in caudal and pectoral fins [128–131]. The phenotype is similar to developmental defects in limb, axial and craniofacial skeleton observed in chick [132] and mouse [133, 134] embryos exposed to excessive levels of retinoic acid.

The zebrafish provides a good model for mechanistic study of the teratogenic effects of retinoic acid and other pollutants. Retinoic acid action is mediated through specific receptors localized in the nucleus of the target cells. Retinoic acid receptor (RAR) and retinoid X receptors (RXR) are ligand-activated transcription factors that control the expression of developmentally important genes. It has been shown by *in situ* hybridization that RA inhibits Hh gene expression in zebrafish embryos [120]. Two transgenic zebrafish lines, *twhh-GFP* and *shh-GFP*, that express green fluorescent protein (GFP) under the control of two different Hh promoters are available [125, 135]. These transgenic lines provide useful models for analyzing the effect of retinoic acid on Hh gene expression. Moreover, transgenic zebrafish, developed by Perz-Edwards et al. [136], that express GFP driven by the retinoic acid-

responsive elements provide another excellent model for analyzing the effects of retinoic acid on skeletal formation and mechanisms of actions.

17.7 Conclusions

In summary, zebrafish have recently become a model of choice among developmental biologists because this species is a well-established system for molecular and genetic studies [137]. Genetic analyses in zebrafish have been instrumental for providing invaluable clues to the elucidation of complex molecular processes in vertebrate biology [138]. Since the completion of the two large-scale mutagenesis screens carried out at the Max-Planck Institute and Massachusetts General Hospital, many of the recovered mutations have been cloned and the functions of the mutated genes studied. With more specifically defined screens being carried out in numerous laboratories globally, the zebrafish will certainly become an even more popular model for basic and medical research. Future achievements certainly will not be limited to specific structures and organ systems, and studies with zebrafish may even provide important insights to more complicated biological processes such as behavior and memory.

Acknowledgments

We thank John Stubblefield for English editing, Lauren Ireland and Brad Oberlander for taking care of the zebrafish, and Olivier Peraud for assistance in using the confocal microscope. This research was supported by a grant from NIH to S. J. D. (R01GM58537-01A1) and a Maryland Sea Grant to S. D. J. This publication is contribution number [05-106] from the Center of Marine Biotechnology, University of Maryland Biotechnology Institute.

References

[1] N. Sims, C. Baron, in *Skeletal Growth Factors* (Ed. E. Canalis), Lippincott Williams & Wilkins, Philadelphia, PA, **2000**, pp. 1–16.
[2] G. A. Rodan, T. J. Martin, *Science* **2000**, *289*, 1508–1514.
[3] A. Erlebacher, E. H. Filvaroff, S. E. Gitelman, R. Derynck, *Cell* **1995**, *80*, 371–378.
[4] B. R. Olsen, A. M. Reginato, W. Wang, *Annu. Rev. Cell Dev. Biol*. **2000**, *16*, 191–220.
[5] W. A. Horton, *Lancet* **2003**, *362*, 560–569.
[6] J. Geraudie, W. J. Landis, *Am. J. Anat.* **1982**, *163*, 141–156.
[7] W. J. Landis, J. Geraudie, *Anat. Rec*. **1990**, *228*, 383–391.

[8] B. L. M. Hogan, *Gene Dev*. **1996**, *10*, 1580–1594.
[9] G. Karsenty, in *Skeletal Growth Factors* (Ed. E. Canalis), Lippincott Williams & Wilkins, Philadelphia, PA, **2000**, pp. 291–298.
[10] P. Ducy, T. Schinke, G. Karsenty, *Science* **2000**, *289*, 1501–1504.
[11] R. P. Barman, *Rec. Zool. Sur. India Occ. Paper* **1991**, *137*, 1–91.
[12] C. Nüsslein-Volhard, *Science* **1994**, *266*, 572–574.
[13] G. Vogel, *Science* **2000**, *288*, 1160–1161.
[14] T. F. Schilling, *BioEssays*, **1997**, *19*, 459–468.
[15] P. Haffter, M. Granato, M. Brand, M. C. Mullins, M. Hammerschmidt, D. A. Kane, J. Odenthal, F. J. M. van Eeden, Y.-J. Jiang, C.-P. Heisenberg, R. N. Kelsh, M. Furutani-Seiki, E. Vogelsang, D. Beuchle, U. Schach, C. Fabian, C. Nüsslein-Volhard, *Development* **1996**, *123*, 1–36.
[16] W. Driever, L. Solnica-Krezel, A. F. Schier, S. C. F. Neuhauss, J. Malicki, D. L. Stemple, D. Y. R. Stainier, F. Zwartkruis, S. Abdelilah, Z. Rangini, J. Belak, C. Boggs, *Development* **1996**, *123*, 37–46.
[17] T. F. Schilling, T. Piotrowski, H. Grandel, M. Brand, C. P. Heisenberg, Y. J. Jiang, D. Beuchle, M. Hammerschmidt, D. A. Kane, M. C. Mullins, F. J. van-Eeden, R. N. Kelsh, M. Furutani-Seiki, M. Granato, P. Haffter, J. Odenthal, R. M. Warga, T. Trowe, C. Nüsslein-Volhard, *Development* **1996**, *123*, 329–344.
[18] T. Piotrowski, T. F. Schilling, M. Brand, Y. J. Jiang, C. P. Heisenberg, D. Beuchle, H. Grandel, F. J. van-Eeden, M. Furutani-Seiki, M. Granato, P. Haffter, M. Hammerschmidt, D. A. Kane, R. N. Kelsh, M. C. Mullins, J. Odenthal, R. M. Warga, C. Nüsslein-Volhard, *Development* **1996**, *123*, 345–356.
[19] S. C. Neuhauss, L. Solnica-Krezel, A. F. Schier, F. Zwartkruis, D. L. Stemple, J. Malicki, S. Abdelilah, D. Y. Stainier, W. Driever, *Development* **1996**, *123*, 357–367.
[20] C. B. Kimmel, C. T. Miller, G. Kruse, B. Ullmann, R. A. BreMiller, K. D. Larison, H. C. Snyder, *Dev. Biol*. **1998**, *203*, 245–263.
[21] S. Fisher, M. E. Halpern, *Nat. Genet*. **1999**, *23*, 442–446.
[22] S. J. Du, V. Frenkel, G. Kindschi, Y. Zohar, *Dev. Biol*. **2001**, *238*, 239–246.
[23] J. W. Mohler, *North Am. J. Fish Management* **1997**, *17*, 751–756.
[24] V. Frenkel, A. Bart, J. Clark, J. Young, E. Kimmel, Y. Zohar, *Aquaculture* **2002**, *214*, 169–183.
[25] C. C. Cubbage, P. M. Mabee, *J. Morphol*. **1996**, *229*, 121–160.
[26] T. F. Schilling, C. B. Kimmel, *Development* **1997**, *124*, 2945–2960.
[27] E. M. Morin-Kensicki, E. Melançon, J. S. Eisen, *Development* **2002**, *129*, 3851–3860.
[28] N. C. Bird, P. M. Mabee, *Dev. Dyn*. **2003**, *228*, 337–357.
[29] H. Grandel, S. Schulte-Merker, *Mech. Dev*. **1998**, *79*, 99–120.
[30] C. B. Kimmel, C. T. Miller, R. J. Keynes, *J. Anat*. **2001**, *199*, 105–120.
[31] C. B. Kimmel, C. T. Miller, C. B. Moens, *Dev. Biol*. **2001**, *233*, 239–257.
[32] T. F. Schilling, C. B. Kimmel, *Development* **1994**, *120*, 483–494.
[33] S. Horstadius, *The Neural Crest, its Properties and Derivatives in Light of Experimental Research*, Oxford University Press, Oxford, **1950**.
[34] N. M. LeDouarin, *The Neural Crest*, Cambridge University Press, Cambridge, **1982**.
[35] R. M. Langille, B. K. Hall, *Anat. Embryol.* (*Berl.*) **1988**, *177*, 297–305.
[36] R. D. Knight, S. Nair, S. S. Nelson, A. Afshar, Y. Javidan, R. Geisler, G. J. Rauch, T. F. Schilling, *Development* **2003**, *130*, 5755–5768.
[37] A. Barrallo-Gimeno, J. Holzschuh, W. Driever, E. W. Knapik, *Development* **2004**, *131*, 1463–1477.
[38] R. D. Knight, Y. Javidan, S. Nelson, T. Zhang, T. F. Schilling, *Dev. Dyn*. **2004**, *229*, 87–98.
[39] H. Schorle, P. Meier, M. Buchert, R. Jaenisch, P. J. Mitchell, *Nature* **1996**, *381*, 235–238.
[40] J. Zhang, S. Hagopian-Donaldson, G. Serbedzija, J. Elsemore, D. Plehn–Dujowich, A. P. McMahon, R. A. Flavell, T. Williams, *Nature* **1996**, *381*, 238–241.
[41] G. M. Morriss-Kay, *BioEssays*, **1996**, *18*, 785–788.
[42] Y. L. Yan, C. T. Miller, R. M. Nissen, A. Singer, D. Liu, A. Kirn, B. Draper, J. Willoughby, P. A. Morcos, A. Amsterdam, B. C. Chung, M. Westerfield, P. Haffter, N. Hopkins, C. Kimmel, J. H. Postlethwait, R. Nissen, *Development* **2002**, *129*, 5065–5079.

[43] E. F. Chiang, C. I. Pai, M. Wyatt, Y. L. Yan, J. Postlethwait, B. Chung, *Dev. Biol*. **2001**, *231*, 149–163.
[44] T. Wagner, J. Wirth, J. Meyer, B. Zabel, M. Held, J. Zimmer, J. Pasantes, F. D. Bricarelli, J. Keutel, E. Hustert, U. Wolf, N. Tommerup, W. Schempp, G. Scherer, *Cell* **1994**, *79*, 1111–1120.
[45] C. T. Miller, T. F. Schilling, K. Lee, J. Parker, C. B. Kimmel, *Development* **2000**, *127*, 3815–3828.
[46] C. B. Kimmel, B. Ullmann, M. Walker, C. T. Miller, J. G. Crump, *Development* **2003**, *130*, 1339–1351.
[47] C. T. Miller, D. Yelon, D. Y. Stainier, C. B. Kimmel, *Development* **2003**, *130*, 1353–1365.
[48] D. E. Clouthier, K. Hosoda, J. A. Richardson, S. C. Williams, H. Yanagisawa, T. Kuwaki, M. Kumada, R. E. Hammer, M. Yanagisawa, *Development* **1998**, *125*, 813–824.
[49] H. Kempf, C. Linares, P. Corvol, J. M. Gasc, *Development* **1998**, *125*, 4931–4941.
[50] T. Piotrowski, D. G. Gahn, T. F. Schilling, S. Nair, I. Ruvinsky, R. Geisler, G. J. Rauch, P. Haffter, L. I. Zon, Y. Zhou, H. Foott, I. B. Dawid, R. K. Ho, *Development* **2003**, *130*, 5043–5052.
[51] A. K. Ryan, J. A. Goodship, D. I. Wilson, N. Philip, A. Levy, H. Seidel, S. Schuffenhauer, H. Oechsler, B. Belohradsky, M. Prieur, A. Aurias, F. L. Raymond, J. Clayton-Smith, E. Hatchwell, C. McKeown, F. A. Beemer, B. Dallapiccola, G. Novelli, J. A. Hurst, J. Ignatius, A. J. Green, R. M. Winter, L. Brueton, K. Brondum-Nielsen, P. J. Scambler, *J. Med. Genet*. **1997**, *34*, 798–804.
[52] C. P. Heisenberg, M. Tada, G. J. Rauch, L. Saude, M. L. Concha, R. Geisler, D. L. Stemple, J. C. Smith, S. W. Wilson, *Nature* **2000**, *405*, 76–81.
[53] T. L. Payne-Ferreira, P. C. Yelick, *Dev. Dyn*. **2003**, *228*, 683–696.
[54] T. L. Payne, J. H. Postlethwait, P. C. Yelick, *Mech. Dev*. **2001**, *100*, 275–289.
[55] K. A. Mintzer, M. A. Lee, G. Runke, J. Trout, M. Whitman, M. C. Mullins, *Development* **2001**, *128*, 859–869.
[56] N. B. David, L. Saint-Etienne, M. Tsang, T. F. Schilling, F. M. Rosa, *Development* **2002**, *129*, 4457–4468.
[57] J. Walshe, I. Mason, *Dev. Biol.* **2003**, *264*, 522–536.
[58] J. Wilson, A. S. Tucker, *Dev. Biol*. **2004**, *266*, 138–150.
[59] V. Prince, A. Lumsden, *Development* **1994**, *120*, 911–923.
[60] P. A. Trainor, R. Krumlauf, *Nat. Rev. Neurosci*. **2000**, 116–124.
[61] M. R. Capecchi, *Cold Spring Harb. Symp. Quant. Biol.* **1997**, *62*, 281–283.
[62] A. Amores, A. Force, Y. L. Yan, L. Joly, C. Amemiya, A. Fritz, R. K. Ho, J. Langeland, V. Prince, Y. L. Wang, M. Westerfield, M. Ekker, J. H. Postlethwait, *Science* **1998**, *282*, 1711–1714.
[63] H. Popperl, H. Rikhof, H. Chang, P. Haffter, C. B. Kimmel, C. B. Moens, *Mol. Cell* **2000**, *6*, 255–267.
[64] K. L. Cooper, W. M. Leisenring, C. B. Moens, *Dev. Biol*. **2003**, *253*, 200–213.
[65] V. E. Prince, C. B. Moens, C. B. Kimmel, R. K. Ho, *Development* **1998**, *125*, 393–406.
[66] C. B. Moens, S. P. Cordes, M. W. Giorgianni, G. S. Barsh, C. B. Kimmel, *Development* **1998**, *125*, 381–391.
[67] M. Gendron-Maguire, M. Mallo, M. Zhang, T. Gridley, *Cell* **1993**, *75*, 1317–1331.
[68] M. P. Hunter, V. E. Prince, *Dev. Biol*. **2002**, *247*, 367–389.
[69] A. Fleming, R. Keynes, D. Tannahill, *Development* **2004**, *131*, 873–880.
[70] E. M. Morin-Kensicki, J. S. Eisen, *Development* **1997**, *124*, 159–167.
[71] L. R. Parenti, *Zool. J. Linnean Soc*. **1986**, *87*, 37–51.
[72] S. Ekanayake, B. K. Hall, *Am. J. Anat*. **1988**, *182*, 241–249.
[73] S. Ekanayake, B. K. Hall, *J. Morphol*. **1987**, *193*, 253–261.
[74] R. Remak, *Untersuchungen über die Entwicklung der Wirbeltiere*, Reimer, Berlin, **1850**.
[75] F. J. van Eeden, M. Granato, U. Schach, M. Brand, M. Furutani-Seiki, P. Haffter, M. Hammerschmidt, C. P. Heisenberg, Y. J. Jiang, D. A. Kane, R. N. Kelsh, M. C. Mullins, J. Odenthal, R. M. Warga, M. L. Allende, E. S. Weinberg, C. Nüsslein-Volhard, *Development* **1996**, *123*, 153–164.
[76] C. Nüsslein-Volhard, E. Wieschaus, *Nature* **1980**, *287*, 795–801.

[77] M. Hammerschmidt, A. Brook, A. P. McMahon, *Trends Genet*. **1997**, *13*, 14–21.
[78] R. L. Johnson, M. P. Scott, *Curr. Opin. Genet. Dev*. **1998**, *8*, 450–456.
[79] P. W. Ingham, A. P. McMahon, *Genes Dev*. **2001**, *15*, 3059–3087.
[80] C. Chiang, Y. Litingtung, E. Lee, K. E. Young, J. L. Corden, H. Westphal, P. A. Beachy, *Nature* **1996**, *383*, 407–413.
[81] D. Miao, H. Liu, P. Plut, M. Niu, R. Huo, D. Goltzman, J. E. Henderson, *Exp. Cell Res.* **2004**, *294*, 210–222.
[82] R. Mo, A. M. Freer, D. L. Zinyk, M. A. Crackower, J. Michaud, H. H. Heng, K. W. Chik, X. M. Shi, L. C. Tsui, S. H. Cheng, A. L. Joyner, C. Hui, *Development* **1997**, *124*, 113–123.
[83] L. Buttitta, R. Mo, C. C. Hui, C. M. Fan, *Development* **2003**, *130*, 6233–6243.
[84] F. Long, U. I. Chung, S. Ohba, J. McMahon, H. M. Kronenberg, A. P. McMahon, *Development* **2004**, *131*, 1309–1318.
[85] A. Vortkamp, K. Lee, B. Lanske, G. V. Segre, H. M. Kronenberg, C. J. Tabin, *Science* **2000**, *273*, 613–622.
[86] B. St-Jacques, M. Hammerschmidt, A. P. McMahon, *Genes Dev*. **1999**, *13*, 2072–2086.
[87] P. D. Currie, P. W. Ingham, *Nature* **1996**, *382*, 452–455.
[88] C. Blagden, P. D. Currie, P. W. Ingham, S. M. Hughes, *Gene Dev*. **1997**, *11*, 2163–2175.
[89] S. J. Du, S. H. Devoto, M. Westerfield, R. T. Moon, *J. Cell Biol.* **1997**, *139*, 145–156.
[90] S. J. Du, M. Dienhart, *Differentiation* **2001**, *67*, 84–91.
[91] J. M. Wozney, V. Rosen, A. J. Celeste, L. M. Mitsock, M. J. Whitters, R. W. Kriz, R. M. Hewick, E. Wang, *Science* **1988**, *242*, 1528–1543.
[92] S. Pathi, J. B. Rutenberg, R. L. Johnson, A. Vortkamp, *Dev. Biol*. **1999**, *209*, 239–253.
[93] W. Balemans, W. Van Hul, *Dev. Biol*. **2002**, *250*, 231–250.
[94] S. Piccolo, Y. Sasai, B. Lu, E. M. De Robertis, *Cell* **1996**, *86*, 589–598.
[95] L. B. Zimmerman, J. M. De Jesus-Escobar, R. M. Harland, *Cell* **1996**, *86*, 599–606.
[96] I. J. Brunet, J. A. McMahon, A. P. MacMahon, R. M. Harland, *Science* **1998**, *280*, 1455–1457.
[97] M. K. Khokha, D. Hsu, L. J. Brunet, M. S. Dionne, R. M. Harland, *Nat. Genet*. **2003**, *34*, 303–307.
[98] M. C. Mullins, *Method Cell Biol*. **1999**, *59*, 159–178.
[99] M. Hammerschmidt, M. C. Mullins, *Results Prob. Cell Differ*. **2002**, *40*, 72–95.
[100] G. Marques, M. Musacchio, M. J. Shimell, K. Wunnenberg-Stapleton, K. W. Cho, M. B. O'Connor, *Cell* **1997**, *91*, 417–426.
[101] M. C. Mullins, *Trends Genet.* **1998**, *14*, 127–129.
[102] S. A. Connors, J. Trout, M. Ekker, M. C. Mullins, *Development* **1999**, *126*, 3119–3130.
[103] R. Owen, *On the Nature of Limbs*, J. Van Voor, London, **1849**.
[104] S. Krauss, J. P. Concordet, P. W. Ingham, *Cell* **1993**, *75*, 1431–1444.
[105] P. Sordino, F. van der Hoeven, D. Duboule, *Nature* **1995**, *375*, 678–681.
[106] K. Hatta, R. Bremiller, M. Westerfield, C. B. Kimmel, *Development* **1991**, *112*, 821–832.
[107] M. Ekker, J. Wegner, M. A. Akimenko, M. Westerfield, *Development* **1992**, *116*, 1001–1010.
[108] R. D. Riddle, R. L. Johnson, E. Laufer, C. Tabin, *Cell* **1993**, *75*, 1401–1416.
[109] Y. Echelard, D. J. Epstein, B. St-Jacques, L. Shen, J. Mohler, J. A. McMahon, A. P. McMahon, *Cell* **1993**, *75*, 1417–1430.
[110] H. Roelink, A. Augsburger, J. Heemskerk, V. Korzh, S. Norlin, A. Ruiz i Altaba, Y. Tanabe, M. laczek, T. Edlund, T. M. Jessell, J. Dodd, *Cell* **1994**, *76*, 761–775.
[111] G. Oliver, C. V. Wright, J. Hardwicke, E. M. De Robertis, *Cell* **1988**, *55*, 1017–1024.
[112] A. Molven, C. V. Wright, R. Bremiller, E. M. De Robertis, C. B. Kimmel, *Development* **1990**, *109*, 279–288.
[113] A. C. Burke, C. E. Nelson, B. A. Morgan, C. Tabin, *Development* **1995**, *121*, 333–346.
[114] F. J. van Eeden, M. Granato, U. Schach, M. Brand, M. Furutani-Seiki, P. Haffter, M. Hammerschmidt, C. P. Heisenberg, Y. J. Jiang, D. A. Kane, R. N. Kelsh, M. C. Mullins, J. Odenthal, R. M. Warga, C. Nüsslein-Volhard, *Development* **1996**, *123*, 255–262.
[115] H. Grandel, B. W. Draper, S. Schulte-Merker, *Development* **2000**, *127*, 4169–4178.
[116] S. L. Johnson, P. Bennett, *Methods Cell Biol.* **1999**, *59*, 301–311.
[117] M. A. Akimenko, M. Mari-Beffa, J. Becerra, J. Geraudie, *Dev. Dyn*. **2003**, *226*, 190–201.

[118] E. Quint, A. Smith, F. Avaron, L. Laforest, J. Miles, W. Gaffield, M. A. Akimenko, *Proc. Natl Acad. Sci. USA* **2002**, *99*, 8713–8718.
[119] J. Geraudie, M. A. Akimenko, M. Smith, in *Cellular and Molecular Basic of Regeneration: From Invertebrates to Humans* (Eds P. Ferretti, J. Geraudie), Wiley, New York, **1998**. pp. 167–185.
[120] L. Laforest, C. W. Brown, G. Poleo, J. Geraudie, M. Tada, M. Ekker, M. A. Akimenko, *Development* **1998**, *125*, 4175–4184.
[121] J. Geraudie, A. Brulfert, M. J. Monnot, P. Ferretti, *J. Exp. Zool*. **1994**, *269*, 12–22.
[122] J. Geraudie, M. J. Monnot, A. Brulfert, P. Ferretti, *Int. J. Dev. Biol*. **1995**, *39*, 373–381.
[123] B. E. Chang, P. Blader, N. Fischer, P. W. Ingham, U. Strahle, *EMBO J.* **1997**, *16*, 3955–3964.
[124] S. Fisher, P. Jagadeeswaran, M. E. Halpern, *Dev. Biol*. **2003**, *264*, 64–76.
[125] S. J. Du, M. Dienhart, *Dev. Dyn*. **2001**, *222*, 655–666.
[126] W. Haschek, C. Rousseaux, *Fundamentals of Toxicologic Pathology*, Academic Press, New York, **1998**.
[127] J. M. Spitsbergen, M. L. Kent, *Toxicol. Pathol*. **2003**, *31*, 62–87.
[128] Y. Haga, T. Takeuchi, T. Seikai, *Fish. Sci*. **2002**, *68*, 560–570.
[129] Y. Haga, T. Suzuki, T. Takeuchi, *Zool. Sci*. **2002**, *19*, 1105–1112.
[130] L. Hoffman, J. Miles, F. Avaron, L. Laforest, M. A. Akimenko, *Int. J. Dev. Biol*. **2002**, *46*, 949–956.
[131] M. W. Vandersea, R. A. McCartrhy, P. Fleming, D. Smith, *Biol. Bull*. **1998**, *194*, 281–296.
[132] A. Tamarin, A. Crawley, J. Lee, C. Tickle, *J. Embryol. Exp. Morphol*. **1984**, *84*, 105–123.
[133] E. H. Goulding, A. M. Jetten, B. D. Abbott, R. M. Pratt, *Reprod. Toxicol*. **1988**, *2*, 91–98.
[134] R. M. Pratt, E. H. Goulding, B. D. Abbott, *J. Craniofac. Genet. Dev. Biol.* **1987**, *7*, 205–217.
[135] C. L. Neumann, C. Nüsslein-Volhard, *Science* **2000**, *289*, 2137–2139.
[136] A. Perz-Edwards, N. L. Hardison, E. Linney, *Dev. Biol*. **2001**, *229*, 89–101.
[137] C. Nüsslein-Volhard, R. Dahm, *Zebrafish*, Oxford University Press, Oxford **2002**.
[138] G. E. Ackermann, B. W. Paw, *Front. Biosci.* **2003**, *8*, d1227–1253.

New Methods

Biomineralization: From Biology to Biotechnology and Medical Application,
Second Edition. Edited by E. Bäuerlein

ISBN: 3-527-31065-7

18 Modern Methods of Investigation in Biomineralization

Matthias Epple

18.1 Introduction

Our knowledge of the elementary processes of biomineralization is continuously increasing. This is partly due to the improved dialog between researchers from the biological field (like biologists and physicians) and researchers from the field of materials (like chemists, physicists, engineers). As the interaction between (bio-)organic compounds and inorganic crystals constitutes the decisive step in the formation of biominerals (which are generally organic/inorganic composites), our knowledge has been substantially advanced by modern physico-chemical methods used to:

- Study the structure of biologically formed biominerals, sometimes on animals in different steps of development.
- Study the growth of inorganic crystals in the presence of artificial or biologically derived substances which influence crystal size, morphology, polymorphic phase, etc.

Of at least equal or maybe even stronger impact are modern genetic and molecular biological methods to elucidate the relationship between the genome and the biominerals formed. However, despite remarkable progress in all these fields, there remains a considerable gap between biology and materials science that needs to be closed in the future.

This chapter is restricted to newer developments in the application of physico-chemical methods in the field of biomineralization. Its aim is to describe these methods in a way that enables non-specialists to understand their potential and to stimulate their application, thereby helping to bridge the gap between biology and materials science. Note that some selection was necessary in the number of methods to be described, given the large number of available techniques. There are, of course, many analytical methods available in modern science and some of them still await their application in the field of biomineralization.

18.2 Infrared (IR) Spectroscopy

IR spectroscopy and its sister technology, Raman spectroscopy, both detect molecular vibrations which are excited by IR radiation. Chemical bonds like O–H, C–H

Biomineralization: From Biology to Biotechnology and Medical Application, Second Edition. Edited by E. Bäuerlein

ISBN: 3-527-31065-7

or C=O are found in distinct positions in the IR spectrum. In the case of solid crystals [including inorganic ones like $CaCO_3$ or $Ca_{10}(PO_4)_6(OH)_2$], characteristic lattice vibrations (phonons) are additionally excited. These are often quite characteristic for the polymorphic phase and can be used to distinguish between phases, e.g. calcite from aragonite or vaterite. Weiss et al. have reported a study on molluscean larval shells with IR and Raman spectroscopy where they could show how the crystalline part of the shell changed with age. Amorphous calcium carbonate (ACC) was shown to be a precursor for aragonite, the final biomineral in the shells of the marine bivalves *Mercenaria mercenaria* and *Crassostrea gigas* [1].

18.3 Scanning Probe Microscopy

Since the invention of scanning tunneling microscopy (STM) by Binnig and Rohrer (Nobel prize 1986) [2], scanning probe microscopy has evolved into almost a routine method in the chemical and physical laboratory. The principle of these methods is always the same – a very sharp tip is moved over a surface, and the force between the tip and surface is detected. With STM, the electrical current between the tip and surface is measured to control the distance between the tip and surface. An electrically conducting substrate like a metal or semiconductor is needed. This makes the method usually not useful for biominerals. Of more importance is scanning force microscopy [''atomic force microscopy'' (AFM)]. In this case, a sharp tip is moved over the surface and the deflection by the surface roughness is measured. This method does not require a conducting surface and can also applied in solution.

An application for biomineralization research is the *in situ* study of crystal growth processes (Fig. 18.1). A defined crystal surface is brought into contact with an oversaturated solution of the same material. The crystal will grow into the solution, usually by a step-wise growth process (layer per layer or in a spiral that emerges from a screw dislocation). Thus, crystallization kinetics and mechanisms can be studied *in situ* with almost atomic resolution if the tip is moved continuously over the same area of the surface. The crystallization behavior of pure substances (like $CaCO_3$) can therefore be studied and compared to that in the presence of additives (like amino acids or proteins) that adsorb to the surface. It is well known that such adsorbing bio-organic additives play a prominent role in biomineralization by controlling crystal growth [3, 4]. Sometimes, crystallization experiments are evaluated *ex situ* because it is not possible to monitor the surface during crystal growth at high resolution. In a fundamental experiment, Teng et al. studied the growth of calcite with and without aspartic acid, and observed the effect of the additive on the crystal growth [5].

Scanning near-field optical microscopy (SNOM) is a special technique that is able to overcome the classical Abbé diffraction limit of about one half wavelength by light scattering from a sharp tip. A resolution of about 10 nm was possible for visible light. It can be expected that the study of biomineralized surfaces will strongly benefit from this technique [6, 7].

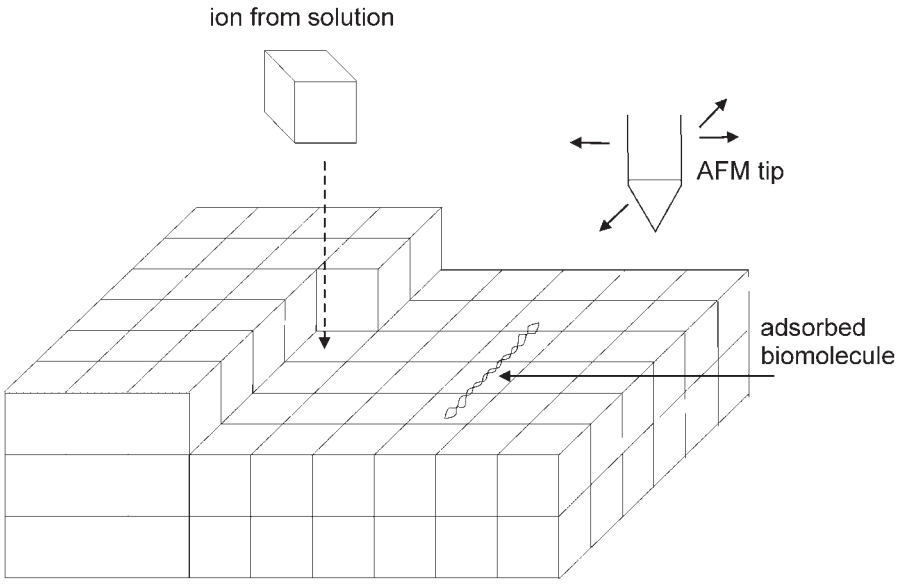

Figure 18.1 Schematic setup of an *in situ* scanning force microscopy experiment for crystallization. The ions of a growing crystal are schematically depicted as cubes. Crystal growth occurs when an ion from solution attaches to the surface and finds its proper place. Biomolecules (like proteins) may adsorb on the surface and thereby prevent the crystal growth process in certain directions. This can be followed *in situ* with AFM where a fine tip is continuously moved over the surface and monitors the surface roughness.

18.4 Synchrotron Radiation Sources

Synchrotron radiation sources have been routinely available for users from all fields of science for about 30 years. These modern light sources were derived from storage rings and accelerators which were originally devoted to high-energy physics, i.e. to the study of the properties of elementary particles at high energy. Such particles are accelerated to a speed near that of light. If such particles are kept in a non-linear pathway (like in a storage ring), the highly intense synchrotron radiation is tangentially emitted (Fig. 18.2). This is electromagnetic radiation with a continuous spectrum, ranging from low energies (like IR, ultraviolet) to the X-ray region (Fig. 18.3). Its main advantage over laboratory sources (like X-ray tubes) is the much higher intensity (equal to the number of photons) – several orders of magnitude more than conventional laboratory sources (Fig. 18.4). In addition, the synchrotron radiation is emitted in the plane of the ring with small divergence, resulting in better optics at the sample. For research with biominerals, it is the X-rays from synchrotron sources that are of the main importance. They are used for diffraction experiments (powders and single crystals), for X-ray absorption spectroscopy [X-ray absorption near edge structure (XANES) and extended X-ray absorption fine struc-

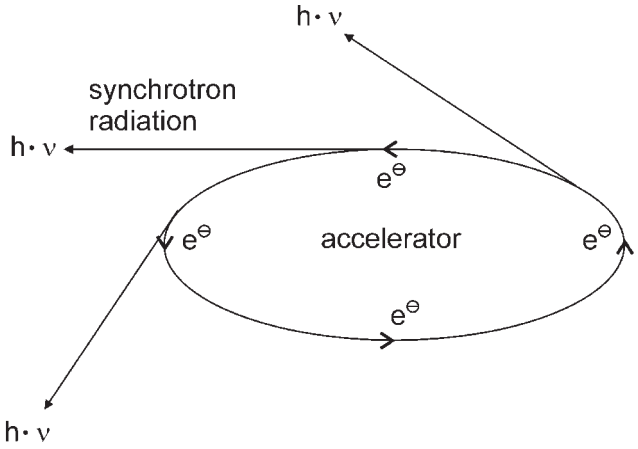

Figure 18.2 Principal setup of a synchrotron radiation source (storage ring or accelerator). When elementary particles are forced on a curved trajectory with a speed near that of the light, they emit very intense synchrotron radiation tangentially and in the plane of the ring. It is therefore highly focused.

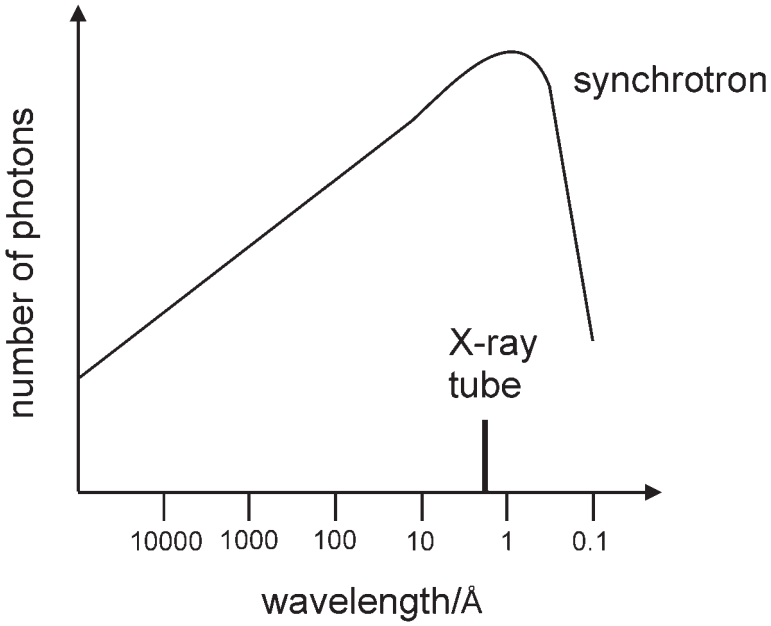

Figure 18.3 The continuous energy spectrum of synchrotron radiation covers a wide range of radiation, from the IR over visible and UV to hard X-rays. This is in contrast to conventional X-ray tubes, which usually emit X-radiation of only one wavelength (the characteristic X-radiation, like Cu K_α). Furthermore the intensity (the number of photons with a given wavelength) is much higher for synchrotron radiation.

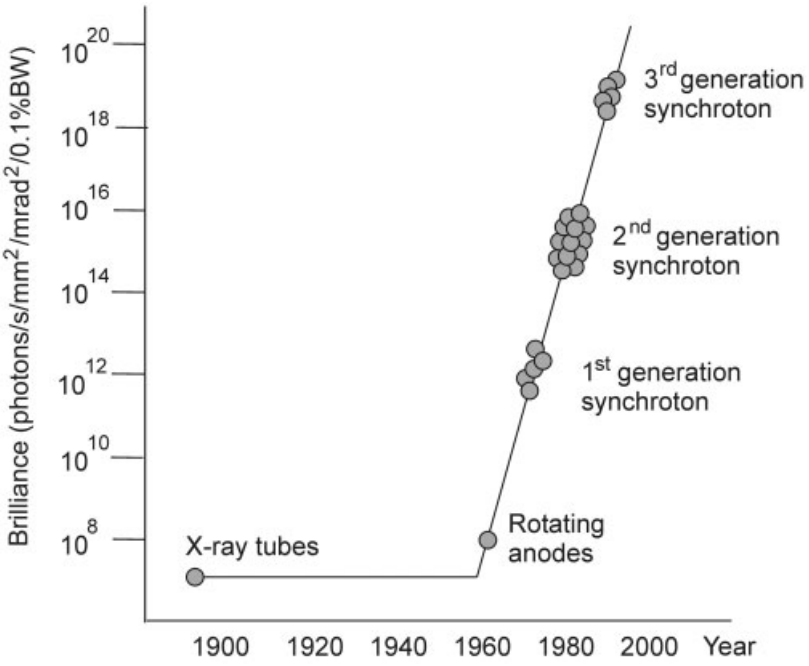

Figure 18.4 Brilliance (a measure for the number of photons on a sample) as a function of time. Note the extreme increase in brilliance with the introduction of synchrotron sources and also the logarithmic scale for brilliance.

ture (EXAFS)] and for small-angle X-ray scattering (SAXS). The much higher intensity gives a better signal-to-noise ratio that can be used to improve the data quality or to lower the detection limit (e.g. for phase analysis).

18.5 Diffraction Methods

Diffraction methods rely on the ordered arrangement of atoms in a crystal. If there is a long-range order of more than about 5 nm, diffraction peaks can be observed when a sample is irradiated with X-rays or neutrons. Due to the much easier accessibility, X-ray diffraction is much more prominent than neutron diffraction [8, 9]. If a transmission electron microscope is available, there is also the possibility for electron diffraction. In general, diffraction methods can be applied to powders and to single crystals. We will first discuss powder diffraction [10, 11].

In biomineralization research, X-ray powder diffraction is certainly the most important of these three methods, with electron diffraction being second in importance. X-ray diffractometers are usually available in chemical or crystallographic

laboratories and can be used for the quick identification of crystalline biominerals. The material must be thoroughly ground to particle sizes of the order of micrometers and only a few milligrams of sample are necessary. It is a destruction-free method. A powder diffractogram consists of a number of intensity maxima (peaks or reflections) at certain diffraction angles (usually given in °2Θ). We can derive the following information from such a diffraction pattern:

1. The set of peak positions depends on the crystal structure of the biomineral and can be used for identification. Thousands of reference compounds are listed in the Joint Committee on Powder Diffraction Standards (JCPDS) database that can be used to identify an unknown compound. The diffraction pattern can serve as a unique "fingerprint" for each crystal structure.
2. The intensity of the diffraction peaks depends on the amount of biomineral present in a mixture and can be used for quantification in a mixture. The Rietveld method can be used to compute such mass fractions [12].
3. The width of the diffraction peaks [usually given as full width at half maximum (FWHM)] can be used to estimate the particle size (Fig. 18.5). The Scherrer equation can serve as a means for such a rough estimate:

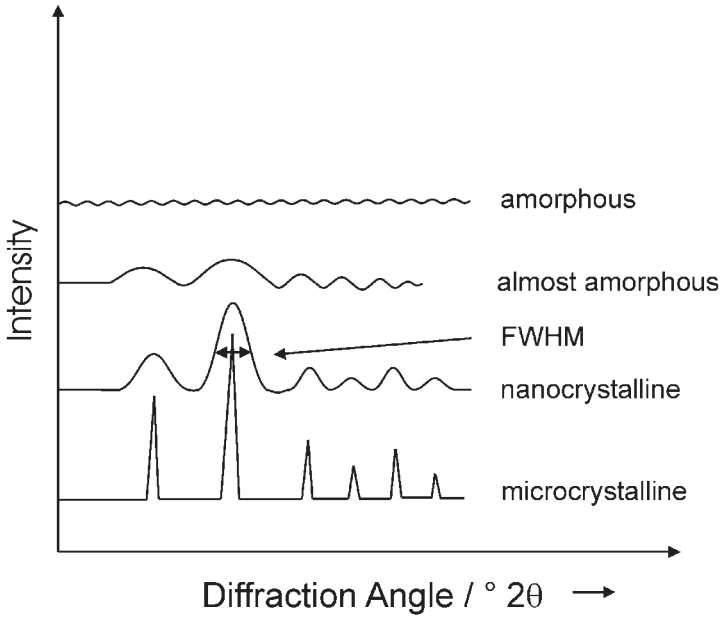

Figure 18.5 Schematic picture of the change of X-ray diffraction peaks as a function of sample crystallinity. Microcrystalline samples ("well-crystalline") give sharp diffraction peaks and nanocrystalline samples give broad diffraction peaks. X-ray diffraction cannot be applied to amorphous samples because no diffraction peaks are present. The gradual increase of the peak width (as FWHM) with decreasing particle size can be used to estimate the crystallite size in a semi-quantitative way.

$$\beta_{1/2} = (\mathrm{K} \cdot \lambda \cdot 57.3)/(D \cdot \cos\Theta) \quad (1)$$

Here, $\beta_{1/2}$ is the peak width (as FWHM) in °2Θ, K is a constant that is usually set to 1, λ is the X-ray wavelength in Å, D is the average domain size in Å (roughly the crystallite size) and Θ is the diffraction angle of the corresponding reflex. This equation gives an estimate of the crystallite size. It should be noted, however, that structural disorder and strain phenomena, e.g. caused by carbonate substitution in hydroxyapatite, can also lead to peak-broadening effects. For anisotropic crystals (like the platelet-like bone mineral crystals), the Scherrer equation can be used to determine the anisotropic crystallite dimensions when diffraction peaks belonging to different crystallographic planes, like (100), are analyzed individually (see [13] for a synchrotron study on bone mineral).

It is important to note that amorphous substances (like glass-like solids and solids without long-range order) cannot be studied by diffraction methods. They often give rise to a broad, unspecific diffraction peak at low angles (at about 10–20°2Θ). However, this cannot be used for identification. Essentially, powder diffraction is ''blind'' for all amorphous compounds. This means that a proportion of an amorphous biomineral (like ACC besides calcite) is simply invisible and may easily escape the researcher's investigation.

There is a smooth transition from well-crystalline compounds (with sharp diffraction peaks) over nanocrystalline compounds (with broad diffraction peaks) to amorphous compounds (with no diffraction peaks). The initially sharp peaks become broader and smaller until they vanish in the background (Fig. 18.5).

Electron diffraction is possible on very small crystals. Plate et al. have thoroughly investigated bone mineral and have shown the ultrastructure of calcium phosphate within matrix vesicles from osteoblasts [14–16].

Single-crystal diffraction gives the full crystal structure, i.e. the positions of all atoms within the elementary cell. Diffraction on biogenic single crystals can be applied if they are available in sufficient size and quality. Many biominerals are polycrystalline and therefore only powder diffraction is applicable. However, two examples will be given where a single crystalline biomaterial was successfully investigated.

Aizenberg et al. have studied single crystalline sea urchin spines by synchrotron radiation [17]. By careful analysis of the diffraction peak widths they were able to derive the position of the macromolecules (proteins) in these single crystals. They could show that they were incorporated to absorb potential cracks in this material which easily breaks along the crystallographic (104) plane.

We have studied single crystalline statoliths of deep-sea medusae. By analysis with synchrotron radiation it could be shown that they consist of calcium sulfate hemihydrate ($CaSO_4 \cdot 0.5H_2O$) instead of the expected calcium sulfate dihydrate (gypsum; $CaSO_4 \cdot 2H_2O$) [18].

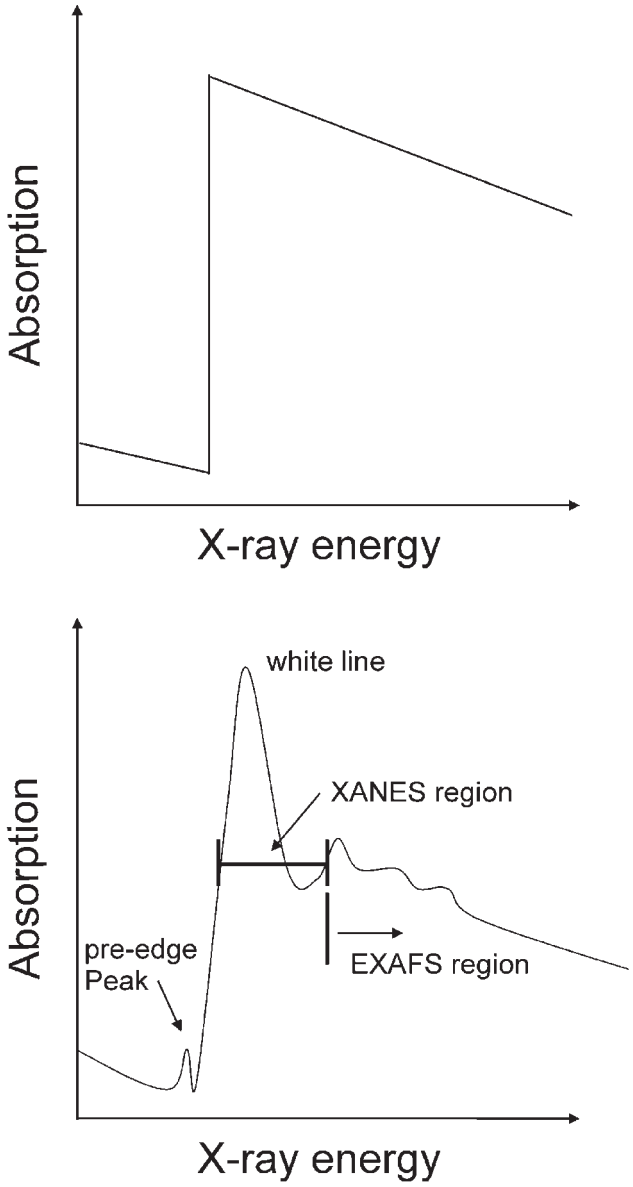

Figure 18.6 The principle of X-ray absorption spectroscopy. X-rays are absorbed by matter with decreasing absorption coefficient when the X-ray energy increases. A discontinuity occurs when an absorption edge is reached, i.e. when the energy of the incoming photon is sufficient to ionize the atom and to create a photoelectron. For single atoms, the absorption edge is simply a step (top). If the atom has neighbors (like in a solid, liquid or diatomic gas molecule), there is a fine structure (bottom). This is due to electronic excitation into bound states of the electron at high energy (pre-edge peak and white line; also possible for isolated atoms) and to scattering of the photoelectron at neighboring atoms. The XANES region and the EXAFS region can be distinguished (see text). Structural information is mainly available from the EXAFS region.

18.6 X-ray Absorption Spectroscopy (EXAFS)

A comparatively new method in biomineralization is X-ray absorption spectroscopy, which has been routinely available at synchrotron sources since the 1980s [19, 20]. Basically, it involves measuring the absorption spectrum of a compound in the X-ray region, i.e. the absorption of X-rays as a function of the wavelength. When an absorption edge is reached, the absorption coefficient increases sharply, because the X-rays now have the necessary energy to create a photoelectron, i.e. to ionize the atom. For isolated atoms (like gaseous noble gases), the photoelectron is simply emitted and there is no fine structure of the absorption spectrum (Fig. 18.6).

In all other cases, a special effect occurs – the emitted photoelectron is partially backscattered by the neighboring atoms (Fig. 18.7). This leads to oscillations in the spectrum after the absorption edge, the so-called EXAFS. Their origin can only be understood in the context of quantum mechanics. Both the outgoing photoelectron as well as the backscattered photoelectron behave as waves in terms of the wave–particle dualism model. These two waves can interfere constructively or destructively. A constructive interference means a high probability of the electron being outside the absorbing atom, i.e. a high rate of ionization, and consequently a high absorption coefficient. On the other hand, a destructive interference means a low absorption coefficient (Fig. 18.8).

It is clear that the interference between the outgoing and the incoming wave depends primarily on the distance between the absorbing (ionized) atom and the backscattering atom, and on the wavelength of the photoelectron. The wavelength is given by the energy of the incoming X-ray photon minus the binding energy of the photoelectron (this is the energy at the absorption edge). Furthermore, it turns out that the nature of the neighboring atom and the number of neighboring atoms influence the amplitude of the oscillations. All these parameters influence the fine structure of the absorption spectrum.

Consequently, it is possible to extract all this information by thorough analysis of the EXAFS spectrum, i.e. the oscillations. Indeed, it is possible to extract information about the environment of the absorbing atom on an Ångstrom scale, i.e. usually up to 5–6 Å distance. A Fourier transformation of the absorption spectrum gives a kind of radial distribution function with maxima at the distance of neighboring atoms. Careful analysis of the phase and amplitude of the spectrum yields:

- The kind of neighbors (like O, Ca, etc.).
- The number of neighbors in one shell (coordination number).
- The distance between absorbing atom and neighbors (like a bond length).
- Information on the degree of static and dynamic disorder in the system (like vibrations).
- Angles between the absorber and two neighbors.

The main advantage is the possibility to study non-crystalline samples. If single crystals are available, a good X-ray structure analysis gives all the above data with very high accuracy. However, if the samples are nanocrystalline or X-ray amor-

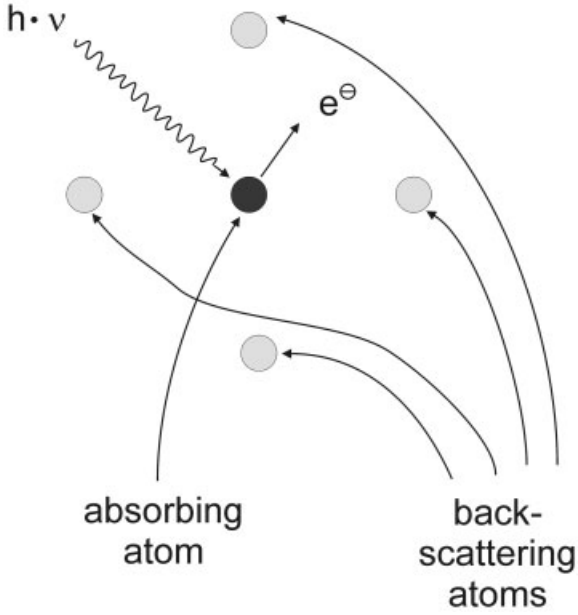

Figure 18.7 The irradiation of an atom with a photon of sufficient energy creates a photoelectron. This leaves the absorbing atom and interacts with neighboring atoms (''backscattering atoms'').

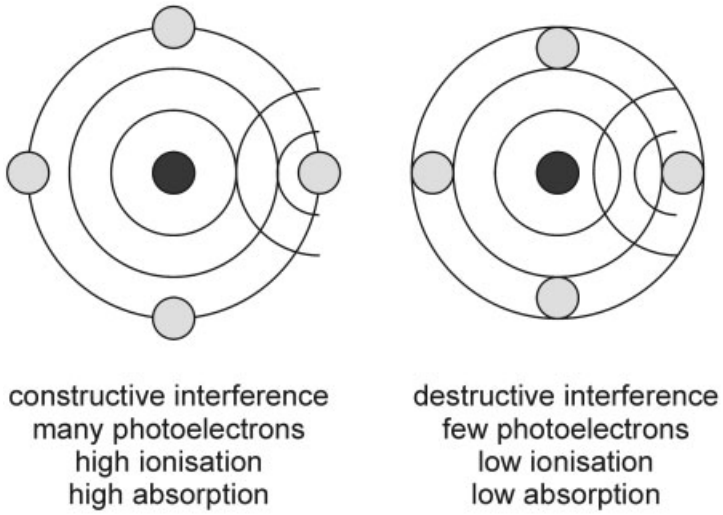

Figure 18.8 The interaction of an outgoing photoelectron with neighboring atoms. Quantum mechanically, the photoelectron is a wave originating from the absorbing atom. Its interference with neighboring atoms leads to backscattering, i.e. to waves returning to the absorbing atom. Two extreme cases can be distinguished: constructive interference (left) leads to high absorption and destructive interference (right) leads to low absorption. Between these two extremes, there is a gradual transition. As the degree of interference depends on the wavelength of the photoelectron, we observe oscillations in the EXAFS spectrum.

phous, EXAFS can be a very useful tool to derive structural information. If absorption spectra from different elements being present in a sample are obtained, each yields a radial distribution function and structural information around the corresponding element. An unfortunate limitation is the fact that only elements which are heavier than phosphorous, sulfur and chlorine can be routinely studied. This means that the most important elements, i.e. carbon, nitrogen and oxygen, are not susceptible to EXAFS experiments. However, two important elements in biomineralization, i.e. calcium and iron, are well suited. It is easily possible to distinguish, for example, the polymorphs calcite, aragonite, and vaterite, and also to identify ACC.

Between the edge and the EXAFS region there is the so-called XANES region. In this region, the kinetic energy of the photoelectron is very small (due to the small difference between the energy of the incoming photoelectron and the binding energy at the edge). This leads to multiple scattering phenomena, i.e. the outgoing photoelectron is backscattered not only once (like in EXAFS), but multiple times. The underlying theory is much more complicated and usually XANES spectra are used as fingerprints to distinguish different coordination geometries (like tetrahedral versus octahedral) [20].

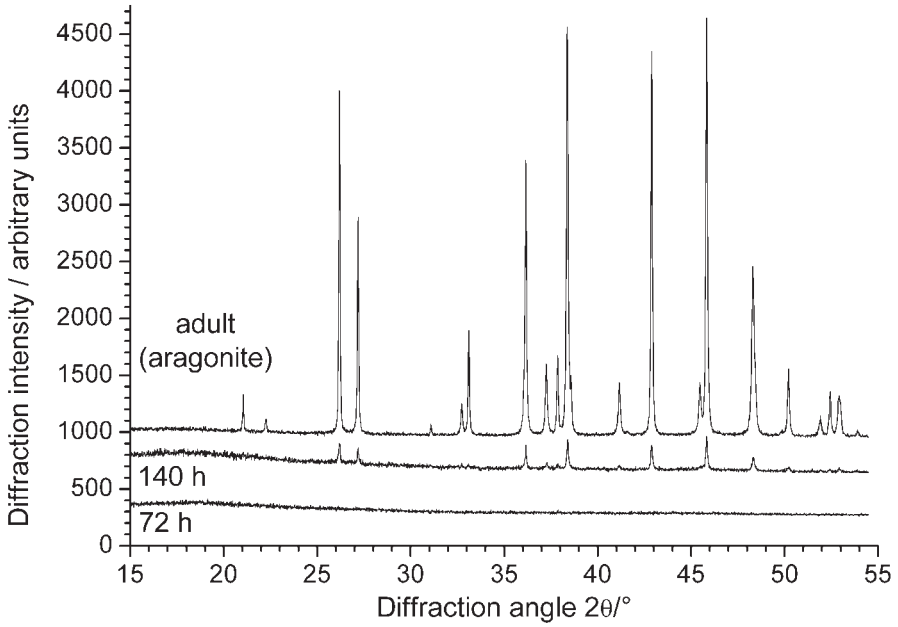

Figure 18.9 Synchrotron X-ray powder diffraction data of integral embryos (72 and 140 h; shortly before hatching) and of the shell of adult freshwater snails *B. glabrata* (X-ray wavelength 1.5418 Å). Only diffraction peaks of aragonite ($CaCO_3$) can be observed in adult snails and in 140-h embryos. The narrow diffraction peaks in both cases show that the shell is well-crystalline in both cases. The smaller intensity with the 140-h embryos shows that there is a lot of organic material present in the sample (as is to be expected for integral embryos). In embryos at 72 h there is no detectable crystalline phase, although histologic data clearly shows the presence of a shell.

18.7 Two Examples for the Combined use of X-ray Diffraction and X-ray Absorption Spectroscopy (at Synchrotron Radiation Sources)

18.7.1 Development of the Shells in Embryos of *Biomphalaria glabrata*

We have followed the development of the shell in embryos of the freshwater snail *B. glabrata*. We combined both high-resolution X-ray diffraction data and X-ray absorption spectroscopy at the calcium K-edge. The first detects only crystalline phases (Fig. 18.9) and the second also detects amorphous phases containing calcium (Figs 18.10 and 18.11). The work was supplemented by electron microscopy data on

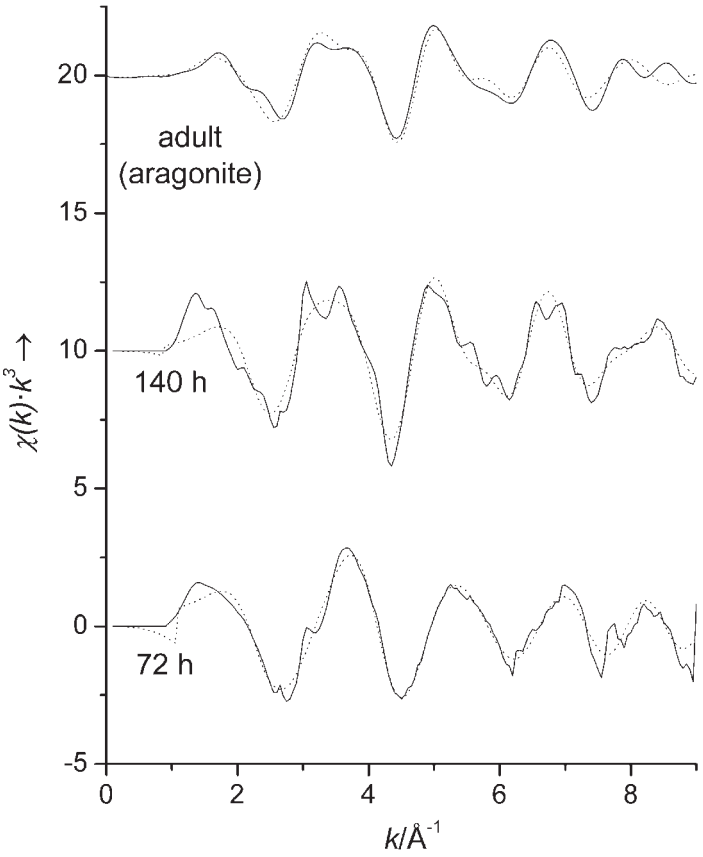

Figure 18.10 Primary Ca K-edge EXAFS data of integral embryos (72 and 140 h) and the shell of *B. glabrata*. The EXAFS oscillations are comparable in the three cases and prove the presence of calcium in a structured environment. Experimental data are shown as solid lines and calculated data are shown as dotted lines.

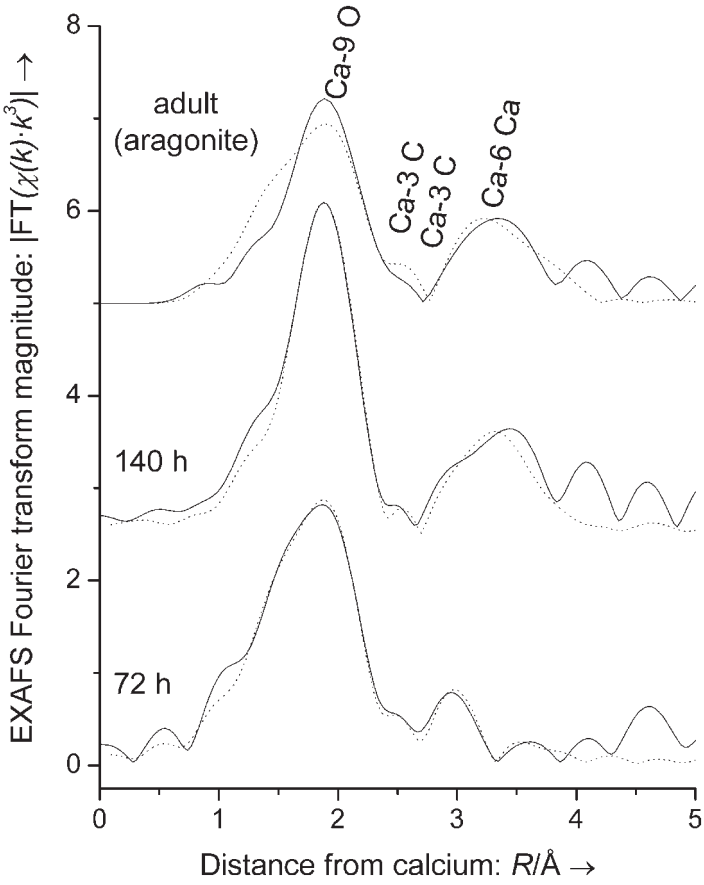

Figure 18.11 Fourier transform Ca K-edge EXAFS data of integral embryos (72 and 140 h) and the shell of *B. glabrata*. Radial distribution functions around calcium are obtained. Groups of atoms ("shells") around calcium appear as maxima. They can be quantitatively identified by fits of the experimental data (solid line) to theoretical data (dotted line). The data are very similar in the three cases, demonstrating that an aragonite-like environment of calcium is present even in the X-ray amorphous sample (72-h embryos).

the forming shell [21, 22]. It could be shown that the first crystalline phase detectable was aragonite (140 h), as in the adult snails. However, in the X-ray amorphous shell of embryos of 72 h, a short-range order around calcium was found which was very similar to that of aragonite. We may therefore conclude that the structure of the final crystalline biomineral (aragonite) is already "imprinted" into the structure of its amorphous precursor. The metastable modification vaterite was not detected. This might have been proposed according to Ostwald's step rule which states that the least-stable polymorphs are formed first upon crystallization.

In adult snails, vaterite could be quantitatively identified by high-resolution,

high-intensity synchrotron X-ray diffraction as a small impurity (0–0.6 wt %) in the shell, possible resulting from a kind of "pathological" mineralization in the shell [21].

18.7.2 Intermediate Storage of ACC in *Porcellio scaber*

An additional study was carried out on amorphous deposits of calcium carbonate on the belly of the crustacea *P. scaber* (woodlice). These animals decalcify their shell (cuticle) in order to save calcium before it is shed off. This calcium is stored in micrometer-sized spheres on the belly while the new cuticle is formed and then re-mineralized. These deposits are fully X-ray amorphous (Fig. 18.12), but contain a fine structure that can be identified as ACC (Fig. 18.13).

Most interestingly, there are different kinds of ACC if such microstructural methods are applied (Table 18.1). This was also studied and discussed extensively by Addadi, Weiner, Raz et al. [1, 23–27].

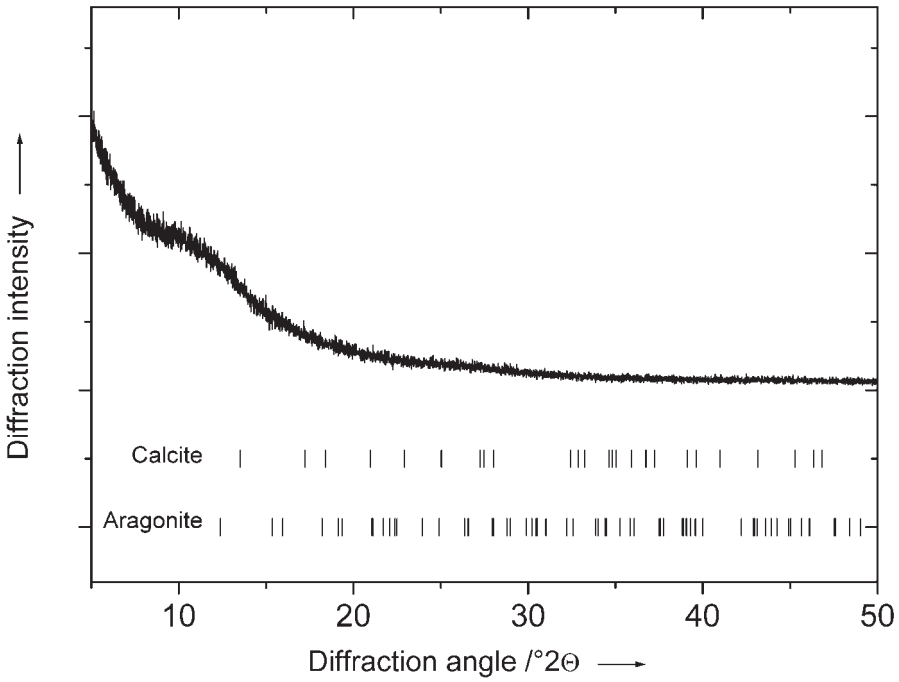

Figure 18.12 Synchrotron X-ray powder diffraction data of sternal deposits of calcium carbonate in *P. scaber* (X-ray wavelength 0.90826 Å). The material is fully X-ray amorphous. For comparison, the expected peak positions of the calcium carbonate polymorphs calcite and aragonite are indicated.

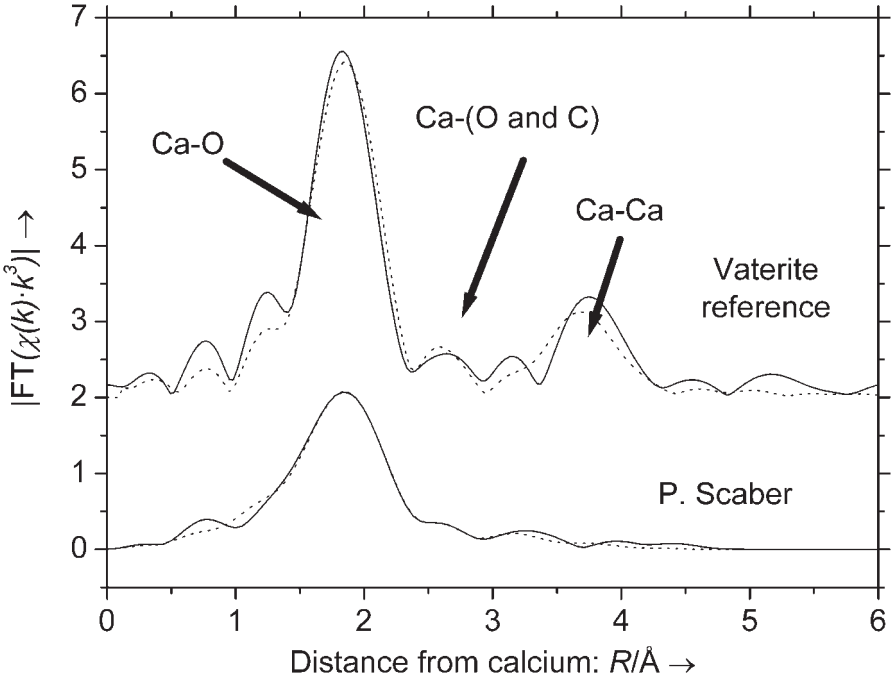

Figure 18.13 Fourier transform Ca K-edge EXAFS data of sternal deposits of ACC in *P. scaber* (bottom) and vaterite (top). There is a first-neighbor peak for the amorphous carbonate which indicates an ordered environment of calcium on the Ångstrom scale. There is, however, less order than in the crystalline vaterite when higher shells are considered.

18.8 X-ray Microtomography (*μ*-CT)

This method has a long tradition in clinical medicine where patients' tissues are studied by X-rays in order to detect bone fractures, etc. Its basis is the recording of a number of two-dimensional transmission pictures (showing weakly and strongly absorbing regions; like medical X-ray projections). If a number of such two-dimensional transmission pictures is recorded, they can be assembled by suitable computer algorithms to create a three-dimensional representation of the sample, i.e. to achieve a transition from two-dimensional "pixels" to three-dimensional "voxels". This is a standard technique in medical imaging; however, the advent of synchrotron radiation sources has strongly enhanced the potential of this method [30–34].

This is due to the very high intensity (giving a good statistics at the sample), the monochromatized X-radiation from synchrotron sources (leading to fewer artifacts) and the possibility to tune the X-ray wavelength to a desired value. If these effects are exploited, one can, for example, work close to an absorption edge (see Fig.

Table 18.1 Results reported in the literature for EXAFS spectra of X-ray amorphour calcium carbonate (ACC) found in biology, together with crystalline phases

Sample	Shell distance by EXAFS in Å			
	Shell 1: Ca–O	Shell 2: Ca–C or Ca–O	Shell 3: Ca–C or Ca–O	Shell 4: Ca–6 Ca
ACC in carapaces of *Homarus american* [26]	2.27	–[a]	3.47	3.79
ACC in plant cystoliths of *Ficus microcarpa* [26]	2.31	–[a]	3.48	3.79
Calcite [28]	2.34	3.30	3.64	4.05
Calcite [29]	2.35	3.23	3.48	3.98
ACC in plant cystoliths of *Ficus retusa* [29]	2.36	3.22	3.39	4.06
Calcite [23]	2.37	3.21	3.52	4.11
Monohydrocalcite [23]	2.37	3.03	3.36	–[a]
Vaterite [28]	2.37	3.09	–[a]	4.24
ACC in spicules of *Pyura Pachydermatina* [23]	2.37	3.03	3.36	–[a]
ACC in sternal deposits of *P. scaber* [28]	2.38	3.00	3.72	(3.89)
ACC in larval shells of *B. glabrata* [21, 22]	2.44	–[a]	–[a]	3.92
Aragonite [28]	2.47	2.98	3.26	3.94

The entries are sorted with ascending distance of the first coordination shell of oxygen. The second, third and fourth shells in the sternal deposits of *P. scaber* are weak and of poor significance.
[a] Shell was not included in fit.

18.6), achieving a maximum contrast or use photons of very high energy which are able to penetrate an optically very dense tissue (like bone or teeth). Figure 18.14 shows a typical picture of a natural bone sample (with the soft tissue and bone marrow having been removed). The maximum resolution of the method is about 1 μm^3 voxel size. It may be predicted that this destruction-free method will find increasing application in the study of biominerals in the future, e.g. to study ''hidden'' structures, like the inside of an egg or a snail shell.

18.9 Micromechanical Experiments

A new approach that combines mechanical studies with biomineralization was recently presented by Hamm et al. [35]. They have crushed different species of diatomea with micrometer-sized glass needles and measured the necessary force to destroy the silica shell (frustrules). Therefore, mechanical properties could be ob-

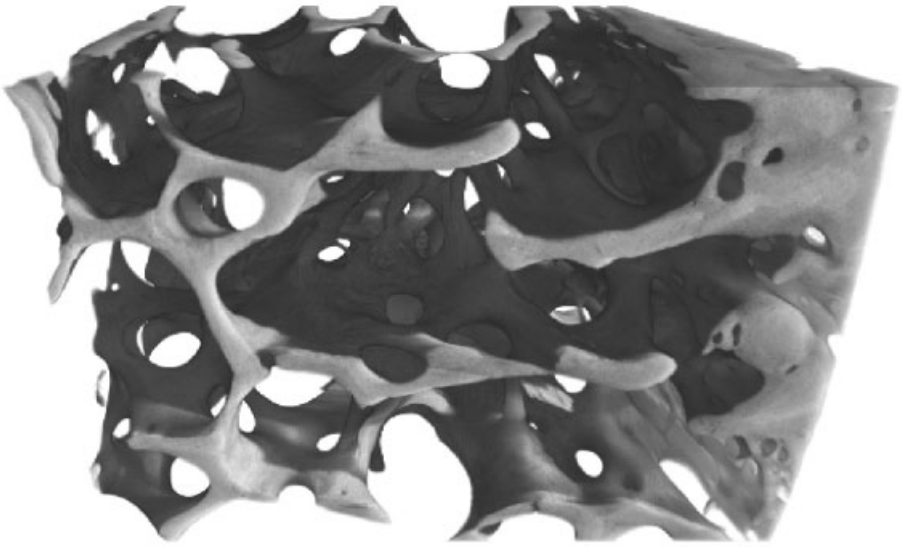

Figure 18.14 Synchrotron X-ray μ-CT of a bone sample, showing the transition from cortical (dense) bone to spongy (porous) bone from right to left.

tained. In addition, the stress distribution in the shell was calculated by finite element methods. Compared to the small size of the diatoms, very high forces were required to break the shells and it was concluded that the shells were developed for mechanical protection of the cells. Diatoms are prey to some predators in the ocean, and therefore this represents a kind of "arms race" between diatoms and their predators. Figure 18.15 shows the principal setup of this micromechanical method.

18.10 Solid-state Nuclear Magnetic Resonance (NMR) Spectroscopy

Classically, NMR spectroscopy is carried out in solution. It is now a standard tool in chemistry. However, the development of new techniques in the last two decades has made solid-state NMR spectroscopy a tool which is almost as versatile as the classical method in solution. Ground samples are brought into rapidly spinning sample containers ["magic angle spinning" (MAS)]. The NMR-active elements which are most important for biomineralization are ^{1}H (possible only in special cases), ^{13}C (for carbonates), ^{29}Si (for silica), and ^{31}P (for calcium phosphates). Two examples will be presented here. Cho et al. studied bone samples by a two-dimensional NMR technique sensitive for the protons in bone mineral only. Most surprisingly, only 20 % of the amount expected of stoichiometric hydroxyapatite,

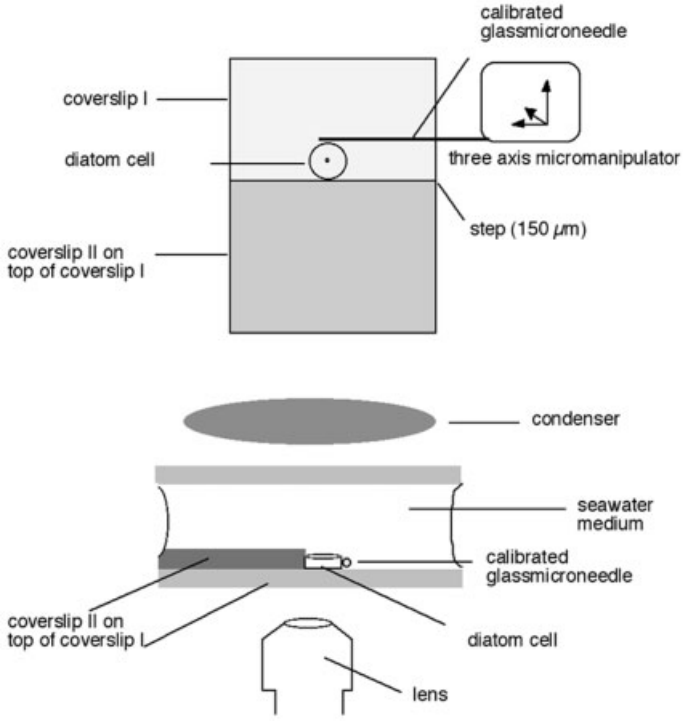

Figure 18.15 Schematic picture of the micromechanical setup to perform crash tests on diatomea. Left: View from above; right: side view.

$Ca_5(PO_4)_3OH$, were found [36]. Diatom shells were studied by Kinrade et al. and Bertermann et al., giving insight into the nature of the silicon coordination inside the shells [37, 38].

18.11 Conclusions

Biomineralization research is currently progressing in two main directions – the application of modern genetic methods and the structural investigation of biomineralized tissues. There is still a large gap between both approaches; however, with the advent of new methods in both areas, the future may finally see a merger of the two areas of ''bioscience'' and ''materials science''. The potential of physicochemical methods which are only little or not at all applied to biominerals is definitely high, but their advancement will require the will and ability of researchers from both areas to understand each other's questions and answers. This chapter was written to stimulate the interest of ''biological community'' in such physicochemical methods.

References

[1] I. M. Weiss, N. Tuross, L. Addadi, S. Weiner, *J. Exp. Zool.* **2002**, *293*, 478.
[2] G. Binnig, H. Rohrer, *Angew. Chem.* **1987**, *99*, 622.
[3] S. Albeck, S. Weiner, L. Addadi, *Chem. Eur. J.* **1996**, *2*, 278.
[4] G. Falini, S. Albeck, S. Weiner, L. Addadi, *Science* **1996**, *271*, 67.
[5] H. H. Teng, P. M. Dove, C. A. Orme, J. J. de Yoreo, *Science* **1998**, *282*, 724.
[6] R. Hillenbrand, T. Taubner, F. Keilmann, *Nature* **2002**, *418*, 159.
[7] F. Keilmann, R. Hillenbrand, *Phil. Trans. R. Soc. Lond. A* **2004**, *362*, 787.
[8] A. K. Cheetham, P. Day, *Solid State Chemistry: Techniques*, Oxford University Press, Oxford, **1987**.
[9] A. K. Cheetham, A. P. Wilkinson, *Angew. Chem. Int. Ed. Engl.* **1992**, *31*, 1557.
[10] H. P. Klug, L. E. Alexander, *X-ray Diffraction Procedures for Polycrystalline and Amorphous Materials*, Wiley-Interscience, New York, **1974**.
[11] D. L. Bish, J. E. Post, *Rev. Mineral.* **1989**, *20*, 369.
[12] R. A. Young, *Monogr. Crystallogr.* **1993**, *5*, 298.
[13] F. Peters, K. Schwarz, M. Epple, *Thermochim. Acta* **2000**, *361*, 131.
[14] U. Plate, S. Arnold, L. Reimer, H. J. Höhling, A. Boyde, *Cell Tissue Res.* **1994**, *278*, 543.
[15] U. Plate, T. Kotz, H. P. Wiesmann, U. Stratmann, U. Joos, H. J. Höhling, *J. Microsc.* **1996**, *183*, 102.
[16] U. Stratmann, K. Schaarschmidt, H. P. Wiesmann, U. Plate, H. J. Höhling, *Cell Tissue Res.* **1996**, *284*, 223.
[17] J. Aizenberg, J. Hanson, T. F. Koetzle, S. Weiner, L. Addadi, *J. Am. Chem. Soc.* **1997**, *119*, 881.
[18] H. Tiemann, I. Sötje, G. Jarms, C. Paulmann, M. Epple, B. Hasse, *J. Chem. Soc. Dalton Trans.* **2002**, 1266.
[19] B. K. Teo, *EXAFS: Basic Principles and Data Analysis, Vol. 9*, Springer, Berlin, **1986**.
[20] H. Bertagnolli, T. S. Ertel, *Angew. Chem. Int. Ed. Engl.* **1994**, *33*, 45.
[21] B. Hasse, H. Ehrenberg, J. C. Marxen, W. Becker, M. Epple, *Chem. Eur. J.* **2000**, *6*, 3679.
[22] J. C. Marxen, W. Becker, D. Finke, B. Hasse, M. Epple, *J. Molluscan Studies* **2003**, *69*, 113.
[23] Y. Levi-Kalisman, S. Raz, S. Weiner, L. Addadi, I. Sagi, *J. Chem. Soc. Dalton Trans.* **2000**, 3977–3982.
[24] S. Raz, S. Weiner, L. Addadi, *Adv. Mater.* **2000**, *12*, 38.
[25] J. Aizenberg, G. Lambert, S. Weiner, L. Addadi, *J. Am. Chem. Soc.* **2002**, *124*, 32.
[26] Y. Levi-Kalisman, S. Raz, S. Weiner, L. Addadi, I. Sagi, *Adv. Funct. Mater.* **2002**, *12*, 43.
[27] L. Addadi, S. Raz, S. Weiner, *Adv. Mater.* **2003**, *15*, 959.
[28] A. Becker, U. Bismayer, M. Epple, H. Fabritius, B. Hasse, J. Shi, A. Ziegler, *J. Chem. Soc. Dalton Trans.* **2003**, 551.
[29] M. G. Taylor, K. Simkiss, G. N. Greaves, M. Okazaki, S. Mann, *Proc. R. Soc. Lond. B* **1993**, *252*, 75.
[30] F. Beckmann, U. Bonse, T. Biermann, *Proc. SPIE* **1999**, *3772*, 179.
[31] R. J. Fajardo, T. M. Ryan, J. Kappelman, *Am. J. Phys. Anthropol.* **2002**, *118*, 1.
[32] P. Weiss, L. Obadia, D. Magne, X. Bourges, C. Rau, T. Weitkamp, I. Khairoun, J. M. Bouler, D. Chappard, O. Gauthier, G. Daculsi, *Biomaterials* **2003**, *24*, 4591.
[33] M. Itoh, A. Shimazu, I. Hirata, Y. Yioshida, H. Shintani, M. Okazaki, *Biomaterials* **2004**, *25*, 2577.
[34] D. Tadic, F. Beckmann, T. Donath, M. Epple, *Mat.-wiss. u. Werkstofftech.* **2004**, *35*, 240–244.
[35] C. E. Hamm, R. Merkel, O. Springer, P. Jurkoj, C. Maier, K. Prechtel, V. Smetacek, *Nature* **2003**, *421*, 841.
[36] G. Cho, Y. Wu, J. L. Ackermann, *Science* **2003**, *300*, 1123.
[37] S. D. Kinrade, A. M. E. Gillson, C. T. G. Knight, *J. Chem. Soc. Dalton Trans.* **2002**, 307.
[38] R. Bertermann, N. Kröger, R. Tacke, *Anal. Bioanal. Chem.* **2003**, *375*, 630.

Index

Biomineralization: From Biology to Biotechnology and Medical Application, Second Edition. Edited by E. Bäuerlein

ISBN: 3-527-31065-7